Understanding the Origins of Photoexcited XUV Spectra

Thesis by
ISABEL MCMILLAN KLEIN

In Partial Fulfillment of the Requirements for
the Degree of
Doctor of Philosophy

CALIFORNIA INSTITUTE OF TECHNOLOGY
Pasadena, California

2023
Defended December 2, 2022

Isabel McMillan Klein
ORCID: 0000-00016134-6732

ACKNOWLEDGEMENTS

I undoubtedly would not be where I am today without the support, assistance, and push of a tremendous number of people. While these notes are by no means all encompassing, there are some individuals who bear specific acknowledgement.

First and foremost, I will be forever grateful to my advisor, Scott Cushing. Without his support and guidance, both scientific and personal, I am confident I would not have finished my PhD work. His willingness to allow me to explore different projects – ranging from synthetic organic chemistry to computational and theoretical spectroscopy – was the proving ground I needed to grow into the scientist I am today.

Secondly, the other members of my thesis committee, Professors Ryan Hadt, Greg Fu, and Geoff Blake deserve my gratitude. Their comments and feedback have pushed me to bridge the gap between the big picture and the details, a skill that will no doubt serve me well far into the future.

The beginnings of my scientific journey would be incomplete without mentioning Dr. Eva Campodonico and Jack Coakley, the first teachers to introduce me to science as a serious pursuit. Without them, I surely would have steered as far from chemistry as I could. Professors Andrew Crowther and Xavier Roy provided me the space and guidance I needed in college to explore scientific research. Their encouragement paved the way for me to go to graduate school.

Here at Caltech, my friends and colleagues have provided more support than I imagined possible. Anna Overholts, Corey Husic, Brooke Versaw, and Ross Barber were my first introductions to true collegial support and guidance. Ross deserves a special thanks as he both taught me and put up with me as I tried (and failed) to master organic chemistry. Anna's collaborations in the pursuit of cross disciplinary research were also particularly impactful over the course of my PhD.

The entire Cushing group deserves my thanks. Hanzhe Liu was the incredible post doc who guided us and helped us. Ultimately, we would not have achieved nearly as much as we did without him. While we disagree more than we agree, Jonathan Michelsen is the kind of colleague I will be searching for for the rest of my career – someone who pushes me to the limits of my knowledge and intellect and is then waiting to catch me when I fall over the brink of my understanding. Manni He and Danika Nimlos were also invaluable companions as we braved being Scott's first students together.

The other friends and companions at Caltech and in Pasadena include Griffin Mead, Sadie Dutton, Gracie Zhang, Mark Wronkiewicz, Aiva Ievins, Ricky Novaes, Kshitij Sadasivan, Noah Krim, Mayukh Sen, and Natelie Hills. Griffin, Sadie, and Gracie were simultaneously graduate school friends and not, moving between that divide seamlessly to remind me who I was both inside of this program and out. Mark and Aiva provided me an example of what life looks like after graduate school and were unfailingly supportive of my pursuits in that direction (and many others). They provided hope and a light at the end of the tunnel. Ricky, K, Noah, Mayukh and Nat couldn't have cared less that I was in a PhD program, which was exactly the friendships I most needed. (Another thank you to Jonathan for the introductions.)

One of my saving graces during graduate school was my CrossFit gym, Resistance Athletics. Not only am I grateful to the gym and community writ large, but I would be remiss if I didn't acknowledge Cassidy Cooper, Katie Alleman, Maggie Kennedy, and Savannah Horne (along with Wes and Monroe Horne). The Saturday morning workouts and coffee have been a highlight of my week for years and will be one of the things I miss when I move to Boston. The unquestioning love and support from these women and this community, and Katie and Cass in particular, cannot be overstated. Savannah also let me into her life and family, and gave me the space to connect with her incredible children who made my life richer and more interesting and continue to do so.

My country (and world) wide support system of friends and loved ones who always listened, advised, and consoled me during this time include Brenna Forristall, Aubri Juhasz, Julien Reiman, Linda Gordon (and her parents Bonnie Taub and David Gordon), and Matt Romer. They have seen me through thick and thin and I have relied on them more than even they know. This group of supporters would be incomplete without mentioning my parents, Carrie and Jason Klein, and my brother and sister-in-law, Max and Keelin Klein. When I first moved to LA, Max and Keelin were living here and gave me the grounding and love I so desperately needed, and I will be forever grateful to them for that. My parents, having no idea what I was doing in graduate school, supported me anyways and gave me all the love I needed.

And finally, the most important acknowledgement by far, is to my partner Bryce Hickam. Bryce's unending love and support carried me through the hard times and elevated the good ones. There is no one with whom I would rather have gone through this grand challenge and no one with whom I want to go through the rest of life's adventures. Bryce, I can't even begin to express the depth of my love and appreciation for you, from the hard conversations to doing the grocery shopping and talking to strangers. My life is fuller with you in it.

ABSTRACT

A full measurement of photoexcited dynamics, from excitation to recombination, is required to understand the photochemical processes at the heart of solar energy materials and devices. Measuring these complete dynamics is often unachievable with a single experimental tool. Transient X-ray spectroscopies, however, have proven to be powerful techniques as they can separately measure electron and hole dynamics, as well as vibrational and structural modes, all with elemental specificity. The interpretation of these measurements is still challenging, as the core-hole created following a core-level transition distorts the measured spectrum. This thesis aims to develop complementary experimental and computational techniques to measure and interpret transient X-ray spectra. Initially, the measured photoexcited dynamics of ZnTe and $CuFeO_2$, which reveal polaron formation and lattice coupling, as well as electron and hole kinetics and band gap dynamics, are presented. Following this experimental work, we develop an *ab initio* computational method for modeling transient X-ray and extreme ultraviolet (XUV) spectra. The *ab initio* method is a Bethe-Salpeter equation (BSE) approach based on the previously developed Obtaining Core Excitations from *Ab initio* electronic structure and the NIST BSE solver (OCEAN) code. Building on the foundations of the OCEAN code, we incorporate photoexcited states for a range of transition metal oxides and demonstrate the method's ability to simulate the effects of state filling, isotropic thermal expansion and polaron states on XUV absorption spectra. Importantly, our method is also able to fully decompose the calculated spectra into the constituent components of the X-ray transition Hamiltonian, providing further insight into the origins and nature of spectral features. The XUV absorption spectra for the ground, photoexcited, and polaron states of α-Fe_2O_3, as well as for the ground, photoexcited, and thermally expanded states of other first row transition metal oxides – TiO_2, α-Cr_2O_3, β-MnO_2, Co_3O_4, NiO, CuO, and ZnO – are calculated to demonstrate the accuracy of our approach. This method is easily generalized to K, L, M, and N edges to provide a general approach for analyzing transient X-ray absorption or reflection data.

PUBLISHED CONTENT AND CONTRIBUTIONS

1. **Klein, I. M.**; Husic, C. C.; Kovács, D. P.; Choquette, N. J.; Robb, M. J. Validation of the CoGEF Method as a Predictive Tool for Polymer Mechanochemistry. *Journal of the American Chemical Society* **2020**. https://doi.org/10.1021/jacs.0c06868.
   I.M.K. ran calculations, prepared data, and helped write the manuscript.

2. Liu, H.; **Klein, I. M.**; Michelsen, J. M.; Cushing, S. K. Element-Specific Electronic and Structural Dynamics Using Transient XUV and Soft X-Ray Spectroscopy. *Chem* **2021**, *7* (10), 2569–2584. https://doi.org/10.1016/j.chempr.2021.09.005.
   I.M.K. helped write the manuscript.

3. **Klein, I. M**.; Liu, H.; Nimlos, D.; Krotz, A.; Cushing, S. K. *Ab Initio* Prediction of Excited-State and Polaron Effects in Transient XUV Measurements of α-Fe_2O_3. *Journal of the American Chemical Society* **2022**, jacs.2c03994. https://doi.org/10.1021/jacs.2c03994.
   I.M.K. participated in the conception of the project, ran calculations and prepared data, and wrote the manuscript.

4. **Klein, I. M**.; Krotz, A.; Lee, W.; Michelsen, J. M.; Cushing, S. K. *Ab Initio* Calculations of XUV Ground and Excited States for First-Row Transition Metal Oxides. *J. Phy. Chem.* **2022**. (in revisions) *arXiv:2209.06347*.
5. I.M.K. participated in the conception of the project, ran calculations and prepared data, and wrote the manuscript.

6. Liu, H.; Michelsen, J. M.; **Klein, I. M**.; Cushing, S. K. Measuring Photoexcited Electron and Hole Dynamics in ZnTe and Modeling Excited State Core-Valence Effects in Transient XUV Reflection Spectroscopy. *arXiv:2108.02262.* **2021**. (in revisions)
   I.M.K. participated in the conception of the project, helped construct the instrument and collect data, and helped write the manuscript.

7. Liu, H.; Michelsen, J. M.; **Klein, I. M.**; Mendes, J.; Cushing, S. K. Measurement and Modeling of Photoexcited Dynamics in $CuFeO_2$ with Transient XUV Reflection Spectroscopy. (manuscript in preparation)
   I.M.K. helped construct the instrument, collect data, and write the manuscript.

8. Liu, H.; Michelsen, J. M.; **Klein, I. M.**; Mendes, J.; Cushing, S. K. Measurement and Modeling of Photoexcited Dynamics in $Re_6Se_8Cl_2$ with Transient XUV Reflection Spectroscopy. (measurements in progress)
   I.M.K. participated in the conception of the project, helped construct the instrument and collect data, and helped write the manuscript.

TABLE OF CONTENTS

LIST OF FIGURES, SCHEMES, CHARTS, AND TABLES

Number *Page*

Chapter 1

INTRODUCTION

To understand photochemical and photoelectrochemical processes, a complete measurement of excitation, thermalization, transport, and recombination of charge carriers is needed. These measurements are particularly important for solar energy materials and devices, as ultrafast dynamics can dictate macroscopic device performance. Capturing the full variety of coupled electronic and structural dynamics, however, is a challenging task for a single experimental tool. Transient X-ray absorption spectroscopy can separate electron and hole dynamics from vibrational modes, parse photoexcited dynamics by atomic contribution, and track photoexcited dynamics across layers in a multilayer device. However, the interpretation of photoexcited changes to an X-ray edge is not as simple as directly probing a transition with optical or infrared wavelengths. The core hole left by the core-level transition distorts the measured absorption and reflection spectra, both hiding and revealing different aspects of a photoinduced process. In this thesis, we first describe the implementation of transient X-ray experiments. Subsequently, we outline and demonstrate the accuracy of an *ab initio* computational method for predicting and interpreting X-ray spectra.

Some of this chapter has been adapted with permission from Liu, H.; Klein, I. M.; Michelsen, J. M.; Cushing, S. K. *Chem* **2021**, *7* (10), 2569–2584.

1.1 Pump-Probe Spectroscopy

Dynamics on the femtosecond to nanosecond timescale can be deterministic in defining a device's overall performance. Often, carriers thermalize and couple to vibronic states on sufficiently short timescales that their effects on the overall device performance can be ignored. Other times, as is the case for polaron formation or inter-system crossings, however, the coupled electronic-structural dynamics on ultrafast timescales determine overall device functionality.[1–5] Most next-generation solar energy devices attempt to extract more energy per incident photon by relying on ultrafast non-equilibrium dynamics instead of ignoring them.[1,6,7] For example, non-equilibrium vibronic states can tune the selectivity of certain reactions and products in molecular catalysts.[8,9] The excess kinetic energy of photoexcited hot electrons and holes can boost device efficiency.[6,7] The light-induced hybridization or creation of new states could potentially drive hydrogen evolution or CO_2 reduction. Measuring these ultrafast dynamics is therefore an important step for the implementation of next-generation solar energy devices.

When using ultraviolet, visible, or infrared light as a probe, overlapping spectral features in the valence states can make it difficult to deconvolute the electronic and vibrational dynamics, especially in the multi-element compounds or integrated multi-layer samples common in photoelectrochemistry.[10] Electron and hole dynamics are also difficult to separate in the signal because their joint density of states is measured. Further, it is helpful to isolate the photoexcited dynamics in terms of different dopants or atomic species, as these often play a major role in material dynamics and macroscopic functionality. Transient X-ray spectroscopy, as shown in Figure 1.1, aims to overcome these issues by probing a core-to-valence transition instead of a valence-valence transition or a vibrational resonance. X-ray spectroscopies overcome the challenges with traditional optical spectroscopy because the core-to-valence transitions are element specific probes of bonding, oxidation states, geometries, and more.

1.2 Extreme Ultraviolet (XUV) Spectroscopy

Core-level transitions span energies from tens of eV to tens of keV. Every element has multiple edges (or core-to-valence transitions) within this broad energy range. The

most important step in designing a transient extreme ultraviolet (XUV) / X-ray experiment is to select an appropriate absorption edge in the material. Selection of an edge depends on dipole allowed transitions and the dynamics of interest. In solids, the orbital contributions to the valence density of states must be considered for the dipole selection rules. Probing different dipole-allowed transitions of the same element can provide different information about the photoexcited dynamics. For example, low energy XUV photons <250 eV (10-100 nm) probe the delocalized valence dynamics but can only infer structural information through changes in core-valence excitons and exchange effects.[2,11–14] While harder to interpret because of the strong core-valence coupling and exchange effects, the resulting features allow electrons and holes to be measured simultaneously with strong structural distortions such as polarons. [2,4,12,13,15–17] On the other hand, high energy hard X-rays at several keV (sub-nm) give atomic-site specific electronic dynamics as well as direct structural information, but do not probe the valence dynamics in the same way that XUV transitions do.[18–20] Soft X-rays fall in between XUV and hard X-rays in terms of the probed valence dynamics, but again are only able to infer structural dynamics through changes in valence couplings.[21]

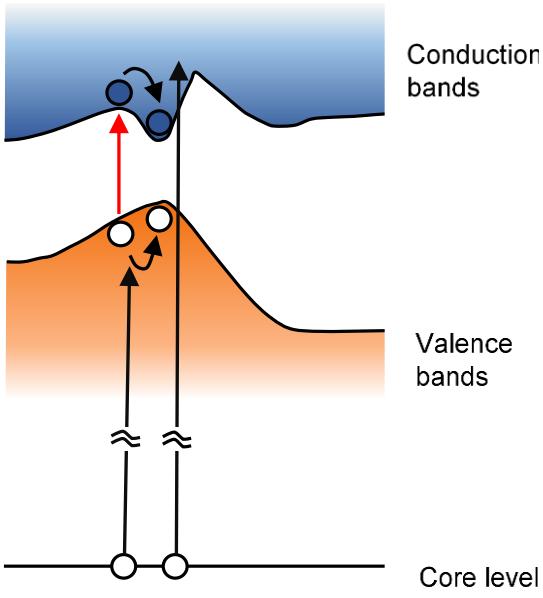

Figure 1.1 Overview of transient X-ray spectroscopy. Simplified depiction of a time-resolved X-ray absorption experiment. The red arrow indicates transitions with optical pulses, while the broken black arrows indicate an X-ray transition from a core level. The optical pulse excites valence electrons, and the X-ray pulse probes the ensuing photodynamics.

The absorption edge energy also largely determines what XUV/X-ray source is best suited for the experiment. There are various experimental methods for generating ultrashort X-ray pulses for transient measurements. An X-ray free-electron laser (XFEL) or a synchrotron facility can generate hard X-rays above 1 keV.[22] XFEL, synchrotron, and tabletop XUV experiments start to overlap at intermediate soft X-ray energies from 300

eV to 1 keV.[23] Ultrashort, coherent XUV pulses are generally created from a table-top setup using a scheme known as high-harmonic generation (HHG).[24] Whereas synchrotrons or XFELs modulate relativistic free electrons to create X-rays, HHG uses the strong electric field of an optical pulse to photoionize, accelerate, and recombine electrons from a noble gas atom to create XUV photons.[24] Since HHG is a coherent process, the spatial and temporal characteristics of the driving pulse are preserved in the XUV pulses that are generated.[25,26] The resulting XUV pulse duration can be significantly shorter (attoseconds) than the driving optical pulse (femtoseconds).[25] The broad bandwidth of HHG emission makes it useful for measuring multiple atomic edges in one measurement.

In Chapter 2, initial development of an XUV spectrometer is described in detail and subsequent use of this instrument is discussed. Pulse compression and high harmonic generation are highlighted as core competencies that enable extremely sensitive transient measurements (~ 0.1 mOD). Experimental investigations into the photoexcited dynamics of the solar energy materials ZnTe and $CuFeO_2$ are undertaken. These studies demonstrate the capability of the instrument to separately measure excited state electron and hole populations and band gap dynamics, as well as small polaron formation, equilibration, and annihilation.

1.3 Computational Interpretation of XUV Spectra

While the benefits of transient X-ray and XUV spectroscopies are numerous, there are also significant challenges associated interpreting experimental data. As a first approximation, the transition probability of the X-ray, and thus the measured absorption spectrum, would be proportional to the unoccupied valence density of states because of the narrow energy width of the core level including any dipole selection rules. However, the core-hole that is created during the X-ray transition perturbs the final transition valence density of states (Figure 1.2).[18,27,28] The strength and extent of this perturbation determines what information can be extracted from the transient X-ray experiment.

The general ranking of different core-hole perturbation effects, from strongest to weakest, is angular momentum effects (atomic multiplet and spin orbit effects resulting from the interaction between unpaired valence electrons and the unpaired core electron),

ligand field effects on these angular momentum perturbations, and the creation of core-valence excitons between the X-ray excited electron and the core-hole. The ability of the valence orbitals to screen the core-hole perturbations determines the peak amplitudes and spectral shifts within this general ordering, often resulting in XUV absorption spectra that do not follow the form of the valence of states.[2,29]

For X-ray transitions to localized d-orbitals, such as the M-edges of the first-row transition metals, angular momentum and spin-orbit effects are dominant in the X-ray spectra. Atomic multiplet coupling between the core level and valence states leads to a redistribution of the ground state, unoccupied density of states across tens of eV (Figure 1.2a). Exchange effects are edge dependent, with exchange interactions generally being stronger for M edges compared to L edges, while not present in K edges. Within each edge, the core-level character also plays a role (assigned as $X_{4,5}$ for d-core levels, $X_{2,3}$ for p-core levels, and X_1 for s-core levels where X is the orbital number with N=4, M=3, L=2, K=1). The angular momentum effects make extracting exact electron and hole energies difficult, but also make the edge sensitive to dynamic bonding and structural changes. Screening and ligand field effects determine the exact strength and separation of the peaks. A lower energy peak is therefore not necessarily a lower energy valence orbital. Theoretical methods are used to map out to which states X-ray peaks correspond.[27,28,30] A photoexcited change in oxidation state / screening is usually observed in the measured spectra, such as the ligand-to-metal-charge-transfer (LMCT), but the electrons and holes are not always spectrally resolved.[2]

For elements with s- and p-orbital valence electrons, the angular momentum coupling is moderate. The primary perturbation affecting the X-ray absorption structure is the creation of core-valence excitons. The core-valence exciton is usually narrow in linewidth and shifted lower in energy from the expected orbital with a modulated amplitude (Figure 1.2b). In a molecule, the core-valence exciton is quite pronounced because valence orbitals are highly localized and therefore do not screen the core-hole.[21] In a solid, the delocalized electron and hole wavefunctions can screen the core-hole and weaken the excitons amplitude and energy shift. The XUV spectrum is then more closely (but not exactly) related to the ground state, valence density of states of the material.[31] After

photoexcitation, electrons block existing X-ray transitions while holes allow new X-ray transitions, generically leading to negative and positive peaks in a transient X-ray spectrum.[12,13] Changes in the occupation and energy of electrons and holes can often be measured and extracted, sometimes even without the need for in-depth theoretical modeling.[12,13] However, more generally, the change in photoexcited valence occupation screens any core-valence excitons, with the resulting renormalization causing spectral changes across the full X-ray absorption spectrum, as seen in the Si $L_{2,3}$ edge.[14,31] In this case, relying only on positive and negative changes in the transient absorption measurement is misleading and in-depth theoretical modeling is needed.

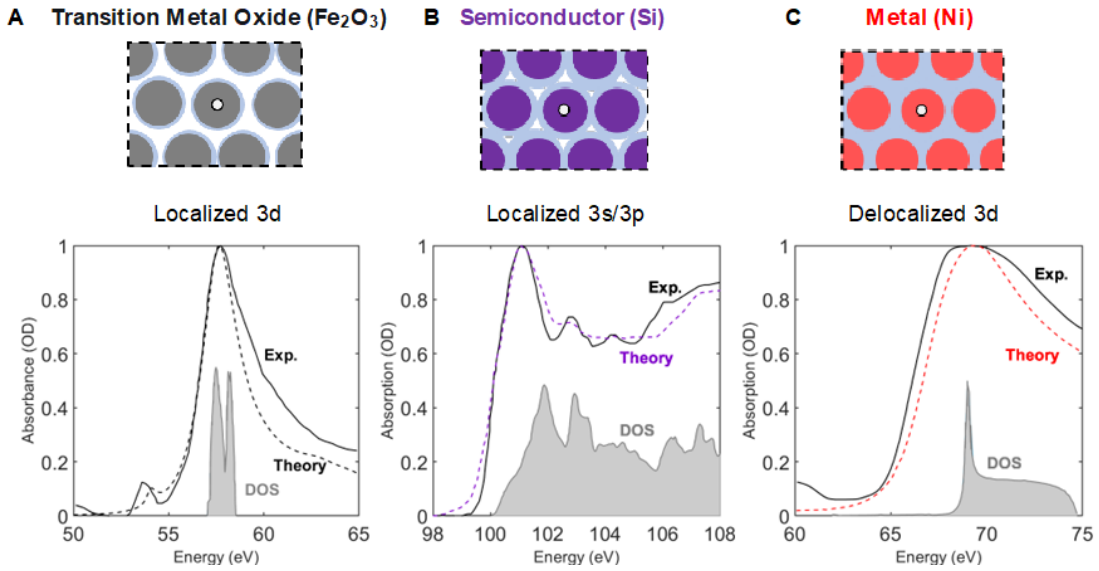

Figure 1.2 The XUV absorption in different classes of solid-state materials compared to their unoccupied density of states. **A** In a metal oxide, the localized d levels interact strongly with the core-hole of the XUV transition. The final transition density of states is dominated by atomic multiple splitting and is therefore distorted from the unoccupied valence states. **B** In a covalent semiconductor, the delocalized electrons shield the core-valence exciton, and the measured experimental absorption is close to the unoccupied density of states. **C** In metals, many-body effects lead to an increased absorption near the Fermi level and a power law tail as compared to the underlying density of states. Adapted with permission from Cushing et al.[12]

For metals, many-body interactions between the core-hole and free electrons dominate X-ray absorptions.[32] For example, the renormalization from the core-hole creates an exponentially increasing density of states near the Fermi level in the otherwise narrow bandwidth and partially filled d-valence bands. The resultant many-body effect leads to a strong increase in absorption, or white line effect, at the X-ray edge energy and a power

law decaying tail (Figure 1.2c).[33] The X-ray absorption spectrum is thus broadened and redistributed from the underlying empty orbitals, even though atomic multiplet effects are minor. The shift in the edge with photoexcitation, however, usually aligns with the change in quasi-Fermi level after excitation, allowing average electron or hole energies to be generically extracted.

Regardless of the edge or the material, as the photoexcited carriers relax by coupling with vibrational modes (phonons), a longer timescale, 10-100 picosecond, acoustic phonon signal can sometimes be measured in the transient X-ray spectra.[14] A lattice expansion can occur from the anharmonicity of the excited vibrational modes, created by phonon-phonon scattering of optical phonons or direct electron-phonon scattering at energies near the band edge. The resultant lattice expansion can decrease the bond hybridization and the band gap of the material, so the interaction of the core-hole with surrounding atoms is decreased and the overall X-ray spectrum is shifted to lower energy.[14] This apparent heating feature can be used to study heat transport between materials in a junction. In addition, comparing its kinetics with the change in carrier energy versus time, the electron-optical phonon and the optical-to-acoustic phonon scattering events can also be kinetically extracted.

While these general principles and considerations are both interesting and important to keep in mind when analyzing photoexcited X-ray spectra, ultimately computational modeling of sample responses to photoexcitation is invaluable. Specifically, the interpretation of photoexcited X-ray spectra requires theoretical modelling to accurately extract charge carrier and structural dynamics, regardless of the energy range used.[18,27,28,30] To that end, we developed a materials agnostic, *ab initio*, Bethe-Salpeter equation (BSE) based method to model measured XUV and X-ray ground and photoexcited states. This method is detailed in Chapter 3, where the theoretical basis is described and modifications to the code to enable transient modeling are discussed. In addition, modifications that allow the extraction of the various core-hole exciton Hamiltonian components are described.

Chapters 4 and 5 demonstrate our ability to use this method model the photoexcited, thermally expanded, and polaron states of a range of transition metal oxides. Not only is

the utility and accuracy of this method shown, but key takeaways are also highlighted. For both ground and excited state spectra, the decomposed X-ray transition Hamiltonian provides insight into the origins and nature of measured spectra, demonstrating specific examples of the influence of angular momentum coupling, exchange effects and screening on X-ray spectra, complementing the discussion in this section. Additionally, trends in photoexcited and thermally expanded transient spectra are analyzed and show that assumptions involving the spectral response of transient features, including "heating" features, do not always hold true. These findings underscore the importance of computational modeling to complement experimental work. While our approach is shown to work for transition metal $M_{2,3}$ edges, it can be easily expanded to other X-ray edges and materials systems.

1.4 XUV Spectroscopy and Polymer Mechanochemistry

While XUV spectroscopy is extremely powerful for investigating photoexcited processes in solid-state solar energy materials, it holds the potential to investigate any non-equilibrium dynamics. Mechanochemistry has emerged as an important field of polymer chemistry, and increasingly, physical organic chemistry, due to the novel reactivities and material properties it accesses. Mechanochemistry investigates the use of mechanical force to initiate productive chemical reactions of mechanophores, mechanically-sensitive molecules that undergo selective transformations under force.[34] Mechanophores have been shown to access a variety of interesting properties and novel reactivities, including color change,[35,36] conductivity switching,[37,38] gated reactivities,[39–43] and, of particular note, thermally-forbidden processes.[44–46] The interest here in mechanophores and mechanochemistry is motivated by a desire to understand the difference between a chemical reaction under typical reaction conditions and in a stressed reference frame. Towards that end, an overarching project was designed to study mechanochemical transformations with time-resolved XUV spectroscopy. While the ultimate aims of this project have yet to be achieved, progress has been made towards the development of a spatiotemporally resolved activation method to enable time-resolved spectroscopy.

In Chapter 6, the development and evaluation of laser-induced cavitation for mechanochemical activation is laid out. The similarities between ultrasound-induced cavitation, a prototypical activation method in the field, and laser-induced cavitation are highlighted, with the distinction that laser-induced cavitation enables spatial and temporal control over activation, potentially enabling time-resolved spectroscopy. Attempts at time-resolved optical measurements with this activation method are discussed and possible future solutions to the encountered challenges are provided.

Changing direction slightly, Chapter 7 shows our validation study of the widely deployed computational method *Constrained Geometries simulate External Force* (CoGEF) that is used to model mechanochemical reactions.[47] This comprehensive study of every mechanophore reported in the literature (as of publication on September 9th, 2020) demonstrates the ability of the CoGEF method to predict reactivity of proposed mechanophores, circumventing the cumbersome synthetic and experimental methods previously used.

Section I

Extreme Ultraviolet Spectroscopy

Chapter 2

ELEMENT-SPECIFIC ELECTRONIC AND STRUCTURAL DYNAMICS USING TRANSIENT XUV SPECTROSCOPY

Transient X-ray absorption techniques can measure ultrafast dynamics of elemental edges in a material or multiple layer junction, giving these measurements immense potential for deconvoluting concurrent processes. These measurements are especially important for solar energy materials, as the ultrafast dynamics dictate longer timescale activities, and for multilayer junctions in which different material layers provide different functionalities and facilitate charge transport differently. That said, the execution of these experiments is not trivial. Herein, we describe the construction, implementation, and interpretation of several transient extreme ultraviolet (XUV) experiments. A brief discussion of the benefits of XUV spectroscopy relative to other X-ray techniques highlights the importance of furthering these techniques and leads to the construction of a table-top instrument. Of note are the methods used for pulse compression and high harmonic generation (HHG) for continuous energy XUV pulses. Ultimately, the photoexcited dynamics of ZnTe and $CuFeO_2$ are investigated, revealing the concurrent measurement of polaron formation and lattice coupling, electron and hole kinetics, and band gap dynamics.

Same of this chapter has been adapted with permission from Liu, H.; Klein, I. M.; Michelsen, J. M.; Cushing, S. K. *Chem* **2021**, *7* (10), 2569–2584 and Liu, H., et al., Measuring Photoexcited Electron and Hole Dynamics in ZnTe and Modeling Excited State Core-Valence Effects in Transient XUV Reflection Spectroscopy. (in preparation).

2.1 Introduction

Capturing the full variety of coupled electronic and structural dynamics is a challenging task for any experimental tool. This hurdle is especially true when materials and molecules are combined in the active junctions of solar energy devices.[10,11,29,48] Transient XUV absorption spectroscopy can separate electron and hole dynamics from the vibrational modes that lead to their relaxation and scattering.[49,50] When a sample includes multiple elemental edges, the photoexcited dynamics can be separated by atomic contribution.[15,49,50] In a multi-layer junction, the photoexcited dynamics can be separated into each layer and the transport of charge carriers and thermal energy can then be mapped throughout a full device.[11,29,48] Charge selective contacts, plasmonic or hot carrier junctions, light absorbers-catalyst interfaces, and reaction products can be studied in their entirety.

As previously described, ultraviolet, visible, or infrared light spectroscopies are insufficient for measuring the full range of dynamics necessary to understand these materials and photoexcited processes.[10] Overlapping spectral features, electron and hole joint density of states and the impact of different atomic species work in concert to obscure and prevent the extraction of desired information from measured spectra. X-rays offer benefits in terms of penetration depth,[29] measuring electronic and structural dynamics simultaneously,[2,14] element specificity,[15] the ability to measure insulating or oxidized samples,[51] trap and mid gap states,[2,13,52] spin crossovers,[5,53] and oxidations state changes.[54,55] For these measurements, however, a tabletop XUV spectrometer must be constructed.

A few comments should be made on the practical challenges of tabletop XUV/soft X-ray sources. At XFELs and synchrotron sources, experimental difficulties center around limited access time and the inability to construct extensive experiment-specific apparatus at the facility. For tabletop XUV experiments, unlimited access is traded for low XUV/soft X-ray fluxes. In general, the HHG process has a conversion efficiency of 10^{-5}~10^{-7} with commonly used noble gases and <20 fs optical driving pulses. Even with high intensity lasers, the produced XUV flux from HHG is limited to the pJ to nJ range.[56] The low conversion efficiency of the HHG process and its reliance on peak intensity adds to the

cost and complexity of the experiment. The low flux and short absorption depth of XUV radiation (~100 nm for p-block and ~10 nm for d-block elements) also necessitate special sample preparation. These samples can include transmission measurements on a silicon nitride or diamond window,[2,12,13] reflection measurements on smooth solid samples,[4,11,16] or few- and sub-micron liquid jet methods.[57–60] Signal to noise ratios allow resolution of transient changes on the order of a few mOD with multiple hours of data acquisition using an XUV CCD spectrometer. Better signal to noise ratios are possible through lock-in detection with an XUV photodiode, but the better signal to noise ratio must be balanced against now having to take thousands of scans at different energies to replace a CCD image.[61]

Herein, we describe the construction of the transient XUV reflection spectrometer and its use in subsequent measurements of excited state dynamics in $CuFeO_2$ and ZnTe. We focus on pulse compression and high harmonic generation (HHG) in the construction, as they dictate signal to noise ratios and sensitivity, as well as XUV energy range.[62] Measurements of $CuFeO_2$ and ZnTe both demonstrate the instrument's capabilities, as well as provide new insights into the photoexcited dynamics of these materials. Specifically, polaron formation and subsequent interaction with the host lattice was measured in $CuFeO_2$, while electron, hole, and band gap dynamics were separately measured in ZnTe.

2.2 Instrumentation Building

The output of a 1 kHz, 38 fs, 13 mJ, 800 nm centered Ti:Sapphire laser is split by a 25:75 beam splitter, with the more intense ~ 10 mJ beam used to pump an optical parametric amplifier (OPA), generating output signal and idler beams between 1160 nm to 2600 nm. A piece of this beam can also be used for the generation of a 10 – 200 μJ, 400 nm pump beam to initiate photoexcitation in transient measurements. The less intense, ~3 mJ beam is used for pulse compression and high harmonic generation. The full optical set-up is shown in Figure 2.3 and will be discussed in more depth in subsequent sections.

2.2.1 Pulse Compression

To generate continuous XUV spectrum, we first needed a source of intense, single-cycle white light. Temporal compression of femtosecond optical pulses requires an increase in the optical bandwidth of the input pulse. The temporal duration and spectral width of a pulse cannot vary independently of one another.[63] A transform-limited pulse has the minimum possible time-bandwidth product (TBP), which is the product of the temporal duration (Δt) and spectral width ($\Delta\omega$) of the pulse. The TBP must be greater than a numerical constant (c_B) that is dependent on the pulse shape,

$$\Delta\omega\Delta t \geq 2\pi c_{\boldsymbol{B}}. \tag{2.1}$$

The interdependence of temporal duration and bandwidth therefore necessitates spectral broadening prior to compression. Subsequently, dispersion compensation is used to obtain the bandwidth- or Fourier-transform-limited pulse.

To achieve spectral broadening of the 38 fs, 800 nm pulse, the beam is focused into a 500 μm core diameter, 1 m long hollow core fiber using a f = 3 m lens. Imaging the focus showed a ~ 330 μm diameter spot size, an appropriate size for coupling into a 500 μm core diameter fiber.[62] The fiber is filled with a nonlinear medium for self-phase modulation. Differentially pumped Ar and statically filled Ne have both been used as the nonlinear medium. The results discussed here will focus on Ne at 50 psi. When the beam is focused into the fiber, propagation of the electromagnetic wave through the gas leads to changes in the electronic structure of the gas. The polarization of the gas (P) is related to the electric field (E) of the pulse by the susceptibilities ($X^{(n)}$) of the material,

$$P = \varepsilon_o(X^{(1)}E + X^{(2)}E^2 + X^{(3)}E^3 \ldots). \tag{2.2}$$

At high field strengths, the nonlinear contributions to the polarization become important and the high susceptibilities lead to several nonlinear processes as pulses propagate through media. In particular, the nonlinear effects of an electric field traveling through isotropic media leads to self-phase modulation, which results in spectral broadening. As the pulse travels through the Ne filled fiber, the refractive index of the gas changes due to the optical Kerr effect. The time-dependent refractive index then leads to a nonlinear phase shift in the pulse. This process then repeats and, through interactions with the gas, the pulse modulates its own phase, i.e. self-phase modulation. The instantaneous frequency, $\omega(t)$, is dependent

on the initial frequency, ω_o, as well as the time-dependent nonlinear refractive index, $n(t)$, over the length of the fiber,

$$\omega(t) = \omega_o - \frac{2\pi}{\lambda_o} n(t) \frac{dI}{dt} L. \quad (2.3)$$

When the time-dependent refractive index is greater than zero, the pulse is continuously spectrally broadened as it propagates through the gas-filled fiber.[62,64] Focusing our beam into the hollow core fiber filled with 50 psi of Ne, we obtained a spectrally broadened pulse from 500 nm to 900 nm (Figure 2.1c).

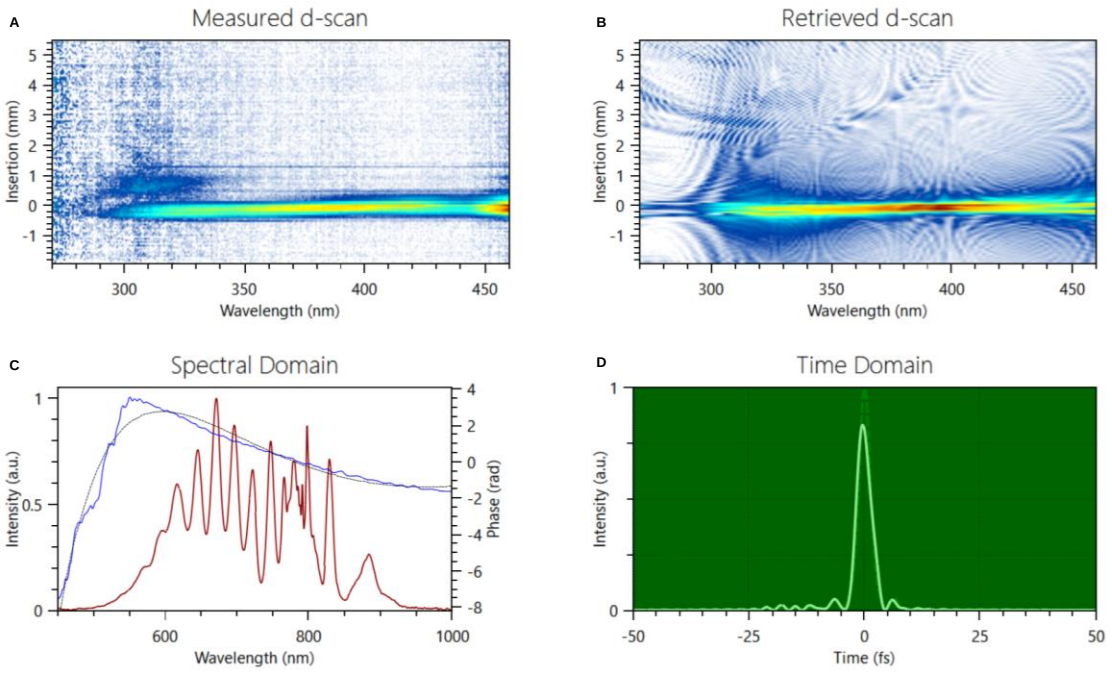

Figure 2.1 Measured d-scan trace of HHG driving pulse after spectral broadening and compression. **A** shows the measured d-scan trace of the pulse, retrieved in **B** to show the accuracy of the measurement and the dispersion of the pulse. The spectral width of the pulse is shown in **C**, while the temporal width is measured in **D**.

Following spectrally broadened, temporal pulse compression leads to a few-cycle, few-fs pulse. Self-phase modulation leading to spectral broadening introduces a large amount of temporal chirp into the pulse. The fiber output is collimated and steered through two sets of chirped mirrors, at 5º and 19º, to compensate for phase oscillations. The chirped mirrors have a negative nominal group delay dispersion (GDD) of – 40 fs^2 per bounce. By changing the number of bounces on the chirped mirrors, the temporal chirp introduced to the pulse by spectral broadening is compensated. Thin fused silica pieces can also be used

as they will introduce + 36 fs^2/mm of second order dispersion into the beam and can correct for an overcorrection by the chirped mirrors. It is the combination of spectral broadening in the hollow core fiber and dispersion compensation with the chirped mirrors that allows us to obtain large bandwidth, ultrashort pulses. The typical pulse generated is measured in Figure 2.1 using a dispersion scan (d-scan), showing the sub-5 fs temporal width (Figure 2.1d) of the pulse that was spectrally broadened to span a 400 nm bandwidth.

2.2.2 High Harmonic Generation

XUV and soft X-rays are produced through a process called high-harmonic generation (HHG). HHG is a nonlinear process in which the frequency of a pulse is converted to its integer multiples. HHG occurs when a linearly polarized high intensity laser pulse tunnel ionizes an electron from a gaseous atom out of the Coulomb potential (Figure 2.2, t_1).[65] Due to the oscillations of the electric field of the laser pulse, the electron is accelerated first away from and then towards the nucleus from which it was ionized (Figure 2.2, t_2). When the electron has returned to the initial nuclear position, it can recombine with the ion, emitting a harmonic, the frequency of which is an integer multiple of that of the input beam (Figure 2.2, t_3).[66]

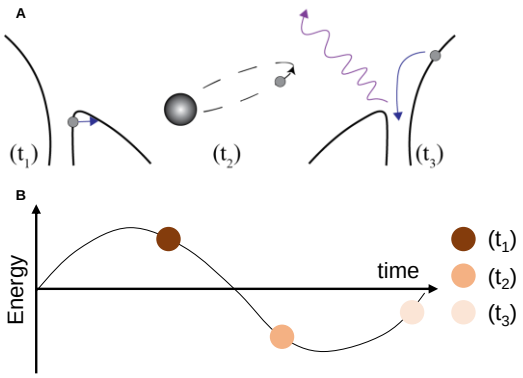

Figure 2.2 Theory of high-harmonic generation. **A** Path of the electron over the course of HHG. **B** HHG as a function of electric field propogation.[61–63]

Harmonic spectra of a single element show a decline in intensity for the first few harmonics and then plateau at a relatively constant intensity, until an abrupt cutoff is reached. As the intensity of the input beam increases, the harmonic intensities and the length of the plateau also increases. The plateau intensity is dependent on the ionization rate of the gas, which in turn depends on the laser intensity.[65] The cutoff energy (E_c) is dictated by the ionization potential of the gas (I_p) and the intensity (I) and frequency (ω) of the laser beam,

$$E_c = I_p + \frac{3I}{4\omega^2}. \quad (2.4)$$

Finally, it is important to note that only odd harmonics are generated in HHG. Ionization occurs every half cycle of the electric field, which means that harmonics are generated as a delta function at $\frac{t}{2}n$ where t is the time of a single cycle and n is an integer. The Fourier transform of this function is only non-zero for odd multiples of ω_o, which corresponds to only odd harmonics being generated.[66,67] A combined 800 nm + 400 nm driving pulse can be used to break the symmetry of the field, leading to both even and odd harmonics.[68] HHG using single-wavelength driving pulses will result in discrete harmonics, while HHG with a single-cycle broadband driving pulse will produce a continuum.

Following pulse compression, the driving beam is focused with a f = 40 cm concave focusing mirror into the HHG vacuum chamber. Changing the polarization of the white light from P to S into the vacuum line increased the HHG flux 20-fold, increasing signal-to-noise of the XUV pulses. The HHG chamber contains a gas jet with a 150 μm hole, into which the beam is focused. Argon (or Ne or He) is flowed through the gas jet as the medium in which HHG occurs. Once harmonics are generated, the beam is passed through an Al (or Zr) filter to remove residual fundamental light, focused with a toroidal mirror, and passed through a recombination chamber. The pump beam enters the recombination chamber at a 90º angle and is focused collinearly with the XUV probe beam on the sample. In the reflectance geometry, the incident angle of the pump and probe beams on the sample can be tuned from 3 to 40º. A catching mirror is used to reflect the XUV light onto a grating that disperses the X-rays on a CCD. Another Al filter is placed directly prior to the CCD to further remove any residual fundamental light.

Initial tests using 38 fs, 800 nm pulses to generate high harmonics were performed in the transmission geometry and then expanded to the reflectance geometry. Using 800 nm light is much simpler, as the hollow core fiber and chirped mirrors can be bypassed but limits the ability to the generated harmonics to discrete integers of 800 nm. After the HHG beamline was optimized with 800 nm, harmonics were generated with the sub-10 fs white light continuum. When a few-fs, white light continuum is used, the harmonics become essentially continuous in the extreme ultraviolet region.[69] When higher wavelengths are used, i.e. 1800 nm, higher energy harmonics can be reached.[69,70] Using the white light as a

pump generated continuous harmonics, however temporal fluctuations make transient measurements challenging. In addition, the reflectivity of different samples at different angles and energies has proven to be fickler than anticipated. However, both these and other experimental challenges have been overcome to allow for transient XUV measurements to be acquired. Future work can look to increase temporal stability, sample reflectivity, and signal to noise, as well as enable multi-angle reflectivity measurements.

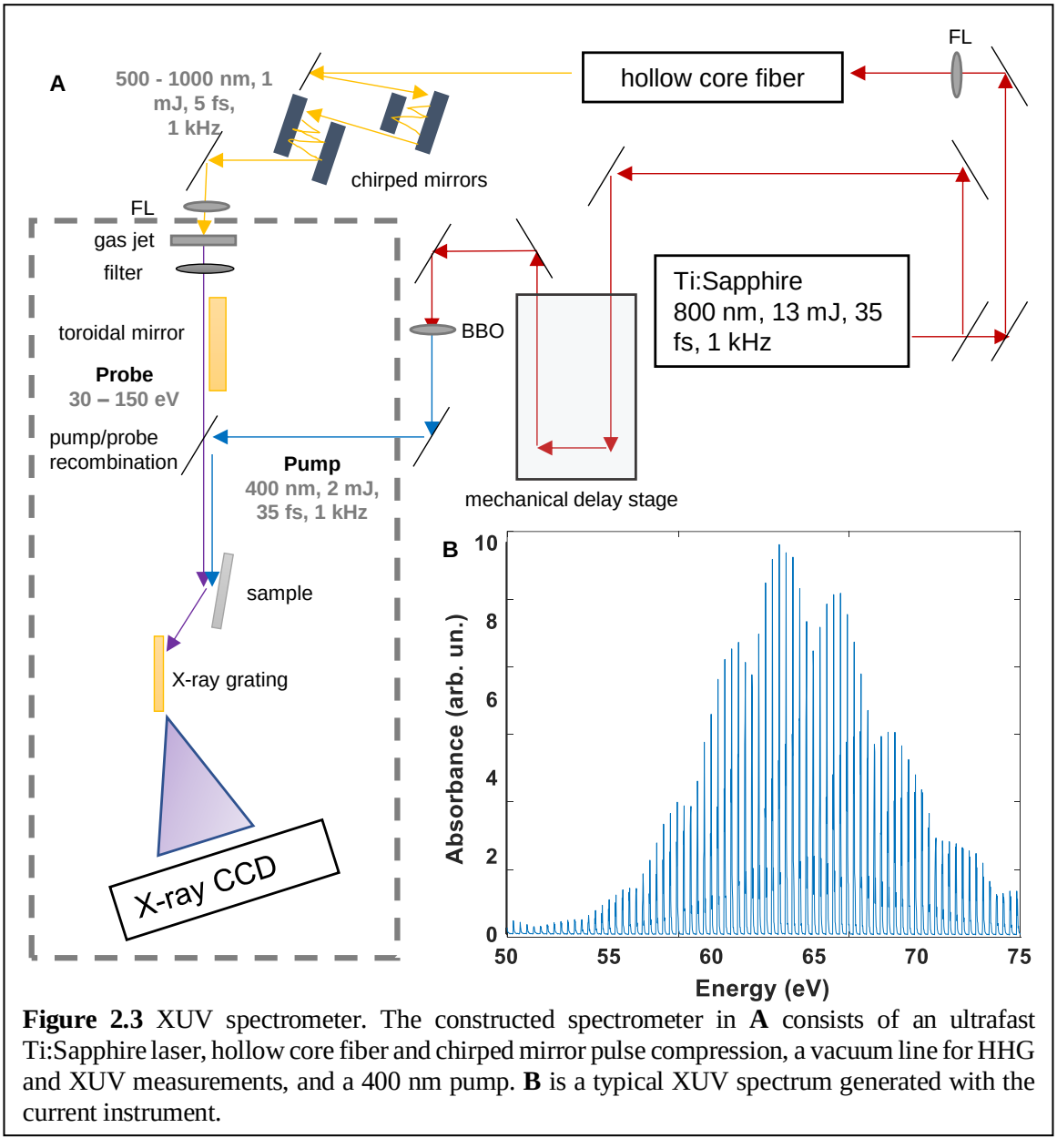

Figure 2.3 XUV spectrometer. The constructed spectrometer in **A** consists of an ultrafast Ti:Sapphire laser, hollow core fiber and chirped mirror pulse compression, a vacuum line for HHG and XUV measurements, and a 400 nm pump. **B** is a typical XUV spectrum generated with the current instrument.

2.3 Time-Resolved XUV Spectroscopy

For time-resolved spectroscopy to work, there needs to be a spatiotemporally resolved pump pulse that can initiate the dynamics of interest which the probe pulse then investigates. In addition, the pump and probe pulses must be delayed relative to each other. Typically, this delay is introduced through an optomechanical delay stage, as the speed of light is 0.3 mm/ps, so the delay between the pulses can be finely controlled with the introduction of additional length to one of the beam paths. In the transient measurements discussed here, the pump pulse photoexcites carriers across the band gap and XUV transitions are measured as a function of time following excitation.

2.3.1 Pump Pulse

In these studies, the probe pulse is the XUV pulse described, while the pump is a 10 – 200 mW, 400 nm pulse. This wavelength was chosen because it matches or exceeds the band gaps of the materials of interest (3 eV). In addition, 400 nm is easily generated from 800 nm through second harmonic generation (SHG) and thus the initial 800 nm pulse from the Legend Elite Duo can be used for both pump and probe pulse generation, simplifying pulse delay and timing.

SHG is a nonlinear effect of frequency mixing inside a non-centrosymmetric crystal as a high intensity IR light propagates through the material. This process is described by the second order effects of an electric field on the polarization of a material, $P = \varepsilon_o X^{(2)} E^2$. When

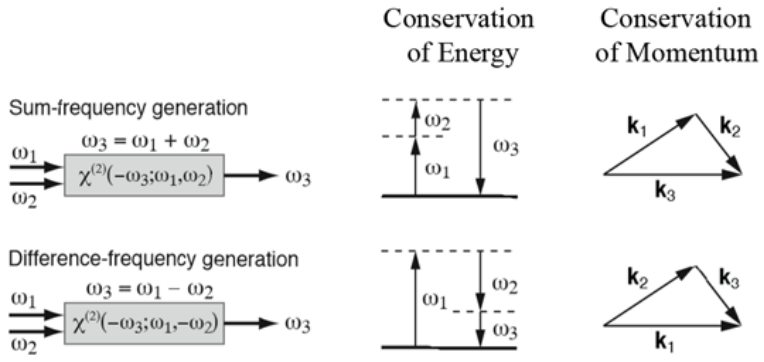

Figure 2.4 Frequency mixing occurs when two pulses of light are converted into one pulse, or vice versa. In both situations, sum and difference frequency generation, respectively, the energy and momentum of the pulses must be conserved.

two, non-identical electric fields propagate through the crystal the polarization depends on both fields by

$$P = \varepsilon_o X^{(2)} E_1 E_2 = \varepsilon_o X^{(2)} \frac{E_o^2}{2} [\cos(\omega_1 - \omega_2)\, t + \cos(\omega_1 + \omega_2)\, t]. \quad (2.5)$$

When a fs pulse with a small Δt propagates through an appropriate material, frequency mixing occurs between the different frequency components of the pulse. This mixing can occur within an ultrashort pulse due to the large associated Δω. Sum- and difference-frequency generation (SFG and DFG, respectively) can occur when $\omega_1 \neq \omega_2$, and second-harmonic generation (SHG) occurs when $\omega_1 = \omega_2$.[71–73] Here, a β-barium borate (BBO) crystal is used for SHG of 800 nm to create a 400 nm pulse. BBOs are useful for SHG because they are birefringent and provide for a wide frequency range in which phase-matching occurs (Figure 2.4).

2.3.2 Transient Absorption vs Transient Reflectivity

The low flux and short absorption depth of XUV radiation necessitate special sample preparation. Samples can be probed either with transmission measurements in which the sample is mounted on a silicon nitride or diamond window or with reflection measurements where the samples must be smooth and solid.[2,4,11,16,74] Both transmission and reflectivity measurements have benefits and pitfalls in terms of sample preparation, however they both produce useful information regarding the photodynamic of the sample of interest.

Optical excitation promotes electrons from the valence band to the otherwise empty conduction bands, blocking allowed XUV transitions to the same states in the transient spectrum. On the other hand, the creation of photoexcited holes allows new core electron transitions to the valence band. In a transmission measurement, transient negative features typically correspond to blocked XUV transitions, while transient positive features correspond to newly allowed XUV transitions. Contrastingly, the change in the transient reflection after optical excitation is defined

$$\Delta OD = -\log_{10}\left(\frac{I_{pump\ on}}{I_{pump\ off}}\right) \quad (2.6)$$

where negative transient reflectivity often corresponds to an increase in absorption due to excited state absorption and positive transient reflectivity is due to a decrease in absorption due to state blocking. This definition is often termed as reflection-absorption, due to the negative sign.[75] Further, transmission measurements are dominated by the imaginary component of the complex refractive index of the material (k), while the reflection spectrum is sensitive to both the real (n) and imaginary (k) components of the complex refractive index, $N = n + ik$.[76]

2.4 Application of XUV Spectroscopy in Solar Energy Materials

Following the construction of the UV pump, XUV probe transient spectrometer outlined above, a brief discussion of the experimental investigations undertaken is warranted. Both experimental measurements discussed below were complemented by the theoretical model described in detail in Chapter 3.

2.4.1 Polarons – $CuFeO_2$

Small polaron formation occurs when an electron or hole interacts with a polar lattice to localize the respective wavefunction at a single atomic site.[2–4] The localization occurs through a distortion of the bonds surrounding the initial charge transfer. The transformation from a free electron-like wave to a trapped, defect-like charge severely limits charge carrier mobility and increases recombination events. Photoexcited small polaron formation explains why metal oxide photocatalysts have never reached the photoconversion efficiencies suggested by their band gaps.[2,4] Small polarons are especially prevalent in transition metals with partially-filled d-orbitals because of the orbitals' localized nature (Fe containing compounds, for example). The localized d-orbitals lead to efficient molecular catalysis but also have a small energy cost for the formation of a small polaron. For largely unfilled or nearly fully filled d-orbitals (e.g. TiO_2 and ZnO), large polarons are formed.[77] Large polarons refer to trapped charges and associated lattice distortions extended over multiple unit cells to the point where it is only a slight impediment to charge transport.[77–80] Photoexcited polaron formation is still an active area of research, and many intermediate cases such as $BiVO_4$ remain debated.[81] It is becoming

increasingly apparent that the photocatalysis community must avoid or reduce small polaron effects to create efficient photocatalysts.

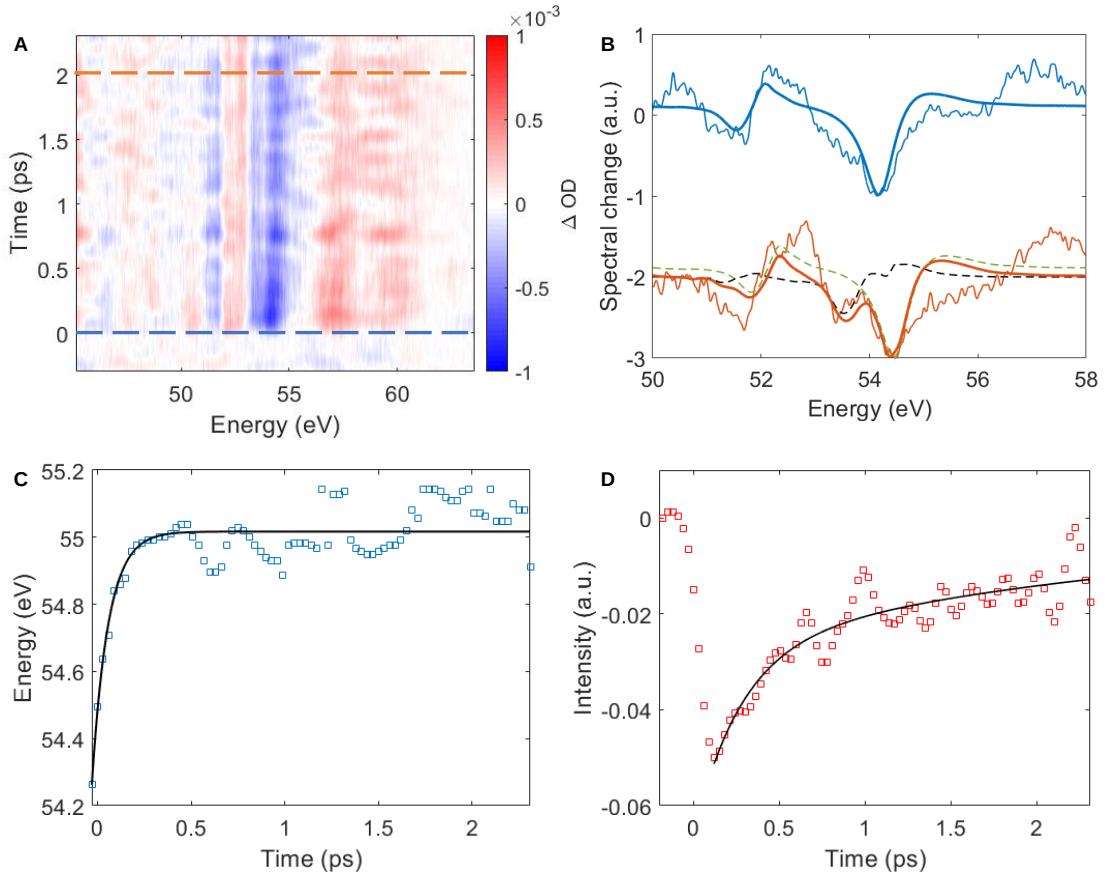

Figure 2.5 Transient XUV reflectivity measurements of $CuFeO_2$. **A** Measured transient XUV reflection-absorption near the Fe $M_{2,3}$ edge after photoexcitation with 3.1 eV (400 nm) pulses. The main features include an ultrafast blueshift in the Fe M2,3 edge (54.2 eV to 55.2 eV), corresponding to the initial charge transfer, followed by peak splitting at the Fe M2,3 edge, corresponding to polaron lattice expansion. **B** Differential lineouts from **A** that show the spectral change initially (blue) and after 2 ps (orange). Thin lines correspond to experimental data, thick solid lines are the computationally modeled differential spectra, black dashed line in the expansion model and green dashed line is polaron charge transfer model. **C** shows the polaron formation kinetics with a time constant of 90 ± 20 fs, while **D** shows the local and lattice expansions on 280 ± 190 fs and 3.1 ± 2.3 ps, respectively.

As an XUV application example, transient XUV reflectivity measurements of the Fe $M_{2,3}$ edge of $CuFeO_2$ at 55 eV confirm the formation of small polarons around Fe sites in a few picoseconds after optical excitation in this material (Figure 2.5a).[2] Optical excitation induces electron transfer from an O site to the Fe center. The charge transfer process reduces the Coulomb interaction between the Fe center and the surrounding O atoms. The reduced Coulomb interaction causes a local lattice expansion, trapping the

electron at the Fe center. The XUV core-level transition is sensitive to the environment surrounding the atom through the core-hole perturbation of the transition state, as will be discussed later. After decomposition of the differential reflectivity, the small polaron formation in $CuFeO_2$ was measured to occur in 90 ± 20 fs matching the first electron-phonon scattering events (Figure 2.5c). Interestingly, the Fe $M_{2,3}$ edge of $CuFeO_2$ was also able to measure subsequent lattice reorganization to accommodate the polaron on the order of 280 ± 190 fs and ultimately the polaron to optical phonon transition after 3.1 ± 2.3 ps (Figure 2.5d). These phenomena and time constants were extracted from the experimental data and computational modeling, as will be discussed in Chapter 3. Specifically, the peak shifting, splitting, and oscillations around the Fe $M_{2,3}$ edge indicate these dynamics. Understanding the few picosecond polaron formation and equilibration dynamics is important as it will determine any later photocatalytic steps.

2.4.2 Energy-Resolved Electron and Hole Kinetics – ZnTe

As highlighted by small polaron formation, controlling the relaxation pathways of photoexcited carriers is crucial for better optimizing solar energy devices. Efficient extraction of the excess kinetic energy of hot (non-thermalized) electrons and holes can overcome the theoretical Shockley-Queisser efficiency limit.[1,6,7] Hot electrons and holes created by plasmonic nanoparticles can create new photoproducts not reachable with thermalized carriers.[82] The ability of transient X-ray spectroscopy to separately measure the electron and hole energies as a function of time is very useful for these applications, whether the device utilizes thermalized or non-thermalized carriers.

Here, we used surface-sensitive femtosecond XUV reflection spectroscopy to separately measure photoexcited electron, hole, and band gap dynamics of ZnTe, a promising photocathode for CO_2 reduction. Experimentally, transient XUV reflection spectra were measured at the Te $N_{4,5}$ edge ($4d_{3/2,\ 5/2}$ core states) around 40 eV following photoexcitation (Figure 2.6). The hot electron thermalization rate was measured to be 150 ± 150 fs, with a hot hole thermalization rate of 340 ± 320 fs (Figure 2.6d). Using the modified Bethe-Salpeter equation approach, outlined in Chapter 3, the hot carrier thermalization pathways can be mapped back onto the band structure. The electron and

hole diffusion rate in real space is determined to be at 2.21 ± 1.12 ps and 3.91 ± 3.58 ps, respectively (Figure 2.6e). Photoexcited carrier concentration-dependent band gap dynamics with a time constant of 730 ± 170 fs were also observed.

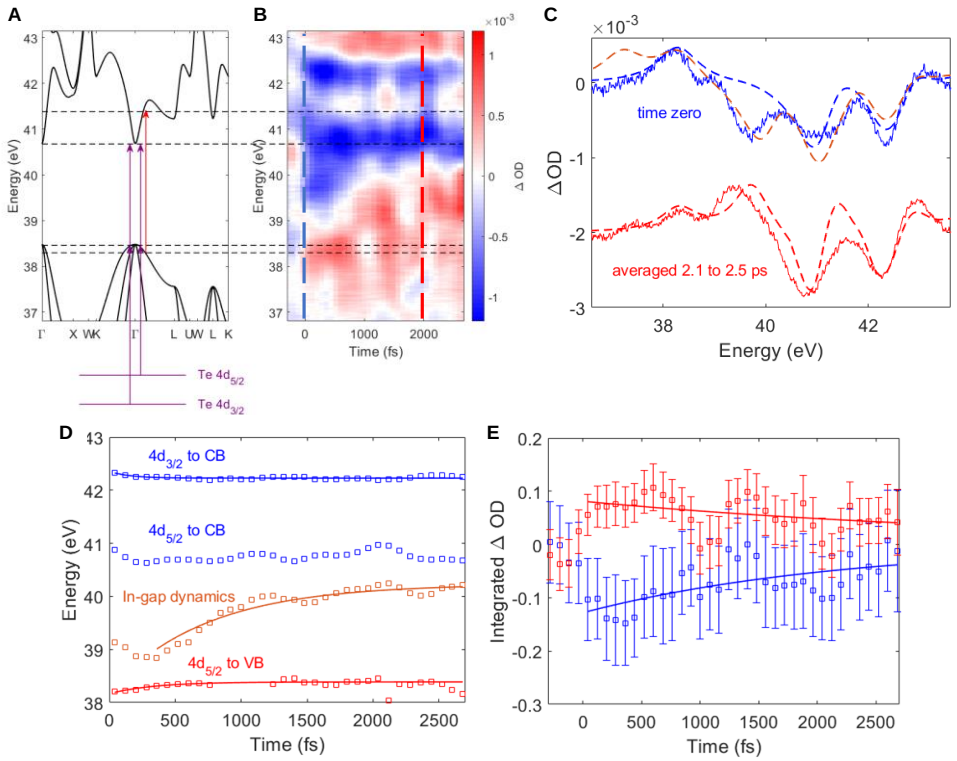

Figure 2.6 Transient XUV reflection spectra of photoexcited ZnTe. **A** Calculated band structure of ZnTe overlaid with optical photoexcitation (red arrow) and core-to-valence XUV transitions (purple arrows). **B** Measured transient XUV reflection-absorption near the Te $N_{4,5}$ edges after photoexcitation. Main transient features due to state blocking include an increase in reflection between 40.2 eV and 41.3 eV, as well as between 41.8 eV and 42.7 eV (blue features). A decrease in reflection is measured starting at 38 eV and blue shifted to 39.5 eV approximately 1 ps after optical excitation (red features). Additionally, in-gap dynamics are observed, showing an initial decrease in absorption below 40 eV, which blue shifts and disappears over time. The alignment of the transient spectral features to the valence and conduction band are shown by the dashed lines. **C** Comparison of experimental (solid) and theoretical (dashed) spectra for initial hot carrier states (blue) and fully thermalized final states (red). The in-gap spectral feature at 39.8 eV (solid blue line) is not shown in the single core-valence exciton theory, suggesting its many-body interaction nature. The in-gap spectral feature can be qualitatively reproduced by red-shifting the theoretical spectrum and convoluting it with the original spectrum, mimicking a smaller band gap transition that would result from band gap renormalization (orange dashed line). **D** Extracted electron, hole, and band gap renormalization dynamics from the experimental spectra using the DFT+BSE approach. Fitting ranges are chosen before the energy and intensity modulation from the acoustic phonons dominate the spectra. The band gap renormalization dynamics are extracted by tracing the energy shift of the spectral zero-crossing for the $4d_{5/2}$ to conduction band transition. **E** Spectral intensity for electrons (blue) integrated between 41.75 eV to 42.56 eV, spectral intensity for holes (red) integrated between 37.88 eV to 38.75 eV.

2.5 Conclusions

Transient XUV spectroscopy is a powerful tool for measuring the ultrafast photoexcited dynamics in a range of materials and has been leveraged here to specifically examine the impact of these dynamics on the macroscopic functionality of solar energy materials. These measurements can only be performed, however, after the construction of a tabletop XUV spectrometer, as described in detail. Different aspects of the experimental set-up greatly influence the measurable dynamics, in particular regarding signal to noise considerations. The sub 1 mOD signal to noise ratios achieved in the experiments discussed herein are at the forefront of the field, enabling the detection of otherwise obscured transient signals.

Chapter 3

AB INITIO MODELING AND INTERPRETATION OF X-RAY AND XUV SPECTRA

As transient spectroscopy becomes more advanced, probing increasingly complex dynamics in increasingly complex systems, experimental data must be complemented with theoretical modeling to accurately assess the origins and implications of measured spectral features. To that end, an *ab initio* computational method for modeling transient X-ray and extreme ultraviolet (XUV) spectra is developed based on the Bethe-Salpeter equation (BSE). While previous approaches have had some success modeling ground state X-ray spectra and excited state spectra with extreme computational investment, this method is computationally inexpensive and is materials agnostic in its modeling of excited state as well as ground state spectra. Importantly, it is also able to fully decompose the calculated spectra into the constituent components of the X-ray transition Hamiltonian, providing further insight into the origins and nature of spectral features.

Part of this chapter has been adapted with permission from Klein, I. M.; Liu, H.; Nimlos, D.; Krotz, A.; Cushing, S. K. *Journal of the American Chemical Society* **2022**, https://doi.org/10.1021/jacs.2c03994.

3.1 Introduction

The capabilities and strengths of transient XUV spectroscopy measurements are numerous, as demonstrated in the previous chapter, and the importance of computational modeling in those studies cannot be overstated. While transient spectroscopic studies generally rely on computational modeling for assistance interpreting complex measurements, theoretical work is essential to transient XUV experiments, as these measurements contain even more complexities than optical ones. The X-ray pulse excites a core-level transition to a valence state leaving behind a core-hole. The core-hole couples with valence states, perturbing the measured X-ray spectrum from the underlying orbitals or density of states.[18] The formation of core-valence excitons can therefore obscure electron and hole occupations. On the other hand, the core-valence exciton can allow structural information to be inferred through changes in bonding lengths and the valence states, as the excitation cross-section in this energy region is highly sensitive to details of the chemical bonding and electronic structure of a material.[2,21] The energetically narrower valence states in molecules lead to easier to interpret transient X-ray absorption spectra.[21] In a crystal, however, the complexity of the valence and conduction bands with screening and many-body effects obfuscates the measurement, placing a higher demand on theory for proper interpretation.[27,30] While multiple theoretical approaches exist for predicting the ground state X-ray structure accurately,[18,27,28,30] the prediction of excited state dynamics over femtosecond to nanosecond timescales is still an ongoing development.[83]

Previous theoretical work has used a variety of approaches to model and understand the measured X-ray spectra of both ground and excited states for a variety of materials. These methods have spanned density functional theory (DFT) to wave function theory and include response and polarization propagator theories. Some of these methods, including static exchange, transition potential DFT (TP-DFT), and the core-valence separation (CSV) approximation, were specifically designed for the simulation of X-ray spectroscopies and it is challenging to appropriately integrate both core-excited and valence-excited states within these methods.[84–89] Other approaches, including time-dependent DFT (TDDFT) methods, multiconfigurational wave function theory, and coupled cluster methods, are more generalizable and can be used to assess both types of excited states previously

mentioned.[84,90–96] Real time TDDFT has been successfully used to evaluate the dynamic behavior, both in the X-ray region and at higher wavelengths, of a variety of materials, including α-Fe_2O_3 and Cr_2O_3.[97–100] The strength of RT-TDDFT methods is that they usually allow the determination of the spectral response over the entire energy range of interest from a single time propagation.[84] That said, RT-TDDFT methods are computationally expensive, which makes computing longer timescale dynamics difficult. In addition, while local expressions of electron-hole interactions provided by TDDFT are an attractive approach for spectroscopy, they are currently limited by poor approximations to the exchange-correlation potential that limit agreement with experiment.[101] Other works have used the assumptions of a semi-empirical atomic multiplet theoretical approach to model $M_{2,3}$ edge measurements that rely on a parameterized fitting of the experimental spectra.[102–108]

In addition to the assumptions inherent to the theoretical methods described above, modeling transient measurements often requires numerous additional assumptions about the behavior and nature of different excited states in these materials. While these approximations are accurate for some of the materials studied, these approaches are not generalizable, with new models needing to be developed for each new material studied.[109–112] In addition, using these computational tools can validate the assumptions regarding excited state dynamics, but provide no additional insight into the origins of observed spectral signals.

Here, we extend the Obtaining Core Excitations from *Ab initio* electronic structure and the NIST BSE solver (OCEAN) code to include excited state effects. This approach is based on the linear response of conduced matter to a photon field. Specifically, the condensed matter can be considered in a quasi-particle framework in which the excitations take the form of quasi-electrons or quasi-holes that then couple to the rest of the system. As excitations in interacting systems inherently are affected by the rest of the system, we can treat these many-body effects as perturbations of excitations of the non-interacting system.[101] Ultimately, the power of this approached for experimentalists lies in the fact that it is an *ab initio* method that lacks a multitude of free adjustable parameters.[101]

The OCEAN code has previously been verified for ground state K, L, M, and N edge calculations.[110,113–117,117–120] The ground state core-level spectrum is calculated in three steps. The core-level transition matrix elements are first determined by projecting an all-electron atomic calculation of the core levels onto a density functional theory (DFT) calculation of the valence wavefunctions using a projector augmented wave (PAW)-style optimal projector functions (OPFs) with a GW scissor correction of the band gap.[101,121,122] The inclusion of the Hubbard-like U term applied to transition metal 3d electrons mitigates the self-interaction error of the GGA functionals, while the GW scissor correction accounts for the misestimation of the band gap in transition metal oxides from DFT+U.[123] The DFT packaged used here was QuantumEspresso.[124,125] Second, screening of the core electrons in the presence of the core-hole is determined self-consistently.[101,122] Atomic multiplet effects are included through core-hole spin-orbit splitting and atomic multipole interactions.[121] Finally, the ground state absorption spectrum is obtained by iteratively solving the BSE using a Haydock recursive algorithm.[101,122] Alternatively, the real-space wavefunction of the core-valence excitons can be calculated using the Generalized Minimal Residual (GMRES) method.

The base OCEAN code has been expanded in this thesis in three ways. First, the core-valence excitons that underly the XUV absorption spectrum are calculated and projected onto the band structure. Second, the X-ray transition matrix elements are decomposed into their fundamental components and are also projected onto the band structure. Finally, photoexcited changes to the band occupations, phonon modes, and polaronic-type effects are included for the prediction of excited state spectra.

In this chapter, the theoretical models (DFT and BSE) underlying the OCEAN code are first described in sections 3.2 and 3.3. Subsequently the methodologies for decomposing the X-ray transition matrix elements, projecting the exciton densities onto band structures, and incorporating excited state effects are outlined in sections 3.4 and 3.5. Future directions for this approach and general considerations for interpreting X-ray spectra, even without detailed calculations are laid out in sections 3.6 and 3.7. Finally, in Chapters 4 and 5, the use of this code to accurately model the ground, photoexcited, and polaron states of numerous transition metal oxides is discussed.

3.2 Density Functional Theory

Density functional theory (DFT) is one of the most widely used computational tools available to chemists and physicists. DFT essentially involves using functionals of the density of a system alone to determine ground state properties of that system. Fifty-five years ago, Kohn and Sham showed that the ground state density of a non-interacting fermion with a density-dependent potential, V_{xc}, will exactly match that of the interacting system, allowing a Hamiltonian of the form[126]

$$H = V_{ext} + \sum_i -\frac{1}{2}\nabla_i^2 + \int dr' \frac{n(r')}{|r_i - r'|} + V_{xc}[n]. \quad (3.1)$$

In this equation, the external potential, V_{ext}, is a fixed, classical potential that describes contributions from ions in the system. The next two terms are a kinetic term and a modified Coulomb term, respectively, that are single particle analogues of expected many-body terms. The V_{xc} term is known as the exchange-correlation potential, which arises from the portion of the Coulomb interaction neglected in the modified Coulomb term and considering repulsive interactions between electrons that are not accounted for using the noninteracting kinetic term. The exchange-correlation potential can be defined from the exchange-correlation energy,

$$V_{xc}[n] = \frac{\partial E_{xc}}{\partial n}. \quad (3.2)$$

Within the framework of DFT, an exact functional for the density of any system is unknown, however approximate functionals have been developed with wide success. These included the local density approximation (LDA), which utilizes the exchange and correlation energies from the free electron gas, and the generalized gradient approximation (GGA), a higher-order ab initio functional that depends on both the local density and its gradient.

Generally, DFT calculations are performed by self-consistently iterating the density until some ground state property, such as the total energy, is appropriately converged. This process involves taking a trial density, solving the DFT Hamiltonian for the eigenfunctions and energies, and using the *N* orbitals with the lowest energies to define the new ground state density until the chosen ground state property is converged.[101] There are several

available codes used for DFT calculations, including Spartan described in Chapter 7, in Chapters 3, 4, and 5 the QuantumEspresso package is used.[124,125]

3.2.1 Pseudopotentials and the PAW formalism

A common approximation made in DFT calculations is the use of pseudopotentials. The electrons in any system can be categorized into core and valence electrons based on their energy. The core electrons are assumed to be unaffected by the condensed environment and do not participate in chemical bonding. Because of the non-interacting nature of core electrons, the all-electron (ae), ionic potential V^{ae} in the DFT Hamiltonian can be replaced by a pseudopotential (ps), V^{ps}. The use of pseudopotentials allows for a significant reduction in computational cost. Pseudopotentials come in many different varieties, including LDA and GGA approximations, and which electrons to include as core or valence electrons can greatly impact the calculation outcomes. Here, pseudopotentials for all elements with d-type valence states include semi-core states of s and p orbitals.

The approach used here is dependent upon determining the ground state wavefunctions from a band structure, pseudopotential based DFT code. The single electron wave functions are written as

$$\phi_j^{ps} = \phi_{nk\sigma}^{ps}(r) = e^{ikr} \sum_G C_G^{nk\sigma} e^{iGr} \tag{3.3}$$

where k is restricted to the first Brillouin zone, r is restricted to the unit cell, and the set of vectors {G} are integer units of a reciprocal lattice vector. Pseudopotentials are constructed so that the all-electron and pseudo wavefunctions are equivalent outside of some critical radius, r_c, but are inherently different within that radius as the all-electron wavefunctions include nodes and orthogonality to core-level wave functions, while the pseudo wavefunctions do not have those properties. Because X-ray spectroscopies involve transitions from, and interactions with, the core-level electrons, the pseudo wavefunctions must be transformed to all-electron wavefunctions to investigate these processes. Here, the projector augmented wave (PAW) formalism of Blöchl is used as a straightforward and accurate method for transforming between these two wavefunctions.[101]

The PAW formalism transforms the pseudopotential-based wavefunction solution φ_i^{ps} with the corresponding all-electron wave function φ_i^{ae}. Because these wavefunctions

are only different within the critical radius, r_c, a local basis consisting of radial functions $\{R_{vl}\}$ and spherical harmonics Y_{lm} can be used for this transformation. M is the standard azimuthal quantum number, l is the principle angular quantum number, and the v index allows for multiple functions per l. Radial functions are determined by solving the radial Schrödinger equation for the DFT Hamiltonian,

$$\left[-\frac{1}{2r^2}\frac{d}{dr}\left(r^2\frac{d}{dr}\right)+\frac{l(l+1)}{2r^2}+V_{ion}^{\overline{ps}}+V_{xc}\left[n^{\overline{ps}}(r)\right]\right]R_{vl}^{\overline{ps}}(r)=E_{vl}R_{vl}^{ps/ae}(r). \quad (3.4)$$

The set of energies $\{E_{vl}\}$ define the corresponding radial functions and are chosen to ensure that the PAW basis is complete for the bands of interest. The above definition of the radial functions does not enforce the orthogonality of the all-electron wavefunction, so projectors for the radial functions are defined by

$$\langle p_{vl}|R_{v'l'}^{ps}\rangle=\delta_{v,v'}. \quad (3.5)$$

The all-electron and pseudo wavefunctions are then equated by taking the overlap between the projector and the pseudo wavefunction where the calculated coefficient determines the amount of pseudo character that must be removed and the amount of all-electron character that must be included.

$$\phi_i^{ae}(\boldsymbol{r})=\phi_i^{ps}(\boldsymbol{r})+\sum_{vlm}[(R_{vl}^{ae}(x)Y_{lm}(\hat{x})-R_{vl}^{ps}(x)Y_{lm}(\hat{x}))\int_0^{r_c}d^3\boldsymbol{x}p_{vl}(x)Y_{lm}(\hat{x})\phi_i^{ps}(x+\tau_a)] \quad (3.6)$$

where $x = r + \tau_a$ is the position vector with respect to the site of the ion. Because of the pseudopotential-based DFT used here, a separate atomic DFT code is implemented for the calculation of the core-level wavefunctions.[101]

3.3 Bethe-Salpeter Equation Approach

The Bethe-Salpeter Equation (BSE) governs the time evolution of an electron-hole pair and was originally formulated for relativistic particles.[127] When an excited electron and hole pair (an exciton) moves within a condensed matter system, all of the other electrons and heavy ions in that system must be considered. Because heavy ions are several

orders of magnitude heavier, there is a significant difference between the timescales of the ionic motion of the heavy ions, the electrons, and the exciton. Because of this difference, the ionic motion can be decoupled from the electrons. Here, the ions as completely fixed, and the electronic response of the system is probed. In addition, because the hole is well-localized for core-level spectroscopies, scaling of the behavior of the exciton can be limited without losing accuracy.

3.3.1 BSE and Linear Response

The linear response of the system can be understood starting with the equation of motion of an electron-hole exciton creation operator, i.e., a destruction operator acting on an occupied core or valence state and a creation operator acting on a conduction band state. Using explicit states where $|\Psi_0\rangle$ is the many-body ground state with energy set to 0 and $|\Psi\rangle$ is an excited state with energy E,

$$\langle\Psi|[H, \hat{a}_i^\dagger \hat{a}_j]|\Psi_0\rangle = E\langle\Psi|\hat{a}_i^\dagger \hat{a}_j|\Psi_0\rangle. \tag{3.7}$$

Here H is the full many-body Hamiltonian and the subscripts {i, j} contain the necessary quantum numbers to fully describe the set of single-electron states. The initial state, i, describes a conduction state above the Fermi level and the final state, j, describes a valence or core state below the Fermi level. In a band structure formalism, the set of states {i} refers to {nkσ}, where n is the band index, k is the crystal momentum, and σ labels the spin. This equation can be expanded to give

$$\sum_{i,j} C_{ij}\left(E_i - E_j - E\right) = -\sum_{i',j'}\langle i,j|V_x - V_D|i',j'\rangle \tag{3.8}$$

where E_i and E_j are the single-particle energies of unoccupied occupied states, respectively and the direct and exchange interaction terms both involve Coulombic operators.

The overall transition rate, Γ_O, can be written

$$\Gamma_O(\omega, \mathbf{q}) = 2\pi \sum_F \left|\langle I|\hat{O}(\omega, \mathbf{q})|F\rangle\right|^2 \delta(\omega + E_I - E_F) \tag{3.9}$$

where Γ_O is the overall transition rate and $\hat{O}$ is the many-body electron-photon interaction operator. Summing over all possible excited states *F*, the transition probability, or XUV cross section, is calculated. Given the cumbersome nature of this summation and the completeness of the sum over all final states, the following equations can be used.

$$\Gamma_O(\omega, \mathbf{q}) = 2\pi \sum_F \langle I|\hat{O}(\omega, \mathbf{q})|F\rangle\langle F|\hat{O}^\dagger(\omega, \mathbf{q})|I\rangle \delta(\omega + E_I - E_F) \quad (3.10)$$

$$\Gamma_O(\omega, \mathbf{q}) = -Im[\langle I|\hat{O}(\omega, \mathbf{q}) G_2(\omega, \mathbf{q}) \hat{O}^\dagger(\omega, \mathbf{q})|I\rangle] \quad (3.11)$$

G_2 is the two-particle Green's function, which is related to BSE Hamiltonian,

$$G_2 = [\omega - H_{BSE}]^{-1} \quad (3.12)$$

where

$$H_{BSE} = H_e - H_h + H_{AM} + H_C + H_M \quad (3.13)$$

where H_e is the electron Hamiltonian, H_h is the hole Hamiltonian, H_{AM} is the angular momentum Hamiltonian, H_C is the central potential Hamiltonian and H_M is the multipole Hamiltonian. The H_e includes the electron-band energy, H_h includes the average core-level binding energy, H_{AM} includes the core-level spin-orbit and angular momentum coupling H_C describes the central potential of the core-hole and H_M includes multipolar terms.

The electron Hamiltonian is built up of Kohn-Sham orbitals and includes solid-state effects. H_e can include self-energy effects through an optional GW calculation. Within that GW correction, a quasi-particle picture of the system is adopted, and the many-body states are treated as perturbations of the non-interacting system, the many-body Hamiltonian can be divided into a single-particle and an interaction term,

$$H_e = H_0 + \Sigma = H_0 + iGW \quad (3.14)$$

where Σ is the electron self-energy operator and contains information about all interactions between the electron and the rest of the electrons in the system, H_0 is the non-interacting Hamiltonian, G is Green's function and W is the screened coulomb interaction. The electron Hamiltonian, H_e, contains information about the electron-electron interactions. Self-energy calculations are often carried out using the Kohn-Sham orbitals as a basis for the non-interacting Green's function.

An approximation for the screening of the interaction between the core-hole and excited electron is used

$$W(\mathbf{r}, \omega) \approx W_0 + \sum_{l=1}^{\infty} W_l. \quad (3.15)$$

The screened Coulomb operator can be separated into the core potential (V_c) and the short and long-ranged valence responses (W_u),

$$W_0(r) = \Delta V_c(r) + W_v^{(1)}(r) + W_v^{(2)}(r). \quad (3.16)$$

The partition of the screening operator into core and valence components allows for the positive charge of the core-hole to be considered in the core component, while the negative charge of the electron can be considered in the long-range valence component. The difference between the potential of the standard ion and the N-1 version is the core response (ΔV_c). The short-range response of the valence electrons to this core-screened potential $W_v^{(1)}(r)$ is determined by the dielectric response of the system, ϵ^{-1}, where

$$W_v^{(1)}(r) = \int d^3\mathbf{r}' \frac{1}{\epsilon^{(1)}(\mathbf{r},\mathbf{r}')} V^{(1)}(r'). \quad (3.17)$$

The dielectric response is governed by the Coulomb interaction and the polarizability of the system. The polarizability operator is a measure of how charge in a material adjusts to the presence of an external field and the simplest expression for the polarizability is the random phase approximation (RPA). The screening of the long-ranged potential is

$$W_v^{(2)}(r) = \int d^3\mathbf{r}' \int d^3\mathbf{r}'' \upsilon(\mathbf{r}', r)\upsilon(\mathbf{r}'', R)\chi_M(\mathbf{r}', \mathbf{r}'') \quad (3.18)$$

where χ_M is a function modeling the reducible polarizability of the system. The screening and the direct interaction are inversely related; the better screened the core-valence exciton is, the weaker its interaction and the smaller the binding energy.

The hole Hamiltonian is defined as

$$H_h = E_h - i\Gamma_j + \chi_j \quad (3.19)$$

where E_h is the hole binding energy, χ_j is the spin-orbit splitting and Γ_j is the life-time broadening.

The angular momentum interaction term is

$$H_{AM} = \frac{1}{2r^3}\hat{\mathbf{S}} \cdot \hat{\mathbf{L}} = \frac{1}{2r^3}\left(\hat{J}^2 - \hat{S}^2 - \hat{L}^2\right) \quad (3.20)$$

where J is the total angular momentum, S is the total spin angular momentum and L is the total orbital angular momentum. This term means that for a given edge the spin-orbit term χ_j is a matrix in the $\{m_l,\mathrm{s}\}$ basis.

The central potential term, H_C, and the multipolar term, H_M, describe interaction effects between the excited electron and core-hole using Slater F_k and G_k integrals.[128,129] Specifically, the H_C term describes electron-hole exchange while the H_M term describes the electron-electron repulsive interaction and multiplet effects.

The decomposition of these components shows how the BSE Hamiltonian can provide insight into the different effects that influence the core-valence exciton and XUV absorption spectrum. The BSE portion of the OCEAN code operates on the state vector of the system through subroutines, wherein each subroutine is a piece of the Hamiltonian. The solutions can then be projected onto the band structures. For subsequent figures and discussions in Chapters 4 and 5, the "angular momentum" describes the impact of the H_{AM} on the states, the "long range screening" term is the magnitude of the long-range screening of the core-hole by the excited electron, the "central potential electron hole exchange" term is the magnitude of the H_C acting on the states, and the "electron-electron exchange" term describes electron-electron repulsive exchange interactions and atomic multiplet effects in H_M.

3.4 Decomposition and Projection of Core-Valence Excitons

Following the calculation of the ground state X-ray spectrum, the components of the X-ray transition Hamiltonian can be decomposed. There are two ways to understand how the core-valence exciton density and the associated components are projected onto the band structure. First, equations 3.9 and 3.11 show that the transition rate and probability, and therefore the core-valence exciton density, are dependent on the k-points of the initial and final states under investigation. The transition probability between initial and final states is calculated for each k-point and then this k-space dependent core-exciton density is projected onto the band structure.

The core-valence exciton density can be further decomposed into the components of the BSE Hamiltonian The BSE portion of the OCEAN code operates on the state vector of the

system through subroutines, wherein each subroutine is a piece of the Hamiltonian. The solutions are then projected onto the band structures. For subsequent figures and discussions, "angular momentum" describes the projection of the H_{AM} subroutine operating on the final X-ray transition, the "screening" term defines the magnitude of the long-range screening of the core-hole by the excited electron, and the "exchange" term is the magnitude of the H_C subroutine acting on the transition of interest, projected onto the band structure. The "electron-electron exchange" term describes electron-electron interactions and atomic multipole effects in H_M. The k-point dependence of the transition probability and the magnitudes of these effects allows for plotting of the core-valence exciton densities directly on the band structure.

Another way to understand the projection of the core-valence exciton density and associated components onto the band structure is as follows. The core-valence exciton wavefunction, $|\psi\rangle$, is given as an expansion in the basis of Kohn-Sham states, $|n,k,\sigma\rangle$, given by the DFT calculations, where n is the valence band index, k is the crystal momentum, and σ labels the spin. The projection, D, of $|\psi\rangle$ onto the band structure for a given term of the BSE Hamiltonian, H, is given by

$$D = |\langle\psi|n,k,\sigma\rangle\langle n,k,\sigma|H_{BSE}|\psi\rangle|^2 \tag{3.21}$$

where the projection operator is $|n,k,\sigma\rangle\langle n,k,\sigma|$. The projection values are then interpolated in reciprocal-space along the paths of the band structure diagram and plotted on the band structure.

Once the core-valence exciton and individual contribution densities are calculated, the relative magnitudes of these contributions can be compared. In comparing the projections of the exciton onto the band structure of a system, the colored bubbles for the ground state calculation can be normalized and thus the size of the different bubbles can be compared to determine the relative strengths of different contributions within a single state of the system. To compare trends of these components between different states, the differential of the core-valence exciton density between the ground state and the excited states under investigation can be calculated. The magnitude of the differential compares trends between different states and determines how much different contributions change

between the ground state and excited states, thus providing information regarding the origins of measured excited state changes.

3.5 Incorporation of Transient Features

Exited state effects are included under the adiabatic approximation that the core-hole lifetime is shorter than any of the modeled optically excited state processes. Since the excited state predictions of interest in this thesis deal with electron-electron and electron-phonon scatterings that occur on the few-femtosecond or longer timescales, this assumption is valid, however it would not hold true for few cycle or attosecond effects.[121] For the excited state calculations, the valence and conduction band occupations can be modified to reflect the change in carrier occupation due to photoexcitation (Figure 3.1). For polaron calculations, the atom in one of the metal sites is replaced with an atom of one higher atomic number (i.e. Fe was replaced with Co) to introduce an additional localized electron. The system was relaxed to determine the local lattice change, and then the original atom is replaced for the final self-consistent calculation.[130–132] Within this approximation, the polaron expands the metal-oxygen and metal-metal bonds bond.[130,133] The resultant wavefunctions and lattice configurations are used as the input for calculating the XUV absorption using the OCEAN code. To model thermal isotropic lattice expansion, the undistorted unit cell was isotopically expanded, corresponding to a temperature increase from 300 K to 650 K, and the OCEAN calculation was run with the expanded lattice.[134]

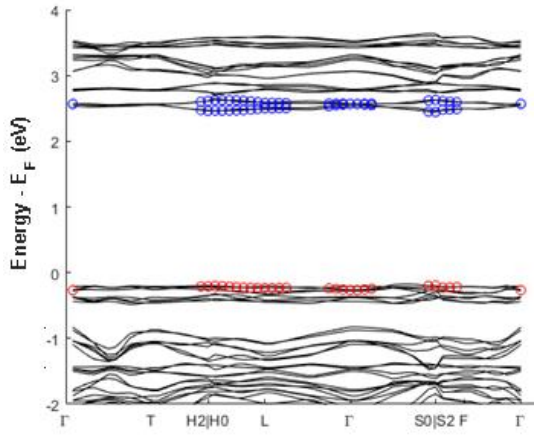

Figure 3.1 Band structure of α-Fe_2O_3 showing state filling (electrons, blue and holes, red). Modeled pump is 0.46 eV above the band edge.

3.6 Future Directions for the BSE Approach

While the underlying theoretical approach is easily extended to any K, L, M, or N edge as long as an accurate underlying DFT calculation is possible for the material, DFT

does not accurately model all systems.[113–116,135–137] In particular, DFT struggles with strongly correlated systems, specifically to accurately predict the band gap and structure of these materials.[138] These challenges are especially prescient in this thesis as the first-row transition metal studied in Chapters 4 and 5 fall into this category. Further work will involve incorporating a full GW self-energy calculation to better understand the screening and band gap renormalization effects.

The BSE formalism outlined here is restricted to the electronic response of a single core electron-hole pair, where interactions with spectator electrons are limited to the mean-field, static screening of the core-hole potential. While the charge-transfer response of the system can be approximated by changing the band structure populations as described above, inclusion of secondary charge-transfer terms in the screening is important, as a localized valence band exciton can dynamically screen the core exciton. In addition, dynamic phonon coupling can be important, especially when considering final state broadening. For example, the differences in peak widths of the e_g and t_{2g} peaks of the Ti $L_{2,3}$ edge in $SrTiO_3$ have been attributed to phonon coupling and its effect on edge broadening.[139] Addressing these issues and incorporating dynamic phonon coupling would be another area of advancement for the OCEAN code.

Given the relatively low computational expense of the underlying BSE method outlined above, the modified package that includes excited state predictions could be used to back-extract quantities from measured spectra by predicting multiple possible configurations such as time-dependent electron and hole distributions. While highly-screen semiconductors like Si or Ge have been able to quantitively extract hot electron and hole distributions as the X-ray structure resembles the unoccupied density of states, the method developed here would allow for more complex materials to be modeled.[110,111] In particular, this kind of back extraction algorithm would be especially useful in the case of complex, angular momentum split spectra and would allow for the hot carrier distributions in these types of systems to be modeled.

Chapter 4

AB INITIO PREDICTION OF EXCITED STATE AND POLARON EFFECTS IN TRANSIENT XUV MEASUREMENTS OF α-Fe_2O_3

Transient X-ray and extreme ultraviolet (XUV) spectroscopies have become invaluable tools for studying photoexcited dynamics due to their sensitivity to carrier occupations and local chemical or structural changes. One of the most studied materials using transient XUV spectroscopy is α-Fe_2O_3 because of its rich photoexcited dynamics, including small polaron formation. The interpretation of carrier and polaron effects in α-Fe_2O_3 is currently done using a semi-empirical method that is not transferrable to most materials. Here, our *ab initio*, Bethe-Salpeter equation (BSE) approach that can incorporate photoexcited state effects for arbitrary materials systems is shown to work for α-Fe_2O_3. The accuracy of this approach is proven by calculating the XUV absorption spectra for the ground, photoexcited, and polaron states of α-Fe_2O_3. Furthermore, the theoretical approach allows for the projection of the core-valence excitons and different components of the X-ray transition Hamiltonian onto the band structure, providing new insights into old measurements. From this information, a physical intuition about the origins and nature of the transient XUV spectra can be built. A route to extracting electron and hole energies is even shown possible for highly angular momentum split XUV peaks. This method is easily generalized to K, L, M, and N edges to provide a general approach for analyzing transient X-ray absorption or reflection data.

Most of this chapter has been reprinted with permission from Klein, I. M.; Liu, H.; Nimlos, D.; Krotz, A.; Cushing, S. K. *Journal of the American Chemical Society* **2022**, https://doi.org/10.1021/jacs.2c03994.

4.1 Introduction

Transient extreme ultraviolet (XUV) spectroscopy has been used to measure electron and hole populations, phonon modes, polaronic states, and charge-transfer in layered photoelectrodes – making it a new favorite tool for studying photocatalytic and photoelectrochemical systems.[76,106,109–111,140–143] The low energy (10-150 eV) and long wavelength of the XUV transition makes it more sensitive to delocalized valence states relative to soft or hard X-rays. Local structural changes can be indirectly probed, including polarons and acoustic phonons. However, the combination of this information makes the interpretation of photoexcited XUV spectra particularly challenging. Unlike molecules where orbitals are localized, solids are subject to the added complexity of cluttered band structures, core-hole screening, and other many-body effects that must be taken into account when analyzing XUV spectra.[53,90,91,102,144,145] Hard X-ray transitions are computed using a modified pseudopotential in a supercell to replicate core-hole effects, however this method is not accurate for modeling low energy XUV transitions.[94]

Hematite (α-Fe_2O_3) has become the prototypical material for transient XUV experiments because of its many photoexcited dynamics, including small polaron physics, and relevance to photocatalysis and photoelectrochemistry.[54,102–105,107,146–149] Small polaron formation traps photoexcited electrons at Fe sites, significantly limiting carrier mobilities and lifetimes.[102,150–152] Transient XUV spectroscopy has been used to evaluate how defects, nanostructuring, doping, surface decoration, and other material aspects can modulate small polaron formation to improve performance.[54,102–105,140,153] To date, these studies have all used the assumptions of a semi-empirical atomic multiplet theoretical approach, a change in oxidation state upon excitation, and polaron splitting of the 3p core level to model measurements.[102–108] These approximations are accurate for α-Fe_2O_3 because of the highly localized Fe 3d orbitals, however, this approach is not generalizable, with new models developed for each new material studied.[109–112] Real-time time-dependent density functional theory (RT-TDDFT) has also been successfully used to evaluate the dynamic behavior of α-Fe_2O_3 and other solids.[97–99]

Here, we demonstrate that the *ab initio* Bethe-Salpeter equation (BSE) approach outlined in Chapter 3 can accurately predict photoexcited changes in the transient XUV

spectra, including photoexcited electron and hole distributions, polarons, and thermal effects. The theory is used to reproduce previous results for α-Fe_2O_3, both to test its accuracy and to show that it can provide new insights into the measured dynamics from past experimental data. Our modified BSE method allows for the peak structure of the Fe $M_{2,3}$ edge to be mapped directly onto the band structure. The spectrum can be further decomposed into the components of the X-ray transition Hamiltonian to help develop a physical intuition into the origins and nature of the ground and photoexcited spectra. Going beyond previous models, we show that electron and hole energies could theoretically be extracted from an angular momentum split XUV spectrum, which was previously only possible in highly screened semiconductors.[110,111] The results in this chapter demonstrate a general and facile technique for understanding time-resolved X-ray spectra for synchrotron, table-top XUV, or free electron laser measurements. Given the complexity of these experiments, it is invaluable to be able to predict whether the excited state phenomena of interest will be measurable for a given X-ray edge.

4.2 Methods

The theoretical approach is based on modifications to the Obtaining Core Excitations from *Ab initio* electronic structure and the NIST BSE solver (OCEAN) code, as outlined in Chapter 3.[121,122] For this study specifically, several models were used for excited state calculations. For initial comparisons between the state-filling model and experimental data for α-Fe_2O_3, a 400 nm pump was used to approximate appropriate state-filling. The polaron excited state is modeled by first replacing one of the iron sites with a cobalt atom to introduce an additional localized electron, relaxing the system to determine the local lattice change, and then replacing the original iron atom for the final self-consistent calculation.[130–132] Within this approximation, the polaron expands the Fe-O bond length 0.4 % and contracts the Fe-Fe bond 1.8 %, consistent with other reports.[130,133] The resultant wavefunctions and lattice configurations are used as the input for calculating the XUV absorption using the OCEAN code (Figure B2). Given the differential measurement type calculated in this study, only the locally effected photoexcited atoms are included in the polaron model, as the background spectrum is subtracted out. We further distinguish

the polaron spectral features from thermal isotropic lattice expansion. To model thermal expansion, the undistorted α-Fe_2O_3 unit cell was isotopically expanded up to 0.8 %, corresponding to a temperature increase from 300 K to 650 K, and the OCEAN calculation was run with the expanded lattice (Figure B3).[134] In all cases, the differential transient XUV spectra are calculated, subtracting the calculated ground state spectrum from the relevant excited state spectrum. Full details of ground state and excited state calculations are provided in Appendix B.

4.3 Results and Discussion

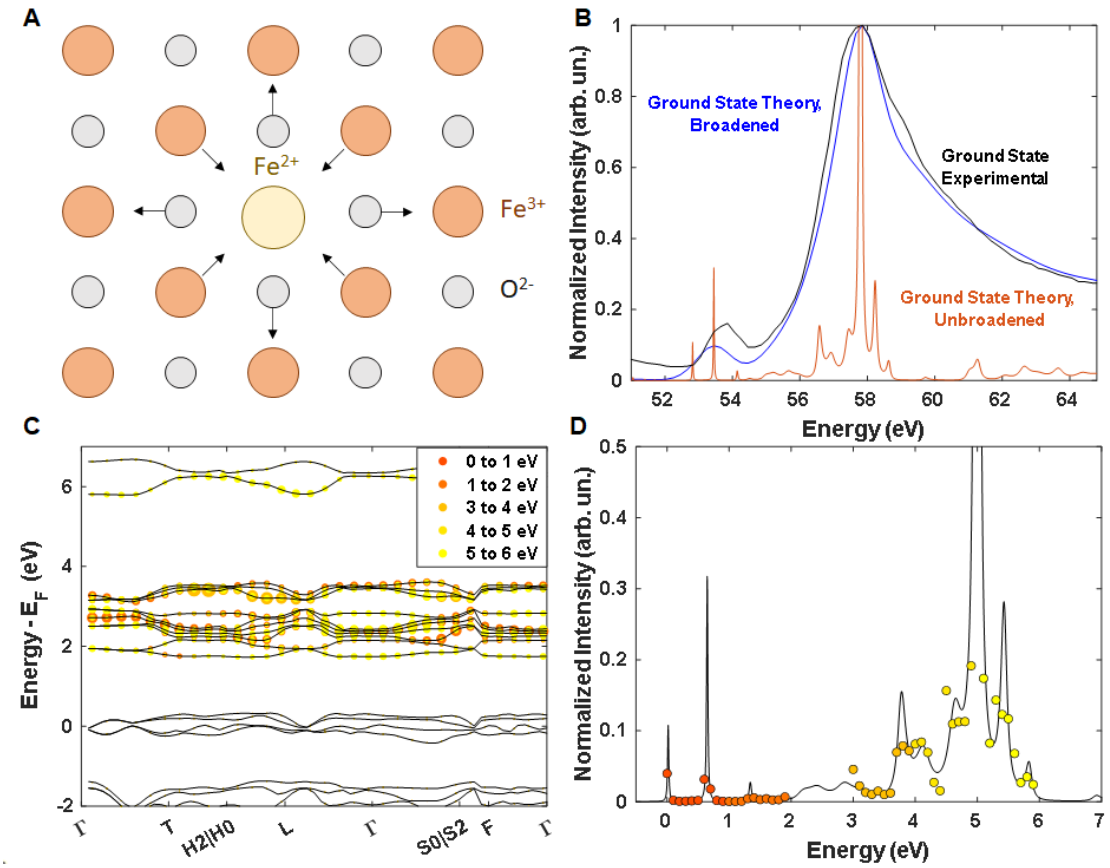

Figure 4.1 Simulation of the Fe $M_{2,3}$ Edge of α-Fe_2O_3. **A** Schematic showing how the initial excitation of α-Fe_2O_3 leads to an oxygen (grey) to iron (orange) charge-transfer transition. Electron-phonon scattering then leads to charge localization as a small polaron, locally modifying the lattice. **B** The experimental (black), OCEAN calculated unbroadened (orange), and OCEAN calculated with energy-dependent broadening (blue) spectra are compared. **C** Distribution of the core-valence exciton density in the band structure. **D** Distribution of the core-valence exciton density over the unbroadened XUV absorption spectrum (black line).

Figure 4.1a shows schematically the lattice change that occurs during small polaron formation in α-Fe_2O_3. Calculated values for the lattice distortions are provided in Appendix A. For the Fe $M_{2,3}$ edge of α-Fe_2O_3, the XUV absorption corresponds to the transition between the Fe 3p core level and the unoccupied Fe 3d DOS, as modified by interactions with the created Fe 3p core hole. Figure 4.1b shows the calculated, broadened ground state absorption spectrum of the Fe $M_{2,3}$ edge (Figure 4.1b, blue trace) as compared to an experimental measurement (Figure 4.1b, black trace). The OCEAN calculation (Figure 4.1b, orange trace) is broadened with an energy-dependent Gaussian with a high energy Fano correction for direct comparison with previous reports.[110,116] The broadening method adequately accounts for the different lifetimes of the angular momentum and atomic multiplet split peaks, as well as the Fano-type line shape of the $M_{2,3}$ edge, and is fully discussed in Appendix B.

To a first approximation, the XUV absorption spectrum should match the dipole-allowed transitions to the unoccupied Fe 3d density of states (DOS) (Figure B4). This approximation is true if the core-hole doesn't perturb the final transition state. However, the core-hole strongly perturbs the final transition state through a variety of core-hole screening, angular momentum coupling, and atomic exchange effects.[144] The core-valence exciton density for the α-Fe_2O_3 XUV absorption spectrum (Figure 4.1d) is projected onto the band structure (Figure 4.1c), where the size of the dots refers to the amplitude and the color denotes the energy range within the spectrum. Figure 4.1c and 4.1d reveal how strongly the core-hole perturbation splits the originally narrow Fe 3d conduction band into absorption peaks more than 4 eV apart, highlighting the difficulty in modeling and interpreting XUV spectra.[54]

To further understand the relationship between the band structure and the measured XUV spectrum, the core-valence exciton density can be broken down into the dominant terms of the X-ray transition Hamiltonian. Figure 4.2 shows that the XUV absorption spectrum comes from a combination, in decreasing order of influence, of spin-orbit angular momentum coupling, core-hole screening, and atomic exchange effects between the $3p^63d^5$ ground state and the $3p^53d^6$ XUV excited state.[91] The angular momentum contribution refers to the angular momentum spin-orbit coupling of the core-hole and the

valence state, the screening term describes the ability of the valence electron to screen the core-valence exciton, and exchange effects arise from the overlap between the core and valence wavefunctions in the final $3p^5 3d^6$ state. The angular momentum contribution is mainly in the middle of the Fe 3d bands and explains the splitting into two dominant peaks in the XUV absorption spectrum (Figure 4.1). The screening contribution is less pronounced and concentrated near the bottom of the conduction band, mainly between the Γ and L points. Both electron-electron and electron-hole exchange effects are minimal (Figure B13).

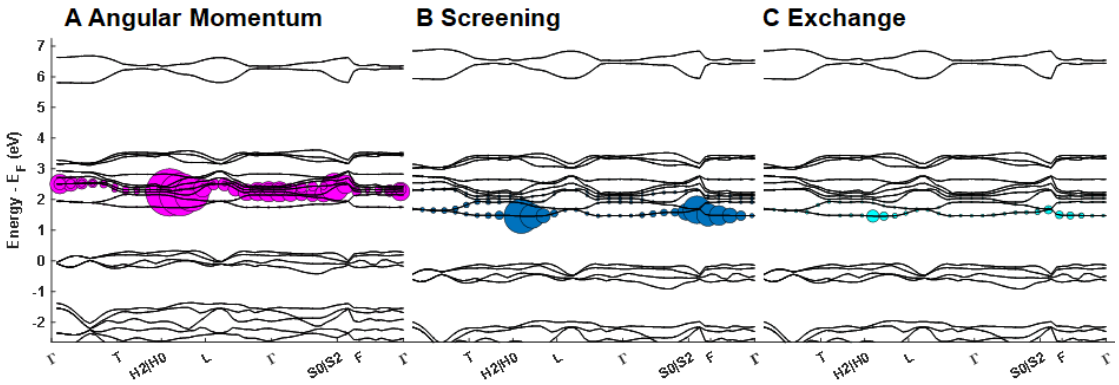

Figure 4.2 Decomposition of the Core-Valence Exciton into X-ray Transition Hamiltonian Components. The **A** spin-orbit angular momentum coupling, **B** core-hole screening, and **C** exchange components of the core-valence exciton of the ground state are normalized and projected onto the band structure. The different Hamiltonian components determine how the valence DOS is distorted into the XUV absorption spectrum by the core-hole.

Photoexcitation of α-Fe_2O_3 initiates a ligand-to-metal charge transfer between the majority O 2p valence band and the majority Fe 3d conduction bands (Figures B5 and B7). Photoexcitation changes the occupation, or state-filling, of the conduction band. Since the Fe 3d orbitals that make up the conduction band are highly localized, this process is often referred to as an effective reduction of the Fe^{3+} center to a Fe^{2+}. However, it is more accurately described as a change in state-filling, which refers to the photoexcited addition of electrons to the conduction band and the emergence of holes in the valence band. According to the X-ray Hamiltonian components shown in Figure 4.2, photoexcited electrons will decrease angular momentum splitting effects, while increasing the screening of the core-valence excitons. These changes will immediately red shift the overall XUV absorption spectrum relative to the ground state. In comparison, if small polarons and

thermal expansion dominate, there will be a change in wavefunction overlap that will mostly affect the angular momentum contributions, leading to a change in peak splitting and ordering.

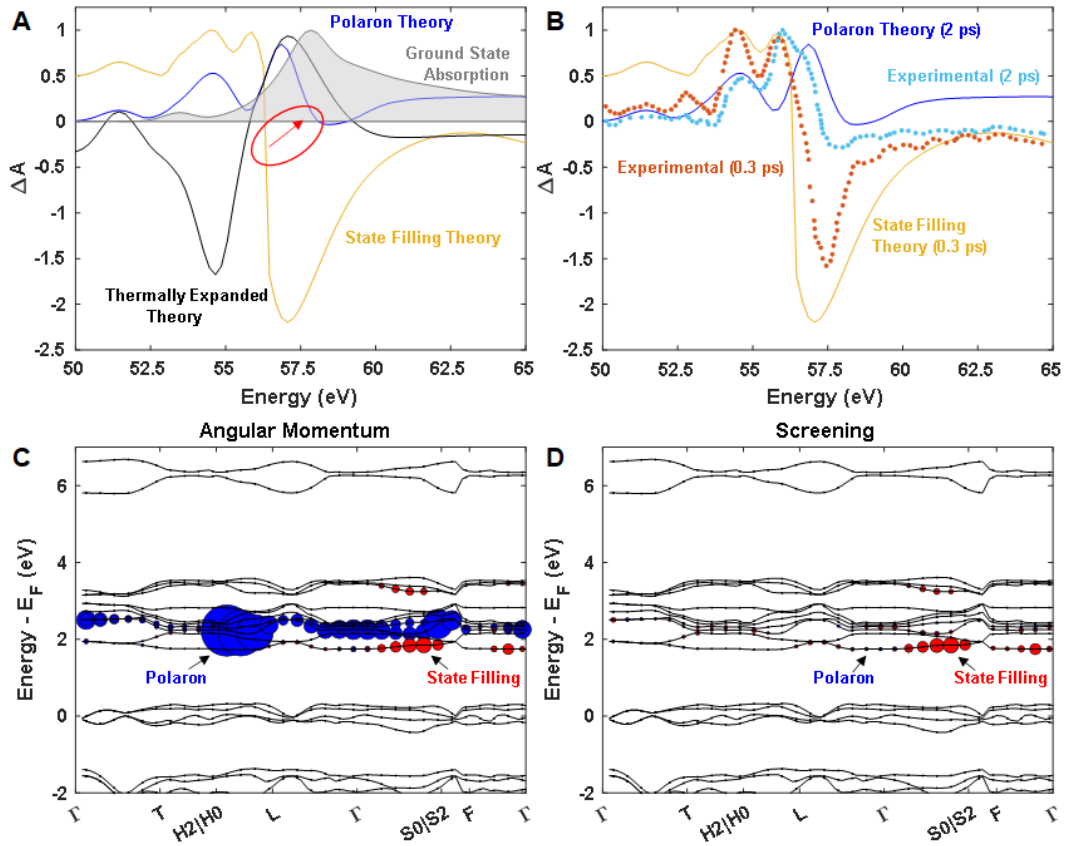

Figure 4.3. Excited State Calculations of the Fe $M_{2,3}$ Edge of α-Fe_2O_3. **A** Theoretically predicted differential absorption between the ground state and the state-filling (yellow), polaron (blue), and thermally expanded (black) states. The red circle and arrow indicate the shift of the zero-crossing commonly used to measure polaron formation. The light grey curve is the ground state XUV absorption of α-Fe_2O_3 to provide a reference of where in the spectrum the differential features arise. **B** Calculated differential absorption compared to experimental data at two time points. The calculated state-filling (yellow) and polaron state (dark blue) are shown as lines while the experimentally measured excited state at 0.3 ps (orange dots) and at 2 ps (light blue dots) from ref. 12 are shown as dots. **C** Differential plots of the change in angular momentum contributions for calculated state-filling (red) and polaron (blue) excited states. **D** Differential plots of the change in screening contributions for calculated state-filling (red) and polaron (blue) excited states.

Figure 4.3a compares the calculated differential spectra for the photoexcited, polaron, and thermally expanded states. The ground state absorption spectrum is also shown for reference of where in the spectra differential features arise. Figure 4.3b compares

the calculated differential spectra to measured experimental data from reference 102 at 0.3 ps and 2 ps, respectively, to show the accuracy of the theoretical approach.[102] The thermal differential signature is not consistent with experimental data, in particular the trace at 2 ps, further confirming the assignment of these measured dynamics to the polaron state. Including photoexcited carriers in the polaron calculation increases the magnitude of the negative feature above 57.5 eV, as shown in Figure B24. The experimental data lies in between the polaron models with and without photoexcited carriers, as in the experiment the bands are not completely filled, but fractional occupations are unable to be incorporated in the current theoretical approach.

Figure 4.3c and 4.3d show the change in the angular momentum and screening contributions to the X-ray transition Hamiltonian in the photoexcited state-filling and polaron cases, as compared to the ground state. Consistent with the intuitive understanding from Figure 2, Figure 4.3c and 4.3d show that state-filling (red) changes both screening and angular momentum components of the core-valence exciton with the same relative magnitude. The polaron state (blue), meanwhile, almost exclusively changes the angular momentum coupling. Since state-filling better screens the core-hole perturbation, the resultant spectrum is red-shifted, leading to the derivative-like features seen in Figure 3a. The change in the angular momentum coupling in the polaron state leads to a mostly positive feature that resembles the two angular momentum split peaks getting closer together in energy. The progression from a differential-like feature to a mostly positive line shape creates the signature blue-shift of the zero-crossing point (Figure 4.3a) that is used as a reference for polaron formation in literature.[102,104,105,149]

The Hamiltonian components in Figures 4.2 and 4.3 are not linearly distributed throughout the conduction band. As photoexcited carriers thermalize, the differential spectra will therefore shift and change in a nonlinear fashion, making extraction of electron and hole energies difficult. Figure 4.4 presents the differential spectra calculated for electrons occupying several energies above the conduction band minimum. Angular momentum coupling is most changed when carriers are in the middle of the conduction band (Figure 4.3c), which is best represented by the growth of the positive feature around 53 eV. Screening is increasingly changed as carriers approach the conduction band

minimum (Figure 4.3d) as indicated by the differential negative feature at 59 eV increasing in depth as the spectrum is further red-shifted, especially in the ~0.2 eV above the conduction band minimum. The nonlinear evolution seen in Figure 4.4 explains why the extraction of hot carrier distributions was believed to be impossible in the presence of strong angular momentum coupling, especially when compared to highly-screened materials like Si or Ge, where the X-ray structure resembles the unoccupied density of states.[110,111] While complex, the computational approach developed here does show that hot carriers and holes can be monitored by their unique spectral signatures. To do so quantitatively requires a back-extraction algorithm like we have used previously for ZnTe.[154] For α-Fe_2O_3, however, the polaron state forms on the timescale of the first electron phonon scattering and dominates the differential absorption, preventing such a procedure.

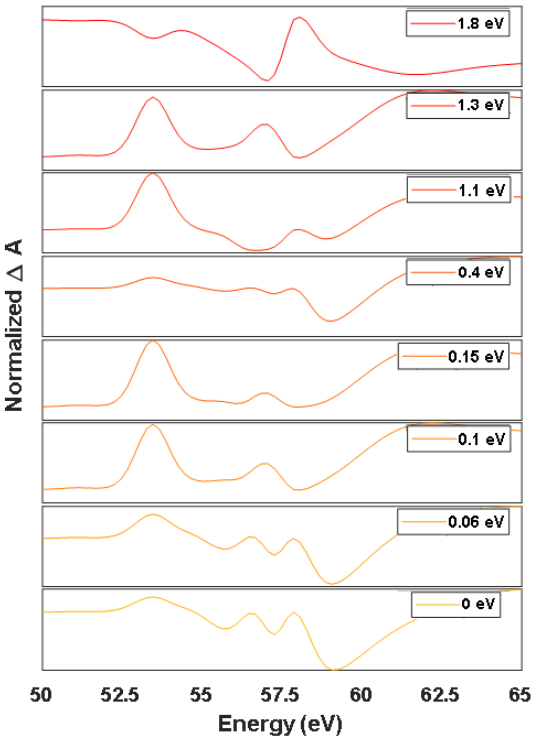

Figure 4.4 Excitation Energy Dependent Calculations. Differential spectra around the Fe $M_{2,3}$ edge of a-Fe_2O_3 following state-filling with different excitation energies above the band gap.

4.5 Conclusions and Outlook

The ab initio method developed in Chapter 3 is used to model excited state effects in the transient XUV spectra of solid-state materials. The method is verified by accurately modeling the complex photophysics of α-Fe_2O_3 and small polaron formation, one of the most studied materials using transient XUV spectroscopy. The ab initio method allows for an in-depth analysis of the XUV spectrum by projecting the core-valence exciton density and major X-ray transition Hamiltonian components on to a material's band structure. The decomposition of the XUV spectrum facilitates an intuitive understanding of the origins of

excited state changes, even in a highly angular-momentum-splitting controlled XUV absorption spectrum. If polaron effects weren't dominant, it could even be possible to extract electron and hole energies from the transient XUV spectra, using the theoretical approach outline here. The technique has obvious extension to X-ray signatures of intermediate and large polarons in other photocatalytic materials, such as those in $BiVO_4$, TiO_2, ZnO, and various perovskites. More broadly, however, the technique presents a BSE-centered, materials-independent method to interpret transient K, L, M, and N edge measurements, whether made using synchrotrons, table-top XUV spectrometers, or X-ray free electron lasers.

Chapter 5

AB INITIO CALCULATIONS OF XUV GROUND AND EXCITED STATES FOR FIRST-ROW TRANSITION METAL OXIDES

Transient X-ray spectroscopies have become ubiquitous in studying photoexcited dynamics in solar energy materials due to their sensitivity to carrier occupations and local chemical or structural dynamics. The interpretation of solid-state photoexcited dynamics, however, is complicated by the core-hole perturbation and the resulting many-body dynamics. Here, our *ab initio*, Bethe-Salpeter equation (BSE) approach is used to calculate the extreme ultraviolet (XUV) absorption spectra for the ground, photoexcited, and thermally expanded states of first row transition metal oxides – TiO_2, α-Cr_2O_3, β-MnO_2, α-Fe_2O_3, Co_3O_4, NiO, CuO, and ZnO – demonstrating the accuracy of this approach. The theory is used to decompose the core-valence excitons into the separate components of the X-ray transition Hamiltonian for each of the transition metal oxides investigated. The decomposition provides a physical intuition about the origins of XUV spectral features as well as how the spectra will change following photoexcitation. The method is easily generalized to other K, L, M, and N edges to provide a general approach for analyzing transient X-ray absorption or reflection data.

Most of this chapter has been reprinted with permission from Klein, I. M.; Krotz, A.; Lee, W.; Michelsen, J.; Cushing, S. K. *J. Phy. Chem.* **2022** (under review).

5.1 Introduction

Transient extreme ultraviolet (XUV) spectroscopy has been used to measure electron and hole populations, charge-transfer dynamics in multilayer junctions, electron-phonon coupling, and polaron state formation in a variety of materials.[76,106,109–111,140–143] The relatively low energy (10 – 150 eV) of the XUV transitions makes the core-level transition sensitive to delocalized valence states, which, while providing new insights, also adds additional complexity to interpreting measurements. The measurements of transition metal $M_{2,3}$ edges are particularly popular because they provide information about the oxidation state, hybridization, coordination geometry, and spin state of the transition metal.[54,55,106,107,145,155,156] Dipole selection rules make XUV transitions from 3p states sensitive to *d* states. This sensitivity means that lower energy XUV transitions are able to measure how the *d* orbitals influence delocalized valence interactions, while higher energy X-ray transitions are not well-suited for these investigations. XUV spectroscopy is therefore a promising route to probing the large range of phenomena that come from transition metals. Theoretical approaches to predicting ground and excited-state XUV transitions, however, are still in development, especially for solids, where complex band structures, core-hole screening, and other many-body effects can obscure the underlying carrier and lattice dynamics.[53,90,91,102,144,145]

Previous theoretical work has used a variety of approaches to model and understand measured XUV spectra. These methods have included density functional theory (DFT), wave function theory, and response and polarization propagator theories.[84] Some of these methods, including static exchange, transition potential DFT (TP-DFT), and the core-valence separation (CVS) approximation, were specifically designed for the simulation of X-ray spectroscopies. However, appropriate integration of both core-excited and valence-excited states has proven difficult.[84–88,157] Other approaches, including time-dependent DFT (TDDFT) methods, multiconfigurational wave function theory, and coupled cluster methods, are more generalizable and can be used to predict X-ray transitions.[84,90–96] Real time TDDFT (RT-TDDFT) has been used to successfully evaluate photoexcited perturbations to X-ray edges for a variety of materials, including α-Fe_2O_3 and α-Cr_2O_3.[97–100] The strength of RT-TDDFT methods is that they can determine the spectral response

from a single time propagation.[84] That said, RT-TDDFT methods are computationally expensive, which makes computing picosecond and longer timescales photodynamics or back-extracting information from measured dynamics difficult.

Transition metal $M_{2,3}$ edges challenge these methods for several reasons. The $M_{2,3}$ edges of transition metal oxides have strong angular momentum and exchange effects. A commonly used and highly successful approach for modeling the $M_{2,3}$ edge in XUV spectra has been a semi-empirical atomic multiplet theoretical approach, Charge Transfer Multiplet program for X-ray Absorption Spectroscopy (CTM4XAS).[102–108] This method has been successfully applied to transition metal oxide spectra, but the method is not *ab initio* and does not accurately capture the many-body effects that are important in solids. Incorporating excited state effects and dynamics into CTM4XAS calculations also requires assumptions about changes in oxidation state and crystal field parameters to align simulations with experiment.[93,102–107]

In this chapter, we explore the validity of a Bethe-Salpeter equation (BSE) approach for predicting the XUV spectrum of various transition metal oxides in both the ground and excited states.[158] Based on the Obtaining Core Excitations from *Ab initio* electronic structure and the NIST BSE solver (OCEAN) framework, which has previously been applied to various K and L edges,[113–116,135–137] we include new capabilities to the code that allow the XUV spectrum to be related to the underlying band structure, as well as an adiabatic approximation to include photoexcited dynamics.[158] With the given modifications, the X-ray transition Hamiltonian is decomposed into its constituent parts, shedding light on the fundamental origins of the X-ray absorption spectra. The range of calculations performed here can serve as a guide for future X-ray measurements of transition metals, as well as other complex, angular momentum coupled peaks. Moreover, these methods provide a general and accurate approach for modeling time-resolved X-ray spectra for synchrotron, table-top XUV, or free electron laser measurements.[113–116,135–137]

5.2 Methods

The theoretical approach is based on modifications to the OCEAN code, as described in Chapter 3.[121,122,158] For the state filling calculations that model photoexcitation

on short timescales, the valence and conduction band occupations are modified to reflect a change in carrier occupation at the band edges (Figures C6, C19, C32, C44, C57, C70, C82, and C95). To model thermal isotropic lattice expansion that occurs from acoustic phonons, the unit cells were isotopically expanded between 0.3 and 1.2 % (Table S3), corresponding to a temperature increase from 300 K to 650 K, and the OCEAN calculation was run with the expanded lattice.[134] This temperature range was chosen to simulate the expansion experienced by these materials following thermalization of photoexcited carriers. As reported elsewhere, polaron states can also be included in the underlying DFT calculation to predict their effect.[158] In all cases, the differential transient XUV spectra are calculated by subtracting the calculated ground state spectrum from the relevant excited state spectrum. Full details of ground state and excited state calculations are provided in Appendix B.

5.3 Results and Discussion

The rest of the chapter is divided into the following sub-sections for clarity. Initial calculations are performed to demonstrate the robustness of the OCEAN technique in modeling the $M_{2,3}$ edge XUV absorption spectra of transition metal oxides in Section 5.3.1, *Ground State Validation.* Next, in Section 5.3.2 on *Ground State Hamiltonian Discussion*, we decompose the ground state X-ray transition Hamiltonians into their constituent parts and explain how the angular momentum coupling, core-hole screening, and exchange effects underpin the XUV spectra for the transition metal oxides investigated here. The methods are extended in Section 5.3.3, *Excited State Validation*, to include photoexcited state effect. Finally, a discussion of how both the ground state and excited state Hamiltonian contributions influence the transient spectral features is undertaken in Section 5.3.4 on *Excited State Trends and Hamiltonian Discussion*. In each discussion, the relationships between physical characteristics of transition metal oxides, Hamiltonian contributions, and XUV spectral features are explained.

5.3.1 Ground State Validation

Comparisons between the measured and calculated ground state $M_{2,3}$ edge absorption spectra are shown in Figure 5.1 and highlight the accuracy of the BSE approach. Figure 5.1 shows the calculated ground state $M_{2,3}$ edge absorption spectra (dashed lines) of rutile TiO_2, α-Cr_2O_3, β-MnO_2, α-Fe2O3, Co_3O_4, NiO, CuO, and ZnO compared to experimentally measured spectra (solid lines).[102,106,109,155,159–161] VO_2 is excluded as the near room temperature phase change dynamics under thermal and optical excitation are outside the scope of this study.[162] Only an experimental reflectivity spectrum was available for α-Cr_2O_3, see Appendix C for details concerning the conversion of the calculated absorption to the calculated reflectivity.[106] No experimental data was available for comparison to ZnO. The OCEAN calculated spectra are broadened with an energy-dependent Gaussian with a high energy Fano correction for direct comparison with previous reports.[110,116] The broadening method adequately accounts for the different lifetimes of the angular momentum and atomic multiplet split peaks, as well as the Fano-type line shape of the $M_{2,3}$ edge that arises from the many-body renormalization due to the half-filled d orbitals in transition metal oxides.[163] The broadening scheme is fully discussed in Appendix C, along with the unbroadened calculated spectra (Figures C3, C15, C28, C41, C53, C66, C79, and C91).

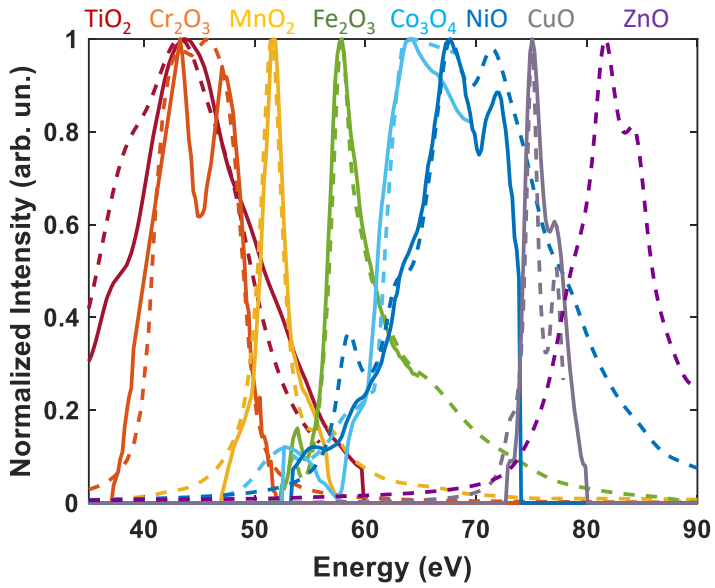

Figure 5.1. Comparing Calculated and Experimental $M_{2,3}$ Edge of First Row Transition Metal Oxides. Experimentally measured XUV absorption spectra are shown as solid lines and calculated spectra are shown as dashed lines. The different transition metal oxides are labelled above the graph in the same color as the curves to which they correspond. The experimental and calculated spectra for Cr_2O_3 are reflectivity spectra. There is no experimental data for ZnO.

A first approximation of an XUV absorption spectrum is the dipole-allowed transitions to the unoccupied 3d density of states. However, this approximation does not consider the core-hole perturbation of the final transition state. An XUV absorption spectrum (eq. 2) comes from a combination of spin-orbit angular momentum coupling (H_{AM}), core-hole screening (W), and exchange effects on the core-hole excited state (H_C) that all act to perturb the final transition DOS.[91,144] The angular momentum contribution refers to the spin-orbit coupling of the core-hole and the valence state, exchange effects arise from the exchange interaction between the core and valence wavefunctions in the final core-hole excited state, and the screening term describes the ability of the excited electron to screen the resultant core-valence exciton.[164] Combined, these components are what influence the formation of the core-valence excitons in the BSE calculation and thus the calculated spectra. Understanding these sub-terms is therefore critical to understanding the origins of the XUV spectra.

5.3.2 Ground State Hamiltonian Discussion

The OCEAN code was modified to project the magnitude of the linearly separable BSE Hamiltonian components onto the band structure. The full projections are shown in Figures C8, C21, C34, C46, C59, C72, C84, and C97, however it is more instructive to look at the relative magnitude of each component, summed across k-space. The fractional contribution of each Hamiltonian component is plotted in Figure 5.2. Moving across the 3d row, from TiO_2 to Co_3O_4, the relative contribution of the angular momentum coupling to the overall BSE Hamiltonian increases while the importance of the screening and exchange components

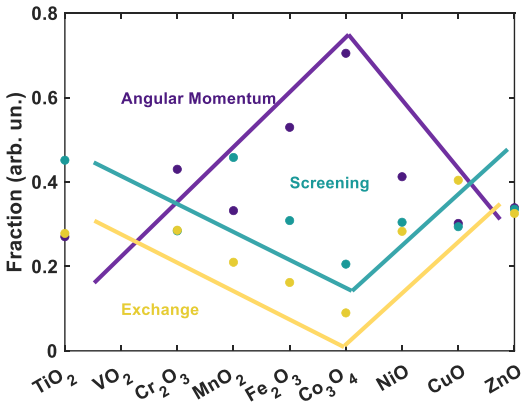

Figure 5.2. Relative Fractional Contributions of the Angular Momentum Spin-Orbit Coupling, Core-Hole Screening, and Exchange Effects on Ground State X-ray Transition Hamiltonians. Colored lines are added as a guides for the eye. These contributions elucidate the origins of ground state spectral features and help explain the observed trends in the transition metal oxide spectra.

decrease. Then, from Co_3O_4 to ZnO, these trends invert and the importance of the screening and exchange components increase while the contribution of the angular momentum coupling term decreases.

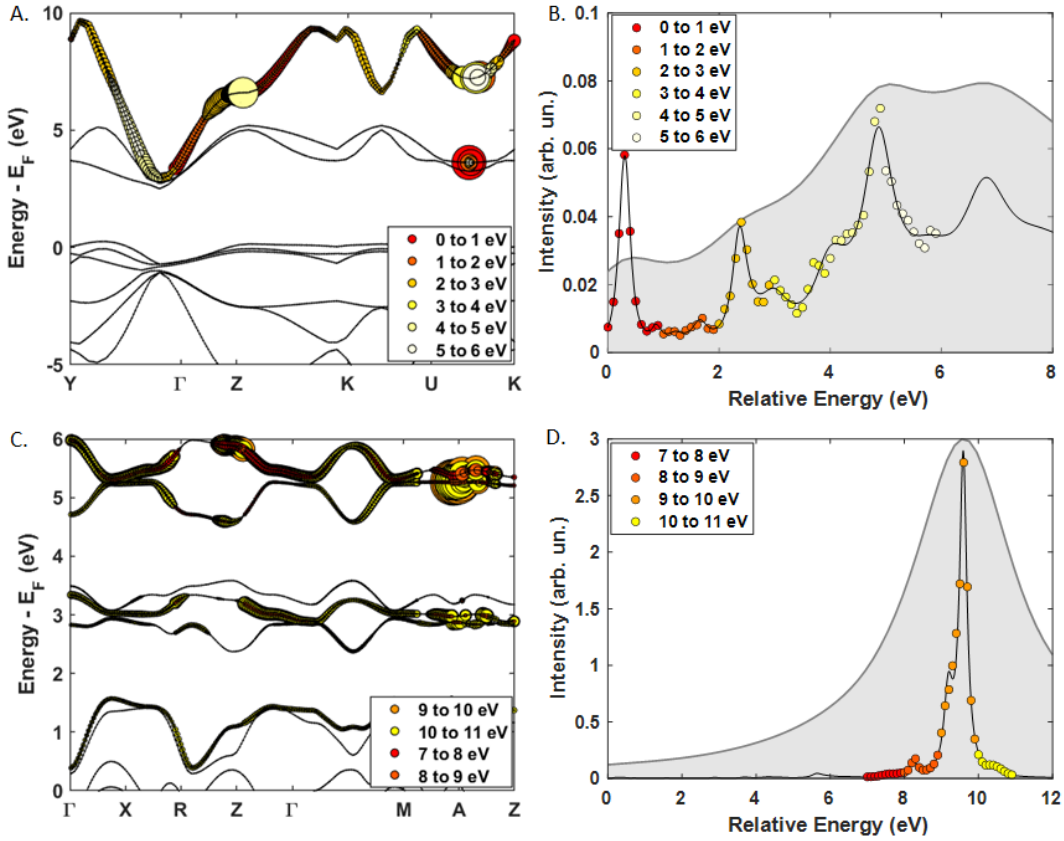

Figure 5.3. Total X-ray Core-Valence Exciton Distribution. The NiO exciton is projected onto the **A** band structure and **B** calculated XUV absorption spectrum. The β-MnO_2 exciton is projected onto the **C** band structure and **D** calculated XUV absorption spectrum. The size of the dots in **A** and **C** refers to the amplitude of the core-valence transition and the color denotes the energy range within the XUV spectra of panels **B** and **D**. The black lines in **B** and **D** are the unbroadened, OCEAN calculated spectra and the gray curve is the broadened spectra. The x axis is relative to the respective $M_{2,3}$ edge onset energies and would need to be appropriately shifted to compare directly to experiment. The projected exciton densities highlight the importance of angular momentum coupling in explaining peak splitting, or lack thereof, in calculated and measured XUV spectra.

The qualitative trends in Figure 5.2 follow the filling of the d-orbitals, flipping at the half-filled point. The trend in the angular momentum can be understood in terms of unpaired valence electrons. From TiO_2 to Co_3O_4, the number of unpaired electrons in the 3d band increases as the formal d count increases from d^0 to d^6/d^7 (Figure C102b). The increase in the number of unpaired electrons increases the angular momentum coupling

between the core-hole and valence state. From NiO to ZnO, the formal d count continues to increase from d^8 to d^{10}, leaving fewer unpaired electrons in the 3d band, leading to decreased angular momentum coupling. Angular momentum coupling is usually the dominant Hamiltonian contribution to the XUV spectra as seen in Figure 5.2.

To demonstrate the impact of angular momentum coupling, Figure 5.3 shows the energy-decomposed core-valence exciton distribution for NiO as projected onto the NiO band structure and calculated spectrum. Comparing the band structure in Figure 5.3a to the XUV absorption in Figure 5.3b shows how angular momentum coupling redistributes core-valence excitons even within a single band. The energy range of the band for NiO spans approximately 6 eV, the same energy range of the XUV spectrum. The exciton distribution within the band, however, does not correspond one-to-one to the distribution of the excitons in the XUV spectrum. The exciton redistribution highlights that the XUV spectrum is not simply the dipole-allowed density of states, especially when it comes to transition metal oxides. Underlying peaks (black trace, Figure 5.3b) are often hidden by core-hole and experimental broadening, which lead to very broad spectra (grey curve, Figure 5.3b) that may otherwise be misinterpreted. The findings for NiO can be contrasted with those for CuO (Figures C79 – 81), where the peaks in the XUV spectrum arise from transitions to different bands in the conduction band and do more closely mirror the dipole-allowed density of states. Figure 5.3 highlights the difficulty of interpreting XUV spectra without theoretical support.[54]

The trends in screening can also be understood in terms of the d-electron filling, although from a different perspective than the angular momentum coupling. As the d-states are filled, transition metal oxides in the middle of the periodic table have more localized 3d electrons and lower carrier mobilities, as compared to the unfilled or completely filled TiO_2 and ZnO that have more delocalized valence electrons and higher carrier mobilities.[165–167] Delocalized carriers better screen the core-valence exciton, reducing angular momentum splitting within the XUV spectra. In addition, from α-Fe_2O_3 to Co_3O_4 to NiO, the M-O bond covalency increases, leading to increased hybridization, and ultimately increased screening.[107] This phenomenon is seen in the spectra of β-MnO_2 (Figure 5.3d). Based on its d-count, β-MnO_2 should have strong angular momentum

splitting, like α-Fe_2O_3, but strong screening is observed through the decomposition of the X-ray transition Hamiltonian (Figure C34b). The effects of screening are apparent when the energy-decomposed core-valence exciton distribution for β-MnO_2 is projected onto the band structure (Figure 5.3c) and absorption spectrum (Figure 5.3d), and clearly result in a single peak, even before experimental broadening is considered Increased screening reduces the apparent angular momentum and multiplet splitting in the XUV spectrum as it reduces the core-valence exciton binding energy in the direct interaction.

The exchange interaction follows the trend in screening, not angular momentum, as it depends on the number of possible configurations created by exchange of the core-hole and valence-electron.[168] As the d-count increases from TiO_2 to α-Fe_2O_3, the number of possible configurations also increases. From α-Fe_2O_3 to ZnO, as the d-count continues to increase, additional valence electrons block potential configurations, decreasing the exchange effects. In contrast to screening, exchange effects act to redistribute the core-valence exciton transitions across the band structure. Even though a material like TiO_2 or ZnO may have relatively minimal angular momentum coupling, there is still a redistribution of the underlying d-orbital conduction bands in the XUV spectra due to exchange effects (see Figures C3 and C91).

5.3.3 Excited State Validation

The ground state Hamiltonian contributions allows us to form an intuition about how photoexcitation perturbs the XUV spectra. The accuracy of the excited state approximation is first verified in Figure 5.4 by comparing the initial photoexcited differential spectra measured experimentally (yellow) with simulated state filling (purple). For these materials, the photoexcited state is often modelled as a ligand-to-metal charge transfer (LMCT) state, where the electron is localized at the metal center. More accurate and generalizable, we take the approach of changing the occupation of the band structure to replicate photoexcited carrier distributions.[54,76,158] The experimental and theoretical transient XUV spectra immediately after photoexcitation (Figure 5.4) agree with good accuracy for TiO_2, α-Fe_2O_3, Co_3O_4, and NiO using this approach. The experimental (grey) picosecond timescale dynamics are also shown. The acoustic phonons created during

optical phonon decay and electron-phonon scattering on the 10's to 100's of picoseconds timescale lead to a thermally expanded lattice, the calculated differential for which is shown in the green line. In these experiments, as compared to semiconductors like Si, Ge, and ZnTe, polarons are dominant on the 1-10 picosecond timescale, so the thermally expanded spectra do not match the long timescales experimental data, but these spectra are still given for reference.[169] The predictions for all the studied materials are given in Figure 5.5, along with the calculated ground state spectra for reference.

5.3.4 Excited State Trends and Hamiltonian Discussion

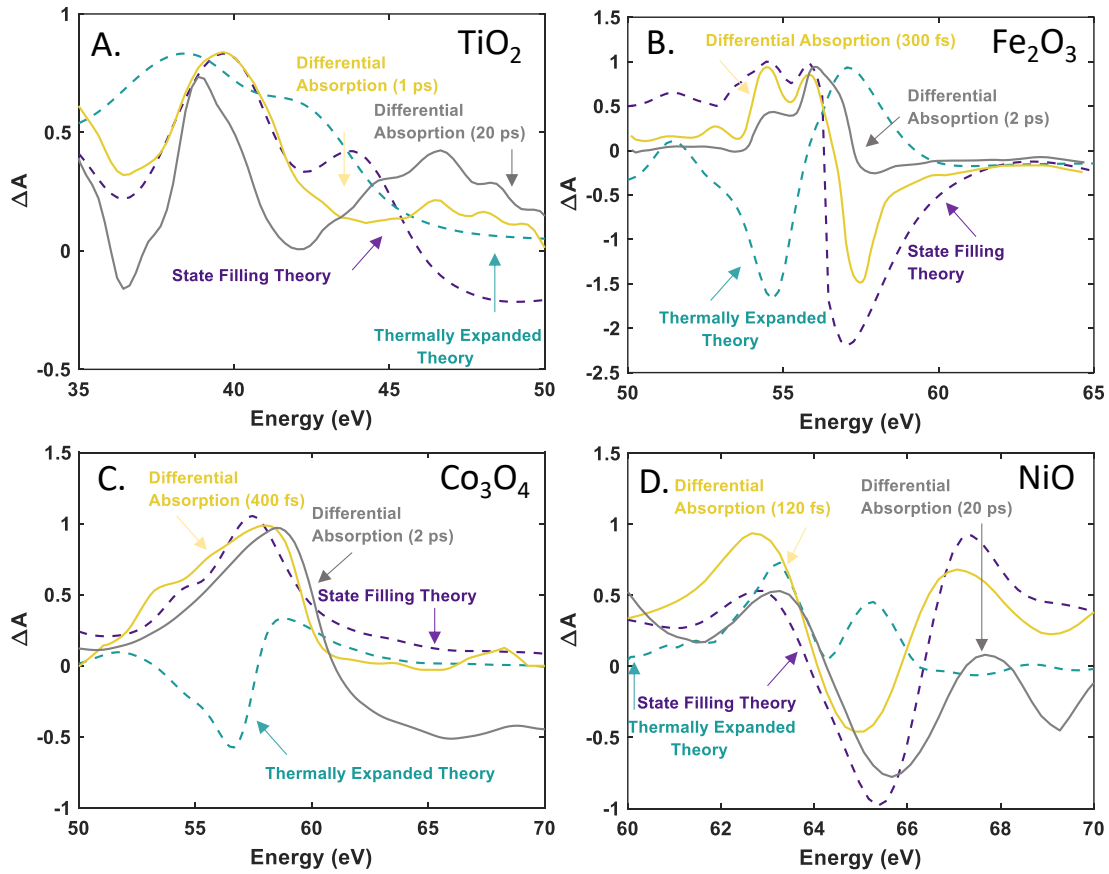

Figure 5.4. Comparing Experimental and Calculated Differential Absorption at the Metal $M_{2,3}$ Edge. Comparisons for **A** TiO_2,[1] **B** α-Fe_2O_3,[18] **C** Co_3O_4,[12] and **D** NiO[12] show the ability of the BSE approach to approximate photodynamics. Yellow curves are experimental data on short (<1ps) timescales, gray are experimental data on longer (>2ps) timescales, purple curves are state filling theory minus the ground state and green curves are thermally expanded theory minus the ground state.[1,12,18] The experimental 1 ps dynamics were used for TiO_2 as carriers generated with 266 nm pump have thermalized to the band edge for comparison with theory.

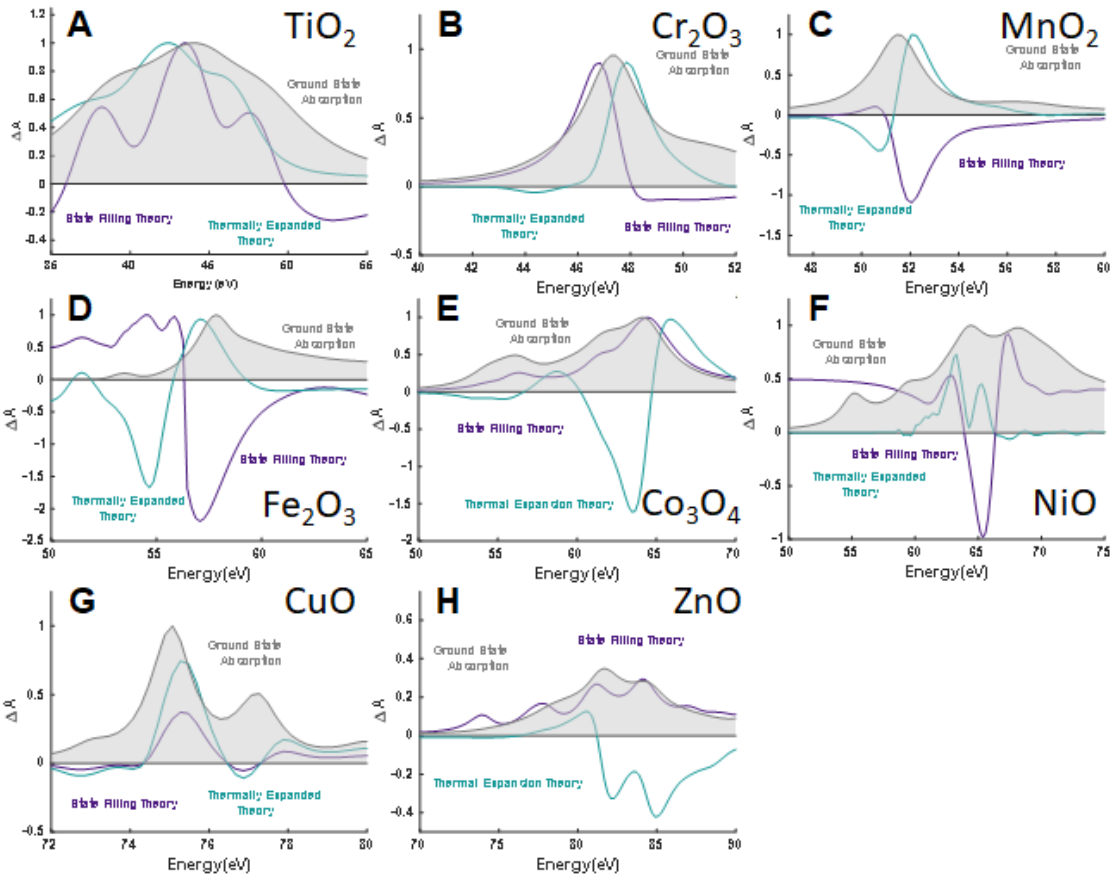

Figure 5.5. Comparing the Calculated Ground State and Differential Absorption at the Metal $M_{2,3}$ Edge. Spectra for **A** TiO_2, **B** α-Cr_2O_3, **C** β-MnO_2, **D** α-Fe_2O_3, **E** Co_3O_4, **F** NiO, **G** CuO, and **H** ZnO are shown. Grey curves are the ground states, purple curves are state filling theory minus ground state and green curves are thermally expanded theory minus the ground state.

In general, the changes in the angular momentum and exchange effects are the largest contributors to the excited state spectra (Figure 5.6a) for all compounds. The LMCT transition common to transition metal oxides is the main reason for this observed trend; as the photoexcited electron transfers from the predominantly O 2p valence bands to the predominantly metal 3d conduction bands, the number of unpaired electrons changes, perturbing the peak splitting. From d^0 to d^{10}, adding an extra electron to the 3d band has a decreasing impact on the core-hole screening (Figure 5.6a). Meanwhile, adding the extra electron has an increasing effect on the angular momentum coupling and exchange interactions with increasing d-orbital occupation. Unsurprisingly, the exchange interaction becomes a dominant term in the excited state because of the change in the possible configurations. Combined, the interplay of increased angular momentum coupling and

exchange interactions versus decreasing screening leads to the observed photoexcited peak shifts and splitting in Figure 5.5 (purple traces) and the overall negative to positive center of mass peak shift trend upon photoexcitation shown in Figure 5.6c. For example, when the angular momentum coupling contribution is large and increases with photoexcitation, and the screening is small, such as for Co_3O_4, photoexcitation predominately changes peak splitting. The increase in splitting can appear as an overall increase in absorption, even when a state blocking model would suggest a decrease in peak absorption. This finding is why an oxidation state picture is not always correct for photoexcitation.

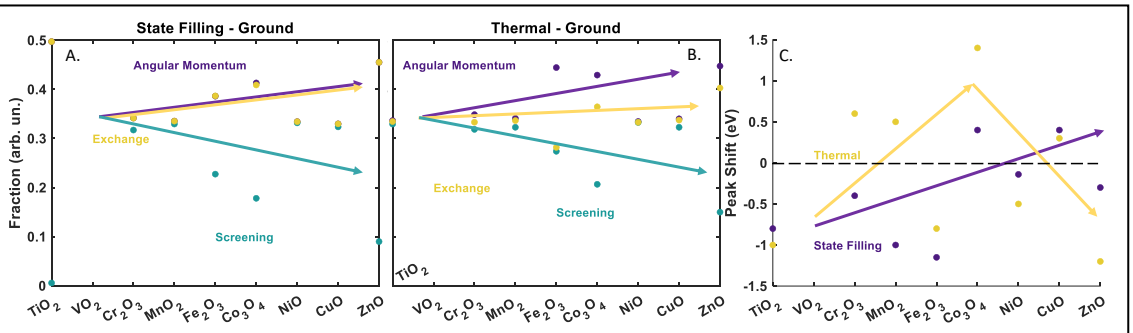

Figure 5.6. Differential X-ray Transitions. Fractional differential contributions to the X-ray transition Hamiltonians for the **A** state filling and **B** thermally expanded states. Colored lines are added as a guide for the eye to demonstrate the observed trends in the changes in the BSE exciton components. These contributions help explain the observed excited state spectral features and trends for first row transition metal oxides. **C** Center of mass peak shifts for state filling and thermally expanded spectra relative to the ground states. Colored lines are added as a guide for the eye.

Some special comments should be made about the observation of state filling effects. In most materials studied to date with delocalized valence states – Si, Ge, ZnTe – an increase or decrease in absorption is measured because X-ray transitions are blocked or allowed due to changes in the photoexcited carrier distribution in the band structure.[110,141,142,170] In all these predicted compounds, however, the change in angular momentum and exchange effects dominate the photoexcitation, distorting the XUV spectra, and acting to block the creation of distinct state filling trends. Instead, the energy and carrier density must be judged by the overall spectral shift and the increase or decrease in peak splitting and amplitude, depending on the material. ZnO and TiO_2 are of particular interest because, while they have highly mobile carriers, they experience the largest change in angular momentum coupling from photoexcitation because there are no unpaired

electrons in the ground states of these materials. While exchange effects and angular momentum coupling played a small role in the ground state spectra (Figure 5.2), these components dominate the changes in the photoexcited spectrum (Figure 5.6a). Resultantly, a negative shift of the overall spectra is the only indicator of the excitation energy and carrier density, and the extraction of electron and hole energies versus time would have to be extracted by calculating the XUV spectrum at each time point.

The change in the XUV spectrum after thermal expansion follows a different trend than the photoexcitation. Again, however, the observed trend is not surprising as the d-band filling remains unchanged, so the trends should mimic the ground state Hamiltonian (Figure 5.2) as they do (Figure 5.6b). Instead, the dominant effect in thermal expansion is that the decreased metal-ligand wavefunction overlap will lead to more localized d-states and a smaller crystal field. Accordingly, angular momentum coupling will dominate as screening and exchange interactions decrease (Figure 5.6b). Again, thermal expansion in these materials leads to a counterintuitive trend as compared to the delocalized semiconductors measured in the past (Si, Ge, ZnTe).[110,141,142,170] In these materials, heating leads to a decreased bandgap and the spectra have been measured to redshift as a result. However, as the thermally expanded transients in Figure 5.5 and the center of mass peak shifts in Figure 6c show, the dominant change in angular momentum coupling leads to complex spectral features that do not always follow the redshift seen in traditional semiconductors. This finding highlights the importance of not making assumptions when analyzing measured spectra as the measured spectral signatures could be falsely assigned.

5.4 Conclusion

There are several key takeaways from this study. First, a Bethe-Salpeter equation approach is proven a facile method for calculating the challenging M edges of the transition metal oxides. This study supports the universality of our excited state approximation, as proven in previous studies on simpler semiconductors like Si, Ge, and ZnTe. The underlying DFT calculation allows easy inclusion of phase changes, polarons, and other structural dynamics into the excited state calculation while the changes in state filling are addressed in the BSE stage. Further work will involve incorporating a full GW self-energy

calculation to better understand the screening and band gap renormalization effects. Moreover, decomposing the X-ray transition Hamiltonian into its fundamental components and projecting it onto the band structure gives a physical intuition for the otherwise complex XUV spectra. The methods used here should be generalizable to higher energy X-ray edges and therefore prove powerful for understanding tabletop, synchrotron, and X-ray free electron laser experiments.

Section II

Polymer Mechanochemistry

Chapter 6

LASER-INDUCED CAVITATION MECHANOPHORE ACTIVATION

The emergent field of polymer mechanochemistry uses mechanical force to initiate productive chemical reactions in molecules termed mechanophores. Mechanophores can be embedded in polymer chains and then the polymer chains are used to transduce force to the mechanically sensitive moiety. These systems have both fundamental and applied impacts across fields ranging from organic synthesis and soft materials to theoretical chemistry. Of particular note are the numerous novel small molecule reactivities that have been demonstrated with mechanical force. Reactions that proceed through concerted mechanisms under thermal and photochemical inputs may proceed instead through multistep mechanisms when initiated with mechanical force. Certain electrocyclic ring opening reactions have been shown to proceed through formally disallowed disrotatry pathways under mechanical activation. Although the outcomes of these reactions have been demonstrated experimentally, the force-modification of reaction potential energy surfaces has only been computationally investigated. The lack of spectroscopic probes into these reaction dynamics is partially due to the lack of a spatiotemporally controllable activation method. Here, we introduce a method of triggering mechanophore activation using laser-induced cavitation to apply force to the mechanophore with spatial and temporal resolution. The proof-of-concept for this method is demonstrated with the fluorescent anthracene-maleimide mechanophore and is then further refined, optimizing the lens focal length, solution temperature, and irradiation intensity for activation. Ultimately, the kinetics of laser-induced cavitation activation are shown to be the same as ultrasound activation, further validating the use of this method to activate polymer-embedded mechanophores. Eventually, this activation method could enable time-resolved spectroscopic investigations of mechanophores.

6.1 Introduction

There are several different mechanophores, or molecules that undergo productive chemical reactions under mechanical stress, that demonstrate previously unobserved reactivities, including *gem*-dihalocyclopropanes, benzocyclobutenes, and ladderenes. Thermal and photochemical electrocyclic ring-opening reactions of cyclopropanes and cyclobutanes proceed through concerted processes, whereas the mechanochemical ring-opening of *gem*-difluorocyclopropanes (gDFC) and ladderenes have been shown to proceed through multistep, diradical mechanisms.[37,44,171,172] Additionally, the mechanochemical reactions of both *gem*-dichlorocyclopropanes (gDCC) and benzocyclobutenes (BCB) produce reaction products that are formally thermally forbidden by the Woodward-Hoffman rules. *cis*-gDCC produces the thermally disallowed conrotatory product and *cis*-BCB gives the thermally disallowed disrotatory product under mechanochemical activation.[45] The *trans*-gDCC and *trans*-BCB, however, both produce thermally allowed products. These mechanophores experimentally demonstrate that mechanochemical activation is inherently distinct from thermal and photochemical activation and requires further investigation to understand.

The fundamental interest in mechanophores is therefore not just in their application to materials development and polymer science, but also in how a reaction in a stressed reference frame will differ from one in the non-stressed state. Depending on the direction of the force relative to the reaction coordinate, the potential energy surface is predicted to be lowered, tilted, or even bifurcated.[173] These reaction kinetics are predicted to occur on a picosecond or quicker timescale.[174,175] The force is also applied on the order of picoseconds, such that the application of stress and the reaction occur on similar timescales.

Only time-averaged methods have previously been used to experimentally investigate mechanochemical mechanisms, including radical trapping studies.[44,171] A variety of computational work has gone into elucidating these mechanisms as well.[176,177,177–179] Time-resolved spectroscopy is needed to measure the kinetics and electronics on the timescales of chemical reactions, but pump-probe experiments have yet to be expanded to mechanochemically-initiated systems. Femtosecond laser measurements are required to measure chemical kinetics on these timescales, but an optical transition

leads to dynamics on the excited state potential energy surface, whereas the applied force acts on the ground state potential energy surface. Additionally, the optical absorption of the mechanophores and intermediates overlap in the UV region, such that separating the kinetics of the different states can prove difficult using UV or visible probe beams.[180,181] Even in the classic case of a mechanochemical ring opening of benzocyclobutene, neither the mechanical change in the transition state, nor the difference between the transition states for the *cis*- and *trans*- isomers has been measured. To study any transition states and possible intermediates of mechanochemical reactions, pump-probe spectroscopy of mechanophores must be developed. To date, no time-resolved studies have been able to probe these dynamics, primarily because the activation methods currently used in polymer mechanochemistry do not lend themselves to time-resolved investigations.

6.1.1 Cavitation Activation of Mechanophores

The most widely used activation methods are ultrasonication and single-molecule force spectroscopy (SMFS).[17,104,153,164,165,171–17] Ultrasonication of polymer solutions leads to acoustic cavitation, during which the collapse of transiently formed bubbles generates elongational flows that exert force on the polymer chain, activating the embedded mechanophore (Figure 6.1). These collapsing bubbles subject the mechanophore-containing polymer chains to solvodynamic shear forces. A velocity gradient exists along the backbone that elongates the polymer until it is under tension, exerting force on the polymer and thus the embedded mechanophore, activating it.[182] This technique probes ensemble behavior, as the composition of these solutions can be characterized with gel permeation chromatography (GPC), NMR and optical spectroscopies. A useful way of confirming the mechanochemical reactivity of a cleavable mechanophore is to measure both the change in molecular weight and the change in absorption or photoluminescence over the course of a sonication experiment as compared to these changes in a chain-end control system. If the mechanophore only reacts under mechanical force or stress, then the chain-centered system will show mechanochemical activity, while the chain-end system will not, because the force is concentrated in the chain-center, not at the chain-end. Ultrasonication is facile and allows for high throughput experimental validation of

mechanophores and mechanophore behavior.[183,184] SMFS, alternatively, offers precise control over force exerted on single polymer chains and thus single mechanophores. Alternative activation methods include powder milling, extruding a melt, exerting tension or compression on a film, and using high-intensity focused ultrasound (HIFU).[184,185]

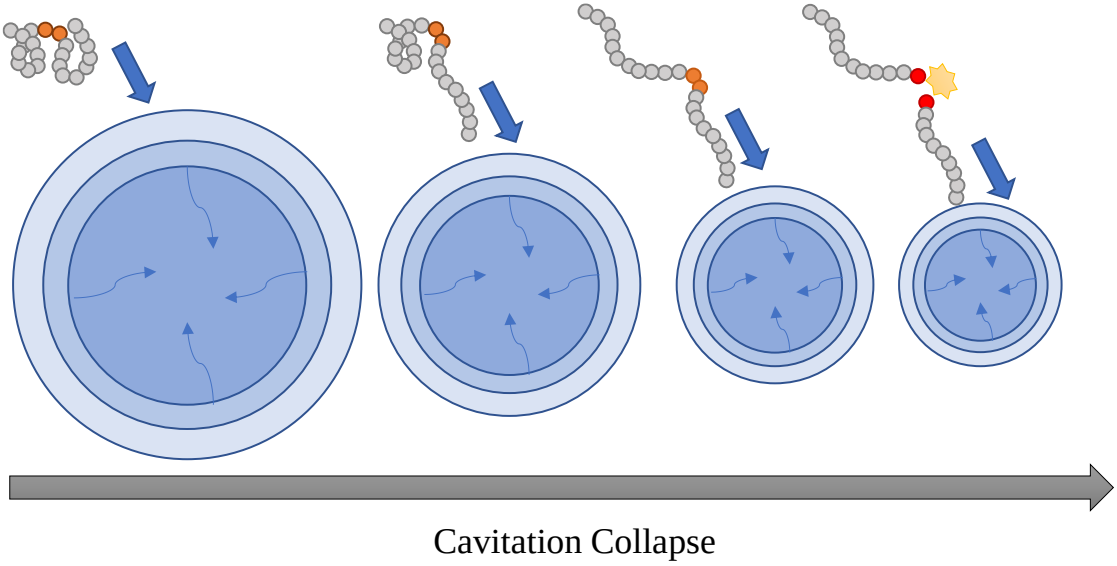

Figure 6.1 Cavitation activation of polymer chain-centered mechanophores. As the cavitation bubble collapses (blue), one end of the polymer chain is elongated more rapidly than the other, which exerts solvodynamic shear forces on the polymer backbone (grey beads). Those forces are concentrated in the center of the polymer chain where the mechanophore is located (orange beads), eventually leading to mechanophore activation (red beads).

While all these methods have been invaluable in the development of the field of polymer mechanochemistry, an activation method that has spatial and temporal resolution is needed to enable time-resolved measurements of these reactions.[186] Laser-induced cavitation bubbles have the advantage of temporal and spatial specificity, as well as increased control of bubble properties compared to ultrasonication.[186–197] Laser-induced breakdown is a non-linear absorption process that can occur in gases and liquids. After surpassing a breakdown energy threshold, a high peak power laser pulse irradiating a liquid or gaseous sample will form a plasma through the ionization of the media via multiphoton absorption or electron cascade processes. Liquids concentrate the laser pulse, creating the field amplification effect that lowers the breakdown threshold.[198] Once the plasma has been generated, it absorbs visible radiation much more strongly than the transparent media in which it was formed, thus rapidly heating the sample to ~ 10^4 K, just as with ultrasonication

induced cavitation.[187,199,200] At these high temperatures, the plasma continues to expand and vaporizes the liquid surrounding it, creating a cavitation bubble centered on the breakdown site. When the plasma starts to decay and the sample cools, the internal pressure is reduced and the vaporized liquid condenses, leading to cavitation bubble collapse.[191] The breakdown threshold depends on the ionization potential and the refractive index of the medium.[190]

The properties of a laser-induced breakdown based cavitation bubble and an acoustically-generated cavitation bubble are extremely similar, and because of these similarities, laser-induced cavitation can be used to initiate mechanochemical transformations in polymer chain-centered mechanophores.[187] Laser-induced cavitation also has the potential to increase control over the spatial, temporal, and force properties of cavitation bubble collapse and mechanophore activation, lending itself to potential use in time-resolved pump-probe investigations of mechanophores.

Herein, we report on the development of a laser-induced cavitation method for activating mechanochemical transformations and evaluate the ability of this method to trigger activation of an anthracene-maleimide (AM) mechanophore embedded in poly(methyl acrylate) (PMA) through mechanical deformation. Laser-induced cavitation was able to achieve upwards of 30% mechanophore activation in 20 minutes, on par with traditional ultrasonication methods.[201] The goal of this project was to develop a spatiotemporally resolved method of activating mechanophores such that transient XUV measurements of these molecules could be explored. Although these aims were ultimately not achieved, the findings presented here demonstrate the feasibility of using laser-induced cavitation to initiate mechanochemical reactions in polymer chain-centered mechanophores. As an intermediate step towards time-resolved XUV measurements on mechanophores, attempts were made to use this method to study these reactions with transient fluorescence and absorption in the visible range. While the bubble dynamics were investigated using spatial transmittance modulation, the mechanochemical dynamics proved elusive.[202] Efforts towards this goals are reported and potential future directions are considered. Ultimately, this method is the first step in the development of time-resolved, pump-probe spectroscopic studies of mechanophores.

6.2 Methods

The samples used in this study were prepared according to previously reported synthetic procedures (Scheme 1).[203,204] Briefly, commercially available 9-(hydroxymethyl)anthracene and *N*-(hydroxyethyl)maleimide were reacted to form the Diels-Alder dihydroxy compound **1**. An esterification with 2-bromoisobutyryl bromide installed polymerization initiator groups on each terminus to form bis-initiator **2**. Polymerization of methyl acrylate yielded poly(methyl acrylate) polymer **3** with the anthracene-maleimide Diels-Alder adduct mechanophore located at the chain center. The control **4** was formed in an analogous fashion employing *N*-methylmaleimide to produce a chain-end instead of chain-centered mechanophore.

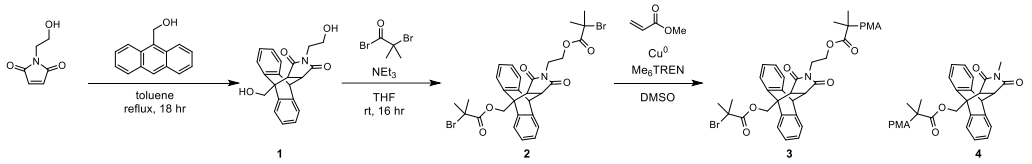

Scheme 6.1 Synthesis of chain-centered anthracene-maleimide mechanophore in poly(methyl acrylate)

First, we investigated how varying the experimental parameters, including irradiation time and power, polymer chain length, focal length, and solution temperature, affected the mechanochemical activation resulting from the cavitation bubbles. Once the test material **3** was prepared, approximately 3 mL of solution was placed inside a cuvette in a Quantum Northwest Flash 300 temperature-controlled cuvette holder. The cuvette holder and cuvette were in the beam path of an 800 nm, 1 kHz, 13 W Coherent Legend Elite Duo laser system. The beam used in these experiments was attenuated to sub-200 mW to prevent cuvette damage or excessive heating and then focused with a spherical lens into the sample solution. The sample was irradiated and the photoluminescence of the anthracene, the result of mechanophore activation, was measured using a Shimadzu RF-6000 spectrofluorophotometer with a quartz microcuvette (Starna 18F-Q-10-GL14-S). Each of the test parameters – irradiation time, beam power, polymer chain length, lens focal length, and solution temperature – were varied to determine the correct baseline parameters to use. The same studies were executed for chain-end control system. Finally,

a kinetic study was performed using a 210 kDa polymer held at 2 °C and irradiated with 110 mW of power focused with a 5 cm focal length lens, where samples were taken every few minutes to track the anthracene generation due to mechanochemical activation.

Following the static investigation of the ensemble dynamics described above, attempts were made to study the time-resolved dynamics of mechanophores using laser-induced cavitation. The pump beam was the same as previously described. The probe beam, a 349 nm, <5ns, 60 mW Spectra-Physics Explorer One laser, was triggered using a TTL pulse from a pulse generator, electronically delayed relative to the pump laser pulse. The delay could be varied from ~1 ns up to ~100 ms to cover all relevant timescales. To probe the bubble dynamics, a spatial transmittance modulation technique was used, as previously reported, where a change in the optical transmission of a CW probe beam generated by the cavitation bubble itself is measured.[202] The bubble probe beam was a CW, 632 nm HeNe. The 800 nm pump, 349 nm mechanophore probe and the 632 nm bubble probe beams were aligned colinearly, with overlapping focal regions. The spatial modulation of the HeNe was measured using a Si photodiode placed directly after the cuvette, while changes in the fluorescence due to 349 nm irradiation were collected perpendicular to the initial beam path and measured with a GaP photodiode.

6.3 Results and Discussion

Initially, to demonstrate both the feasibility of laser-induced cavitation for mechanochemical activation and the selectivity of laser-induced cavitation for chain-centered rather than chain-end mechanophores, a polymer length activation trial was undertaken (Figure 6.2). The activation of chain-centered mechanophore polymers of 210 kDa and 55 kDa with laser-induced cavitation was compared to the activity of a chain-end mechanophore, irradiated for 30 minutes at 2ºC with 100 mW of 1 kHz, 800 nm light. The photoluminescence data shown in Figure 6.2 demonstrates that both the mechanophores embedded in the 210 kDa polymer and those embedded in the 55 kDa polymer system activate more strongly than the chain-end mechanophore. While the PL data appears to demonstrate that the 55 kDa system is more active than the 210 kDa system, it is important to note that the 210 kDa system has approximately a quarter of the mechanophore

concentration as the 55 kDa system. Taking the difference of mechanophore concentration into account, the 210 kDa polymer in fact reaches nearly twice the activation efficiency of the 55 kDa system and at least six times that of the control.[201] The control signal does not display the characteristic anthracene peak shape and is at such a low intensity as to not be statistically resolvable within the signal-to-noise ratio of the instrument. These findings are consistent with previous work on chain-centered mechanophores, which has shown that mechanophores embedded in longer polymer chains activate at a faster rate. In addition, the control studies demonstrate that laser-induced cavitation does not activate the control through passive heating or radical generation.

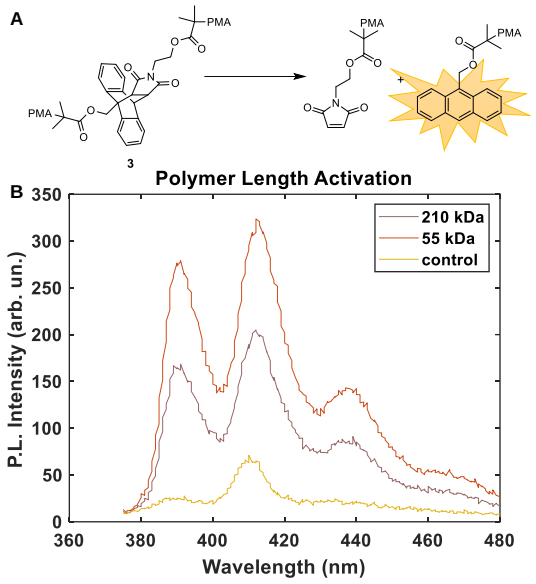

Figure 6.2 Laser-induced cavitation activation of PMA-AM-PMA samples. **A** Mechanophore and activation reaction investigated here. **B** Initial studies showing the difference in activity between a control small molecule, a 55 kDa polymer sample and a 210 kDa sample.

Following confirmation that laser-induced cavitation effectively activates chain-centered mechanophores, the parameters of laser-induced cavitation were tuned to increase the amount of mechanochemical activation observed. As the irradiation intensity was modulated from 90 mW to 130 mW, an increase in activation from 90 mW to 120 mW, is observed and a decrease in activation with a 130 mW beam relative to the 120 mW beam was measured (Figure 6.3a). Increasing the irradiation intensity for laser-induced cavitation experiments with a chain-end control showed a slight increase in the amount of anthracene generated through mechanophore cleavage, without changing the activation of control (Figure 6.3b). The initial increase in activity as the pump pulse increases in energy is intuitively consistent with the understanding that more energy in the focus increases the number of cavitation events occurring, which in turn increases the number of mechanophores that can be activated with each pulse. The reversal in this trend when the

energy is increased from 120 mW to 130 mW may be due to several factors, including threshold power, super heating, and mechanophore destruction.

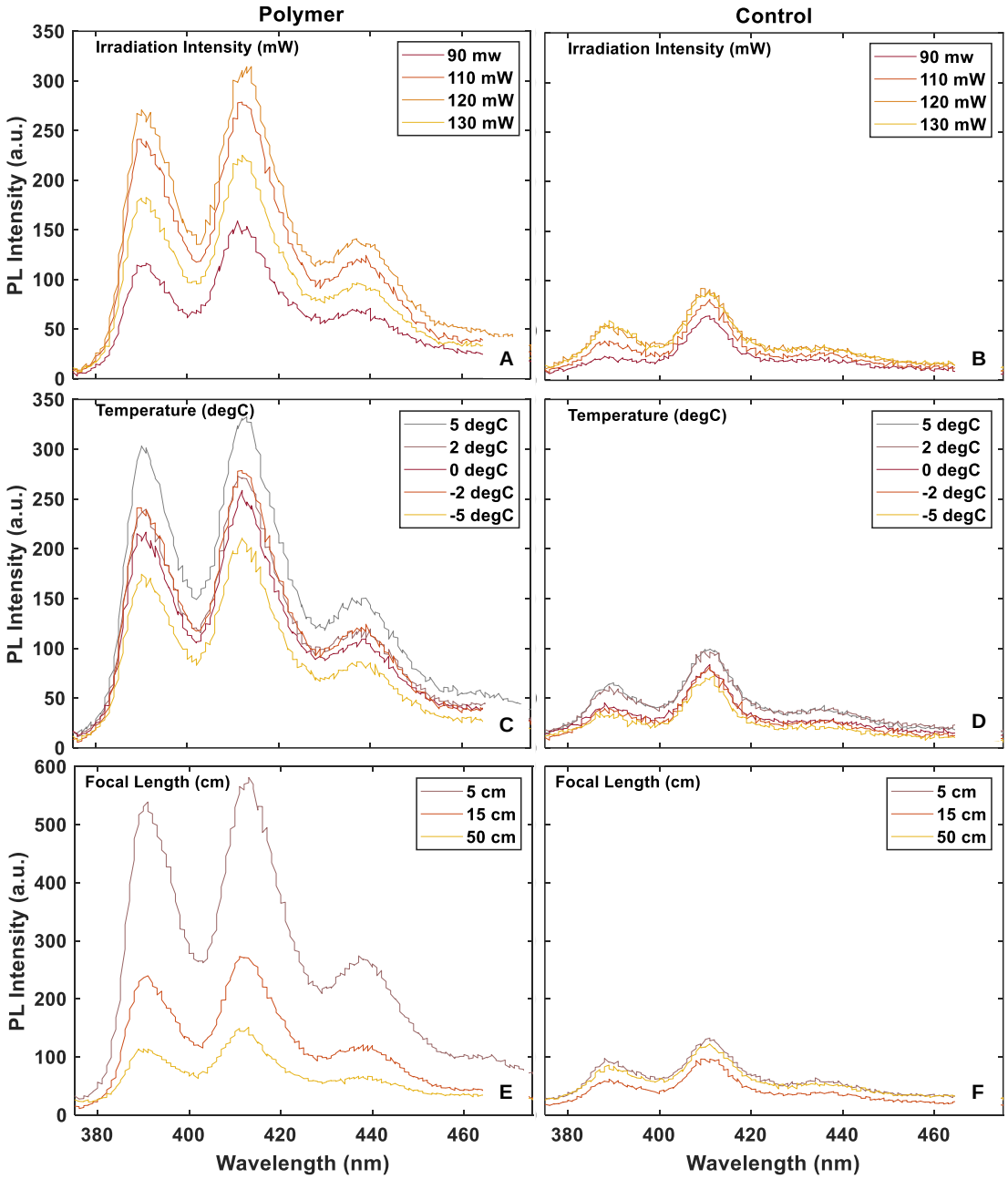

Figure 6.3 Parameter testing for laser-induced cavitation mechanophore activation. Investigating the effect of irradiation intensity on **A** polymer samples and **B** small molecule controls shows that activation does not continuously increase with increasing irradiation intensity. For solution temperature, the colder solutions show less activation in **C**, but does not appear to have an impact on the control samples in **D**. The most drastic impact of activation parameters is the lens focal length. For mechanophore samples in **E**, the shorter focal length lenses lead to higher leaves of activation. The control sample, however, does not appear to be impacted by lens focal length, **F**.

Modulation of the solution temperature over the course of irradiation showed that higher temperatures facilitated mechanophore cleavage. Going from 5 °C to -5 °C decreased the generated anthracene content in the chain-centered solution by almost 50 %, while the chain-end control was modulated less than 20 %, as shown in Figure 6.3b and c. The higher activity of the chain-centered mechanophore regardless of the solution temperature further confirms that the measured anthracene is being generated predominantly through mechanochemical activation and not passive heating. That said, mechanochemical activity, and the force required to initiate mechanochemical reactions, does depend on the temperature. This temperature dependence may be due to the effect of environmental temperature on the activation energy and the relationship between activation energy and mechanical force required to initiate a mechanochemical reaction.[183] Numerous computational studies have shown that applied force fundamentally alters the potential energy surfaces of the mechanophores, making the chemical reaction pathways barrierless at threshold forces.[176] Some studies have suggested that the applied force does not fundamentally change the electronic structure of these systems, but simply changes the relative energies of different states, facilitating the certain pathways.[178] Given that the relative energies of the different states involved in these reaction pathways are fundamentally affected by both the environmental temperature and the force, it makes sense that changing the solution temperature has impacts on mechanochemical activity outside of simple passive heating.

Finally, the focal length of the lens used to focus the beam to generate laser-induced cavitation bubbles was varied from 50 cm to 5 cm. For the chain-centered mechanophore sample, decreasing the focal length of the lens dramatically increased the observed mechanochemical activation by almost six times (Figure 6.3e), however it had no apparent effect on the amount of anthracene generated in the chain-end control (Figure 6.3f). The consistently low control activity indicates that tighter focusing is not simply heating the solution to trigger the retro-Diels-Alder reaction. Rather, the increased activity of the active sample with a decreased focal length suggests that a shorter focal length tightens the focal region, contracting the energy used in liquid breakdown, facilitating the formation of cavitation bubbles and thus the activation of chain-centered mechanophores.[205]

Next, a kinetic study was undertaken to investigate the dynamics of mechanochemical activation using laser-induced cavitation. GPC and photoluminescence measurements were taken at various timepoints over the 60 minute irradiation time to monitor the mechanochemical retro-Diels-Alder reaction (Figure 6.4a-b). GPC traces show the retention time of the polymer sample increasing with irradiation time, indicating that the polymer chains are getting shorter as mechanophore activation events lead to chain cleavage. The evolution of the photoluminescence (PL) intensity at 413 nm over the course of irradiation, shown in Figure 6.4c, is fit to the equation

$$I = A(1 - e^{-kt})$$

where I is the PL intensity at 413 nm and time t, A is the maximum intensity, and k is the rate constant.[201] Based on this fit, the mechanochemical rate constant under these conditions is 91×10^{-3} min^{-1}. This rate constant is on the same order of magnitude as that determined for a 210 kDa polymer with this mechanophore under ultrasonication conditions, further demonstrating the commensurate nature of these techniques.[201] While this kinetic study was undertaken with the fully optimized parameters described above, it might be useful for future work to perform kinetic studies under a range of conditions to understand the dynamics of mechanophore activation under an assortment of variables.

Future studies might further look to extend the parameter testing detailed above by controlling and testing even more variables that influence laser-induced cavitation.[205] Changing the repetition rate of the driving laser pulses, the duration of the laser pulses,[206] the laser wavelength and pulse energy,[187,188,197] and solvent identity would all have implications for the laser-induced breakdown, cavitation, and mechanochemical activation. Given the same set of conditions, lower pulse energies produce bubbles with smaller maximum radii and lower maximum bubble wall velocities.[188] Generally, lower pulse energy is required to produce breakdown for shorter pulses, and shorter pulse durations also decrease cavitation bubble diameters.[206] For different uses of cavitation bubbles, including as a scalpel in laser surgery, laser pulses with high repetition rates and low energies, with large numerical aperture lenses, have proven to be the optimal choice for

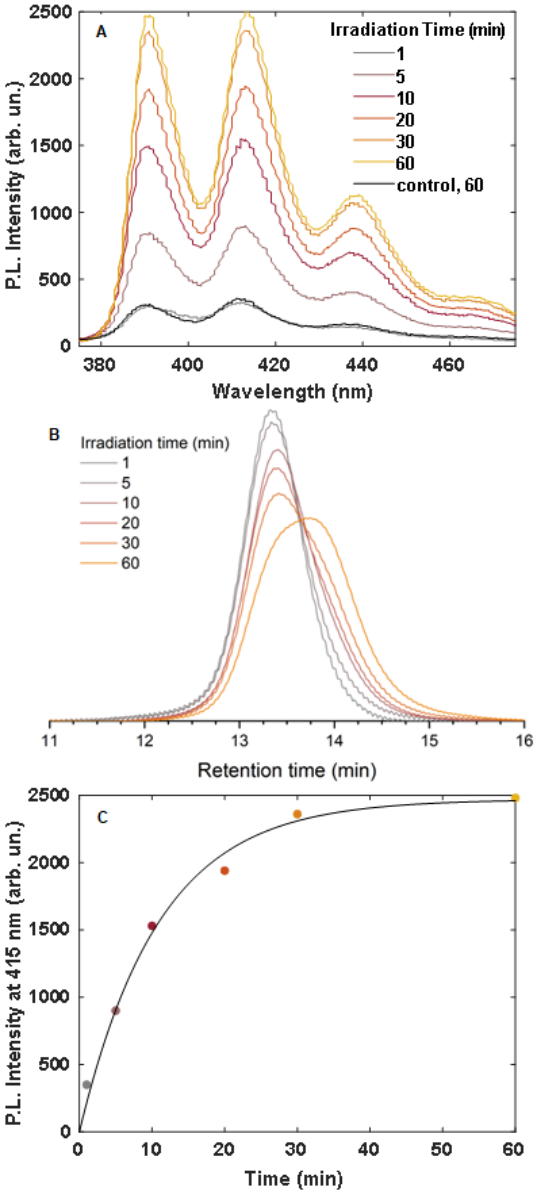

Figure 6.4 Kinetics study of laser-induced cavitation mechanophore activation. The **A** photoluminescence spectra and **B** GPC traces over the course of an irradiation experiment show continuous activation over time. The **C** kinetic fit of the experiment yields a time constant on the same order of magnitude as that determined for ultrasound activation.

controlling cavitation bubbles.[205] While the same parameters might not be optimal for laser-induced cavitation activation of chain-centered mechanophores, this example highlights the importance of understanding and optimizing the parameters that influence these dynamics so as to control them.

Following the confirmation that laser-induced cavitation does lead to mechanochemical activation, pump-probe spectroscopic studies of mechanophore reactivities were attempted using laser-induced cavitation as the pump. As described in the methods section, the pump was an 800 nm, 1 kHz laser beam attenuated to 120 mW, focused with a 5 cm lens into a cuvette filled with 2 mg/mL solution of 210 kDa PMA-AM-PMA. The probe beam used to interrogate the cavitation bubble dynamics was a 632 nm CW HeNe, while the chemical probe was a 349 nm, <5ns, 1 kHz laser, electronically delayed and triggered relative to the pump pulse that was absorbed and caused the activated anthracene to fluoresce. All three beams were collinear, the HeNe signal was collected along the beam path, and the fluorescence signal was collected at a 90° angle to the beam path.

While the CW HeNe was able to measure the time-resolved expansion and collapse of the cavitation bubble, all attempts at measuring the mechanochemically induced anthracene fluorescence were futile. In the future, if these measurements continue to be attempted, there are several takeaways from the failed measurements.

1. Any attempt at measuring transient mechanophore absorption or fluorescence in the beam path is obscured by the bubble dynamics. The mechanophore probe beam is influenced by the bubble in much the same way as the CW HeNe beam. This finding was what led us to attempt to measure the fluorescence perpendicular to the beam path.
2. The amount of mechanophore left to activate rapidly decreases. After approximately 30 minutes of irradiation at the conditions described above, there is no change in the solution's PL intensity. Therefore, a continuously circulated flow cell design might be optimal for the experiments that require more than 30 minutes of data acquisition to measure appreciable transient signal.
3. It is extremely challenging, if not impossible, to achieve consistent cavitation events. Post-processing of the data to select for only the cavitation events with the same profile in the HeNe trace was attempted, however no significant signal was detected in the fluorescence trace.
4. The fluorescence signal is extremely weak and may simply have been too weak to detect with the GaP photodiodes that were used. Subsequent experiments could attempt using a single photon avalanche photon detector (SPAD) to increase the sensitivity of these measurements.
5. The timing between the cavitation initiation and the pulsed 349 nm probe may have been a source of error in these experiments. Attempts were made at both transient absorption and transient fluorescence with a CW white light source, however given the broadband and CW nature of the source, it may have not been intense enough to elicit a measurable response in the system. Attempts in the future could use a single wavelength (350 nm), high power laser diode.
6. Furthermore, these experiments could be conducted with a mechanophore that exhibits chemiluminescence, one that emits light following mechanochemical

cleavage *without* the need for an external light source. These mechanophores are quite challenging to synthesize, however, so this experimental route might not be feasible.

6.4 Conclusion

While time-resolved measurements of the mechanochemical activation of anthracene-maleimide Diels-Alder adducts were not achieved, the spatiotemporally resolved initiation method was proven to work extremely well. Laser-induced cavitation activation of this system was shown to resemble ultrasound-induced cavitation activation qualitatively and quantitatively, further supporting its use as a method for activating mechanochemically responsive systems. While it is always interesting to develop a new activation technique, this method is especially important as it is a first step towards the achievement of transient measurements of these reactions. Future work should continue to attempt those time-resolved measurements to gain a deeper understanding of how the potential energy surfaces of these reactions are influenced by mechanical force.

Chapter 7

VALIDATION OF THE COGEF METHOD AS A PREDICTIVE TOOL FOR POLYMER MECHANOCHEMISTRY

The development of force-responsive molecules called mechanophores is a central component of the field of polymer mechanochemistry. Mechanophores enable the design and fabrication of polymers for a variety of applications ranging from sensing to molecular release to self-healing. Nevertheless, an insufficient understanding of structure−activity relationships limits experimental development, and thus computation is necessary to guide the structural design of mechanophores. The Constrained Geometries simulate External Force (CoGEF) method is a highly accessible and straightforward computational technique that simulates the effect of mechanical force on a molecule and enables the prediction of mechanochemical reactivity. Here, we use the CoGEF method to systematically evaluate every covalent mechanophore reported to as of September 9th, 2020 and compare the predicted mechanochemical reactivity to experimental results. Molecules that are mechanochemically inactive are also studied as negative controls. In general, mechanochemical reactions predicted with the CoGEF method at the common B3LYP/6-31G* level of density functional theory are in excellent agreement with reactivities determined experimentally. Moreover, bond rupture forces obtained from CoGEF calculations are compared to experimentally measured forces and demonstrated to be reliable indicators of mechanochemical activity. This investigation validates the CoGEF method as a powerful tool for predicting mechanochemical reactivity, enabling its widespread adoption to support the developing field of polymer mechanochemistry. Secondarily, this study provides a contemporary catalog of over 100 mechanophores developed as of September 9th, 2020.

Most of this chapter has been reprinted and adapted with permission from Klein, I. M. et. al. *Journal of the American Chemical Society* **2020**. https://doi.org/10.1021/jacs.0c06868.

7.1 Introduction

The emergent field of mechanochemistry looks to controllably direct the chemical transformation of mechanophores, small-molecule functional units that undergo well-defined chemical changes upon mechanochemical activation.[34] In polymer mechanochemistry, force is transduced to the mechanophore through covalently attached polymer chains.[207,182] Polymer mechanochemistry provides a novel method of initiating chemical reactions, accessing interesting molecule reactivities and material properties.[45,208,46,178,209,37] The development of new mechanophores is crucial to further our understanding of the fundamental nature of mechanochemical reactivity and to expand the repertoire of mechanically responsive materials. Designing novel mechanophores can be arduous, however, as the synthesis of a proposed mechanophore can be intensive and may ultimately yield a final molecule that is not mechanically active. For this reason, a reliable, easy-to-use, and fast computational method for validating mechanophore design prior to synthesis is desirable.

Several computational methods have been developed over the past two decades that investigate molecules and materials under mechanical stress. These methods include, but are not limited to the calculation of full *force-modified potential energy surfaces*, where the first-principles forces are directly modified to incorporate applied forces;[210] the *external force is explicitly included* method,[177] where the explicitly defined external force is included in the calculation of potential energy surfaces starting from the Born-Oppenheimer potential energy surface; and through *ab initio steered molecular dynamics*,[211] where constant pulling velocities simulate external forces. While these computational methods can probe mechanisms and energetic rationales of mechanochemical reactions, they are too computationally expensive to be useful in the rapid screening of potential mechanophores.

The method of *Constrained Geometries simulate External Force* (CoGEF), on the other hand, is both relatively computationally inexpensive and easy to use, and can be leveraged to test proposed mechanophore structures. Developed by Beyer in 2000, CoGEF is a first-principles approach that aims to probe how chemical bond strengths change as a function of applied force using constrained geometry optimizations. In this method, the

terminal ends of a molecule are held at increasingly large separation distances and a constrained geometry optimization is performed at each step.[212] CoGEF is implemented in several commercially available computational packages, including *Spartan* and *Gaussian*; is capable of simulating moderately sized mechanophores (up to 70 heavy atoms) on desktop computers; and is relatively fast (on the order of hours and days, rather than weeks or months). Due to the relative advantages of this method, it has been widely employed in the field of mechanochemistry to test proposed mechanophores and corroborate experimental observations.[213,214] However, no benchmarking or validation studies of this method have been undertaken to date.

We report a comprehensive investigation and validation of the CoGEF method for the screening and computational assessment of mechanophores. We find that CoGEF is an effective tool for the rapid screening of proposed mechanophores as it is able correctly predict the outcome of mechanochemical activation for both mechanophores and control molecules, those with domains often found in known mechanophores that have been experimentally determined to be not mechanically active. Below, we provide a brief overview of the CoGEF methods used herein and comprehensive results tables of the computational outputs for all 128 molecules investigated. We also explore the relationship between a series of outputs from CoGEF calculations and experimental observables and conclude that calculated force is a good indicator of mechanochemical activity.

7.2 Computational Methods

CoGEF calculations were run on structures designed to include the mechanophore core, the domain that undergoes a mechanochemical transformation, and tethers that appropriately truncate the polymeric material in which the mechanophore was studied experimentally. The equilibrium geometry of the unconstrained model structure is first computed at the B3LYP/6-31G* level of DFT. To run a CoGEF calculation, a distance constraint is then placed between the two terminal atoms (D_{eq}) (blue methyl groups, Figure 7.1a). The terminal atoms chosen are the attachment points for the extended polymer in experimental systems. The distance between the terminal atoms is extended in 0.05 Å steps (D) and a constrained geometry optimization is performed after every step. This process is

repeated until a mechanochemical transformation is predicted to occur (Figure 7.1b). Determining the energy of the molecule under force is easily done by setting this constraint and performing a constrained geometry optimization of the system. The CoGEF potential relative to the equilibrium energy is determined as a function of the distance constraint (Figure 7.1c).[212]

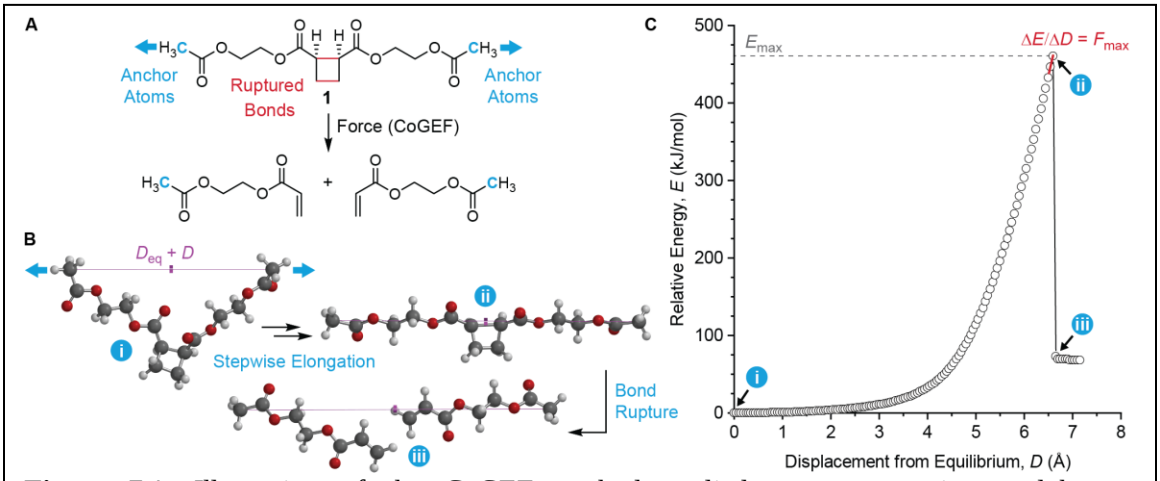

Figure 7.1. Illustration of the CoGEF method applied to representative cyclobutane mechanophore **1**. **A** Structures of the truncated mechanophore and products resulting from a formal retro-[2+2] cycloaddition reaction upon stepwise mechanical elongation predicted at the B3LYP/6-31G* level of theory. Blue carbon atoms designate the anchor points defining the distance constraint. Bonds that are broken in the calculation are colored red. **B** Computed structures at critical points in the CoGEF calculation: (i) the force-free equilibrium geometry, (ii) the constrained geometry immediately prior to bond rupture, and (iii) the predicted product(s). The corresponding points in the CoGEF curve are indicated in part C. **C** Relative energy, E, plotted as a function of displacement from equilibrium, D. E_{max} is the bond dissociation energy associated with the covalent transformation and F_{max} is the maximum force, calculated from the slope of the curve immediately prior to bond rupture.

As the distance between attachment points is increased, the energy of the system increases until a mechanochemical reaction occurs. These simulations provide the predicted products of the transformation, as shown in Figure 7.1b. Using the outcome structure(s) of these calculations, we determined whether the simulation has correctly predicted the experimentally determined reaction or if another outcome occurred. The CoGEF calculation was determined to be successful if the predicted products were consistent with the experimental products of the mechanochemical reaction. Looking to the numerical data generated through CoGEF calculations, the derivative of the CoGEF curve (Δ) gives the relative force necessary to reach a specific elongation, while the point

at which the sign of the derivative changes provides the maximum force (F_{max}) experienced by the mechanophore prior to undergoing a mechanochemical transformation. The bond dissociation energy is defined as the maximum relative energy immediately prior to bond rupture (E_{max}). The force-bond angle is calculated as the angle between the force vector and the reactive bond in the highest energy geometry, $\angle\overrightarrow{AB}$ and $\overrightarrow{CD}$.[36]

The B3LYP/6-31G* level of theory was chosen for the initial set of CoGEF calculations as it is the one most commonly used in mechanochemistry literature and we were interested in confirming the validity of this choice.[34] For calculations that gave false negatives, i.e. the calculation predicted a reaction that was inconsistent with the chemical transformation shown experimentally, we explored the use of the larger basis sets 6-311G(2d,p) and ccp-pVDZ with the B3LYP functional, the alternate functionals M06-2X and ωB97X-D with the 6-31G* basis set, and the wavefunction-based electronic structure method MP2 with the 6-31G* basis set. In addition, we also examined the effect of including dispersion corrections in the functional for CoGEF calculations of representative molecules using the B3LYP-D3/6-31G* level of DFT and performing CoGEF calculations at the B3LYP/6-31G* level of theory using unrestricted DFT.

7.3 Computational Results for Studied Reactions

CoGEF calculations were performed for 120 experimentally reported mechanophores, as well as eight controls. All structures investigated are presented in Charts 7.1 – 7.8 and the results of CoGEF calculations performed at the B3LYP/6-31G* level of theory are presented in associated Tables 7.1 – 7.8. All mechanophores that have been experimentally investigated are associated with one of eight categories: formal retro-[2+2] cycloaddition reactions, formal retro-[4+2] cycloaddition reactions, formal retro-[4+4] cycloaddition reactions, 2π electrocyclic ring-opening reactions, 4π electrocyclic ring-opening reactions, 6π electrocyclic ring-opening reactions, homolytic bond cleavages and heterolytic bond cleavages. The tested structures and outcomes have been categorized accordingly.[34] Control molecules are categorized based on their core structure; i.e. a control Diels-Alder adduct will be presented with the formal retro-[4+2] cycloaddition reactions. The bonds that are predicted to break in the CoGEF calculations are colored red. The

overall reaction predicted by each CoGEF calculation is identified as being either consistent (✓) or inconsistent (✗) with the reported experimental mechanochemical reactivity. We discuss some cases in which the calculation is inconsistent with the reported reactivity in which the available experimental data are either insufficient or suggest that a structural revision may be necessary. Calculated values of F_{max} and E_{max} are summarized in the tabulated data for each structure. The results of CoGEF calculations performed using alternate basis sets, a variety of functionals, and at the MP2 level of theory are presented when relevant. Following our validation of the use of CoFEF for investigating the mechanochemical activity of mechanophores, we show how CoGEF outputs are related to experimental observables, highlighting how F_{max} is related to observed trends in mechanochemical reactivity.

7.3.1 Retro-[2+2] Cycloaddition Reactions

The mechanochemical reactivity of molecules containing four-membered rings has been extensively studied. Moore and coworkers reported the mechanochemical generation of cyanoacrylate functional groups resulting from the formal retro-[2+2] cycloaddition reaction of cyano-substituted cyclobutanes in 2010.[215] Subsequently, a number of other cyclobutane mechanophores have been identified as well as mechanochemically active heterocyclic 1,2-dioxetane,[216] beta-lactam,[217] and 1,2-diazetidinone[218] compounds (Chart 7.1). CoGEF calculations successfully predict the anticipated mechanochemical reaction for 32 of the 34 structures in this category (Table 7.1).

In a seminal paper published in 2011,[219] Kryger *et al.* reported a systematic study of the relative reactivity of substituted cyclobutane mechanophores, comparing the results of ultrasound-induced mechanochemical activation experiments to predictions from CoGEF calculations. A threshold molecular weight was determined for each chain-centered cyclobutane derivative and used as a proxy for mechanochemical activity, with a lower molecular weight threshold indicating a more reactive substrate. The trends in experimental reactivity were generally found to be consistent with the results of CoGEF calculations. In our hands, CoGEF calculations performed on analogous cyclobutane compounds **1**–**6** produce similar results; however, subtle variation in the truncation of the computed

structures compared to those investigated by Kryger *et al.* reveals an important consideration. Here, cyclobutane mechanophores **1**–**6** include longer tethers compared to the structures computed by Kryger *et al.*, which contained terminal methyl ester groups directly attached to the cyclobutane cores. Despite the differences in truncation, our calculated values of F_{max} closely match those reported previously; however, the calculated values of E_{max} are highly variable, differing by more than 350 kJ/mol for cyclobutane **2**, for instance. This case study typifies a general observation that F_{max} is a robust quantitative metric obtained from CoGEF calculations and a better descriptor of relative mechanochemical activity than E_{max}. We therefore focus on the calculated values of F_{max} in the discussion of quantitative mechanochemical relationships for illustrative examples within each class of mechanochemical reactions and return to a more general discussion of quantitative aspects of CoGEF toward the end of the article.

Chart 7.1. Structures associated with formal retro-[2+2] cycloaddition reactions.

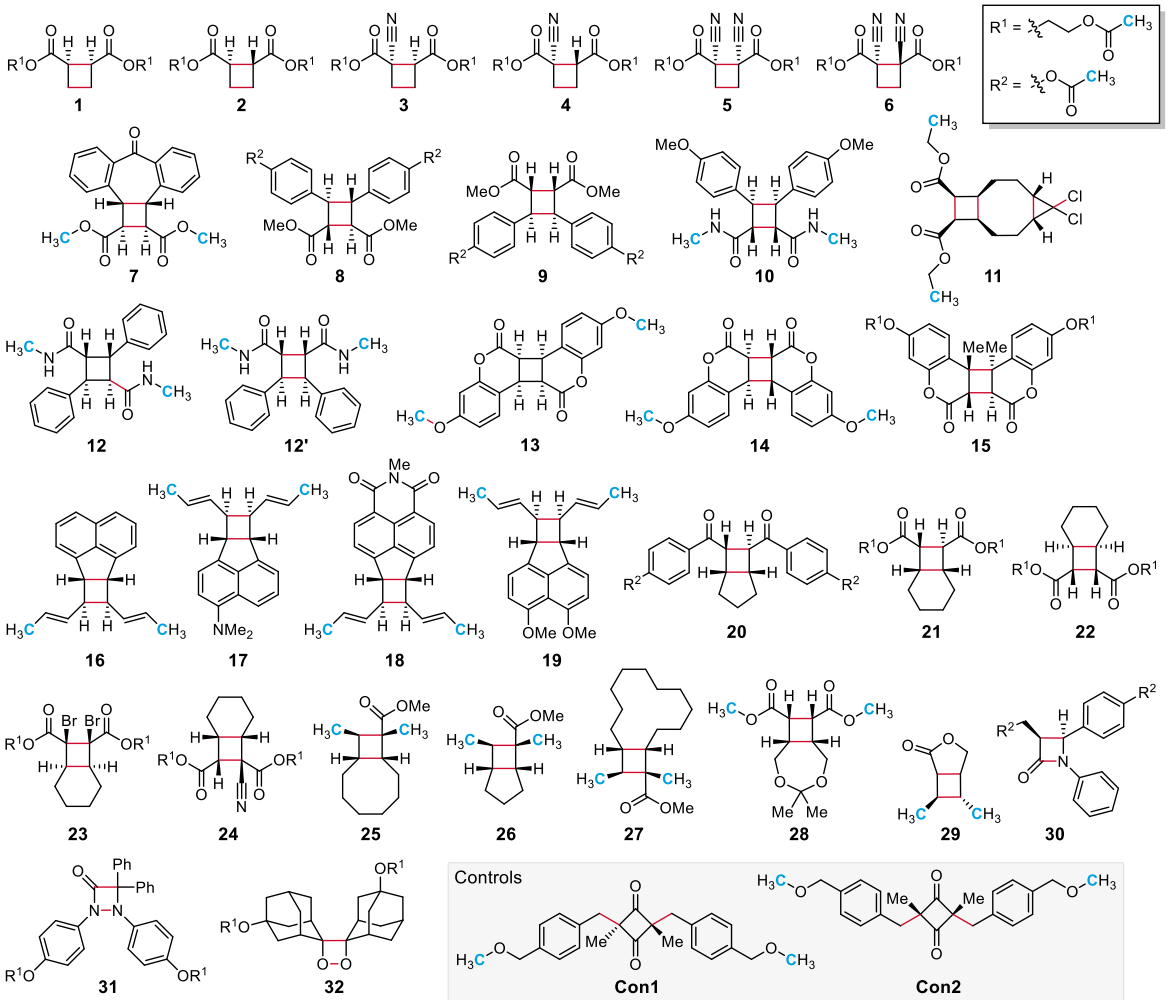

The influence of both stereochemistry and regiochemistry at the polymer attachment positions is evident in the CoGEF results for this class of mechanophores. Another consistent feature that emerges from the data is the impact of *cis* versus *trans* stereochemistry at the pulling positions. In particular, cyclobutanes containing a *cis* pulling geometry are predicted to have lower values of F_{max} compared to the corresponding *trans* isomer, which is again consistent with previous observations of Kryger *et al.* for cyclobutanes **1**–**6**.[219] Furthermore, we note that the reactions predicted for different mechanophores often proceed with a range of synchronicity. In many cases, the reaction occurs in a single elongational step, while asynchronous or stepwise fragmentation of other mechanophores is observed. These variations potentially reflect differences in mechanism, such as diradicaloid character in an asynchronous reaction,[219] although mechanistic interpretations should be treated carefully due to the constraints imposed on the system and the level of theory employed. Nevertheless, the results presented herein suggest that many mechanistic features are accurately captured using the CoGEF method.

Compound **11** is unique among this class of mechanophores, as it possesses two distinct mechanochemically active subunits. Wang *et al.* demonstrated that each subunit is activated in sequence upon mechanical elongation, illustrating the concept of mechanical gating whereby the ring-opening reaction of the *gem*-dichlorocyclopropane unit is contingent upon the cycloelimination reaction of the cyclobutane motif.[220] CoGEF simulations are consistent with this result, predicting initial fragmentation of the cyclobutane group via a formal retro-[2+2] cycloaddition reaction with an F_{max} value of 4.7 nN followed by further molecular extension that ultimately leads to ring-opening of the more reactive *gem*-dichlorocyclopropane at a lower F_{max} value of 3.8 nN. The concept of gating has led to a number of developments in polymer mechanochemistry recently being applied to mechanically gated photoswitching,[221] photochemically gated chain scission,[222] mechanically triggered molecular release,[223] and mechanically gated polymer degradation.[224,225]

For cyclobutane compound **12**, the CoGEF calculation predicts C–C bond cleavage at a location peripheral to the four-membered ring that is inconsistent with the reported reactivity. Each of the four-membered-ring mechanophores for which CoGEF correctly

predicts a formal cycloelimination reaction exhibits a 1,2-disubstitution pattern for the positions of polymer attachment. In contrast, cinnamamide dimer **12** was reported to have a 1,3-disubstitution geometry on the cyclobutane ring.[226,227] The available experimental data are insufficient to confirm the structure of the dimer in question, but the photodimerization of cinnamic acid and related derivatives has been shown to produce the head-to-head dimer corresponding to the 1,2-disubstituted cyclobutane.[228,229] CoGEF calculations performed on alternative head-to-head dimer **12′** predict a formal cycloelimination reaction upon mechanical elongation, in agreement with the computational results for other 1,2- disubstituted cyclobutane mechanophores. Based on this evaluation, we speculate that the fluorogenic mechanochemical activity previously observed for the cinnamamide dimer mechanophore may originate from the reaction of the 1,2-disubstituted compound **12′**. Additionally, the CoGEF calculation performed on head-to-tail coumarin dimer **13** predicts scission of the C–O bond adjacent to the pulling position, rather than the experimentally observed retro-[2+2] cycloaddition reaction. Compared to head-to-head coumarin dimer **14**, the head-to-tail dimer was demonstrated to be significantly less reactive.[233]

Table 7.1. CoGEF results for formal retro-[2+2] cycloaddition reactions[§]

Structure	Result[a]	F_{max} (nN)	E_{max} (kJ/mol)	Ref.
1	✓	4.6	460	219
2	✓	5.9	746	219
3	✓	4.0	335	219
4	✓	4.8	426	219
5	✓	3.4	285	215,219
6	✓	5.0	444	215,219
7	✓	4.5	413	230
8	✓	5.0	417	231
9	✓	2.5	253	231
10	✓	4.4	364	232
11	✓	4.7, 3.8[b]	395, 291[b]	220
12	×	5.9	498	226,227
12′	✓[c]	4.4	359	-
13	×	6.3	658	233
14	✓	5.6	633	233
15	✓	5.9	1017	234
16	✓	3.3	244	235
17	✓	3.3	241	235
18	✓	3.3	244	235
19	✓	3.3	236	235
20	✓	5.5	692	236
21	✓	5.2	562	237
22	✓	4.6	469	237
23	✓	3.6	332	237
24	✓	4.0	313	237
25	✓	3.8	302	238
26	✓	3.5	278	238
27	✓	3.7	306	238
28	✓	4.4	345	224
29	✓	5.4	331	225
30	✓	3.5	284	217
31	✓	3.6	260	218
32	✓	4.4	495	216
Con1	✓	6.3	947	239
Con2	✓	6.4	959	239

[§]B3LYP/6-31G* level of DFT. [a]Consistency between CoGEF prediction and reported experimental reactivity. [b]Computed values associated with reaction of the *g*DCC subunit. [c]Structural revision results in CoGEF prediction matching expected reactivity.

Although the number of compounds that have been reported in the literature to exhibit non-productive reactivity under mechanical force is relatively limited, the ability to

accurately identify this type of behavior in negative controls is critical to validate the CoGEF method as a reliable predictive tool. Two such examples are available in this class of mechanochemical reactions. The mechanochemical reactivity of *cis* and *trans* disubstituted 1,3-cyclobutanedione molecules **Con1** and **Con2** was investigated by Sijbesma and coworkers and both molecules were found to undergo non-specific bond scission under ultrasound-induced mechanical force rather than formal cycloelimination.[239] Consistent with these experimental observations, CoGEF calculations predict C–C bond scission peripheral to the cyclobutanedione core. Intriguingly, both benzylic C–C bonds cleave simultaneously in the CoGEF calculations to form a product consistent with the structure of 1,3-dimethylbicyclo[1.1.0]butane-2,4-dione for both the *cis* and *trans* cyclobutanedione stereoisomers. These results further reinforce the apparent regiochemical constraints for mechanochemical activation of four-membered-ring compounds and point to the privileged mechanochemical reactivity derived from 1,2-disubstitution.

7.3.2 Retro-[4+2] Cycloaddition Reactions

Mechanically activated formal retro-[4+2] cycloaddition reactions have also been demonstrated for a variety of mechanophores (Chart 7.2). Within this category, retro-Diels–Alder reactions are prominent transformations that have garnered significant attention for applications including stress sensing[221,248,253] and triggered small molecule release.[223,240] CoGEF calculations successfully reproduce the reported experimental mechanochemical reactivity for 13 of the 18 structures in this category (Table 7.2).

Table 7.2. CoGEF results for formal retro-[4+2] cycloaddition reactions[§]

Structure	Result[a]	F_{max} (nN)	E_{max} (kJ/mol)	Ref.
33	×	6.2	676	240,241
34	×	6.0	693	242
35	×	5.8	736	243
36	×	2.9	295	244
37	×	6.5	772	245
38	✓	4.1	306	246,247
39	✓	4.0	372	248
40	✓	3.9	230	249
41	✓	4.8	504	249
42	✓	4.1	285	249,250
43	✓	4.0	264	251
44	✓	4.0	245	223
45	✓	3.8	284	252
46	✓	4.6	396	221
47	✓	3.9	243	222
Con3	✓	6.0	843	248
Con4	✓	6.0	832	246
Con5	✓	6.0	650	249

[§]B3LYP/6-31G* level of DFT. [a]Consistency between CoGEF prediction and reported experimental reactivity.

For mechanophores **33**–**37**, CoGEF calculations result in C–C, C–O, or C–S bond rupture that is inconsistent with the reported

cycloelimination reactions. The mechanochemical reaction of oxanorbornadiene mechanophore **33** was achieved under compression in crosslinked elastomers resulting in the release of a small molecule furan derivative.[240] Mechanical activation of **33** was hypothesized to proceed via a unique "flex activation" mechanism whereby force-induced bond-bending motions promote the desired retro-[4+2] cycloaddition reaction. Other computational studies have suggested that this reaction manifold is less sensitive to external mechanical perturbation and that a significant thermal component is still required for activation under relatively large forces.[254] Poor orientational alignment between the scissile bonds and the direction of applied force along the reaction coordinate results in weak mechanochemical coupling in these systems, and mechanical force alone is insufficient for activation. The formal retro-Diels–Alder reaction of phenyltriazolinedione–anthracene adduct **34** was also investigated experimentally in crosslinked elastomers under tension where mechanical activation is expected to proceed via force-induced planarization.[242] In addition to mechanical strain, simultaneous heating was required to achieve activation on the order of ~1% at 125 °C, indicating a relatively low level of mechanochemical reactivity. The reaction of **35** was recently reported to produce singlet oxygen under mechanical stress via a similar planarization process,[243] although it is important to note that control experiments to rule out thermal activation were not presented. For these flex-activated mechanophores, proper consideration of the thermal energy is critical to accurately model their reactivity. CoGEF calculations performed on compound **36** predict C–S bond scission instead of a retro-[4+2] cycloaddition reaction. Characterization data suggest that the bis-hetero-Diels–Alder adduct investigated was symmetric,[255] although the reported structure of **36** differs in the configuration of each adduct.[244] Nevertheless, CoGEF calculations performed on simple models of individual hetero-Diels–Alder adducts comprising all of the different possible regio- and stereoisomers result in the same C–S bond scission (Figure D1). We cautiously note that additional experimental investigation is warranted to confirm the mechanochemical reactivity of the hetero-Diels–Alder adduct(s) represented by compound **36**, as well as compound **35**.

Chart 7.2. Structures associated with formal retro-[4+2] cycloaddition reactions.

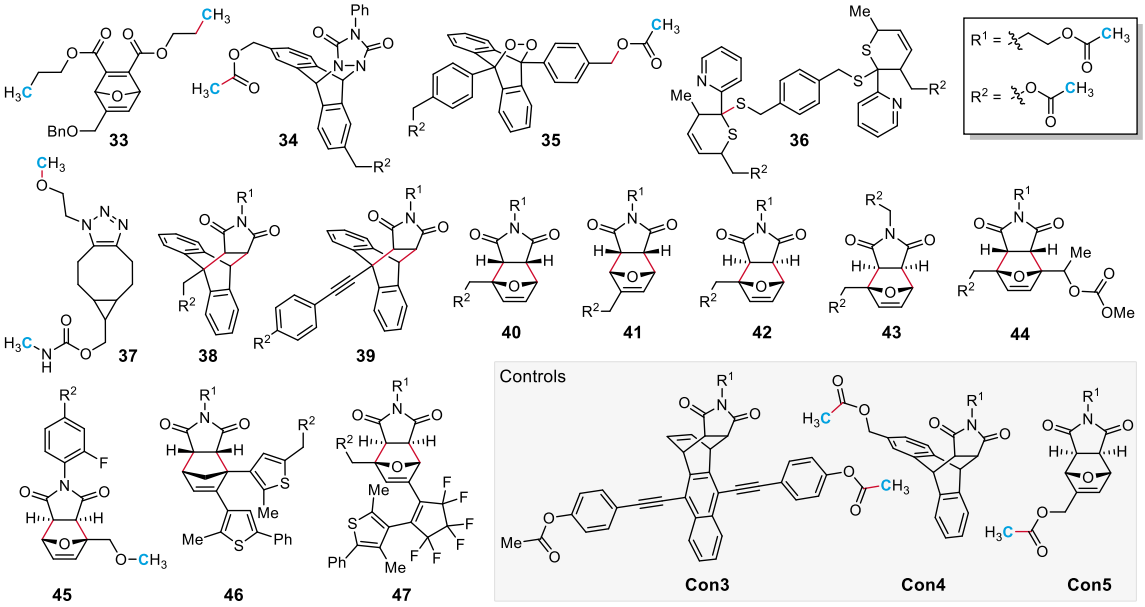

The mechanochemical cycloreversion of 1,2,3-triazoles has been the subject of debate in the mechanochemistry literature.[256,257] This transformation has piqued interest due to the ubiquitous use of azide–alkyne cycloaddition "click" chemistry.[258] Blank and coworkers previously demonstrated that the CoGEF method predicts a retro-[4+2] cycloaddition reaction for some 1,2,3-triazoles, although the reactivity is highly sensitive to pulling geometry.[259] For triazoles derived from terminal alkynes, the cycloreversion reaction is only predicted for the 1,5-regioisomer, whereas non-specific bond scission adjacent to the triazole ring is expected for the 1,4-regioisomer accessed through the popular copper-catalyzed cycloaddition reaction.[260,261] Stauch and Dreuw further demonstrated that even for 1,5-substitued 1,2,3-triazoles, cycloreversion competes with rupture of the C–N bond at the location of polymer attachment on the triazole ring because the forces associated with both processes are similar.[262] Experimentally, the cycloreversion reaction of a 1,5-disubstituted 1,2,3-triazole was investigated using atomic force microscopy (AFM) methods leading to inconclusive results.[263] In another AFM study, the mechanochemical cycloreversion reaction of the strain-promoted azide–alkyne cycloaddition product **37** was probed, which suggested that cycloreversion of the triazole was achieved at the single molecule level as deduced through a series of subsequent labeling experiments.[245] Nevertheless, the methods employed in the study did not permit

conclusive chemical analysis of the reaction products. The CoGEF calculation for compound **37** predicts C–O bond scission in the tether and not the cycloreversion reaction, similar to the results of previous computational studies on this scaffold.[259]

Three molecules have been studied experimentally that serve as negative controls for this category of formal retro-[4+2] cycloaddition reactions. In contrast to mechanophores **38** and **39** that reveal fluorescent anthracene derivatives upon mechanochemical activation, anthracene–maleimide Diels–Alder adducts **Con3** and **Con4** with distal pulling geometries do not undergo a retro-[4+2] cycloaddition reaction under force.[246,248] CoGEF calculations are consistent with these experimental results, predicting C–C bond scission at a terminal position in the tether groups instead of cycloelimination. In addition, Stevenson and De Bo elegantly illustrated the impact of both regiochemistry and stereochemistry on the mechanochemical reactivity of furan–maleimide adducts.[249] Compound **Con5** with *exo* stereochemistry and a distal pulling position relative to the furan–maleimide junction was demonstrated to be mechanically inert under ultrasound-induced elongational force due to poor alignment of the scissile bonds with the force vector. This behavior is accurately captured by the CoGEF calculation for this substrate, which predicts C–C bond rupture adjacent to the terminal pulling position rather than the retro-[4+2] cycloaddition reaction observed in the CoGEF calculations for experimentally verified mechanophores **40**–**42**. In addition, the calculated values of F_{max} for these three furan–maleimide mechanophores are also consistent with their experimentally determined reactivity. For example, *proximal–endo* isomer **40** exhibited the lowest threshold molecular weight while *distal–endo* isomer **41** had the highest threshold molecular weight of the mechanochemically active adducts. The calculated values of F_{max} for mechanophores **40** and **41** are 3.9 nN and 4.8 nN, respectively.

7.3.3 Retro-[4+4] Cycloaddition Reactions

Anthracene dimers **48** and **49** have been reported to undergo a formal retro-[4+4] cycloaddition reaction under mechanical compression in polymeric materials to generate fluorescent anthracene moieties (Chart 7.3).[264,265] CoGEF calculations do not predict the

Chart 7.3. Structures associated with formal retro-[4+4] cycloaddition

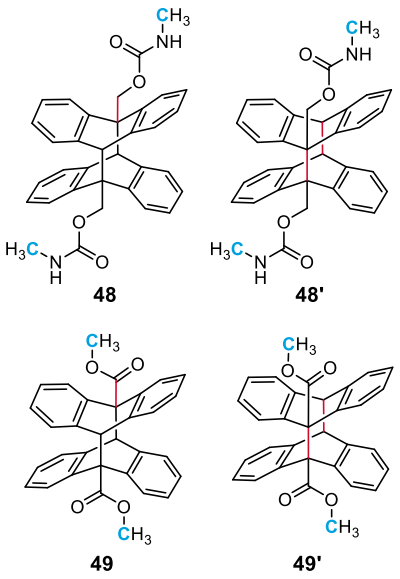

anticipated cycloelimination reaction for either compound, instead suggesting unproductive C–C or C–N bond scission near the pulling point (Table 7.3). However, unlike the bond elongation process typically operative in the activation of other mechanophores, we envisioned that the structure of these adducts may be uniquely susceptible to mechanical activation through compression-induced planarization. Modified CoGEF calculations were performed on **48** and **49** in which two carbon atoms in opposing phenyl rings were brought closer together in a typical series of constrained geometry calculations at the B3LYP/6-31G* level of theory. For both compounds, this alternative CoGEF model does indeed predict the formal retro-[4+4] cycloaddition reaction to generate a pair of anthracene products (Figure D2). These results may suggest that typical CoGEF calculations do not properly reflect the mode of mechanical activation for anthracene dimer mechanophores. However, it is important to note that the unconventional constrained geometry calculations were designed specifically to emulate the geometric distortions that are anticipated to occur for the anthracene dimers under compressive stress. We caution against applying these alternative methods broadly because they do not represent a realistic mode of mechanical activation for most mechanophores.

Table 7.3. CoGEF results for formal retro-[4+4] cycloaddition reactions[§]

Structure	Result[a]	F_{max} (nN)	E_{max} (kJ/mol)	Ref.
48	×	6.9	844	[264]
48′	✓[b]	2.3	140	-
49	×	5.8	557	[265]
49′	✓[b]	2.2	167	-

[§]B3LYP/6-31G* level of DFT. [a]Consistency between CoGEF prediction and reported experimental reactivity. [b]Structural revision results in CoGEF prediction matching expected reactivity.

Based on the regiochemical effects observed for other classes of mechanophores, we were also curious to investigate the impact of regiochemistry on the predicted mechanochemical reactivity of the anthracene dimer. The photodimerization of anthracene derivatives typically produces the head-to-tail isomer selectively; however, the head-to-

head configuration is also accessible under certain conditions.[266,267] The typical CoGEF operation performed on alternative head-to-head dimers **48′** and **49′** predicts the desired cycloelimination reactions. Although mechanistic interpretations should again be treated with caution, the CoGEF simulations performed on the anthracene dimer indicate that the cycloelimination reaction does not proceed via a concerted retro-[4+4] cycloaddition reaction. Instead, the calculations suggest a stepwise reaction involving sequential, discrete bond-breaking events before ultimately generating the two anthracene products. This behavior is observed for both the head-to-tail and head-to-head dimers regardless of the simulated mode of mechanical activation.

7.3.4 2π Electrocyclic Ring-Opening Reactions

Since first reported by Craig and coworkers in 2009,[268] the mechanochemical 2π electrocyclic ring-opening reaction of *gem*-dihalocyclopropane (gDHC) mechanophores to generate 2,3-dihaloalkenes has been studied extensively. In addition to cyclopropanes, the mechanochemical reactivity of three-membered heterocycles including epoxides[269,270] and aziridines[271] has also been explored (Chart 7.4). Unlike most of the mechanophores presented above that undergo cycloelimination reactions, mechanophores that undergo electrocyclic ring-opening reactions are non-scissile, allowing for the incorporation of many reactive units per polymer chain, thus enabling a greater degree of activation per stretching event.[272] CoGEF calculations successfully predict a 2π electrocyclic ring-opening reaction that is consistent with the determined experimental behavior for 16 of the 19 structures in this category (Table 7.4).

Chart 7.4. Structures associated with formal 2π Electrocyclic Ring-Opening

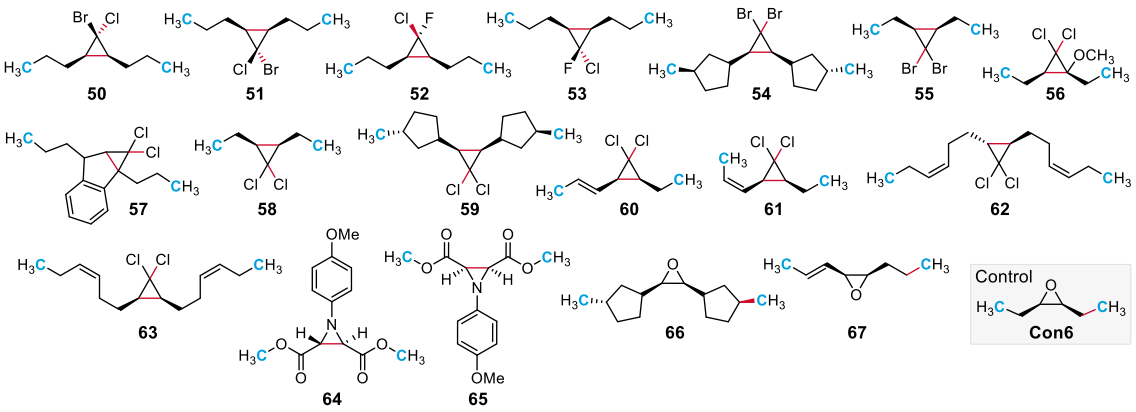

CoGEF calculations correctly predict the C–C bond cleavage and concerted halide migration to form a 2,3-dihaloalkene product consistent with the anticipated 2π electrocyclic ring-opening reaction of *g*DHCs with only one exception, as noted below. The halide *anti* to the outwardly rotating alkyl substituents is the preferred leaving group for the thermal electrocyclic ring-opening reaction according to the Woodward–Hoffman–DePuy (WHD) rules.[283–285] For *gem*-bromochlorocyclopropanes (*g*BCC) **50** and **51**, CoGEF calculations follow the WHD predicted pathways and occur with migration of chlorine and bromine, respectively, which are *anti* to the alkyl substituents in each case. These results are consistent with experiments for the mechanical activation of a copolymer containing each *g*BCC isomer, which proceeded to form both the chlorine and bromine migration products.[274] On the other hand, CoGEF calculations predict chlorine migration for both *gem*-chlorofluorocyclopropane (gCFC) mechanophores **52** and **53**, which contradicts the WHD rules, but again is consistent with experimental findings.[275] In this case, radical trapping experiments indicate that *syn*-Cl isomer **52** reacts via a mechanism involving a transition state with considerable diradicaloid character, similar to the isomerization reaction of *gem*-difluorocyclopropane (*g*DFC) mechanophores (*vide infra*). The value of F_{max} calculated for *syn*-Cl *g*CFC **52** is approximately 0.3 nN larger than the F_{max} for *anti*-Cl *g*CFC **53**, which also agrees with the relative reactivity of the two mechanophores observed from SMFS experiments.[275] Finally, we note that CoGEF calculations performed on mechanophores **56** and **57** successfully predict the expected 2π electrocyclic ring-opening reactions accompanied by chlorine migration; however, the corresponding 2,3-dichloroalkene products in these cases are thermally unstable and undergo subsequent elimination of HCl in the laboratory,[279,280] which is not captured in the simulations, as expected.

The diversity of structural variations for the *g*DHC mechanophores provides an opportunity to compare the results of CoGEF calculations to experimentally determined structure–property relationships. For example, comparing mechanophores **58**, **59**, and **60** reveals the impact of a so-called lever-arm effect[276] that has been demonstrated to reduce the force required for ring-opening by providing more efficient force transfer to the mechanophore. SMFS experiments confirm that a polynorbornene backbone attached to

the *gem*-dichlorocycloproprane (*g*DCC) mechanophore (**59**) or the addition of an *E*-alkene substituent (**60**) lowers the force required to promote the mechanochemical ring-opening reaction from approximately 1.3 nN for **58** to 0.9 and 0.8 nN for **59** and **60**, respectively.[276,281] The results of CoGEF calculations are consistent with these experimentally determined trends in reactivity. The CoGEF calculation performed on *cis*-*g*DCC mechanophore **58** with simple alkyl substituents predicts an F_{max} value of 3.8 nN. Modifying the tethers to include terminal cyclopentyl groups that mimic the structure of a polynorbornene backbone lowers the calculated value of F_{max} to 3.4 nN for **59**, while incorporation of an *E*-alkene adjacent to the *g*DCC results in a calculated F_{max} of 3.2 nN for **60**. The incorporation of a *Z*-alkene substituent is less effective than the *E*-alkene, requiring a force of approximately 1.2 nN to achieve the ring-opening reaction in SMFS experiments.[281] The relative impact of the *Z*-alkene is also accurately reflected in the CoGEF calculation with a predicted F_{max} value of 3.7 nN for **61**, just below the calculated value of F_{max} for dialkyl substituted mechanophore **58**.

Table 7.4. CoGEF results for formal 2π electrocyclic ring-opening reactions[§]

Structure	Result[a]	F_{max} (nN)	E_{max} (kJ/mol)	Ref.
50	✓	3.6	216	273,274
51	✓	3.3	184	273,274
52	✓	3.5	262	275
53	✓	3.2	183	275
54	✓	3.3	164	276
55	✓	3.7	180	277,273,274,278
56	✓	3.6	166	279
57	✓	5.7	448	280
58	✓	3.8	205	268,273,276
59	✓	3.4	190	276
60	✓	3.2	148	281
61	✓	3.7	202	281
62	×	5.2	557	268,282
63	✓	3.8	340	268,282
64	✓	5.4	300	271
65	✓	5.6	416	271
66	×	6.4	729	269
67	×	6.2	549	270
Con6	✓	6.2	607	269

[§]B3LYP/6-31G* level of DFT. [a]Consistency between CoGEF prediction and reported experimental reactivity.

The CoGEF calculation performed on *trans*-*g*DCC mechanophore **62** does not predict a 2π electrocyclic ring-opening reaction with concurrent halide migration to generate a 2,3-dichloroalkene product. Instead, the predicted transformation mirrors the CoGEF results for the *g*DFC mechanophores described below, indicating cleavage of the central C–C bond to form a product consistent with a transient diradical species. Although the mechanochemical reaction of *cis* and *trans* *g*DCC isomers was previously demonstrated to occur with nearly equal probability under ultrasonication conditions,[268] SMFS measurements revealed substantially different plateau forces of 1.3 nN and 2.3 nN for *cis*-

*g*DCC and *trans*-*g*DCC, respectively.[282] Despite the different reaction pathways predicted by CoGEF, the calculated values of F_{max} reflect the impact of *cis* and *trans* stereochemistry on the *g*DCC mechanophore observed in SMFS experiments. The value of F_{max} calculated for the electrocyclic ring-opening reaction of *cis*-*g*DCC mechanophore **63** is 3.8 nN, while the F_{max} value predicted for the reaction of *trans*-*g*DCC analog **62** is 5.2 nN. The significantly larger force measured for the reaction of the *trans*-*g*DCC mechanophore is consistent with an electrocyclic ring-opening reaction that proceeds via a formally symmetry-forbidden conrotatory pathway.[282] Alternatively, the CoGEF results for **62** suggest another intriguing mechanistic possibility, in analogy to the reactivity observed for *g*DFC mechanophores.[286] That is, isomerization of the *trans*-*g*DCC into the *cis* isomer via a transient mechanical force and subsequent reaction via the expected electrocyclic ring-opening pathway would ultimately furnish the 2,3-dichloroalkene product. To the best of our knowledge, this hypothesis has not been tested experimentally.

The mechanochemical ring-opening reaction of epoxides to generate carbonyl ylide intermediates has been demonstrated for mechanophores **66** and **67**, although the reactivity is low.[269,270] SMFS measurements have revealed that the rate of ring-opening for even the most mechanochemically reactive allylic epoxide **67** is very slow under significantly large forces of approximately 2.5 nN,[270] suggesting that ring-opening likely competes with non-specific bond scission in the polymer backbone. CoGEF calculations performed on these epoxide mechanophores fail to reproduce the ring-opening behavior and instead predict C–C bond scission adjacent to the pulling point. The mechanochemical ring-opening reaction of epoxidized polybutadiene has also been characterized by SMFS measurements, which did not reveal any evidence for epoxide ring-opening at forces up to 2.5 nN.[269] Again, the cyclopentyl groups of structure **66** reflect a polynorbornene backbone, which has been suggested to provide more efficient force transduction compared to polybutadiene.[276] Similar to the other epoxides, the CoGEF calculation performed on **Con6** does not predict a ring-opening reaction, which in this case is consistent with the experimental observation that epoxidized polybutadiene is mechanochemically inactive.

7.3.5 4π Electrocyclic Ring-Opening Reactions

In 2007, Moore and coworkers described the mechanochemical 4π electrocyclic ring-opening reaction of benzocyclobutene.[45] Remarkably, both the *cis* and *trans* 1,2-disubstituted benzocyclobutenes were demonstrated to undergo formal disrotatory and conrotatory electrocyclic ring-opening reactions, respectively, to generate identical *E*,*E*-*ortho*-quinodimethide intermediates. For the formally symmetry-forbidden disrotatory electrocyclic ring-opening reaction of the *cis*-isomer, FMPES calculations suggest that mechanical force reduces the activation barrier of the concerted pathway, which becomes barrierless at sufficiently high forces.[289] Six benzocyclobutene congeners have been investigated experimentally that differ in the substitution and stereochemistry at the positions of polymer attachment (Chart 7.5). CoGEF calculations predict a formal 4π electrocyclic ring-opening reaction for all six benzocyclobutene compounds reported in the literature (Table 7.5).

Chart 7.5. Structures associated with formal 4π electrocyclic ring-opening

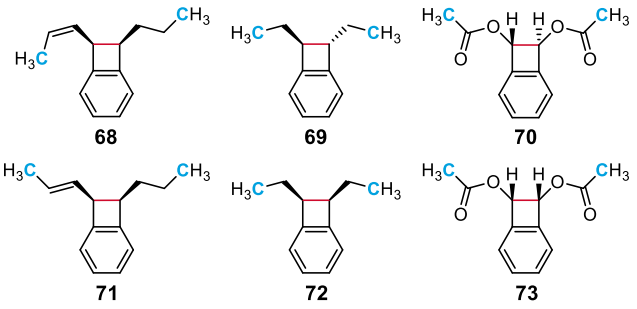

Table 7.5. CoGEF results for formal 4π electrocyclic ring-opening reactions[§]

Structure	Result[a]	F_{max} (nN)	E_{max} (kJ/mol)	Ref.
68	✓	3.7	282	287
69	✓	4.1	186	282
70	✓	4.1	211	45,288
71	✓	3.1	244	287
72	✓	3.7	367	282
73	✓	3.0	310	45,288

[§]B3LYP/6-31G* level of DFT. [a]Consistency between CoGEF prediction and reported experimental reactivity.

The CoGEF calculations performed on *cis* and *trans* 1,2-disubstitued benzocyclobutenes result in the formation of the same *ortho*-quinodimethide products, consistent with experimental measurements. The simulated ring-opening reactions of **68**–**71** are consistent with a synchronous transformation in which the breaking and reformation of bonds occurs over a single elongation step in the CoGEF profile. On the other hand, the CoGEF calculations performed on mechanophores **72** and **73** appear to proceed through a highly asynchronous ring-opening process, which could suggest the formation of significant diradicaloid character prior to formation of the *ortho*-quinodimethide product. This behavior is not consistent with orbital symmetry arguments as the predicted ring-

opening reaction of other *cis*-disubstituted benzocyclobutenes **68** and **71** occurs synchronously, so the origin of these qualitative differences in the CoGEF profiles is unclear.

The impact of *cis* and *trans* stereochemistry of the pulling positions on the four-membered-ring follows the same trends as the cyclobutane and *gem*-dichlorocyclopropane mechanophores presented above. The predicted F_{max} is lower for *cis*-isomer **72** compared to the corresponding *trans*-isomer **69**, with calculated values of 3.7 and 4.1 nN, respectively. This trend is also consistent with the relative forces measured experimentally using SMFS.[282] Similar to the lever arm effect observed for *gem*-dichlorocyclopropanes,[281] the *E*-alkene substituent of *cis*-disubstituted benzocyclobutene **71** results in a lower calculated F_{max} value of 3.1 nN compared to *cis*-dialkyl substituted analog **72** with a calculated F_{max} of 3.7 nN, which is again consistent with the relative forces measured by SMFS.[287]

7.3.6 6π Electrocyclic Ring-Opening Reactions

Spiropyran[288] and naphthopyran[298] undergo a 6π electrocyclic ring-opening reaction under mechanical force to generate colored merocyanine dyes (Chart 7.6). The mechanochromic behavior of these mechanophores makes them useful as molecular force probes for visual stress sensing applications. The mechanochemical reactivity of a variety of spiropyran and naphthopyran structures has been studied experimentally, providing insight into structure–mechanochemical activity relationships. CoGEF calculations successfully predict the expected 6π electrocyclic ring-opening reaction for 16 out of 18 reported structures in this class (Table 7.6).

Table 7.6. CoGEF results for formal 6π electrocyclic ring-opening reactions[§]

Structure	Result[a]	F_{max} (nN)	E_{max} (kJ/mol)	Ref.
74	✓	4.4	381	290,288,291,292
75	✓	2.7	165	242,291–293
76	✓	2.6	150	294
77	✓	2.0	74	295
78	✓	3.5	271	293,296
79	✓	3.2	248	293
80	×	5.9	536	297
81	×	5.7	567	296
82	✓	4.8	386	296
83	✓	4.3	418	298
84	✓	4.4	483	299
85	✓	4.1	370	299
86	✓	3.7	348	299
87	✓	3.7	334	299
88	✓	3.9	332	299
89	✓	4.1, 4.6	652, 740	300
Con7	✓	6.0	716	298
Con8	✓	6.0	650	298

[§]B3LYP/6-31G* level of DFT. [a]Consistency between CoGEF prediction and reported experimental reactivity.

Spiropyran is one of the most widely studied mechanophores in the literature. Similar to the *g*DHC mechanophores, the mechanochemical reactivity of a number of different spiropyran mechanophores with varying connectivity and substitution has been investigated using different experimental techniques enabling the elucidation of important structure–activity relationships. The two most commonly employed spiropyran mechanophores, **74** and **75**, vary in the position of polymer attachment on the indoline portion of the molecule resulting in different mechanochemical activity in SMFS experiments.[291] Attachment at the indoline nitrogen for mechanophore **75** leads to a greater mechanical advantage compared to **74**, which is manifested in different plateau forces of 0.24 and 0.26 nN, respectively. The F_{max} values calculated from CoGEF are qualitatively consistent with this trend in reactivity; however, as discussed in greater detail below, the F_{max} value of 4.4 nN calculated for mechanophore **74** is unexpectedly large compared to the F_{max} value of 2.7 nN calculated for spiropyran **75**. Notably, spirothiopyran **77** is predicted to have one of the lowest predicted values of F_{max} (2.0 nN) of any mechanophore studied, although the force required for this ring-opening reaction has not been measured experimentally.

Chart 7.6. Structures associated with formal 6π electrocyclic ring-opening

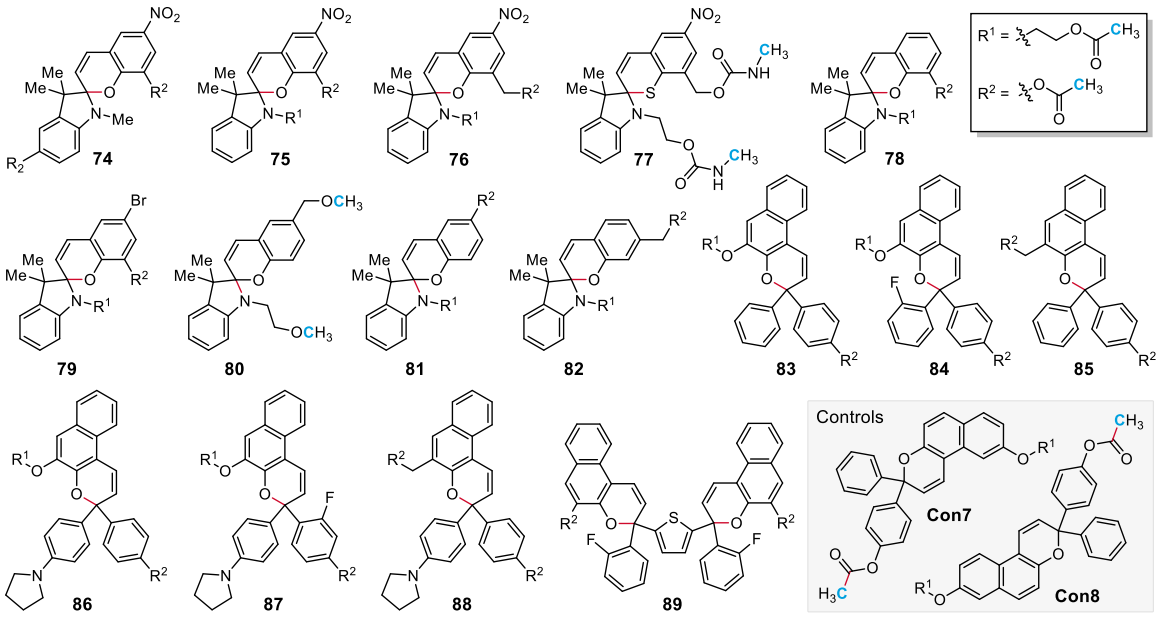

The effect of electronic substitution on the mechanochemical reactivity of spiropyran has also been recently studied using SMFS.[293] The force required for ring opening was shown to vary depending on the nature of the substituent *para* to the oxygen on the benzopyran portion of the molecule following a classic Hammett relationship. The plateau forces measured for the ring-opening reaction of mechanophores **78**, **79**, and **75** were 0.41, 0.36, and 0.24 nN, respectively, indicating enhanced stabilization of negative charge in the transition state as the electron withdrawing power of the substituent increases going from hydrogen to bromine to a nitro group. The values of F_{max} calculated for **78** (R = H), **79** (R = Br), and **75** (R = NO_2) are 3.5, 3.2, and 2.7 nN, respectively, which are in agreement with the trend in reactivity determined from SMFS experiments.

Spiropyran mechanophores **80** and **81** with pulling positions *para* to the pyran oxygen on the benzopyran fragment of the molecule are both predicted to undergo cleavage of the spiro C–N bond instead of the expected C–O bond. The C–N bond scission appears to be heterolytic in nature and occurs with predicted F_{max} values of 5.9 nN (**80**) and 5.7 nN (**81**), which are significantly higher than values of F_{max} computed for the ring-opening reaction of other spiropyran mechanophores. A prior investigation of the effects of regiochemistry on the mechanochemical activation of spiropyran in bulk materials revealed that *para*-substituted mechanophore **81** is significantly less sensitive to mechanical force than analogous mechanophores with polymer attachment at the *ortho* and *meta* positions (**78** and **82**, respectively).[296] Interestingly, CoGEF calculations predict the expected C–O bond cleavage reaction leading to merocyanine formation for structure **81** when the pulling point is changed to a hydrogen atom at either the *meta* or *ortho* position on the benzopyran portion of the molecule, indicating that the computed reactivity is affected strongly by the pulling geometry and not purely electronic factors (Figure D3). We further note that the computed visible absorption spectrum of the product resulting from C–N bond cleavage of spiropyran **81** is similar to that of the merocyanine species resulting from the expected 6π electrocyclic ring-opening reaction, possibly confounding the interpretation of colorimetric analyses if this competing reaction pathway is indeed experimentally accessible.

Similar to the regiochemical effects discussed above for spiropyran and other classes of mechanophores, the mechanochemical activity of naphthopyran is highly

dependent upon the positions of polymer attachment. While naphthopyrans **83**–**88** are mechanochemically active, regioisomers **Con7** and **Con8** do not undergo electrocyclic ring-opening reactions in polymeric materials under tension.[298] This behavior is accurately reproduced in the CoGEF calculations, which predict C–C bond scission adjacent to the pulling point for both control molecules. The regioisomer-specific mechanochemical reactivity of naphthopyran **83** was previously attributed to better alignment between the labile C–O pyran bond and the direction of the applied force, which was quantified by a specific angle denoted here as the force–bond angle.[298] The angle between the C–O pyran bond and the external force vector at maximum extension was calculated from molecular models to be relatively narrow for mechanophore **83**, whereas the angle is substantially wider for the two unreactive naphthopyran regioisomers **Con7** and **Con8**. While proper orientation between the external force vector and the labile bond in a mechanophore is a critical parameter that influences mechanochemical coupling, in general we find no correlation between force–bond angle and mechanochemical activity when analyzed broadly across the entire library of mechanophores and control structures (Figure D4).

Another notable example in this reaction class is bis-naphthopyran mechanophore **89**, which contains two separate reactive sites and exhibits force-dependent changes in visible absorption due to distinctly colored merocyanine products resulting from the ring-opening reaction of either one or both pyrans.[300] While the CoGEF calculation performed on bis-naphthopyran **89** predicts that both pyrans successfully undergo the anticipated ring-opening reactions under force, the geometry constraints imposed by the CoGEF method necessitate a sequential ring-opening process upon molecular extension. Experiments indicate, however, that both rings open in tandem under ultrasound-induced mechanical elongation. Multiple chain scission reactions have been observed for cyclic polymers during a single high-strain-rate extensional event that suggest potentially important dynamic effects under ultrasonication conditions,[301] which are not accurately captured by the CoGEF method.

7.3.7 Homolytic Reactions

In a seminal report by Moore and coworkers in 2005, the mechanochemical site-specific chain scission of polymers containing mechanophore **90** with a mechanically weak azo group near the chain midpoint was demonstrated to occur through the putative homolytic expulsion of nitrogen.[302] A number of mechanophores have since been developed that react via radical pathways (Chart 7.7). This category includes mechanochromic mechanophores **94**–**97** that generate colored stable free radicals under mechanical force,[303–306] and ladderenes **98** and **99** that unzip to generate semiconducting polyacetylene.[37,307] CoGEF calculations successfully predict the expected homolytic bond scission reactions for 23 out of 25 experimental mechanophores in this class (Table 7.7).

Chart 7.7. Structures associated with homolytic reactions.

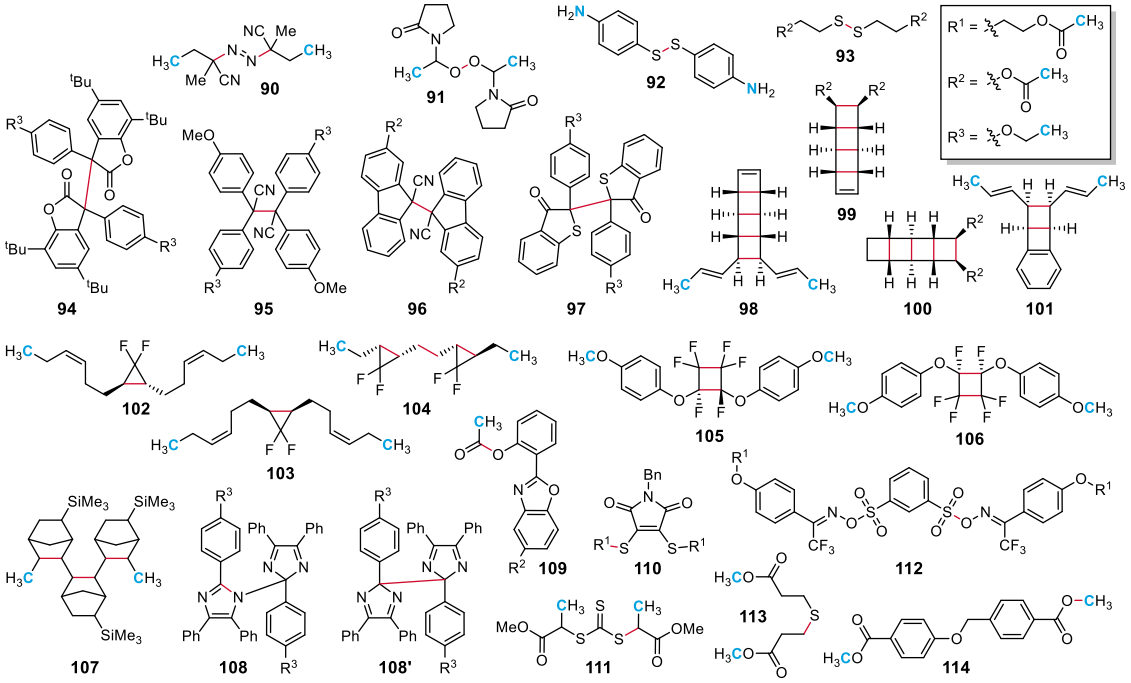

In addition to transformations involving simple homolytic bond scission, CoGEF calculations also successfully capture the mechanochemical behavior of more complex, multistep reactions. In many cases, CoGEF calculations accurately reproduce computations performed using more sophisticated approaches. According to FMPES calculations, the unzipping reaction of ladderene and ladderane mechanophores **98**–**100** proceeds via a mechanism that involves two transient diradical transition states.[37,307] The

complex stepwise unzipping reaction of these mechanophores is successfully captured by CoGEF calculations. While the mechanochemical reaction mechanism of benzoladderene **101** has not been confirmed experimentally, we include it in this category in the context of other ladderene structures.[308] Notably, the CoGEF calculation performed on benzoladderene **101** predicts that the ring-opening reaction occurs through a stepwise mechanism similar to the other ladderene mechanophores. In contrast to the electrocyclic ring-opening reactions of other *g*DHCs described above, *gem*-difluorocyclopropane (*g*DFC) mechanophores **102** and **103** undergo homolytic bond scission leading to a transient diradical intermediate under force.[286] As an interesting example, the CoGEF calculation performed on a representative dimer structure **104** predicts sequential ring-opening reactions of the *cis* followed by the *trans* disubstituted *g*DFC groups to generate an apparent tetraradical species, which subsequently disproportionates to form two identical 3,3-difluoroalkene radicals. This reactivity predicted by CoGEF is consistent with experimental characterization of reaction products by ^{1}H and ^{19}F NMR spectroscopy following ultrasound-induced mechanochemical activation and reproduces the results from AISMD simulations.[314] Similarly, the mechanochemical reaction of perfluorocyclobutane mechanophores **105** and **106** has been demonstrated to proceed via a stepwise mechanism with a diradical intermediate,[316] which is accurately reflected in the CoGEF calculations performed on these two structures. In another interesting example, the ring-opening reaction of vinyl-addition

Table 7.7. CoGEF results for homolytic reactions[§]

Structure	Result[a]	F_{max} (nN)	E_{max} (kJ/mol)	Ref.
90	✓	3.7	366	302,309
91	✓	5.2	230	310
92	✓	2.0	114	311
93	✓	3.6	271	312
94	✓	3.5	169	303,313
95	✓	4.5	294	304
96	✓	4.3	326	305
97	✓	4.4	287	306
98	✓	3.2, 3.9	236, 239	37,307
99	✓	4.2, 4.0	451, 346	307
100	✓	4.2, 3.9	511, 326	307
101	✓	3.3	245	308
102	✓	4.8	466	282,286,314
103	✓	3.4	292	282,286,314,315
104	✓	4.9	771	314
105	✓	4.2	455	316
106	✓	3.4	409	316
107	✓	3.5, 2.6, 3.5	348, 521, 617	317
108	×	5.1	536	318
108′	✓[b]	4.3	258	-
109	✓	4.7	369	319
110	✓	4.3	472	320
111	✓	4.3	227	321
112	✓	4.3	625	322
113	✓	4.6	626	309
114	×	6.1	611	309

[§]B3LYP/6-31G* level of DFT. [a]Consistency between CoGEF prediction and reported experimental reactivity. [b]Structural revision results in CoGEF prediction matching expected reactivity.

polynorbornene surrogate **107** is predicted to occur in a stepwise fashion to produce the ROMP-type polynorbornene repeat unit structure observed experimentally.[317]

The CoGEF calculation performed on triphenylimidazole dimer **108** predicts bond scission that differs from the anticipated reaction. Compound **108** was reported to undergo homolytic cleavage of the central C–N bond to generate a pair of stable triphenylimidazolyl radicals under force.[318] Instead, CoGEF calculations predict fragmentation of a C–N bond in one of the imidazole rings. While the imidazole dimer containing a central C–N linkage is expected to be the major product of oxidative coupling, this species exists in equilibrium with other isomers.[318] Performing the CoGEF calculation on isomer **108′** comprising a structure in which the imidazole rings are coupled via a central C–C bond results in the expected homolytic cleavage producing two identical triphenylimidazolyl radicals consistent with the experimentally observed behavior. The CoGEF calculations performed on compounds **109**–**113** predict homolytic bond scission that is consistent with the reported reactivity of these compounds, although we note that the products of these mechanochemical transformations have not been fully characterized. The CoGEF calculation performed on **114**, however, predicts scission of the C–O bond in a terminal ester group, rather than the anticipated C–O bond of the benzyl ether moiety. In fact, the reactivity of benzyl phenyl ether **114** was found to be surprisingly low.[309] Poor mechanochemical coupling was attributed to contraction of the molecule as the benzyl carbon atom rehybridizes from sp^3 to sp^2 upon formation of the benzyl radical. In that scenario, the CoGEF process may bias the reaction along a trajectory that does not correspond to the global minimum energy force-coupled pathway.

7.3.8 Heterolytic Reactions

Mechanochemical reactions that involve heterolytic fragmentation of covalent bonds to generate charged species are less common.[323–327] Nevertheless, several mechanophores have been reported in the literature to undergo heterolytic covalent bond cleavage under mechanical force (Chart 7.8). The CoGEF calculations performed on models of all such structures successfully reproduce the experimentally demonstrated reactivity (Table 7.8). Notably, a series of N-heterocyclic carbene precursors (**115**–**117**)

was recently discovered that undergoes selective C–C bond scission under mechanical force via three concomitant dissociation pathways.[327] CoGEF calculations predict the heterolytic fragmentation of all three compounds; however, experiments demonstrated that the proportion of heterolytic fragmentation diminishes with decreasing fluorination of the aryl group, favoring a concerted mechanism for mechanophores **116** and **117** with a less polarized scissile bond.

Chart 7.8. Structures associated with heterolytic reactions.

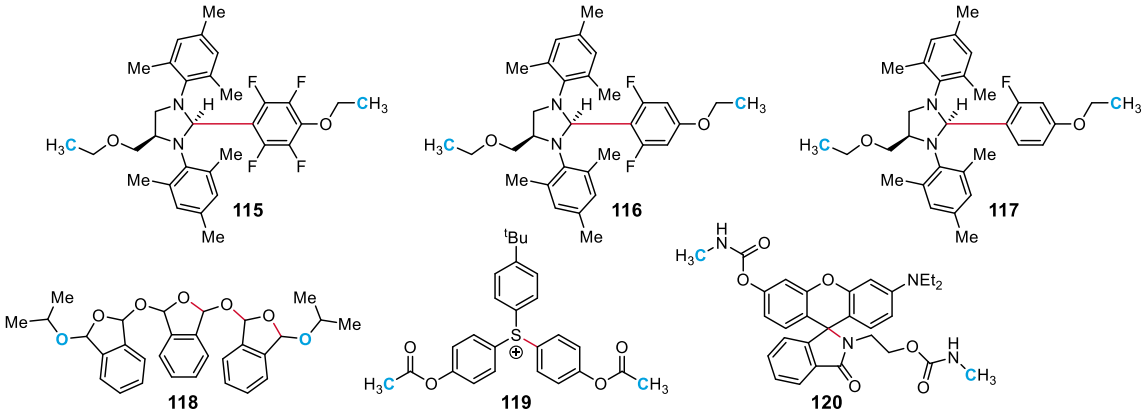

Poly(*o*-phthalaldehyde) undergoes a mechanically triggered unzipping reaction above its ceiling temperature to generate *o*-phthalaldehyde monomers.[323,324] The proposed mechanism, which is supported by AISMD simulations, involves mechanochemical chain cleavage via an initial heterolytic bond scission event followed by a depolymerization cascade.[323] The CoGEF calculation performed on model structure **118**, which represents a short repeating unit segment of poly(*o*-phthalaldehyde), predicts the simultaneous cleavage of three C–O bonds along the oligomer backbone including one central linking bond and two internal bonds on adjacent monomer units. The chemical transformation predicted by the CoGEF method is consistent with heterolytic fragmentation and two concurrent ring-opening reactions to generate two new aldehyde functional groups, with an oxocarbenium ion and

Table 7.8. CoGEF results for heterolytic reactions[§]

Structure	Result[a]	F_{max} (nN)	E_{max} (kJ/mol)	Ref.
115	✓	5.2	388	327
116	✓	5.5	438	327
117	✓	5.8	499	327
118	✓	5.6	507	323,324
119	✓	3.7	266	325
120	✓	4.6	368	326,328

[§]B3LYP/6-31G* level of DFT. [a]Consistency between CoGEF prediction and reported experimental reactivity.

an oxyanion localized on the separate portions. These results are in excellent agreement with the prior mechanistic findings for mechanically initiated depolymerization of poly(*o*-phthalaldehyde).

Triarylsulfonium compound **119** was reported to undergo heterolytic scission of the central polarized C–S bond to afford a phenyl cation, which was demonstrated experimentally through trapping experiments.[325] The CoGEF calculation performed on mechanophore **119** predicts the rupture of the anticipated C–S bond that is consistent with the reported mechanochemical behavior. In addition, rhodamine mechanophore **120** undergoes a force-induced ring-opening reaction that leads to a change in color and fluorescence in polymeric materials.[326,328] Although the mechanism has not been studied in detail, the C–N bond is presumed to cleave heterolytically, possibly with assistance from the diethylamine substituent *para* to the developing carbocation. The CoGEF calculation performed on mechanophore **120** predicts the selective scission of the anticipated central C–N bond. However, in the absence of a polarizable continuum model to simulate a polar solvent environment, a [1,3]-sigmatropic rearrangement is predicted to occur, resulting in the formation of a new oxygen-containing five-membered ring bearing an exocyclic C–N double bond. When the CoGEF calculation is repeated with a polar solvent model, heterolytic cleavage of the central C–N bond is observed without any rearrangement (see Appendix D for details).

7.4 F_{max} as a Reliable Descriptor of Mechanochemical Reactivity

Calculated values of F_{max} are reliable and consistent indicators of the relative mechanochemical reactivity of mechanophores, as demonstrated above for various reactions within each formal mechanistic category. The value of F_{max} from each successful CoGEF calculation across every reaction class is illustrated in Figure 7.2. For mechanophores where the predicted reactivity from the CoGEF calculation agrees with experimental results, the values of F_{max} range from the lowest of 2.0 nN for spirothiopyran **77** and diaryldisulfide **92** to the highest of 5.9 nN for *trans*-cyclobutane **2**. Notably, there is a clear distinction between the values of F_{max} calculated for each mechanophore and the values of F_{max} associated with bond scission in the negative controls, which in every case

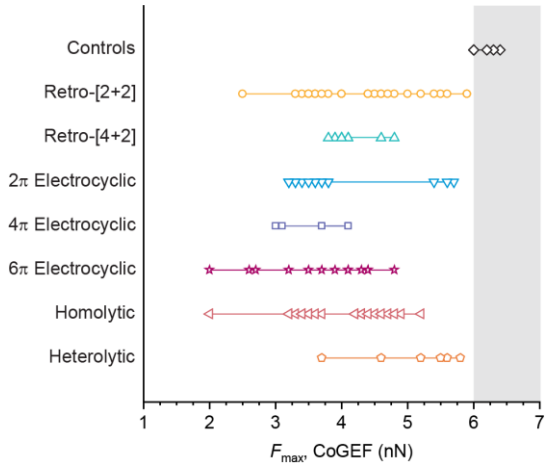

Figure 7.2. Summary of F_{max} values calculated by the CoGEF method across all mechanistic categories. Data from calculations that are inconsistent with reported experimental reactivity are excluded.

are ≥ 6.0 nN. In contrast, the CoGEF results for control structures are universally indistinguishable from the mechanophores when alternative quantitative metrics E_{max} and force–bond angle are compared (Figure D4). While the values of E_{max} generally exhibit a positive correlation with F_{max}, there is no such correlation with force–bond angle (Figure D5). It is worth reiterating, however, that the magnitude of E_{max} values from CoGEF calculations is highly variable, whereas F_{max} is a more robust predictor of mechanochemical activity. We mention in passing that the use of unrestricted calculations and dispersion corrections appears to have minimal influence on the results of CoGEF calculations (Figures D6 and D7).

Calculated values of F_{max} obtained from CoGEF calculations also correlate well with the mechanochemical reactivity of different mechanophores determined experimentally (Figure 7.3). While systematic studies of structure–reactivity relationships using threshold molecular weight as a quantitative metric are limited to substituted cyclobutanes[219] and furan–maleimide Diels–Alder adducts,[249] there is a positive correlation between the calculated values of F_{max} and the experimentally measured threshold molecular weight for these mechanophores (Figure 7.3a). Mechanochemical reactivity is more accurately quantified using SMFS, which has been performed consistently on a relatively large number of mechanophores including spiropyrans,[291,293] benzocyclobutenes,[282,287] and cyclopropanes.[275,276,281,282] Again, there is a positive correlation between the values of F_{max} calculated using CoGEF and the forces measured experimentally using SMFS (Figure 7.3b). As mentioned previously, spiropyran mechanophore **74** is a notable exception to this trend with an anomalously high calculated F_{max} value of 4.4 nN compared to the exceptionally low measured force of 0.26 nN.[291] The

rupture forces calculated with the CoGEF method are consistently greater than forces determined from experiments, in part because thermal effects are neglected.[256] In addition, the forces measured using SMFS are dependent upon the loading velocity, with all of the forces considered here measured with a loading velocity of 300 nm/s. Nevertheless, the relationship between calculated values of F_{max} and experimentally determined forces demonstrates that the CoGEF method can reliably predict the relative mechanochemical activity of mechanophores, reinforcing the qualitative trends in reactivity.

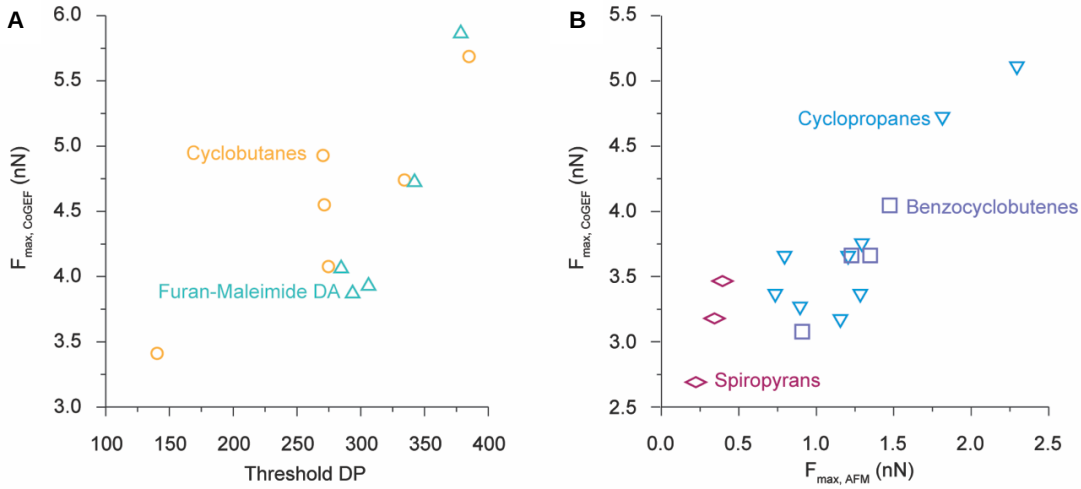

Figure 7.3. Values of F_{max} from CoGEF calculations compared to experimentally determined values of **A** threshold molecular weight obtained from rates of ultrasound-induced mechanochemical activation, and **B** forces determined from single molecule force spectroscopy measurements.

In addition to investigating the use of alternate basis sets, functionals, and levels of theory on CoGEF calculations, we also tested the effect of including dispersion corrections in the DFT functional for representative mechanophores. As most calculations performed in the mechanochemistry literature are done without including dispersion corrections, we were interested in exploring the validity of this choice. We performed CoGEF calculations with both B3LYP and B3LYP-D3 functionals for a series of representative mechanophores, one from each class, as well as for a variety of retro-[4+2] cycloaddition reactions. There have been a number of computational studies that have shown the importance of including dispersion corrections to accurately model transition states and calculate transition state energies, especially for Diels-Alder reactions.[329] Intuitively, the stereo- and regioselectivity of Diels-Alder reactions are greatly influenced by long-range

dispersion interactions and thus computational investigations of these reactions should include these considerations.[330] We found no significant difference in the CoGEF curves or outcomes obtained for calculations performed with B3LYP and B3LYP-D3 functionals for any mechanophore investigated. In addition, the F_{max} values extracted from the CoGEF curves showed no difference between calculations with dispersion corrections and those without (see Appendix D). The absence of discrepancies between CoGEF calculations performed with and without dispersion corrections supports the use of uncorrected functionals in past and future CoGEF calculations. We believe that mechanochemically-induced retro-[4+2] cycloaddition reactions can be accurately characterized computationally without including dispersion corrections because the mechanism, and thus the transition state, of this reaction is fundamentally quite different than that of the forward, thermally-initiated cycloaddition.

Further validating the use of the B3LYP/6-31G* level of DFT for these calculations, we performed the calculations in an unrestricted framework to investigate the modeling of radicals and radical mechanisms for mechanochemical reactions. Looking at two mechanophores known to undergo homolytic bond cleavages that produce radicals, HABI (**86**)[331] and a disulfide linkage (**93**),[312] we see no difference in the CoGEF predicted outcomes between restricted and unrestricted DFT at the B3LYP/6-31G* level of theory. HABI is reported to undergo a specific homolytic mechanochemical cleavage, however CoGEF predicted a different C-N cleavage than that which has been experimentally determined. Performing CoGEF in an unrestricted framework did not correct the predicted outcome. The calculated E_{max} for the disulfide homolytic cleavage was slightly higher for the restricted calculation than for the unrestricted case (350 kJ vs 300 kJ), but F_{max} was the same (3.6 nN) (Figure D6). As F_{max} is the metric of mechanochemical activity, the consistency between the F_{max} values for the restricted and unrestricted calculations indicates that there is no difference in the performing CoGEF in these two frameworks. Additionally, we tested the use of unrestricted DFT for mechanophores that do not undergo radical mechanisms, performing CoGEF calculations on *trans*-bicycloheptane (**13**)[332] and *cis*-benzocyclobutene (**59**).[45] Here again we looked at one mechanophore for which CoGEF predicted the experimentally observed outcome, **59**, and one for which CoGEF and

experiment are inconsistent, **13**. For both **59** and **13**, we see no difference in CoGEF predicted outcomes or outputs between restricted and unrestricted DFT. Performing CoGEF calculations in an unrestricted framework does not appear to change how it models mechanochemical reactions.

Another experimentally reported phenomenon that describes the relative reactivity of different mechanophores is the lever arm effect.[333] Specifically, the lever arm effect allows comparison of mechanophores with the same active domain and different tethers. Experimental studies have shown that introducing a stiff, extended tether to the mechanophore core acts as a lever arm, reducing the force necessary to achieve mechanochemical activation. Comparing F_{max} for mechanophores with the same core functionality and different tethers, or lever arms, we see the same reactivity trends seen experimentally in the CoGEF outputs (Figure 7.4).[46,172,333–336] The F_{max} for the mechanophore without addition lever arms is shown in teal and the F_{max} for the mechanophore with lever arms is shown in orange. While the mechanistic explanation for the observed lever arm effect remains unclear, it is important to note for this study that we have shown consistency between CoGEF calculations and relative trends in mechanochemical activity.

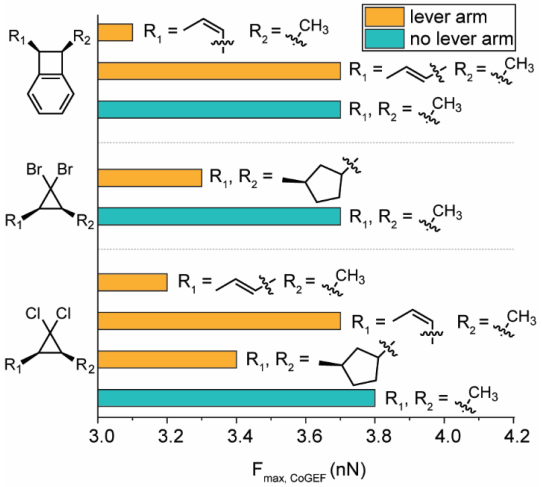

Figure 7.4. Experimentally observed lever arm effect mirrored in CoGEF calculated F_{max}

Following the confirmation that the calculated F_{max} is a good indication of relative mechanochemical activity (Figures 7.3 and 7.4), in addition to being a binary confirmation of any mechanochemical activity (Figure 7.2), we were curious as to whether CoGEF can provide any insight into the relative reactivates of different mechanophores. There have been a variety of different methods for using CoGEF in this manner; one such method examined how the active or "scissile" bond length changed as a function of the end-to-end mechanophore distance as the system was displaced from equilibrium.[337]

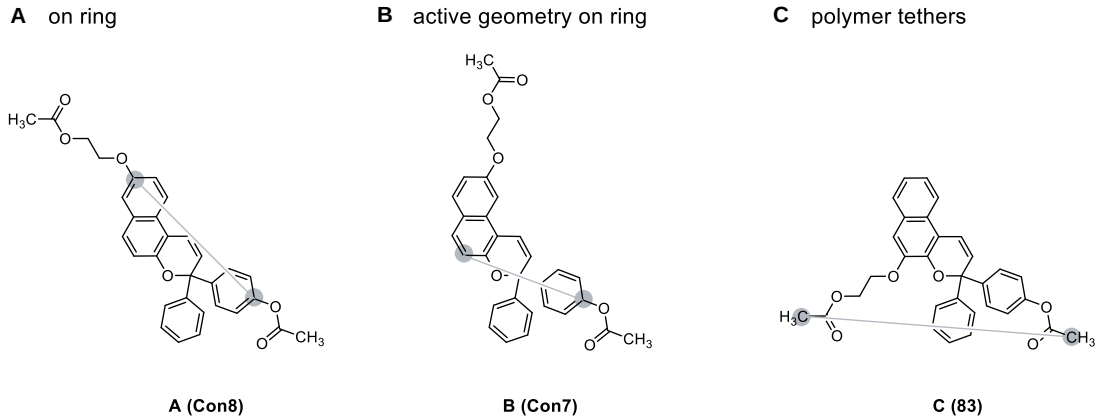

	Napthopyran A	Naphthopyran B	Naphthopyran C
Polymer Tethers	6.0 nN*	6.0 nN*	4.3 nN
On ring	6.6 nN*	6.5 nN*	4.8 nN
Bond	3.5 nN	3.4 nN	3.4 nN
Active geometry on ring	4.7 nN	4.6 nN	4.8 nN

Figure 7.5. Napthopyran mechanophore activity as a function of pulling position. An asterisk (*) denotes a non-productive bond cleavage, see Appendix D for details on which bond cleaves. (a) shows on the "on ring" constraint, (b) shows the "active geometry on ring" constraint, and (c) shows the "polymer tethers" constraint. "Bond" indicates that the spiro C-O bond of interest was elongated at 0.05 Å increments until cleavage was observed.

In addition to examining the relationship between bond elongation and productive mechanochemical activation, we investigated the relationship between pulling position and activation for a series of naphthopyrans. Naphthopyrans A (**Con8**) and B (**Con7**) are both control molecules that have been experimentally reported to not undergo a productive mechanochemical transformation. Naphthopyran C (**83**) is an experimentally validated mechanophore and undergoes a 6π electrocyclization reaction under mechanical activation. For prototypical CoGEF calculations, shown as "polymer tethers" in Figure 7.5c, and for "on ring" calculations, shown in Figure 7.5a, the outcomes are consistent with experimental observations. For CoGEF calculations in which the spiro carbon-oxygen bond of interest was systematically elongated in 0.05 Å steps, all three bonds cleave at approximately the same force. This result demonstrates that the spiro C-O bond is no stronger in the control naphthopyrans A and B than in the mechanically active naphthopyran C. Given this finding, it appears that mechanochemical activity of naphthopyran C is due to the effective transduction of force to the spiro C-O bond through the attachment at the 5-position, as

opposed to attachments at the 8- or 9-positions. This hypothesis is further validated when CoGEF calculations were performed pulling at the "active geometry on the ring," as shown in Figure 7.5b. All three naphthopyrans showed productive spiro C-O mechanochemical cleavages at approximately the same force, indicating that the geometry of force transduction is responsible for the differential mechanical susceptibility of naphthopyrans A – C.

The study of pulling position and activation in naphthopyrans suggests that the geometry of force transduction is critically important to determining whether mechanochemical activation will occur. From both literature and CoGEF, for the same core mechanophore, a *cis* geometry of the pulling tethers is more reactive than the *trans* pulling geometry.[338,339,239,231,334,208] This reactivity trend is quite pronounced when F_{max} for the *cis* and *trans* attachment geometries of the same mechanophore are directly compared, as the *cis* geometry always activates at a lower F_{max} value than the *trans* geometry. While we see no significant correlation between the force-bond angle and F_{max} for mechanophores in general (Figure D5), it is apparent that mechanophores with *cis* pulling attachments have both lower calculated F_{max} values and smaller force-bond angles than those with *trans* pulling attachments. We believe that, for the same mechanically active core, the better the alignment between the force vector and the active bond, the lower the force required to achieve mechanochemical activation.

Looking at both the naphthopyran studies and the relationship between F_{max} and force-bond angle, the geometry of force transduction is an important aspect in understanding mechanochemical activation. That said, the geometry of force transduction is only one component of the structural and electronic considerations that govern mechanochemical reactions and mechanochemical reactivity trends. The inconsistency of the correlations between F_{max} and force-bond angle for all mechanophore reaction classes highlights this fact. Different principles influence the reactivity of different mechanophores differently. Different mechanophores are activated through different mechanisms, and as such the considerations for these specific mechanisms must be appreciated when designing new mechanophores.

7.6 Conclusions

The CoGEF method is an operationally simple and highly accessible quantum chemistry technique that enables prediction of mechanochemical reactivity. In this study, we applied the CoGEF method systematically to every covalent mechanophore reported in the literature and compared the predicted reactivity against the experimentally determined behavior. CoGEF calculations are also performed on molecules that have been determined to be mechanochemically inactive as negative controls. Out of the 128 structures investigated with reactions that span eight distinct mechanistic categories, CoGEF calculations performed at the B3LYP/6-31G* level of DFT predict mechanochemical transformations that are consistent with the reported experimental reactivity for 112 molecules, including every negative control. In total, this corresponds to a success rate of 88%; however, analysis suggests that the accuracy of the CoGEF method is likely even higher. In some cases, for example, computational results combined with experimental characterization data indicate that revision of prior structural assignments may be merited or that additional experiments are needed to substantiate the reported reactivity.

The utility of the CoGEF method is revealed not only in its general ability to accurately predict covalent bond transformations, but also in quantitative comparisons of mechanochemical reactivity. We demonstrate that the maximum force predicted for bond rupture in CoGEF calculations is correlated with forces measured using single molecule force spectroscopy, suggesting that the CoGEF method is a reliable predictor of the relative activity of mechanophores. On the other hand, some notable limitations of the CoGEF method are revealed. The inability of CoGEF to account for thermal effects as a static quantum chemistry method limits its use in calculating the mechanochemical reactivity of "flex activated" mechanophores, for instance, where proper consideration of the contribution from thermal energy to the overall activation is essential. Additionally, the inherent geometric constraints imposed by CoGEF can obscure dynamic effects, such as those that may be involved in some specific reactions under high strain rate conditions, or possibly bias reactions by stretching molecules along trajectories that do not correspond to global minimum energy force-coupled pathways. Nevertheless, the ability of the CoGEF

method to reproduce more sophisticated computations as well as accurately predict remarkable transformations, like those that formally violate classical orbital-symmetry rules or proceed in a complex stepwise process, suggest that the technique can provide important insight into mechanochemical reactions beyond identifying scissile bonds.

BIBLIOGRAPHY

(1) Smith, M. B.; Michl, J. Singlet Fission. *Chemical Reviews* **2010**, *110* (11), 6891–6936. https://doi.org/10.1021/cr1002613.
(2) Carneiro, L. M.; Cushing, S. K.; Liu, C.; Su, Y.; Yang, P.; Alivisatos, A. P.; Leone, S. R. Excitation-Wavelength-Dependent Small Polaron Trapping of Photoexcited Carriers in α-Fe_2O_3. *Nature Materials* **2017**, *16* (8), 819–825. https://doi.org/10.1038/nmat4936.
(3) Pastor, E.; Park, J.-S.; Steier, L.; Kim, S.; Grätzel, M.; Durrant, J. R.; Walsh, A.; Bakulin, A. A. In Situ Observation of Picosecond Polaron Self-Localisation in α-Fe_2O_3 Photoelectrochemical Cells. *Nature Communications* **2019**, *10* (1), 3962. https://doi.org/10.1038/s41467-019-11767-9.
(4) Bandaranayake, S.; Hruska, E.; Londo, S.; Biswas, S.; Baker, L. R. Small Polarons and Surface Defects in Metal Oxide Photocatalysts Studied Using XUV Reflection–Absorption Spectroscopy. *Journal of Physical Chemistry C* **2020**, *124* (42), 22853–22870. https://doi.org/10.1021/acs.jpcc.0c07047.
(5) Auböck, G.; Chergui, M. Sub-50-Fs Photoinduced Spin Crossover in $[Fe(bpy)_3]^{2+}$. *Nature Chemistry* **2015**, *7* (8), 629–633. https://doi.org/10.1038/nchem.2305.
(6) Garin, M.; Heinonen, J.; Werner, L.; Pasanen, T. P.; Vähänissi, V.; Haarahiltunen, A.; Juntunen, M. A.; Savin, H. Black-Silicon Ultraviolet Photodiodes Achieve External Quantum Efficiency above 130%. *Physical Review Letters* **2020**, *125* (11), 117702. https://doi.org/10.1103/PhysRevLett.125.117702.
(7) Schaller, R. D.; Agranovich, V. M.; Klimov, V. I. High-Efficiency Carrier Multiplication through Direct Photogeneration of Multi-Excitons via Virtual Single-Exciton States. *Nature Physics* **2005**, *1* (3), 189–194. https://doi.org/10.1038/nphys151.
(8) Thomas, A.; Lethuillier-Karl, L.; Nagarajan, K.; Vergauwe, R. M. A.; George, J.; Chervy, T.; Shalabney, A.; Devaux, E.; Genet, C.; Moran, J.; Ebbesen, T. W. Tilting a Ground-State Reactivity Landscape by Vibrational Strong Coupling. *Science* **2019**, *363* (6427), 615–619. https://doi.org/10.1126/science.aau7742.
(9) Campos-Gonzalez-Angulo, J. A.; Ribeiro, R. F.; Yuen-Zhou, J. Resonant Catalysis of Thermally Activated Chemical Reactions with Vibrational Polaritons. *Nature Communication* **2019**, *10* (1), 4685. https://doi.org/10.1038/s41467-019-12636-1.
(10) D. Tran, P.; H. Wong, L.; Barber, J.; C. Loo, J. S. Recent Advances in Hybrid Photocatalysts for Solar Fuel Production. *Energy & Environmental Science* **2012**, *5* (3), 5902–5918. https://doi.org/10.1039/C2EE02849B.
(11) Biswas, S.; Husek, J.; Londo, S.; Fugate, E. A.; Baker, L. R. Identifying the Acceptor State in NiO Hole Collection Layers: Direct Observation of Exciton Dissociation and Interfacial Hole Transfer across α-Fe_2O_3/NiO Heterojunction. *Physical Chemistry Chemical Physics* **2018**, *20* (38), 24545–24552. https://doi.org/10.1039/C8CP04502J.
(12) Zürch, M.; Chang, H.-T.; Borja, L. J.; Kraus, P. M.; Cushing, S. K.; Gandman, A.; Kaplan, C. J.; Oh, M. H.; Prell, J. S.; Prendergast, D.; Pemmaraju, C. D.; Neumark, D. M.; Leone, S. R. Direct and Simultaneous Observation of Ultrafast Electron and Hole Dynamics in Germanium. *Nature Communications* **2017**, *8* (1), 15734. https://doi.org/10.1038/ncomms15734.
(13) Zürch, M.; Chang, H.-T.; Kraus, P. M.; Cushing, S. K.; Borja, L. J.; Gandman, A.; Kaplan, C. J.; Oh, M. H.; Prell, J. S.; Prendergast, D.; Pemmaraju, C. D.; Neumark, D. M.; Leone, S. R. Ultrafast Carrier Thermalization and Trapping in Silicon-Germanium Alloy Probed by Extreme Ultraviolet Transient Absorption Spectroscopy. *Structural Dynamics* **2017**, *4* (4), 044029. https://doi.org/10.1063/1.4985056.

(14) Cushing, S. K.; Zürch, M.; Kraus, P. M.; Carneiro, L. M.; Lee, A.; Chang, H.-T.; Kaplan, C. J.; Leone, S. R. Hot Phonon and Carrier Relaxation in Si(100) Determined by Transient Extreme Ultraviolet Spectroscopy. *Structural Dynamics* **2018**, *5* (5), 054302. https://doi.org/10.1063/1.5038015.
(15) Attar, A. R.; Chang, H.-T.; Britz, A.; Zhang, X.; Lin, M.-F.; Krishnamoorthy, A.; Linker, T.; Fritz, D.; Neumark, D. M.; Kalia, R. K.; Nakano, A.; Ajayan, P.; Vashishta, P.; Bergmann, U.; Leone, S. R. Simultaneous Observation of Carrier-Specific Redistribution and Coherent Lattice Dynamics in 2H-$MoTe_2$ with Femtosecond Core-Level Spectroscopy. *ACS Nano* **2020**, *14* (11), 15829–15840. https://doi.org/10.1021/acsnano.0c06988.
(16) Kaplan, C. J.; Kraus, P. M.; Ross, A. D.; Zürch, M.; Cushing, S. K.; Jager, M. F.; Chang, H.-T.; Gullikson, E. M.; Neumark, D. M.; Leone, S. R. Femtosecond Tracking of Carrier Relaxation in Germanium with Extreme Ultraviolet Transient Reflectivity. *Physical Review B* **2018**, *97* (20), 205202. https://doi.org/10.1103/PhysRevB.97.205202.
(17) Biswas, S.; Wallentine, S.; Bandaranayake, S.; Baker, L. R. Controlling Polaron Formation at Hematite Surfaces by Molecular Functionalization Probed by XUV Reflection-Absorption Spectroscopy. *Journal of Chemical Physics* **2019**, *151* (10), 104701. https://doi.org/10.1063/1.5115163.
(18) de Groot, F. High-Resolution X-Ray Emission and X-Ray Absorption Spectroscopy. *Chemical Reviews* **2001**, *101* (6), 1779–1808. https://doi.org/10.1021/cr9900681.
(19) Bergmann, U.; Kern, J.; Schoenlein, R. W.; Wernet, P.; Yachandra, V. K.; Yano, J. Using X-Ray Free-Electron Lasers for Spectroscopy of Molecular Catalysts and Metalloenzymes. *Nature Review Physics* **2021**, *3* (4), 264–282. https://doi.org/10.1038/s42254-021-00289-3.
(20) Bostedt, C.; Boutet, S.; Fritz, D. M.; Huang, Z.; Lee, H. J.; Lemke, H. T.; Robert, A.; Schlotter, W. F.; Turner, J. J.; Williams, G. J. Linac Coherent Light Source: The First Five Years. *Reviews of Modern Physics* **2016**, *88* (1), 015007. https://doi.org/10.1103/RevModPhys.88.015007.
(21) Attar, A. R.; Bhattacherjee, A.; Pemmaraju, C. D.; Schnorr, K.; Closser, K. D.; Prendergast, D.; Leone, S. R. Femtosecond X-Ray Spectroscopy of an Electrocyclic Ring-Opening Reaction. *Science* **2017**, *356* (6333), 54–59. https://doi.org/10.1126/science.aaj2198.
(22) Pellegrini, C.; Marinelli, A.; Reiche, S. The Physics of X-Ray Free-Electron Lasers. *Reviews of Modern Physics* **2016**, *88* (1), 015006. https://doi.org/10.1103/RevModPhys.88.015006.
(23) Popmintchev, T.; Chen, M.-C.; Popmintchev, D.; Arpin, P.; Brown, S.; Ališauskas, S.; Andriukaitis, G.; Balčiunas, T.; Mücke, O. D.; Pugzlys, A.; Baltuška, A.; Shim, B.; Schrauth, S. E.; Gaeta, A.; Hernández-García, C.; Plaja, L.; Becker, A.; Jaron-Becker, A.; Murnane, M. M.; Kapteyn, H. C. Bright Coherent Ultrahigh Harmonics in the KeV X-Ray Regime from Mid-Infrared Femtosecond Lasers. *Science* **2012**, *336* (6086), 1287–1291. https://doi.org/10.1126/science.1218497.
(24) Lewenstein, M.; Balcou, Ph.; Ivanov, M. Yu.; L'Huillier, A.; Corkum, P. B. Theory of High-Harmonic Generation by Low-Frequency Laser Fields. *Physical Review A* **1994**, *49* (3), 2117–2132. https://doi.org/10.1103/PhysRevA.49.2117.
(25) Krausz, F.; Ivanov, M. Attosecond Physics. *Reviews of Modern Physics* **2009**, *81* (1), 163–234. https://doi.org/10.1103/RevModPhys.81.163.
(26) Brabec, T.; Krausz, F. Intense Few-Cycle Laser Fields: Frontiers of Nonlinear Optics. *Reviews of Modern Physic* **2000**, *72* (2), 545–591. https://doi.org/10.1103/RevModPhys.72.545.
(27) Vinson, J.; Rehr, J. J.; Kas, J. J.; Shirley, E. L. Bethe-Salpeter Equation Calculations of Core Excitation Spectra. *Physical Review B* **2011**, *83* (11), 115106. https://doi.org/10.1103/PhysRevB.83.115106.
(28) Groot, F. de. Multiplet Effects in X-Ray Spectroscopy. *Coordination Chemistry Reviews* **2005**, *249* (1), 31–63. https://doi.org/10.1016/j.ccr.2004.03.018.

(29) Cushing, S. K.; Porter, I. J.; Roulet, B. R. de; Lee, A.; Marsh, B. M.; Szoke, S.; Vaida, M. E.; Leone, S. R. Layer-Resolved Ultrafast Extreme Ultraviolet Measurement of Hole Transport in a Ni-TiO_2-Si Photoanode. *Science Advances* **2020**, *6* (14), eaay6650. https://doi.org/10.1126/sciadv.aay6650.
(30) Ankudinov, A. L.; Ravel, B.; Rehr, J. J.; Conradson, S. D. Real-Space Multiple-Scattering Calculation and Interpretation of x-Ray-Absorption near-Edge Structure. *Physical Review B* **1998**, *58* (12), 7565–7576. https://doi.org/10.1103/PhysRevB.58.7565.
(31) Cushing, S. K.; Lee, A.; Porter, I. J.; Carneiro, L. M.; Chang, H.-T.; Zürch, M.; Leone, S. R. Differentiating Photoexcited Carrier and Phonon Dynamics in the Δ, L, and Γ Valleys of Si(100) with Transient Extreme Ultraviolet Spectroscopy. *Journal of Physical Chemistry C* **2019**, *123* (6), 3343–3352. https://doi.org/10.1021/acs.jpcc.8b10887.
(32) Chang, H.-T.; Guggenmos, A.; Cushing, S. K.; Cui, Y.; Din, N. U.; Acharya, S. R.; Porter, I. J.; Kleineberg, U.; Turkowski, V.; Rahman, T. S.; Neumark, D. M.; Leone, S. R. Electron Thermalization and Relaxation in Laser-Heated Nickel by Few-Femtosecond Core-Level Transient Absorption Spectroscopy. *Physical Review B* **2021**, *103* (6), 064305. https://doi.org/10.1103/PhysRevB.103.064305.
(33) Brown, M.; Peierls, R. E.; Stern, E. A. White Lines in X-Ray Absorption. *Physical Review B* **1977**, *15* (2), 738–744. https://doi.org/10.1103/PhysRevB.15.738.
(34) Li, J.; Nagamani, C.; Moore, J. S. Polymer Mechanochemistry: From Destructive to Productive. *Accounts of Chemical Research* **2015**, *48* (8), 2181–2190. https://doi.org/10.1021/acs.accounts.5b00184.
(35) Davis, D. A.; Hamilton, A.; Yang, J. L.; Cremar, L. D.; Van Gough, D.; Potisek, S. L.; Ong, M. T.; Braun, P. V.; Martinez, T. J.; White, S. R.; Moore, J. S.; Sottos, N. R. Force-Induced Activation of Covalent Bonds in Mechanoresponsive Polymeric Materials. *Nature* **2009**, *459* (7243), 68–72. https://doi.org/10.1038/nature07970.
(36) Robb, M. J.; Kim, T. A.; Halmes, A. J.; White, S. R.; Sottos, N. R.; Moore, J. S. Regioisomer-Specific Mechanochromism of Naphthopyran in Polymeric Materials. *Journal of the American Chemical Society* **2016**, *138* (38), 12328–12331. https://doi.org/10.1021/jacs.6b07610.
(37) Chen, Z. X.; Mercer, J. A. M.; Zhu, X. L.; Romaniuk, J. A. H.; Pfattner, R.; Cegelski, L.; Martinez, T. J.; Burns, N. Z.; Xia, Y. Mechanochemical Unzipping of Insulating Polyladderene to Semiconducting Polyacetylene. *Science* **2017**, *357* (6350), 475–478. https://doi.org/10.1126/science.aan2797.
(38) Su, J. K.; Feist, J. D.; Yang, J.; Mercer, J. A. M.; Romaniuk, J. A. H.; Chen, Z.; Cegelski, L.; Burns, N. Z.; Xia, Y. Synthesis and Mechanochemical Activation of Ladderene–Norbornene Block Copolymers. *Journal of the American Chemical Society* **2018**. https://doi.org/10.1021/jacs.8b08908.
(39) Wang, J. P.; Kouznetsova, T. B.; Boulatov, R.; Craig, S. L. Mechanical Gating of a Mechanochemical Reaction Cascade. *Nature Communications* **2016**, *7*. https://doi.org/10.1038/ncomms13433.
(40) Diesendruck, C. E.; Steinberg, B. D.; Sugai, N.; Silberstein, M. N.; Sottos, N. R.; White, S. R.; Braun, P. V.; Moore, J. S. Proton-Coupled Mechanochemical Transduction: A Mechanogenerated Add.Journal of the American Chemical Society **2012**, *134* (30), 12446–12449. https://doi.org/10.1021/ja305645x.
(41) Hu, X. R.; McFadden, M. E.; Barber, R. W.; Robb, M. J. Mechanochemical Regulation of a Photochemical Reaction. *Journal of the American Chemical Society* **2018**, *140* (43), 14073–14077. https://doi.org/10.1021/jacs.8b09628.
(42) Hu, X.; Zeng, T.; Husic, C. C.; Robb, M. J. Mechanically Triggered Small Molecule Release from a Masked Furfuryl Carbonate. *Journal of the American Chemical Society* **2019**. https://doi.org/10.1021/jacs.9b08663.

(43) Piermattei, A.; Karthikeyan, S.; Sijbesma, R. P. Activating Catalysts with Mechanical Force. *Nature Chemistry* **2009**, *1* (2), 133–137. https://doi.org/10.1038/nchem.167.
(44) Wang, J. P.; Kouznetsova, T. B.; Craig, S. L. Reactivity and Mechanism of a Mechanically Activated Anti-Woodward-Hoffmann-DePuy Reaction.Journal of the American Chemical Society **2015**, *137* (36), 11554–11557. https://doi.org/10.1021/jacs.5b06168.
(45) Hickenboth, C. R.; Moore, J. S.; White, S. R.; Sottos, N. R.; Baudry, J.; Wilson, S. R. Biasing Reaction Pathways with Mechanical Force. *Nature* **2007**, *446* (7134), 423–427. https://doi.org/10.1038/nature05681.
(46) Wang, J. P.; Kouznetsova, T. B.; Niu, Z. B.; Rheingold, A. L.; Craig, S. L. Accelerating a Mechanically Driven Anti-Woodward-Hoffmann Ring Opening with a Polymer Lever Arm Effect. *Journal of Organic Chemistry* **2015**, *80* (23), 11895–11898. https://doi.org/10.1021/acs.joc.5b01465.
(47) Klein, I. M.; Husic, C. C.; Kovács, D. P.; Choquette, N. J.; Robb, M. J. Validation of the CoGEF Method as a Predictive Tool for Polymer Mechanochemistry. *Journal of the American Chemical Society* **2020**. https://doi.org/10.1021/jacs.0c06868.
(48) Marsh, B. M.; Vaida, M. E.; Cushing, S. K.; Lamoureux, B. R.; Leone, S. R. Measuring the Surface Photovoltage of a Schottky Barrier under Intense Light Conditions: Zn/p-Si(100) by Laser Time-Resolved Extreme Ultraviolet Photoelectron Spectroscopy. *Journal of Physical Chemistry. C* **2017**, *121* (40), 21904–21912. https://doi.org/10.1021/acs.jpcc.7b06406.
(49) Kraus, P. M.; Zürch, M.; Cushing, S. K.; Neumark, D. M.; Leone, S. R. The Ultrafast X-Ray Spectroscopic Revolution in Chemical Dynamics. *Nature Reviews Chemistry* **2018**, *2* (6), 82–94. https://doi.org/10.1038/s41570-018-0008-8.
(50) Geneaux, R.; Marroux, H. J. B.; Guggenmos, A.; Neumark, D. M.; Leone, S. R. Transient Absorption Spectroscopy Using High Harmonic Generation: A Review of Ultrafast X-Ray Dynamics in Molecules and Solids. *Philosophical Transactions of the Royal Society A* **2019**, *377* (2145), 20170463. https://doi.org/10.1098/rsta.2017.0463.
(51) Géneaux, R.; Kaplan, C. J.; Yue, L.; Ross, A. D.; Bækhøj, J. E.; Kraus, P. M.; Chang, H.-T.; Guggenmos, A.; Huang, M.-Y.; Zürch, M.; Schafer, K. J.; Neumark, D. M.; Gaarde, M. B.; Leone, S. R. Attosecond Time-Domain Measurement of Core-Level-Exciton Decay in Magnesium Oxide. *Physical Review Letters* **2020**, *124* (20), 207401. https://doi.org/10.1103/PhysRevLett.124.207401.
(52) Cushing, S. K.; Zurch, M.; Kraus, P. M.; Carneiro, L. M.; Lee, A.; Chang, H. T.; Kaplan, C. J.; Leone, S. R. Hot Phonon and Carrier Relaxation in Si(100) Determined by Transient Extreme Ultraviolet Spectroscopy. *Structural Dynamics* **2018**, *5* (5), 054302. https://doi.org/10.1063/1.5038015.
(53) Zhang, K.; Ash, R.; Girolami, G. S.; Vura-Weis, J. Tracking the Metal-Centered Triplet in Photoinduced Spin Crossover of $Fe(phen)_3^{2+}$ with Tabletop Femtosecond M-Edge X-Ray Absorption Near-Edge Structure Spectroscopy. *Journal of the American Chemical Society* **2019**, *141* (43), 17180–17188. https://doi.org/10.1021/jacs.9b07332.
(54) Vura-Weis, J.; Jiang, C.-M.; Liu, C.; Gao, H.; Lucas, J. M.; de Groot, F. M. F.; Yang, P.; Alivisatos, A. P.; Leone, S. R. Femtosecond $M_{2,3}$ -Edge Spectroscopy of Transition-Metal Oxides: Photoinduced Oxidation State Change in α-Fe_2O_3. *Journal of Physical Chemistry Letters* **2013**, *4* (21), 3667–3671. https://doi.org/10.1021/jz401997d.
(55) Zhang, K.; Lin, M.-F.; Ryland, E. S.; Verkamp, M. A.; Benke, K.; de Groot, F. M. F.; Girolami, G. S.; Vura-Weis, J. Shrinking the Synchrotron: Tabletop Extreme Ultraviolet Absorption of Transition-Metal Complexes. *Journal of Physical Chemistry Letters* **2016**, *7* (17), 3383–3387. https://doi.org/10.1021/acs.jpclett.6b01393.
(56) Hergott, J.-F.; Kovacev, M.; Merdji, H.; Hubert, C.; Mairesse, Y.; Jean, E.; Breger, P.; Agostini, P.; Carré, B.; Salières, P. Extreme-Ultraviolet High-Order Harmonic Pulses in the Microjoule Range. *Physical Review A* **2002**, *66* (2), 021801. https://doi.org/10.1103/PhysRevA.66.021801.

(57) Koralek, J. D.; Kim, J. B.; Brůža, P.; Curry, C. B.; Chen, Z.; Bechtel, H. A.; Cordones, A. A.; Sperling, P.; Toleikis, S.; Kern, J. F.; Moeller, S. P.; Glenzer, S. H.; DePonte, D. P. Generation and Characterization of Ultrathin Free-Flowing Liquid Sheets. *Nature Communications* **2018**, *9* (1), 1353. https://doi.org/10.1038/s41467-018-03696-w.
(58) Ekimova, M.; Quevedo, W.; Faubel, M.; Wernet, P.; Nibbering, E. T. J. A Liquid Flatjet System for Solution Phase Soft-x-Ray Spectroscopy. *Structural Dynamics* **2015**, *2* (5), 054301. https://doi.org/10.1063/1.4928715.
(59) Luu, T. T.; Yin, Z.; Jain, A.; Gaumnitz, T.; Pertot, Y.; Ma, J.; Wörner, H. J. Extreme–Ultraviolet High–Harmonic Generation in Liquids. *Nature Communications* **2018**, *9* (1), 3723. https://doi.org/10.1038/s41467-018-06040-4.
(60) Smith, A. D.; Balčiūnas, T.; Chang, Y.-P.; Schmidt, C.; Zinchenko, K.; Nunes, F. B.; Rossi, E.; Svoboda, V.; Yin, Z.; Wolf, J.-P.; Wörner, H. J. Femtosecond Soft-X-Ray Absorption Spectroscopy of Liquids with a Water-Window High-Harmonic Source. *Journal of Physical Chemical Letters* **2020**, *11* (6), 1981–1988. https://doi.org/10.1021/acs.jpclett.9b03559.
(61) Kato, K.; Mashiko, H.; Kunihashi, Y.; Omi, H.; Gotoh, H.; Oguri, K. Highly Sensitive Transient Reflection Measurement in Extreme Ultraviolet Region for Tracking Carrier and Coherent Phonon Dynamics. *Optical Express, OE* **2020**, *28* (2), 1595–1602. https://doi.org/10.1364/OE.381585.
(62) Froemel, Paul. Generation of few-cycle laser pulses by hollow-core fiber compression for high harmonic generation. Master's Thesis, Humboldt University, Berlin.
(63) Diels, J.-C.; Rudolph, W. *Ultrashort Laser Pulse Phenomena: Fundamentals, Techniques, and Applications on a Femtosecond Time Scale*, 2nd ed.; Optics and photonics; Elsevier / Academic Press: Amsterdam ; Boston, 2006.
(64) Shen, Y. R.; Yang, G.-Z. Theory of Self-Phase Modulation and Spectral Broadening. In *The Supercontinuum Laser Source*; Alfano, R. R., Ed.; Springer: New York, NY, 1989; pp 1–32. https://doi.org/10.1007/978-1-4757-2070-9_1.
(65) Krause, J. L.; Schafer, K. J.; Kulander, K. C. High-Order Harmonic Generation from Atoms and Ions in the High Intensity Regime. *Physical Review Letters* **1992**, *68* (24), 3535–3538. https://doi.org/10.1103/PhysRevLett.68.3535.
(66) Ishikawa, K. L. High-Harmonic Generation.
(67) Iravani, H.; Vafaee, M. Breakdown of Odd-Harmonic Rule in the High Harmonic Generation Spectra of the Hydrogen Molecular Ion. *Journal of Physics: Conference Series* **2017**, *869*, 012004. https://doi.org/10.1088/1742-6596/869/1/012004.
(68) Sayrac, M.; Kolomenskii, A. A.; Dong, J.; Schuessler, H. A. Generation of Even and Odd Harmonics in the XUV Region with Controlling the Relative Delay and Polarization of Two-Color Fields. *Optik* **2021**, *226*, 165966. https://doi.org/10.1016/j.ijleo.2020.165966.
(69) Barreau, L.; Ross, A. D.; Garg, S.; Kraus, P. M.; Neumark, D. M.; Leone, S. R. Efficient Table-Top Dual-Wavelength Beamline for Ultrafast Transient Absorption Spectroscopy in the Soft X-Ray Region. *Scientific Reports* **2020**, *10* (1), 5773. https://doi.org/10.1038/s41598-020-62461-6.
(70) Popmintchev, T.; Chen, M.-C.; Bahabad, A.; Gerrity, M.; Sidorenko, P.; Cohen, O.; Christov, I. P.; Murnane, M. M.; Kapteyn, H. C. Phase Matching of High Harmonic Generation in the Soft and Hard X-Ray Regions of the Spectrum. *Proceedings of the National Academy of Sciences* **2009**, *106* (26), 10516–10521. https://doi.org/10.1073/pnas.0903748106.
(71) Wilke, I.; Sengupta, S. Nonlinear Optical Techniques for THZ Pulse Generation and Detection. 32.
(72) Jazbinsek, M.; Puc, U.; Abina, A.; Zidansek, A. Organic Crystals for THz Photonics. *Applied Sciences* **2019**, *9* (5), 882. https://doi.org/10.3390/app9050882.
(73) Tomasino, A.; Parisi, A.; Stivala, S.; Livreri, P.; Cino, A. C.; Busacca, A. C.; Peccianti, M.; Morandotti, R. Wideband THz Time Domain Spectroscopy Based on Optical Rectification and Electro-Optic Sampling. *Scientific Reports* **2013**, *3* (1), 1–8. https://doi.org/10.1038/srep03116.

(74) Zurch, M.; Chang, H. T.; Kraus, P. M.; Cushing, S. K.; Borja, L. J.; Gandman, A.; Kaplan, C. J.; Oh, M. H.; Prell, J. S.; Prendergast, D.; Pemmaraju, C. D.; Neumark, D. M.; Leone, S. R. Ultrafast Carrier Thermalization and Trapping in Silicon-Germanium Alloy Probed by Extreme Ultraviolet Transient Absorption Spectroscopy. *Structural Dynamics* **2017**, *4* (4), 044029. https://doi.org/10.1063/1.4985056.
(75) Biswas, S.; Husek, J.; Baker, L. R. Elucidating Ultrafast Electron Dynamics at Surfaces Using Extreme Ultraviolet (XUV) Reflection–Absorption Spectroscopy. *Chemical Communications* **2018**, *54* (34), 4216–4230. https://doi.org/10.1039/C8CC01745J.
(76) Cirri, A.; Husek, J.; Biswas, S.; Baker, L. R. Achieving Surface Sensitivity in Ultrafast XUV Spectroscopy: M2,3-Edge Reflection–Absorption of Transition Metal Oxides. *Journal of Physical Chemistry C* **2017**, *121* (29), 15861–15869. https://doi.org/10.1021/acs.jpcc.7b05127.
(77) Franchini, C.; Reticcioli, M.; Setvin, M.; Diebold, U. Polarons in Materials. *Nature Reviews Materials* **2021**, 1–27. https://doi.org/10.1038/s41578-021-00289-w.
(78) Emin, D. Optical Properties of Large and Small Polarons and Bipolarons. *Physical Review B* **1993**, *48* (18), 13691–13702. https://doi.org/10.1103/PhysRevB.48.13691.
(79) Miyata, K.; Atallah, T. L.; Zhu, X.-Y. Lead Halide Perovskites: Crystal-Liquid Duality, Phonon Glass Electron Crystals, and Large Polaron Formation. *Science Advances* **2017**, *3* (10), e1701469. https://doi.org/10.1126/sciadv.1701469.
(80) Guzelturk, B.; Winkler, T.; Van de Goor, T. W. J.; Smith, M. D.; Bourelle, S. A.; Feldmann, S.; Trigo, M.; Teitelbaum, S. W.; Steinrück, H.-G.; de la Pena, G. A.; Alonso-Mori, R.; Zhu, D.; Sato, T.; Karunadasa, H. I.; Toney, M. F.; Deschler, F.; Lindenberg, A. M. Visualization of Dynamic Polaronic Strain Fields in Hybrid Lead Halide Perovskites. *Nature Materials* **2021**, *20* (5), 618–623. https://doi.org/10.1038/s41563-020-00865-5.
(81) Ziwritsch, M.; Müller, S.; Hempel, H.; Unold, T.; Abdi, F. F.; van de Krol, R.; Friedrich, D.; Eichberger, R. Direct Time-Resolved Observation of Carrier Trapping and Polaron Conductivity in BiVO4. *ACS Energy Lett.* **2016**, *1* (5), 888–894. https://doi.org/10.1021/acsenergylett.6b00423.
(82) Brongersma, M. L.; Halas, N. J.; Nordlander, P. Plasmon-Induced Hot Carrier Science and Technology. *Nature Nanotechnology* **2015**, *10* (1), 25–34. https://doi.org/10.1038/nnano.2014.311.
(83) Zhou, J.-J.; Park, J.; Lu, I.-T.; Maliyov, I.; Tong, X.; Bernardi, M. Perturbo: A Software Package for Ab Initio Electron–Phonon Interactions, Charge Transport and Ultrafast Dynamics. *Computer Physics Communications* **2021**, *264*, 107970. https://doi.org/10.1016/j.cpc.2021.107970.
(84) Norman, P.; Dreuw, A. Simulating X-Ray Spectroscopies and Calculating Core-Excited States of Molecules. *Chemical Reviews* **2018**, *118* (15), 7208–7248. https://doi.org/10.1021/acs.chemrev.8b00156.
(85) Ekimova, M.; Quevedo, W.; Szyc, Ł.; Iannuzzi, M.; Wernet, P.; Odelius, M.; Nibbering, E. T. J. Aqueous Solvation of Ammonia and Ammonium: Probing Hydrogen Bond Motifs with FT-IR and Soft X-Ray Spectroscopy. *Journal of the American Chemical Society* **2017**, *139* (36), 12773–12783. https://doi.org/10.1021/jacs.7b07207.
(86) Cederbaum, L. S.; Domcke, W.; Schirmer, J. Many-Body Theory of Core Holes. *Physical Review A* **1980**, *22* (1), 206–222. https://doi.org/10.1103/PhysRevA.22.206.
(87) Barth, A.; Schirmer, J. Theoretical Core-Level Excitation Spectra of N_2 and CO by a New Polarisation Propagator Method. *Journal of Physics B: Atomic and Molecular Physics* **1985**, *18* (5), 867–885. https://doi.org/10.1088/0022-3700/18/5/008.
(88) Triguero, L.; Pettersson, L. G. M.; Ågren, H. Calculations of Near-Edge x-Ray-Absorption Spectra of Gas-Phase and Chemisorbed Molecules by Means of Density-Functional and Transition-Potential Theory. *Physical Review B* **1998**, *58* (12), 8097–8110. https://doi.org/10.1103/PhysRevB.58.8097.
(89) Stöhr, J. *NEXAFS Spectroscopy*.

(90) de Groot, F. High-Resolution X-Ray Emission and X-Ray Absorption Spectroscopy. *Chemical Reviews* **2001**, *101* (6), 1779–1808. https://doi.org/10.1021/cr9900681.
(91) Groot, F. de. Multiplet Effects in X-Ray Spectroscopy. *Coordination Chemistry Reviews* **2005**, *249* (1–2), 31–63. https://doi.org/10.1016/j.ccr.2004.03.018.
(92) Reinholdt, P.; Vidal, M. L.; Kongsted, J.; Iannuzzi, M.; Coriani, S.; Odelius, M. Nitrogen K-Edge X-Ray Absorption Spectra of Ammonium and Ammonia in Water Solution: Assessing the Performance of Polarizable Embedding Coupled Cluster Methods. *Journal of Physical Chemistry Letters* **2021**, *12* (36), 8865–8871. https://doi.org/10.1021/acs.jpclett.1c02031.
(93) Montorsi, F.; Segatta, F.; Nenov, A.; Mukamel, S.; Garavelli, M. Soft X-Ray Spectroscopy Simulations with Multiconfigurational Wave Function Theory: Spectrum Completeness, Sub-EV Accuracy, and Quantitative Reproduction of Line Shapes. *Journal of Chemical Theory and Computation* **2022**, *18* (2), 1003–1016. https://doi.org/10.1021/acs.jctc.1c00566.
(94) Gao, S.-P.; Pickard, C. J.; Payne, M. C.; Zhu, J.; Yuan, J. Theory of Core-Hole Effects in $1s$ Core-Level Spectroscopy of the First-Row Elements. *Physical Review B* **2008**, *77* (11), 115122. https://doi.org/10.1103/PhysRevB.77.115122.
(95) Cederbaum, L. S.; Domcke, W. A Many-body Approach to the Vibrational Structure in Molecular Electronic Spectra. I. Theory. *Journal of Chemical Physics* **1976**, *64* (2), 603–611. https://doi.org/10.1063/1.432250.
(96) Runge, E.; Gross, E. K. U. Density-Functional Theory for Time-Dependent Systems. *Physical Review Letters* **1984**, *52* (12), 997–1000. https://doi.org/10.1103/PhysRevLett.52.997.
(97) Kolesov, G.; Kolesov, B. A.; Kaxiras, E. Polaron-Induced Phonon Localization and Stiffening in Rutile TiO_2. *Physical Review B* **2017**, *96* (19), 195165. https://doi.org/10.1103/PhysRevB.96.195165.
(98) Lian, C.; Ali, Z. A.; Kwon, H.; Wong, B. M. Indirect but Efficient: Laser-Excited Electrons Can Drive Ultrafast Polarization Switching in Ferroelectric Materials. *Journal of Physical Chemistry Letters* **2019**, *10* (12), 3402–3407. https://doi.org/10.1021/acs.jpclett.9b01046.
(99) Wang, Y.; Lopata, K.; Chambers, S. A.; Govind, N.; Sushko, P. V. Optical Absorption and Band Gap Reduction in (Fe1–XCrx)2O3 Solid Solutions: A First-Principles Study. *Journal of Physical Chemistry C* **2013**, *117* (48), 25504–25512. https://doi.org/10.1021/jp407496w.
(100) Konecny, L.; Vicha, J.; Komorovsky, S.; Ruud, K.; Repisky, M. Accurate X-Ray Absorption Spectra near L- and M-Edges from Relativistic Four-Component Damped Response Time-Dependent Density Functional Theory. *Inorganic Chemistry* **2022**, *61* (2), 830–846. https://doi.org/10.1021/acs.inorgchem.1c02412.
(101) Vinson, J. Bethe-Salpeter Equation Approach for Calculations of X-Ray Spectra. Thesis, University of Washington, Seattle, WA, 2013.
(102) Carneiro, L. M.; Cushing, S. K.; Liu, C.; Su, Y.; Yang, P.; Alivisatos, A. P.; Leone, S. R. Excitation-Wavelength-Dependent Small Polaron Trapping of Photoexcited Carriers in α-Fe_2O_3. *Nature Materials* **2017**, *16* (8), 819–825. https://doi.org/10.1038/nmat4936.
(103) Husek, J.; Cirri, A.; Biswas, S.; Baker, L. R. Surface Electron Dynamics in Hematite (α-Fe_2O_3): Correlation between Ultrafast Surface Electron Trapping and Small Polaron Formation †Electronic Supplementary Information (ESI) Available. See DOI: 10.1039/C7sc02826a. *Chemical Science* **2017**, *8* (12), 8170–8178. https://doi.org/10.1039/c7sc02826a.
(104) Biswas, S.; Wallentine, S.; Bandaranayake, S.; Baker, L. R. Controlling Polaron Formation at Hematite Surfaces by Molecular Functionalization Probed by XUV Reflection-Absorption Spectroscopy. *J. Chem. Phys.* **2019**, *151* (10), 104701. https://doi.org/10.1063/1.5115163.
(105) Porter, I. J.; Cushing, S. K.; Carneiro, L. M.; Lee, A.; Ondry, J. C.; Dahl, J. C.; Chang, H.-T.; Alivisatos, A. P.; Leone, S. R. Photoexcited Small Polaron Formation in Goethite (α-FeOOH) Nanorods Probed by Transient Extreme Ultraviolet Spectroscopy. *Journal of Physical Chemistry Letters* **2018**, *9* (14), 4120–4124. https://doi.org/10.1021/acs.jpcLetters8b01525.

(106) Biswas, S.; Husek, J.; Baker, L. R. Elucidating Ultrafast Electron Dynamics at Surfaces Using Extreme Ultraviolet (XUV) Reflection–Absorption Spectroscopy. *Chemical Communications***2018**, *54* (34), 4216–4230. https://doi.org/10.1039/C8CC01745J.
(107) Biswas, S.; Husek, J.; Londo, S.; Baker, L. R. Highly Localized Charge Transfer Excitons in Metal Oxide Semiconductors. *Nano Letters* **2018**, *18* (2), 1228–1233. https://doi.org/10.1021/acs.nanoLetters7b04818.
(108) Stavitski, E.; de Groot, F. M. F. The CTM4XAS Program for EELS and XAS Spectral Shape Analysis of Transition Metal L Edges. *Micron* **2010**, *41* (7), 687–694. https://doi.org/10.1016/j.micron.2010.06.005.
(109) Cushing, S. K.; Porter, I. J.; Roulet, B. R. de; Lee, A.; Marsh, B. M.; Szoke, S.; Vaida, M. E.; Leone, S. R. Layer-Resolved Ultrafast Extreme Ultraviolet Measurement of Hole Transport in a Ni-TiO2-Si Photoanode. *Science Advances* **2020**, *6* (14), eaay6650. https://doi.org/10.1126/sciadv.aay6650.
(110) Cushing, S. K.; Zürch, M.; Kraus, P. M.; Carneiro, L. M.; Lee, A.; Chang, H.-T.; Kaplan, C. J.; Leone, S. R. Hot Phonon and Carrier Relaxation in Si(100) Determined by Transient Extreme Ultraviolet Spectroscopy. *Structural Dynamics* **2018**, *5* (5), 054302. https://doi.org/10.1063/1.5038015.
(111) Kaplan, C. J.; Kraus, P. M.; Ross, A. D.; Zürch, M.; Cushing, S. K.; Jager, M. F.; Chang, H.-T.; Gullikson, E. M.; Neumark, D. M.; Leone, S. R. Femtosecond Tracking of Carrier Relaxation in Germanium with Extreme Ultraviolet Transient Reflectivity. *Physical Review B* **2018**, *97* (20), 205202. https://doi.org/10.1103/PhysRevB.97.205202.
(112) Cannelli, O.; Colonna, N.; Puppin, M.; Rossi, T. C.; Kinschel, D.; Leroy, L. M. D.; Löffler, J.; Budarz, J. M.; March, A. M.; Doumy, G.; Al Haddad, A.; Tu, M.-F.; Kumagai, Y.; Walko, D.; Smolentsev, G.; Krieg, F.; Boehme, S. C.; Kovalenko, M. V.; Chergui, M.; Mancini, G. F. Quantifying Photoinduced Polaronic Distortions in Inorganic Lead Halide Perovskite Nanocrystals. *Journal of the American Chemical Society* **2021**, *143* (24), 9048–9059. https://doi.org/10.1021/jacs.1c02403.
(113) Vinson, J.; Jach, T.; Müller, M.; Unterumsberger, R.; Beckhoff, B. Quasiparticle Lifetime Broadening in Resonant X-Ray Scattering of NH_4NO_3. *Physical Review B* **2016**, *94* (3), 035163. https://doi.org/10.1103/PhysRevB.94.035163.
(114) Li, L.; Zhang, R.; Vinson, J.; Shirley, E. L.; Greeley, J. P.; Guest, J. R.; Chan, M. K. Y. Imaging Catalytic Activation of CO_2 on Cu_2O (110): A First-Principles Study. *Chemistry of Materials* **2018**, *30* (6), 1912–1923. https://doi.org/10.1021/acs.chemmater.7b04803.
(115) Geondzhian, A.; Gilmore, K. Demonstration of Resonant Inelastic X-Ray Scattering as a Probe of Exciton-Phonon Coupling. *Physical Review B* **2018**, *98* (21), 214305. https://doi.org/10.1103/PhysRevB.98.214305.
(116) Attar, A. R.; Chang, H.-T.; Britz, A.; Zhang, X.; Lin, M.-F.; Krishnamoorthy, A.; Linker, T.; Fritz, D.; Neumark, D. M.; Kalia, R. K.; Nakano, A.; Ajayan, P.; Vashishta, P.; Bergmann, U.; Leone, S. R. Simultaneous Observation of Carrier-Specific Redistribution and Coherent Lattice Dynamics in 2H-MoTe2 with Femtosecond Core-Level Spectroscopy. *ACS Nano* **2020**, *14* (11), 15829–15840. https://doi.org/10.1021/acsnano.0c06988.
(117) Kvashnina, K. O.; Butorin, S. M. High-Energy Resolution X-Ray Spectroscopy at Actinide M4,5 and Ligand K Edges: What We Know, What We Want to Know, and What We Can Know. *Chemical Communications***2022**, *58* (3), 327–342. https://doi.org/10.1039/D1CC04851A.
(118) Nattino, F.; Marzari, N. Operando XANES from First-Principles and Its Application to Iridium Oxide. *Physical Chemistry Chemical Physics* **2020**, *22* (19), 10807–10818. https://doi.org/10.1039/C9CP06726D.
(119) Charles, N.; Yu, Y.; Giordano, L.; Jung, R.; Maglia, F.; Shao-Horn, Y. Toward Establishing Electronic and Phononic Signatures of Reversible Lattice Oxygen Oxidation in Lithium Transition

Metal Oxides For Li-Ion Batteries. *Chemistry of Materials* **2020**, *32* (13), 5502–5514. https://doi.org/10.1021/acs.chemmater.0c00245.
(120) Wansleben, M.; Vinson, J.; Holfelder, I.; Kayser, Y.; Beckhoff, B. Valence-to-Core X-Ray Emission Spectroscopy of Ti, TiO, and TiO_2 by Means of a Double Full-Cylinder Crystal von Hamos Spectrometer. *X-Ray Spectrometry* **2019**, *48* (2), 102–106. https://doi.org/10.1002/xrs.3000.
(121) Vinson, J.; Rehr, J. J.; Kas, J. J.; Shirley, E. L. Bethe-Salpeter Equation Calculations of Core Excitation Spectra. *Physical Review B* **2011**, *83* (11), 115106. https://doi.org/10.1103/PhysRevB.83.115106.
(122) Gilmore, K.; Vinson, J.; Shirley, E. L.; Prendergast, D.; Pemmaraju, C. D.; Kas, J. J.; Vila, F. D.; Rehr, J. J. Efficient Implementation of Core-Excitation Bethe–Salpeter Equation Calculations. *Computer Physics Communications* **2015**, *197*, 109–117. https://doi.org/10.1016/j.cpc.2015.08.014.
(123) Piccinin, S. The Band Structure and Optical Absorption of Hematite (α-Fe_2O_3): A First-Principles GW-BSE Study. *Physical Chemistry Chemical Physics* **2019**, *21* (6), 2957–2967. https://doi.org/10.1039/C8CP07132B.
(124) Giannozzi, P.; Baroni, S.; Bonini, N.; Calandra, M.; Car, R.; Cavazzoni, C.; Ceresoli, D.; Chiarotti, G. L.; Cococcioni, M.; Dabo, I.; Dal Corso, A.; de Gironcoli, S.; Fabris, S.; Fratesi, G.; Gebauer, R.; Gerstmann, U.; Gougoussis, C.; Kokalj, A.; Lazzeri, M.; Martin-Samos, L.; Marzari, N.; Mauri, F.; Mazzarello, R.; Paolini, S.; Pasquarello, A.; Paulatto, L.; Sbraccia, C.; Scandolo, S.; Sclauzero, G.; Seitsonen, A. P.; Smogunov, A.; Umari, P.; Wentzcovitch, R. M. QUANTUM ESPRESSO: A Modular and Open-Source Software Project for Quantum Simulations of Materials. *J Phys Condensed Matter* **2009**, *21* (39), 395502. https://doi.org/10.1088/0953-8984/21/39/395502.
(125) Giannozzi, P.; Andreussi, O.; Brumme, T.; Bunau, O.; Buongiorno Nardelli, M.; Calandra, M.; Car, R.; Cavazzoni, C.; Ceresoli, D.; Cococcioni, M.; Colonna, N.; Carnimeo, I.; Dal Corso, A.; de Gironcoli, S.; Delugas, P.; DiStasio, R. A.; Ferretti, A.; Floris, A.; Fratesi, G.; Fugallo, G.; Gebauer, R.; Gerstmann, U.; Giustino, F.; Gorni, T.; Jia, J.; Kawamura, M.; Ko, H.-Y.; Kokalj, A.; Küçükbenli, E.; Lazzeri, M.; Marsili, M.; Marzari, N.; Mauri, F.; Nguyen, N. L.; Nguyen, H.-V.; Otero-de-la-Roza, A.; Paulatto, L.; Poncé, S.; Rocca, D.; Sabatini, R.; Santra, B.; Schlipf, M.; Seitsonen, A. P.; Smogunov, A.; Timrov, I.; Thonhauser, T.; Umari, P.; Vast, N.; Wu, X.; Baroni, S. Advanced Capabilities for Materials Modelling with Quantum ESPRESSO. *Journal of Physics and Condensed Matter* **2017**, *29* (46), 465901. https://doi.org/10.1088/1361-648X/aa8f79.
(126) Kohn, W.; Sham, L. J. Self-Consistent Equations Including Exchange and Correlation Effects. *Physical Review* **1965**, *140* (4A), A1133–A1138. https://doi.org/10.1103/PhysRev.140.A1133.
(127) Salpeter, E. E.; Bethe, H. A. A Relativistic Equation for Bound-State Problems. *Physical Review* **1951**, *84* (6), 1232–1242. https://doi.org/10.1103/PhysRev.84.1232.
(128) Shirley, E. L.; Vinson, J. T.; Gilmore, K. The OCEAN Suite: Core Excitations; International Union of Crystallography, 2020. https://doi.org/10.1107/S157487072000333X.
(129) Shirley, E. L.; Pettersson, L. G. M.; Prendergast, D. Core-Hole Potentials and Related Effects; 2021. https://doi.org/10.1107/S1574870720011039.
(130) Pham, T. D.; Deskins, N. A. Efficient Method for Modeling Polarons Using Electronic Structure Methods. *Jounral of Chemical Theory and Computation* **2020**, *16* (8), 5264–5278. https://doi.org/10.1021/acs.jctc.0c00374.
(131) Shibuya, T.; Yasuoka, K.; Mirbt, S.; Sanyal, B. A Systematic Study of Polarons Due to Oxygen Vacancy Formation at the Rutile TiO_2 (110) Surface by GGA + *U* and HSE06 Methods. *Journal of Physics: Condensed Matter* **2012**, *24* (43), 435504. https://doi.org/10.1088/0953-8984/24/43/435504.
(132) Deskins, N. A.; Dupuis, M. Electron Transport via Polaron Hopping in Bulk Ti O 2 : A Density Functional Theory Characterization. *Physical Review B* **2007**, *75* (19), 195212. https://doi.org/10.1103/PhysRevB.75.195212.

(133) Shelton, J. L.; Knowles, K. E. Thermally Activated Optical Absorption into Polaronic States in Hematite. *Journal of Physical Chemistry Letters* **2021**, *12* (13), 3343–3351. https://doi.org/10.1021/acs.jpcLetters0c03751.
(134) Smyth, J. R.; Jacobsen, S. D.; Hazen, R. M. Comparative Crystal Chemistry of Dense Oxide Minerals. *Reviews in Mineralogy and Geochemistry* **2000**, *41* (1), 157–186. https://doi.org/10.2138/rmg.2000.41.6.
(135) Soldatov, M. A.; Martini, A.; Bugaev, A. L.; Pankin, I.; Medvedev, P. V.; Guda, A. A.; Aboraia, A. M.; Podkovyrina, Y. S.; Budnyk, A. P.; Soldatov, A. A.; Lamberti, C. The Insights from X-Ray Absorption Spectroscopy into the Local Atomic Structure and Chemical Bonding of Metal–Organic Frameworks. *Polyhedron* **2018**, *155*, 232–253. https://doi.org/10.1016/j.poly.2018.08.004.
(136) Guda, S. A.; Guda, A. A.; Soldatov, M. A.; Lomachenko, K. A.; Bugaev, A. L.; Lamberti, C.; Gawelda, W.; Bressler, C.; Smolentsev, G.; Soldatov, A. V.; Joly, Y. Optimized Finite Difference Method for the Full-Potential XANES Simulations: Application to Molecular Adsorption Geometries in MOFs and Metal–Ligand Intersystem Crossing Transients. *Journal of Chemical Theory and Computation* **2015**, *11* (9), 4512–4521. https://doi.org/10.1021/acs.jctc.5b00327.
(137) Woicik, J. C.; Weiland, C.; Rumaiz, A. K.; Brumbach, M.; Quackenbush, N. F.; Ablett, J. M.; Shirley, E. L. Revealing Excitonic Processes and Chemical Bonding in $\mathrm{Mo}{\mathrm{S}}_{2}$ by X-Ray Spectroscopy. *Physical Review B* **2018**, *98* (11), 115149. https://doi.org/10.1103/PhysRevB.98.115149.
(138) Burke, K. Perspective on Density Functional Theory. *Journal of Chemical Physics* **2012**, *136* (15), 150901. https://doi.org/10.1063/1.4704546.
(139) Gilmore, K.; Shirley, E. L. Numerical Quantification of the Vibronic Broadening of the SrTiO$\less$sub$\greater$3$\less$/Sub$\greater$Ti L-Edge Spectrum. *Journal of Physics: Condensed Matter***2010**, *22* (31), 315901. https://doi.org/10.1088/0953-8984/22/31/315901.
(140) Biswas, S.; Husek, J.; Londo, S.; Fugate, E. A.; Baker, L. R. Identifying the Acceptor State in NiO Hole Collection Layers: Direct Observation of Exciton Dissociation and Interfacial Hole Transfer across a Fe_2O_3/NiO Heterojunction. *Physical Chemistry Chemical Physics* **2018**, *20* (38), 24545–24552. https://doi.org/10.1039/C8CP04502J.
(141) Zürch, M.; Chang, H.-T.; Borja, L. J.; Kraus, P. M.; Cushing, S. K.; Gandman, A.; Kaplan, C. J.; Oh, M. H.; Prell, J. S.; Prendergast, D.; Pemmaraju, C. D.; Neumark, D. M.; Leone, S. R. Direct and Simultaneous Observation of Ultrafast Electron and Hole Dynamics in Germanium. *Nature Communications* **2017**, *8* (1), 1–11. https://doi.org/10.1038/ncomms15734.
(142) Zürch, M.; Chang, H.-T.; Kraus, P. M.; Cushing, S. K.; Borja, L. J.; Gandman, A.; Kaplan, C. J.; Oh, M. H.; Prell, J. S.; Prendergast, D.; Pemmaraju, C. D.; Neumark, D. M.; Leone, S. R. Ultrafast Carrier Thermalization and Trapping in Silicon-Germanium Alloy Probed by Extreme Ultraviolet Transient Absorption Spectroscopy. *Structural Dynamics* **2017**, *4* (4), 044029. https://doi.org/10.1063/1.4985056.
(143) Lin, M.-F.; Verkamp, M. A.; Leveillee, J.; Ryland, E. S.; Benke, K.; Zhang, K.; Weninger, C.; Shen, X.; Li, R.; Fritz, D.; Bergmann, U.; Wang, X.; Schleife, A.; Vura-Weis, J. Carrier-Specific Femtosecond XUV Transient Absorption of PbI_2 Reveals Ultrafast Nonradiative Recombination. *Journal of Physical Chemistry C* **2017**, *121* (50), 27886–27893. https://doi.org/10.1021/acs.jpcc.7b11147.
(144) Liu, H.; Klein, I. M.; Michelsen, J. M.; Cushing, S. K. Element-Specific Electronic and Structural Dynamics Using Transient XUV and Soft X-Ray Spectroscopy. *Chem* **2021**, *7* (10), 2569–2584. https://doi.org/10.1016/j.chempr.2021.09.005.
(145) Ryland, E. S.; Zhang, K.; Vura-Weis, J. Sub-100 Fs Intersystem Crossing to a Metal-Centered Triplet in Ni(II)OEP Observed with M-Edge XANES. *Journal of Physical Chemistry A* **2019**, *123* (25), 5214–5222. https://doi.org/10.1021/acs.jpca.9b03376.

(146) Gedamu Tamirat, A.; Rick, J.; Aregahegn Dubale, A.; Su, W.-N.; Hwang, B.-J. Using Hematite for Photoelectrochemical Water Splitting: A Review of Current Progress and Challenges. *Nanoscale Horizons* **2016**, *1* (4), 243–267. https://doi.org/10.1039/C5NH00098J.
(147) Zandi, O.; Hamann, T. W. The Potential versus Current State of Water Splitting with Hematite. *Physical Chemistry Chemical Physics* **2015**, *17* (35), 22485–22503. https://doi.org/10.1039/C5CP04267D.
(148) Sivula, K.; Le Formal, F.; Grätzel, M. Solar Water Splitting: Progress Using Hematite (α-Fe_2O_3) Photoelectrodes. *ChemSusChem* **2011**, *4* (4), 432–449. https://doi.org/10.1002/cssc.201000416.
(149) Bandaranayake, S.; Hruska, E.; Londo, S.; Biswas, S.; Baker, L. R. Small Polarons and Surface Defects in Metal Oxide Photocatalysts Studied Using XUV Reflection–Absorption Spectroscopy. *Journal of Physical Chemistry C* **2020**, *124* (42), 22853–22870. https://doi.org/10.1021/acs.jpcc.0c07047.
(150) Stoneham, A. M.; Gavartin, J.; Shluger, A. L.; Kimmel, A. V.; Ramo, D. M.; Rønnow, H. M.; Aeppli, G.; Renner, C. Trapping, Self-Trapping and the Polaron Family. *Journal of Physics: Condensed Matter* **2007**, *19* (25), 255208. https://doi.org/10.1088/0953-8984/19/25/255208.
(151) Rettie, A. J. E.; Chemelewski, W. D.; Emin, D.; Mullins, C. B. Unravelling Small-Polaron Transport in Metal Oxide Photoelectrodes. *Journal of Physical Chemistry Letters* **2016**, *7* (3), 471–479. https://doi.org/10.1021/acs.jpcLetters5b02143.
(152) Adelstein, N.; Neaton, J. B.; Asta, M.; De Jonghe, L. C. Density Functional Theory Based Calculation of Small-Polaron Mobility in Hematite. *Physical Review B* **2014**, *89* (24), 245115. https://doi.org/10.1103/PhysRevB.89.245115.
(153) Biswas, S.; Husek, J.; Londo, S.; Baker, L. R. Ultrafast Electron Trapping and Defect-Mediated Recombination in NiO Probed by Femtosecond Extreme Ultraviolet Reflection–Absorption Spectroscopy. *Journal of Physical Chemistry Letters* **2018**, *9* (17), 5047–5054. https://doi.org/10.1021/acs.jpcLetters8b01865.
(154) Liu, H.; Michelsen, J. M.; Klein, I. M.; Cushing, S. K. Measuring Photoexcited Electron and Hole Dynamics in ZnTe and Modeling Excited State Core-Valence Effects in Transient XUV Reflection Spectroscopy. *arXiv:2108.02262 [cond-mat, physics:physics]* **2021**.
(155) Wang, H.; Young, A. T.; Guo, J.; Cramer, S. P.; Friedrich, S.; Braun, A.; Gu, W. Soft X-Ray Absorption Spectroscopy and Resonant Inelastic X-Ray Scattering Spectroscopy below 100 EV: Probing First-Row Transition-Metal M-Edges in Chemical Complexes. *Journal of Synchrotron Radiation* **2013**, *20* (Pt 4), 614–619. https://doi.org/10.1107/S0909049513003142.
(156) Vaida, M. E.; Leone, S. R. Femtosecond Extreme Ultraviolet Photoemission Spectroscopy: Observation of Ultrafast Charge Transfer at the n-TiO2/p-Si(100) Interface with Controlled TiO2 Oxygen Vacancies. *Journal of Physical Chemistry C* **2016**, *120* (5), 2769–2776. https://doi.org/10.1021/acs.jpcc.5b11161.
(157) Stöhr, J. NEXAFS Spectroscopy. In *NEXAFS Spectroscopy*; Stöhr, J., Ed.; Springer Series in Surface Sciences; Springer: Berlin, Heidelberg, 1992; pp 1–7. https://doi.org/10.1007/978-3-662-02853-7_1.
(158) Klein, I. M.; Liu, H.; Nimlos, D.; Krotz, A.; Cushing, S. K. *Ab Initio* Prediction of Excited-State and Polaron Effects in Transient XUV Measurements of α-Fe_2O_3. *Journal of the American Chemical Society* **2022**, jacs.2c03994. https://doi.org/10.1021/jacs.2c03994.
(159) Agarwal, B. K.; Givens, M. P. Soft X-Ray Absorption by Manganese and Manganese Oxide. *Journal of Physics and Chemistry of Solids* **1958**, *6* (2–3), 178–179. https://doi.org/10.1016/0022-3697(58)90092-1.
(160) Jiang, C.-M.; Baker, L. R.; Lucas, J. M.; Vura-Weis, J.; Alivisatos, A. P.; Leone, S. R. Characterization of Photo-Induced Charge Transfer and Hot Carrier Relaxation Pathways in Spinel

Cobalt Oxide (Co_3O_4). *Journal of Physical Chemistry C* **2014**, *118* (39), 22774–22784. https://doi.org/10.1021/jp5071133.
(161) Chiuzbăian, S. G.; Ghiringhelli, G.; Dallera, C.; Grioni, M.; Amann, P.; Wang, X.; Braicovich, L.; Patthey, L. Localized Electronic Excitations in NiO Studied with Resonant Inelastic X-Ray Scattering at the Ni M Threshold: Evidence of Spin Flip. *Physical Review Letters* **2005**, *95* (19), 197402. https://doi.org/10.1103/PhysRevLetters95.197402.
(162) Basu, R.; Srihari, V.; Sardar, M.; Srivastava, S. K.; Bera, S.; Dhara, S. Probing Phase Transition in VO_2 with the Novel Observation of Low-Frequency Collective Spin Excitation. *Scientific Reports* **2020**, *10* (1), 1977. https://doi.org/10.1038/s41598-020-58813-x.
(163) Luo, H. G.; Xiang, T.; Wang, X. Q.; Su, Z. B.; Yu, L. Fano Resonance for Anderson Impurity Systems. *Physical Review Letters* **2004**, *92* (25), 256602. https://doi.org/10.1103/PhysRevLetters92.256602.
(164) van der Heide, P. A. W. Multiplet Splitting Patterns Exhibited by the First Row Transition Metal Oxides in X-Ray Photoelectron Spectroscopy. *Journal of Electron Spectroscopy and Related Phenomena* **2008**, *164* (1), 8–18. https://doi.org/10.1016/j.elspec.2008.04.001.
(165) Lany, S. Semiconducting Transition Metal Oxides. *Journal of Physics: Condensed Matter* **2015**, *27* (28), 283203. https://doi.org/10.1088/0953-8984/27/28/283203.
(166) Tokura, Y. Correlated-Electron Physics in Transition-Metal Oxides. *Physics Today* **2003**, *56* (7), 50–55. https://doi.org/10.1063/1.1603080.
(167) Hozoi, L. Localized States in Transition Metal Oxides. Thesis fully internal (DIV), University of Groningen, Groningen, 2003.
(168) Gagliardi, L.; Truhlar, D. G.; Li Manni, G.; Carlson, R. K.; Hoyer, C. E.; Bao, J. L. Multiconfiguration Pair-Density Functional Theory: A New Way To Treat Strongly Correlated Systems. *Acc. Chem. Res.* **2017**, *50* (1), 66–73. https://doi.org/10.1021/acs.accounts.6b00471.
(169) Reticcioli, M.; Diebold, U.; Kresse, G.; Franchini, C. Small Polarons in Transition Metal Oxides. In *Handbook of Materials Modeling: Applications: Current and Emerging Materials*; Andreoni, W., Yip, S., Eds.; Springer International Publishing: Cham, 2019; pp 1–39. https://doi.org/10.1007/978-3-319-50257-1_52-1.
(170) Cushing, S. K.; Lee, A.; Porter, I. J.; Carneiro, L. M.; Chang, H.-T.; Zürch, M.; Leone, S. R. Differentiating Photoexcited Carrier and Phonon Dynamics in the Δ, L, and Γ Valleys of Si(100) with Transient Extreme Ultraviolet Spectroscopy. *Journal of Physical Chemistry C* **2019**, *123* (6), 3343–3352. https://doi.org/10.1021/acs.jpcc.8b10887.
(171) Lenhardt, J. M.; Ong, M. T.; Choe, R.; Evenhuis, C. R.; Martinez, T. J.; Craig, S. L. Trapping a Diradical Transition State by Mechanochemical Polymer Extension. *Science* **2010**, *329* (5995), 1057–1060. https://doi.org/10.1126/science.1193412.
(172) Lenhardt, J. M.; Black, A. L.; Craig, S. L. Gem-Dichlorocyclopropanes as Abundant and Efficient Mechanophores in Polybutadiene Copolymers under Mechanical Stress.Journal of the American Chemical Society **2009**, *131* (31), 10818-+. https://doi.org/10.1021/ja9036548.
(173) Roessler, A. G.; Zimmerman, P. M. Examining the Ways To Bend and Break Reaction Pathways Using Mechanochemistry. *The Journal of Physical Chemistry C* **2018**, *122* (12), 6996–7004. https://doi.org/10.1021/acs.jpcc.8b00467.
(174) Lenhardt, J. M.; Ong, M. T.; Choe, R.; Evenhuis, C. R.; Martinez, T. J.; Craig, S. L. Trapping a Diradical Transition State by Mechanochemical Polymer Extension. *Science* **2010**, *329* (5995), 1057–1060. https://doi.org/10.1126/science.1193412.
(175) Ong, M. T.; Leiding, J.; Tao, H.; Virshup, A. M.; Martínez, T. J. First Principles Dynamics and Minimum Energy Pathways for Mechanochemical Ring Opening of Cyclobutene. *Journal of the American Chemical Society* **2009**, *131* (18), 6377–6379. https://doi.org/10.1021/ja8095834.

(176) Ribas-Arino, J.; Shiga, M.; Marx, D. Unravelling the Mechanism of Force-Induced Ring-Opening of Benzocyclobutenes. *Chemistry: A European Journal* **2009**, *15* (48), 13331–13335. https://doi.org/10.1002/chem.200902573.
(177) Ribas-Arino, J.; Shiga, M.; Marx, D. Understanding Covalent Mechanochemistry. *Angewandte Chemie International Edition* **2009**, *48* (23), 4190–4193. https://doi.org/10.1002/anie.200900673.
(178) Wollenhaupt, M.; Krupicka, M.; Marx, D. Should the Woodward-Hoffmann Rules Be Applied to Mechanochemical Reactions? *ChemPhysChem* **2015**, *16* (8), 1593–1597. https://doi.org/10.1002/cphc.201500054.
(179) Roessler, A. G.; Zimmerman, P. M. Examining the Ways to Bend and Break Reaction Pathways Using Mechanochemistry. *Journal of Physical Chemistry C* **2018**. https://doi.org/10.1021/acs.jpcc.8b00467.
(180) Ben-Nun, M.; Quenneville, J.; Martínez, T. J. Ab Initio Multiple Spawning: Photochemistry from First Principles Quantum Molecular Dynamics. *The Journal of Physical Chemistry A* **2000**, *104* (22), 5161–5175. https://doi.org/10.1021/jp994174i.
(181) Quenneville, J.; Martínez, T. J. Ab Initio Study of Cis−Trans Photoisomerization in Stilbene and Ethylene. *The Journal of Physical Chemistry A* **2003**, *107* (6), 829–837. https://doi.org/10.1021/jp021210w.
(182) Caruso, M. M.; Davis, D. A.; Shen, Q.; Odom, S. A.; Sottos, N. R.; White, S. R.; Moore, J. S. Mechanically-Induced Chemical Changes in Polymeric Materials. *Chemical Reviews* **2009**, *109* (11), 5755–5798. https://doi.org/10.1021/cr9001353.
(183) Akbulatov, S.; Boulatov, R. Experimental Polymer Mechanochemistry and Its Interpretational Frameworks. *ChemPhysChem* **2017**, *18* (11), 1422–1450. https://doi.org/10.1002/cphc.201601354.
(184) May, P. A.; Moore, J. S. Polymer Mechanochemistry: Techniques to Generate Molecular Force via Elongational Flows. *Chemical Society Reviews* **2013**, *42*, 7497–7506. https://doi.org/10.1039/C2CS35463B.
(185) Kim, G.; Lau, V. M.; Halmes, A. J.; Oelze, M. L.; Moore, J. S.; Li, K. C. High-Intensity Focused Ultrasound-Induced Mechanochemical Transduction in Synthetic Elastomers. *PNAS* **2019**, 201901047. https://doi.org/10.1073/pnas.1901047116.
(186) Feng, Y.; Qin, D.; Wan, M. Laser-Induced Cavitation and Photoacoustic Cavitation. In *Cavitation in Biomedicine: Principles and Techniques*; Wan, M., Feng, Y., Haar, G. ter, Eds.; Springer Netherlands: Dordrecht, 2015; pp 401–455. https://doi.org/10.1007/978-94-017-7255-6_8.
(187) Jasikova, D.; Schovanec, P.; Kotek, M.; Muller, M.; Kopecky, V. Comparison of Ultrasound and LIB Generated Cavitation Bubble. *EPJ Web Conference* **2017**, *143*, 02044. https://doi.org/10.1051/epjconf/201714302044.
(188) Vogel, A.; Busch, S.; Parlitz, U. Shock Wave Emission and Cavitation Bubble Generation by Picosecond and Nanosecond Optical Breakdown in Water. *The Journal of the Acoustical Society of America* **1996**, *100* (1), 148–165. https://doi.org/10.1121/1.415878.
(189) Chýlek, P.; Jarzembski, M. A.; Srivastava, V.; Pinnick, R. G.; Pendleton, J. D.; Cruncleton, J. P. Effect of Spherical Particles on Laser-Induced Breakdown of Gases. *Applied. Optics, AO* **1987**, *26* (5), 760–762. https://doi.org/10.1364/AO.26.000760.
(190) Hsieh, W.-F.; Zheng, J.-B.; Wood, C. F.; Chu, B. T.; Chang, R. K. Propagation Velocity of Laser-Induced Plasma inside and Outside a Transparent Droplet. *Optical Letters, OL* **1987**, *12* (8), 576–578. https://doi.org/10.1364/OL.12.000576.
(191) Kennedy, P. K.; Hammer, D. X.; Rockwell, B. A. Laser-Induced Breakdown in Aqueous Media. *Progress in Quantum Electronics* **1997**, *21* (3), 155–248. https://doi.org/10.1016/S0079-6727(97)00002-5.
(192) Berthe, L.; Fabbro, R.; Peyre, P.; Tollier, L.; Bartnicki, E. Shock Waves from a Water-Confined Laser-Generated Plasma. *Journal of Applied Physics* **1997**, *82* (6), 2826–2832. https://doi.org/10.1063/1.366113.

(193) Ohl, C. D.; Lindau, O.; Lauterborn, W. Luminescence from Spherically and Aspherically Collapsing Laser Induced Bubbles. *PHYSICAL REVIEW LETTERS* **1998**, *80* (2), 4.
(194) Akhatov, I.; Lindau, O.; Topolnikov, A.; Mettin, R.; Vakhitova, N.; Lauterborn, W. Collapse and Rebound of a Laser-Induced Cavitation Bubble. *Physics of Fluids* **2001**, *13* (10), 2805–2819. https://doi.org/10.1063/1.1401810.
(195) Robert, E.; Lettry, J.; Farhat, M.; Monkewitz, P. A.; Avellan, F. Cavitation Bubble Behavior inside a Liquid Jet. *Physics of Fluids* **2007**, *19* (6), 067106. https://doi.org/10.1063/1.2744402.
(196) Jang, D.; Park, J.-G.; Kim, D. Enhancement of Airborne Shock Wave by Laser-Induced Breakdown of Liquid Column in Laser Shock Cleaning. *Journal of Applied Physics* **2011**, *109* (7), 073101. https://doi.org/10.1063/1.3558989.
(197) Avila, S. R. G.; Ohl, C.-D. Fragmentation of Acoustically Levitating Droplets by Laser-Induced Cavitation Bubbles. *Journal of Fluid Mechanics* **2016**, *805*, 551–576. https://doi.org/10.1017/jfm.2016.583.
(198) Hammer, D. X.; Jansen, E. D.; Frenz, M.; Noojin, G. D.; Thomas, R. J.; Noack, J.; Vogel, A.; Rockwell, B. A.; Welch, A. J. Shielding Properties of Laser-Induced Breakdown in Water for Pulse Durations from 5 Ns to 125 Fs. *Applied Optics, AO* **1997**, *36* (22), 5630–5640. https://doi.org/10.1364/AO.36.005630.
(199) Phase Change, Nucleation, and Cavitation. In *Cavitation and Bubble Dynamics*; Brennen, C. E., Ed.; Cambridge University Press: Cambridge, 2013; pp 1–29. https://doi.org/10.1017/CBO9781107338760.002.
(200) Cavitation Bubble Collapse. In *Cavitation and Bubble Dynamics*; Brennen, C. E., Ed.; Cambridge University Press: Cambridge, 2013; pp 59–88. https://doi.org/10.1017/CBO9781107338760.004.
(201) Overholts, A. C.; McFadden, M. E.; Robb, M. J. Quantifying Activation Rates of Scissile Mechanophores and the Influence of Dispersity. *Macromolecules* **2022**, *55* (1), 276–283. https://doi.org/10.1021/acs.macromol.1c02232.
(202) Devia-Cruz, L. F.; Camacho-López, S.; Evans, R.; García-Casillas, D.; Stepanov, S. Laser-Induced Cavitation Phenomenon Studied Using Three Different Optically-Based Approaches – An Initial Overview of Results. *Photonics & Lasers in Medicine* **2012**, *1* (3). https://doi.org/10.1515/plm-2012-0019.
(203) Nguyen, N. H.; Rosen, B. M.; Lligadas, G.; Percec, V. Surface-Dependent Kinetics of Cu(0)-Wire-Catalyzed Single-Electron Transfer Living Radical Polymerization of Methyl Acrylate in DMSO at 25 °C. *Macromolecules* **2009**, *42*, 2379–2386. https://doi.org/10.1021/ma8028562.
(204) Syrett, J. A.; Mantovani, G.; Barton, W. R. S.; Price, D.; Haddleton, D. M. Self-Healing Polymers Prepared via Living Radical Polymerisation. *Polymer Chemistry* **2010**, *1* (1), 102–106. https://doi.org/10.1039/B9PY00316A.
(205) Qi, P.; Su, Q.; Lin, L.; Liu, W. Bubble Dynamics Driven by a Few Successive Femtosecond Laser Pulses in Methanol under 1 KHz. *J. Opt. Soc. Am. B* **2018**, *35* (11), 2727. https://doi.org/10.1364/JOSAB.35.002727.
(206) Noack, J.; Hammer, D. X.; Noojin, G. D.; Rockwell, B. A.; Vogel, A. Influence of Pulse Duration on Mechanical Effects after Laser-Induced Breakdown in Water. *Journal of Applied Physics* **1998**, *83* (12), 7488–7495. https://doi.org/10.1063/1.367512.
(207) Beyer, M. K.; Clausen-Schaumann, H. Mechanochemistry: The Mechanical Activation of Covalent Bonds. *Chemical Reviews* **2005**, *105* (8), 2921–2948. https://doi.org/10.1021/cr030697h.
(208) Wang, J. P.; Kouznetsova, T. B.; Niu, Z. B.; Ong, M. T.; Klukovich, H.; Rheingold, A. L.; Martinez, T. J.; Craig, S. L. Inducing and Quantifying Forbidden Reactivity with Single-Molecule Polymer Mechanochemistry. *Nat Chem* **2015**, *7* (4), 323–327. https://doi.org/10.1038/Nchem.2185.

(209) Nagamani, C.; Liu, H. Y.; Moore, J. S. Mechanogeneration of Acid from Oxime Sulfonates. *Journal of the American Chemical Society* **2016**, *138* (8), 2540–2543. https://doi.org/10.1021/jacs.6b00097.
(210) Ong, M. T.; Leiding, J.; Tao, H. L.; Virshup, A. M.; Martinez, T. J. First Principles Dynamics and Minimum Energy Pathways for Mechanochemical Ring Opening of Cyclobutene. J*ournal of the American Chemical Society* **2009**, *131* (18), 6377-+. https://doi.org/10.1021/ja8095834.
(211) BartłomiejSzyja; Pidko, E.; Groote, R.; Hensen, E.; Sijbesma, R. DFT Study on Mechanochemical Bond Breaking in COGEF and Molecular Dynamics Simulations. *Procedia Computer Science* **2011**, *4*, 1167–1176. https://doi.org/10.1016/j.procs.2011.04.125.
(212) Beyer, M. K. The Mechanical Strength of a Covalent Bond Calculated by Density Functional Theory. *J Chem Phys* **2000**, *112* (17), 7307–7312. https://doi.org/10.1063/1.481330.
(213) Kryger, M. J.; Munaretto, A. M.; Moore, J. S. Structure-Mechanochemical Activity Relationships for Cyclobutane Mechanophores. *Journal of the American Chemical Society* **2011**, *133* (46), 18992–18998. https://doi.org/10.1021/ja2086728.
(214) Stauch, T.; Dreuw, A. Advances in Quantum Mechanochemistry: Electronic Structure Methods and Force Analysis. *Chemical Reviews* **2016**, *116* (22), 14137–14180. https://doi.org/10.1021/acs.chemrev.6b00458.
(215) Kryger, M. J.; Ong, M. T.; Odom, S. A.; Sottos, N. R.; White, S. R.; Martinez, T. J.; Moore, J. S. Masked Cyanoacrylates Unveiled by Mechanical Force. *Journal of the American Chemical Society* **2010**, *132* (13), 4558–4559. https://doi.org/10.1021/ja1008932.
(216) Chen, Y. L.; Spiering, A. J. H.; Karthikeyan, S.; Peters, G. W. M.; Meijer, E. W.; Sijbesma, R. P. Mechanically Induced Chemiluminescence from Polymers Incorporating a 1,2-Dioxetane Unit in the Main Chain. *Nature Chemistry* **2012**, *4* (7), 559–562. https://doi.org/10.1038/Nchem.1358.
(217) Robb, M. J.; Moore, J. S. A Retro-Staudinger Cycloaddition: Mechanochemical Cycloelimination of a Beta-Lactam Mechanophore. *Journal of the American Chemical Society* **2015**, *137* (34), 10946–10949. https://doi.org/10.1021/jacs.5b07345.
(218) Lin, Y.; Chang, C.-C.; Craig, S. L. Mechanical Generation of Isocyanate by Mechanically Induced Retro [2 + 2] Cycloaddition of a 1,2-Diazetidinone Mechanophore. *Organic Chemistry Frontiers* **2019**, *6*, 1052–1057. https://doi.org/10.1039/C9QO00262F.
(219) Kryger, M. J.; Munaretto, A. M.; Moore, J. S. Structure-Mechanochemical Activity Relationships for Cyclobutane Mechanophores. *Journal of the American Chemical Society* **2011**, *133* (46), 18992–18998. https://doi.org/10.1021/ja2086728.
(220) Wang, J. P.; Kouznetsova, T. B.; Boulatov, R.; Craig, S. L. Mechanical Gating of a Mechanochemical Reaction Cascade. *Nature Communications* **2016**, *7*, 13433. https://doi.org/10.1038/ncomms13433.
(221) Hu, X. R.; McFadden, M. E.; Barber, R. W.; Robb, M. J. Mechanochemical Regulation of a Photochemical Reaction. *Journal of the American Chemical Society* **2018**, *140* (43), 14073–14077. https://doi.org/10.1021/jacs.8b09628.
(222) Kida, J.; Imato, K.; Goseki, R.; Aoki, D.; Morimoto, M.; Otsuka, H. The Photoregulation of a Mechanochemical Polymer Scission. *Nature Communications* **2018**, *9*, 3504. https://doi.org/10.1038/s41467-018-05996-7.
(223) Hu, X.; Zeng, T.; Husic, C. C.; Robb, M. J. Mechanically Triggered Small Molecule Release from a Masked Furfuryl Carbonate. *Journal of the American Chemical Society* **2019**, *141* (38), 15018–15023. https://doi.org/10.1021/jacs.9b08663.
(224) Lin, Y.; Kouznetsova, T. B.; Craig, S. L. Mechanically Gated Degradable Polymers. *Journal of the American Chemical Society* **2020**, *142* (5), 2105–2109. https://doi.org/10.1021/jacs.9b13359.
(225) Hsu, T.-G.; Zhou, J.; Su, H.-W.; Schrage, B. R.; Ziegler, C. J.; Wang, J. A Polymer with "Locked" Degradability: Superior Backbone Stability and Accessible Degradability Enabled by

Mechanophore Installation. *Journal of the American Chemical Society* **2020**, *142* (5), 2100–2104. https://doi.org/10.1021/jacs.9b12482.
(226) Nofen, E. M.; Zimmer, N.; Dasgupta, A.; Gunckel, R.; Koo, B.; Chattopadhyay, A.; Dai, L. Stress-Sensing Thermoset Polymer Network via Grafted Cinnamoyl/Cyclobutane Mechanophore Units in Epoxy. *Polymer Chemistry* **2016**, *7*, 7249–7259. https://doi.org/10.1039/C6PY01463A.
(227) Gunckel, R.; Koo, B.; Xu, Y.; Pauley, B.; Hall, A.; Chattopadhyay, A.; Dai, L. L. Grafted Cinnamoyl-Based Mechanophores for Self-Sensing and Photochemical Healing Capabilities in Epoxy. *ACS Applied Polymer Materials* **2020**, DOI: 10.1021/acsapm.0c00599. https://doi.org/10.1021/acsapm.0c00599.
(228) Bernstein, H. I.; Quimby, W. C. The Photochemical Dimerization of Trans-Cinnamic Acid. *Journal of the American Chemical Society* **1943**, *65* (10), 1845–1846. https://doi.org/10.1021/ja01250a016.
(229) Ishigami, T.; Murata, T.; Endo, T. The Solution Photodimerization of (E)-p-Nitrocinnamates. *Bulletin of the Chemical Society of Japan* **1976**, *49* (12), 3578–3583. https://doi.org/10.1246/bcsj.49.3578.
(230) Li, M.; Zhang, H.; Gao, F.; Tang, Z.; Zeng, D.; Pan, Y.; Su, P.; Ruan, Y.; Xu, Y.; Weng, W. A Cyclic Cinnamate Dimer Mechanophore for Multimodal Stress Responsive and Mechanically Adaptable Polymeric Materials. *Polymer Chemistry* **2019**, *10*, 905–910. https://doi.org/10.1039/C8PY01654B.
(231) Zhang, H.; Li, X.; Lin, Y. J.; Gao, F.; Tang, Z.; Su, P. F.; Zhang, W. K.; Xu, Y. Z.; Weng, W. G.; Boulatov, R. Multi-Modal Mechanophores Based on Cinnamate Dimers. *Nature Communications* **2017**, *8*, 1174. https://doi.org/10.1038/s41467-017-01412-8.
(232) Pill, M. F.; Holz, K.; Preusske, N.; Berger, F.; Clausen-Schaumann, H.; Luning, U.; Beyer, M. K. Mechanochemical Cycloreversion of Cyclobutane Observed at the Single Molecule Level. *Chemistry: A European Journal* **2016**, *22* (34), 12034–12039. https://doi.org/10.1002/chem.201600866.
(233) Zhang, Y.; Lund, E.; Gossweiler, G. R.; Lee, B.; Niu, Z.; Khripin, C.; Munch, E.; Couty, M.; Craig, S. L. Molecular Damage Detection in an Elastomer Nanocomposite with a Coumarin Dimer Mechanophore. *Macromolecular Rapid Communications* **2020**, DOI: 10.1002/marc.202000359. https://doi.org/10.1002/marc.202000359.
(234) Kean, Z. S.; Gossweiler, G. R.; Kouznetsova, T. B.; Hewage, G. B.; Craig, S. L. A Coumarin Dimer Probe of Mechanochemical Scission Efficiency in the Sonochemical Activation of Chain-Centered Mechanophore Polymers. *Chemical Communications* **2015**, *51* (44), 9157–9160. https://doi.org/10.1039/c5cc01836f.
(235) Yang, J.; Horst, M.; Werby, S. H.; Cegelski, L.; Burns, N. Z.; Xia, Y. Bicyclohexene-Peri-Naphthalenes: Scalable Synthesis, Diverse Functionalization, Efficient Polymerization, and Facile Mechanoactivation of Their Polymers. *Journal of the American Chemical Society* **2020**, DOI: 10.1021/jacs.0c06454. https://doi.org/10.1021/jacs.0c06454.
(236) Kean, Z. S.; Ramirez, A. L. B.; Yan, Y. F.; Craig, S. L. Bicyclo[3.2.0]Heptane Mechanophores for the Non-Scissile and Photochemically Reversible Generation of Reactive Bis-Enones. *Journal of the American Chemical Society* **2012**, *134* (31), 12939–12942. https://doi.org/10.1021/ja3063666.
(237) Kean, Z. S.; Niu, Z. B.; Hewage, G. B.; Rheingold, A. L.; Craig, S. L. Stress-Responsive Polymers Containing Cyclobutane Core Mechanophores: Reactivity and Mechanistic Insights. *Journal of the American Chemical Society* **2013**, *135* (36), 13598–13604. https://doi.org/10.1021/ja4075997.
(238) Bowser, B. H.; Ho, C.-H.; Craig, S. L. High Mechanophore Content, Stress-Relieving Copolymers Synthesized via RAFT Polymerization. *Macromolecules* **2019**, *52* (22), 9032–9038. https://doi.org/10.1021/acs.macromol.9b01792.

(239) Groote, R.; Szyja, B. M.; Leibfarth, F. A.; Hawker, C. J.; Doltsinis, N. L.; Sijbesma, R. P. Strain-Induced Strengthening of the Weakest Link: The Importance of Intermediate Geometry for the Outcome of Mechanochemical Reactions. *Macromolecules* **2014**, *47* (3), 1187–1192. https://doi.org/10.1021/ma4022339.
(240) Larsen, M. B.; Boydston, A. J. "Flex-Activated" Mechanophores: Using Polymer Mechanochemistry To Direct Bond Bending Activation. *Journal of the American Chemical Society* **2013**, *135* (22), 8189–8192. https://doi.org/10.1021/ja403757p.
(241) Larsen, M. B.; Boydston, A. J. Successive Mechanochemical Activation and Small Molecule Release in an Elastomeric Material. *Journal of the American Chemical Society* **2014**, *136* (4), 1276–1279. https://doi.org/10.1021/ja411891x.
(242) Gossweiler, G. R.; Hewage, G. B.; Soriano, G.; Wang, Q. M.; Welshofer, G. W.; Zhao, X. H.; Craig, S. L. Mechanochemical Activation of Covalent Bonds in Polymers with Full and Repeatable Macroscopic Shape Recovery. *ACS Macro Letters* **2014**, *3* (3), 216–219. https://doi.org/10.1021/mz500031q.
(243) Turksoy, A.; Yildiz, D.; Aydonat, S.; Beduk, T.; Canyurt, M.; Baytekin, B.; U. Akkaya, E. Mechanochemical Generation of Singlet Oxygen. *Royal Society of Chemistry Advances* **2020**, *10* (16), 9182–9186. https://doi.org/10.1039/D0RA00831A.
(244) Wang, Z.; Ma, Z.; Zhang, Z.; Wu, F.; Jiang, H.; Jia, X. Mechanical Activation of a Dithioester Derivative-Based Retro RAFT-HDA Reaction. *Polymer Chemistry* **2014**, *5* (24), 6893–6897. https://doi.org/10.1039/c4py00964a.
(245) Khanal, A.; Long, F.; Cao, B.; Shahbazian-Yassar, R.; Fang, S. Y. Evidence of Splitting 1,2,3-Triazole into an Alkyne and Azide by Low Mechanical Force in the Presence of Other Covalent Bonds. *Chemistry: A European Journal* **2016**, *22* (28), 9760–9767. https://doi.org/10.1002/chem.201600982.
(246) Konda, S. S. M.; Brantley, J. N.; Varghese, B. T.; Wiggins, K. M.; Bielawski, C. W.; Makarov, D. E. Molecular Catch Bonds and the Anti-Hammond Effect in Polymer Mechanochemistry. *Journal of the American Chemical Society* **2013**, *135* (34), 12722–12729. https://doi.org/10.1021/ja4051108.
(247) Li, J.; Shiraki, T.; Hu, B.; Wright, R. A. E.; Zhao, B.; Moore, J. S. Mechanophore Activation at Heterointerfaces. *Journal of the American Chemical Society* **2014**, *136* (45), 15925–15928. https://doi.org/10.1021/ja509949d.
(248) Gostl, R.; Sijbesma, R. P. Pi-Extended Anthracenes as Sensitive Probes for Mechanical Stress. *Chemical Science* **2016**, *7* (1), 370–375. https://doi.org/10.1039/c5sc03297k.
(249) Stevenson, R.; De Bo, G. Controlling Reactivity by Geometry in Retro-Diels-Alder Reactions under Tension. *Journal of the American Chemical Society* **2017**, *139* (46), 16768–16771. https://doi.org/10.1021/jacs.7b08895.
(250) Zhang, M.; De Bo, G. Impact of a Mechanical Bond on the Activation of a Mechanophore. *Journal of the American Chemical Society* **2018**, *140* (40), 12724–12727. https://doi.org/10.1021/jacs.8b08590.
(251) Duan, H. Y.; Wang, Y. X.; Wang, L. J.; Min, Y. Q.; Zhang, X. H.; Du, B. Y. An Investigation of the Selective Chain Scission at Centered Diels-Alder Mechanophore under Ultrasonication. *Macromolecules* **2017**, *50* (4), 1353–1361. https://doi.org/10.1021/acs.macromol.6b02370.
(252) Lyu, B.; Cha, W.; Mao, T.; Wu, Y.; Qian, H.; Zhou, Y.; Chen, X.; Zhang, S.; Liu, L.; Yang, G.; Lu, Z.; Zhu, Q.; Ma, H. Surface Confined Retro Diels–Alder Reaction Driven by the Swelling of Weak Polyelectrolytes. *ACS Applied Material Interfaces* **2015**, *7* (11), 6254–6259. https://doi.org/10.1021/acsami.5b00538.
(253) P. Kabb, C.; S. O'Bryan, C.; D. Morley, C.; E. Angelini, T.; S. Sumerlin, B. Anthracene-Based Mechanophores for Compression-Activated Fluorescence in Polymeric Networks. *Chemical Science* **2019**, *10*, 7702–7708. https://doi.org/10.1039/C9SC02487E.

(254) Roessler, A. G.; Zimmerman, P. M. Examining the Ways to Bend and Break Reaction Pathways Using Mechanochemistry. *Journal of Physical Chemistry C* **2018**, *122* (12), 6996–7004. https://doi.org/10.1021/acs.jpcc.8b00467.
(255) Inglis, A. J.; Sinnwell, S.; Stenzel, M. H.; Barner-Kowollik, C. Ultrafast Click Conjugation of Macromolecular Building Blocks at Ambient Temperature. *Angewandte Chemie International Edition* **2009**, *48* (13), 2411–2414. https://doi.org/10.1002/anie.200805993.
(256) Stauch, T.; Dreuw, A. Advances in Quantum Mechanochemistry: Electronic Structure Methods and Force Analysis. *Chemical Reviews* **2016**, *116* (22), 14137–14180. https://doi.org/10.1021/acs.chemrev.6b00458.
(257) Krupicka, M.; Dopieralski, P.; Marx, D. Unclicking the Click: Metal-Assisted Mechanochemical Cycloreversion of Triazoles Is Possible. *Angewandte Chemie International Edition* **2017**, *56* (27), 7745–7749. https://doi.org/10.1002/anie.201612507.
(258) Kolb, H. C.; Finn, M. G.; Sharpless, K. B. Click Chemistry: Diverse Chemical Function from a Few Good Reactions. *Angewandte Chemie International Edition* **2001**, *40* (11), 2004–2021. https://doi.org/10.1002/1521-3773(20010601)40:11<2004::AID-ANIE2004>3.0.CO;2-5.
(259) Jacobs, M. J.; Schneider, G.; Blank, K. G. Mechanical Reversibility of Strain-Promoted Azide–Alkyne Cycloaddition Reactions. *Angewandte Chemie International Edition* **2016**, *55* (8), 2899–2902. https://doi.org/10.1002/anie.201510299.
(260) Rostovtsev, V. V.; Green, L. G.; Fokin, V. V.; Sharpless, K. B. A Stepwise Huisgen Cycloaddition Process: Copper(I)-Catalyzed Regioselective "Ligation" of Azides and Terminal Alkynes. *Angewandte Chemie International Edition* **2002**, *41* (14), 2596–2599. https://doi.org/10.1002/1521-3773(20020715)41:14<2596::AID-ANIE2596>3.0.CO;2-4.
(261) Tornoe, C. W.; Christensen, C.; Meldal, M. Peptidotriazoles on Solid Phase: [1,2,3]-Triazoles by Regiospecific Copper(I)-Catalyzed 1,3-Dipolar Cycloadditions of Terminal Alkynes to Azides. *J. Org. Chem.* **2002**, *67* (9), 3057–3064. https://doi.org/10.1021/jo011148j.
(262) Stauch, T.; Dreuw, A. Force-Induced Retro-Click Reaction of Triazoles Competes with Adjacent Single-Bond Rupture. *Chemical Science* **2017**, *8*, 5567–5575. https://doi.org/10.1039/C7SC01562C.
(263) Schütze, D.; Holz, K.; Müller, J.; Beyer, M. K.; Lüning, U.; Hartke, B. Pinpointing Mechanochemical Bond Rupture by Embedding the Mechanophore into a Macrocycle. *Angewandte Chemie International Edition* **2015**, *54*, 2556–2559. https://doi.org/10.1002/anie.201409691.
(264) Kan, L.; Cheng, H.; Li, B.; Zhang, X.; Wang, Q.; Wei, H.; Ma, N. Anthracene Dimer Crosslinked Polyurethanes as Mechanoluminescent Polymeric Materials. *New Journal of Chemistry* **2019**, *43* (6), 2658–2664. https://doi.org/10.1039/C8NJ06005C.
(265) Song, Y.-K.; Lee, K.-H.; Hong, W.-S.; Cho, S.-Y.; Yu, H.-C.; Chung, C.-M. Fluorescence Sensing of Microcracks Based on Cycloreversion of a Dimeric Anthracene Moiety. *Journal of Materials Chemistry* **2011**, *22* (4), 1380–1386. https://doi.org/10.1039/C1JM13709C.
(266) Wu, D.-Y.; Zhang, L.-P.; Wu, L.-Z.; Wang, B.; Tung, C.-H. Water-in-Oil Microemulsions as Microreactors to Control the Regioselectivity in the Photocycloaddition of 9-Substituted Anthracenes. *Tetrahedron Letters* **2002**, *43* (7), 1281–1283. https://doi.org/10.1016/S0040-4039(01)02360-7.
(267) Becker, H. Dieter. Unimolecular Photochemistry of Anthracenes. *Chemical Reviews* **1993**, *93* (1), 145–172. https://doi.org/10.1021/cr00017a008.
(268) Lenhardt, J. M.; Black, A. L.; Craig, S. L. Gem-Dichlorocyclopropanes as Abundant and Efficient Mechanophores in Polybutadiene Copolymers under Mechanical Stress. *Journal of the American Chemical Society* **2009**, *131* (31), 10818–10819. https://doi.org/10.1021/ja9036548.
(269) Klukovich, H. M.; Kean, Z. S.; Ramirez, A. L. B.; Lenhardt, J. M.; Lin, J. X.; Hu, X. Q.; Craig, S. L. Tension Trapping of Carbonyl Ylides Facilitated by a Change in Polymer Backbone. *Journal of the American Chemical Society* **2012**, *134* (23), 9577–9580. https://doi.org/10.1021/ja302996n.

(270)Barbee, M. H.; Wang, J.; Kouznetsova, T.; Lu, M.; Craig, S. L. Mechanochemical Ring-Opening of Allylic Epoxides. *Macromolecules* **2019**, *52* (16), 6234–6240. https://doi.org/10.1021/acs.macromol.9b01190.
(271) Jung, S.; Yoon, H. J. Mechanical Force Induces Ylide-Free Cycloaddition of Nonscissible Aziridines. *Angewandte Chemie International Edition* **2020**, *59* (12), 4883–4887. https://doi.org/10.1002/anie.201915438.
(272) Bowser, B.; L Craig, S. Empowering Mechanochemistry with Multi-Mechanophore Polymer Architectures. *Polymer Chemistry* **2018**, *9*, 3583–3593. https://doi.org/10.1039/C8PY00720A.
(273) Lenhardt, J. M.; Black, A. L.; Beiermann, B. A.; Steinberg, B. D.; Rahman, F.; Samborski, T.; Elsakr, J.; Moore, J. S.; Sottos, N. R.; Craig, S. L. Characterizing the Mechanochemically Active Domains in Gem-Dihalocyclopropanated Polybutadiene under Compression and Tension. *Journal of Materials Chemistry***2011**, *21* (23), 8454–8459. https://doi.org/10.1039/C0JM04117C.
(274) Black, A. L.; Orlicki, J. A.; Craig, S. L. Mechanochemically Triggered Bond Formation in Solid-State Polymers. *Journal of Materials Chemistry***2011**, *21*, 8460–8465. https://doi.org/10.1039/C0JM03875J.
(275) Wang, J. P.; Kouznetsova, T. B.; Craig, S. L. Reactivity and Mechanism of a Mechanically Activated Anti-Woodward-Hoffmann-DePuy Reaction. *Journal of the American Chemical Society* **2015**, *137* (36), 11554–11557. https://doi.org/10.1021/jacs.5b06168.
(276) Klukovich, H. M.; Kouznetsova, T. B.; Kean, Z. S.; Lenhardt, J. M.; Craig, S. L. A Backbone Lever-Arm Effect Enhances Polymer Mechanochemistry. *Nature Chemistry* **2013**, *5* (2), 110–114. https://doi.org/10.1038/Nchem.1540.
(277) Ramirez, A. L. B.; Kean, Z. S.; Orlicki, J. A.; Champhekar, M.; Elsakr, S. M.; Krause, W. E.; Craig, S. L. Mechanochemical Strengthening of a Synthetic Polymer in Response to Typically Destructive Shear Forces. *Nature Chemistry* **2013**, *5* (9), 757–761. https://doi.org/10.1038/Nchem.1720.
(278) Wu, D.; Lenhardt, J. M.; Black, A. L.; Akhremitchev, B. B.; Craig, S. L. Molecular Stress Relief through a Force-Induced Irreversible Extension in Polymer Contour Length. *Journal of the American Chemical Society* **2010**, *132* (45), 15936–15938. https://doi.org/10.1021/ja108429h.
(279) Lin, Y.; Kouznetsova, T. B.; Craig, S. L. A Latent Mechanoacid for Time-Stamped Mechanochromism and Chemical Signaling in Polymeric Materials. *Journal of the American Chemical Society* **2020**, *142* (1), 99–103. https://doi.org/10.1021/jacs.9b12861.
(280) Diesendruck, C. E.; Steinberg, B. D.; Sugai, N.; Silberstein, M. N.; Sottos, N. R.; White, S. R.; Braun, P. V.; Moore, J. S. Proton-Coupled Mechanochemical Transduction: A Mechanogenerated Add. *Journal of the American Chemical Society* **2012**, *134* (30), 12446–12449. https://doi.org/10.1021/ja305645x.
(281) Wang, J. P.; Kouznetsova, T. B.; Kean, Z. S.; Fan, L.; Mar, B. D.; Martinez, T. J.; Craig, S. L. A Remote Stereochemical Lever Arm Effect in Polymer Mechanochemistry. *Journal of the American Chemical Society* **2014**, *136* (43), 15162–15165. https://doi.org/10.1021/ja509585g.
(282)Wang, J. P.; Kouznetsova, T. B.; Niu, Z. B.; Ong, M. T.; Klukovich, H.; Rheingold, A. L.; Martinez, T. J.; Craig, S. L. Inducing and Quantifying Forbidden Reactivity with Single-Molecule Polymer Mechanochemistry. *Nature Chemistry* **2015**, *7* (4), 323–327. https://doi.org/10.1038/Nchem.2185.
(283) Woodward, R. B.; Hoffmann, R. Stereochemistry of Electrocyclic Reactions. *Journal of the American Chemical Society* **1965**, *87* (2), 395–397. https://doi.org/10.1021/ja01080a054.
(284) DePuy, C. H.; Schnack, L. G.; Hausser, J. W.; Wiedemann, W. Chemistry of Cyclopropanols. III. The Mechanism of the Solvolysis of Cyclopropyl Tosylates. *Journal of the American Chemical Society* **1965**, *87* (17), 4006–4006. https://doi.org/10.1021/ja01095a056.

(285) DePuy, C. H.; Schnack, L. G.; Hausser, J. W. Chemistry of Cyclopropanols. IV. The Solvolysis of Cycopropyl Tosylates1,2. *Journal of the American Chemical Society* **1966**, *88* (14), 3343–3346. https://doi.org/10.1021/ja00966a029.
(286) Lenhardt, J. M.; Ong, M. T.; Choe, R.; Evenhuis, C. R.; Martinez, T. J.; Craig, S. L. Trapping a Diradical Transition State by Mechanochemical Polymer Extension. *Science* **2010**, *329* (5995), 1057–1060. https://doi.org/10.1126/science.1193412.
(287) Wang, J. P.; Kouznetsova, T. B.; Niu, Z. B.; Rheingold, A. L.; Craig, S. L. Accelerating a Mechanically Driven Anti-Woodward-Hoffmann Ring Opening with a Polymer Lever Arm Effect. *J. Org. Chem.* **2015**, *80* (23), 11895–11898. https://doi.org/10.1021/acs.joc.5b01465.
(288) Potisek, S. L.; Davis, D. A.; Sottos, N. R.; White, S. R.; Moore, J. S. Mechanophore-Linked Addition Polymers. *Journal of the American Chemical Society* **2007**, *129*, 13808–13809. https://doi.org/10.1021/ja076189x.
(289) Ong, M. T.; Leiding, J.; Tao, H. L.; Virshup, A. M.; Martinez, T. J. First Principles Dynamics and Minimum Energy Pathways for Mechanochemical Ring Opening of Cyclobutene. *Journal of the American Chemical Society* **2009**, *131* (18), 6377–6379. https://doi.org/10.1021/ja8095834.
(290) Davis, D. A.; Hamilton, A.; Yang, J. L.; Cremar, L. D.; Van Gough, D.; Potisek, S. L.; Ong, M. T.; Braun, P. V.; Martinez, T. J.; White, S. R.; Moore, J. S.; Sottos, N. R. Force-Induced Activation of Covalent Bonds in Mechanoresponsive Polymeric Materials. *Nature* **2009**, *459* (7243), 68–72. https://doi.org/10.1038/nature07970.
(291) Gossweiler, G. R.; Kouznetsova, T. B.; Craig, S. L. Force-Rate Characterization of Two Spiropyran-Based Molecular Force Probes. *Journal of the American Chemical Society* **2015**, *137* (19), 6148–6151. https://doi.org/10.1021/jacs.5b02492.
(292) Kim, T. A.; Robb, M. J.; Moore, J. S.; White, S. R.; Sottos, N. R. Mechanical Reactivity of Two Different Spiropyran Mechanophores in Polydimethylsiloxane. *Macromolecules* **2018**. https://doi.org/10.1021/acs.macromol.8b01919.
(293) Barbee, M. H.; Kouznetsova, T. B.; Barrett, S. L.; Gossweiler, G. R.; Lin, Y.; Rastogi, S. K.; Brittain, W. J.; Craig, S. L. Substituent Effects and Mechanism in a Mechanochemical Reaction. *Journal of the American Chemical Society* **2018**, *140* (40), 12746–12750. https://doi.org/10.1021/jacs.8b09263.
(294) O'Bryan, G.; Wong, B. M.; McElhanon, J. R. Stress Sensing in Polycaprolactone Films via an Embedded Photochromic Compound. *ACS Applied Material Interfaces* **2010**, *2* (6), 1594–1600. https://doi.org/10.1021/am100050v.
(295) Zhang, H.; Gao, F.; Cao, X. D.; Li, Y. Q.; Xu, Y. Z.; Weng, W. G.; Boulatov, R. Mechanochromism and Mechanical-Force-Triggered Cross-Linking from a Single Reactive Moiety Incorporated into Polymer Chains. *Angewandte Chemie International Edition* **2016**, *55* (9), 3040–3044. https://doi.org/10.1002/anie.201510171.
(296) Lin, Y. J.; Barbee, M. H.; Chang, C. C.; Craig, S. L. Regiochemical Effects on Mechanophore Activation in Bulk Materials. *Journal of the American Chemical Society* **2018**, *140* (46), 15969–15975. https://doi.org/10.1021/jacs.8b10376.
(297) Peterson, G. I.; Larsen, M. B.; Ganter, M. A.; Storti, D. W.; Boydston, A. J. 3D Printed Mechanochromic Materials. *ACS Applied Material Interfaces* **2015**, *7*, 577–583. https://doi.org/10.1021/am506745m.
(298) Robb, M. J.; Kim, T. A.; Halmes, A. J.; White, S. R.; Sottos, N. R.; Moore, J. S. Regioisomer-Specific Mechanochromism of Naphthopyran in Polymeric Materials. *Journal of the American Chemical Society* **2016**, *138* (38), 12328–12331. https://doi.org/10.1021/jacs.6b07610.
(299) Versaw, B. A.; McFadden, M. E.; Husic, C. C.; Robb, M. J. Designing Naphthopyran Mechanophores with Tunable Mechanochromic Behavior. *Chemical Science* **2020**, *11*, 4525–4530.

(300) McFadden, M. E.; Robb, M. J. Force-Dependent Multicolor Mechanochromism from a Single Mechanophore. *Journal of the American Chemical Society* **2019**, *141*, 11388–11392. https://doi.org/10.1021/jacs.9b05280.
(301) Lin, Y.; Zhang, Y.; Wang, Z.; Craig, S. L. Dynamic Memory Effects in the Mechanochemistry of Cyclic Polymers. *Journal of the American Chemical Society* **2019**, *141* (28), 10943–10947. https://doi.org/10.1021/jacs.9b03564.
(302) Berkowski, K. L.; Potisek, S. L.; Hickenboth, C. R.; Moore, J. S. Ultrasound-Induced Site-Specific Cleavage of Azo-Functionalized Poly(Ethylene Glycol). *Macromolecules* **2005**, *38* (22), 8975–8978. https://doi.org/10.1021/ma051394n.
(303) Imato, K.; Irie, A.; Kosuge, T.; Ohishi, T.; Nishihara, M.; Takahara, A.; Otsuka, H. Mechanophores with a Reversible Radical System and Freezing-Induced Mechanochemistry in Polymer Solutions and Gels. *Angewandte Chemie International Edition* **2015**, *54* (21), 6168–6172. https://doi.org/10.1002/anie.201412413.
(304) Sumi, T.; Goseki, R.; Otsuka, H. Tetraarylsuccinonitriles as Mechanochromophores to Generate Highly Stable Luminescent Carbon-Centered Radicals. *Chemical Communications***2017**, *53* (87), 11885–11888. https://doi.org/10.1039/c7cc06913h.
(305) Sakai, H.; Sumi, T.; Aoki, D.; Goseki, R.; Otsuka, H. Thermally Stable Radical-Type Mechanochromic Polymers Based on Difluorenylsuccinonitrile. *ACS Macro Letters* **2018**, *7* (11), 1359–1363. https://doi.org/10.1021/acsmacroLetters8b00755.
(306) Ishizuki, K.; Oka, H.; Aoki, D.; Goseki, R.; Otsuka, H. Mechanochromic Polymers That Turn Green Upon the Dissociation of Diarylbibenzothiophenonyl: The Missing Piece toward Rainbow Mechanochromism. *Chemistry: A European Journal* **2018**, *24* (13), 3170–3173. https://doi.org/10.1002/chem.201800194.
(307) Chen, Z.; Zhu, X.; Yang, J.; Mercer, J. A. M.; Burns, N. Z.; Martinez, T. J.; Xia, Y. The Cascade Unzipping of Ladderane Reveals Dynamic Effects in Mechanochemistry. *Nature Chemistry* **2020**, *12*, 302–309. https://doi.org/10.1038/s41557-019-0396-5.
(308) Yang, J. H.; Horst, M.; Romaniuk, J. A. H.; Jin, Z. X.; Cegelski, L.; Xia, Y. Benzoladderene Mechanophores: Synthesis, Polymerization, and Mechanochemical Transformation. *Journal of the American Chemical Society* **2019**, *141* (16), 6479–6483. https://doi.org/10.1021/jacs.9b01736.
(309) Lee, B.; Niu, Z. B.; Wang, J. P.; Slebodnick, C.; Craig, S. L. Relative Mechanical Strengths of Weak Bonds in Sonochemical Polymer Mechanochemistry. *Journal of the American Chemical Society* **2015**, *137* (33), 10826–10832. https://doi.org/10.1021/jacs.5b06937.
(310) Encina, M. V.; Lissi, E.; Sarasúa, M.; Gargallo, L.; Radic, D. Ultrasonic Degradation of Polyvinylpyrrolidone: Effect of Peroxide Linkages. *Journal of Polymer Science B Polymer Letters Ed.* **1980**, *18* (12), 757–760. https://doi.org/10.1002/pol.1980.130181201.
(311) Luzuriaga, A. R. de; Matxain, J. M.; Ruipérez, F.; Martin, R.; Asua, J. M.; Cabanero, G.; Odriozola, I. Transient Mechanochromism in Epoxy Vitrimer Composites Containing Aromatic Disulfide Crosslinks. *Journal of Materials Chemistry C* **2016**, *4*, 6220–6223. https://doi.org/10.1039/C6TC02383E.
(312) Li, Y. C.; Nese, A.; Matyjaszewski, K.; Sheiko, S. S. Molecular Tensile Machines: Anti-Arrhenius Cleavage of Disulfide Bonds. *Macromolecules* **2013**, *46* (18), 7196–7201. https://doi.org/10.1021/ma401178w.
(313) Imato, K.; Kanehara, T.; Ohishi, T.; Nishihara, M.; Yajima, H.; Ito, M.; Takahara, A.; Otsuka, H. Mechanochromic Dynamic Covalent Elastomers: Quantitative Stress Evaluation and Autonomous Recovery. *ACS Macro Letters* **2015**, *4* (11), 1307–1311. https://doi.org/10.1021/acsmacroLetters5b00717.
(314) Lenhardt, J. M.; Ogle, J. W.; Ong, M. T.; Choe, R.; Martinez, T. J.; Craig, S. L. Reactive Cross-Talk between Adjacent Tension-Trapped Transition States. *Journal of the American Chemical Society* **2011**, *133* (10), 3222–3225. https://doi.org/10.1021/ja107645c.

(315) Wang, J.; Kouznetsova, T. B.; Craig, S. L. Single-Molecule Observation of a Mechanically Activated Cis-to-Trans Cyclopropane Isomerization. *Journal of the American Chemical Society* **2016**, *138*, 10410–10412. https://doi.org/10.1021/jacs.6b06452.
(316) Klukovich, H. M.; Kean, Z. S.; Iacono, S. T.; Craig, S. L. Mechanically Induced Scission and Subsequent Thermal Remending of Perfluorocyclobutane Polymers. *Journal of the American Chemical Society* **2011**, *133* (44), 17882–17888. https://doi.org/10.1021/ja2074517.
(317) Lee, D. C.; Kensy, V. K.; Maroon, C. R.; Long, B. K.; Boydston, A. J. The Intrinsic Mechanochemical Reactivity of Vinyl-Addition Polynorbornene. *Angewandte Chemie International Edition* **2019**, *58*, 5639–5642.
(318) Verstraeten, F.; Gostl, R.; Sijbesma, R. P. Stress-Induced Colouration and Crosslinking of Polymeric Materials by Mechanochemical Formation of Triphenylimidazolyl Radicals. *Chemical Communications* **2016**, *52* (55), 8608–8611. https://doi.org/10.1039/c6cc04312g.
(319) Karman, M.; Verde-Sesto, E.; Weder, C. Mechanochemical Activation of Polymer-Embedded Photoluminescent Benzoxazole Moieties. *ACS Macro Letters* **2018**, *7* (8), 1028–1033. https://doi.org/10.1021/acsmacroLetters8b00520.
(320) Karman, M.; Verde-Sesto, E.; Weder, C.; Simon, Y. C. Mechanochemical Fluorescence Switching in Polymers Containing Dithiomaleimide Moieties. *ACS Macro Letters* **2018**, *7* (9), 1099–1104. https://doi.org/10.1021/acsmacroLetters8b00591.
(321) Gordon, M. B.; Wang, S.; Knappe, G. A.; Wagner, N. J.; Epps, T. H.; Kloxin, C. J. Force-Induced Cleavage of a Labile Bond for Enhanced Mechanochemical Crosslinking. *Polymer Chemistry* **2017**, *8* (42), 6485–6489. https://doi.org/10.1039/c7py01431g.
(322) Nagamani, C.; Liu, H. Y.; Moore, J. S. Mechanogeneration of Acid from Oxime Sulfonates. *Journal of the American Chemical Society* **2016**, *138* (8), 2540–2543. https://doi.org/10.1021/jacs.6b00097.
(323) Diesendruck, C. E.; Peterson, G. I.; Kulik, H. J.; Kaitz, J. A.; Mar, B. D.; May, P. A.; White, S. R.; Martinez, T. J.; Boydston, A. J.; Moore, J. S. Mechanically Triggered Heterolytic Unzipping of a Low-Ceiling-Temperature Polymer. *Nature Chemistry* **2014**, *6* (7), 624–629. https://doi.org/10.1038/Nchem.1938.
(324) Peterson, G. I.; Boydston, A. J. Kinetic Analysis of Mechanochemical Chain Scission of Linear Poly(Phthalaldehyde). *Macromolecular Rapid Communications* **2014**, *35* (18), 1611–1164. https://doi.org/10.1002/marc.201400271.
(325) Shiraki, T.; Diesendruck, C. E.; Moore, J. S. The Mechanochemical Production of Phenyl Cations through Heterolytic Bond Scission. *Faraday Discuss* **2014**, *170*, 385–394. https://doi.org/10.1039/c4fd00027g.
(326) Wang, Z.; Ma, Z.; Wang, Y.; Xu, Z.; Luo, Y.; Wei, Y.; Jia, X. A Novel Mechanochromic and Photochromic Polymer Film: When Rhodamine Joins Polyurethane. *Advanced Materials* **2015**, *27* (41), 6469–6474. https://doi.org/10.1002/adma.201503424.
(327) Nixon, R.; De Bo, G. Three Concomitant C–C Dissociation Pathways during the Mechanical Activation of an N-Heterocyclic Carbene Precursor. *Nature Chemistry* **2020**, DOI: 10.1038/s41557-020-0509-1. https://doi.org/10.1038/s41557-020-0509-1.
(328) Wang, T.; Zhang, N.; Dai, J.; Li, Z.; Bai, W.; Bai, R. Novel Reversible Mechanochromic Elastomer with High Sensitivity: Bond Scission and Bending-Induced Multicolor Switching. *ACS Appl. Mater. Interfaces* **2017**, *9* (13), 11874–11881. https://doi.org/10.1021/acsami.7b00176.
(329) Singh, R. K.; Tsuneda, T. Reaction Energetics on Long-Range Corrected Density Functional Theory: Diels-Alder Reactions. *Journal of Computational Chemistry* **2013**, *34* (5), 379–386. https://doi.org/10.1002/jcc.23145.
(330) Williamson, K. L.; Hsu, Y. F. L. Stereochemistry of Diels-Alder Reaction .2. Lewis Acid Catalysis of Syn-Anti Isomerism. *Journal of the American Chemical Society* **1970**, *92* (25), 7385-+. https://doi.org/10.1021/ja00728a022.

(331) Verstraeten, F.; Gostl, R.; Sijbesma, R. P. Stress-Induced Colouration and Crosslinking of Polymeric Materials by Mechanochemical Formation of Triphenylimidazolyl Radicals. *Chemical Communications* **2016**, *52* (55), 8608–8611. https://doi.org/10.1039/c6cc04312g.
(332) Kean, Z. S.; Ramirez, A. L. B.; Yan, Y. F.; Craig, S. L. Bicyclo[3.2.0]Heptane Mechanophores for the Non-Scissile and Photochemically Reversible Generation of Reactive Bis-Enones. *Journal of the American Chemical Society* **2012**, *134* (31), 12939–12942. https://doi.org/10.1021/ja3063666.
(333) Klukovich, H. M.; Kouznetsova, T. B.; Kean, Z. S.; Lenhardt, J. M.; Craig, S. L. A Backbone Lever-Arm Effect Enhances Polymer Mechanochemistry. *Nature Chemistry* **2013**, *5* (2), 110–114. https://doi.org/10.1038/Nchem.1540.
(334) Wang, J. P.; Kouznetsova, T. B.; Kean, Z. S.; Fan, L.; Mar, B. D.; Martinez, T. J.; Craig, S. L. A Remote Stereochemical Lever Arm Effect in Polymer Mechanochemistry. *Journal of the American Chemical Society* **2014**, *136* (43), 15162–15165. https://doi.org/10.1021/ja509585g.
(335) Wu, D.; Lenhardt, J. M.; Black, A. L.; Akhremitchev, B. B.; Craig, S. L. Molecular Stress Relief through a Force-Induced Irreversible Extension in Polymer Contour Length. *Journal of the American Chemical Society* **2010**, *132* (45), 15936–15938. https://doi.org/10.1021/ja108429h.
(336) Kouznetsova, T. B.; Wang, J.; Craig, S. L. Combined Constant Force and Constant Velocity Single Molecule Force Spectroscopy of the Conrotatory Ring Opening Reaction of Benzocyclobutene. *ChemPhysChem* **2016**. https://doi.org/10.1002/cphc.201600463.
(337) Stevenson, R.; De Bo, G. Controlling Reactivity by Geometry in Retro-Diels-Alder Reactions under Tension. *Journal of the American Chemical Society* **2017**, *139* (46), 16768–16771. https://doi.org/10.1021/jacs.7b08895.
(338) Klukovich, H. M.; Kean, Z. S.; Iacono, S. T.; Craig, S. L. Mechanically Induced Scission and Subsequent Thermal Remending of Perfluorocyclobutane Polymers. *Journal of the American Chemical Society* **2011**, *133* (44), 17882–17888. https://doi.org/10.1021/ja2074517.
(339) Kean, Z. S.; Niu, Z. B.; Hewage, G. B.; Rheingold, A. L.; Craig, S. L. Stress-Responsive Polymers Containing Cyclobutane Core Mechanophores: Reactivity and Mechanistic Insights. *Journal of the American Chemical Society* **2013**, *135* (36), 13598–13604. https://doi.org/10.1021/ja4075997.
(340) Attar, A. R.; Chang, H.-T.; Britz, A.; Zhang, X.; Lin, M.-F.; Krishnamoorthy, A.; Linker, T.; Fritz, D.; Neumark, D. M.; Kalia, R. K.; Nakano, A.; Ajayan, P.; Vashishta, P.; Bergmann, U.; Leone, S. R. Simultaneous Observation of Carrier-Specific Redistribution and Coherent Lattice Dynamics in 2H-$MoTe_2$ with Femtosecond Core-Level Spectroscopy. *arXiv:2009.00721 [cond-mat]* **2020**.

APPENDIX A: COMPLETE MANUAL FOR RUNNING OCEAN CALCULATIONS

1. General Notes and Considerations
    a. Color coding:
        i. Input files and input parameters
        ii. Output files
        iii. Scripts
    b. Ensure appropriate and consistent pseudopotentials
        i. Well separated valence and core levels required to make pseudopotentials a good approximation
        ii. Inclusion of semi-core states based on elements in question
    c. Ensure correct lattice parameters
    d. Energetics of excitation
        i. Low energy edge energies are well represented by dipole approximation
        ii. ~80 eV past edge, pseudopotential approximation breaks down
2. Quantum Espresso – Note: Ensure that the quantum espresso runs before attempting OCEAN calculations. A running QE input file will both ensure that the DFT stage of the OCEAN calculation runs and that the underlying electronic structure is correct.
    a. General notes
        i. Excellent resources for troubleshooting QE can be found online, including
            1. https://www.quantum-espresso.org/Doc/INPUT_PW.html
            2. https://www.quantum-espresso.org/Doc/INPUT_BANDS.html
            3. https://www.quantum-espresso.org/Doc/INPUT_DOS.html
            4. https://www.quantum-espresso.org/Doc/INPUT_PROJWFC.html
            5. Quantum Espresso Tutorial 2019
        ii. Need fhi pseudopotential files to run OCEAN calculations but need UPF pseudopotential files to run QE – can find fhi files on pseudopotential vault and then use fhi2upf.x tool to convert the fhi file to UPF format but BE CAREFUL this is a tricky step!
            1. https://nninc.cnf.cornell.edu/periodic_table.html
            2. the UPF file and the opts file for OCEAN need to be consistent !
        iii. Common errors and fixes
            1. For a namelist error (especially for DOS or band structure), rewrite input file from scratch using vi and the command line
            2. For “fortran runtime error, failed to run wfconvert.x” when trying to run nscf, run in a directory with more space
        iv. To use xcrysden, need to have Xming installed and running and export DISPLAY=:0

v. For scf calculations that are not converging, lower mixing beta, add gaussian smearing, check atomic positions, increase kpoint grid

b. QE Calculations

i. **Geometry relaxation calculation** – QE/bin/pw.x <relax.in> relax.out

&control – this flag sets the computer parameters for the calculation, these flags tell QE what parameters are about to be defined, errors often occur when the flag is misspelled, misplaced, or otherwise slightly incorrect

calculation = 'vc-relax' – this parameter tells QE what kind of calculation to run, vc-relax should be used for solid systems and relax should be used for molecular systems

prefix = 'fe2o3'

restart_mode = 'from_scratch'

wf_collect = .true.

pseudo_dir = './' – this parameter tells QE where to find the pseudopotentials on the computer, ./ means that the pseudopotentials are in the same folder from which the calculation is being run

outdir = './' – this parameter tells QE where to save the generated wavefunctions, changing this can be useful if aspects of the calculation are to be changed and rerun, but you want to save all wavefunctions

/ – this symbol tells QE to close the control flag

&system – this flag sets the system parameters for the calculation

ibrav = 5 – sets the Bravais lattice index, can either use this parameter with A, B, C, cosAB, cosBC, cosAC defined, or can set this parameter to 0 and set cell parameters to define the unit cell of interest

- For geometry optimization/relaxation calculations, set ibrav, A, B, C, cosAB, cosBC, cosAC based on the crystal structure of the material from literature, but use ibrav = 0 and cell parameters for subsequent electronic structure calculations

A = 5.49503193 – traditional a crystallographic constant

B = 5.49503193 – traditional b crystallographic constant

C = 5.49503193 – traditional c crystallographic constant

cosAB = 0.56848497982 – traditional gamma angle crystallographic constant

cosAC = 0.56848497982 – traditional beta angle crystallographic constant

cosBC = 0.56848497982 – traditional alpha angle crystallographic constant

nat = 10 – sets the number of atoms in the unit cell

ntyp = 3 – sets the number of types of inequivalent atoms in the unit cell

ecutwfc = 250 – sets the kinetic energy cutoff for wavefunctions, the higher this number is the more computationally expensive the calculation, but usually the more accurate

occupations = 'smearing' – sets the description of orbital occupancies, smearing should be used for metals and some semiconductors, fixed should be used for insulators with a band gap, there are several different options that can be played with

smearing = 'fermi-dirac' – sets the kind of smearing used, again several different options

degauss = 0.05 – sets value of the gaussian spreading (Ry) for brillouin-zone integration in metals

lda_plus_u = .true. – changes the calculation to a DFT+U calculation, this parameter is especially important for transition metal oxides and other materials for which DFT is not the best electronic structure method, setting the U parameter can sometimes help

Hubbard_U(1) = 4.5 – sets the value of the U parameter for the first type of atom (see Atomic Species), needs to be set between 1 and 10, although the value is somewhat arbitrary, setting these values is especially important for transition metals

Hubbard_U(2) = 4.5 – sets the value of the U parameter for the second type of atom (see Atomic Species)

Hubbard_U(3) = 1 – sets the value of the U parameter for the third type of atom (see Atomic Species)

nspin = 2 – sets the total number of spins

starting_magnetization(1) = 1 – sets the spin of the first type of atom (see Atomic Species)

starting_magnetization(2) = -1 – sets the spin of the second type of atom (see Atomic Species)

starting_magnetization(3) = 0 – sets the spin of the third type of atom (see Atomic Species)

tot_magnetization = 0 – sets the total magnetization, if the material is antiferromagnetic and has equal spin up and spin down atoms, this number should be zero

tot_charge = 0.0 – sets the total charge on the system, this is important for ionic systems

/

&electrons

diagonalization = 'david'

mixing_beta = 0.3 – sets the mixing factor for self-consistency, i.e. how much of the previous wavefunction should be used in constructing the wavefunction for the next step

conv_thr = 1.0d-9 – sets the convergence threshold for self-consistency where the estimated energy error is < convergence threshold, the smaller this number usually the more costly and accurate the calculation, can set this to 1d-1 for a very fast check that the input file runs, but doesn't check the accuracy of the electronic structure

/

&ions – this flag is only used in relaxation or MD calculations

ion_dynamics = 'bfgs' – sets how the calculation moves the atoms during structural relaxation

/

&cell – this flag is only used in relaxation calculations

cell_factor = 2.0 – sets how the calculation constructs pseudopotential tables, should be 2 in vc-relax calculations and otherwise should be 1

cell_dynamics = 'bfgs'– sets how the calculation moves the cell during structural relaxation

/

ATOMIC_SPECIES – this flag sets the parameters for all the indistinguishable atoms, the number of entries in this section should equal the set value of ntyp

Fe1 55.845 26-Fe.GGA.fhi.UPF – sets the details for the first atom, defines the atomic identity of the first type of atoms, the atomic mass, and the pseudopotential to be used

Fe2 55.845 26-Fe.GGA.fhi.UPF – sets the details for the second atom

O 15.999 08-O.GGA.fhi.UPF – sets the details for the third atom

ATOMIC_POSITIONS (crystal) – this flag sets the atomic positions, the units in parentheses define the units for the atomic positions, alat sets cartesian coordinates, bohr and angstrom are themselves, crystal sets coordinates relative to the defined crystal structure, initial positions for relax calculations are available in literature or materials project

Fe1 0.85417500 0.85417500 0.85417500

Fe1 0.14582500 0.14582500 0.14582500

Fe2 0.64582500 0.64582500 0.64582500

Fe2 0.35417500 0.35417500 0.35417500
O 0.44512250 0.05487750 0.75000000
O 0.55487750 0.94512250 0.25000000
O 0.05487750 0.75000000 0.44512250
O 0.94512250 0.25000000 0.55487750
O 0.75000000 0.44512250 0.05487750
O 0.25000000 0.55487750 0.94512250

!CELL_PARAMETERS (angstrom) – this flag sets the lattice vectors for the cell (if ibrav is set to 0), units set in paratheses set the units of the lattice vectors and are typically bohr or angstrom

! 2.5525 -1.4736 1.8316
! 0.0000 2.947 1.8316
! -2.5525 -1.4736 1.8316

K_POINTS automatic – this flag sets the kmesh used to sample reciprocal space, the higher these numbers the more accurate and costly the calculation

8 8 8 0 0 0

relax.out → output file contains the geometry optimized cell parameters and atomic coordinates that can (and should) be used in subsequent electronic structure calculations

i. **SCF calculation** – QE/bin/pw.x <scf.in> scf.out

&control
calculation = 'scf' – scf calculations should be run after the geometry optimization
/
&system
ibrav = 0 – set this value to zero once optimized lattice vectors are calculated
/
&ions – this flag is only used in relaxation or MD calculations, will be ignored if in the scf input file
/
&cell – this flag is only used in relaxation calculations, will be ignored if in the scf input file
/

ATOMIC_POSITIONS (crystal) – this flag sets the atomic positions, the units in parentheses define the units for the atomic positions

- Optimized positions are calculated in the relax calculation and can be found in the associated output file → search “Begin final coordinates” to find the final atomic positions

Fe1 0.85417500 0.85417500 0.85417500
Fe1 0.14582500 0.14582500 0.14582500
Fe2 0.64582500 0.64582500 0.64582500
Fe2 0.35417500 0.35417500 0.35417500
O 0.44512250 0.05487750 0.75000000
O 0.55487750 0.94512250 0.25000000
O 0.05487750 0.75000000 0.44512250
O 0.94512250 0.25000000 0.55487750
O 0.75000000 0.44512250 0.05487750
O 0.25000000 0.55487750 0.94512250

CELL_PARAMETERS (angstrom) – this flag sets the lattice vectors for the cell (if ibrav is set to 0), units set in paratheses set the units of the lattice vectors and are typically bohr or angstrom

- the optimized vectors are calculated in the relax calculation and can be found in the associated output file → search "Begin final coordinates" to find the final cell parameters

2.5525 -1.4736 1.8316
0.0000 2.947 1.8316
-2.5525 -1.4736 1.8316

K_POINTS automatic – don't necessarily need a dense k-point grid for scf calculation
4 4 4 0 0 0
scf.out → output file contains the HOMO and LUMO energies or Fermi energy, total energy, band energies sorted by k-point and the fe2o3.save folder contains the wavefunctions sorted by kpoint

a. **NSCF calculation** – QE/bin/pw.x <nscf.in> nscf.out

&control
calculation = 'nscf' – nscf calculations should be run after the scf calculation
/
ATOMIC_POSITIONS (crystal) – this flag gets ignored and the atomic positions from the previous scf calculation are used in a nscf calculation
K_POINTS automatic – to facilitate subsequent band structure calculations, make the kpoint grid as dense as computationally feasible
12 12 12 0 0 0
nscf.out → output file contains HOMO and LUMO energies or Fermi energy, while the Out or .save folder contains the calculated wavefunctions

a. **Band Structure calculation** – QE/bin/pw.x <band.in> band.out

!! For band structure calculations in QE, set the k-points and kpath based on the symmetry points in the Brillion zone, otherwise the band structures will be off (the OCEAN code does *not* set correct kpaths in their electronic structure calculations, so if you try to plot the band structure from the enkfile, it will look different than literature/the structure you calculate here. That's OK because the electronic structure is still correct, the interpolation path is just off for this) !!

- The coordinates can be determined from the symmetry points in Brillion zone of each crystal structure → can load the scf.out file into xcrysden, under the tools tab open the kpath selector option and then draw out the kpath desired, can save this path to a file and use those coordinates here
  - https://www.cryst.ehu.es/cgi-bin/cryst/programs/nph-table?from=kv has the symmetry points for the Brillion zones of all crystal space groups
- Keeping the kpoints set to a kmesh will still calculate the band structure but it is not a useful comparison to literature or for future use in exciton plotting

&control
calculation = 'bands' – scf and nscf calculations should be run before the bands calculation
/
ATOMIC_POSITIONS (crystal) – this flag gets ignored and the atomic positions from the previous scf calculation are used in a nscf calculation
K_POINTS crystal_b – for band structure calculations, the k-points should be set to reflect the kpath

10 – set the number of k points along the kpath

0.0000000000 0.0000000000 0.0000000000 10 !GAMMA – sets the coordinates of the kpoint and sets the number of points interpolated along the kpath

0.5000000000 0.5000000000 0.5000000000 10 !T
0.7688956561 0.2311043439 0.5000000000 10 !H_2
0.5000000000 -0.2311043439 0.2311043439 10 !H_0
0.5000000000 0.0000000000 0.0000000000 10 !L
0.0000000000 0.0000000000 0.0000000000 10 !GAMMA
0.3655521720 -0.3655521720 0.0000000000 10 !S_0
0.6344478280 0.0000000000 0.3655521720 10 !S_2
0.5000000000 0.0000000000 0.5000000000 10 !F
0.0000000000 0.0000000000 0.0000000000 10 !GAMMA

a. **Band Structure processing** – QE/bin/bands.x <band_proc.in> band_proc.out

&bands – this flag is used for band structure processing
prefix = 'fe2o3'
outdir = './'
filband = 'fe2o3_bands_proc.dat' ' – sets the output file for the processed band structure
/

band_proc.dat → processed band structure file has the bands sorted by kpoint in an easily readable form that can be imported and plotted in matlab

band_proc.dat.gnu →is also a processed band structure file that can be plotted with gnuplot from the terminal or command line

a. **Density of states calculation** – QE/bin/dos.x <dos.in> dos.out

&DOS – this flag is used for density of states calculation
prefix = 'fe2o3'
outdir = './'
DeltaE = 0.1
degauss = 0.01 – sets the broadening of the DOS, usually not an issue, but if the DOS is too broad, can set this to very small value (0.01)
fildos = 'fe2o3.dos'
/

fe2o3.dos → total density of states "# E (eV) dosup(E) dosdw(E) Int dos(E) EFermi = 8.418 eV"

a. **Projected wavefunction calculation** – QE/bin/projwfc.x <projwfc.in> projwfc.out

&projwfc
prefix = 'fe2o3'
outdir = './'
DeltaE = 0.1
filpdos = 'fe2o3.dos'
/

fe2o3.dos.pdos_atm#1(Fe1)_wfc#1(s) → partial density of states for each of the distinguishable atoms in the material calculated, projected wavefunctions of each atom on the total density of states, outputs are files for each relevant wavefunction (orbital contribution) for each atom

3. Ground State OCEAN Calculations
    a. Notes
        i. Need to make sure element of interest is first in all lists (and is consistent) otherwise OPF will not run and will return and “opening” error
        ii. Check the spin-orbit splitting of the edge of interest using the program Hephaestus (i.e. M2 and M3 splitting)
        iii. If you think you’ve fixed a problem and are still encountering an error, try deleting all the previous runs and associated trials and just starting over
    b. Common Errors and Fixes
        i. If the hfk.x in the OPF stage fails to converge, ensure that the pseudopotential has been correctly converted from fhi to UPF and that the opts file is correctly configured to reflect the pseudopotential
            1. This error usually looks like this: “The program hfk.x has exited incorrectly for hfin1.”
        ii. If the PREP stage fails with “Entering PREP stage 0 0 25.000000000094836 25.000000000000000../../DFT/SCREEN/Outlegacy 0 /home/iklein/OCEAN-2.5.2/install/qe_data_file.pl Out/system.save/data-file.xml, At line 59 of file wfconvert2.f90 (unit = 99, file = 'brange.ipt'), Fortran runtime error: Bad integer for item 2 in list input,” try setting occupt to 3 and metal = .true. in the OCEAN input file and rerun the calculation
        iii. If the SCREENING stage fails with “Fortran runtime error: Cannot open file 'zpawinfo/vc_barez029n04l02': No such file or directory…Failed to run screen_driver.x, SCREEN stage failed, Inappropriate ioctl for device at /home/iklein/OCEAN-2.5.2/install/ocean.pl line 287.” The most likely reason is that the vc_bare* files, which are potentials for the core states calculated from the pseudo potential, do not include the requisite core states
            1. If the pseudopotential has been correctly converted and the opts file is correct and you still get this error, you need a new pseudopotential file
            2. The pseudopotential used must include the core state of interest in the edge calculation as a core state in that pseudopotential
        iv. When running a haydock calculation, the bse.in file sometimes doesn’t write itself correctly, so the calculation will fail
            1. “time mpirun -n 11 /home/akrotz/GWDFT/OCEAN_new/OCEAN-2.5.2/installDir//ocean.x > cm.logAt line 1292 of file OCEAN_haydock.f90 (unit = 99, file = 'bse.in')”
            2. To correct this, open bse.in file and make sure that the last line starts with the number of bands (nbands value) used in the calculation, and then rerun ocean.x from the CNBSE folder

c. Inside the calculation directory, need following files:
   i. UPF and fhi pseudopotential files for each of the atoms
   ii. x.opts files for each of the atoms

026 – sets the atomic number of the atomic number of atomic species
3 2 0 0 – sets the number of core states for each angular momentum channel (s,p,d,f) that are filled, these values need to be consistent with the pseudopotentials used
scalar rel – specifies how the relativistic spin-orbit effects are treated
gga – specifies the exchange correlation functional used
2.0 0.0 5.5 0.0 – sets the valence occupation as determined by the pseudopotential, these values need to be consistent with the pseudopotentials used and pseudopotentials are often slightly positively ionic, hence the half value for the d orbital occupation
- matching these values to the pseudopotential used is very important, especially for the semi-core pseudopotentials that are used for transition metals
2.0 0.0 5.5 0.0

   iii. x.fill files for each of the atoms

2 – sets the matrix elements between the core state χα and local orbital φi are calculated up to χα|rpow|φi.
0.2 3.00 0.0001 – sets Epad, Emax, and prec, where the OPF reconstruction starts at energy Epad below the lowest valence state for a given angular momentum channel and attempts to span the space to Emax and prec should be left at the set value
2.8 – sets the cutoff radius in Bohr for the OPF cutoff, the convergence of this parameter should be checked
0.05 20 – sets q step and q max that control the Fourier transform of the projectors from real-space, the defaults should be fine.

   iv. photon1 file

quad – sets the dipole operator
cartesian 0 0 1 – sets the direction for the x-ray polarization vector
end
cartesian 0 1 0 – sets the q-vector direction for the incoming light (for quad dipole operator)
end
54 – sets the X-ray photon energy in eV

a. **OCEAN ground state haydock calculation** – ocean.pl

dft{ qe } – sets the DFT solver, currently can use AbInit or QE
acell {10.2423 10.2423 10.2423} – Magnitude of lattice vectors in Bohr
- these can be calculated using the cell parameters from QE and the rprim

rprim {1.0000000000 0.0000000000 0.0000000000
0.5695664700 0.8219452757 0.0000000000
0.5695664700 0.2982686482 0.7659176521} – cartesian coordinates of primitive lattice vectors, these are specific to the crystal space group of the system under investigation
ntypat 3 – sets the number of types of inequivalent atoms in the unit cell
znucl { 26 26 8 } – sets the atomic numbers of each set of inequivalent atoms
natom 10 – sets the total number of atoms in the unit cell
typat { 1 1 2 2 3 3 3 3 3 3 } – sets the number of each type of inequivalent atoms
xred {0.1433915 0.1433904 0.1433906
0.8566085 0.8566096 0.8566094

0.3566087 0.3566104 0.3566106
0.6433913 0.6433896 0.6433894
0.7500005 0.4472258 0.0527735
0.9472262 0.2499995 0.5527741
0.4472260 0.0527734 0.7500002
0.2499995 0.5527742 0.9472265
0.0527738 0.7500005 0.4472259
0.5527740 0.9472266 0.2499998} – sets the relative positions of all the atoms in the order listed in typat
diemac 25 – sets the static dielectric constant
nspin 2 – sets the total spin where 1 is paramagnetic and 2 is antiferromagnetic
smag {starting_magnetization(1)=1,starting_magnetization(2)=1,starting_magnetization(3)=0, tot_magnetization=0} – sets the initial magnetization (see QE section)
ldau {lda_plus_u=.true. , Hubbard_U(1)=4, Hubbard_U(2)=4, Hubbard_U(3)=1} – sets the U values (see QE section)
zsymb { Fe1 Fe2 O} – sets the element symbol for all ntypat
ppdir { '../' } – sets the pseudopotential directory location
pp_list{ 26-Fe.GGA.fhi
26-Fe.GGA.fhi
08-O.GGA.fhi } – sets the pseudopotentials in the order listed in typat
ecut 250 – sets the kinetic energy cut off
nkpt {8 8 8} – sets the kpoint mesh for the final states
ngkpt { 4 4 4 } – sets the kpoint mesh for the nscf calculation
nbands {100} – sets the number of bands calculated
screen.nbands 200 – sets the number of bands used for screening
occopt 3 – sets the smearing where 1 is fixed (insulator) and 3 is smearing (metals and semiconductor)
toldfe 1.1d-8 – sets the scf energy tolerance (related to convergence threshold)
tolwfr 1.1d-8 – sets the scf wavefunction tolerance
nstep 200 – sets the maximum number of scf iterations
mixing { 0.3 } – sets the scf beta mixing
screen.nkpt {2 2 2} – sets the kpoint mesh for screening
opf.fill{ 26 fe.fill } – sets the fill file for the atom with the edge of interest (see above)
opf.opts{ 26 fe.opts } – sets the opts file for the atom with the edge of interest (see above)
nedges 1 – sets the number of edges to calculate
edges{ 1 3 1 } – sets the atom number, n quantum number and l quantum number of the edge of interest
screen.shells{ 4.5 } – sets the radius for the shell used in the screening
cnbse.rad{ 4.5 }
scfac 1
opf.hfkgrid {2000 50}
CNBSE.xmesh { 8 8 8 }
cnbse.broaden{ 0.01 } – sets the spectral broadening in eV, # 0.1 eV is the default broadening, setting it as low as possible is ideal but too low and the calculation will not converge, enables

post calculation energy dependent broadening that accurately reflects the physics of experimental broadening

cnbse.spect_range{ -1 }

absspct_Fe.0001_3p_01 (in CNBSE folder) → calculated continuous X-ray absorption spectrum for the edge set in the edges parameter flag

enkfile (in CNBSE folder) →band structure calculated with OCEAN using QE (this band structure file isn't as good as the QE ones because the kpath isn't always set correctly)

scf.out (in DFT folder) →self-consistent field calculation output, this file can be used to check the crystal structure used in the OCEAN calculation to ensure the rprim, acell and xred parameters are correctly set

a. OCEAN ground state gmres calculation – ocean.x

a. Gmres calculations should be run after a haydock calculation has been run to verify the accuracy of the calculation spectrum resulting from the OCEAN input file → can tweak some of the input parameters to converge the calculation and/or achieve a correct calculated spectrum
    i. most of the parameters are taken from a converged and accurate QE calculation, so this step shouldn't be arduous

cnbse.solver{ gmres} – sets the CNBSE solver to gmres → this spits out the overlap between the initial and final wavefunctions using either the total Hamiltonian or BSE components of it (based on hamnum)

cnbse.gmres.erange{ 0 20 1 } – sets the energy range and step size of the exciton calculation

hamnum{ 1 1 1 1 1 1 } – determines which BSE components are turned on in the calculation

absspct_Fe.0001_3p_01 (in CNBSE folder) → calculated X-ray absorption at for each step defined in cnbse.gmres.erange for the edge set in the edges parameter flag

echamp_Fe.0001_3p_01.0001.111111 (in CNBSE folder) → exciton wavefunctions projected onto the band structure for each step defined in cnbse.gmres.erange for the edge set in the edges parameter flag

- the atom symbol (Fe), core level (3p), step number (0001) and hamnum (111111) are all written into the file name

a. **OCEAN ground state gmres calculation** – separable BSE components

a. Once the overall gmres calculation has been run, as described above, the values in the hamnum file in the CNBSE folder can be changed and ocean.x can be used to rerun the exciton overlap portion of the calculation in the CNBSE folder
    i. This calculation will spit out echamp files that are specific to the BSE component(s) specified and can be used to look at the magnitude and location of the contributions of these components to the overall exciton

b. hamnum is a list of variables (either 1 or 0) that turn on or off different terms of the BSE Hamiltonian (1 is on, 0 is off, default is all on). The terms that each variable controls are:
    i. lr_act (long range) – screening
    ii. ladder
    iii. bubble
    iv. ct_act (charge transfer) – multiplet

v. fgact (slater/fg integrals)
vi. soact (spin-orbit term) – angular momentum

echamp_Fe.0001_3p_01.0001.111111 (in CNBSE folder) → exciton wavefunctions projected onto the band structure for each step defined in cnbse.gmres.erange for the edge set in the edges parameter flag

- as the hamnum numbers change, the last number change to reflect that – i.e. when hamnum = 000001, then the file name will be echamp_Fe.0001_3p_01.0001.000001, in this way, the echamp files for each BSE component can be kept separate

b. **OCEAN ground state gmres calculation** – energy decomposition
   a. Can rerun the overall OCEAN gmres calculation with different energy ranges and step sizes specified in cnbse.gmres.erange to investigate the magnitude and location of the exciton as it relates to specific peaks in the absorption spectrum
      i. Calculation spits out echamp files that are specific to the energy range specified AND absspct absorption spectrum file that contains discrete spectral points within the energy range specified

echamp_Fe.0001_3p_01.0001.111111 (in CNBSE folder) → exciton wavefunctions projected onto the band structure for each step defined in cnbse.gmres.erange for the edge set in the edges parameter flag

1. Excited State OCEAN Calculations

c. **OCEAN state filling calculations** – manual_state_filling_HOMO_LUMO
   a. Can use different state filling codes to model state filling in two different ways
      i. Can either select state filling states in band structure OR can specify an energy range based on pump energy to fill
   b. To model the X-ray absorption spectrum that corresponds to photoexcited carriers based on energy, use the manual_state_filling_HOMO_LUMO code to generate a new allowarray.dat file (the file in the CNBSE folder that tells the OCEAN code which states are filled or empty) that has holes in the VB and electrons in the CB based on the energy of excitation specified
      i. Allowarray.dat file matches the number of conduction bands x kpoints, arranged in blocks by k-point
      ii. Usually integer values are used, there may be non-linear behavior from using fractional occupations -- needs to further testing.
   c. Copy the CNBSE folder with all files and replace the original allowarray.dat file with the new one generated from the state filling simulation and rerun ocean.x
      i. This method can be used for both haydock (spectrum) and gmres (exciton density) calculation
   d. Can also use multiple different state filling conditions, with multiple allowarray.dat files and iteratively loop the ocean.x calculation

absspct_Fe.0001_3p_01 (in CNBSE folder) → calculated continuous X-ray absorption spectrum for the edge set in the edges parameter flag (when using the haydock solver)
absspct_Fe.0001_3p_01 (in CNBSE folder) → calculated X-ray absorption at for each step defined in cnbse.gmres.erange for the edge set in the edges parameter flag (when using the gmres solver)
echamp_Fe.0001_3p_01.0001.111111 (in CNBSE folder) → exciton wavefunctions projected onto the band structure for each step defined in cnbse.gmres.erange for the edge set in the edges parameter flag (when using the gmres solver)

d. OCEAN thermal expansion calculations

a. To model the X-ray absorption spectrum that corresponds to a thermally expanded sample, the values of acell, the magnitude of the lattice vectors, must be changes. To calculate the new values of acell that correspond to the thermally expanded lattice, need to find the isotropic thermal expansion constant for a given material and choose an appropriate temperature. Use those parameters to calculate the new values of acell and then run the OCEAN calculation as described above.
    i. This method can be used for both haydock (spectrum) and gmres (exciton density) calculation

absspct_Fe.0001_3p_01 (in CNBSE folder) → calculated continuous X-ray absorption spectrum for the edge set in the edges parameter flag (when using the haydock solver)
absspct_Fe.0001_3p_01 (in CNBSE folder) → calculated X-ray absorption at for each step defined in cnbse.gmres.erange for the edge set in the edges parameter flag (when using the gmres solver)
echamp_Fe.0001_3p_01.0001.111111 (in CNBSE folder) → exciton wavefunctions projected onto the band structure for each step defined in cnbse.gmres.erange for the edge set in the edges parameter flag (when using the gmres solver)

1. OCEAN Processing

a. Exciton processing

i. Converting exciton wavefunctions to energies (this step has to be repeated for every permutation of gmres calculation – different energy ranges, different BSE components turned on, etc – as each calculation generates exciton wavefunctions that have to be processed)

1. In the CNBSE folder (or wherever you have copied the echamp files), copy echamp_proc.py and open using text editor
    a. In line 10, change the bands = # to the number of conduction band states
        i. The number of conduction band states can be found in the cm.log file in the CNBSE folder at the line "Dim: 66 512 1" where the first number is the number of conduction band states and the second is the number of kpoints
    b. In line 63, change filenameList=glob.glob("echamp_Fe.000*_3p_*.*.0000

01") to match the pattern for your echamp files (element, edge, and hamnum)

2. In the folder with the processing code file and the echamp files, run python3 echamp_proc_k10.py, this will generate energyOut_512_echamp_Fe.000*_3p_*.*.000001 files
    a. Once the echamp_proc script has been successfully run there should be a number of files with the prefix energyOut_* followed by the number of k-points and the input echamp files.

energyOut_512_echamp_Fe.000*_3p_*.*.111111 → energyOut files are processed echamp files that can be imported, read, and plotted by matlab using the bandSum codes

!! If you screw up the number of bands, the processing code will still run, but it will incorrectly process your echamp files such that they won't have the correct number of bands and k points and you won't be able to process them using the bandSum code → check that you have the correct number of k points in the name of the energyOut files

ii. Plotting exciton energies on band structure – bandSum

iii. Note: To use any of the bandSum matlab files, the bandgen file needs to be in the same folder from which you are running the bandSum matlab. The bandgen file is used to important and reshape the enkfile and energyOut files

1. To plot the ground state excitons on the band structure, use bandSum
    a. This code can be augmented to be used for plotting the excitons of any single state
2. To plot the difference between the ground and excited state excitons on the band structure, use excited state comparisons_bandSum
    a. This code also plots all of the different states' excitons, as well as the differences between them
3. To plot the ground state excitons over different energy ranges, use ground state exciton erange comparisons_bandSum

b. **Broadening** – broadening_matlab

i. Notes: L3:L2 ratios and white lines have very different lifetime broadening

ii. There are a number of different broadening techniques that can be used → try using them in increasing order of complexity (i.e. see if the simplest broadening method works before moving on to more complex ones) because estimating lifetimes is theoretically challenging, so just look to match experiment

1. These include linear broadening, Lorentzian broadening, energy dependent Lorentzian broadening, inelastic mean free path energy dependent convolution broadening, fano broadening, etc.

2. While the simplest should be used first, typically a combination of the above is needed to accurately broaden the calculated spectrum to match the experimental spectrum

APPENDIX B: SUPPLEMENTARY INFORMATION FOR AB INITIO PREDICTION OF EXCITED STATE AND POLARON EFFECTS IN TRANSIENT XUV MEASUREMENTS OF A-FE_2O_3

B1. Computational Methods

a. Computational Input Parameters

Geometry optimization and DFT calculations were performed with the Quantum ESPRESSO package using Perdew-Burke-Ernzerhof (PBE) pseudopotentials under the generalized gradient approximation (GGA). The associated ground state wavefunctions were constructed using a plane wave basis set with components up to a kinetic energy cutoff of 250 Ry. Reciprocal space was sampled using an 4x4x4 Gamma-centered mesh with a 0.02 eV Gaussian smearing of orbital occupancies. DFT simulations were performed on a unit cell of α-Fe_2O_3 containing 10 atoms, measuring 10.24 Å along the *a*-, *b*- and *c*-directions. Self-consistent calculations were performed to a convergence of 10^{-6} eV/atom and forces on ions under 10^{-3} eV/Å. DFT-BSE calculations were conducted using the same parameters. Additionally, an 8x8x8 k-point grid for the screening mesh, 100 bands, a dielectric constant of 25, a cutoff radius of 4.5 Bohr, and a band gap scissor correction of 3 eV were used in the DFT-BSE calculations of the XUV absorption spectra.[123,340]

B2. Structural Data for Calculations

a. Calculations for both the ground state and the state-filling excited state of α-Fe_2O_3 were performed on the following unit cell.

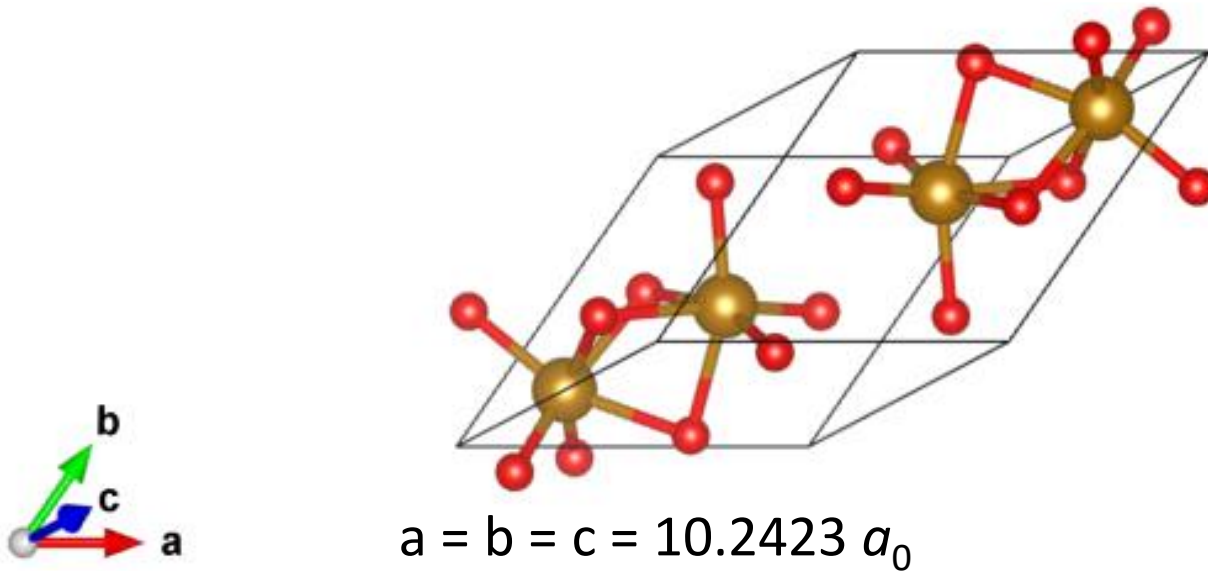

Figure B1. Unit Cell for Ground State and State Filling Excited State OCEAN Calculations.

Primitive Vectors

1.0000000000	0.0000000000	0.0000000000
0.5695664700	0.8219452757	0.0000000000
0.5695664700	0.2982686482	0.7659176521

Reduced coordinates, (x, y, z), of the all n-atoms in the cell were

Fe1	0.1433915	0.1433904	0.1433906
Fe1	0.8566085	0.8566096	0.8566094
Fe2	0.3566087	0.3566104	0.3566106
Fe2	0.6433913	0.6433896	0.6433894
O	0.7500005	0.4472258	0.0527735
O	0.9472262	0.2499995	0.5527741
O	0.4472260	0.0527734	0.7500002
O	0.2499995	0.5527742	0.9472265

O 0.0527738 0.7500005 0.4472259

O 0.5527740 0.9472266 0.2499998

b. Calculations for the polaron excited state of α-Fe_2O_3 were performed using the following unit cell, arrived at by the procedure described in the main text. The Fe2 site is used for the polaron state X-ray site and is highlighted in yellow.

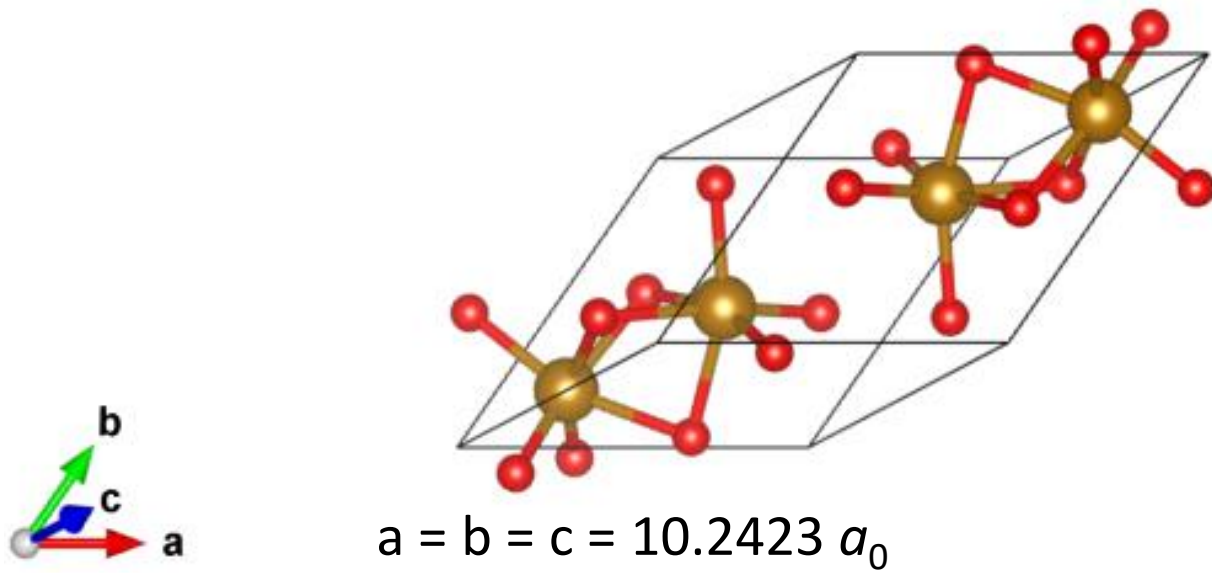

Figure B2. Unit Cell for Polaron Excited State OCEAN Calculations.

Primitive Vectors

1.0000000000 0.0000000000 0.0000000000

0.5695664700 0.8219452757 0.0000000000

0.5695664700 0.2982686482 0.7659176521

Reduced Coordinates, (x, y, z), of the all natom atoms in the cell

Fe1 0.1452347 0.1454904 0.1451297

Fe1 0.8549303 0.8545129 0.8546109

Fe2 0.3544541 0.3549705 0.3547903

Fe2 0.6450367 0.6458038 0.6448248

O 0.7498179 0.4453231 0.0551344

O 0.9451309 0.2494991 0.5553065

O 0.4449728 0.0547092 0.7500116

O 0.2500428 0.5549325 0.9452755

O 0.0553823 0.7494405 0.4452824

O 0.5549975 0.9453182 0.2496338

c. Calculations for the thermally expanded excited state of α-Fe_2O_3 were performed on the unit cell below. The specific change to the scaling of the primitive vectors that models the thermal expansion is highlighted in yellow.

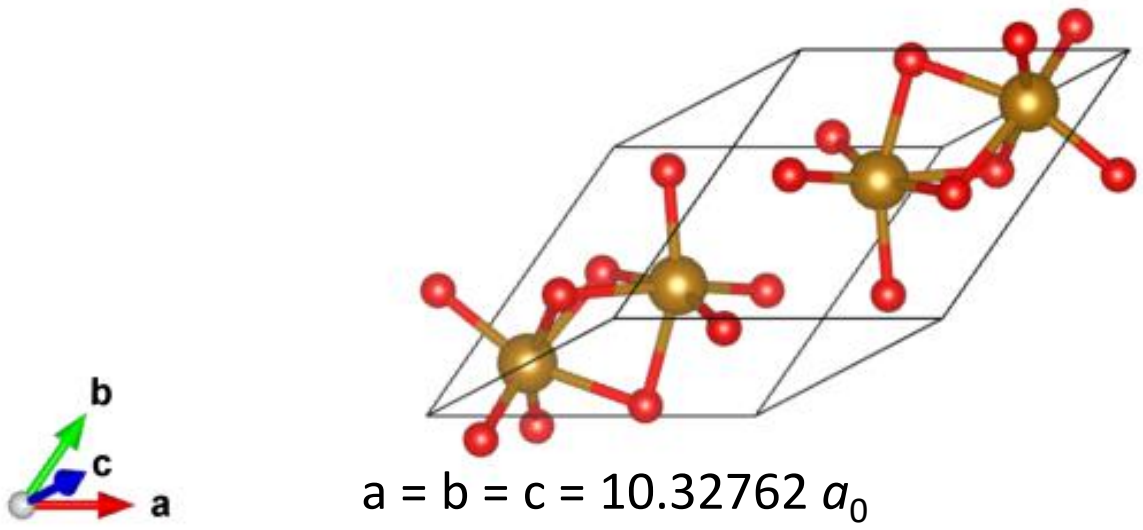

Figure B3. Unit Cell for Thermally Expanded Excited State OCEAN Calculations.

Primitive Vectors

1.0000000000 0.0000000000 0.0000000000

0.5695664700 0.8219452757 0.0000000000

0.5695664700 0.2982686482 0.7659176521

Reduced Coordinates, (x, y, z), of the all natom atoms in the cell

Fe1 0.1433915 0.1433904 0.1433906

Fe1 0.8566085 0.8566096 0.8566094

Fe2 0.3566087 0.3566104 0.3566106

Fe2 0.6433913 0.6433896 0.6433894

O 0.7500005 0.4472258 0.0527735

O 0.9472262 0.2499995 0.5527741

O 0.4472260 0.0527734 0.7500002

O 0.2499995 0.5527742 0.9472265

O 0.0527738 0.7500005 0.4472259

O 0.5527740 0.9472266 0.2499998

d. Comparisons between each excited state and the ground state for the Fe-Fe distance and Fe-O distance are given in Table S1, along with the percent change from the ground state.

Table B1. Bond Distances and Change from the Ground State for each Excite State.

State	**Fe-Fe Distance (Å)**	**Percent Change from Ground (%)**	**Fe-O Distance (Å)**	**Percent Change from Ground (%)**
Ground	2.92755	n/a	1.94192	n/a
Charge Transfer	2.92755	0	1.94192	0
Polaron	2.87585	- 1.77	1.95016	+ 0.4
Thermal (650 K)	2.95194	+ 0.83	1.95810	+ 0.83

B3. Ground State Calculations

a. Initial DFT calculations on the ground state of α-Fe_2O_3 were performed to verify computational parameters used in this study. The OCEAN computational program is not yet able to use hybrid pseudopotentials, and as such it was important to compare the band structure and DOS shown here to previous computational work.[123] Partial DOS with orbital breakdowns are shown to fully understand the DOS and the excitations calculated in the OCEAN calculations. As commented earlier, a scissor shift was used for to correct the band gap because hybrid pseudopotentials could not be used. Since only the conduction band states are needed for the final calculations, the calculation can still be accurate even without a hybrid functional. Accordingly, adjusting the U parameter in the DFT+U calculations had little effect on the final XUV absorption spectrum.

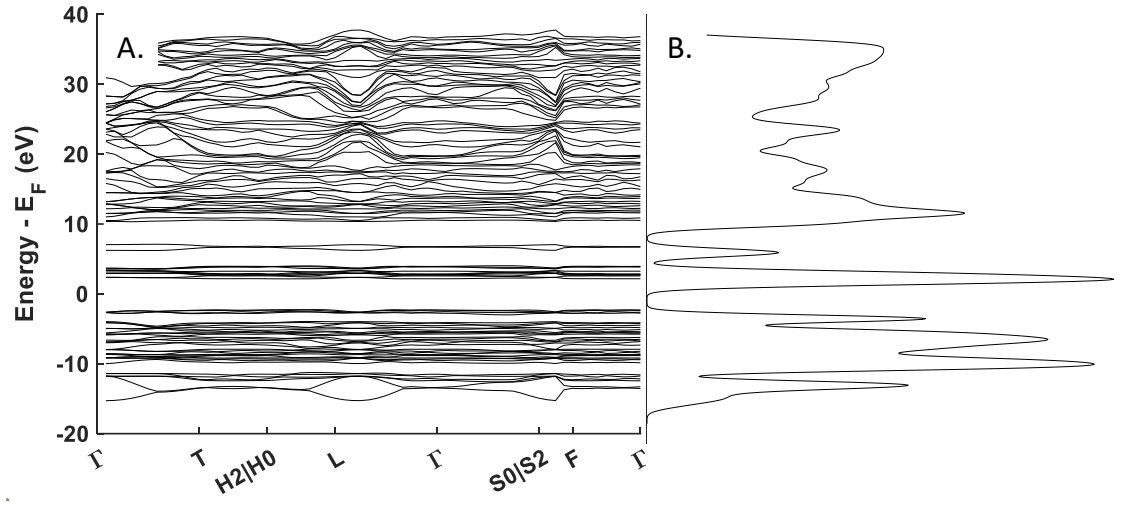

Figure B4. Ground State DFT Outputs for α-Fe_2O_3. (a) Full ground state band structure with the Fermi energy set to 0 eV. (b) Full ground state total density of states. No scissor shift has been included in these calculations.

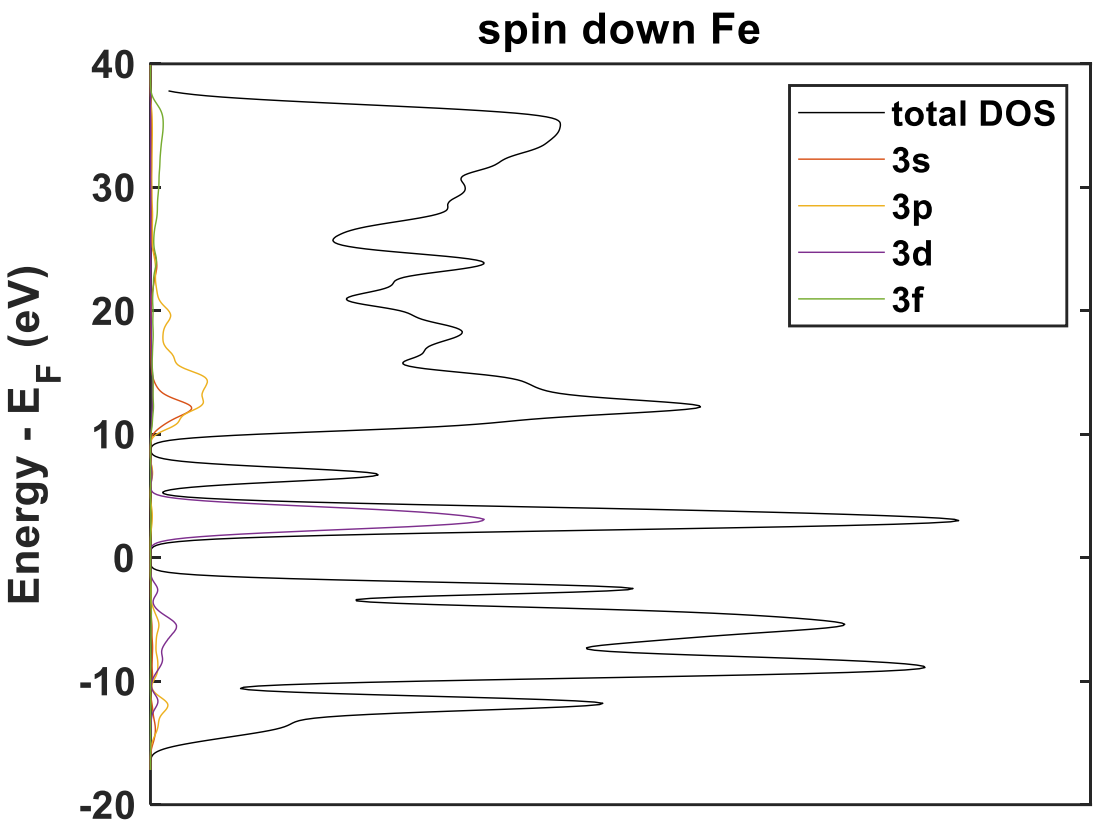

Figure B5. Partial Density of States for α-Fe_2O_3. Spin down Fe partial DOS decomposed into 3s, 3p, 3d, and 3f orbital contributions. No scissor shift has been included in these calculations.

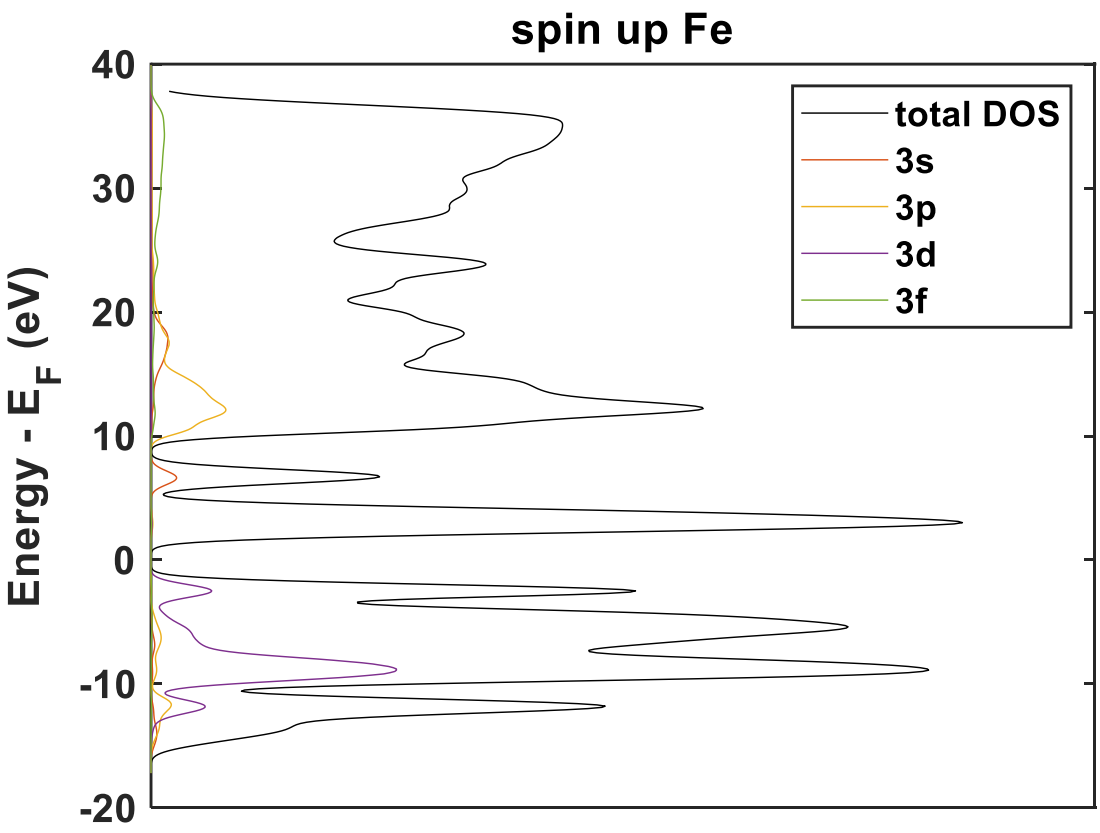

Figure B6. Partial Density of States for α-Fe_2O_3. Spin up Fe partial DOS decomposed into 3s, 3p, 3d, and 3f orbital contributions. No scissor shift has been included in these calculations.

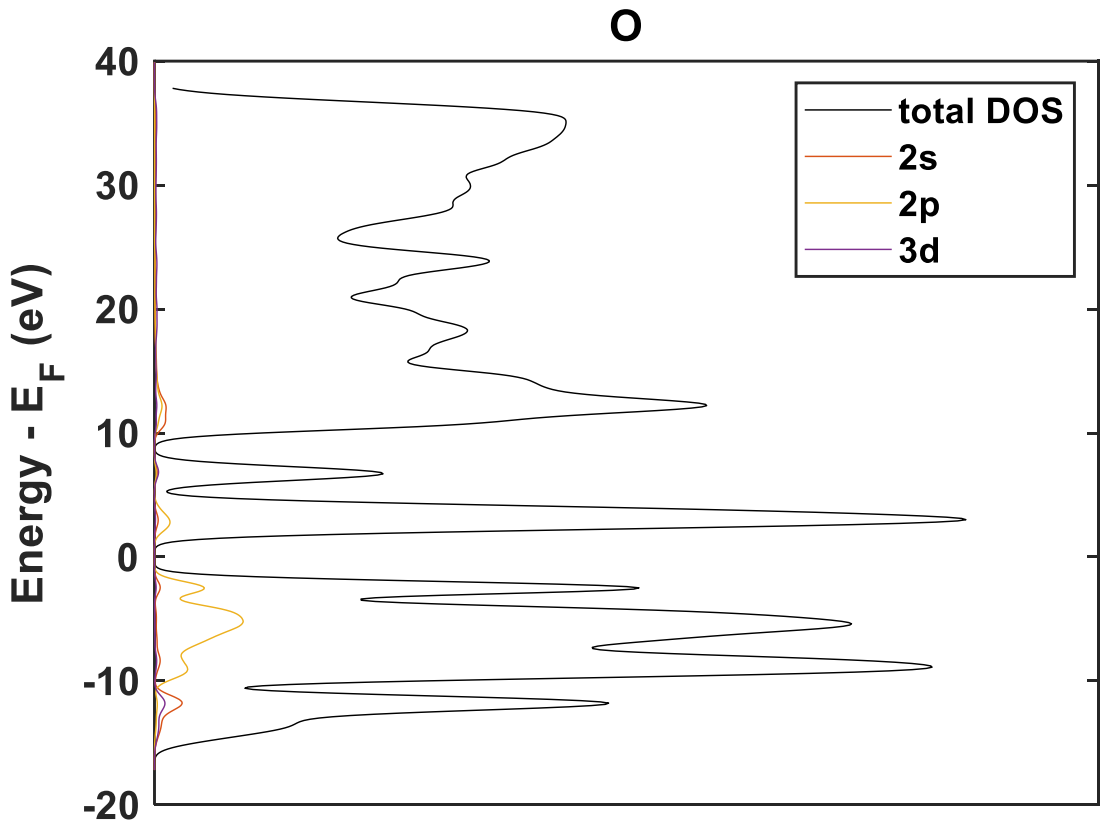

Figure B7. Partial Density of States for α-Fe_2O_3. O partial DOS decomposed into 2s, 2p, and 3d orbital contributions. No scissor shift has been included in these calculations.

b. The ground state XUV absorption was calculated and broadened by convoluting the calculated XUV absorption spectrum with an energy-dependent Gaussian, as described below (consistent with previous literature, as can be compared in Figure S8).[54,110] The calculated ground state spectrum was compared to the LMCT stick spectrum used in previous work.[54]

The matlab script for the broadening is as follows:

$$G(E,w,E_o)= \frac{e^{-(\frac{E-E_o}{\omega\sqrt{2}})^2}}{\omega\sqrt{2\pi}}$$

Fe2O3_calc = initial calculated absorption spectrum
Fe2O3_ground_broad= final broadened calculated absorption spectrum
Fe2O3_broad = broadened calculated absorption spectrum
E(i) = 1 – 200 eV, 0.2 eV steps

```
for i=1:100
   if E(i) <= 58
        Fe2O3_broad=25*Fe2O3_calc(i)*G(E,0.5,E(i));
   elseif E(i) > 58 & E(i) <= 62
        Fe2O3_broad=300*Fe2O3_calc(i)*G(E,(i/200)^0.01 + 0.5,E(i));
   else
        Fe2O3_broad=200*Fe2O3_calc(i)*G(E, (i/200)^-2,E(i));
   end
   Fe2O3_ground_broad = Fe2O3_broad;
end
```

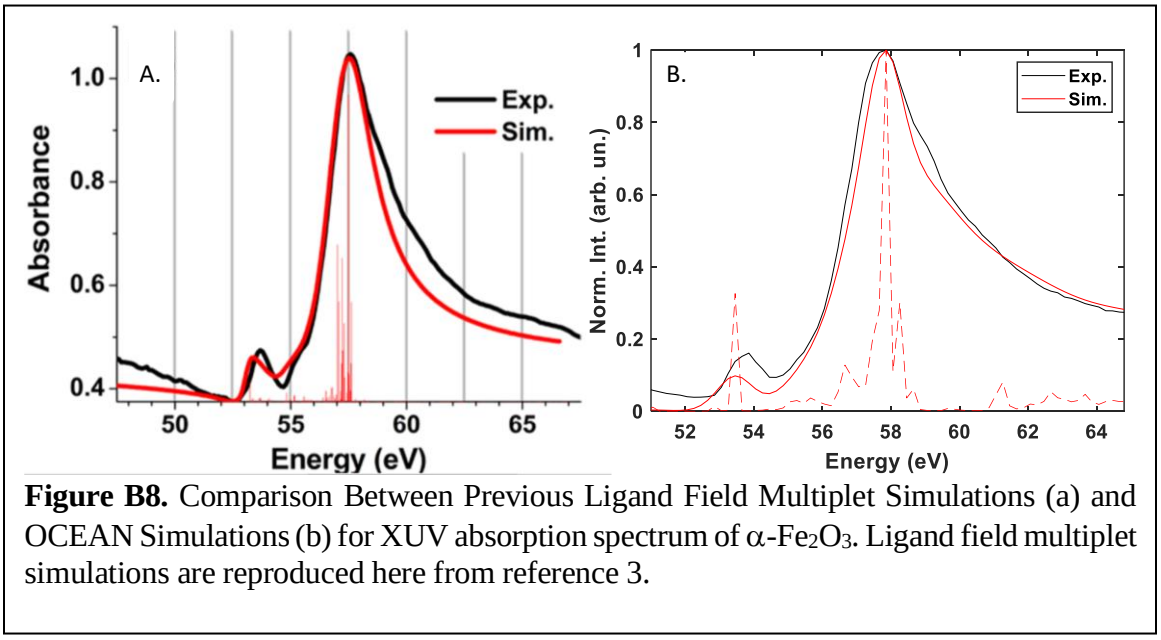

Figure B8. Comparison Between Previous Ligand Field Multiplet Simulations (a) and OCEAN Simulations (b) for XUV absorption spectrum of α-Fe_2O_3. Ligand field multiplet simulations are reproduced here from reference 3.

c. The ground state XUV core-valence exciton density was calculated for specific energy ranges and overlaid on the XUV absorption spectrum and band structure. To calculate the exciton density for these specific energy ranges, a GMRES calculation was used, restricting the energy to a 1 eV range. The range was changed to allow the entire region around the Fermi energy, and around the Fe $M_{2,3}$ edge under investigation, to be calculated.

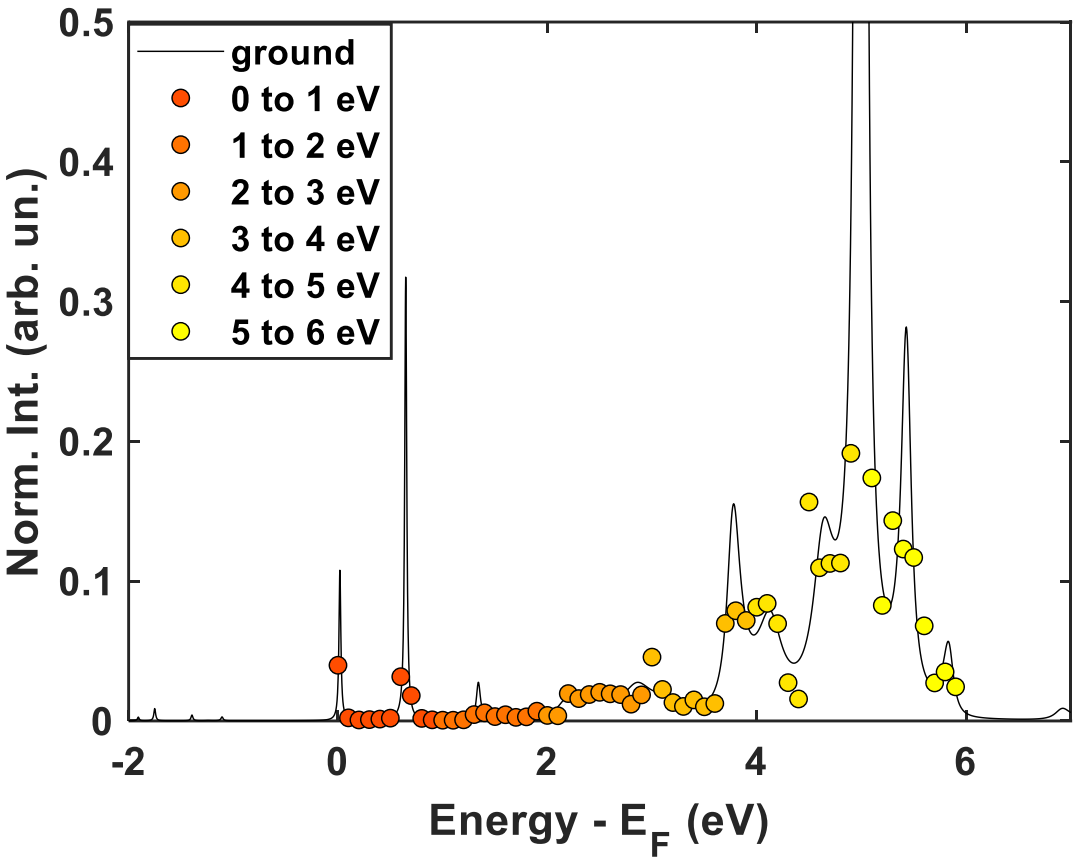

Figure B9. Energy-Resolved Exciton Densities Overlaid on the Calculated XUV Absorption Spectrum for α-Fe_2O_3. Exciton densities overlaid on the calculated XUV absorption spectrum around the Fermi level and the Fe $M_{2,3}$ edge.

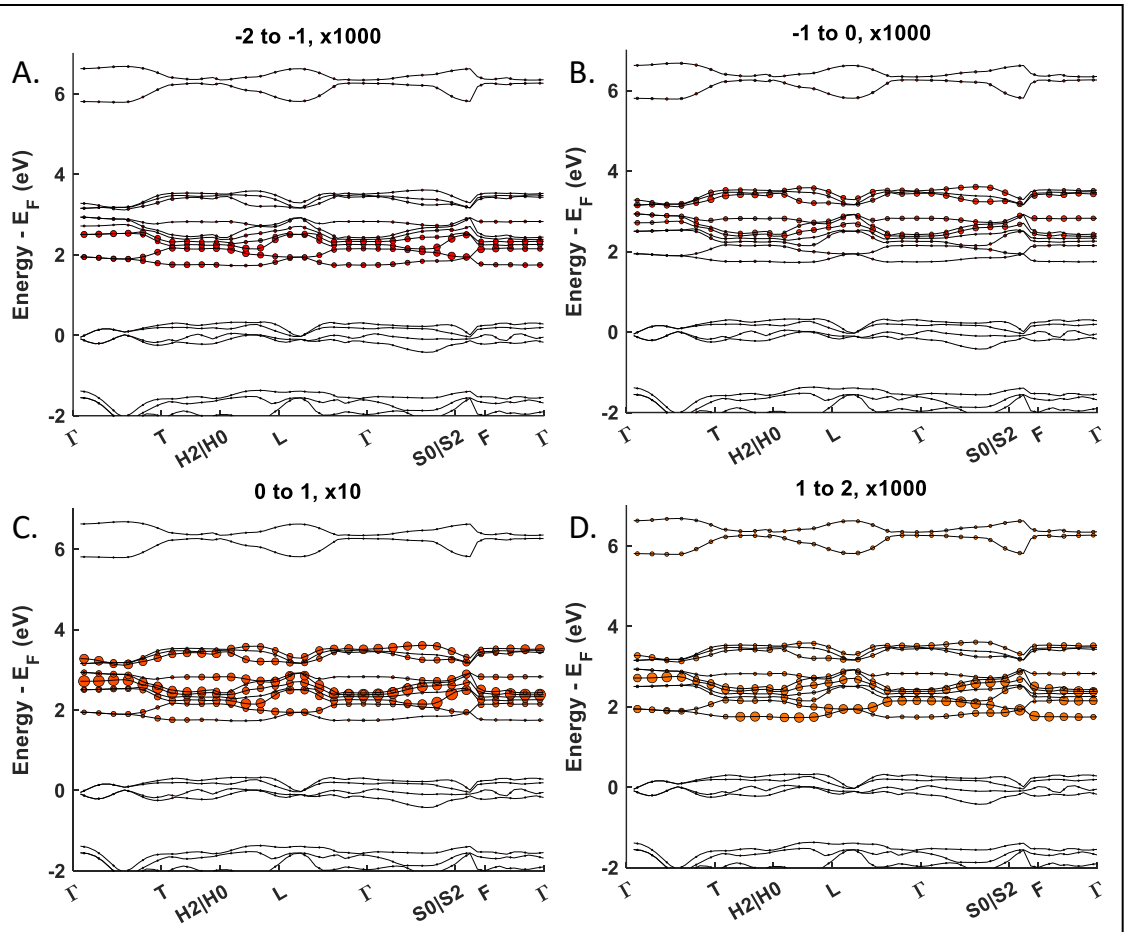

Figure B10. Energy-Resolved Exciton Densities Overlaid on the α-Fe_2O_3 Band Structure. Energy ranges between (a) -2 to -1 eV, (b) -1 to 0 eV, (c) 0 to 1 eV and (d) 1 to 2 eV below the Fermi energy are shown. The necessary amplitude magnification is shown in the title of each band structure, demonstrating the relative strength of the exciton components in different energy ranges.

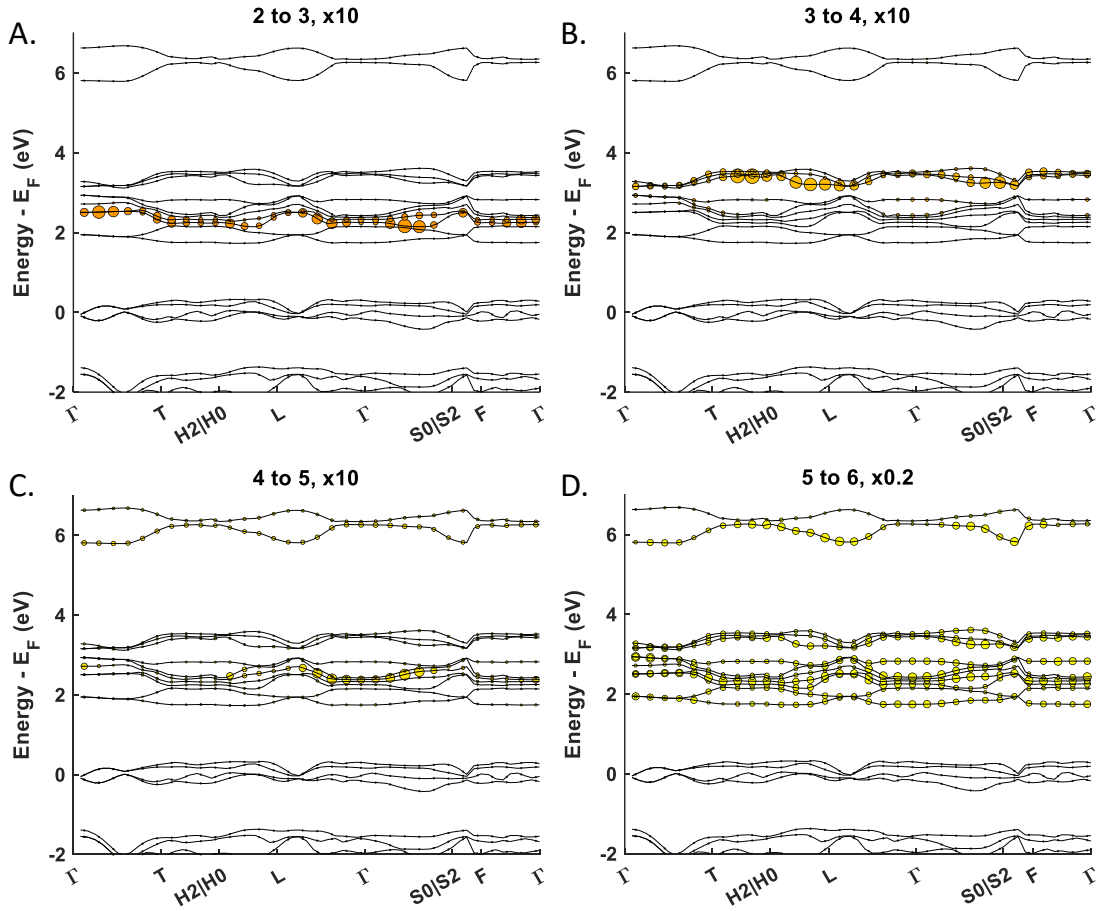

Figure B11. Energy-Resolved Exciton Densities Overlaid on the α-Fe_2O_3 Band Structure. Energy ranges between (a) 2 to 3 eV, (b) 3 to 4 eV, (c) 4 to 5 eV, and (d) 5 to 6 eV below the Fermi energy are shown. The necessary amplitude magnification is shown in the title of each band structure, demonstrating the relative strength of the exciton components in different energy ranges.

B4. Hamiltonian Decompositions

a. Comparisons between the total core-valence exciton density for the four states (ground, state-filling, polaron, and thermally expanded) modeled in this study.

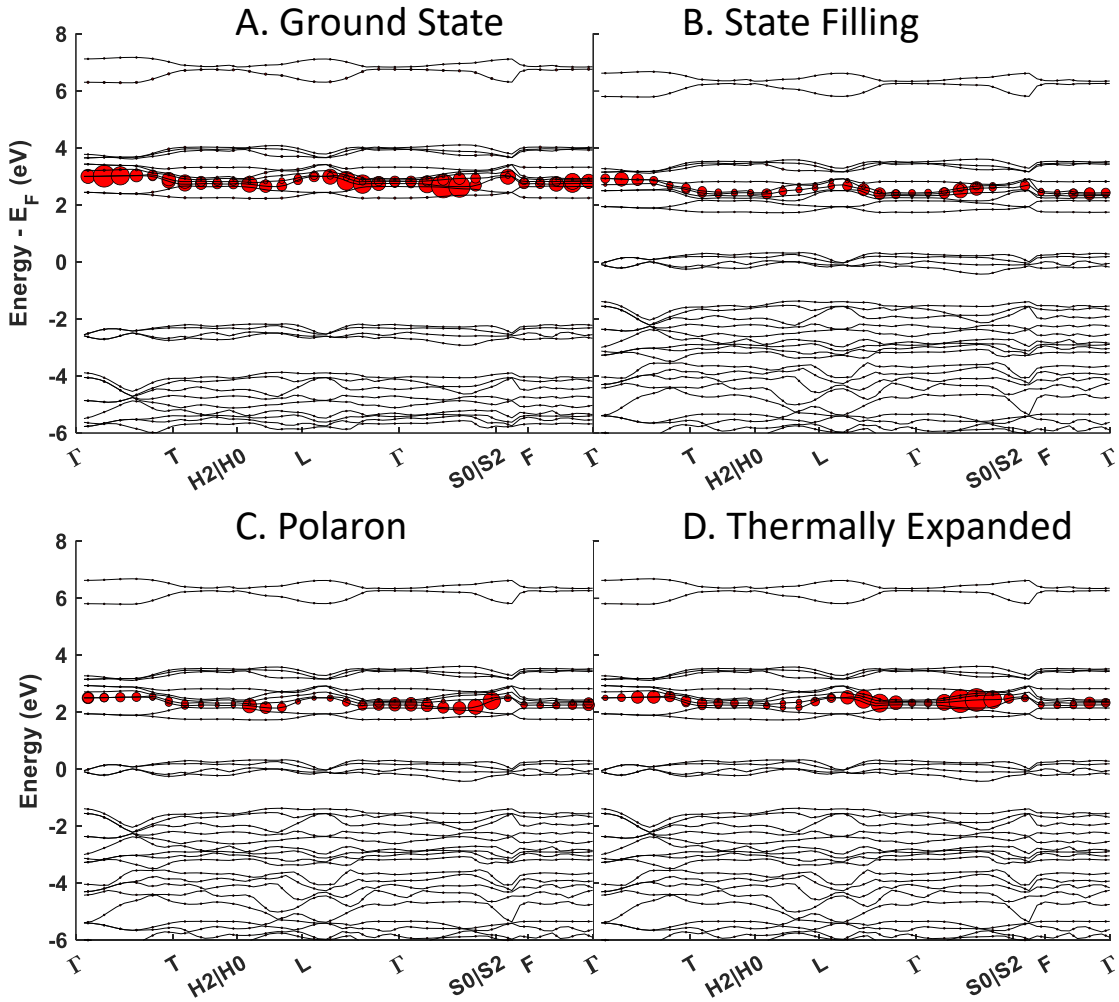

Figure B12. Total Core-Valence Exciton Densities. (a) Ground, (b) state filling, (c) polaron, and (d) thermally expanded states' total core-valence exciton densities overlaid on the band structure of α-Fe_2O_3.

b. Hamiltonian decomposition of the core-valence exciton for the ground state, state filling, polaron, and thermally expanded excited states. These decompositions are projected onto the band structure and are used to qualitatively compare trends between states, as well as quantify the differences between the excited states and the ground state Hamiltonian contributions. All contributions for one state are normalized relative to each other to facilitate direct comparison.

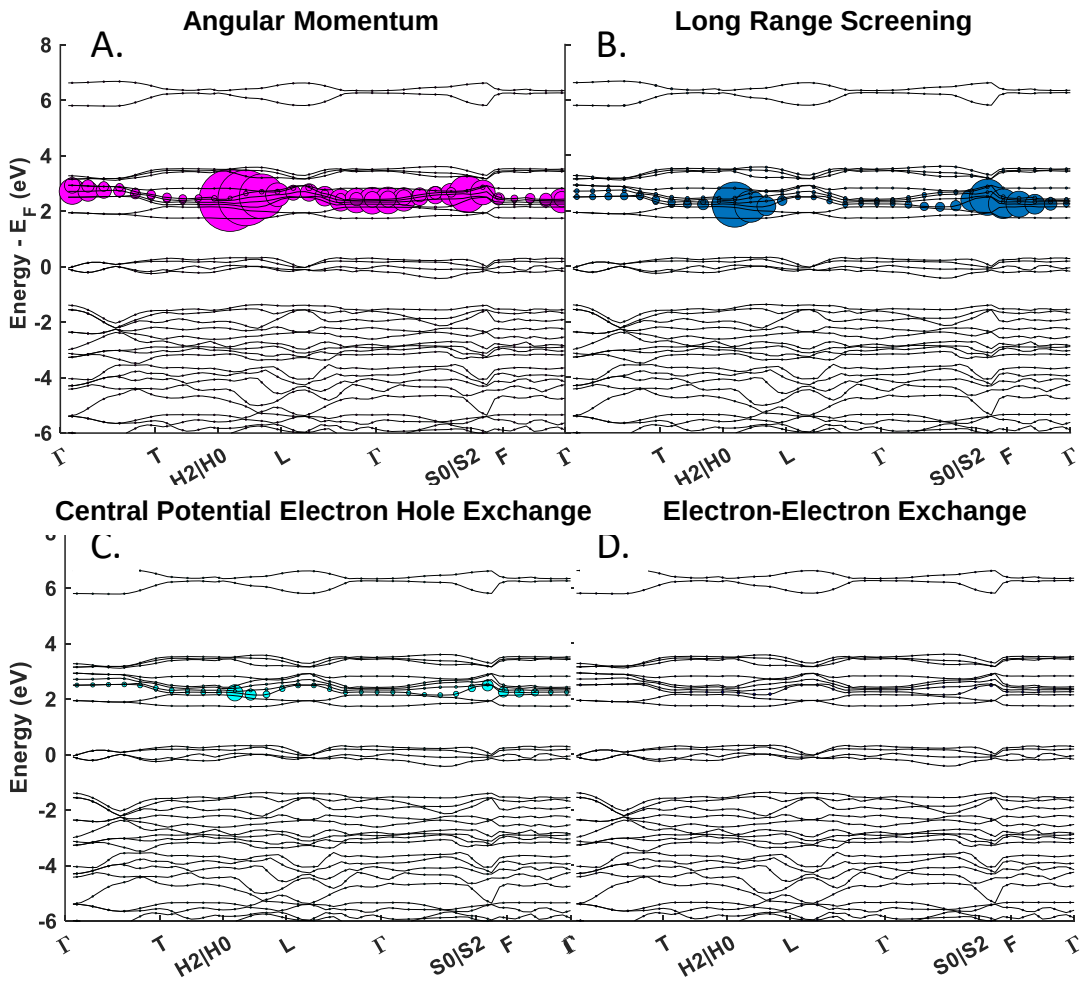

Figure B13. XUV transition Hamiltonian Decomposition of Core-Valence Exciton for the Ground State of α-Fe_2O_3. The (a) angular momentum, (b) core-hole screening, (c) electron-hole exchange, and (d) electron-electron exchange core-valence exciton densities are calculated and normalized to determine the relative contribution of each of these processes to the overall XUV exciton and thus absorption spectrum. The angular momentum, multiplet and screening contributions are included in the main text.

c. Comparisons of the differential between the total core-valence exciton density for the excited states of α-Fe_2O_3 and the ground state modeled in this study.

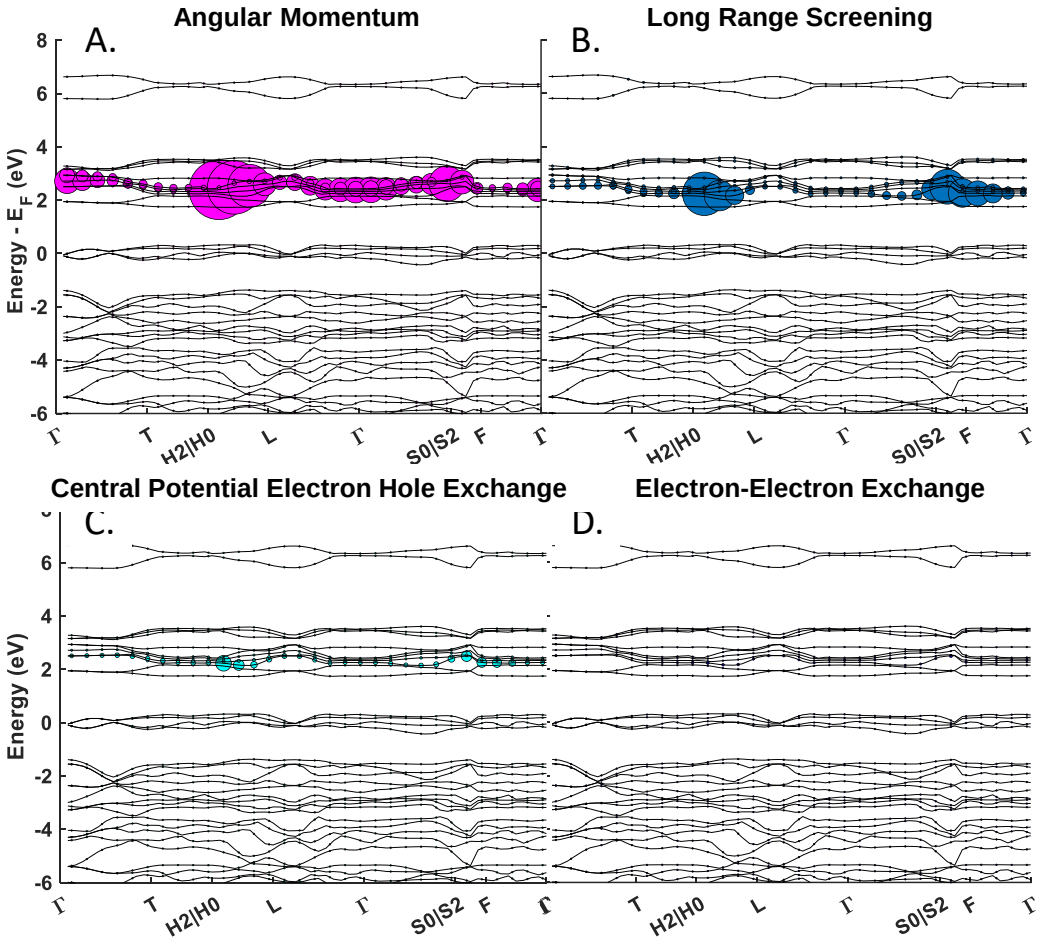

Figure B14. XUV transition Hamiltonian Decomposition of Core-Valence Exciton for the State-Filling Excited State of α-Fe_2O_3. The (a) angular momentum, (b) core-hole screening, (c) electron-hole exchange, and (d) electron-electron exchange core-valence exciton densities are calculated and normalized to determine the relative contribution of each of these processes to the overall XUV exciton and thus absorption spectrum.

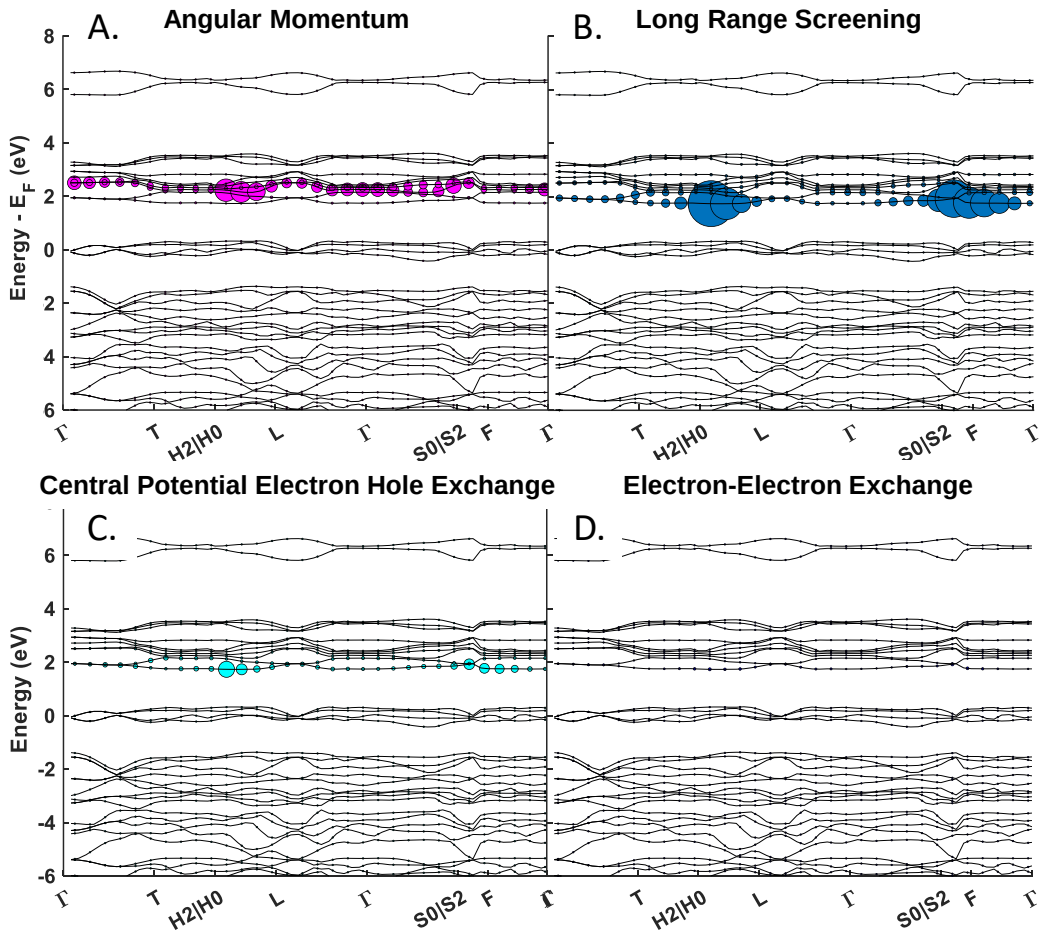

Figure B15. XUV transition Hamiltonian Decomposition of Core-Valence Exciton for the Polaron Excited State of α-Fe_2O_3. The (a) angular momentum, (b) core-hole screening, (c) electron-hole exchange, and (d) electron-electron exchange core-valence exciton densities are calculated and normalized to determine the relative contribution of each of these processes to the overall XUV exciton and thus absorption spectrum.

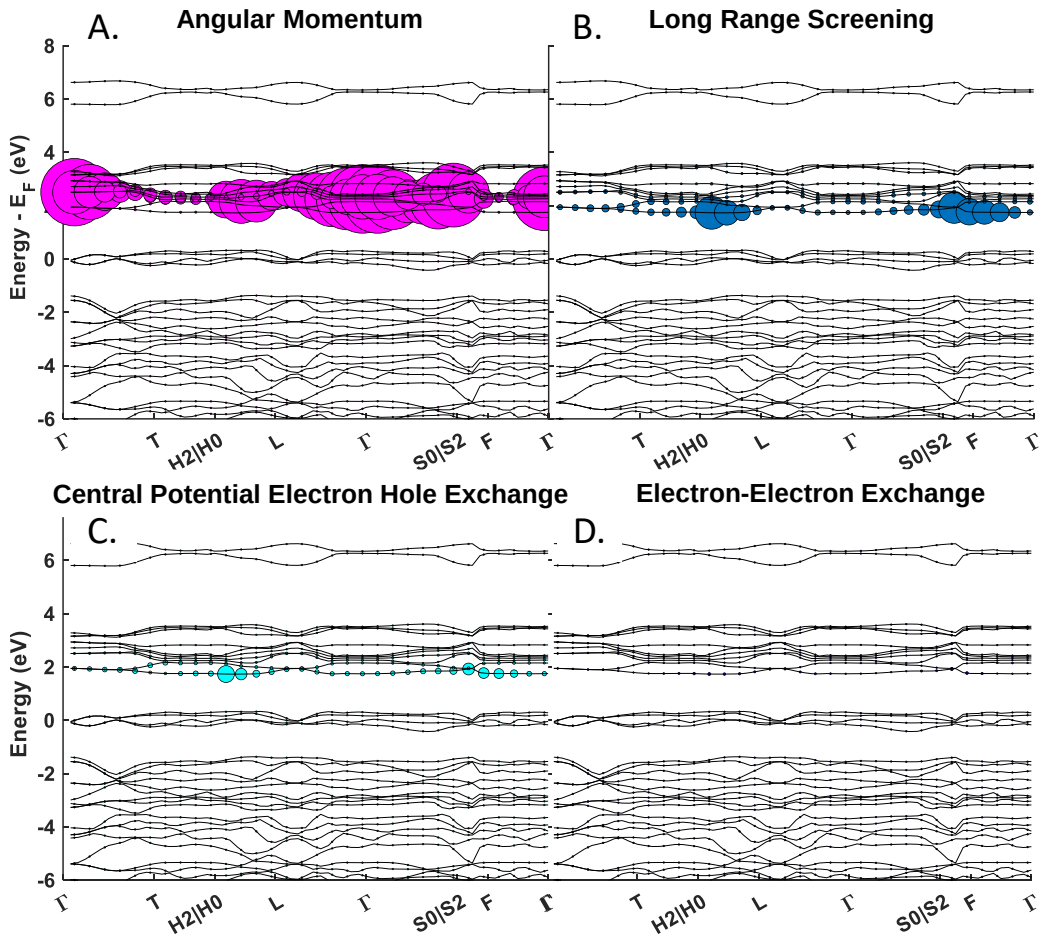

Figure B16. XUV transition Hamiltonian Decomposition of Core-Valence Exciton for the Thermally Expanded Excited State of α-Fe_2O_3. The (a) angular momentum, (b) core-hole screening, (c) electron-hole exchange, and (d) electron-electron exchange core-valence exciton densities are calculated and normalized to determine the relative contribution of each of these processes to the overall XUV exciton and thus absorption spectrum.

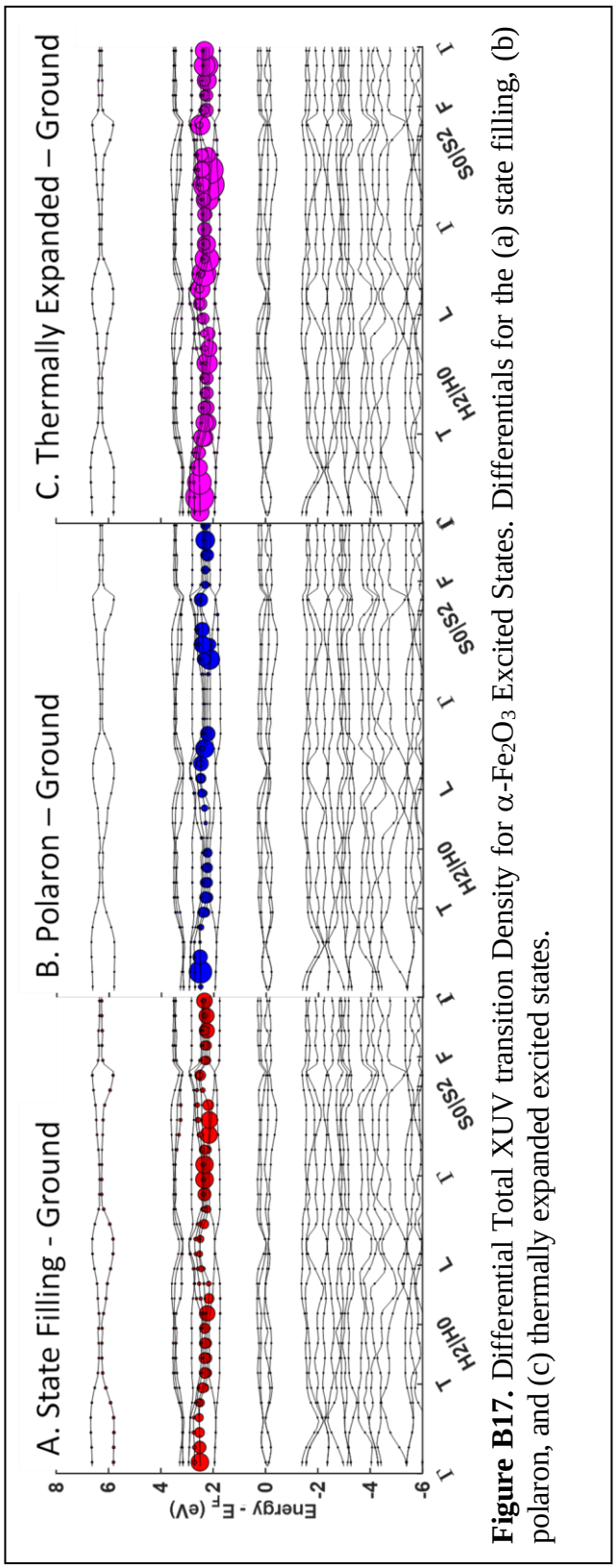

Figure B17. Differential Total XUV transition Density for α-Fe_2O_3 Excited States. Differentials for the (a) state filling, (b) polaron, and (c) thermally expanded excited states.

d. Differential Hamiltonian decompositions for the state filling, polaron, and thermally expanded excited states relative to the ground state are used to quantitatively determine the importance of different components in the transient changes observed experimentally. All contributions are normalized relative to each other to facilitate direct, quantitative comparison.

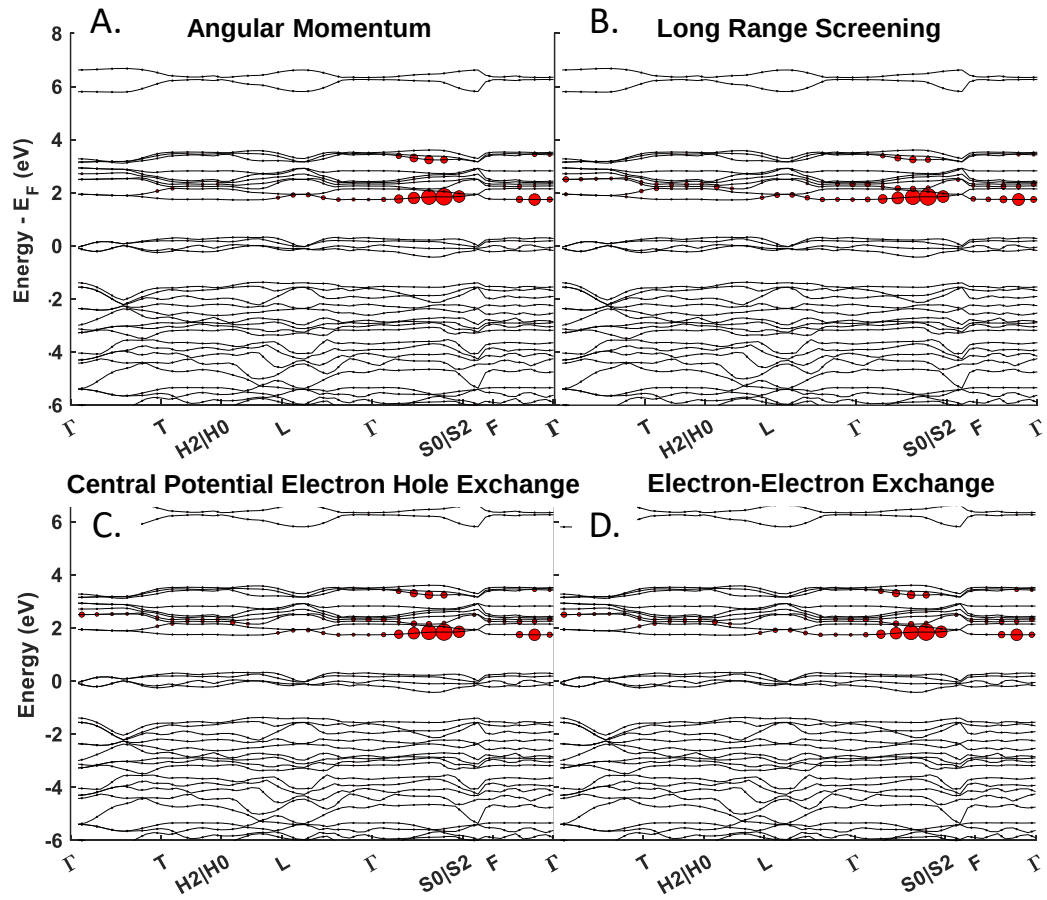

Figure B18. Differential XUV transition Hamiltonian Decomposition of Core-Valence Exciton for the State-Filling Excited State of α-Fe_2O_3. The magnitude of the state-filling minus the ground state components the (a) angular momentum, (b) core-hole screening, (c) electron-hole exchange, and (d) electron-electron exchange core-valence exciton densities are calculated and normalized to determine the relative contribution of each of these processes to excited state effects.

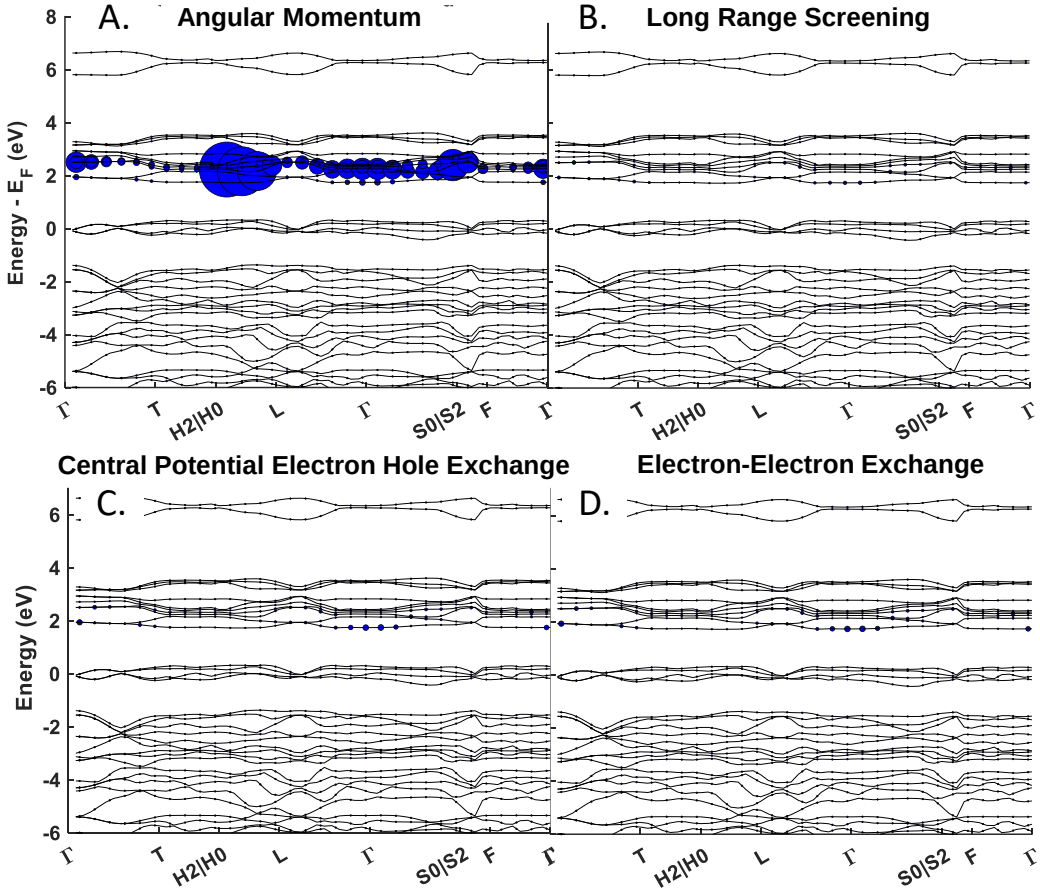

Figure B19. Differential XUV transition Hamiltonian Decomposition of Core-Valence Exciton for the Polaron Excited State of α-Fe_2O_3. The magnitude of the polaron minus the ground state for the components of the (a) angular momentum, (b) core-hole screening, (c) electron-hole exchange, and (d) electron-electron exchange core-valence exciton densities are calculated and normalized to determine the relative contribution of each of these processes to excited state effects.

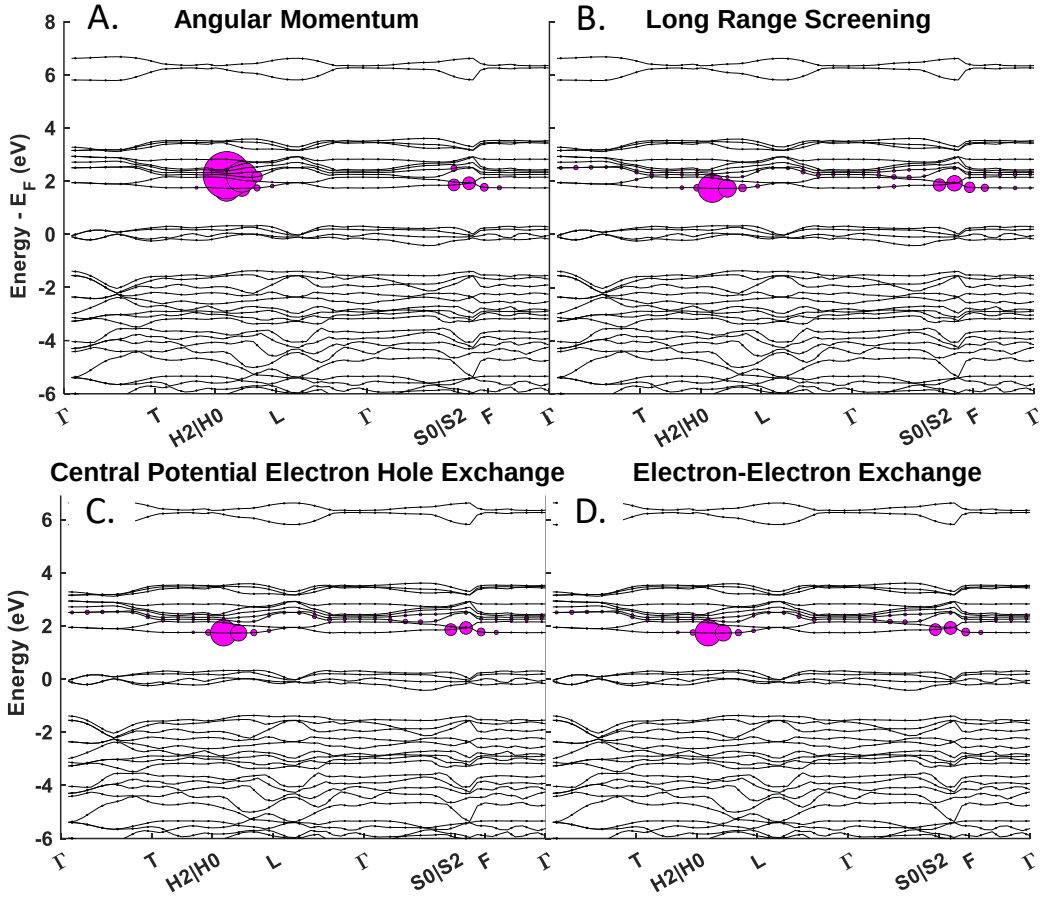

Figure B20. Differential XUV transition Hamiltonian Decomposition of Core-Valence Exciton for the Thermally Expanded Excited State of α-Fe_2O_3. The magnitude of the thermally expanded minus the ground state for the components of the (a) angular momentum, (b) core-hole screening, (c) electron-hole exchange, and (d) electron-electron exchange core-valence exciton densities are calculated and normalized to determine the relative contribution of each of these processes to excited state effects.

B5. Excited State Spectra

a. Excited state spectra were calculated as described in detail in the text, using the same computational parameters as the ground state calculation. Excited state broadening was performed consistent with previously described ground state broadening in SI section 3b.

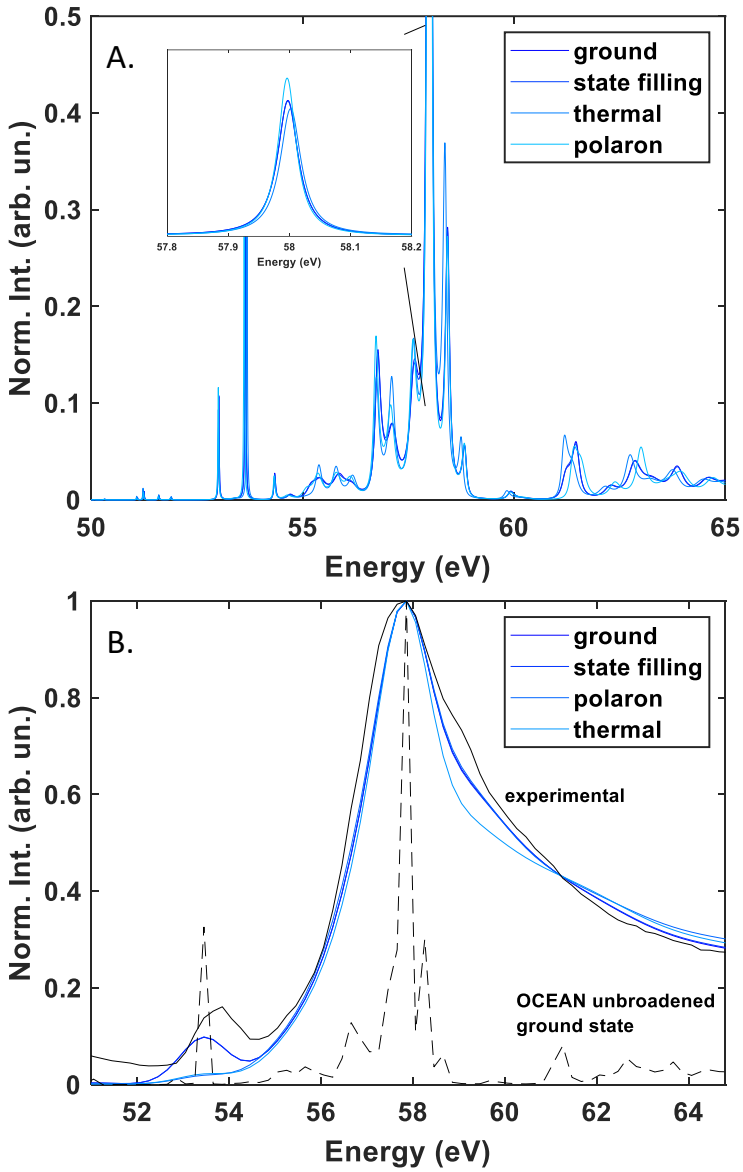

Figure B21. Calculated Spectra for Ground, State Filling, Polaron, and Thermally Expanded States of α-Fe_2O_3. (a) Unbroadened OCEAN output XUV absorption spectra for these states. Inset zooms in on the main peak showing how it shifts in energy. (b) Broadened OCEAN outputs compared to the experimental ground state.

b. A simple exponential broadening scheme to model the differential curve between the excited state and the ground state spectra was shown to produce relatively good agreement between the calculated and experimental data. In the exponential broadening model, the calculated XUV absorption spectra for the ground state and state filling (or polaron) are subtracted (without any initial broadening), and the difference is broadened with an exponential. While this scheme clearly over broadens the differential, it also clearly reproduces the signatures of these two states.

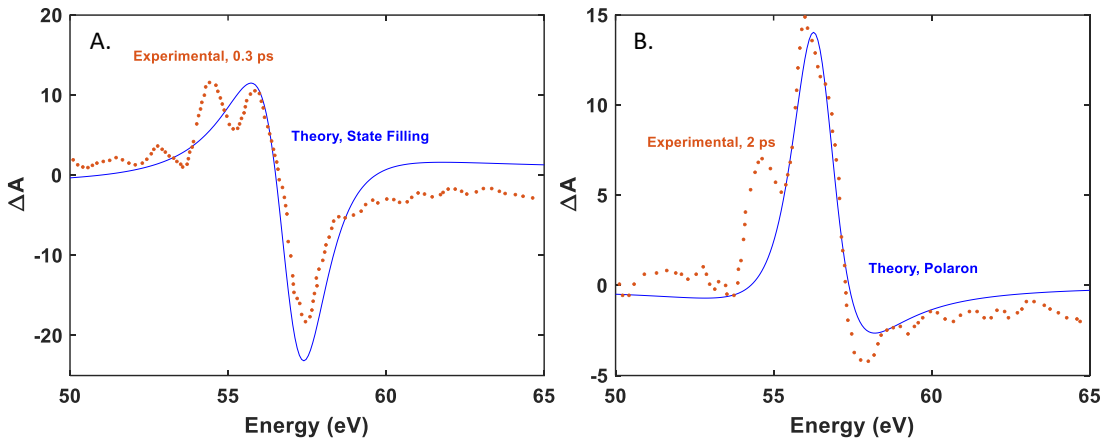

Figure B22. Calculated Differential Spectra for Excited States of α-Fe_2O_3. (a) Comparison between experimental differential after 0.3 ps and state filling differential for exponential broadening. (b) Comparison between experimental differential after 2 ps and polaron differential for exponential broadening.

c. Broadened differential traces, compared without normalization to demonstrate the relative intensities of the different differential signals.

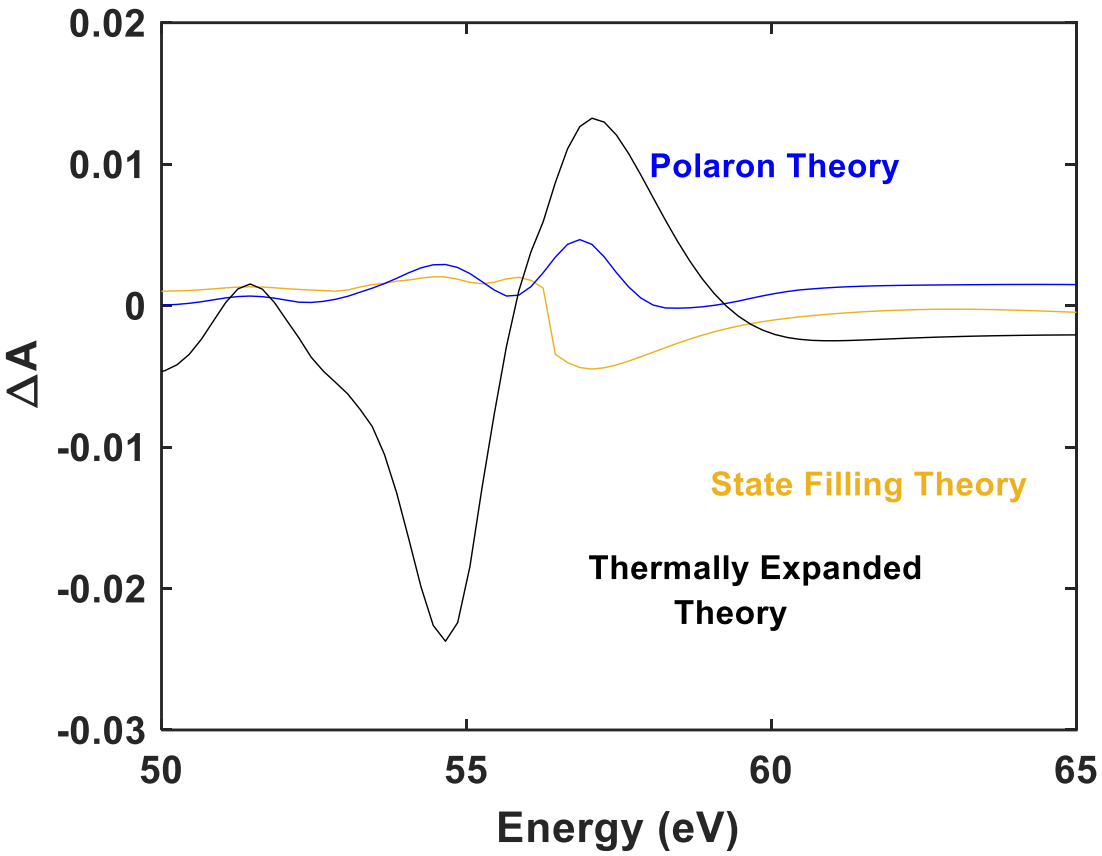

Figure B23. Differential Signals for state filling, polaron, and thermally expanded models of the excited states of α–Fe_2O_3 without normalization.

d. Comparison between calculated polaron states with and without additional state filling shows the relative dominance of the polaron in determining transient signals.

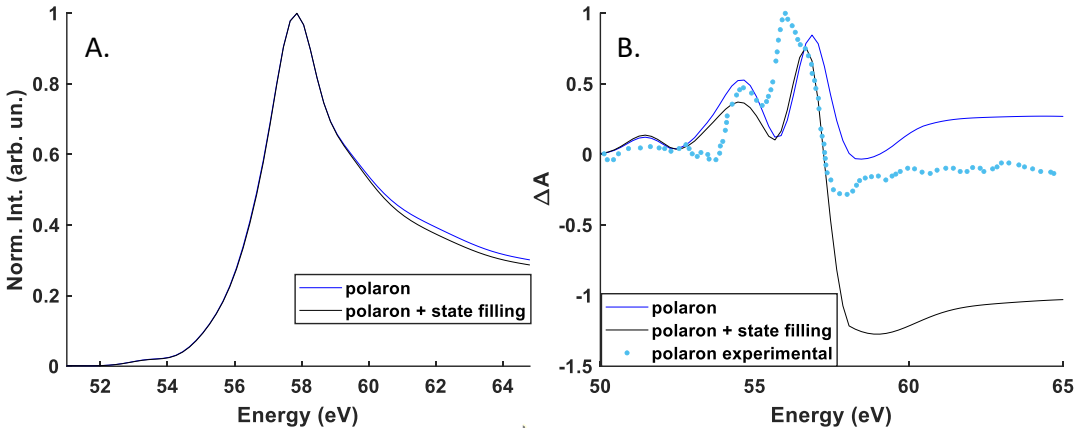

Figure B24. Polaron States of α-Fe_2O_3 with and without State Filling. (a) Initial calculated absorption with energy-dependent Gaussian broadening and (b) differential with additional energy-dependent amplitude corrections. The differential plot includes the experimentally measured polaron state differential spectrum.

e. Different configurations were used to model the state filling excited state, using excitation from 0 eV to 1.8 eV above the conduction band minimum. The electron and hole occupations resulting from excitation with different energies were used in the OCEAN calculation to generate model state filling XUV absorption spectra.

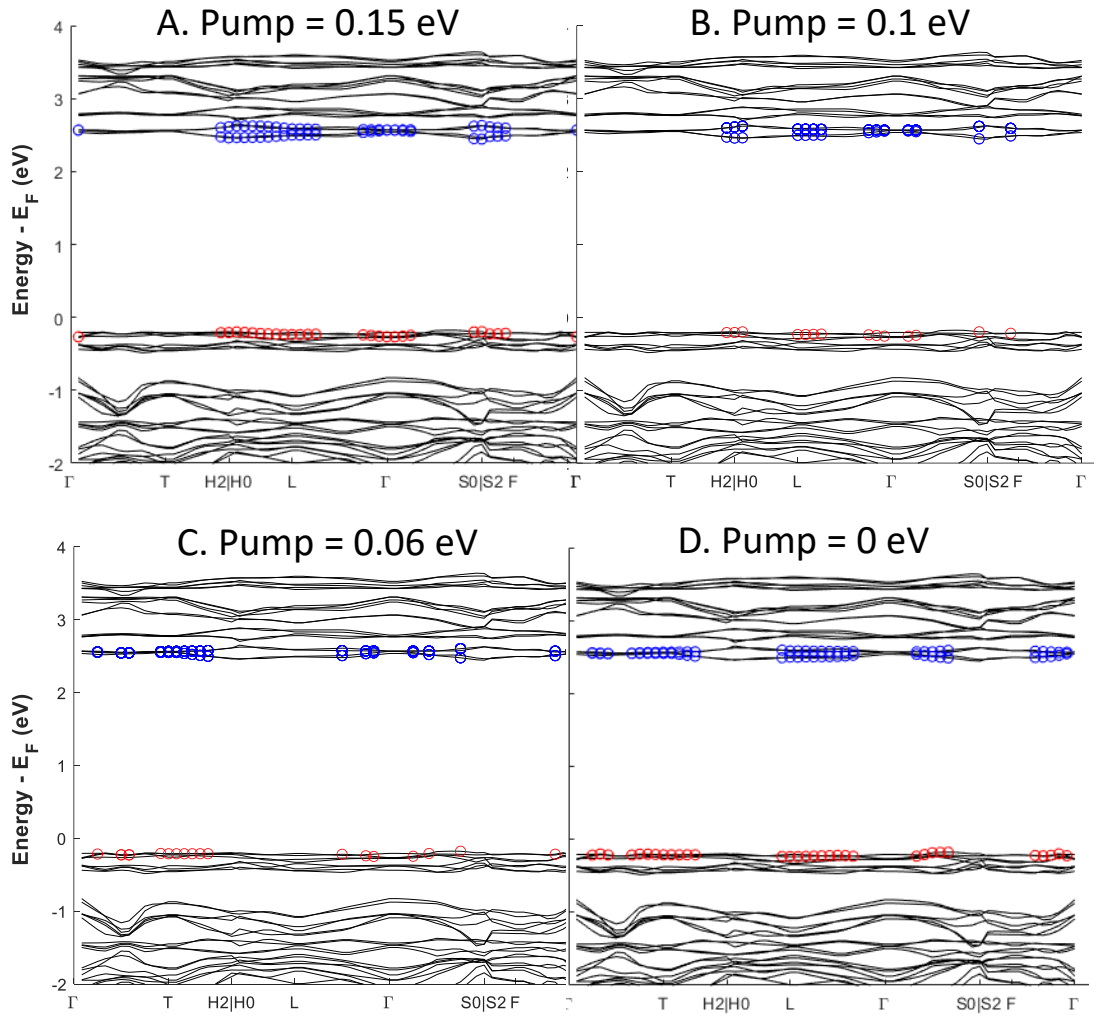

Figure B25. Band Filling for Different Pump Energies Used to Model State Filling. Pump energies from (a) 0.15 eV, (b) 0.1 eV, (c) 0.06 eV, and (d) 0 eV above the conduction band minimum were used to model state filling, as shown in Figure 4.4. Blue circles indicate electron occupation and red circles indicate holes.

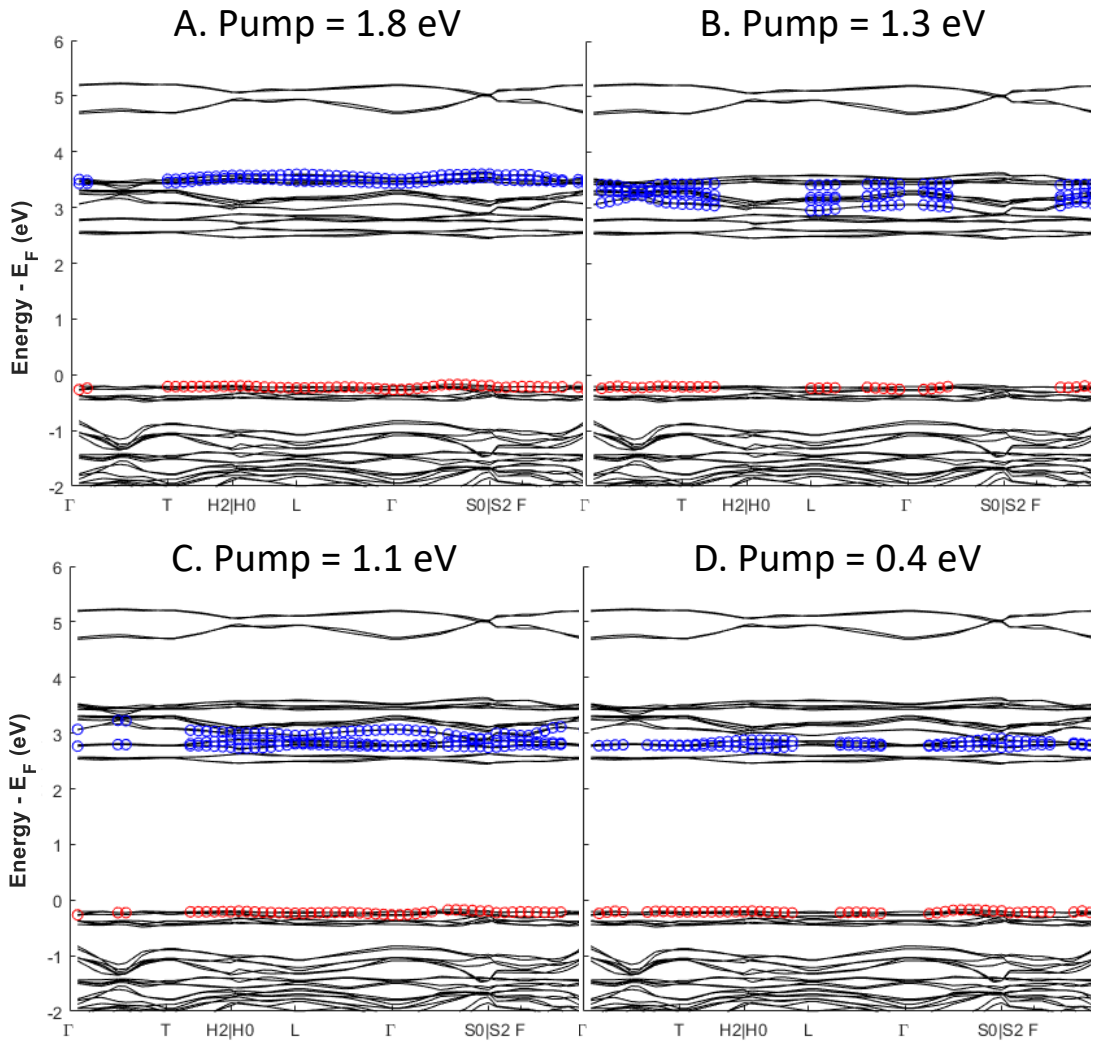

Figure B26. Band Filling for Different Pump Energies Used to Model State Filling. Pump energies from (a) 1.8 eV, (b) 1.3 eV, (c) 1.1 eV, and (d) 0.4 eV above the conduction band minimum were used to model state filling, as shown in Figure B27. Blue circles indicate electron occupation and red circles indicate holes.

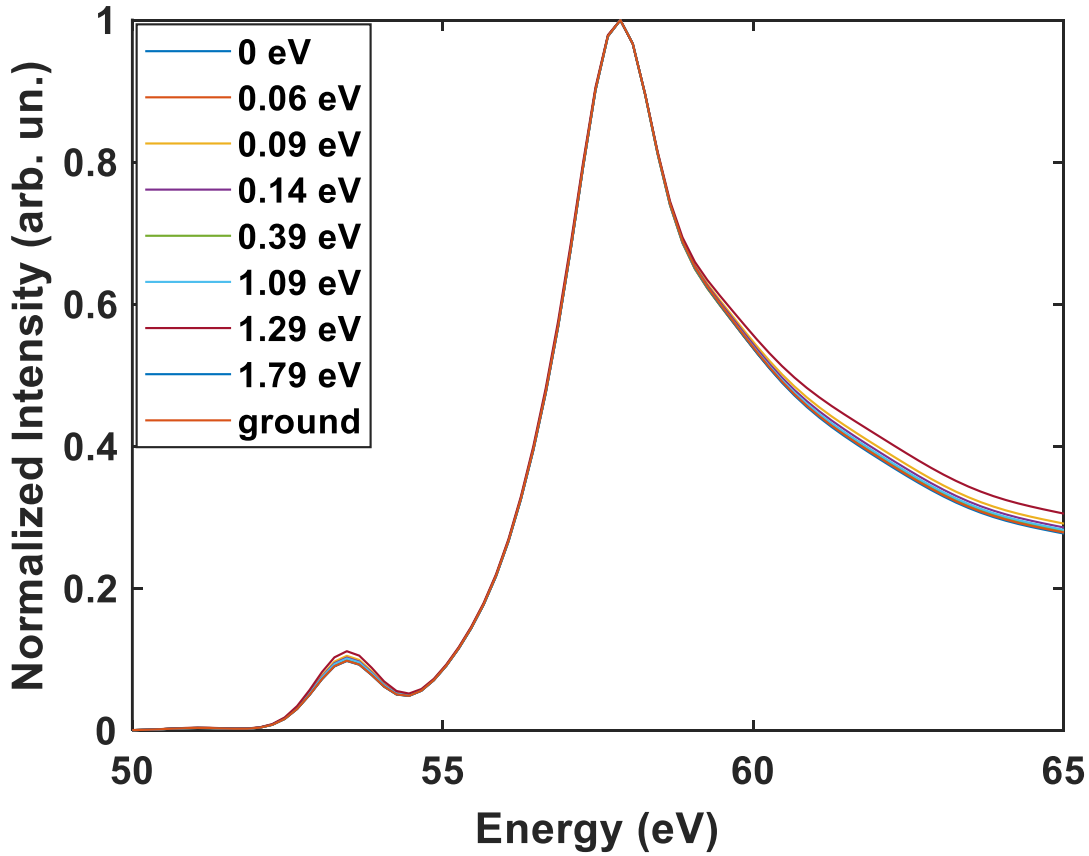

Figure B27. Excitation Energy Dependent XUV Absorption Calculations. Spectra at the Fe $M_{2,3}$ edge of α-Fe_2O_3 following state filling with different excitation energies. Energy above the conduction band minimum for each trace is shown in eV in the legend.

APPENDIX C: SUPPLEMENTARY INFORMATION FOR *AB INITIO* CALCULATIONS OF XUV GROUND AND EXCITED STATES FOR FIRST-ROW TRANSITION METAL OXIDES

C1. Computational Methods

a. Computational Input Parameters

Geometry optimization and DFT calculations were performed with the Quantum ESPRESSO package using Perdew-Burke-Ernzerhof (PBE) pseudopotentials under the generalized gradient approximation (GGA). The associated ground state wavefunctions were constructed using a plane wave basis set with components up to a kinetic energy cutoff of 250 Ry. Reciprocal space was sampled using an 4x4x4 Gamma-centered mesh with a 0.02 eV Gaussian smearing of orbital occupancies. DFT simulations were performed on unit cells of each of the transition metal oxides investigated in this study. Self-consistent calculations were performed to a convergence of 10^{-6} eV/atom and forces on ions under 10^{-3} eV/Å. DFT-BSE calculations were conducted using the same parameters. Additionally, an 8x8x8 k-point grid for the screening mesh, 100 bands, and a cutoff radius of 4.5 Bohr were used in the DFT-BSE calculations of the XUV absorption spectra.[123,340]

Table C1. Computational Parameters of Transition Metal Oxides

Transition Metal Oxide	Dielectric Constant	Hubbard U	Scissor Correction (eV)	Metal Oxidation	Metal Pseudopotential
TiO_2	6			+4	22-Ti.GGA
Cr_2O_3	11	3	-2	+3	24-Cr.GGA
MnO_2	10	4		+4	25-Mn.GGA
Fe_2O_3	25	4	-3	+3	26-Fe.GGA
Co_3O_4	12.8		+2	+2/+3	27-Co.GGA
NiO	11.9			+2	28-Ni.GGA
CuO	6.46			+2	29-Cu.GGA
ZnO	10.4	13		+2	30-Zn.GGA

The 08-O.GGA pseudopotential was used for the oxygen in all of the metal oxide calculations.

b. Energy Dependent Broadening

```
lor = @(E,w,E0) (1/2*pi).*w./((E-E0).^2+(w/2).^2);
lor = @(E,w,E0) lor(E,w,E0)/trapz(E,lor(E,w,E0));
lin_broad_ocean = zeros(size(energy));

for i = 1:size(energy,2);
   lin_broad_ocean=lor(energy,w,energy(i)).*ocean_intp(i);
   lin_broad_ocean= lin_broad_ocean + lin_broad_ocean;
   ocean_broad_lin = lin_broad_ocean + ocean_intp;
End
```

Table C2. Lorentzian Peak Widths used for Transition Metal Oxide Broadening

Transition Metal Oxide	Lorentzian Width (w)
TiO_2	4
Cr_2O_3	2
MnO_2	2
Fe_2O_3	0.5
Co_3O_4	2.5
NiO	2
CuO	1
ZnO	2

While the broadening scheme above was used for all the transition metal oxides, an additional GW stretch was used to correct the energy scaling for TiO_2 and NiO.

C2. TiO_2

a. Structural Data for Calculations

i. Ground State and State Blocking

Unit Cell Parameters, (bohr)

{9.0989 9.0989 5.9151}

Primitive Vectors

{1.0 0.0 0.0

0.0 1.0 0.0

0.0 0.0 1.0}

Reduced coordinates, (x, y, z)

Ti 0.0000 0.0000 0.0000

Ti 0.5000 0.5000 0.5000

O 0.304809167 0.304809167 0.0000

O -0.304809167 -0.304809167 0.0000

O 0.804801130 0.195198870 0.5000

O 0.195198870 0.804801130 0.5000

ii. Thermally Expanded Lattice

Unit Cell Parameters, (bohr)

{9.1899 9.1899 5.9742}

Primitive Vectors

{1.0 0.0 0.0

0.0 1.0 0.0

0.0 0.0 1.0}

Reduced coordinates, (x, y, z)

Ti 0.0000 0.0000 0.0000

Ti 0.5000 0.5000 0.5000

O 0.304809167 0.304809167 0.0000

O -0.304809167 -0.304809167 0.0000

O 0.804801130 0.195198870 0.5000

O 0.195198870 0.804801130 0.5000

b. Ground State Calculations

i. Band Structure and DOS

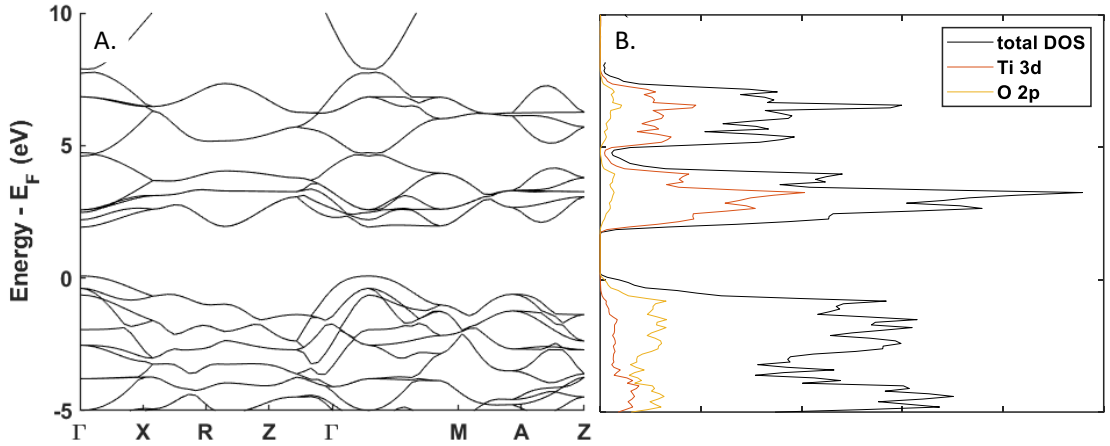

Figure C1. Ground State DFT Outputs for TiO_2. (a) Ground state band structure with the Fermi energy set to 0 eV. (b) Ground state total density of states in black and important orbital contributions around the Fermi energy are shown in color. No scissor shift has been included in these calculations.

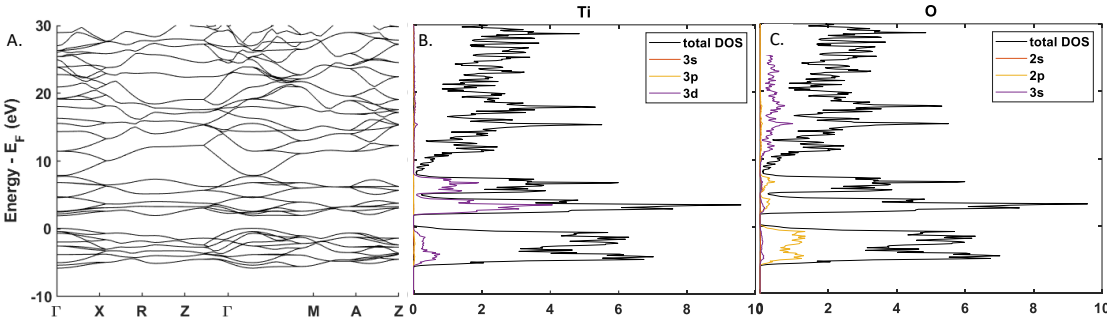

Figure C2. Ground State DFT Outputs for TiO_2. (a) Overall ground state band structure with the Fermi energy set to 0 eV. (b) Overall ground state total density of states in black and Ti partial DOS decomposed into 3s, 3p, and 3d orbital contributions. (c) Overall ground state total density of states in black and O partial DOS decomposed into 2s, 2p, and 3s orbital contributions No scissor shift has been included in these calculations.

ii. Ground State Spectrum[109]

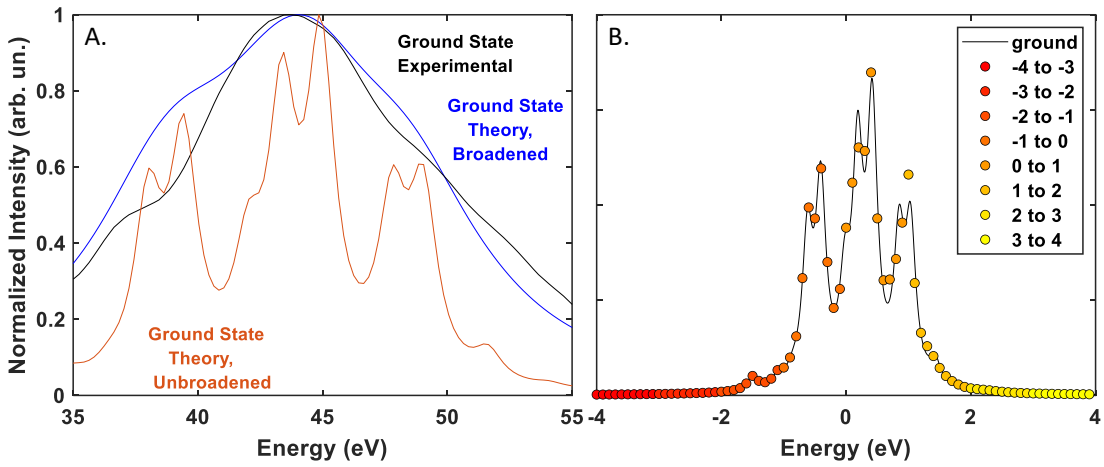

Figure C3. Ground State $M_{2,3}$ edge Absorption Spectrum. (a) The experimental (black), OCEAN calculated unbroadened (orange), and OCEAN calculated with energy-dependent broadening (blue) spectra are compared. A GW stretch was applied following the OCEAN calculation to correct the energy spacing of the observed peaks. (b) Energy-resolved exciton densities overlaid on the calculated XUV absorption spectrum around the Fermi level and the Ti $M_{2,3}$ edge. No GW stretch was applied here.

iii. Ground State GMRES Energy Decomposition

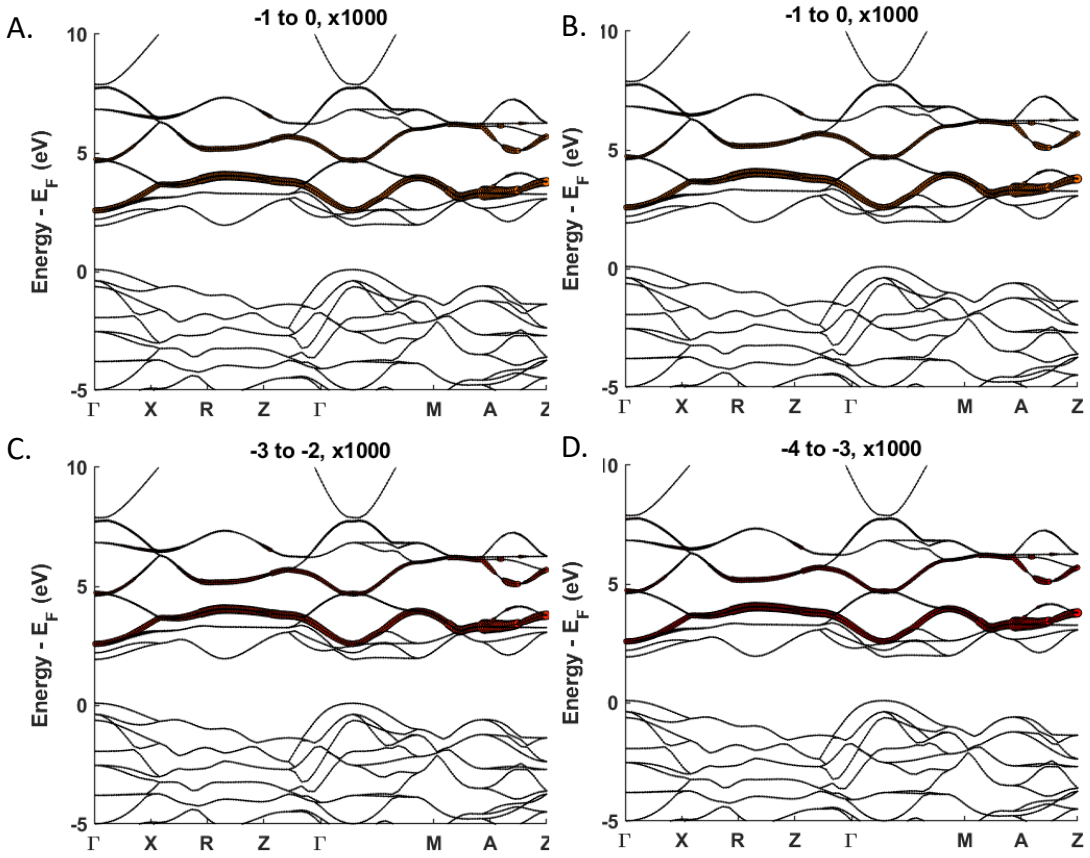

Figure C4. Energy-Resolved Exciton Densities Overlaid on the TiO_2 Band Structure. Energy ranges between (a) -1 to 0 eV, (b) -2 to -1 eV, (c) -2 to -3 eV and (d) -3 to -4 eV below the Fermi energy are shown. The necessary amplitude magnification is shown in the title of each band structure, demonstrating the relative strength of the exciton components in different energy ranges.

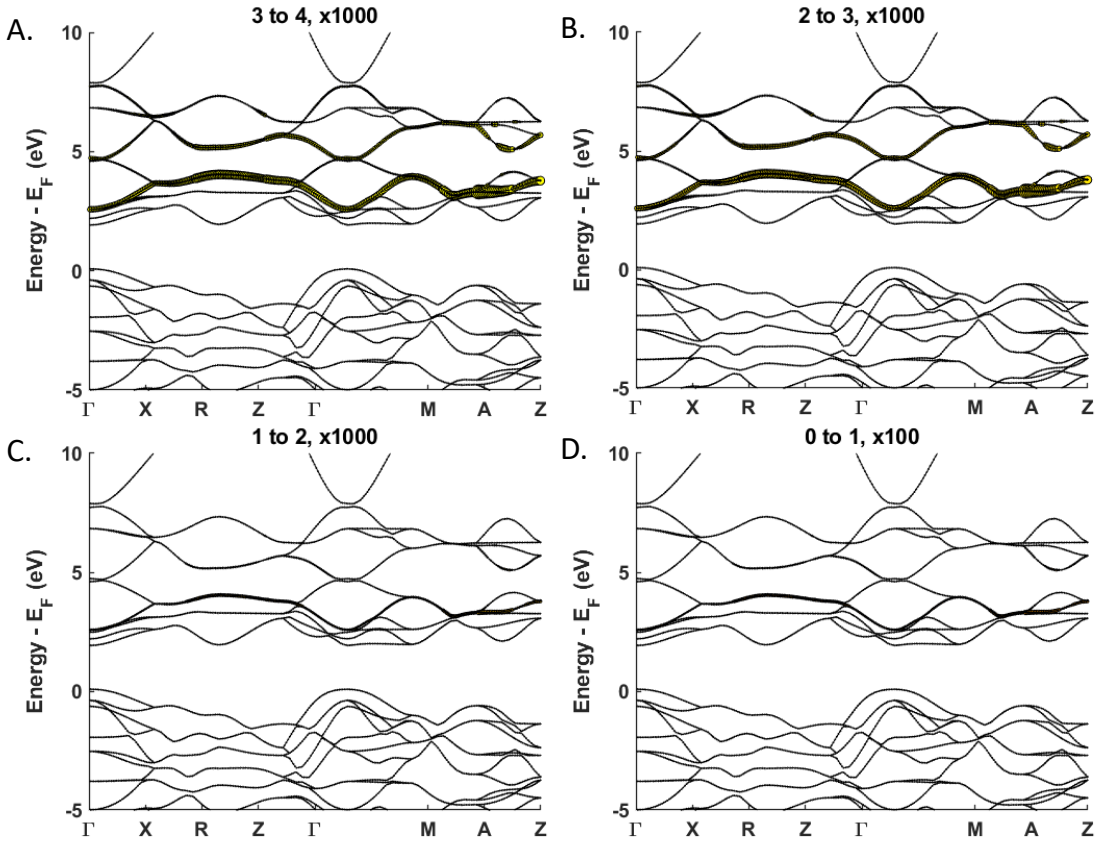

Figure C5. Energy-Resolved Exciton Densities Overlaid on the TiO_2 Band Structure. Energy ranges between (a) 3 to 4 eV, (b) 2 to 3 eV, (c) 1 to 2 eV and (d) 0 to 1 eV below the Fermi energy are shown. The necessary amplitude magnification is shown in the title of each band structure, demonstrating the relative strength of the exciton components in different energy ranges.

c. Excited State Calculations

i. State filling band diagrams and Full Spectra

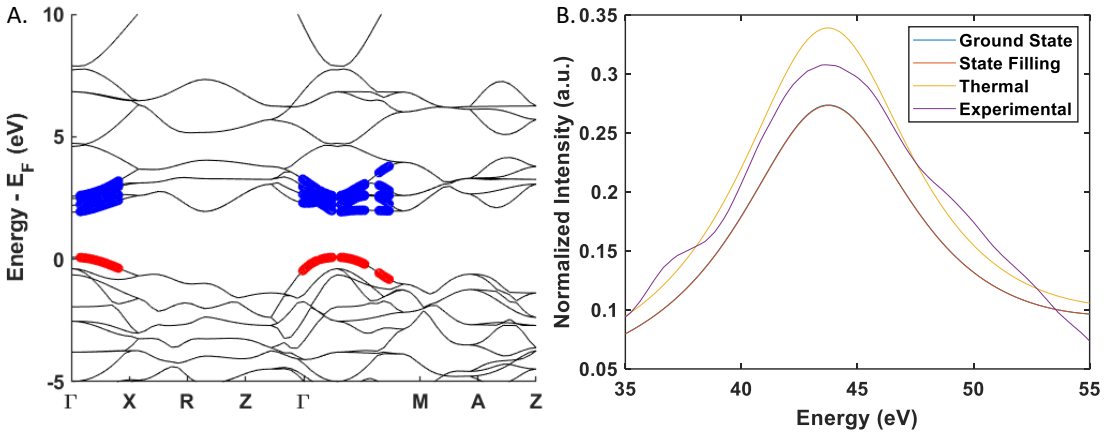

Figure C6. Excited State $M_{2,3}$ edge Absorption Spectrum. (a) State filling occupation used to model charge-transfer where the blue circles indicate electron occupation and red circles indicate holes overlaid on the band structure in black. (b) Broadened spectra for the ground state (blue), state filling (orange), thermal expansion (yellow) and experimental (purple).

d. Hamiltonian Decompositions

i. Total Exciton Comparisons

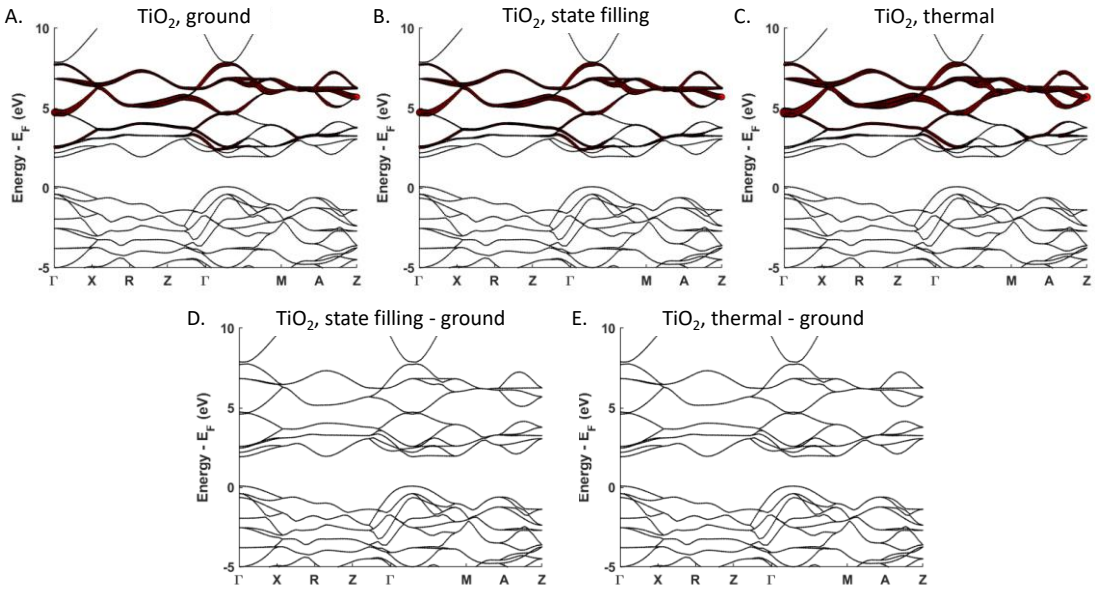

Figure C7. Total Core-Valence Exciton Densities. (a) Ground, (b) state filling, and (c) thermally expanded states' total core-valence exciton densities overlaid on the band structure of TiO_2. Differentials for the (d) state filling, and (e) thermally expanded excited states.

ii. Hamiltonian Decomposition of Exciton Components for ground, state filling, and thermally expanded models.

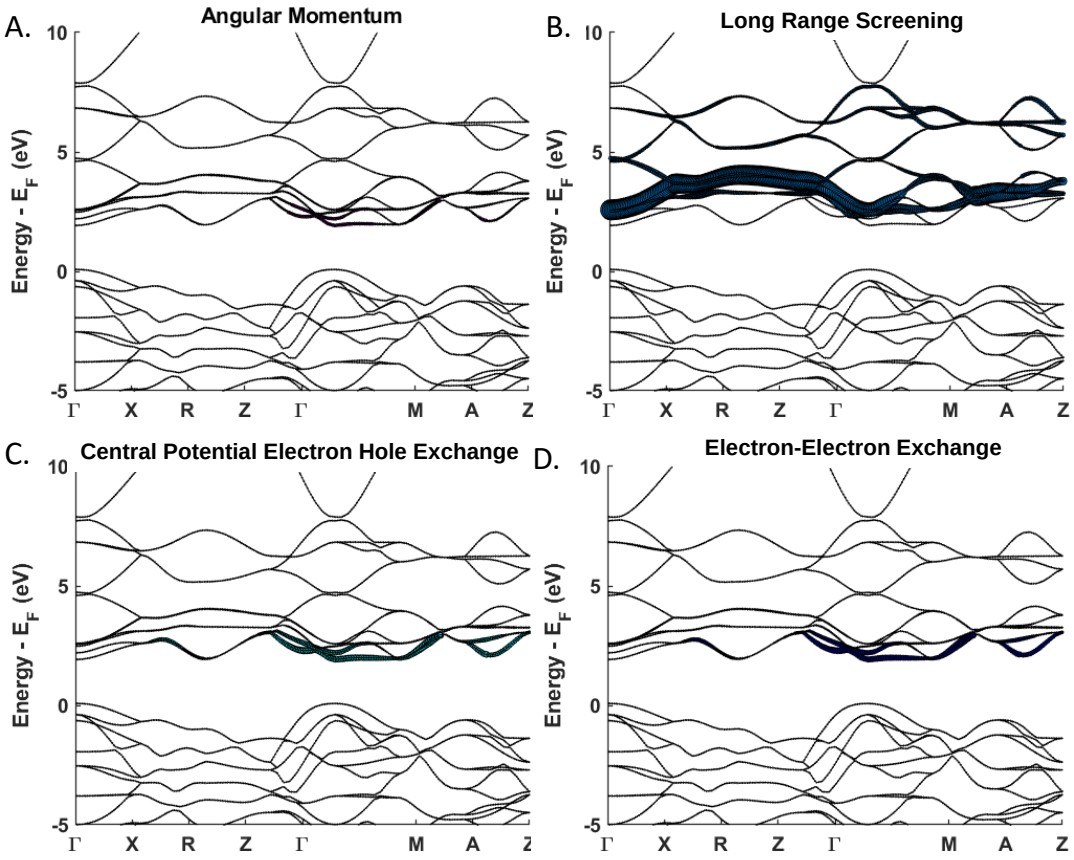

Figure C8. XUV transition Hamiltonian Decomposition of Core-Valence Exciton for the Ground State of TiO_2. The (a) angular momentum, (b) core-hole screening, (c) electron-hole exchange, and (d) electron-electron exchange core-valence exciton densities are calculated and normalized to determine the relative contribution of each of these processes to the overall XUV exciton and thus absorption spectrum.

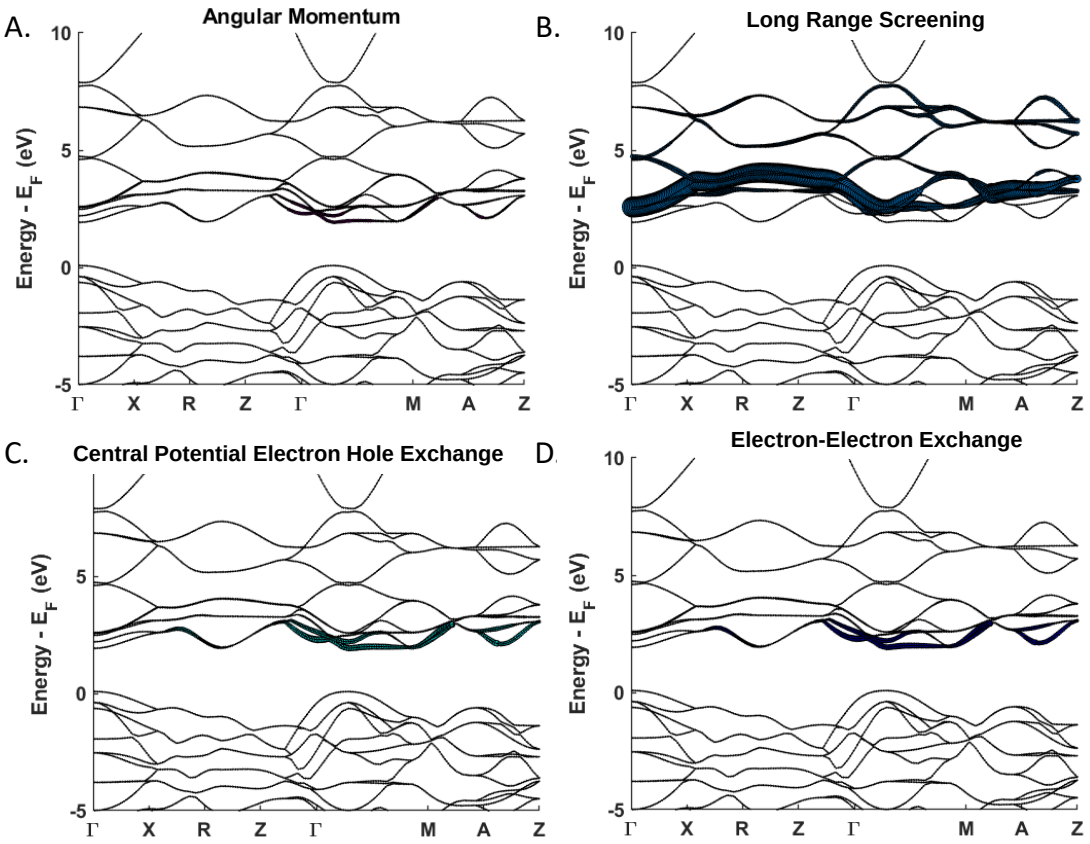

Figure C9. XUV transition Hamiltonian Decomposition of Core-Valence Exciton for the State Filling State of TiO_2. The (a) angular momentum, (b) core-hole screening, (c) electron-hole exchange, and (d) electron-electron exchange core-valence exciton densities are calculated and normalized to determine the relative contribution of each of these processes to the overall XUV exciton and thus absorption spectrum.

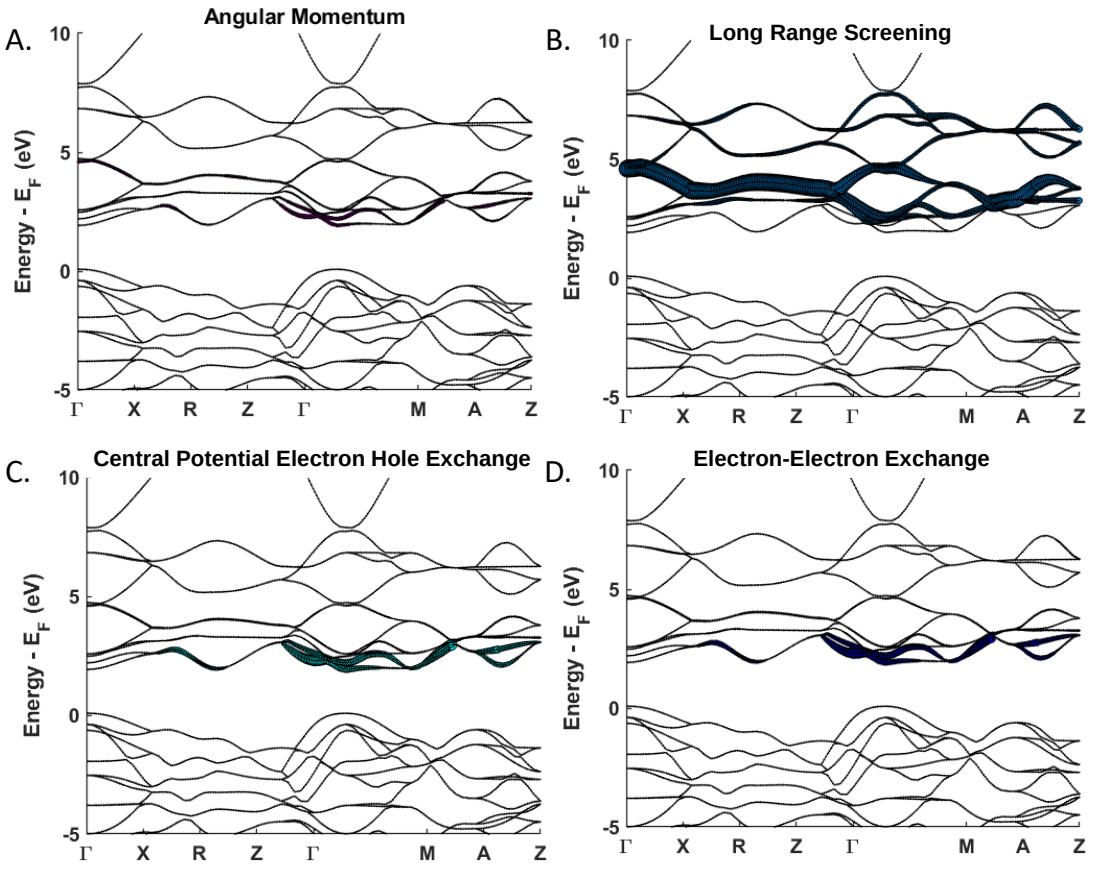

Figure C10. XUV transition Hamiltonian Decomposition of Core-Valence Exciton for the Thermally Expanded State of TiO_2. The (a) angular momentum, (b) core-hole screening, (c) electron-hole exchange, and (d) electron-electron exchange core-valence exciton densities are calculated and normalized to determine the relative contribution of each of these processes to the overall XUV exciton and thus absorption spectrum.

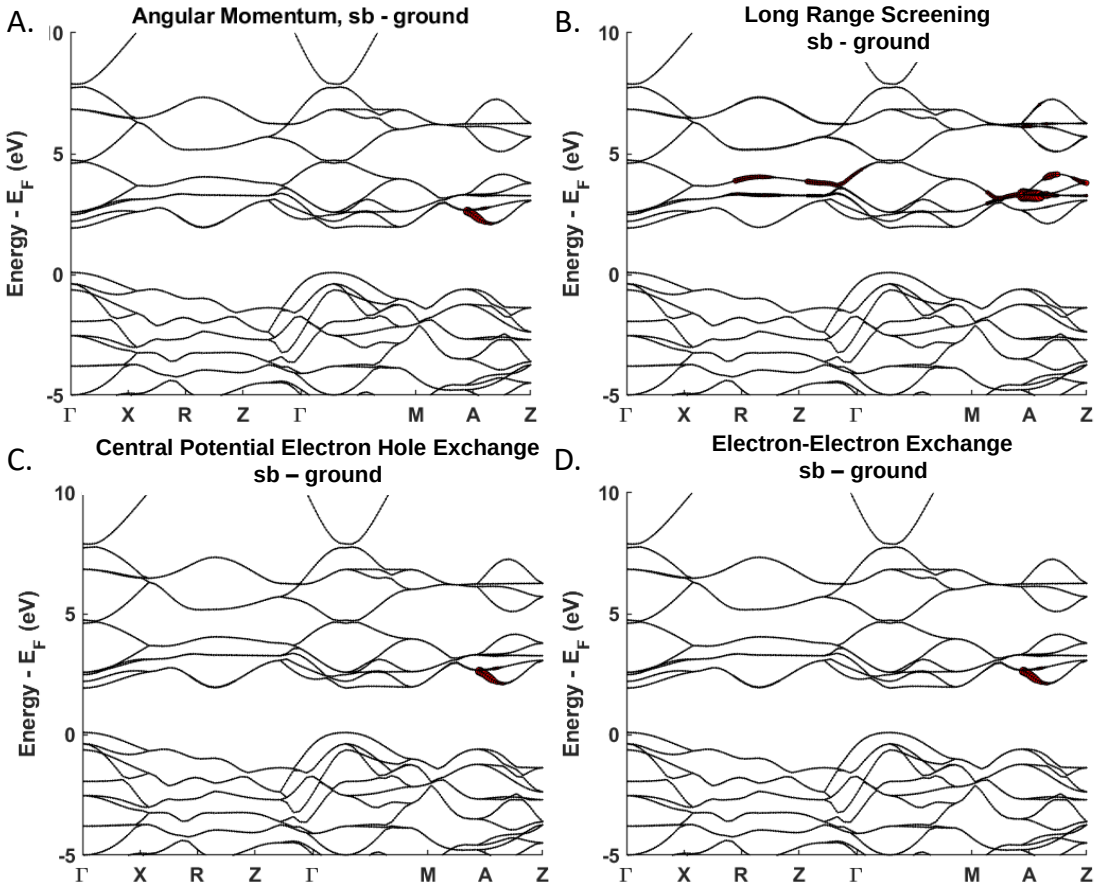

Figure C11. Differential XUV transition Hamiltonian Decomposition of Core-Valence Exciton for the State-Filling Excited State of TiO_2. The magnitude of the state-filling minus the ground state components the (a) angular momentum, (b) core-hole screening, (c) electron-hole exchange, and (d) electron-electron exchange core-valence exciton densities are calculated and normalized to determine the relative contribution of each of these processes to excited state effects.

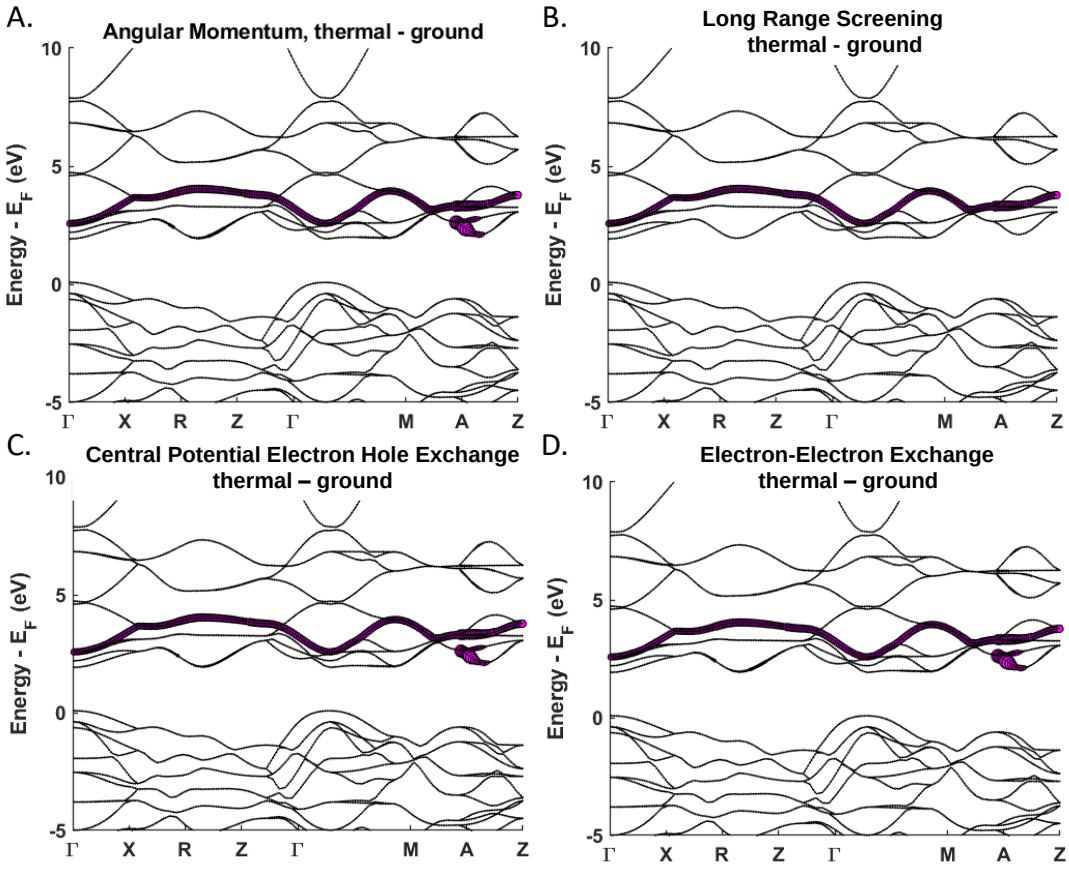

Figure C12. Differential XUV transition Hamiltonian Decomposition of Core-Valence Exciton for the Thermally Expanded Excited State of TiO_2. The magnitude of the state-filling minus the ground state components for the (a) angular momentum, (b) core-hole screening, (c) electron-hole exchange, and (d) electron-electron exchange core-valence exciton densities are calculated and normalized to determine the relative contribution of each of these processes to excited state effects.

C3. Cr_2O_3

As the only available experimental spectrum of Cr_2O_3 was a reflectivity spectrum, the following Matlab code was used to calculate the reflectivity spectrum of Cr_2O_3 from the OCEAN calculated absorption spectrum.

```
Cr2O3_exp = importdata('Cr2O3.csv');
files = dir('absspct_Cr_ground.0001_3p_01');
num_cf = size(files,1);
eps1 = 0;
eps2 = 0;
for i = 1:size(files,1)
   [E,eps1i,eps2i] = import_ocean_epsilon(files(i).name);
   eps1 = eps1 + eps1i;
   eps2 = eps2 + eps2i;
end
eps1 = eps1./num_cf;
eps2 = eps2./num_cf;
figure(1);
plot(E,eps1);
hold on;
%plot(energy,eps2);
title('absorption');
theta = 8*pi/180;
eps_sb = eps2 + eps1.*1i;
n_sb = sqrt(eps_sb);
R_sb = abs( (sqrt(1-(1./n_sb.*sin(theta)).^2)-n_sb.*cos(theta))./(sqrt(1-
(1./n_sb.*sin(theta)).^2)+n_sb.*cos(theta)) ).^2;
figure(2);
plot(E,R_sb);
hold on;
title('reflection');
```

a. Structural Data for Calculations

i. Ground State and State Blocking

Unit Cell Parameters (bohr)

{9.48 9.48 26.72}

Primitive Vectors

{0.5 -0.2887 0.333

0 0.5773 0.333

-0.5 -0.2887 0.333}

Reduced coordinates, (x, y, z)

Cr1 0.344311154 0.344311154 0.344311154

Cr1 0.844318706 0.844318706 0.844318706

Cr2 0.155681294 0.155681294 0.155681294

Cr2 0.655688846 0.655688846 0.655688846

O 0.936543866 0.563452102 0.249999406

O 0.563452102 0.249999406 0.936543866

O 0.249999406 0.936543866 0.563452102

O 0.063456134 0.436547898 0.750000594

O 0.436547898 0.750000594 0.063456134

O 0.750000594 0.063456134 0.436547898

ii. Thermally Expanded Lattice

Unit Cell Parameters (bohr)

{9.54 9.52 26.89}

Primitive Vectors

{0.5 -0.2887 0.333

0 0.5773 0.333

-0.5 -0.2887 0.333}

Reduced coordinates, (x, y, z)

Cr1 0.344311154 0.344311154 0.344311154

Cr1 0.844318706 0.844318706 0.844318706

Cr2 0.155681294 0.155681294 0.155681294

Cr2 0.655688846 0.655688846 0.655688846

O 0.936543866 0.563452102 0.249999406

O 0.563452102 0.249999406 0.936543866

O 0.249999406 0.936543866 0.563452102

O 0.063456134 0.436547898 0.750000594

O 0.436547898 0.750000594 0.063456134

O 0.750000594 0.063456134 0.436547898

i. Band Structure and DOS

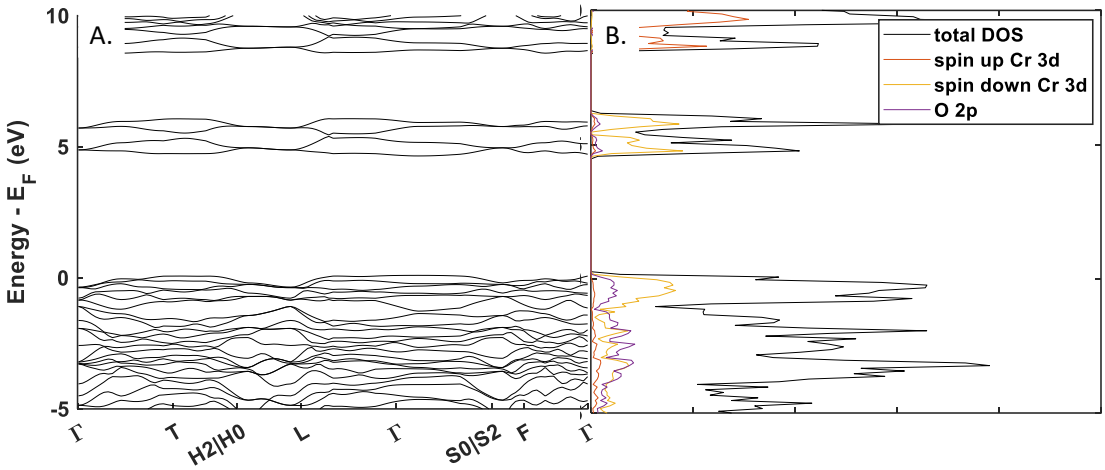

Figure C13. Ground State DFT Outputs for Cr_2O_3. (a) Ground state band structure with the Fermi energy set to 0 eV. (b) Ground state total density of states in black and important orbital contributions around the Fermi energy are shown in color. No scissor shift has been included in these calculations.

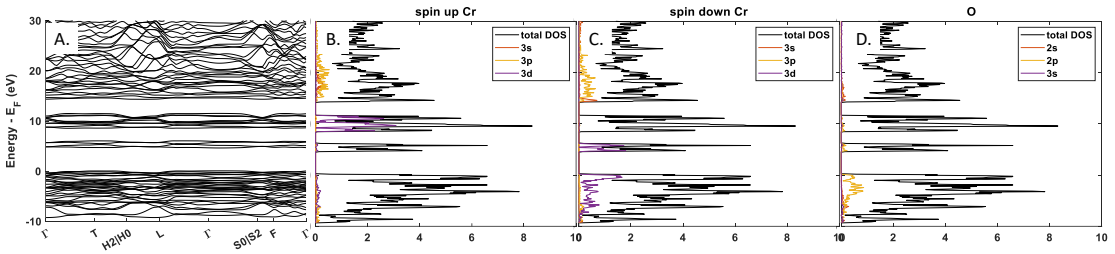

Figure C14. Ground State DFT Outputs for Cr_2O_3. (a) Overall ground state band structure with the Fermi energy set to 0 eV. (b) Overall ground state total density of states in black and spin up Cr partial DOS decomposed into 3s, 3p, and 3d orbital contributions. (c) Overall ground state total density of states in black and spin down Cr partial DOS decomposed into 3s, 3p, and 3d orbital contributions. (d) Overall ground state total density of states in black and O partial DOS decomposed into 2s, 2p, and 3s orbital contributions No scissor shift has been included in these calculations.

ii. Ground State Spectrum[106]

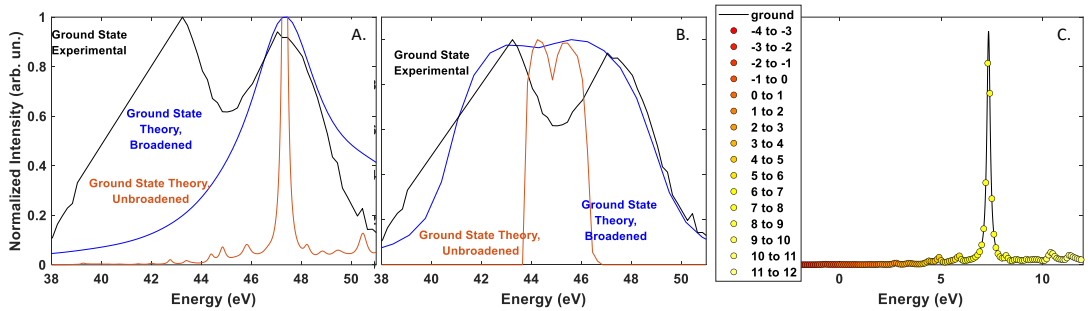

Figure C15. Ground State $M_{2,3}$ edge Spectra. (a) The experimental reflectivity (black), OCEAN calculated unbroadened (orange), and OCEAN calculated with energy-dependent broadening (blue) XUV absorption spectra are compared. (b) The experimental (black), calculated unbroadened (orange), and calculated with energy-dependent broadening (blue) XUV reflectivity spectra are compared. Reflectivity spectra are calculated following the Matlab code presented above. (c) Energy-resolved exciton densities overlaid on the calculated XUV absorption spectrum around the Fermi level and the Cr $M_{2,3}$ edge.

iii. Ground State GMRES Energy Decomposition

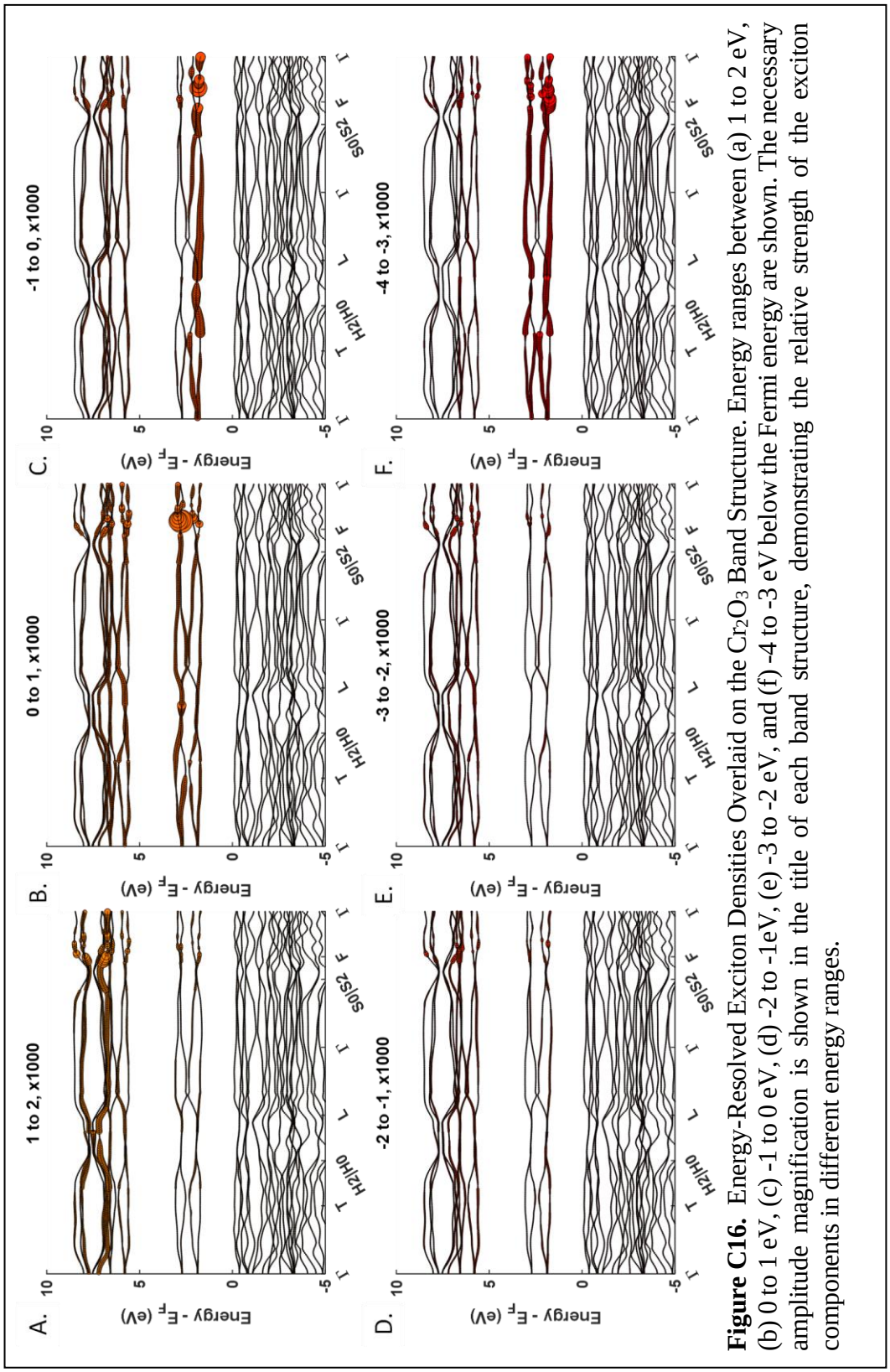

Figure C16. Energy-Resolved Exciton Densities Overlaid on the Cr_2O_3 Band Structure. Energy ranges between (a) 1 to 2 eV, (b) 0 to 1 eV, (c) -1 to 0 eV, (d) -2 to -1eV, (e) -3 to -2 eV, and (f) -4 to -3 eV below the Fermi energy are shown. The necessary amplitude magnification is shown in the title of each band structure, demonstrating the relative strength of the exciton components in different energy ranges.

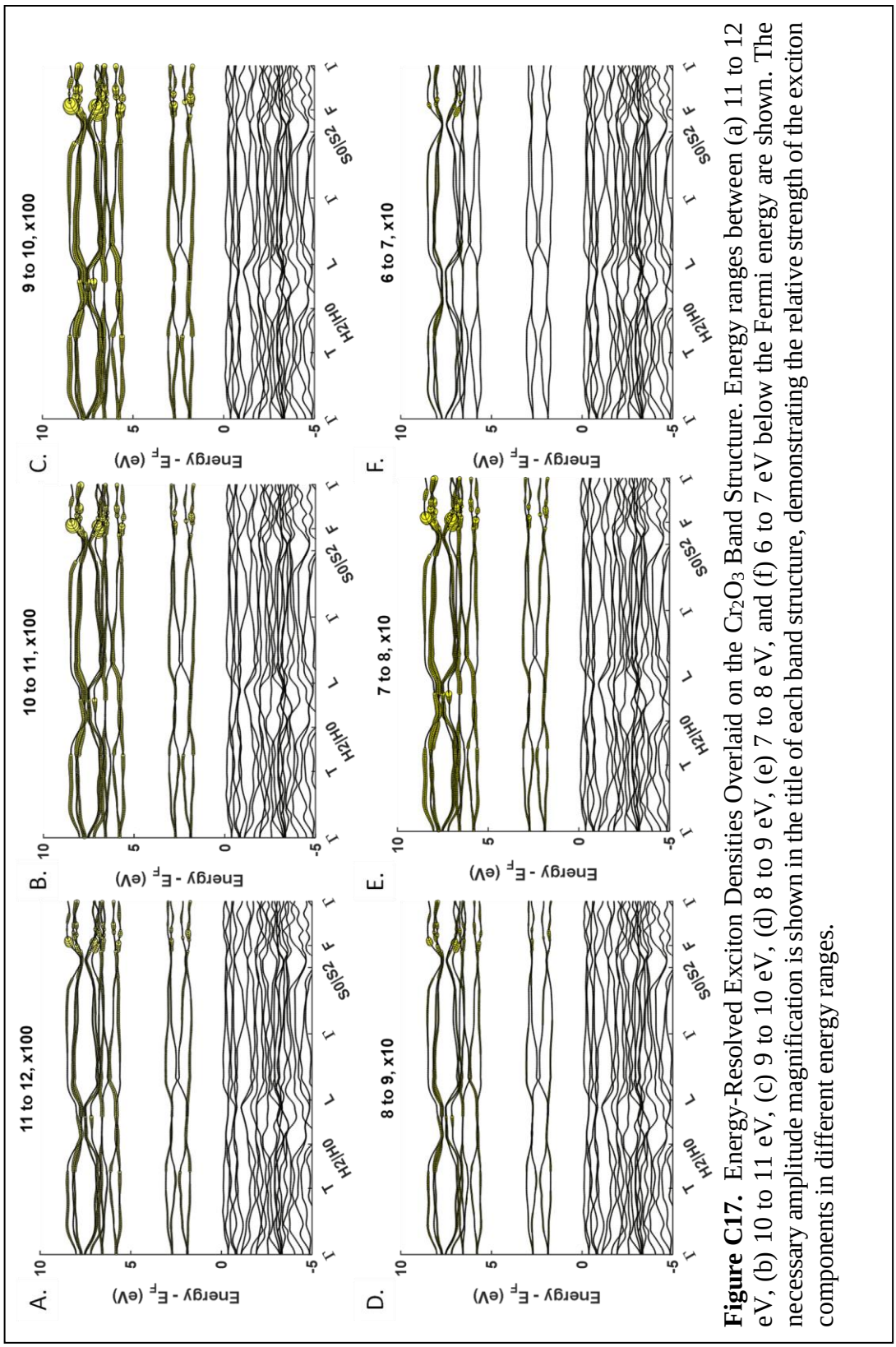

Figure C17. Energy-Resolved Exciton Densities Overlaid on the Cr_2O_3 Band Structure. Energy ranges between (a) 11 to 12 eV, (b) 10 to 11 eV, (c) 9 to 10 eV, (d) 8 to 9 eV, (e) 7 to 8 eV, and (f) 6 to 7 eV below the Fermi energy are shown. The necessary amplitude magnification is shown in the title of each band structure, demonstrating the relative strength of the exciton components in different energy ranges.

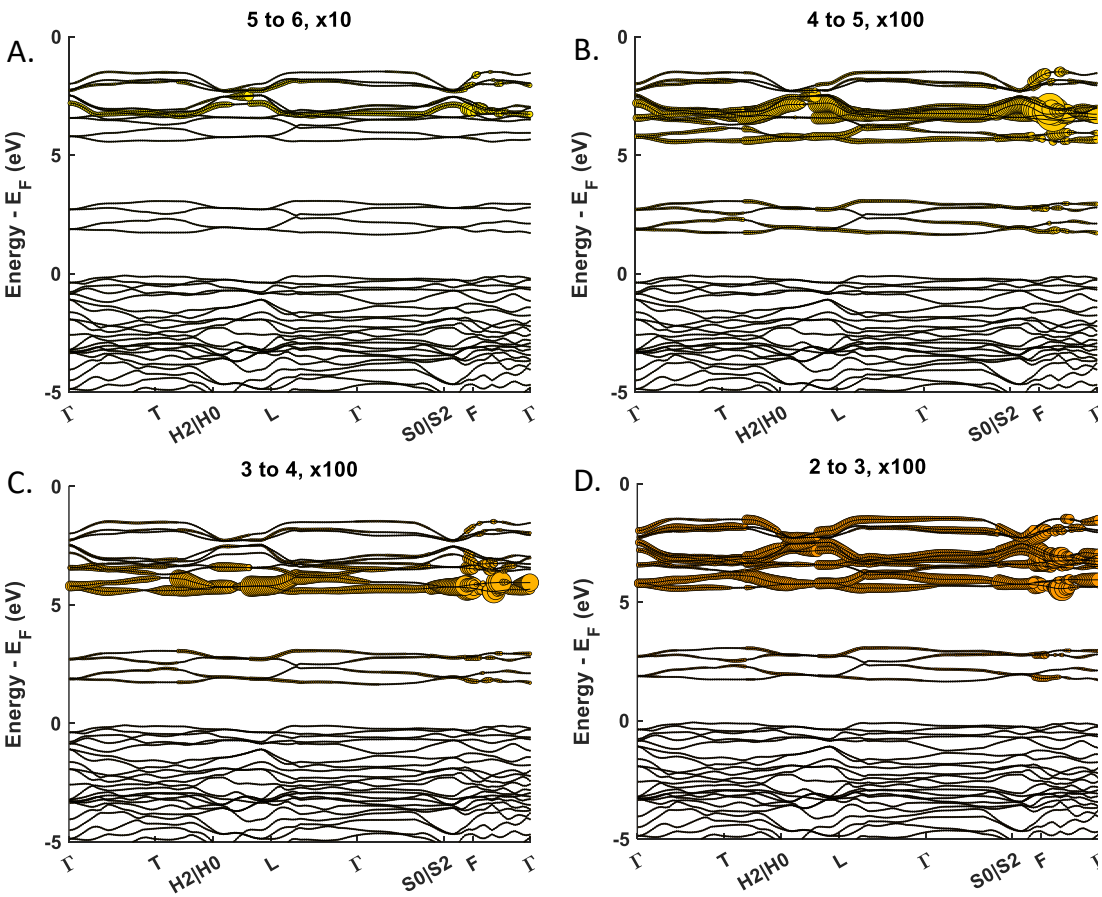

Figure C18. Energy-Resolved Exciton Densities Overlaid on the Cr_2O_3 Band Structure. Energy ranges between (a) 5 to 6 eV, (b) 4 to 5 eV, (c) 3 to 4 eV and (d) 2 to 3 eV below the Fermi energy are shown. The necessary amplitude magnification is shown in the title of each band structure, demonstrating the relative strength of the exciton components in different energy ranges.

c. Excited State Calculations

i. State filling band diagrams and Full Spectra

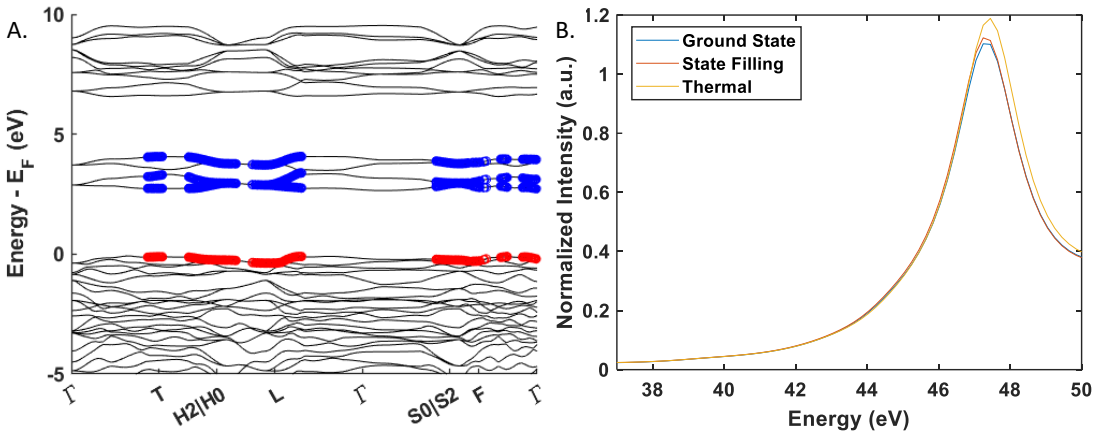

Figure C19. Excited State $M_{2,3}$ edge Absorption Spectrum. (a) State filling occupation used to model charge-transfer where the blue circles indicate electron occupation and red circles indicate holes overlaid on the band structure in black. (b) Broadened spectra for the ground state (blue), state filling (orange), and thermal expansion (yellow).

d. Hamiltonian Decompositions

i. Total Exciton Comparisons

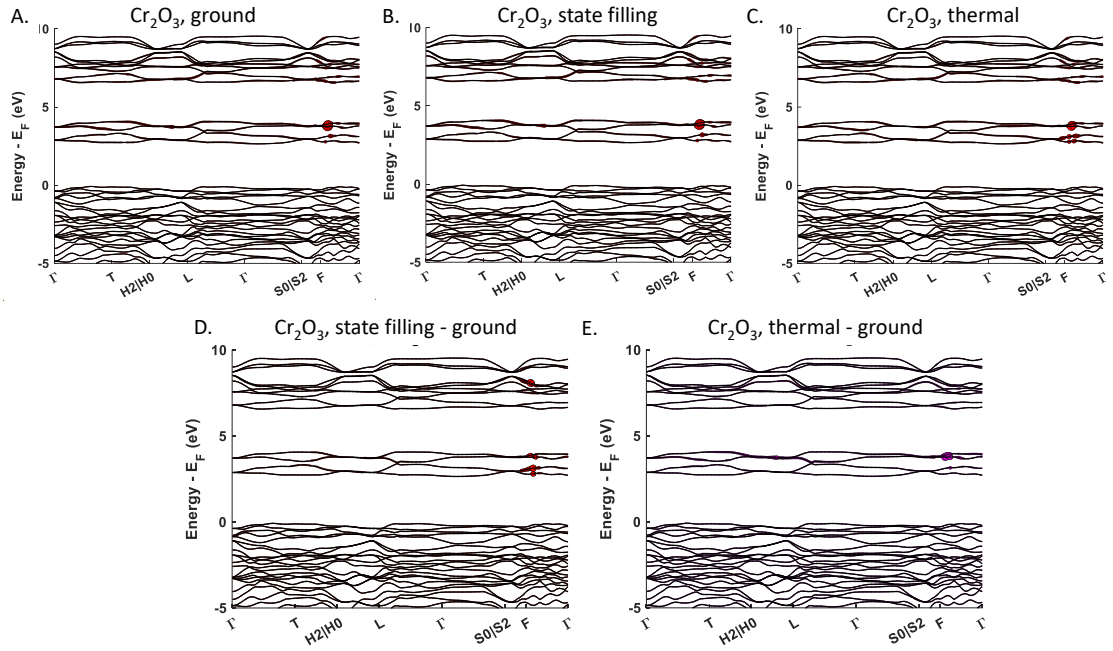

Figure C20. Total Core-Valence Exciton Densities. (a) Ground, (b) state filling, and (c) thermally expanded states' total core-valence exciton densities overlaid on the band structure of Cr_2O_3. Differentials for the (d) state filling, and (e) thermally expanded excited states.

ii. Hamiltonian Decomposition of Exciton Components for ground, state filling, and thermally expanded models.

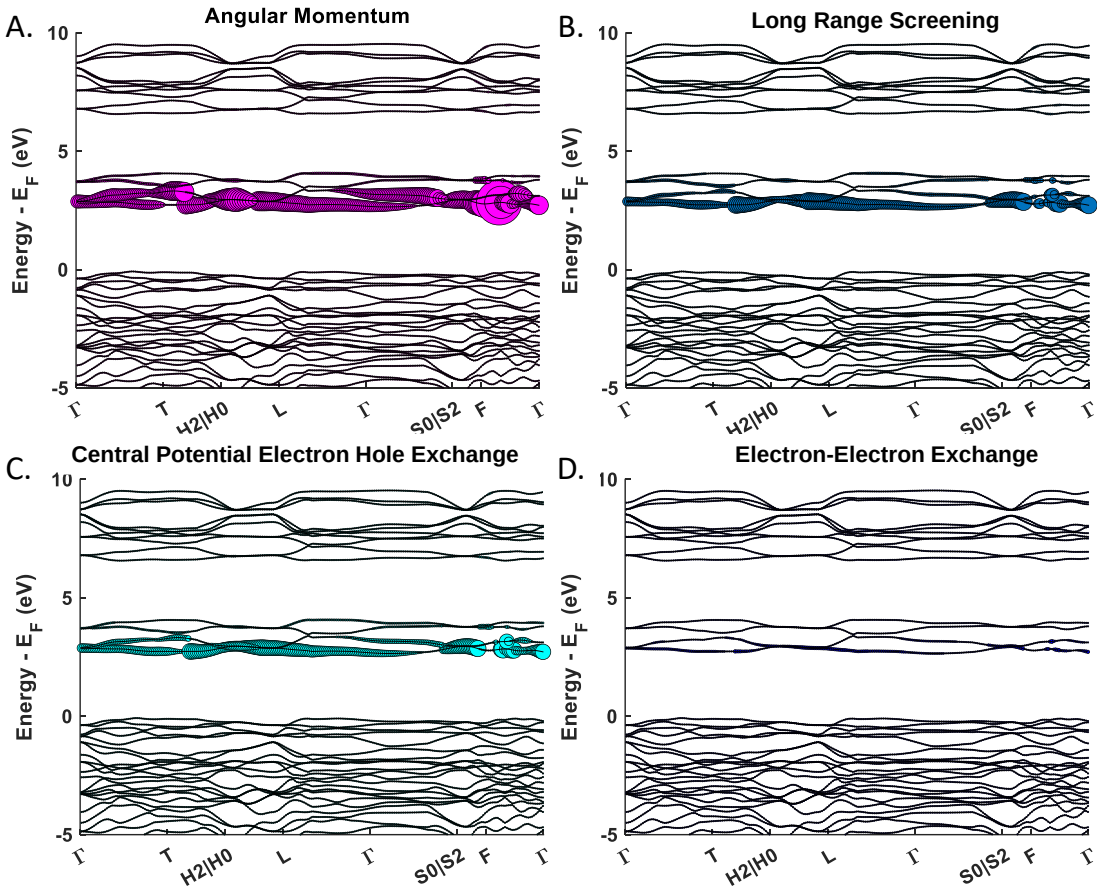

Figure C21. XUV transition Hamiltonian Decomposition of Core-Valence Exciton for the Ground State of Cr_2O_3. The (a) angular momentum, (b) core-hole screening, (c) electron-hole exchange, and (d) electron-electron exchange core-valence exciton densities are calculated and normalized to determine the relative contribution of each of these processes to the overall XUV exciton and thus absorption spectrum.

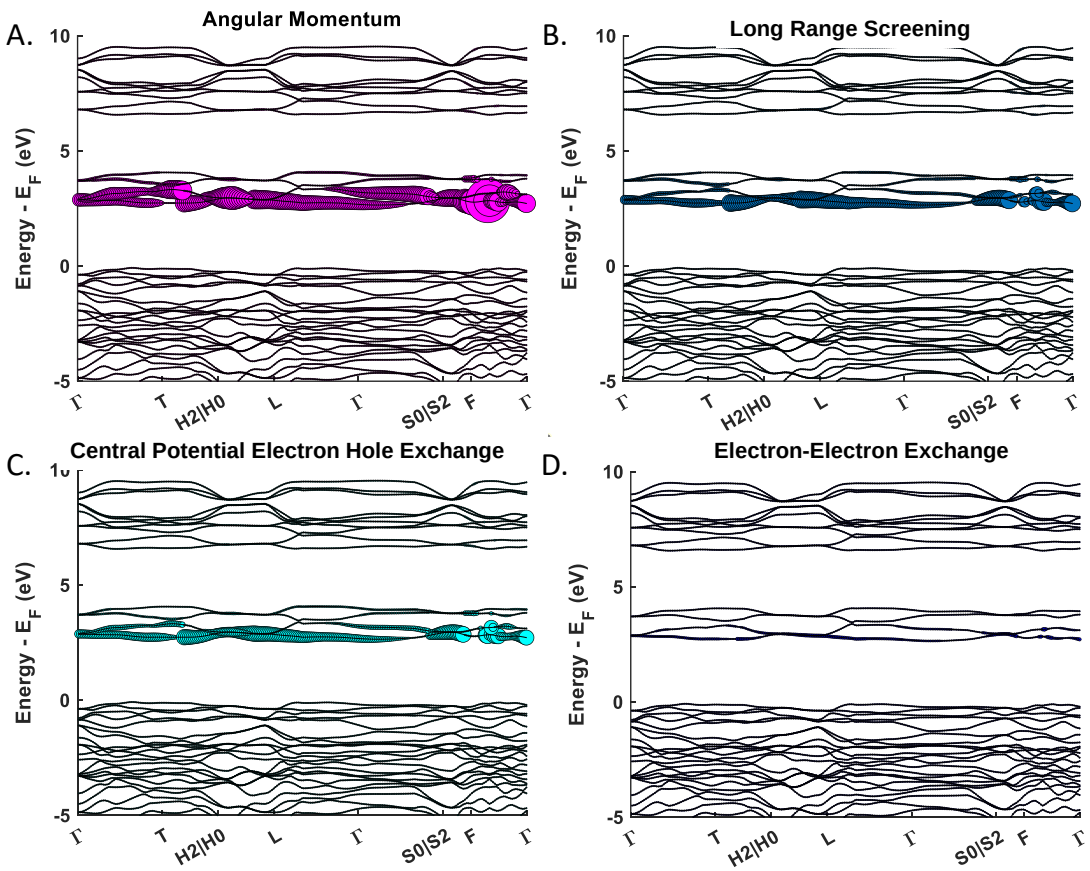

Figure C22. XUV transition Hamiltonian Decomposition of Core-Valence Exciton for the State Filling State of Cr_2O_3. The (a) angular momentum, (b) core-hole screening, (c) electron-hole exchange, and (d) electron-electron exchange core-valence exciton densities are calculated and normalized to determine the relative contribution of each of these processes to the overall XUV exciton and thus absorption spectrum.

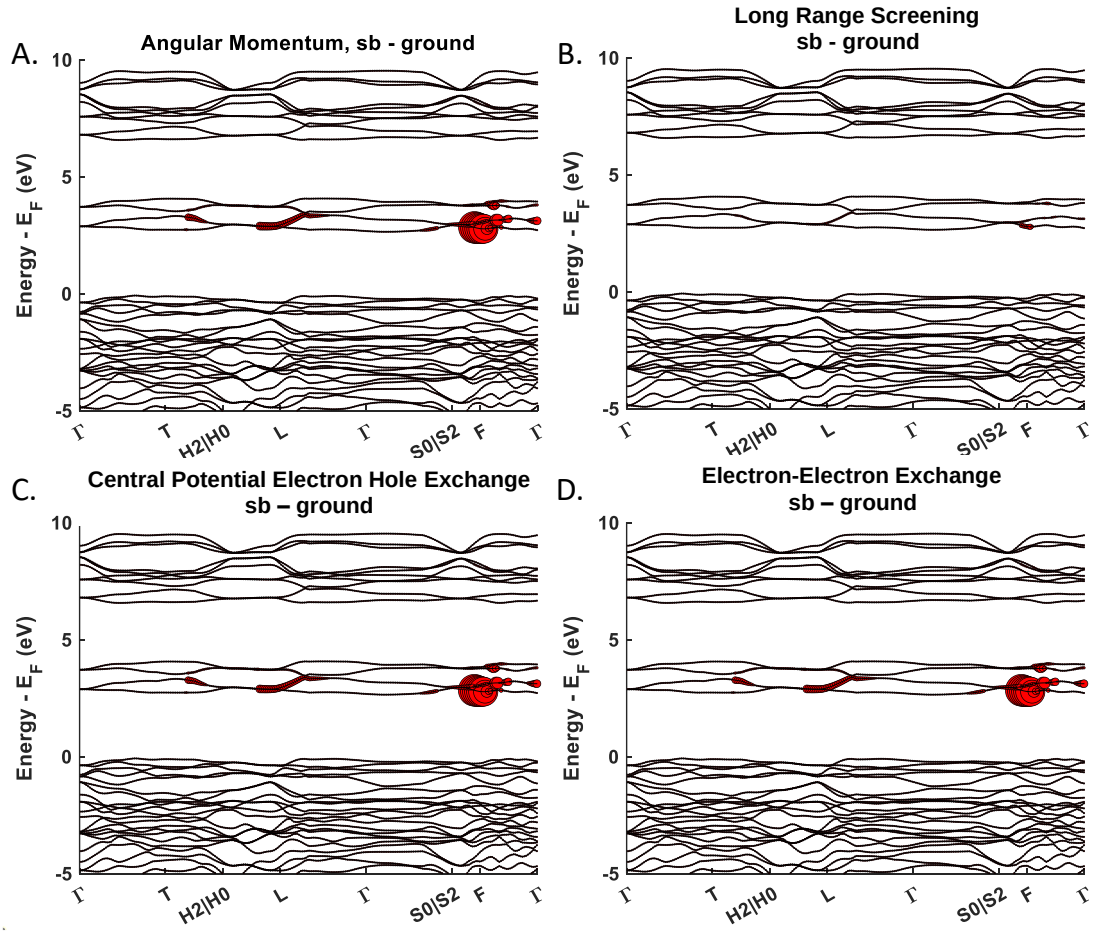

Figure C24. Differential XUV transition Hamiltonian Decomposition of Core-Valence Exciton for the State-Filling Excited State of Cr_2O_3. The magnitude of the state-filling minus the ground state components the (a) angular momentum, (b) core-hole screening, (c) electron-hole exchange, and (d) electron-electron exchange core-valence exciton densities are calculated and normalized to determine the relative contribution of each of these processes to excited state effects.

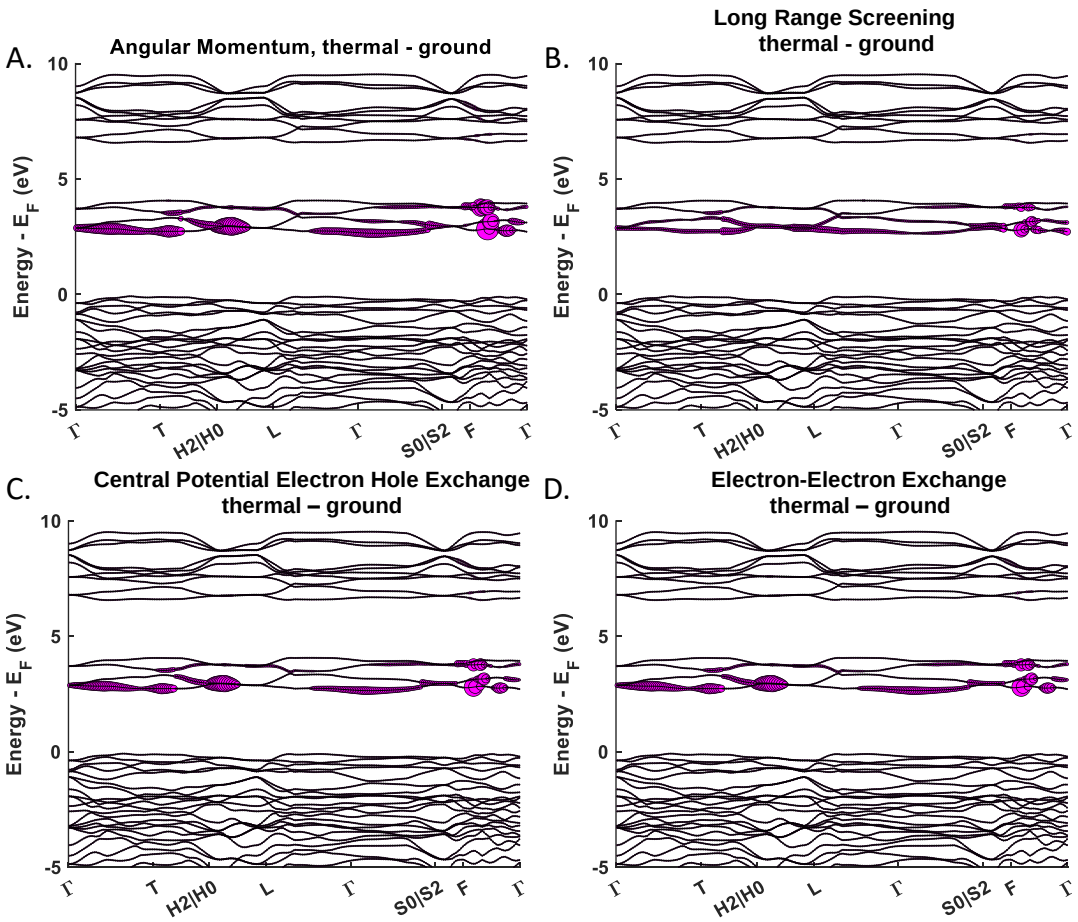

Figure C25. Differential XUV transition Hamiltonian Decomposition of Core-Valence Exciton for the Thermally Expanded Excited State of Cr_2O_3. The magnitude of the state-filling minus the ground state components for the (a) angular momentum, (b) core-hole screening, (c) electron-hole exchange, and (d) electron-electron exchange core-valence exciton densities are calculated and normalized to determine the relative contribution of each of these processes to excited state effects.

C4. MnO_2

a. Structural Data for Calculations

i. Ground State and State Blocking

Unit Cell Parameters (bohr)

{8.4518 8.4518 5.4896}

Primitive Vectors

{10 0

01 0

00 1}

Reduced coordinates, (x, y, z)

Mn1 0.000000000 0.000000000 0.000000000

Mn2 0.500000000 0.500000000 0.500000000

O 0.293959177 0.293959177 -0.000000000

O 0.203610439 0.796389561 0.500000000

O 0.706040823 0.706040823 -0.000000000

O 0.796389561 0.203610439 0.500000000

ii. Thermally Expanded Lattice

Unit Cell Parameters (bohr)

{8.4729 8.4729 5.5033}

Primitive Vectors

{1 00

010

001}

Reduced coordinates, (x, y, z)

Mn1 0.000000000 0.000000000 0.000000000

Mn2 0.500000000 0.500000000 0.500000000

O 0.293959177 0.293959177 -0.000000000

O 0.203610439 0.796389561 0.500000000

O 0.706040823 0.706040823 -0.000000000

O 0.796389561 0.203610439 0.500000000

b. Ground State Calculations

i. Band Structure and DOS

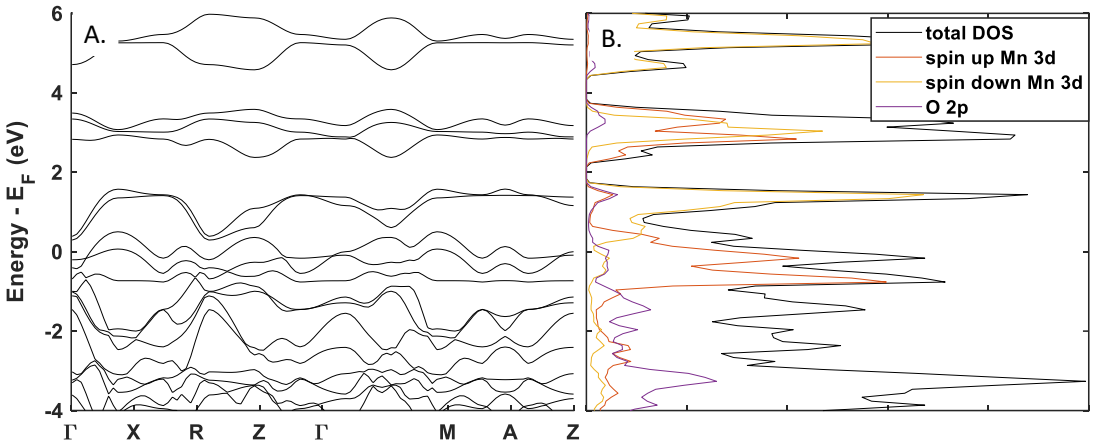

Figure C26. Ground State DFT Outputs for MnO_2. (a) Ground state band structure with the Fermi energy set to 0 eV. (b) Ground state total density of states in black and important orbital contributions around the Fermi energy are shown in color. No scissor shift has been included in these calculations.

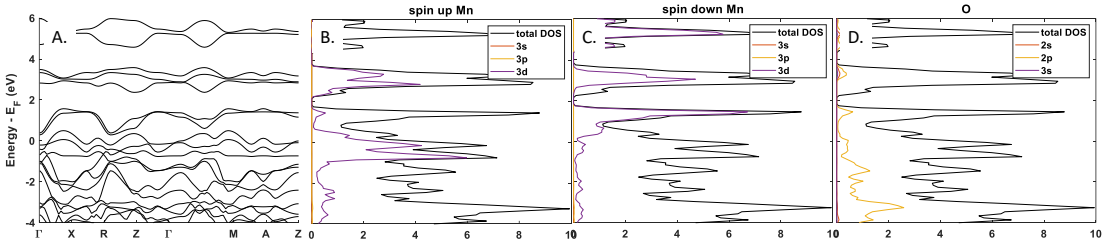

Figure C27. Ground State DFT Outputs for MnO_2. (a) Overall ground state band structure with the Fermi energy set to 0 eV. (b) Overall ground state total density of states in black and spin up Mn partial DOS decomposed into 3s, 3p, and 3d orbital contributions. (c) Overall ground state total density of states in black and spin down Mn partial DOS decomposed into 3s, 3p, and 3d orbital contributions. (d) Overall ground state total density of states in black and O partial DOS decomposed into 2s, 2p, and 3s orbital contributions No scissor shift has been included in these calculations.

ii. Ground State Spectrum[159]

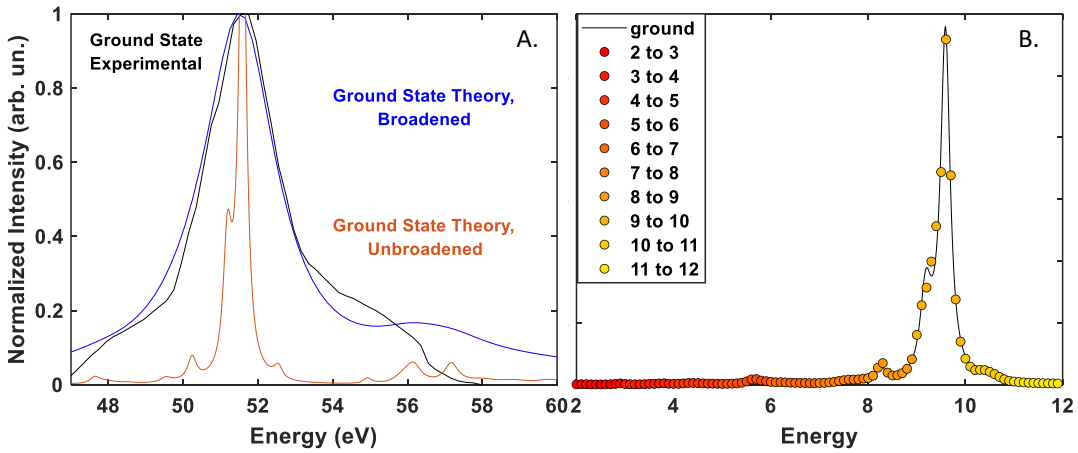

Figure C28. Ground State $M_{2,3}$ edge Absorption Spectrum. (a) The experimental (black), OCEAN calculated unbroadened (orange), and OCEAN calculated with energy-dependent broadening (blue) spectra are compared. (b) Energy-resolved exciton densities overlaid on the calculated XUV absorption spectrum around the Fermi level and the Mn $M_{2,3}$ edge.

iii. Ground State GMRES Energy Decomposition

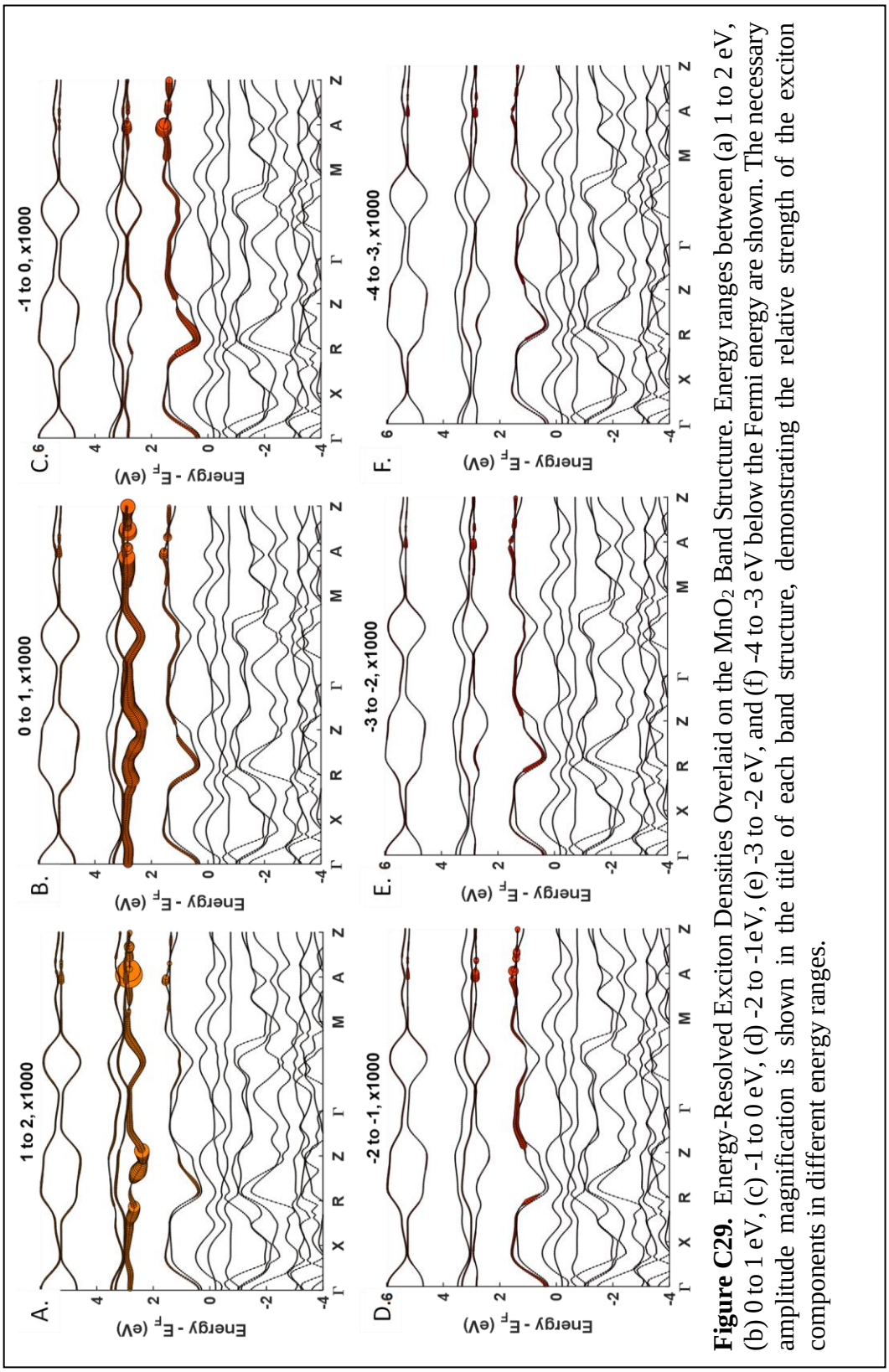

Figure C29. Energy-Resolved Exciton Densities Overlaid on the MnO_2 Band Structure. Energy ranges between (a) 1 to 2 eV, (b) 0 to 1 eV, (c) -1 to 0 eV, (d) -2 to -1eV, (e) -3 to -2 eV, and (f) -4 to -3 eV below the Fermi energy are shown. The necessary amplitude magnification is shown in the title of each band structure, demonstrating the relative strength of the exciton components in different energy ranges.

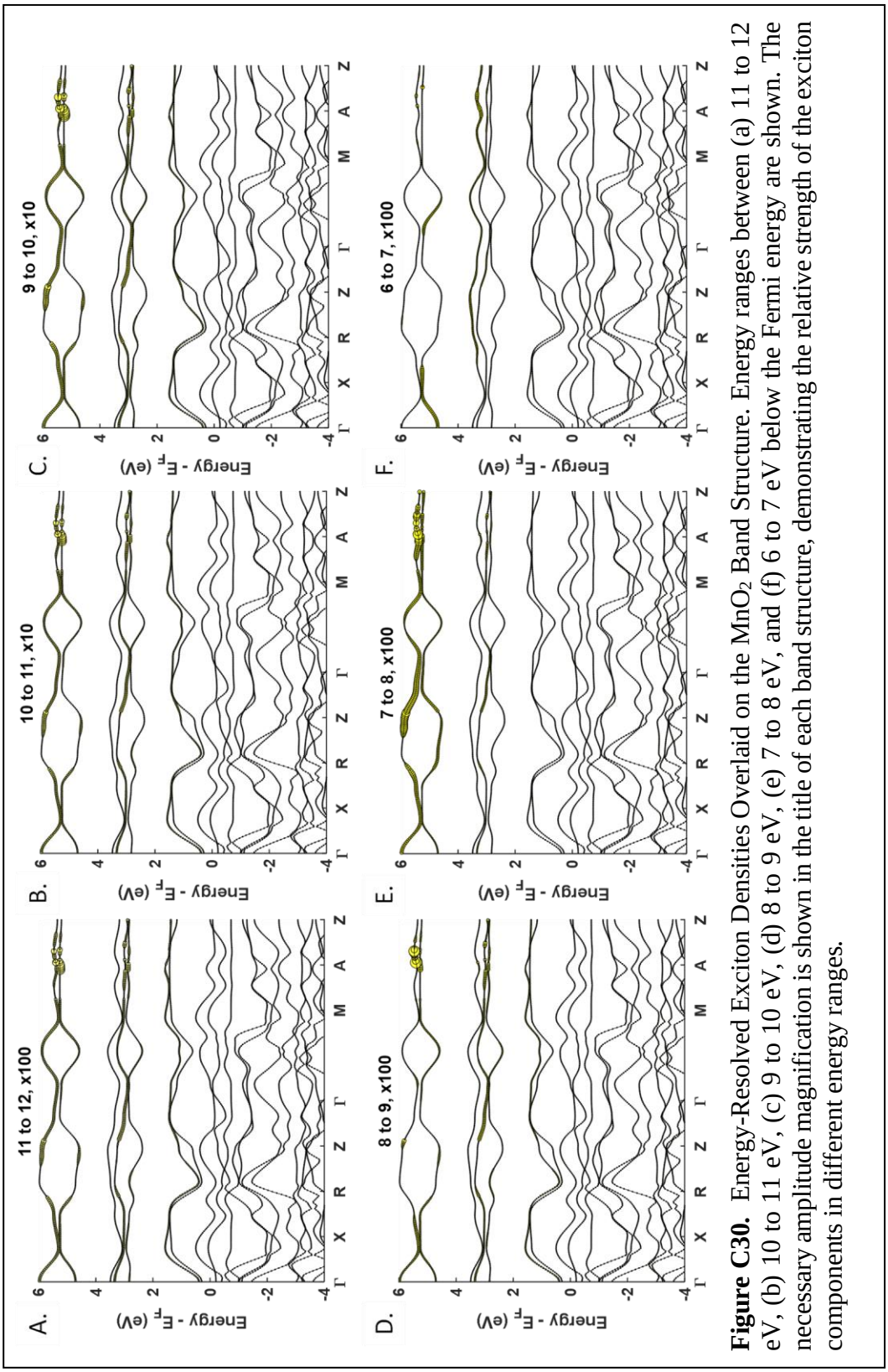

Figure C30. Energy-Resolved Exciton Densities Overlaid on the MnO_2 Band Structure. Energy ranges between (a) 11 to 12 eV, (b) 10 to 11 eV, (c) 9 to 10 eV, (d) 8 to 9 eV, (e) 7 to 8 eV, and (f) 6 to 7 eV below the Fermi energy are shown. The necessary amplitude magnification is shown in the title of each band structure, demonstrating the relative strength of the exciton components in different energy ranges.

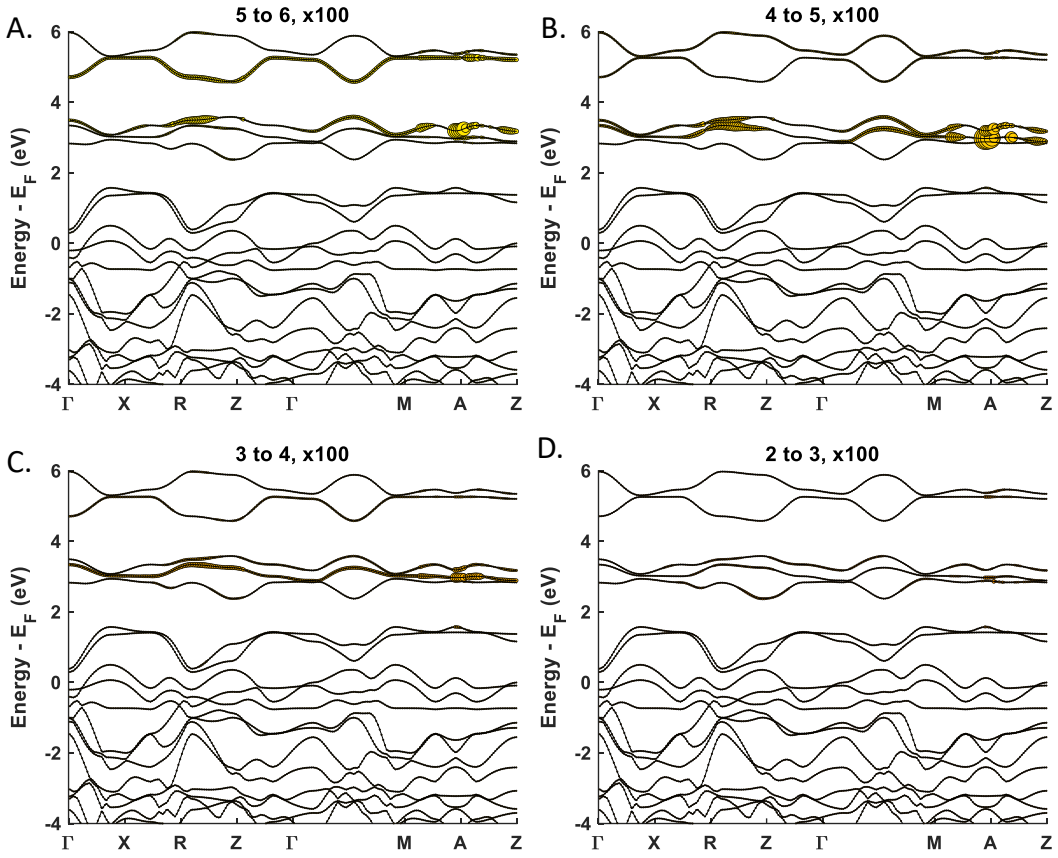

Figure C31. Energy-Resolved Exciton Densities Overlaid on the MnO_2 Band Structure. Energy ranges between (a) 5 to 6 eV, (b) 4 to 5 eV, (c) 3 to 4 eV and (d) 2 to 3 eV below the Fermi energy are shown. The necessary amplitude magnification is shown in the title of each band structure, demonstrating the relative strength of the exciton components in different energy ranges.

c. Excited State Calculations

i. State filling band diagrams and Full Spectra

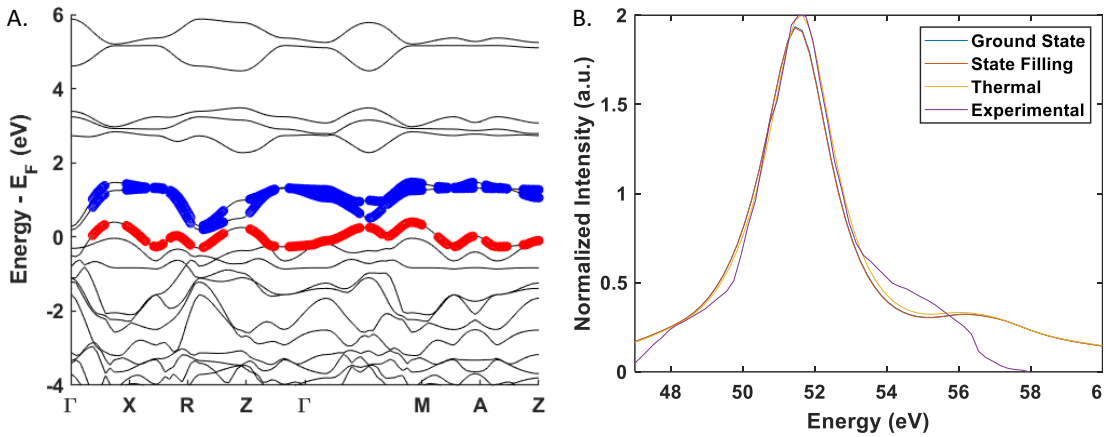

Figure C32. Excited State $M_{2,3}$ edge Absorption Spectrum. (a) State filling occupation used to model charge-transfer where the blue circles indicate electron occupation and red circles indicate holes overlaid on the band structure in black. (b) Broadened spectra for the ground state (blue), state filling (orange), thermal expansion (yellow), and experimental (purple).

d. Hamiltonian Decompositions

i. Total Exciton Comparisons

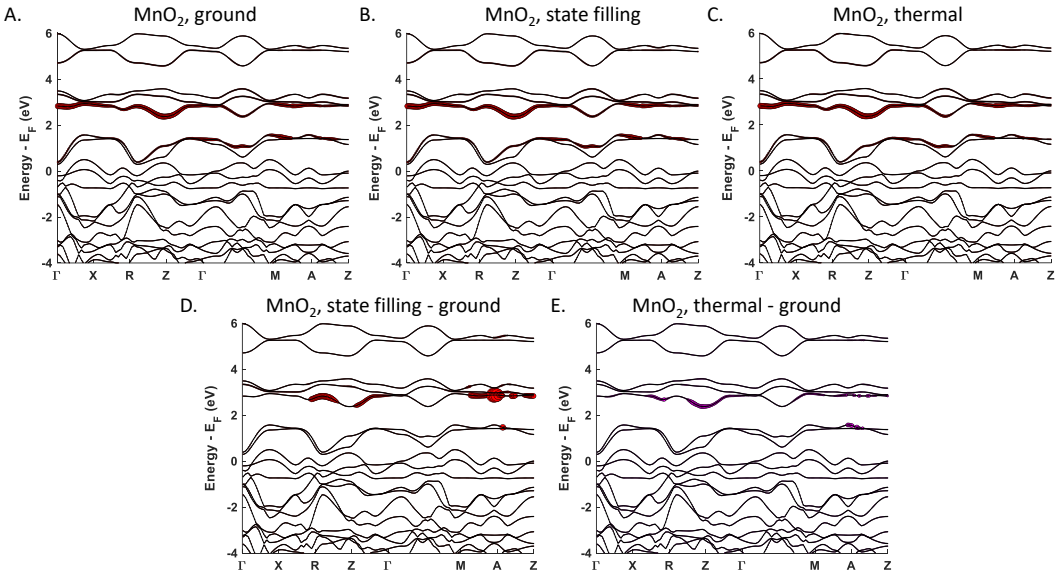

Figure C33. Total Core-Valence Exciton Densities. (a) Ground, (b) state filling, and (c) thermally expanded states' total core-valence exciton densities overlaid on the band structure of MnO2. Differentials for the (d) state filling, and (e) thermally expanded excited states.

ii. Hamiltonian Decomposition of Exciton Components for ground, state filling, and thermally expanded models.

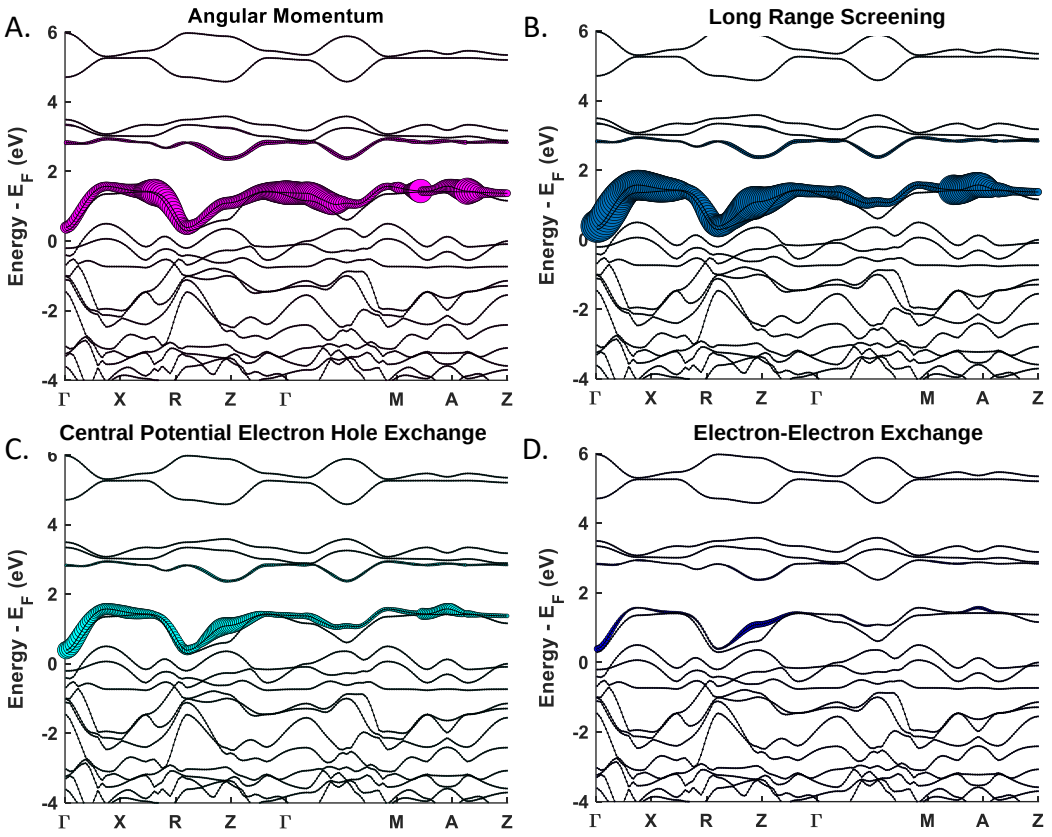

Figure C34. XUV transition Hamiltonian Decomposition of Core-Valence Exciton for the Ground State of MnO_2. The (a) angular momentum, (b) core-hole screening, (c) electron-hole exchange, and (d) electron-electron exchange core-valence exciton densities are calculated and normalized to determine the relative contribution of each of these processes to the overall XUV exciton and thus absorption spectrum.

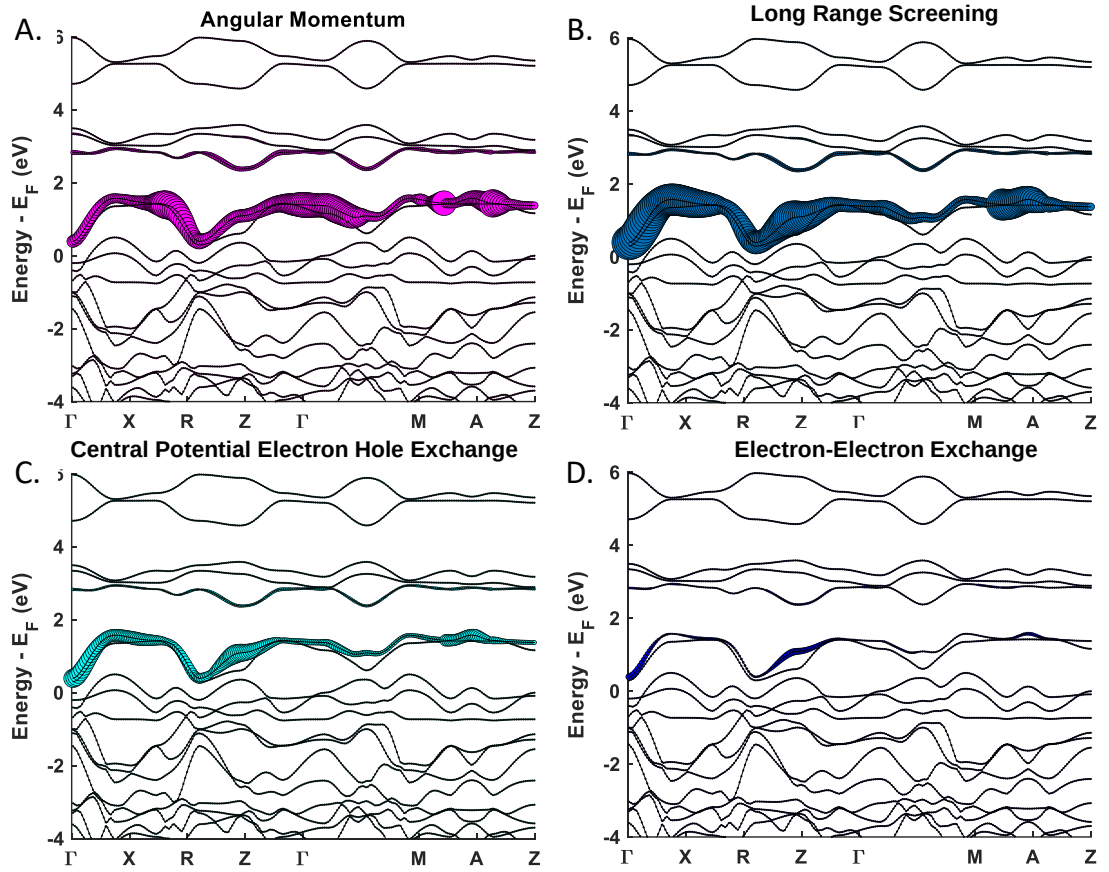

Figure C35. XUV transition Hamiltonian Decomposition of Core-Valence Exciton for the State Filling State of MnO_2. The (a) angular momentum, (b) core-hole screening, (c) electron-hole exchange, and (d) electron-electron exchange core-valence exciton densities are calculated and normalized to determine the relative contribution of each of these processes to the overall XUV exciton and thus absorption spectrum.

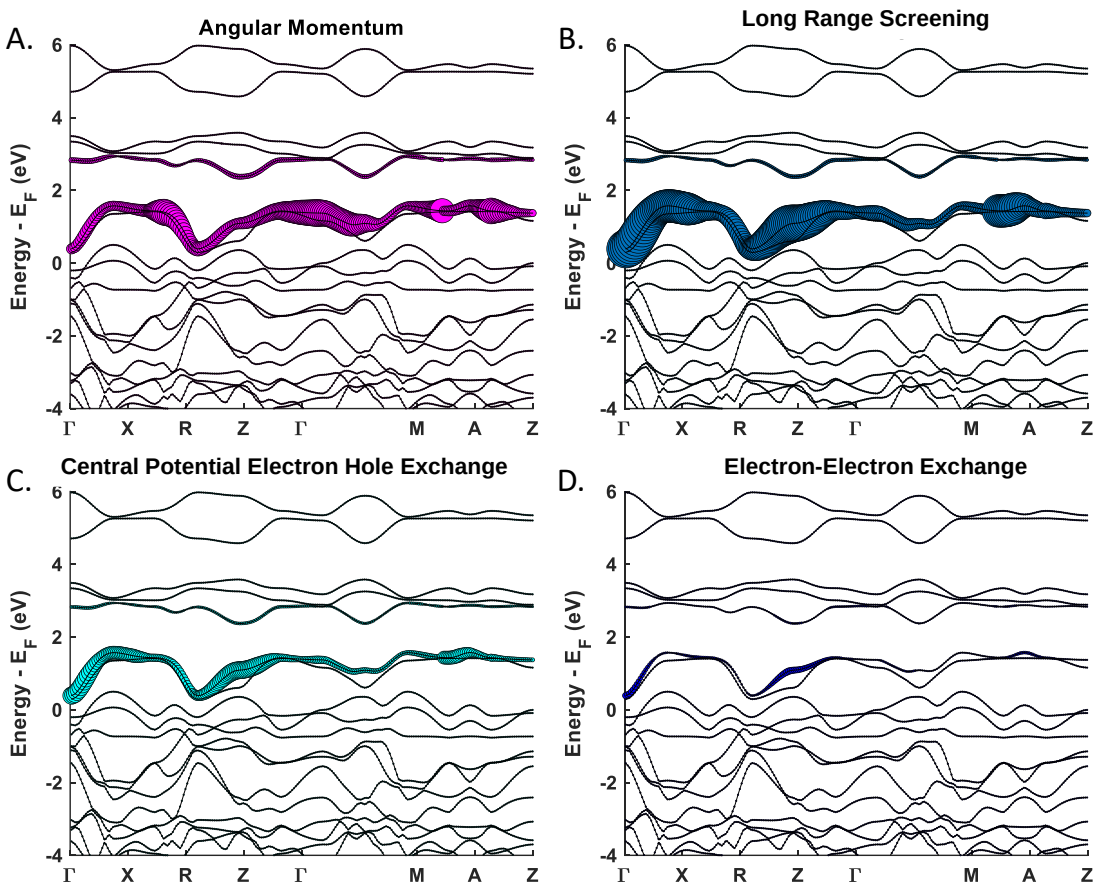

Figure C36. XUV transition Hamiltonian Decomposition of Core-Valence Exciton for the Thermally Expanded State of MnO_2. The (a) angular momentum, (b) core-hole screening, (c) electron-hole exchange, and (d) electron-electron exchange core-valence exciton densities are calculated and normalized to determine the relative contribution of each of these processes to the overall XUV exciton and thus absorption spectrum.

1

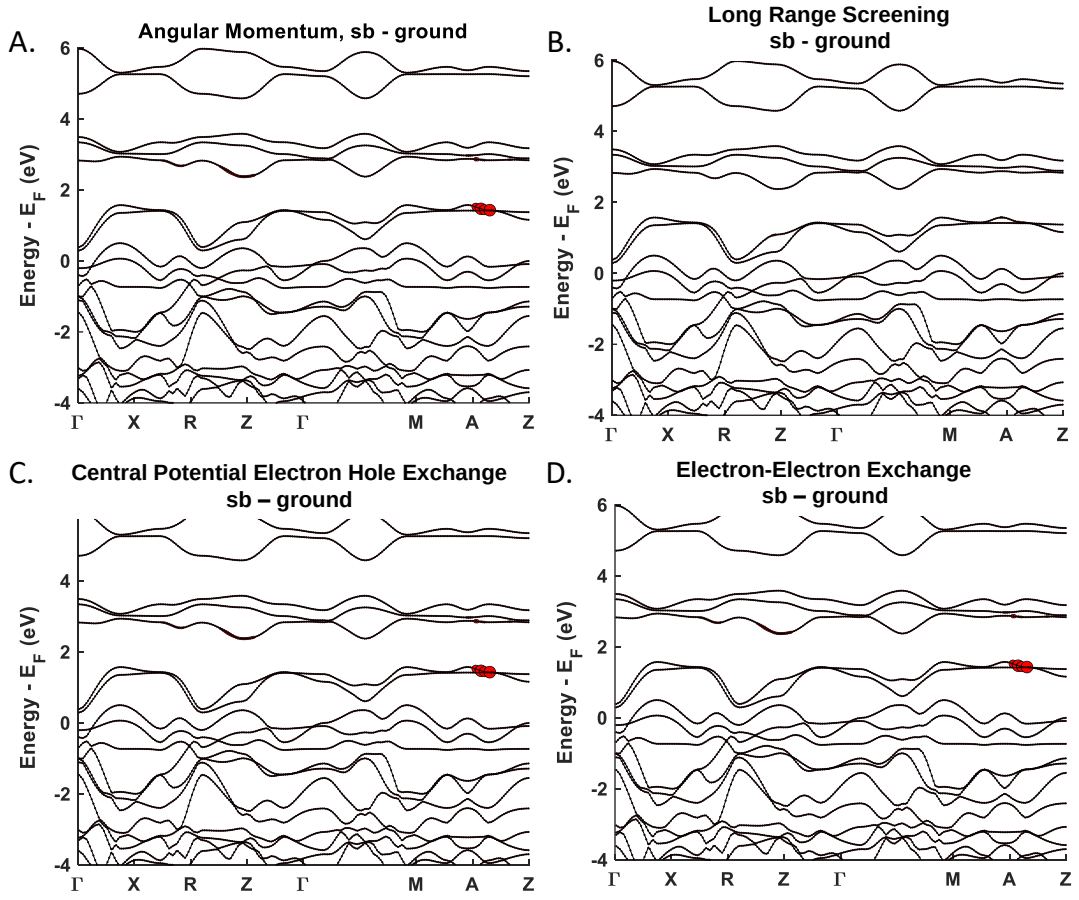

Figure C37. Differential XUV transition Hamiltonian Decomposition of Core-Valence Exciton for the State-Filling Excited State of MnO_2. The magnitude of the state-filling minus the ground state components for the (a) angular momentum, (b) core-hole screening, (c) electron-hole exchange, and (d) electron-electron exchange core-valence exciton densities are calculated and normalized to determine the relative contribution of each of these processes to excited state effects.

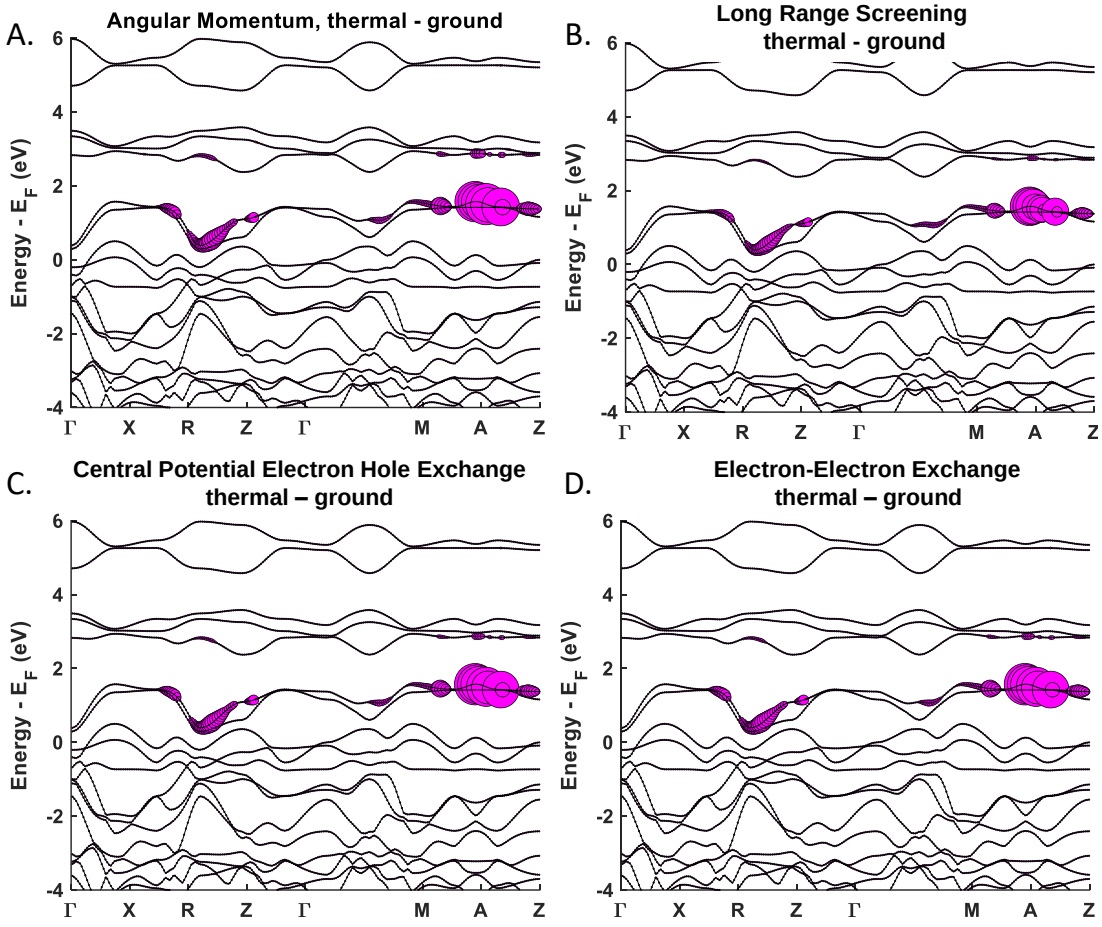

Figure C38. Differential XUV transition Hamiltonian Decomposition of Core-Valence Exciton for the Thermally Expanded Excited State of MnO_2. The magnitude of the state-filling minus the ground state components for the (a) angular momentum, (b) core-hole screening, (c) electron-hole exchange, and (d) electron-electron exchange core-valence exciton densities are calculated and normalized to determine the relative contribution of each of these processes to excited state effects.

C5. α-Fe_2O_3

a. Structural Data for Calculations

i. Ground State and State Blocking

Unit Cell Parameters

{10.2423 10.2423 10.2423}

Primitive Vectors

{1.0000000000 0.0000000000 0.0000000000

0.5695664700 0.8219452757 0.0000000000

0.5695664700 0.2982686482 0.7659176521}

Reduced coordinates, (x, y, z),

Fe1 0.1433915 0.1433904 0.1433906

Fe1 0.8566085 0.8566096 0.8566094

Fe2 0.3566087 0.3566104 0.3566106

Fe2 0.6433913 0.6433896 0.6433894

O 0.7500005 0.4472258 0.0527735

O 0.9472262 0.2499995 0.5527741

O 0.4472260 0.0527734 0.7500002

O 0.2499995 0.5527742 0.9472265

O 0.0527738 0.7500005 0.4472259

O 0.5527740 0.9472266 0.2499998

ii. Thermally Expanded Lattice

Unit Cell Parameters

{10.327 10.327 10.327}

Primitive Vectors

{1.0000000000 0.0000000000 0.0000000000

0.5695664700 0.8219452757 0.0000000000

0.5695664700 0.2982686482 0.7659176521}

Reduced coordinates, (x, y, z)

Fe1 0.1433915 0.1433904 0.1433906

Fe1 0.8566085 0.8566096 0.8566094

Fe2 0.3566087 0.3566104 0.3566106

Fe2 0.6433913 0.6433896 0.6433894

O 0.7500005 0.4472258 0.0527735

O 0.9472262 0.2499995 0.5527741

O 0.4472260 0.0527734 0.7500002

O 0.2499995 0.5527742 0.9472265

O 0.0527738 0.7500005 0.4472259

O 0.5527740 0.9472266 0.2499998

b. Ground State Calculations

i. Band Structure and DOS

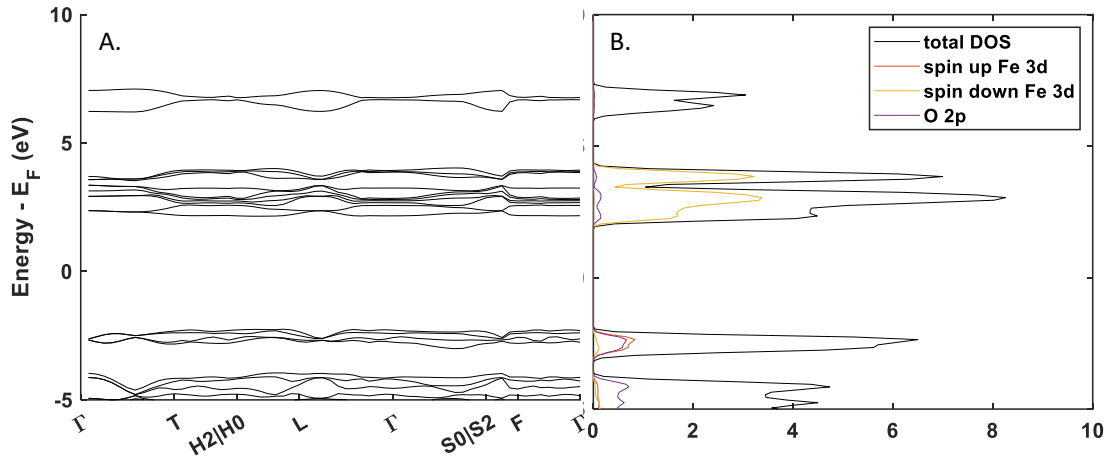

Figure C39. Ground State DFT Outputs for Fe_2O_3. (a) Ground state band structure with the Fermi energy set to 0 eV. (b) Ground state total density of states in black and important orbital contributions around the Fermi energy are shown in color. No scissor shift has been included in these calculations.

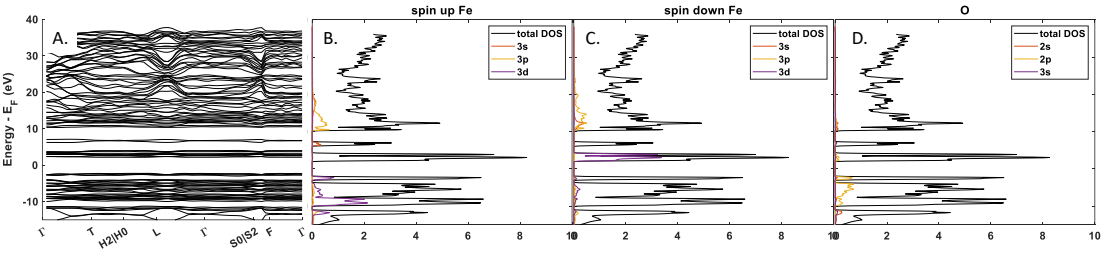

Figure C40. Ground State DFT Outputs for Fe_2O_3. (a) Overall ground state band structure with the Fermi energy set to 0 eV. (b) Overall ground state total density of states in black and spin up Fe partial DOS decomposed into 3s, 3p, and 3d orbital contributions. (c) Overall ground state total density of states in black and spin down Fe partial DOS decomposed into 3s, 3p, and 3d orbital contributions. (d) Overall ground state total density of states in black and O partial DOS decomposed into 2s, 2p, and 3s orbital contributions No scissor shift has been included in these calculations.

ii. Ground State Spectrum[102]

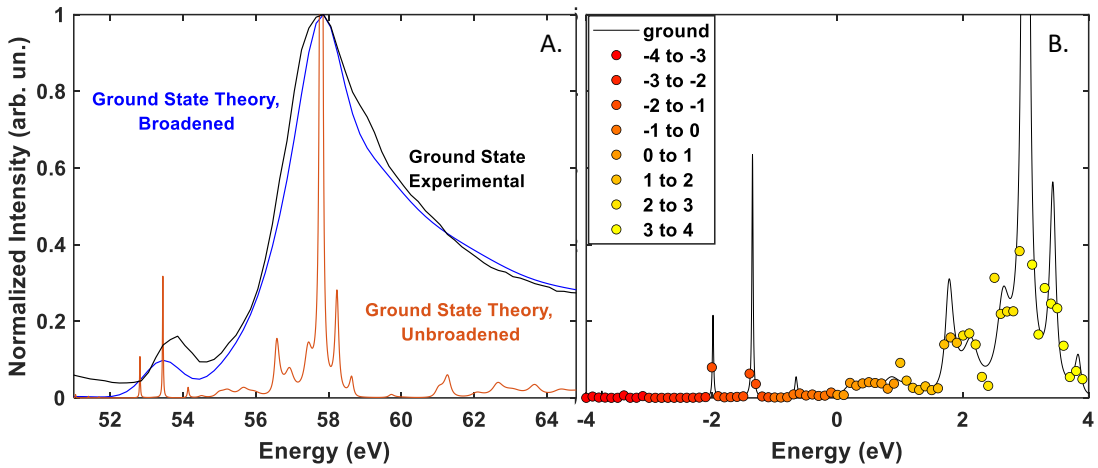

Figure C41. Ground State $M_{2,3}$ edge Absorption Spectrum. (a) The experimental (black), OCEAN calculated unbroadened (orange), and OCEAN calculated with energy-dependent broadening (blue) spectra are compared. (b) Energy-resolved exciton densities overlaid on the calculated XUV absorption spectrum around the Fermi level and the Fe $M_{2,3}$ edge.

iii. Ground State GMRES Energy Decomposition

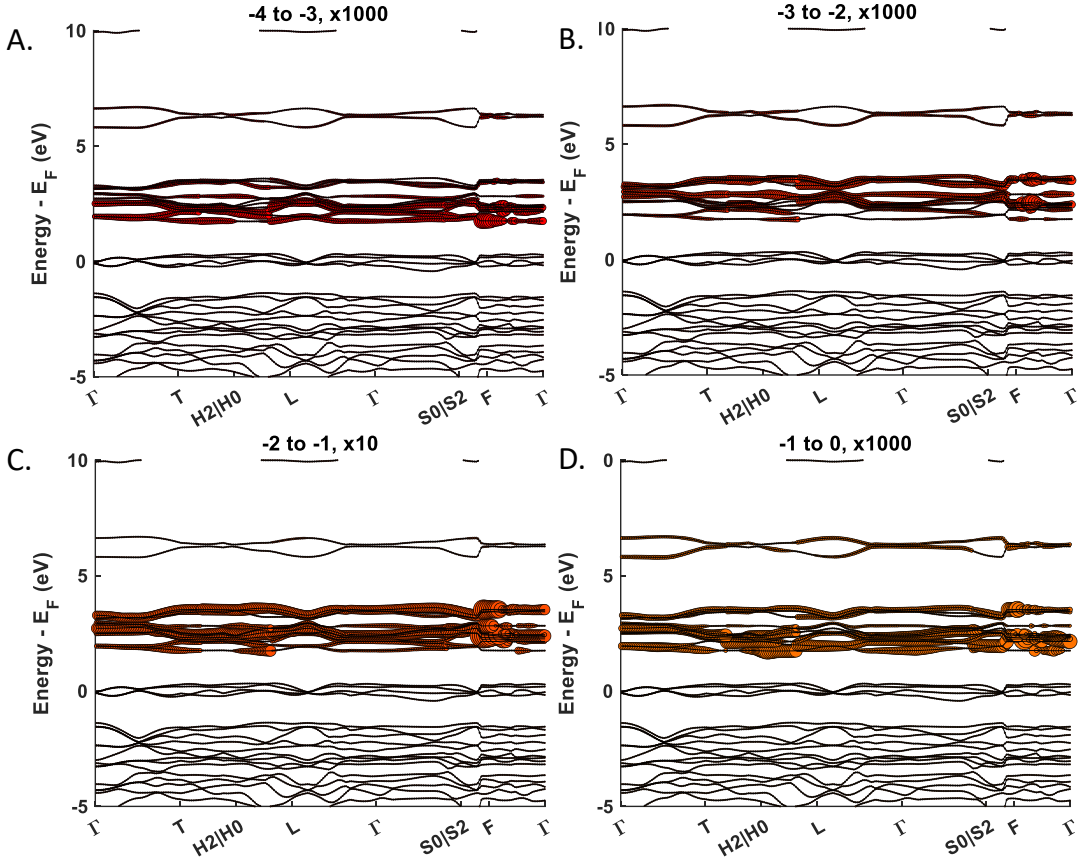

Figure C42. Energy-Resolved Exciton Densities Overlaid on the Fe_2O_3 Band Structure. Energy ranges between (a) -4 to -3 eV, (b) -3 to -2 eV, (c) -2 to -1 eV, and (d) -1 to 0 eV below the Fermi energy are shown. The necessary amplitude magnification is shown in the title of each band structure, demonstrating the relative strength of the exciton components in different energy ranges.

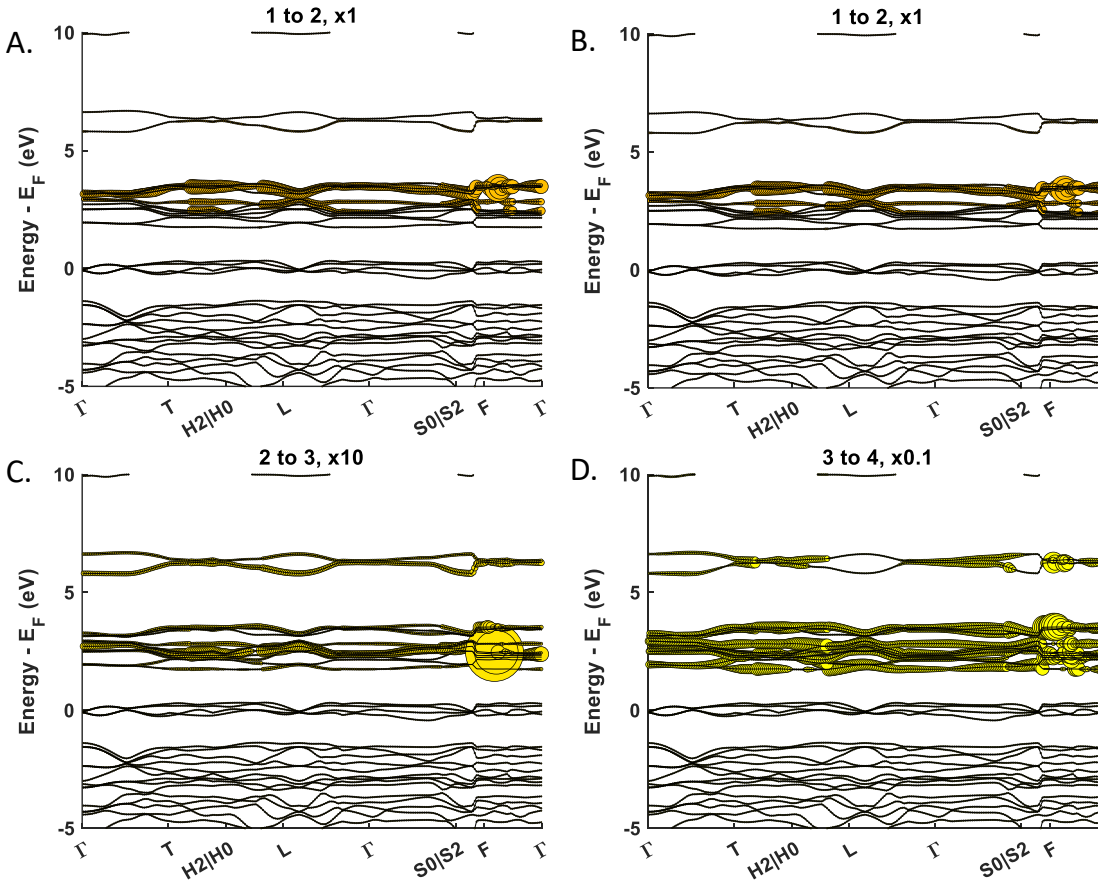

Figure C43. Energy-Resolved Exciton Densities Overlaid on the Fe_2O_3 Band Structure. Energy ranges between (a) 1 to 2 eV, (b) 1 to 2 eV, (c) 2 to 3 eV, and (d) 3 to 4 eV below the Fermi energy are shown. The necessary amplitude magnification is shown in the title of each band structure, demonstrating the relative strength of the exciton components in different energy ranges.

c. Excited State Calculations

i. State filling band diagrams and Full Spectra

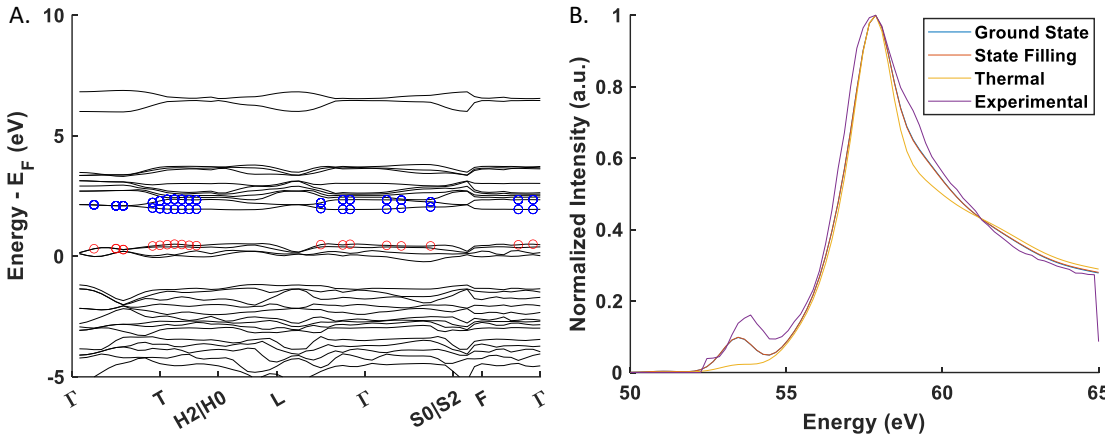

Figure C44. Excited State $M_{2,3}$ edge Absorption Spectrum. (a) State filling occupation used to model charge-transfer where the blue circles indicate electron occupation and red circles indicate holes overlaid on the band structure in black. (b) Broadened spectra for the ground state (blue), state filling (orange), thermal expansion (yellow), and experimental (purple).

d. Hamiltonian Decompositions

i. Total Exciton Comparisons

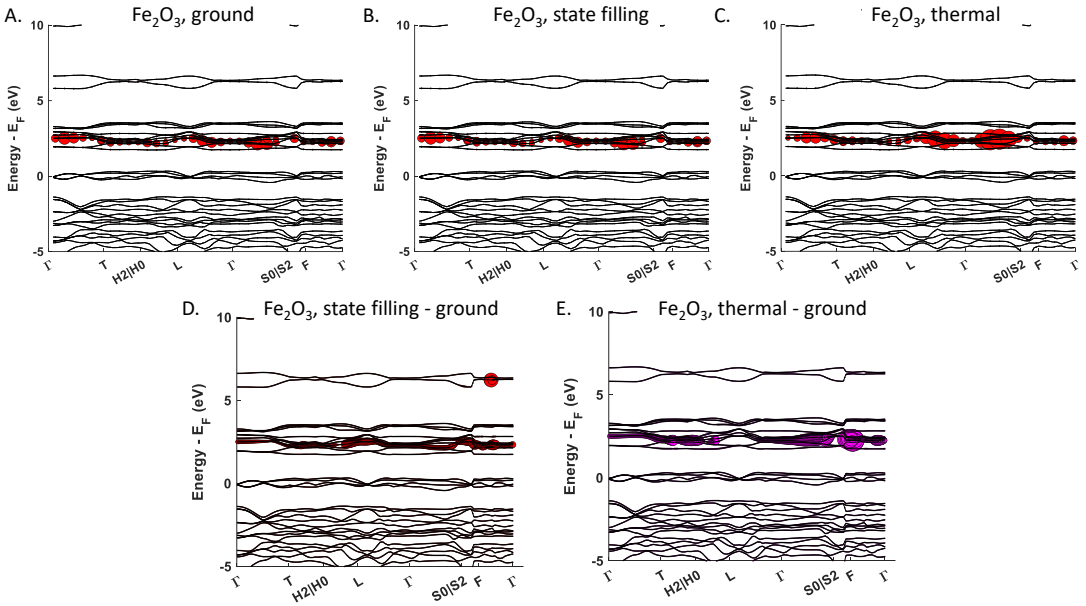

Figure C45. Total Core-Valence Exciton Densities. (a) Ground, (b) state filling, and (c) thermally expanded states' total core-valence exciton densities overlaid on the band structure of Fe_2O_3. Differentials for the (d) state filling, and (e) thermally expanded excited states.

ii. Hamiltonian Decomposition of Exciton Components for ground, state filling, and thermally expanded models.

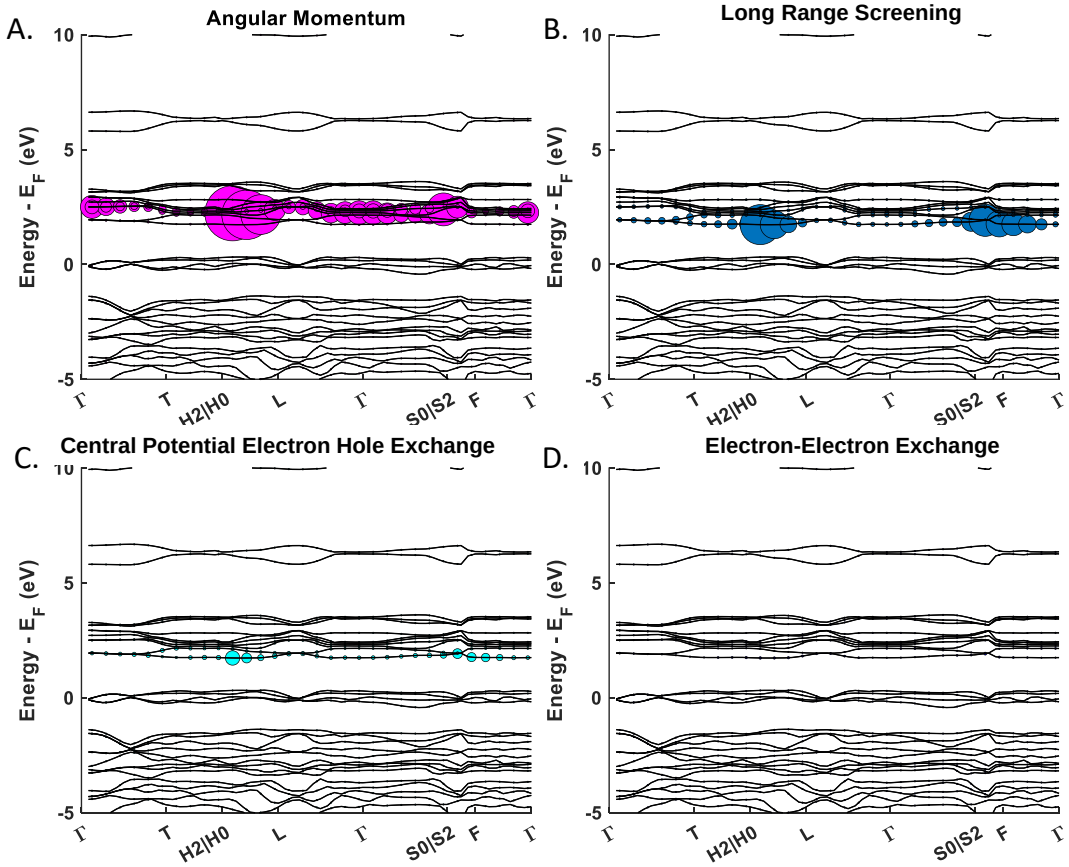

Figure C46. XUV transition Hamiltonian Decomposition of Core-Valence Exciton for the Ground State of Fe_2O_3. The (a) angular momentum, (b) core-hole screening, (c) electron-hole exchange, and (d) electron-electron exchange core-valence exciton densities are calculated and normalized to determine the relative contribution of each of these processes to the overall XUV exciton and thus absorption spectrum.

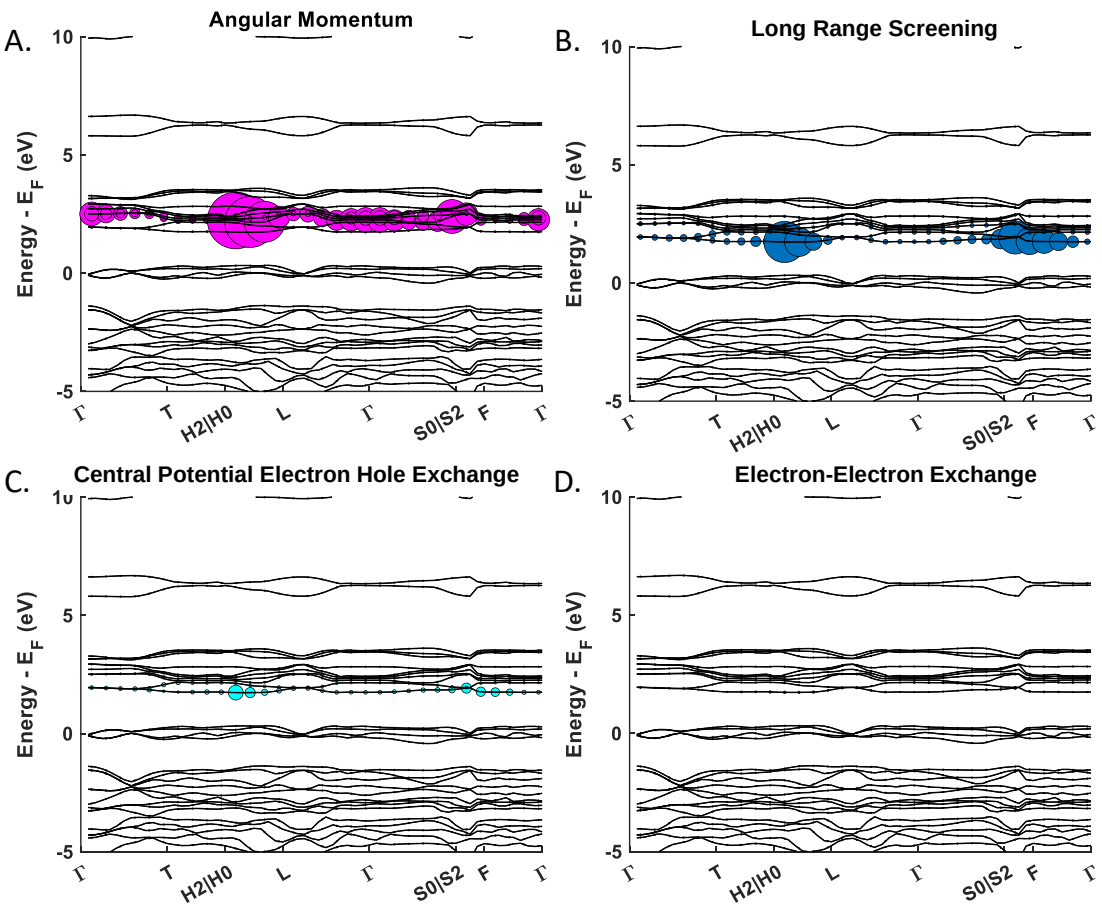

Figure C47. XUV transition Hamiltonian Decomposition of Core-Valence Exciton for the State Filling State of Fe_2O_3. The (a) angular momentum, (b) core-hole screening, (c) electron-hole exchange, and (d) electron-electron exchange core-valence exciton densities are calculated and normalized to determine the relative contribution of each of these processes to the overall XUV exciton and thus absorption spectrum.

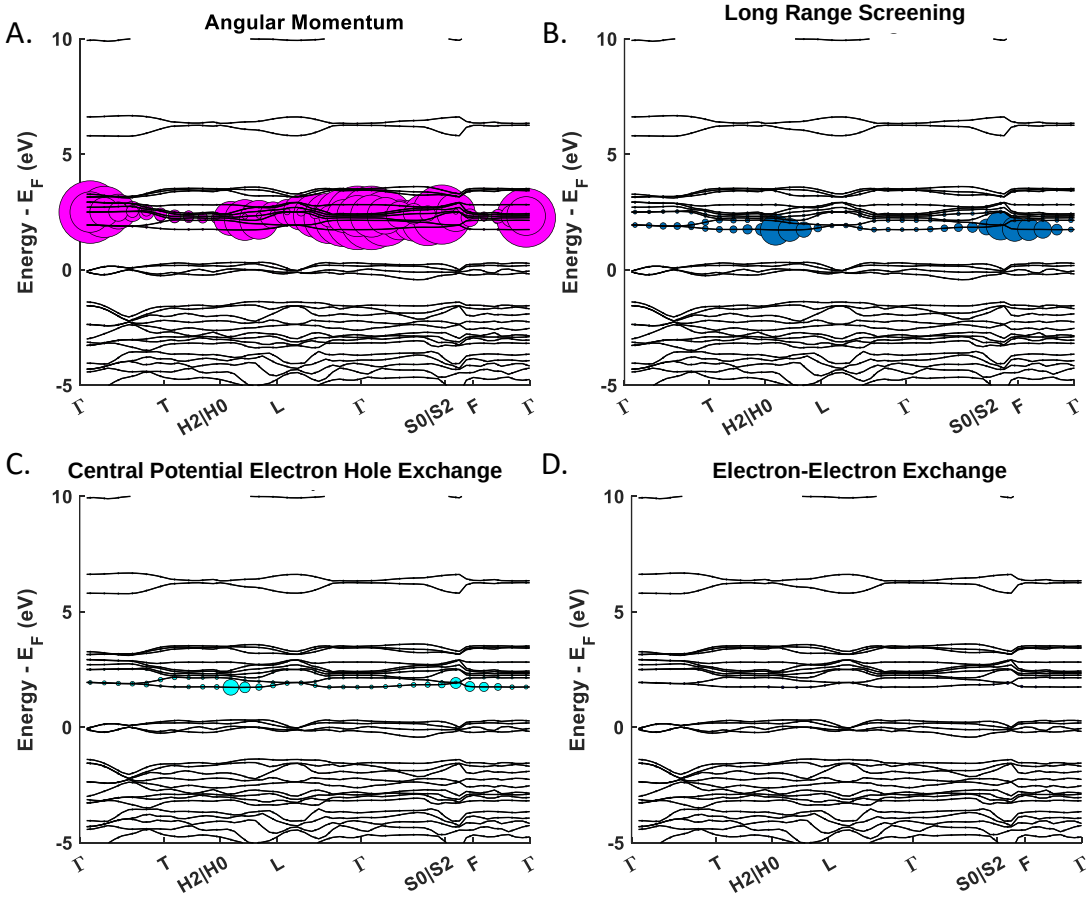

Figure C48. XUV transition Hamiltonian Decomposition of Core-Valence Exciton for the Thermally Expanded State of Fe_2O_3. The (a) angular momentum, (b) core-hole screening, (c) electron-hole exchange, and (d) electron-electron exchange core-valence exciton densities are calculated and normalized to determine the relative contribution of each of these processes to the overall XUV exciton and thus absorption spectrum.

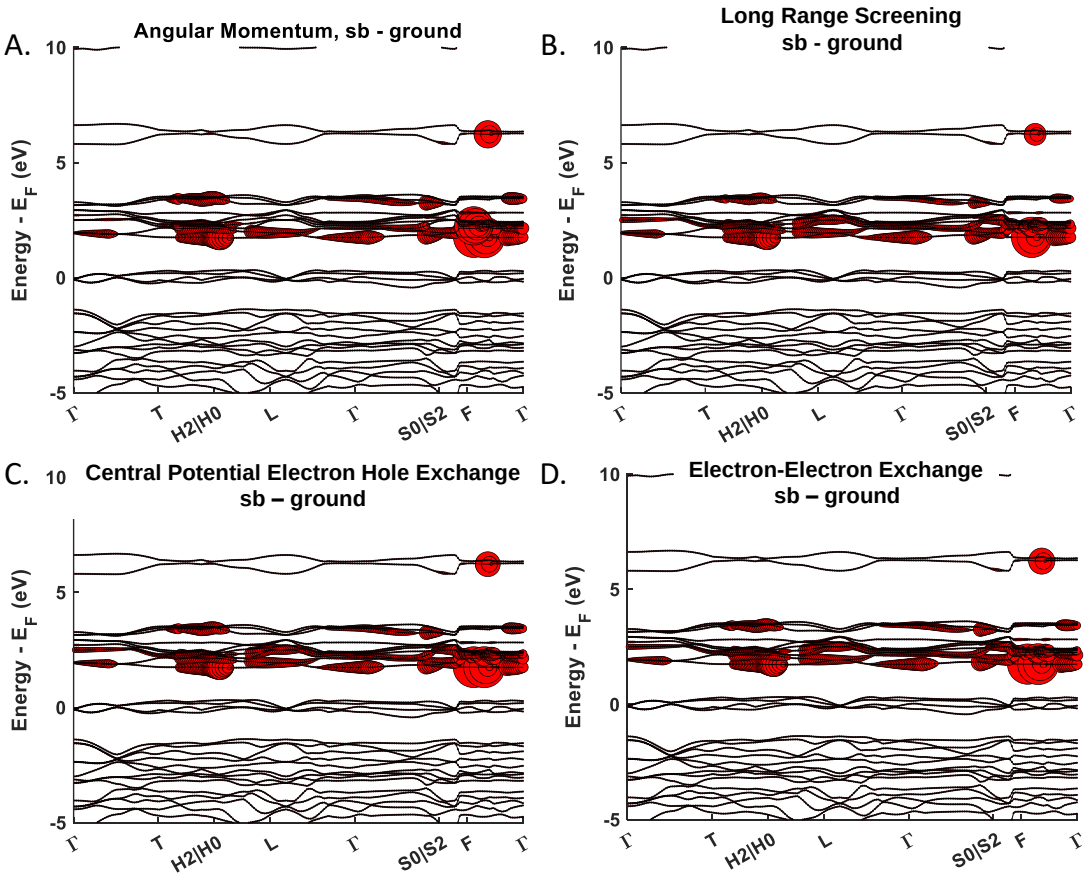

Figure C49. Differential XUV transition Hamiltonian Decomposition of Core-Valence Exciton for the State-Filling Excited State of Fe_2O_3. The magnitude of the state-filling minus the ground state components for the (a) angular momentum, (b) core-hole screening, (c) electron-hole exchange, and (d) electron-electron exchange core-valence exciton densities are calculated and normalized to determine the relative contribution of each of these processes to excited state effects.

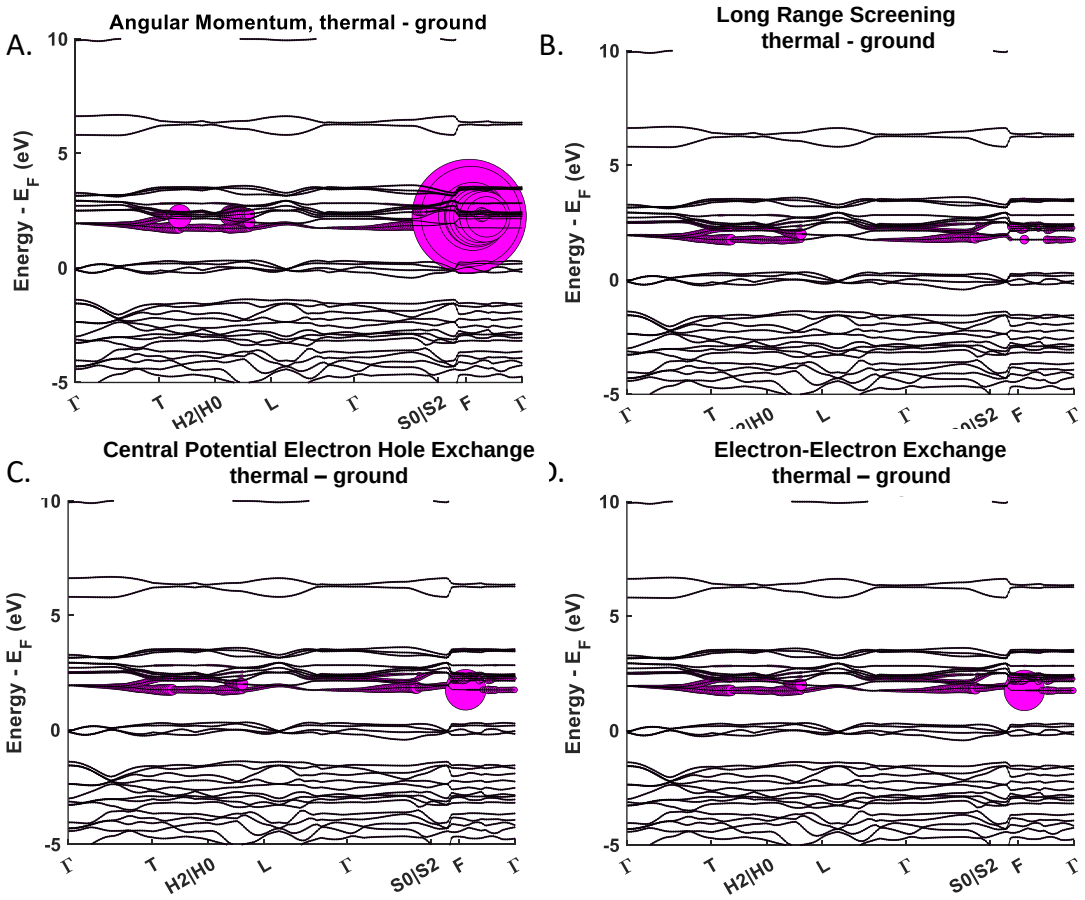

Figure C50. Differential XUV transition Hamiltonian Decomposition of Core-Valence Exciton for the Thermally Expanded Excited State of Fe_2O_3. The magnitude of the state-filling minus the ground state components for the (a) angular momentum, (b) core-hole screening, (c) electron-hole exchange, and (d) electron-electron exchange core-valence exciton densities are calculated and normalized to determine the relative contribution of each of these processes to excited state effects.

C6. Co_3O_4

a. Structural Data for Calculations

i. Ground State and State Blocking

Unit Cell Parameters (bohr)

{11.221 11.221 11.221 }

Primitive Vectors

{0.0 0.5 0.5

0.5 0.0 0.5

0.5 0.5 0.0}

Reduced coordinates, (x, y, z)

Co1 0.125 0.125 0.125

Co1 0.875 0.875 0.875

Co1 0.500 0.500 0.500

Co2 0.500 0.500 0.000

Co2 0.500 0.000 0.500

Co2 0.000 0.500 0.500

O 0.2642 0.2642 0.2642

O 0.2642 0.2642 -0.2926

O 0.2642 -0.2926 0.2642

O -0.2926 0.2642 0.2642

O -0.2642 -0.2642 1.2926

O -0.2642 -0.2642 -0.2642

O -0.2642 1.2926 -0.2642

O 1.2926 -0.2642 -0.2642

ii. Thermally Expanded Lattice

Unit Cell Parameters (bohr)

{11.258 11.258 11.258 }

Primitive Vectors

{0.0 0.5 0.5

0.5 0.0 0.5

0.5 0.5 0.0}

Reduced coordinates, (x, y, z)

Co1 0.125 0.125 0.125

Co1 0.875 0.875 0.875

Co1 0.500 0.500 0.500

Co2 0.500 0.500 0.000

Co2 0.500 0.000 0.500

Co2 0.000 0.500 0.500

O 0.2642 0.2642 0.2642

O 0.2642 0.2642 -0.2926

O 0.2642 -0.2926 0.2642

O -0.2926 0.2642 0.2642

O -0.2642 -0.2642 1.2926

O -0.2642 -0.2642 -0.2642

O -0.2642 1.2926 -0.2642

O 1.2926 -0.2642 -0.2642

b. Ground State Calculations

i. Band Structure and DOS

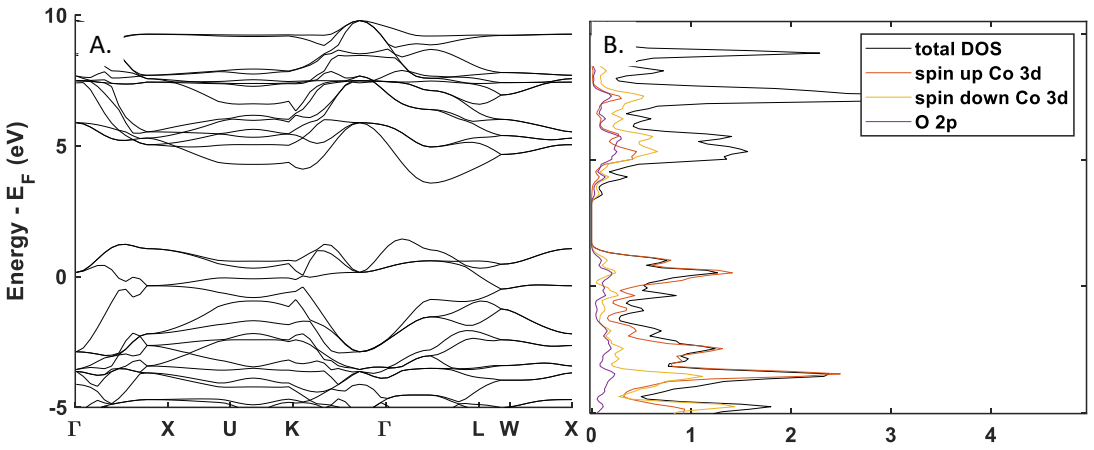

Figure C51. Ground State DFT Outputs for Co_3O_4. (a) Ground state band structure with the Fermi energy set to 0 eV. (b) Ground state total density of states in black and important orbital contributions around the Fermi energy are shown in color. No scissor shift has been included in these calculations.

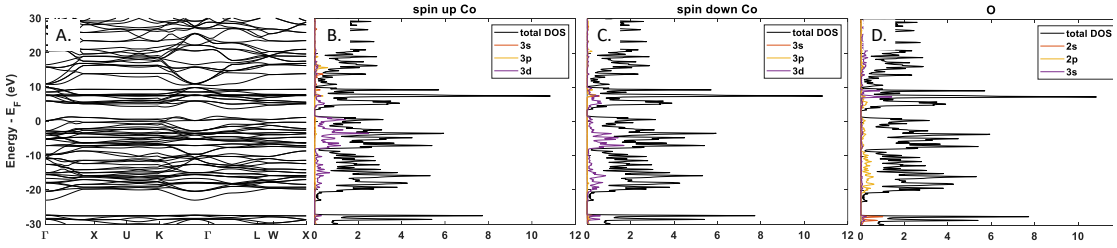

Figure C52. Ground State DFT Outputs for Co_3O_4. (a) Overall ground state band structure with the Fermi energy set to 0 eV. (b) Overall ground state total density of states in black and spin up Co partial DOS decomposed into 3s, 3p, and 3d orbital contributions. (c) Overall ground state total density of states in black and spin down Co partial DOS decomposed into 3s, 3p, and 3d orbital contributions. (d) Overall ground state total density of states in black and O partial DOS decomposed into 2s, 2p, and 3s orbital contributions No scissor shift has been included in these calculations.

ii. Ground State Spectrum[160]

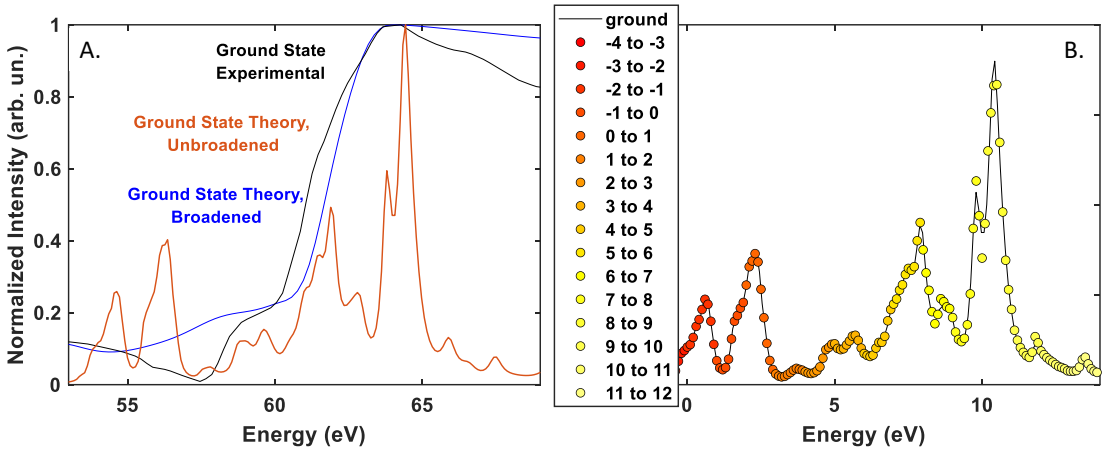

Figure C53. Ground State $M_{2,3}$ edge Absorption Spectrum. (a) The experimental (black), OCEAN calculated unbroadened (orange), and OCEAN calculated with energy-dependent broadening (blue) spectra are compared. (b) Energy-resolved exciton densities overlaid on the calculated XUV absorption spectrum around the Fermi level and the Co $M_{2,3}$ edge.

iii. Ground State GMRES Energy Decomposition

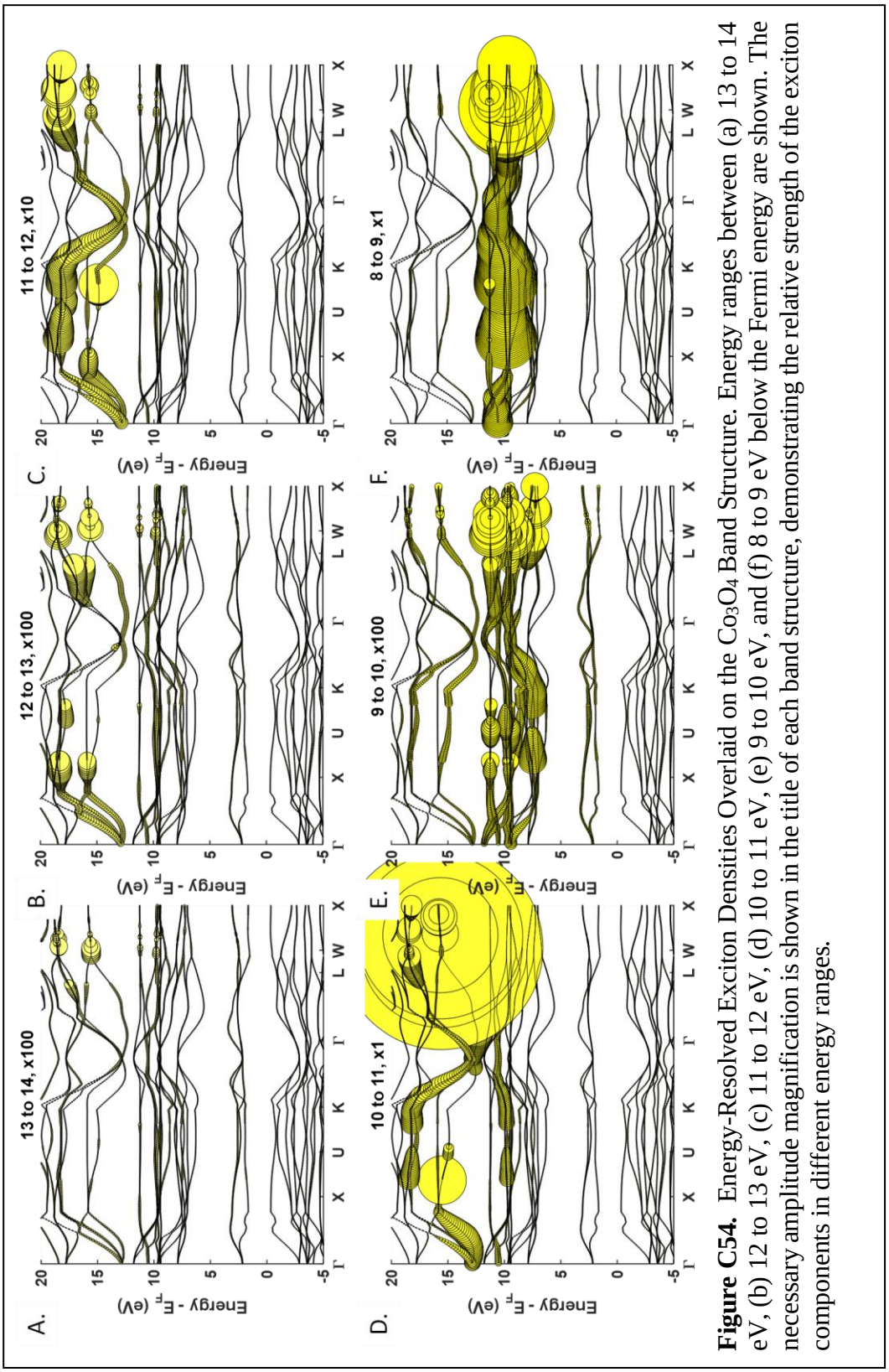

Figure C54. Energy-Resolved Exciton Densities Overlaid on the Co_3O_4 Band Structure. Energy ranges between (a) 13 to 14 eV, (b) 12 to 13 eV, (c) 11 to 12 eV, (d) 10 to 11 eV, (e) 9 to 10 eV, and (f) 8 to 9 eV below the Fermi energy are shown. The necessary amplitude magnification is shown in the title of each band structure, demonstrating the relative strength of the exciton components in different energy ranges.

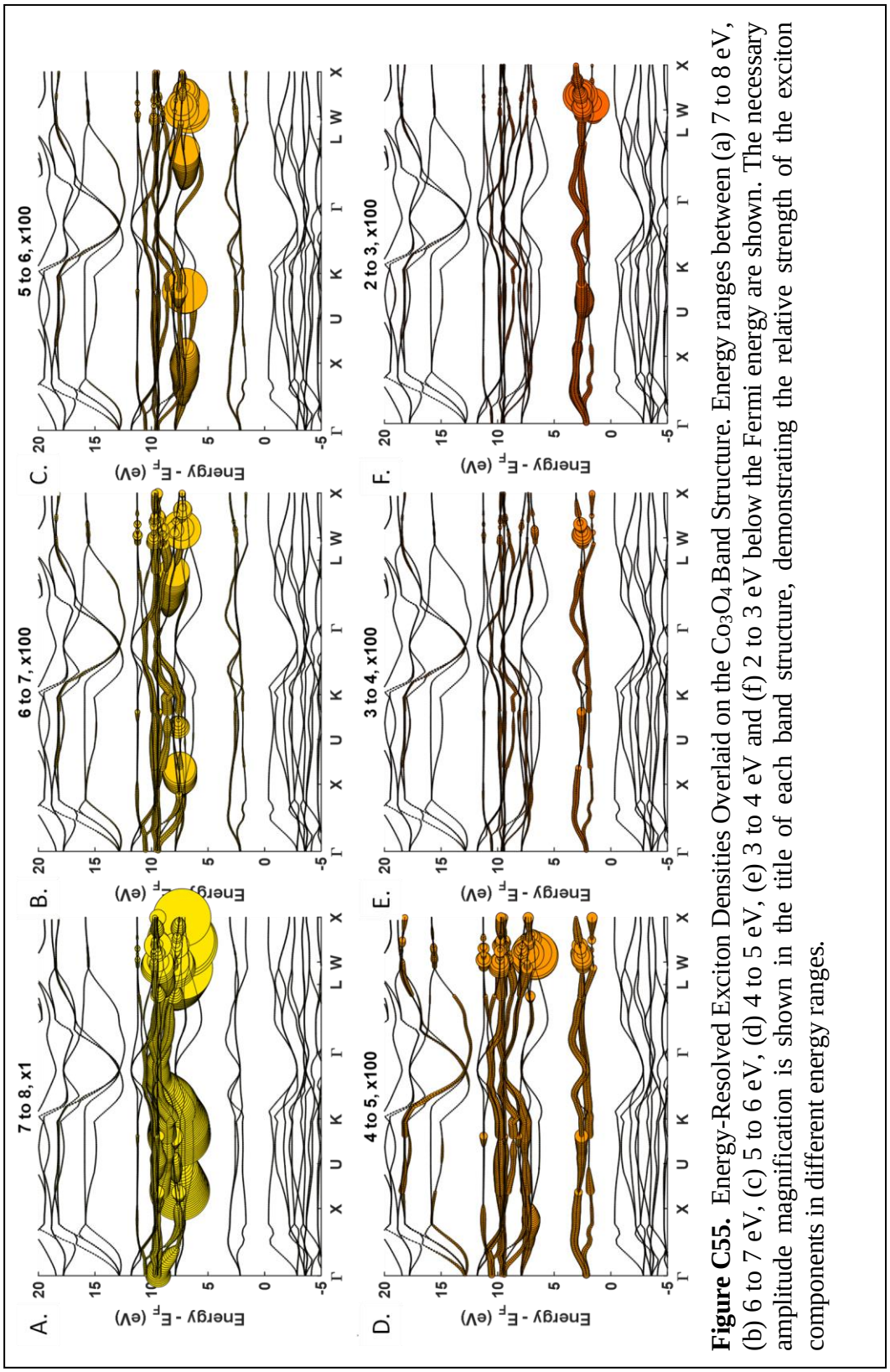

Figure C55. Energy-Resolved Exciton Densities Overlaid on the Co_3O_4 Band Structure. Energy ranges between (a) 7 to 8 eV, (b) 6 to 7 eV, (c) 5 to 6 eV, (d) 4 to 5 eV, (e) 3 to 4 eV and (f) 2 to 3 eV below the Fermi energy are shown. The necessary amplitude magnification is shown in the title of each band structure, demonstrating the relative strength of the exciton components in different energy ranges.

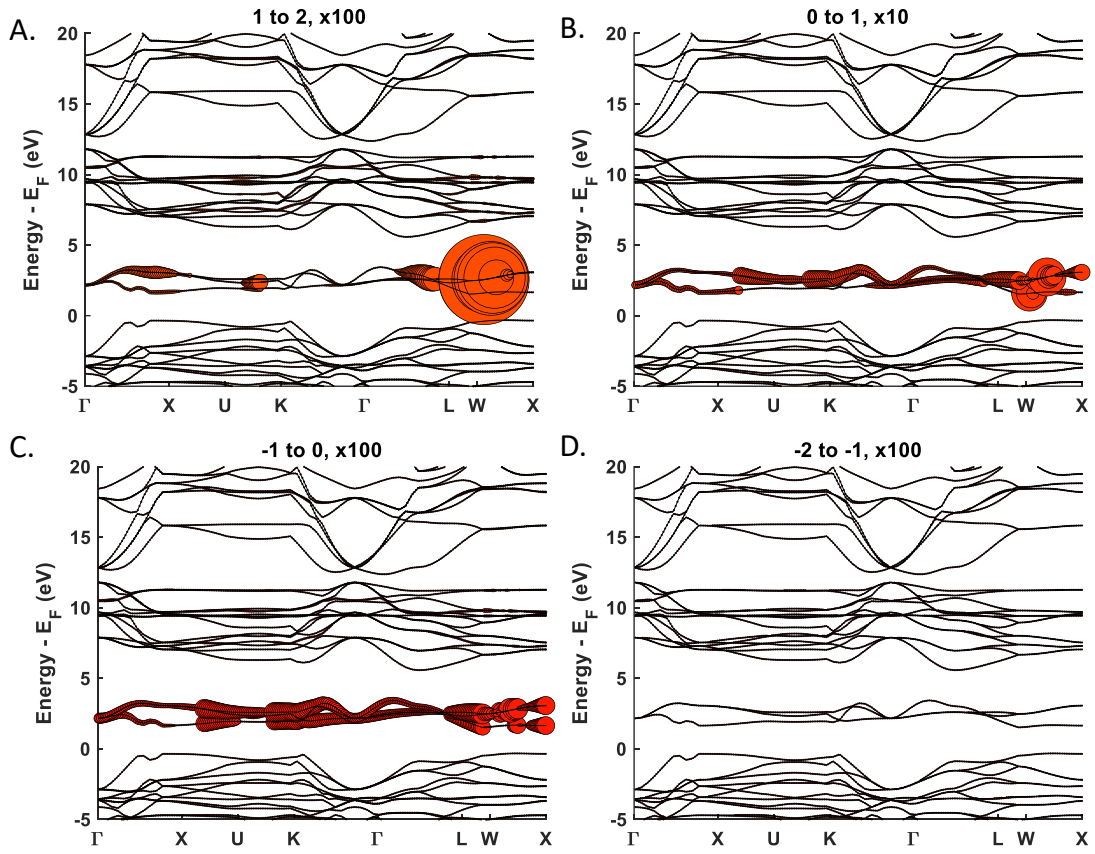

Figure C56. Energy-Resolved Exciton Densities Overlaid on the Co_3O_4 Band Structure. Energy ranges between (a) 1 to 2 eV, (b) 0 to 1 eV, (c) -1 to 0 eV and (d) -2 to -1 eV below the Fermi energy are shown. The necessary amplitude magnification is shown in the title of each band structure, demonstrating the relative strength of the exciton components in different energy ranges.

c. Excited State Calculations

i. State filling band diagrams and Full Spectra

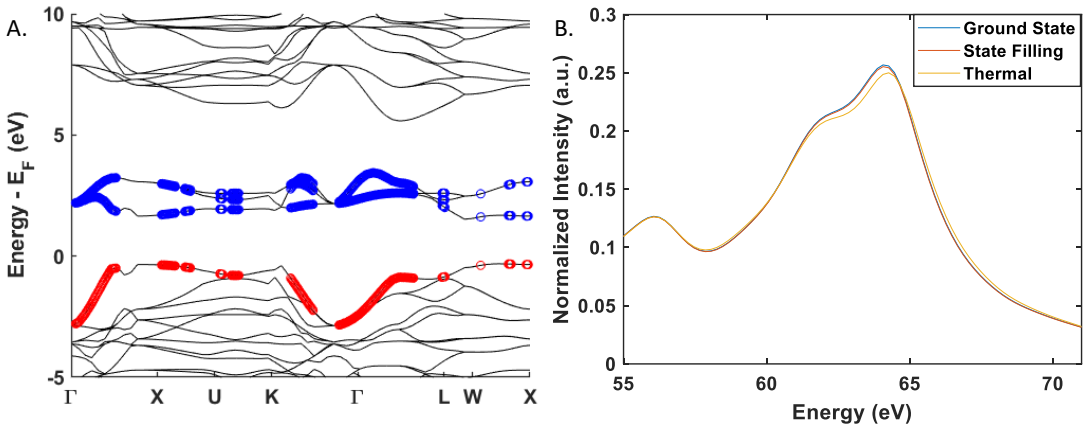

Figure C57. Excited State $M_{2,3}$ edge Absorption Spectrum. (a) State filling occupation used to model charge-transfer where the blue circles indicate electron occupation and red circles indicate holes overlaid on the band structure in black. (b) Broadened spectra for the ground state (blue), state filling (orange), and thermal expansion (yellow).

d. Hamiltonian Decompositions

i. Total Exciton Comparisons

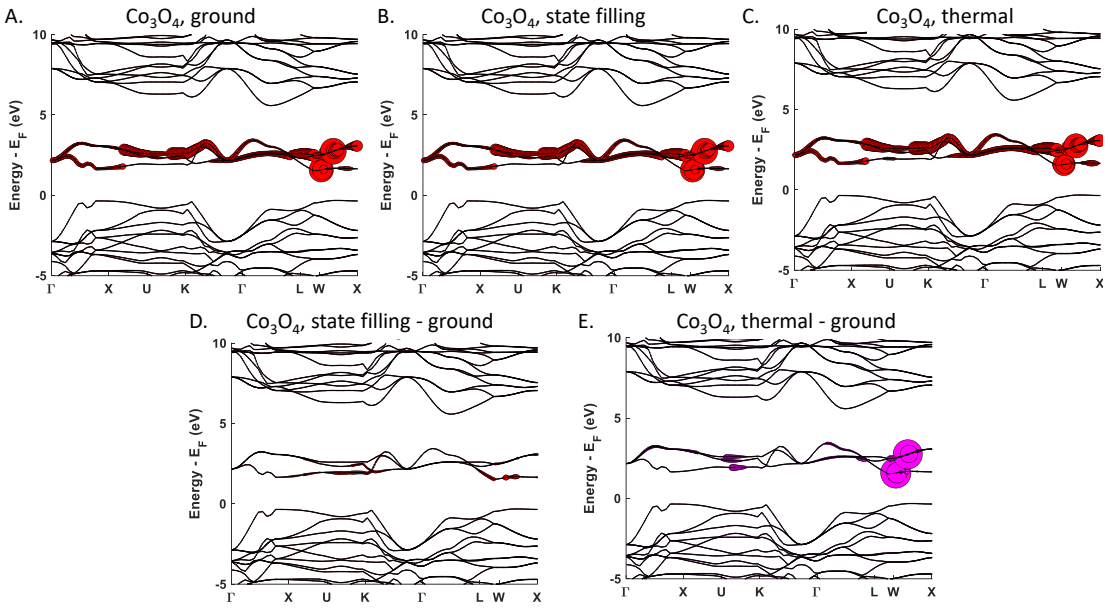

Figure C58. Total Core-Valence Exciton Densities. (a) Ground, (b) state filling, and (c) thermally expanded states' total core-valence exciton densities overlaid on the band structure of Co_3O_4. Differentials for the (d) state filling, and (e) thermally expanded excited states.

ii. Hamiltonian Decomposition of Exciton Components for ground, state filling, and thermally expanded models.

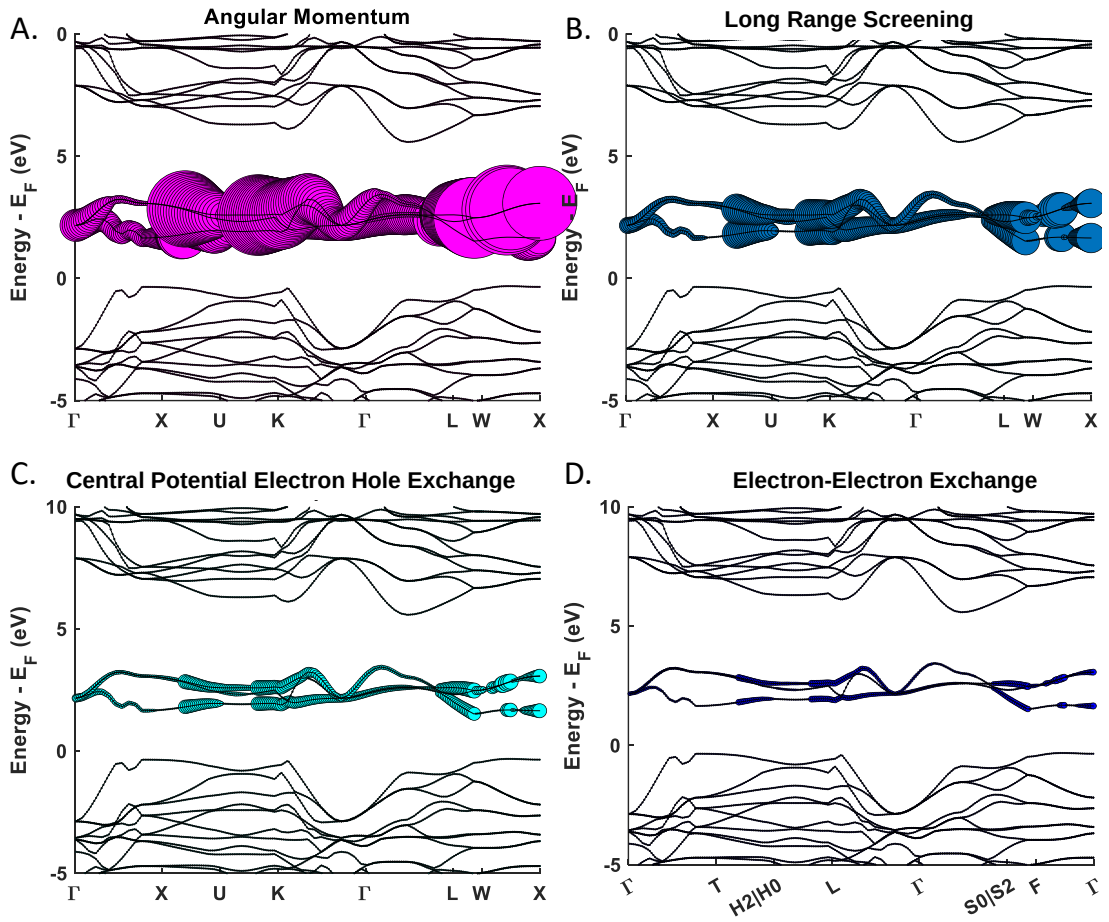

Figure C59. XUV transition Hamiltonian Decomposition of Core-Valence Exciton for the Ground State of Co_3O_4. The (a) angular momentum, (b) core-hole screening, (c) electron-hole exchange, and (d) electron-electron exchange core-valence exciton densities are calculated and normalized to determine the relative contribution of each of these processes to the overall XUV exciton and thus absorption spectrum.

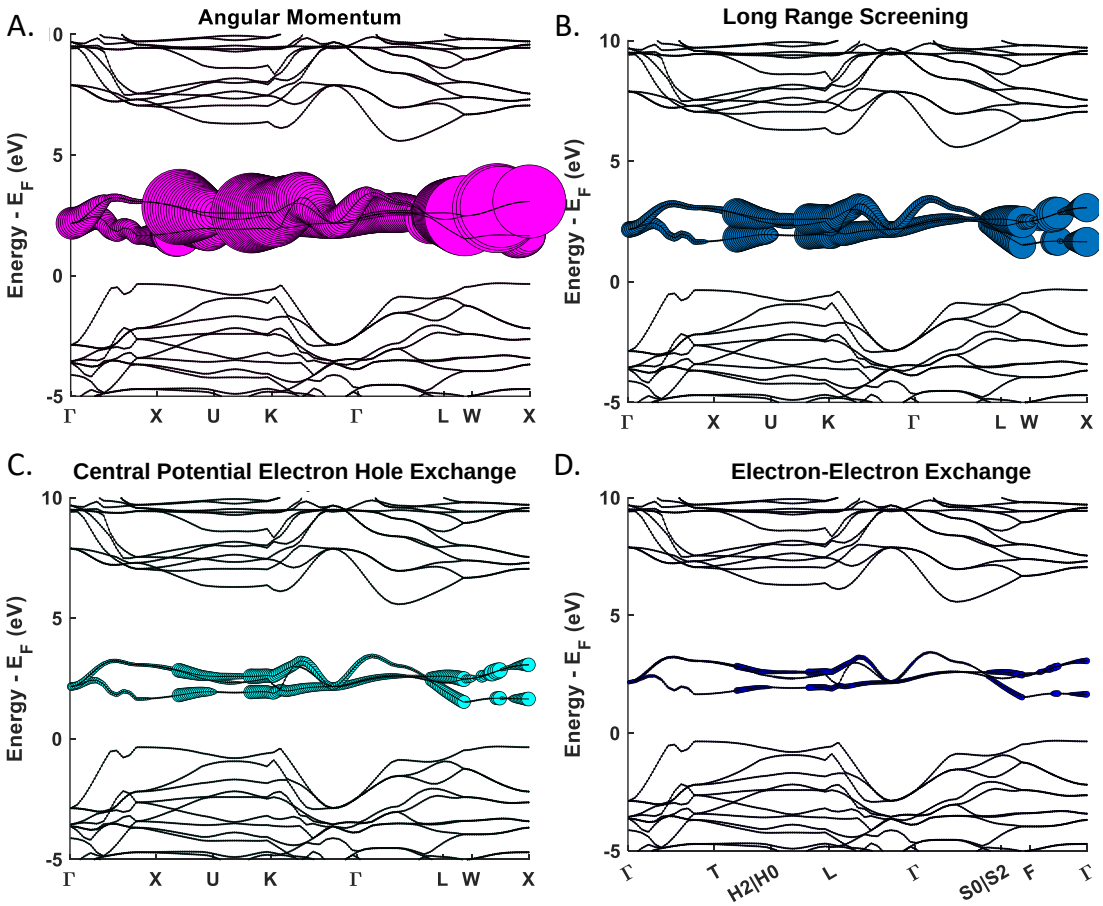

Figure C60. XUV transition Hamiltonian Decomposition of Core-Valence Exciton for the State Filling State of Co_3O_4. The (a) angular momentum, (b) core-hole screening, (c) electron-hole exchange, and (d) electron-electron exchange core-valence exciton densities are calculated and normalized to determine the relative contribution of each of these processes to the overall XUV exciton and thus absorption spectrum.

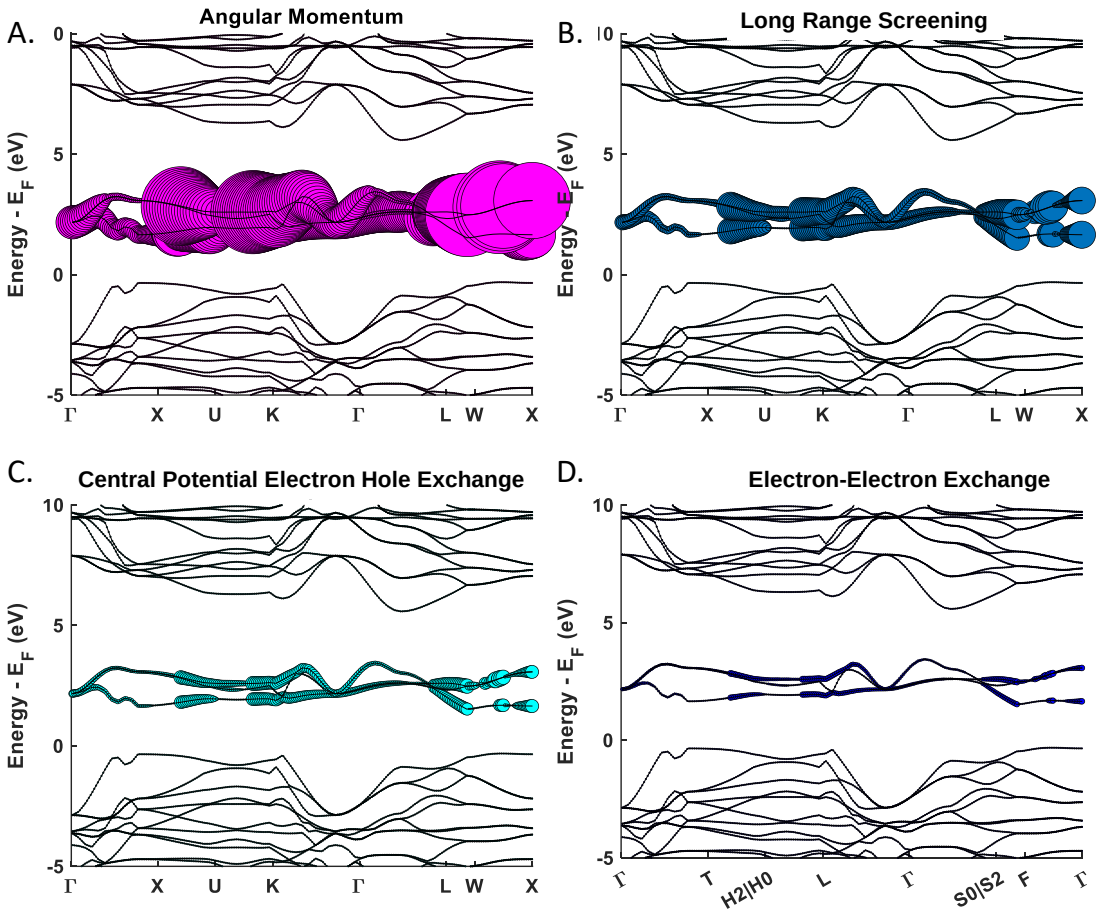

Figure C61. XUV transition Hamiltonian Decomposition of Core-Valence Exciton for the Thermally Expanded State of Co_3O_4. The (a) angular momentum, (b) core-hole screening, (c) electron-hole exchange, and (d) electron-electron exchange core-valence exciton densities are calculated and normalized to determine the relative contribution of each of these processes to the overall XUV exciton and thus absorption spectrum.

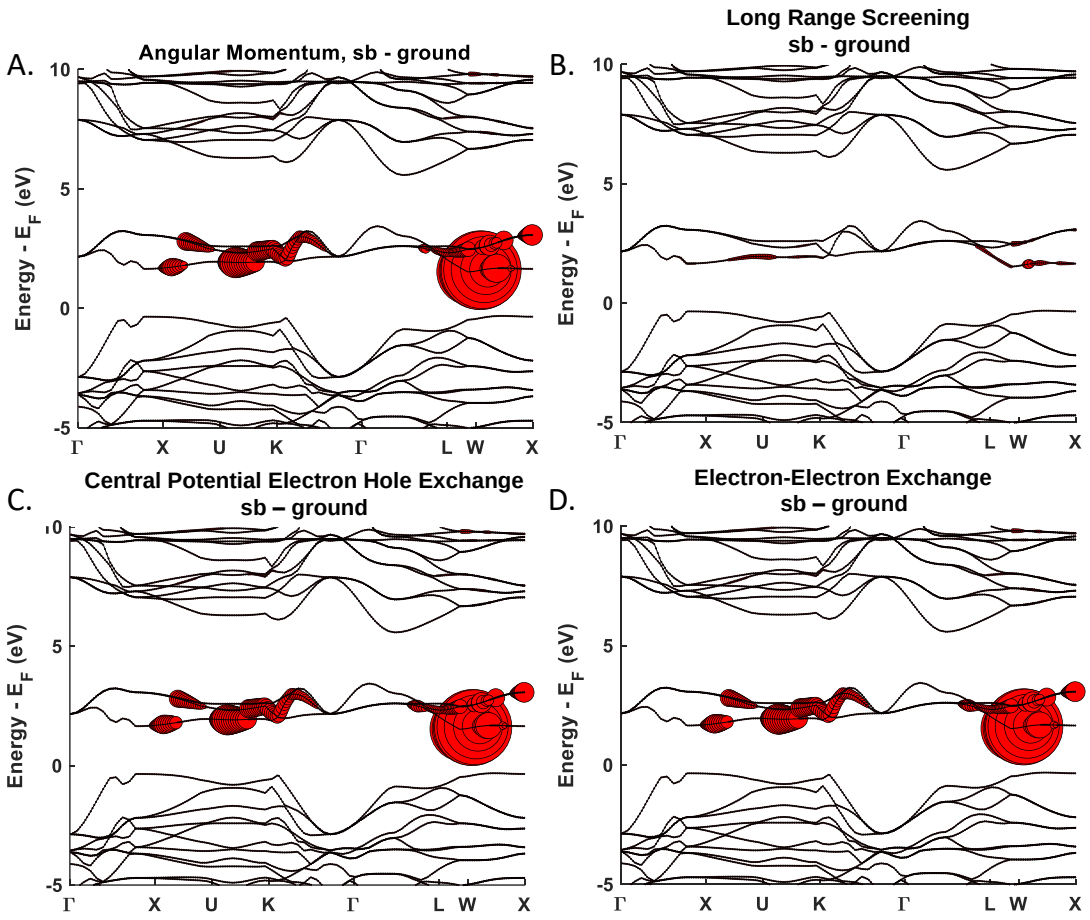

Figure C62. Differential XUV transition Hamiltonian Decomposition of Core-Valence Exciton for the State-Filling Excited State of Co_3O_4. The magnitude of the state-filling minus the ground state components for the (a) angular momentum, (b) core-hole screening, (c) electron-hole exchange, and (d) electron-electron exchange core-valence exciton densities are calculated and normalized to determine the relative contribution of each of these processes to excited state effects.

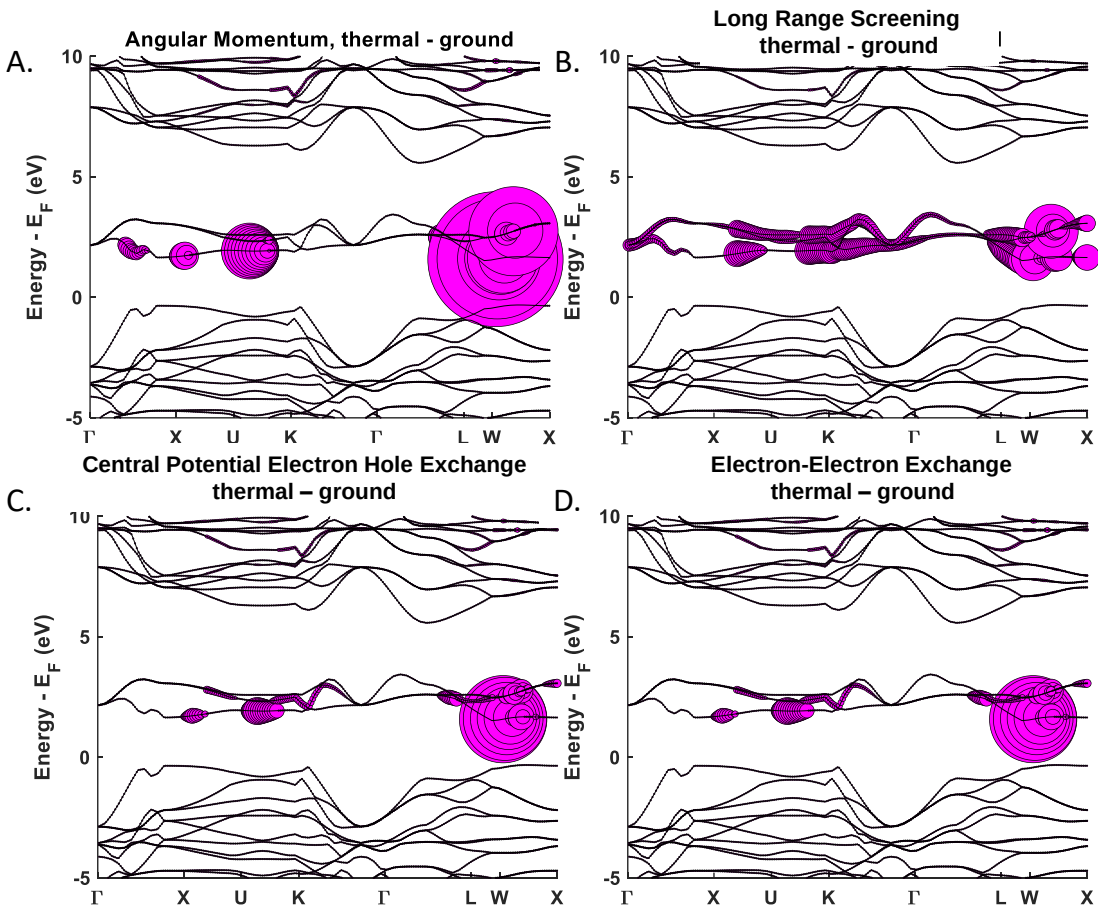

Figure C63. Differential XUV transition Hamiltonian Decomposition of Core-Valence Exciton for the Thermally Expanded Excited State of Co_3O_4. The magnitude of the state-filling minus the ground state components for the (a) angular momentum, (b) core-hole screening, (c) electron-hole exchange, and (d) electron-electron exchange core-valence exciton densities are calculated and normalized to determine the relative contribution of each of these processes to excited state effects.

C7. NiO

a. Structural Data for Calculations

i. Ground State and State Blocking

Unit Cell Parameters (bohr)

{7.9689 8.1564 8.1564}

Primitive Vectors

{0.0 0.5 0.5

0.5 0.0 0.5

0.5 0.5 0.0}

Reduced coordinates, (x, y, z)

Ni 0.5000 0.5000 0.5000

O 0.0000 0.0000 0.0000

ii. Thermally Expanded Lattice

Unit Cell Parameters (bohr)

{8.0646 8.254 8.254 }

Primitive Vectors

{0.0 0.5 0.5

0.5 0.0 0.5

0.5 0.5 0.0}

Reduced coordinates, (x, y, z)

Ni 0.5000 0.5000 0.5000

O 0.0000 0.0000 0.0000

b. Ground State Calculations

i. Band Structure and DOS

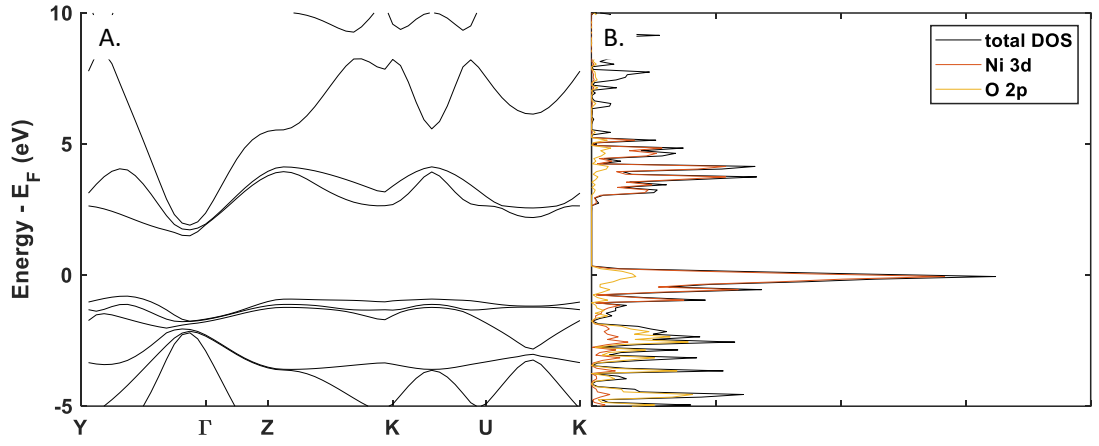

Figure C64. Ground State DFT Outputs for NiO. (a) Ground state band structure with the Fermi energy set to 0 eV. (b) Ground state total density of states in black and important orbital contributions around the Fermi energy are shown in color. No scissor shift has been included in these calculations.

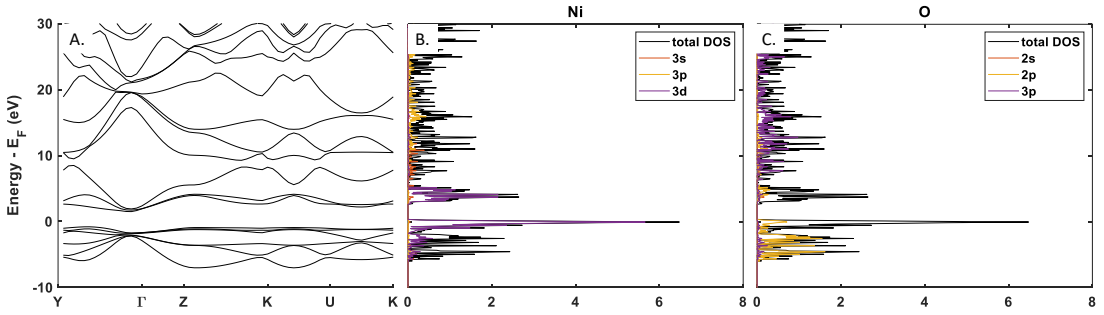

Figure C65. Ground State DFT Outputs for NiO. (a) Overall ground state band structure with the Fermi energy set to 0 eV. (b) Overall ground state total density of states in black and Ni partial DOS decomposed into 3s, 3p, and 3d orbital contributions. (c) Overall ground state total density of states in black and O partial DOS decomposed into 2s, 2p, and 3s orbital contributions No scissor shift has been included in these calculations.

ii. Ground State Spectrum[155]

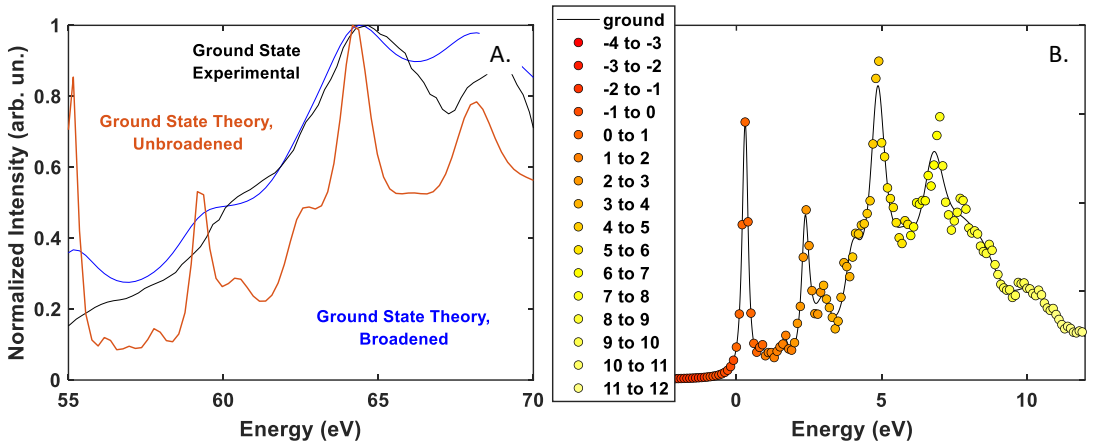

Figure C66. Ground State $M_{2,3}$ edge Absorption Spectrum. (a) The experimental (black), OCEAN calculated unbroadened (orange), and OCEAN calculated with energy-dependent broadening (blue) spectra are compared. (b) Energy-resolved exciton densities overlaid on the calculated XUV absorption spectrum around the Fermi level and the Ni $M_{2,3}$ edge.

iii. Ground State GMRES Energy Decomposition

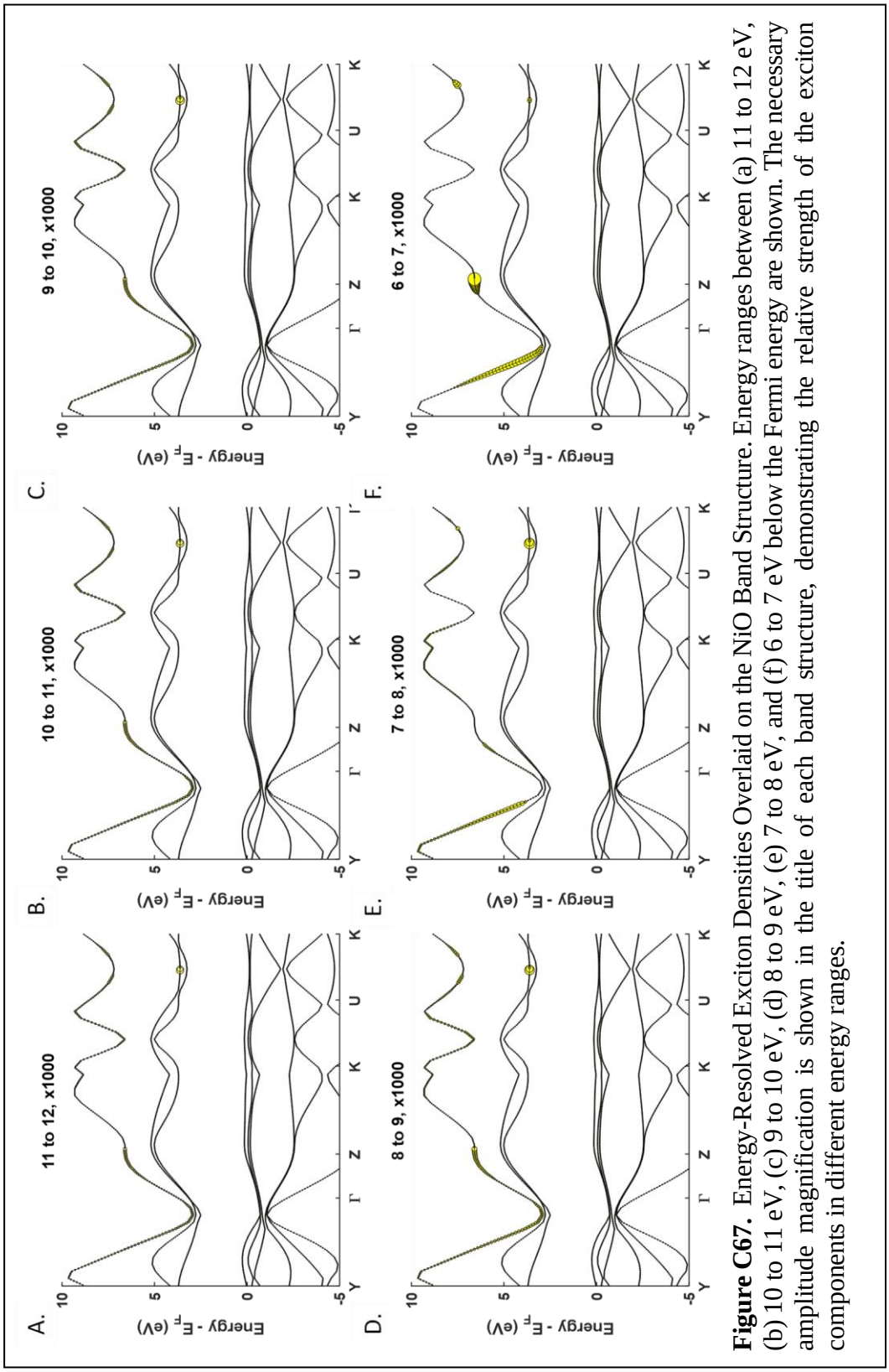

Figure C67. Energy-Resolved Exciton Densities Overlaid on the NiO Band Structure. Energy ranges between (a) 11 to 12 eV, (b) 10 to 11 eV, (c) 9 to 10 eV, (d) 8 to 9 eV, (e) 7 to 8 eV, and (f) 6 to 7 eV below the Fermi energy are shown. The necessary amplitude magnification is shown in the title of each band structure, demonstrating the relative strength of the exciton components in different energy ranges.

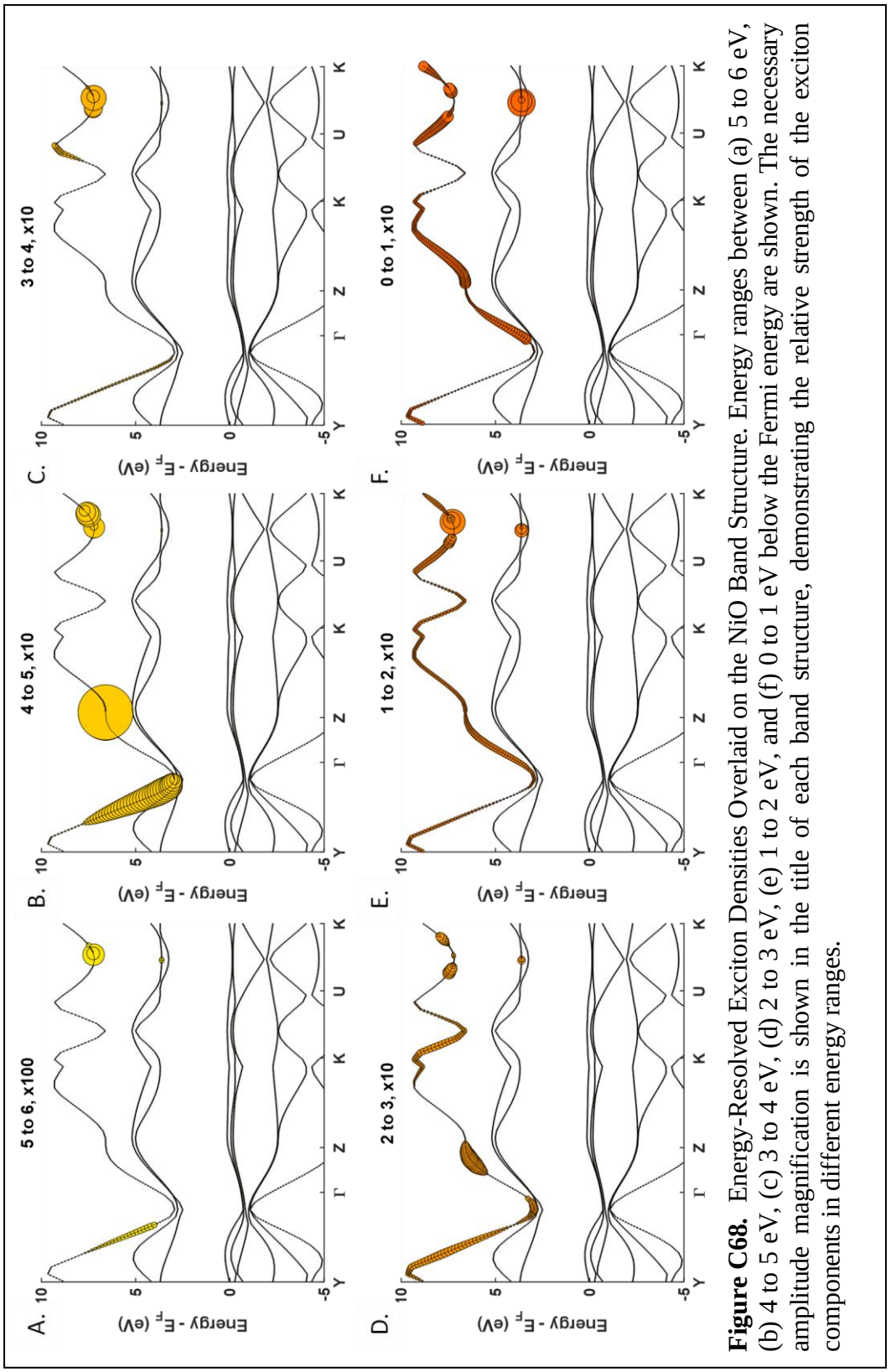

Figure C68. Energy-Resolved Exciton Densities Overlaid on the NiO Band Structure. Energy ranges between (a) 5 to 6 eV, (b) 4 to 5 eV, (c) 3 to 4 eV, (d) 2 to 3 eV, (e) 1 to 2 eV, and (f) 0 to 1 eV below the Fermi energy are shown. The necessary amplitude magnification is shown in the title of each band structure, demonstrating the relative strength of the exciton components in different energy ranges.

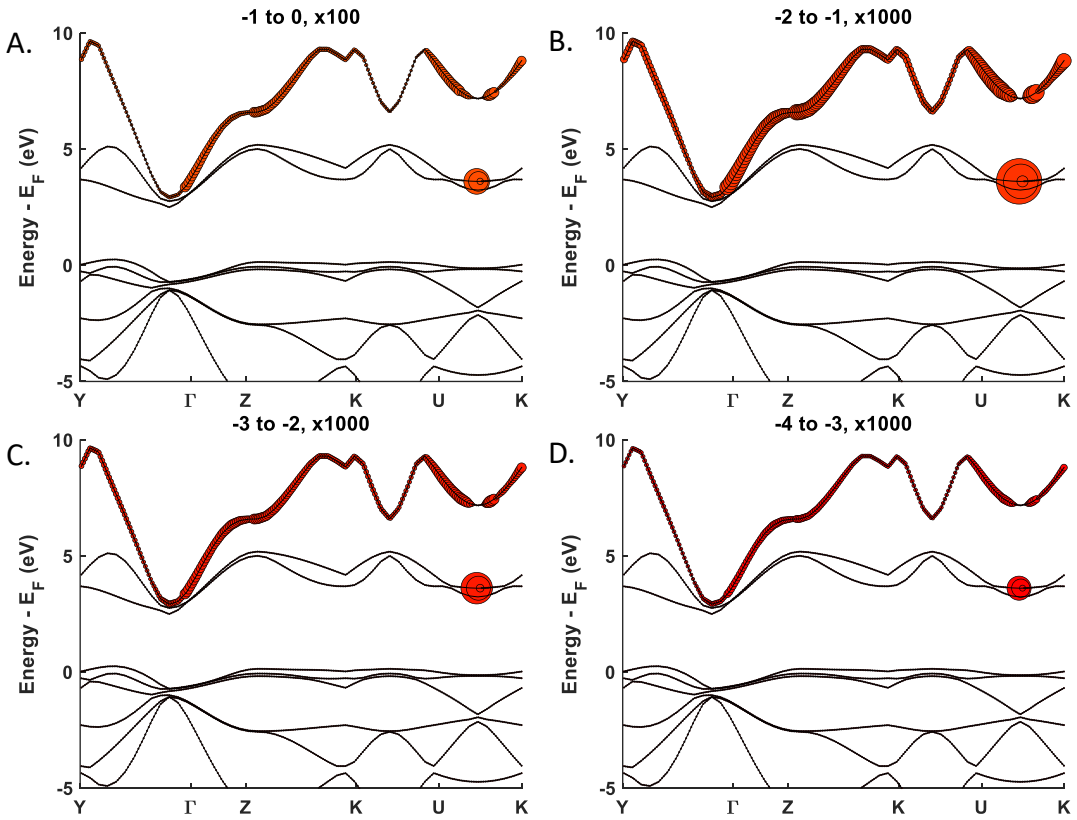

Figure C69. Energy-Resolved Exciton Densities Overlaid on the NiO Band Structure. Energy ranges between (a) -1 to 0 eV, (b) -2 to -1 eV, (c) -3 to -2 eV, and (d) -3 to -4 eV below the Fermi energy are shown. The necessary amplitude magnification is shown in the title of each band structure, demonstrating the relative strength of the exciton components in different energy ranges.

c. Excited State Calculations

i. State filling band diagrams and Full Spectra

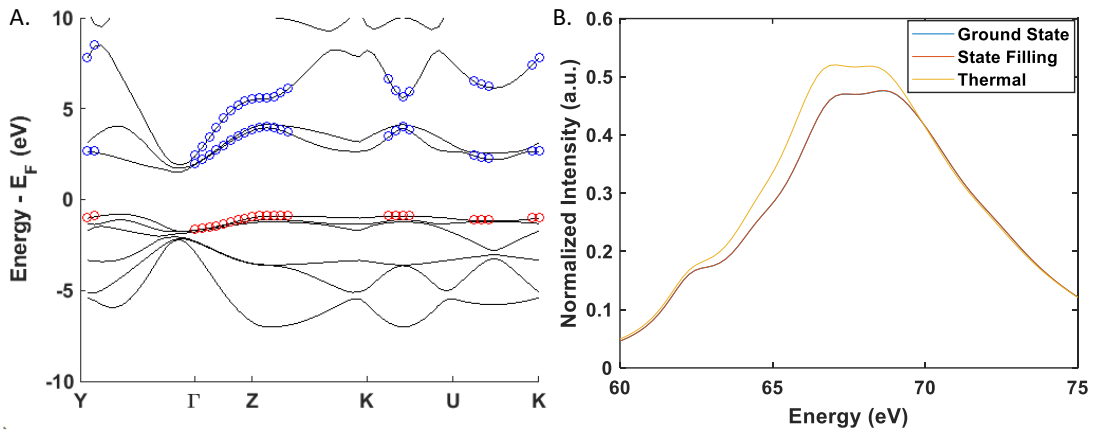

Figure C70. Excited State $M_{2,3}$ edge Absorption Spectrum. (a) State filling occupation used to model charge-transfer where the blue circles indicate electron occupation and red circles indicate holes overlaid on the band structure in black. (b) Broadened spectra for the ground state (blue), state filling (orange), and thermal expansion (yellow).

d. Hamiltonian Decompositions

i. Total Exciton Comparisons

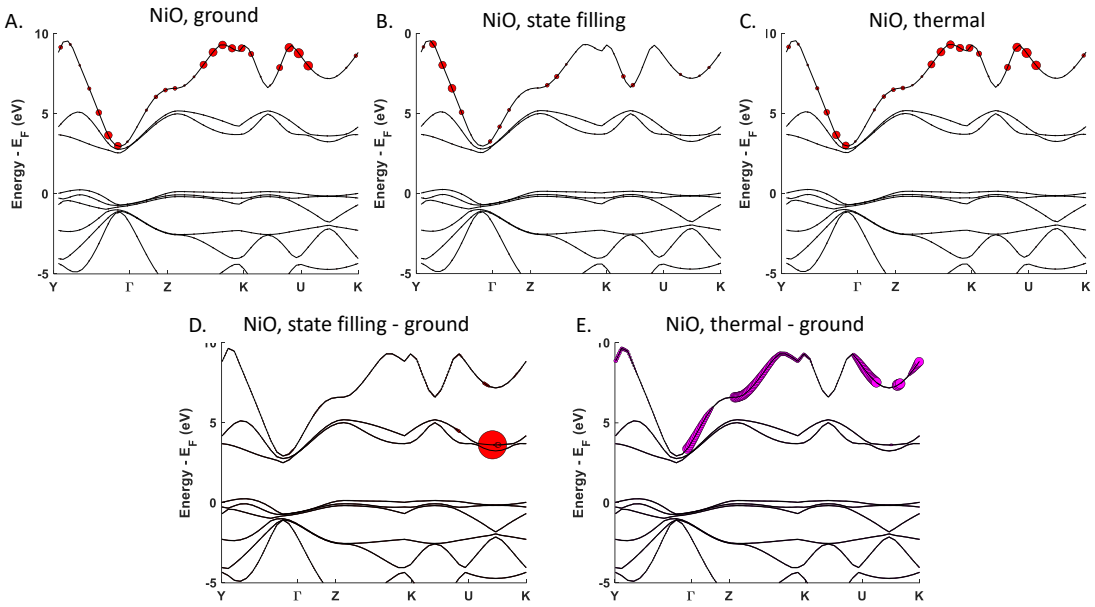

Figure C71. Total Core-Valence Exciton Densities. (a) Ground, (b) state filling, and (c) thermally expanded states' total core-valence exciton densities overlaid on the band structure of NiO. Differentials for the (d) state filling, and (e) thermally expanded excited states.

ii. Hamiltonian Decomposition of Exciton Components for ground, state filling, and thermally expanded model.

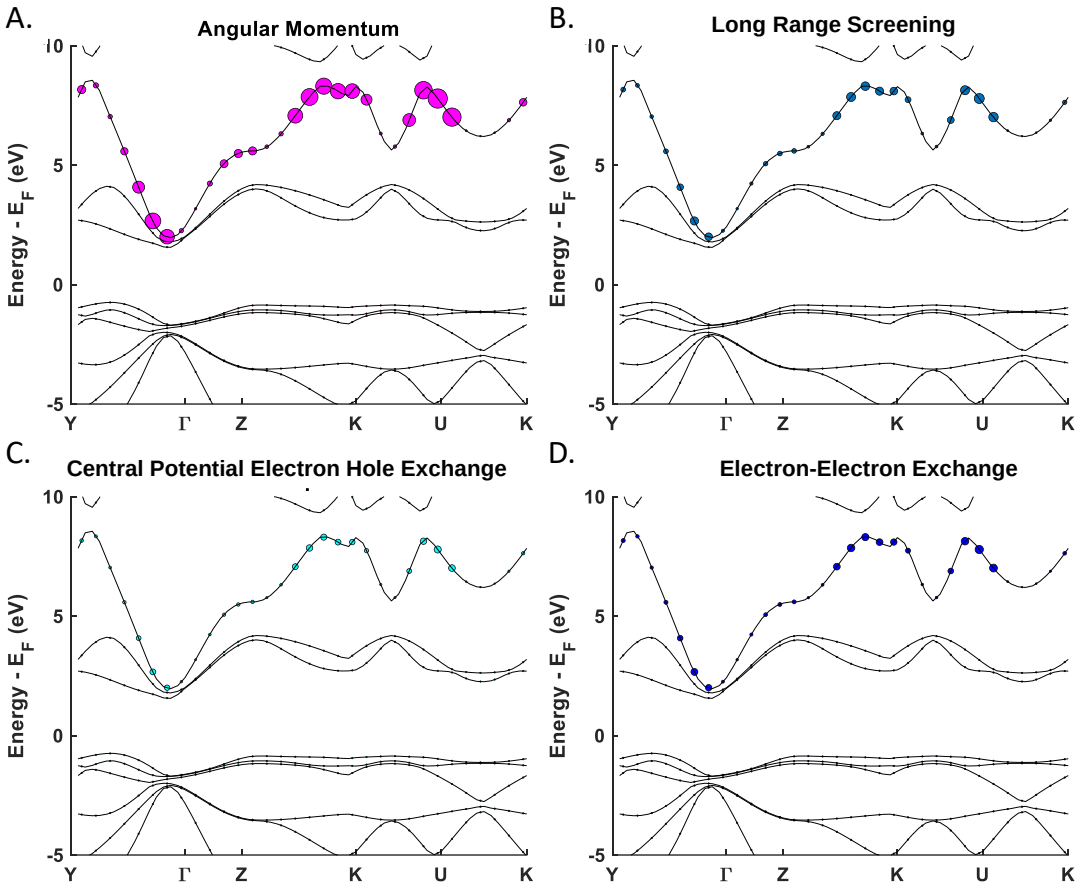

Figure C72. XUV transition Hamiltonian Decomposition of Core-Valence Exciton for the Ground State of NiO. The (a) angular momentum, (b) core-hole screening, (c) electron-hole exchange, and (d) electron-electron exchange core-valence exciton densities are calculated and normalized to determine the relative contribution of each of these processes to the overall XUV exciton and thus absorption spectrum.

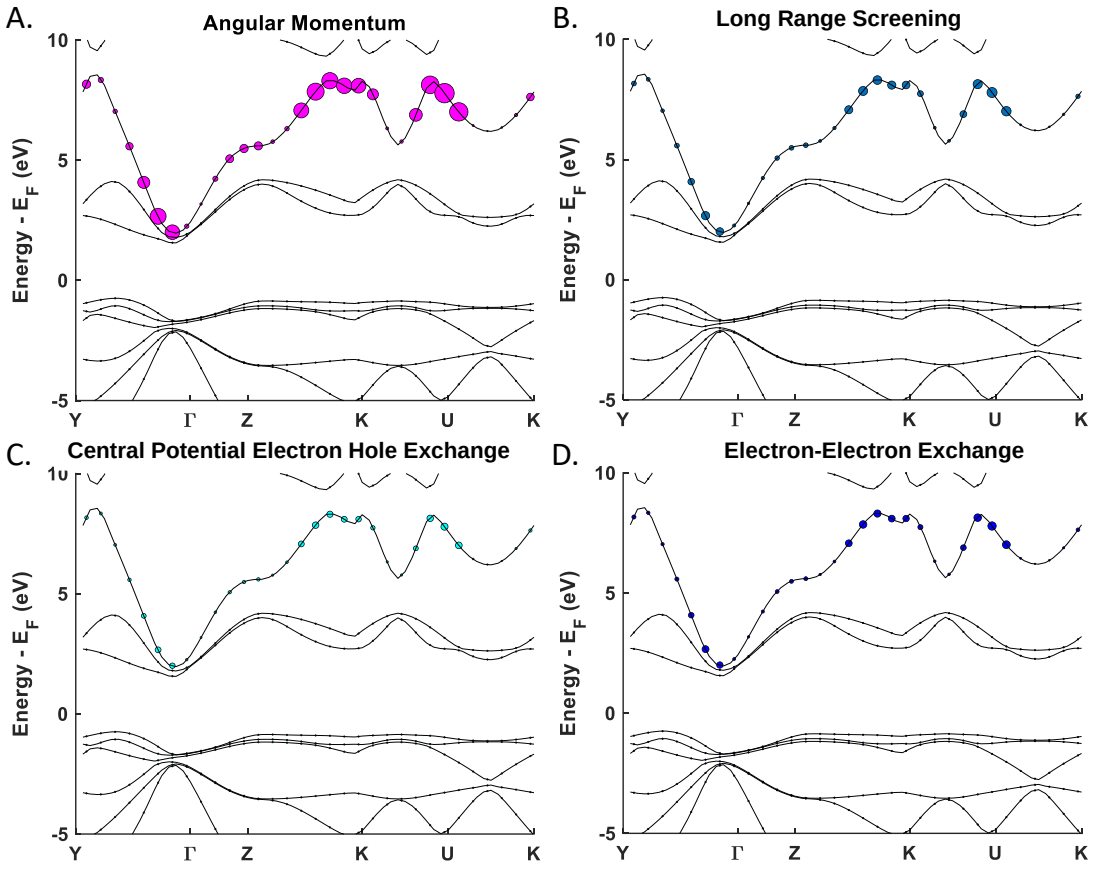

Figure C73. XUV transition Hamiltonian Decomposition of Core-Valence Exciton for the State Filling State of NiO. The (a) angular momentum, (b) core-hole screening, (c) electron-hole exchange, and (d) electron-electron exchange core-valence exciton densities are calculated and normalized to determine the relative contribution of each of these processes to the overall XUV exciton and thus absorption spectrum.

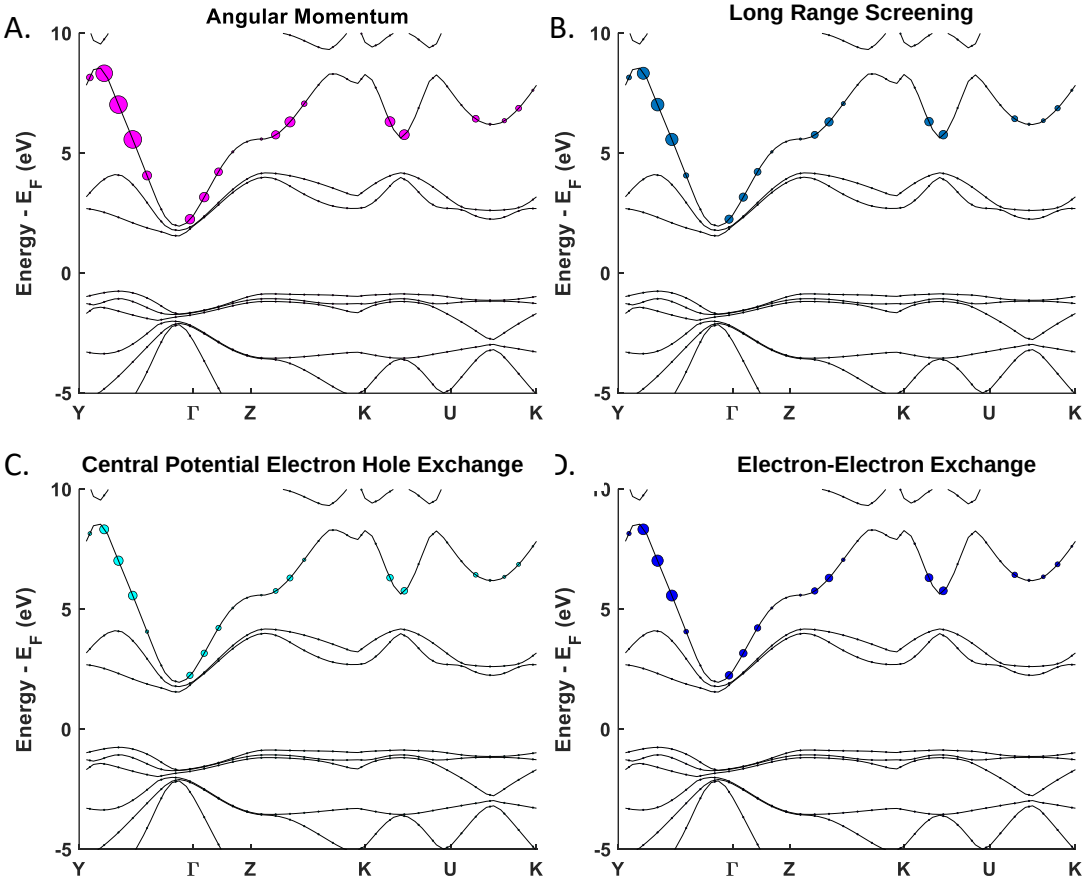

Figure C74. XUV transition Hamiltonian Decomposition of Core-Valence Exciton for the Thermally Expanded State of NiO. The (a) angular momentum, (b) core-hole screening, (c) electron-hole exchange, and (d) electron-electron exchange core-valence exciton densities are calculated and normalized to determine the relative contribution of each of these processes to the overall XUV exciton and thus absorption spectrum.

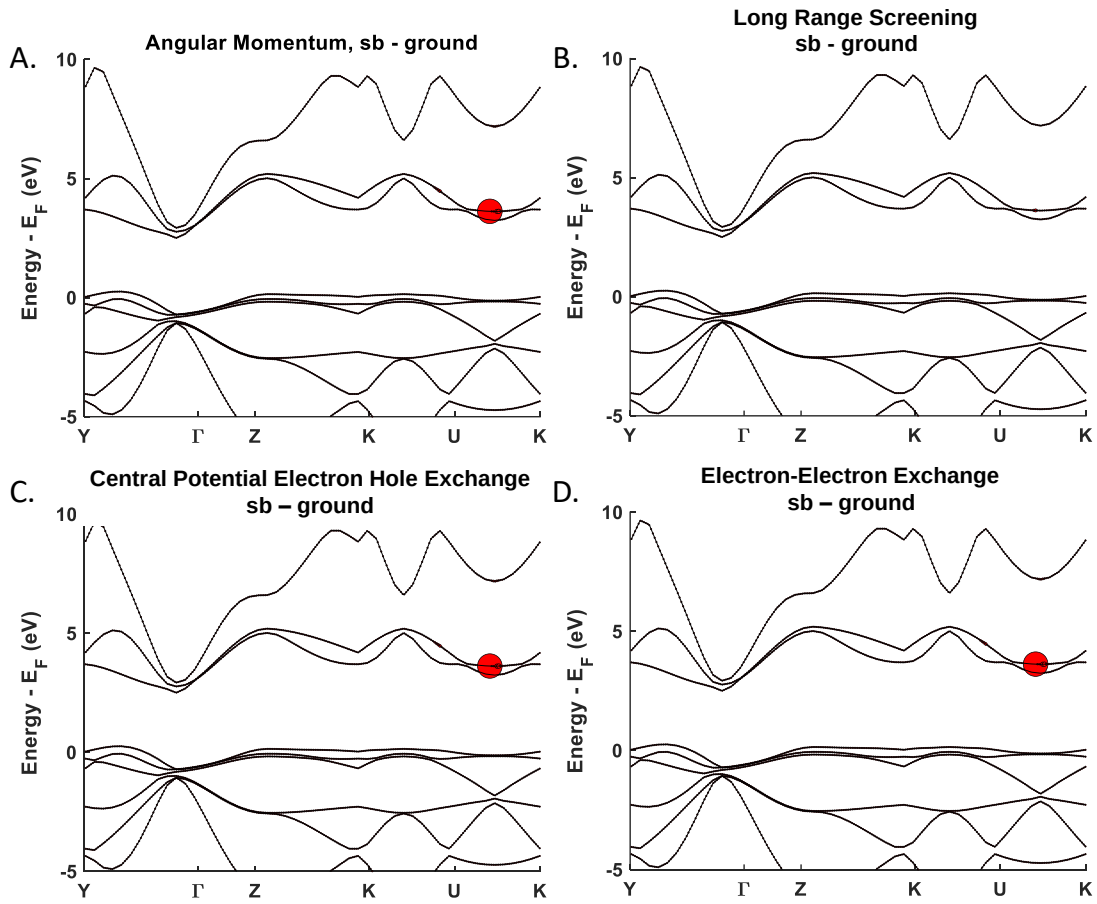

Figure C75. Differential XUV transition Hamiltonian Decomposition of Core-Valence Exciton for the State-Filling Excited State of NiO. The magnitude of the state-filling minus the ground state components for the (a) angular momentum, (b) core-hole screening, (c) electron-hole exchange, and (d) electron-electron exchange core-valence exciton densities are calculated and normalized to determine the relative contribution of each of these processes to excited state effects.

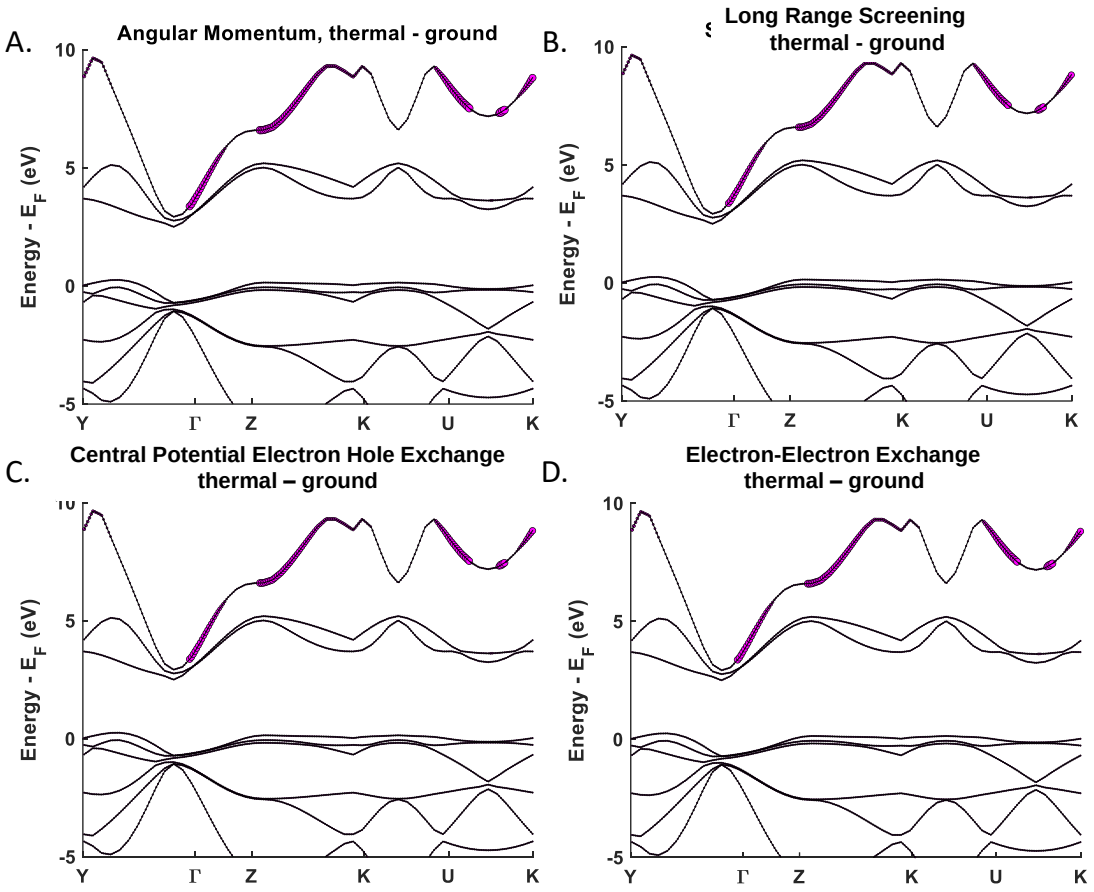

Figure C76. Differential XUV transition Hamiltonian Decomposition of Core-Valence Exciton for the Thermally Expanded Excited State of NiO. The magnitude of the state-filling minus the ground state components for The (a) angular momentum, (b) core-hole screening, (c) electron-hole exchange, and (d) electron-electron exchange core-valence exciton densities are calculated and normalized to determine the relative contribution of each of these processes to excited state effects.

C8. CuO

a. Structural Data for Calculations

i. Ground State and State Blocking

Unit Cell Parameters (bohr)

{7.9984 7.6543 9.7940}

Primitive Vector

{0.5 -0.5 0.1

0.5 0.5 0.1

-0.305 0 0.9784 }

Reduced coordinates, (x, y, z)

Cu 0.000000000 0.500000000 0.000000000

Cu 0.500000000 0.000000000 0.500000000

O 0.503680623 0.496319387 0.250000000

O 0.496319377 0.503680613 0.75000000

ii. Thermally Expanded Lattice

Unit Cell Parameters (bohr)

{8.0264 7.681 9.828}

Primitive Vector

{0.5 -0.5 0.1

0.5 0.5 0.1

-0.305 0 0.9784 }

Reduced coordinates, (x, y, z)

Cu 0.000000000 0.500000000 0.000000000

Cu 0.500000000 0.000000000 0.500000000

O 0.503680623 0.496319387 0.250000000

O 0.496319377 0.503680613 0.75000000

b. Ground State Calculations

i. Band Structure and DOS

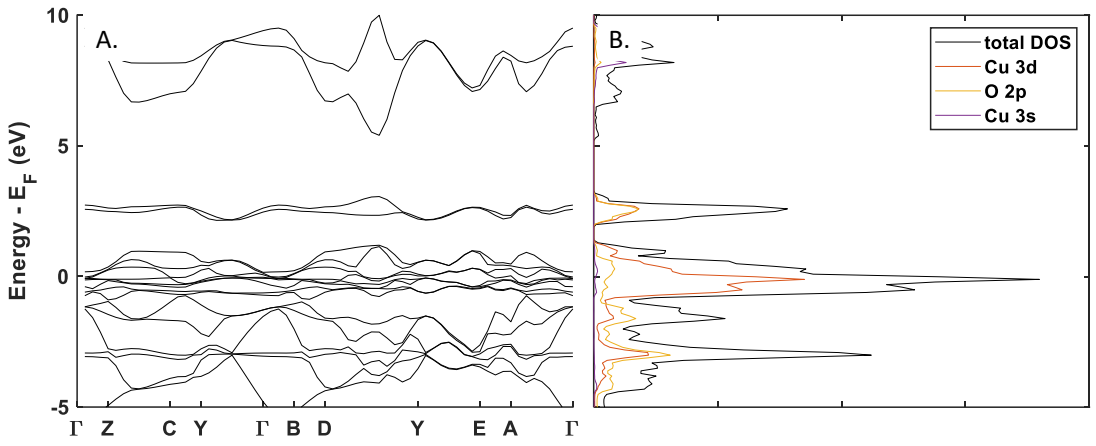

Figure C77. Ground State DFT Outputs for CuO. (a) Ground state band structure with the Fermi energy set to 0 eV. (b) Ground state total density of states in black and important orbital contributions around the Fermi energy are shown in color. No scissor shift has been included in these calculations.

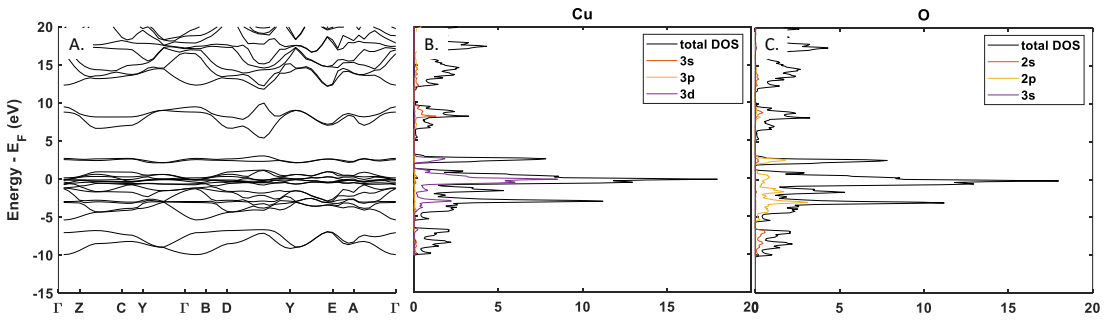

Figure C78. Ground State DFT Outputs for CuO. (a) Overall ground state band structure with the Fermi energy set to 0 eV. (b) Overall ground state total density of states in black and Cu partial DOS decomposed into 3s, 3p, and 3d orbital contributions. (c) Overall ground state total density of states in black and O partial DOS decomposed into 2s, 2p, and 3s orbital contributions No scissor shift has been included in these calculations.

ii. Ground State Spectrum[155]

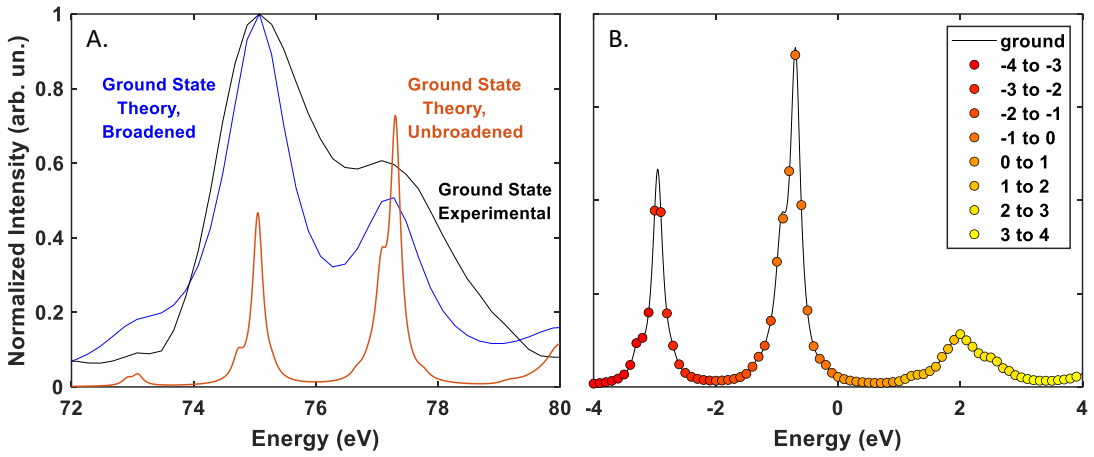

Figure C79. Ground State $M_{2,3}$ edge Absorption Spectrum. (a) The experimental (black), OCEAN calculated unbroadened (orange), and OCEAN calculated with energy-dependent broadening (blue) spectra are compared. (b) Energy-resolved exciton densities overlaid on the calculated XUV absorption spectrum around the Fermi level and the Cu $M_{2,3}$ edge.

iii. Ground State GMRES Energy Decomposition

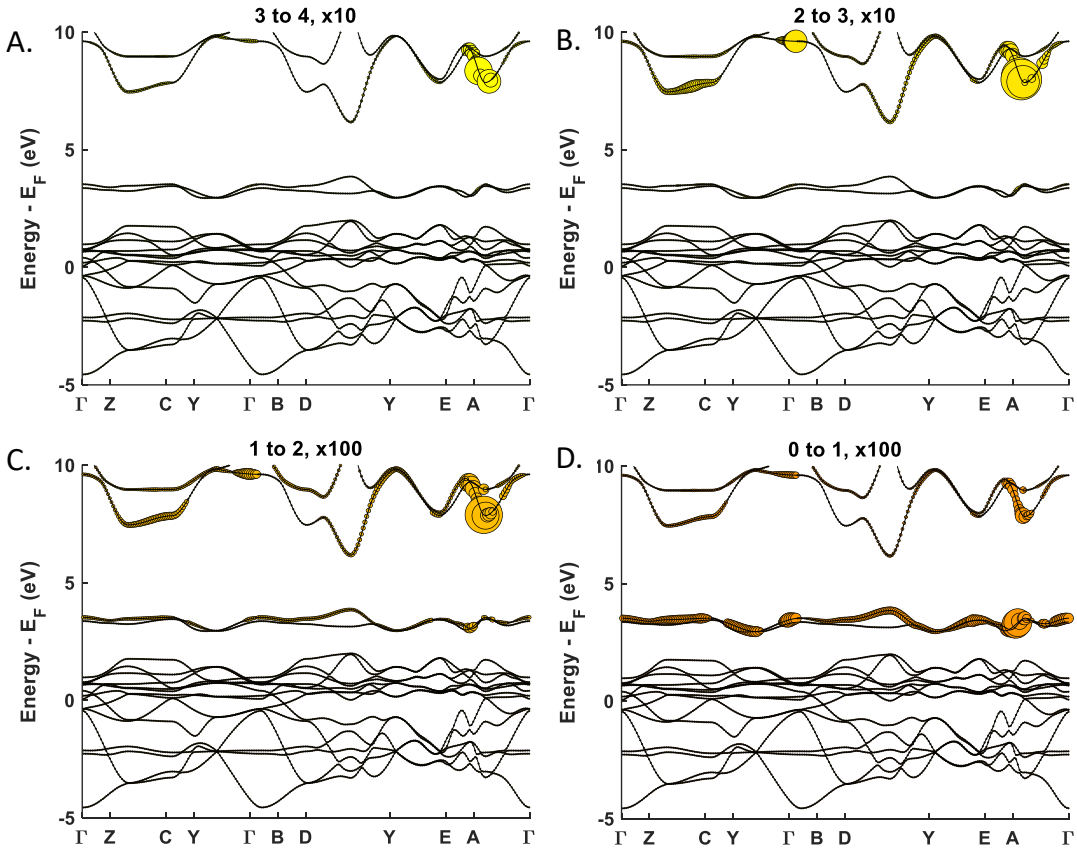

Figure C80. Energy-Resolved Exciton Densities Overlaid on the CuO Band Structure. Energy ranges between (a) 3 to 4 eV, (b) 2 to 3 eV, (c) 1 to 2 eV, and (d) 0 to 1 eV below the Fermi energy are shown. The necessary amplitude magnification is shown in the title of each band structure, demonstrating the relative strength of the exciton components in different energy ranges.

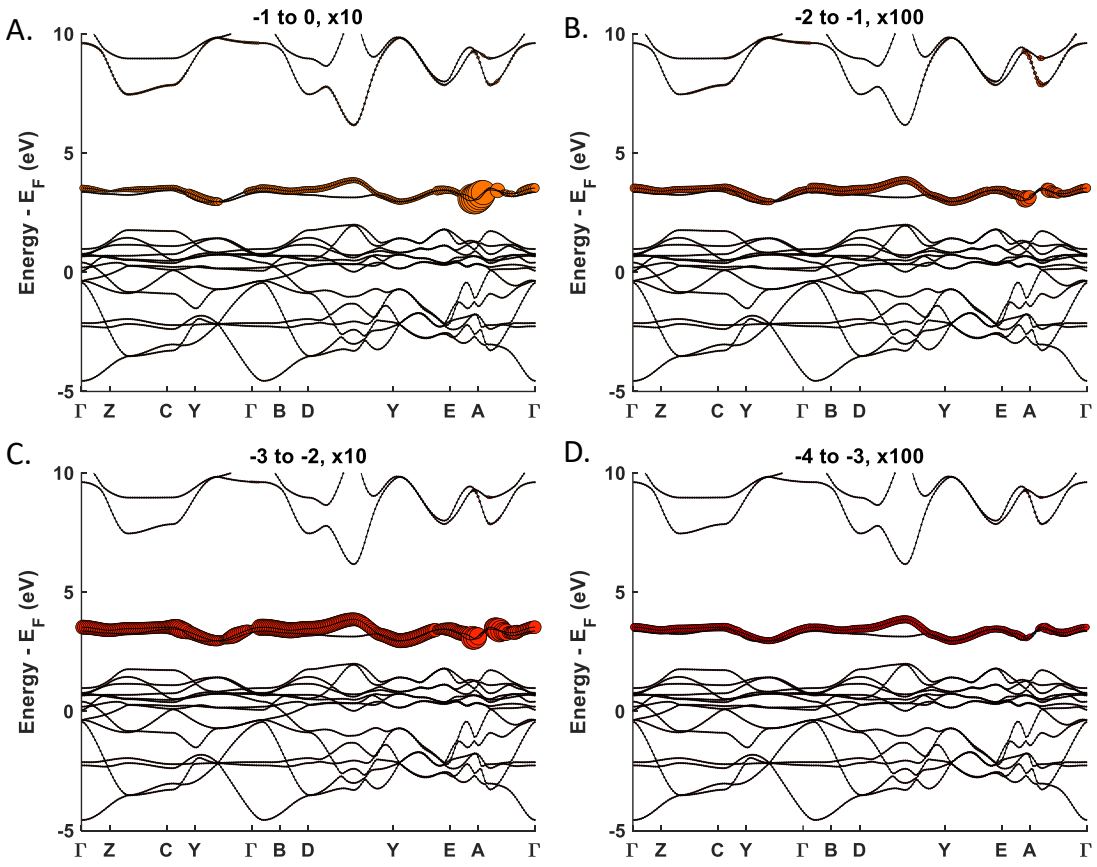

Figure C81. Energy-Resolved Exciton Densities Overlaid on the CuO Band Structure. Energy ranges between (a) -1 to 0 eV, (b) -2 to -1 eV, (c) -3 to -2 eV, and (d) -3 to -4 eV below the Fermi energy are shown. The necessary amplitude magnification is shown in the title of each band structure, demonstrating the relative strength of the exciton components in different energy ranges.

c. Excited State Calculations

i. State filling band diagrams and Full Spectra

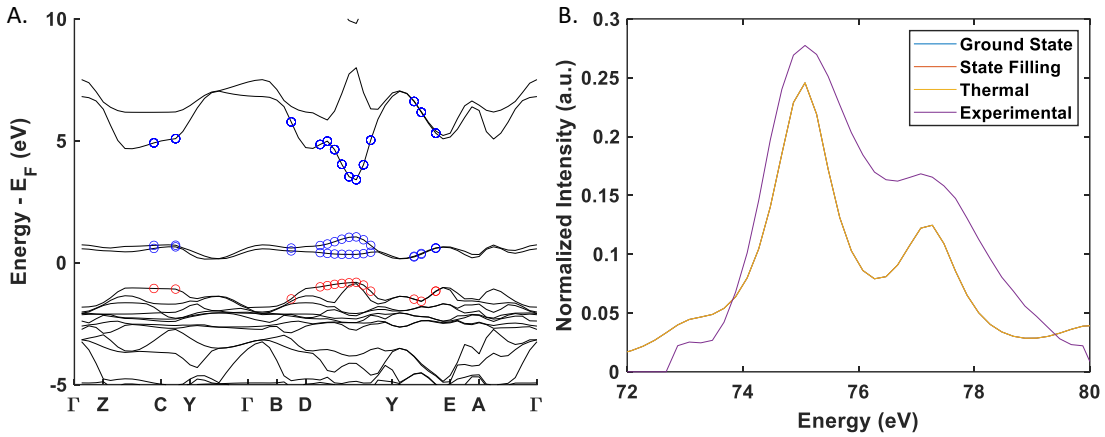

Figure C82. Excited State $M_{2,3}$ edge Absorption Spectrum. (a) State filling occupation used to model charge-transfer where the blue circles indicate electron occupation and red circles indicate holes overlaid on the band structure in black. (b) Broadened spectra for the ground state (blue), state filling (orange), thermal expansion (yellow), and experimental (purple).

d. Hamiltonian Decompositions

i. Total Exciton Comparisons

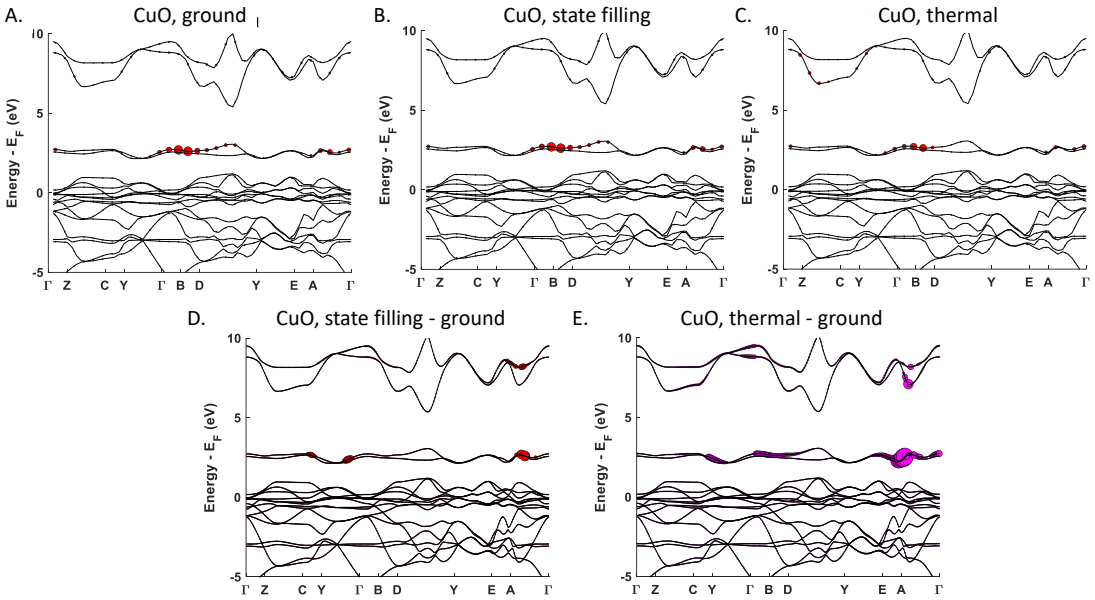

Figure C83. Total Core-Valence Exciton Densities. (a) Ground, (b) state filling, and (c) thermally expanded states' total core-valence exciton densities overlaid on the band structure of CuO. Differentials for the (d) state filling, and (e) thermally expanded excited states.

ii. Hamiltonian Decomposition of Exciton Components for ground, state filling, and thermally expanded models.

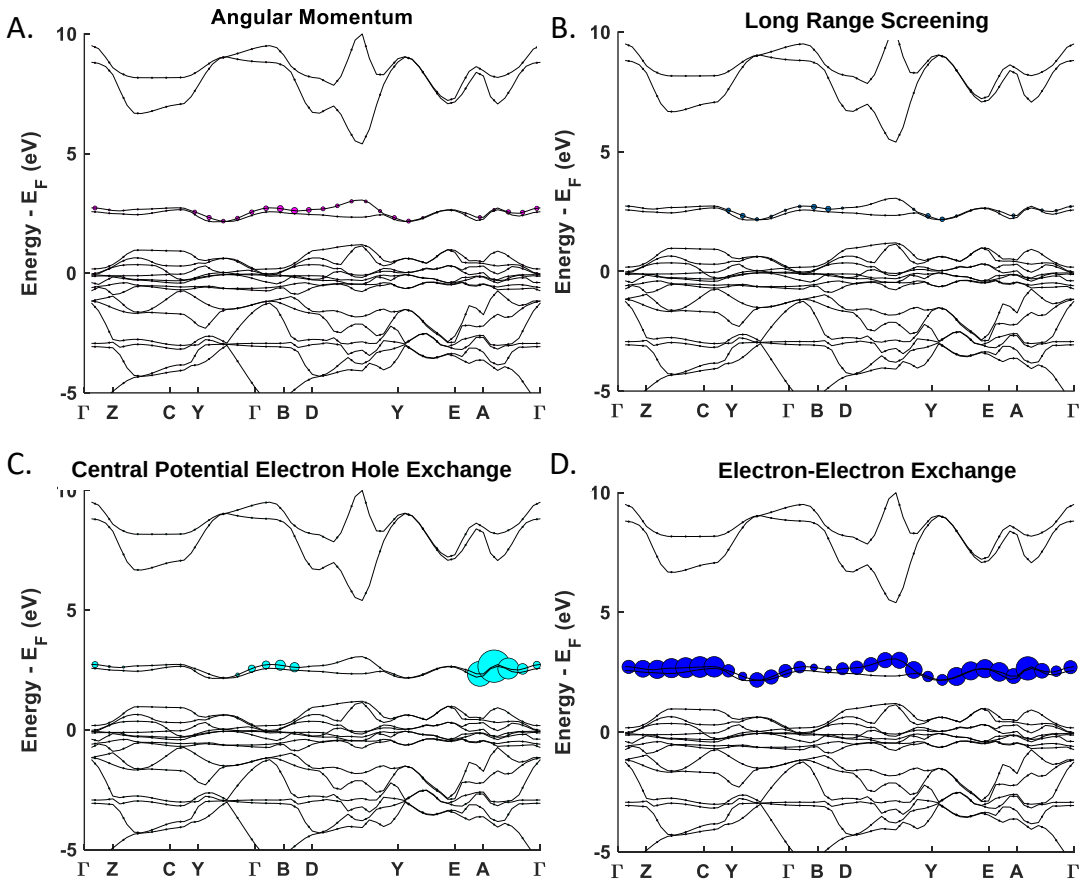

Figure C84. XUV transition Hamiltonian Decomposition of Core-Valence Exciton for the Ground State of CuO. The (a) angular momentum, (b) core-hole screening, (c) electron-hole exchange, and (d) electron-electron exchange core-valence exciton densities are calculated and normalized to determine the relative contribution of each of these processes to the overall XUV exciton and thus absorption spectrum.

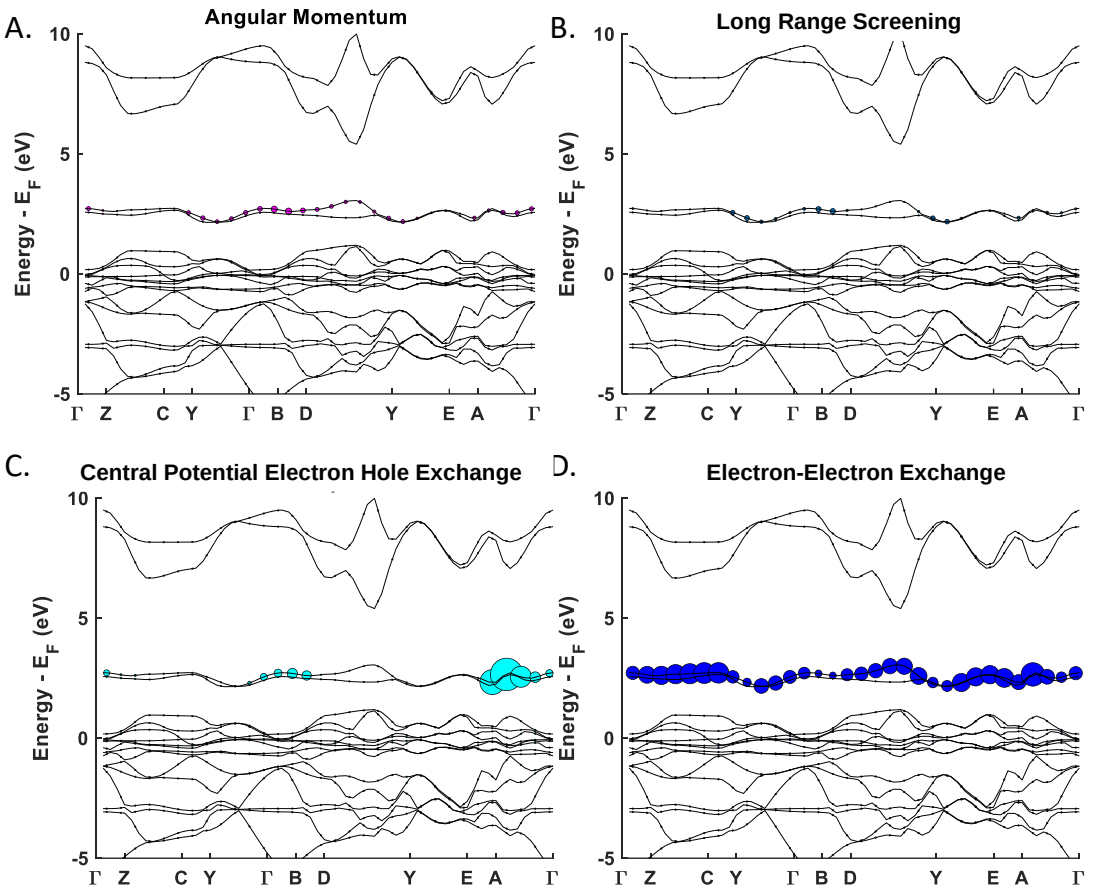

Figure C85. XUV transition Hamiltonian Decomposition of Core-Valence Exciton for the State Filling State of CuO. The (a) angular momentum, (b) core-hole screening, (c) electron-hole exchange, and (d) electron-electron exchange core-valence exciton densities are calculated and normalized to determine the relative contribution of each of these processes to the overall XUV exciton and thus absorption spectrum.

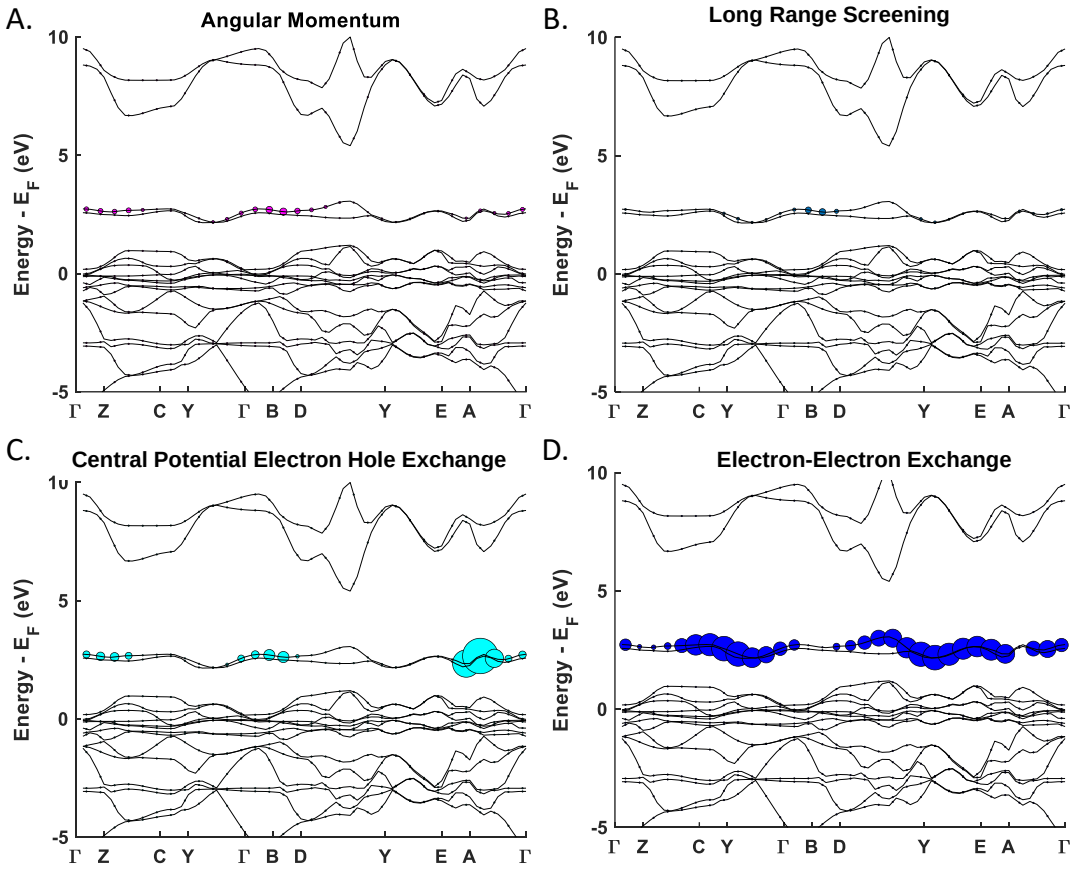

Figure C86. XUV transition Hamiltonian Decomposition of Core-Valence Exciton for the Thermally Expanded State of CuO. The (a) angular momentum, (b) core-hole screening, (c) electron-hole exchange, and (d) electron-electron exchange core-valence exciton densities are calculated and normalized to determine the relative contribution of each of these processes to the overall XUV exciton and thus absorption spectrum.

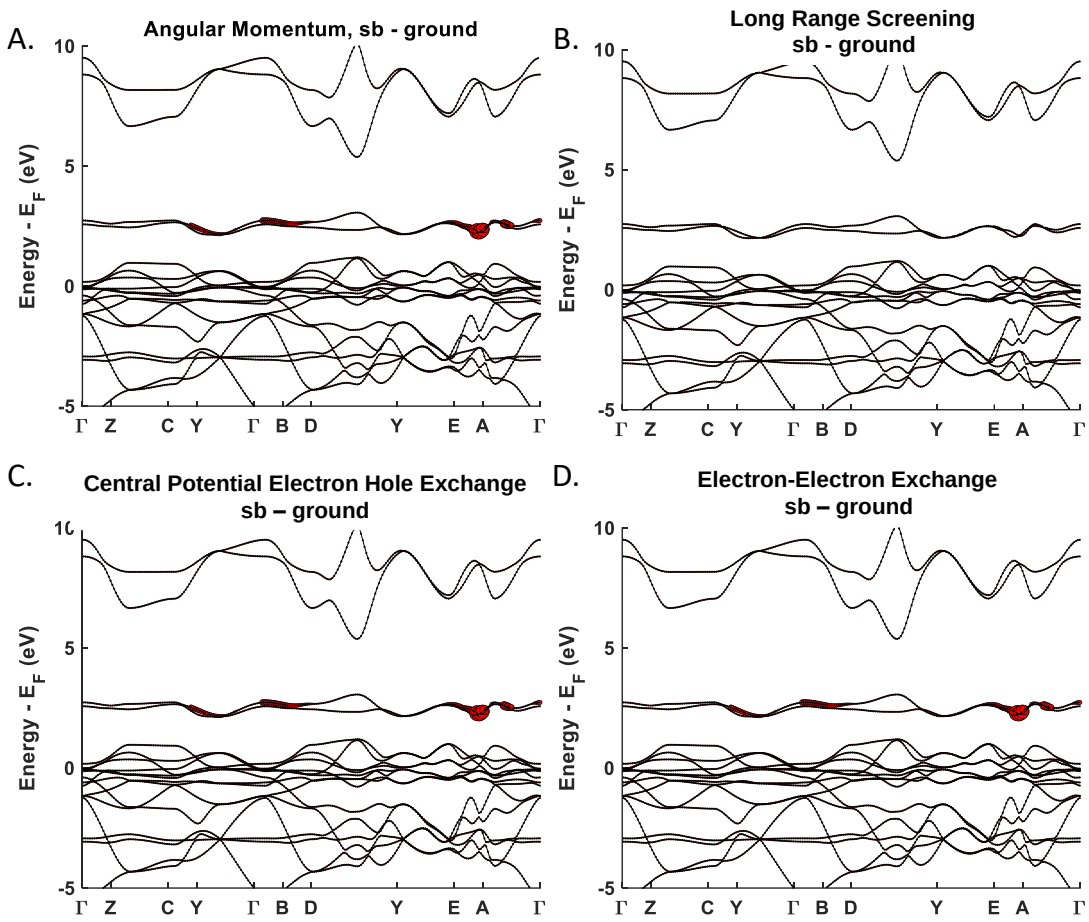

Figure C87. Differential XUV transition Hamiltonian Decomposition of Core-Valence Exciton for the State-Filling Excited State of CuO. The magnitude of the state-filling minus the ground state components for the (a) angular momentum, (b) core-hole screening, (c) electron-hole exchange, and (d) electron-electron exchange core-valence exciton densities are calculated and normalized to determine the relative contribution of each of these processes to excited state effects.

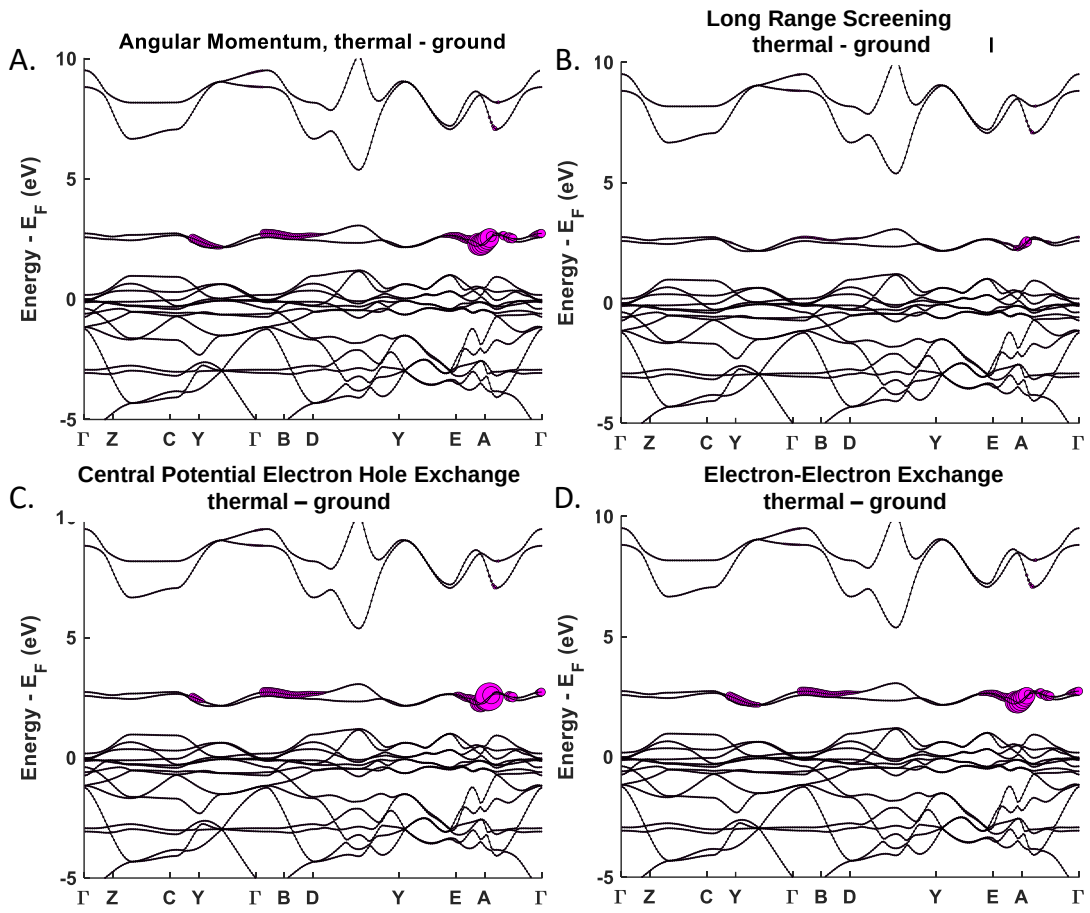

Figure C88. Differential XUV transition Hamiltonian Decomposition of Core-Valence Exciton for the Thermally Expanded Excited State of CuO. The magnitude of the state-filling minus the ground state components for the (a) angular momentum, (b) core-hole screening, (c) electron-hole exchange, and (d) electron-electron exchange core-valence exciton densities are calculated and normalized to determine the relative contribution of each of these processes to excited state effects.

C9. ZnO

a. Structural Data for Calculations

i. Ground State and State Blocking

Unit Cell Parameters (bohr)

{ 6.146932044 6.146932044 9.978075761 }

Primitive Vectors

{0.5 -0.866 0

0.5 0.866 0

00 1}

Reduced coordinates, (x, y, z)

Zn 0.333332565 0.666667435 0.001542181

Zn 0.666667435 0.333332565 0.501542181

O 0.333332311 0.666667689 0.378757819

O 0.666667689 0.333332311 0.878757819

ii. Thermally Expanded Lattice

Unit Cell Parameters (bohr)

{6.18074 6.18074 10.032955 }

Primitive Vectors

{0.5 -0.8660

0.5 0.866 0

001}

Reduced coordinates, (x, y, z)

Zn 0.333332565 0.666667435 0.001542181

Zn 0.666667435 0.333332565 0.501542181

O 0.333332311 0.666667689 0.378757819

O 0.666667689 0.333332311 0.878757819

b. Ground State Calculations

i. Band Structure and DOS

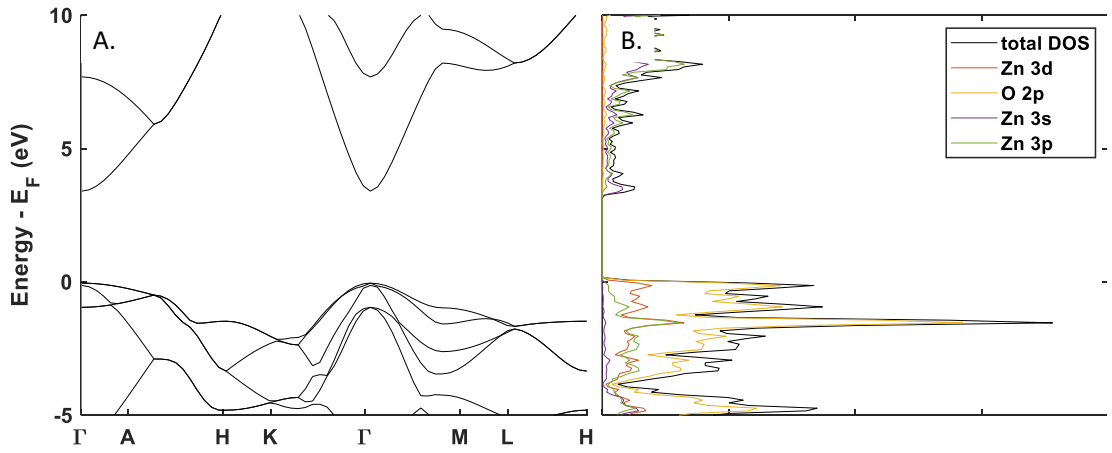

Figure C89. Ground State DFT Outputs for ZnO. (a) Ground state band structure with the Fermi energy set to 0 eV. (b) Ground state total density of states in black and important orbital contributions around the Fermi energy are shown in color. No scissor shift has been included in these calculations.

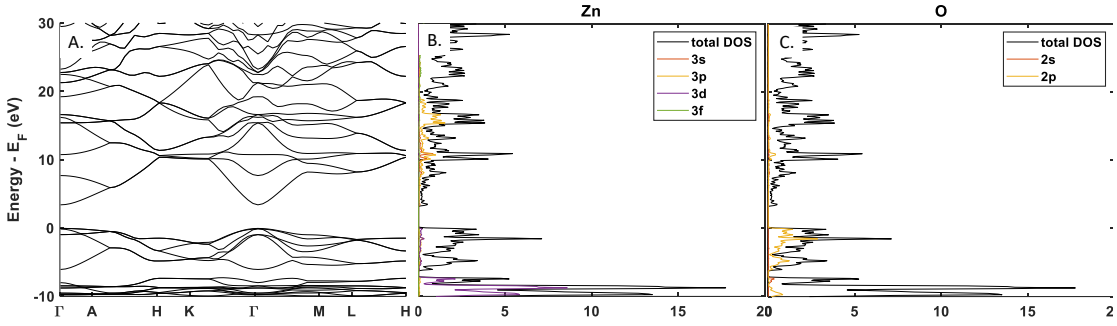

Figure C90. Ground State DFT Outputs for ZnO. (a) Overall ground state band structure with the Fermi energy set to 0 eV. (b) Overall ground state total density of states in black and Zn partial DOS decomposed into 3s, 3p, and 3d orbital contributions. (c) Overall ground state total density of states in black and O partial DOS decomposed into 2s, 2p, and 3s orbital contributions No scissor shift has been included in these calculations.

ii. Ground State Spectrum

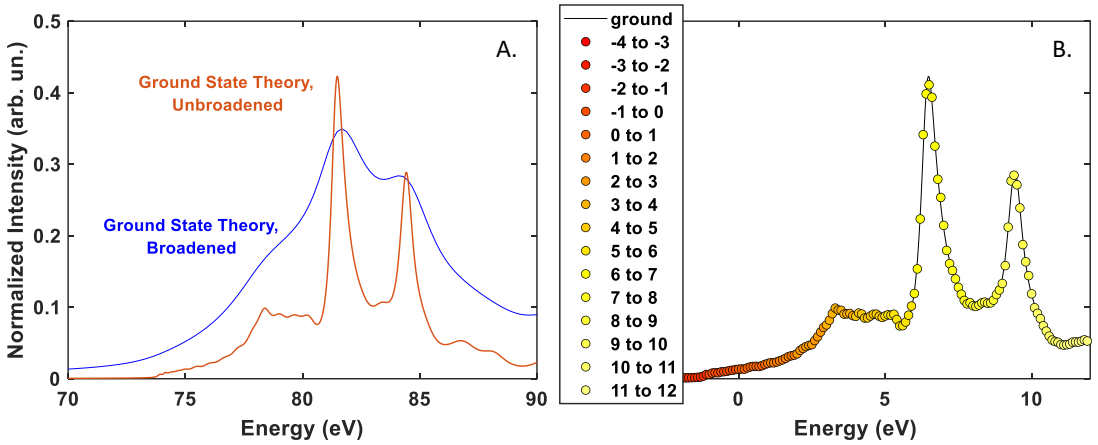

Figure C91. Ground State $M_{2,3}$ edge Absorption Spectrum. (a) The experimental (black), OCEAN calculated unbroadened (orange), and OCEAN calculated with energy-dependent broadening (blue) spectra are compared. (b) Energy-resolved exciton densities overlaid on the calculated XUV absorption spectrum around the Fermi level and the Zn $M_{2,3}$ edge.

iii. Ground State GMRES Energy Decomposition

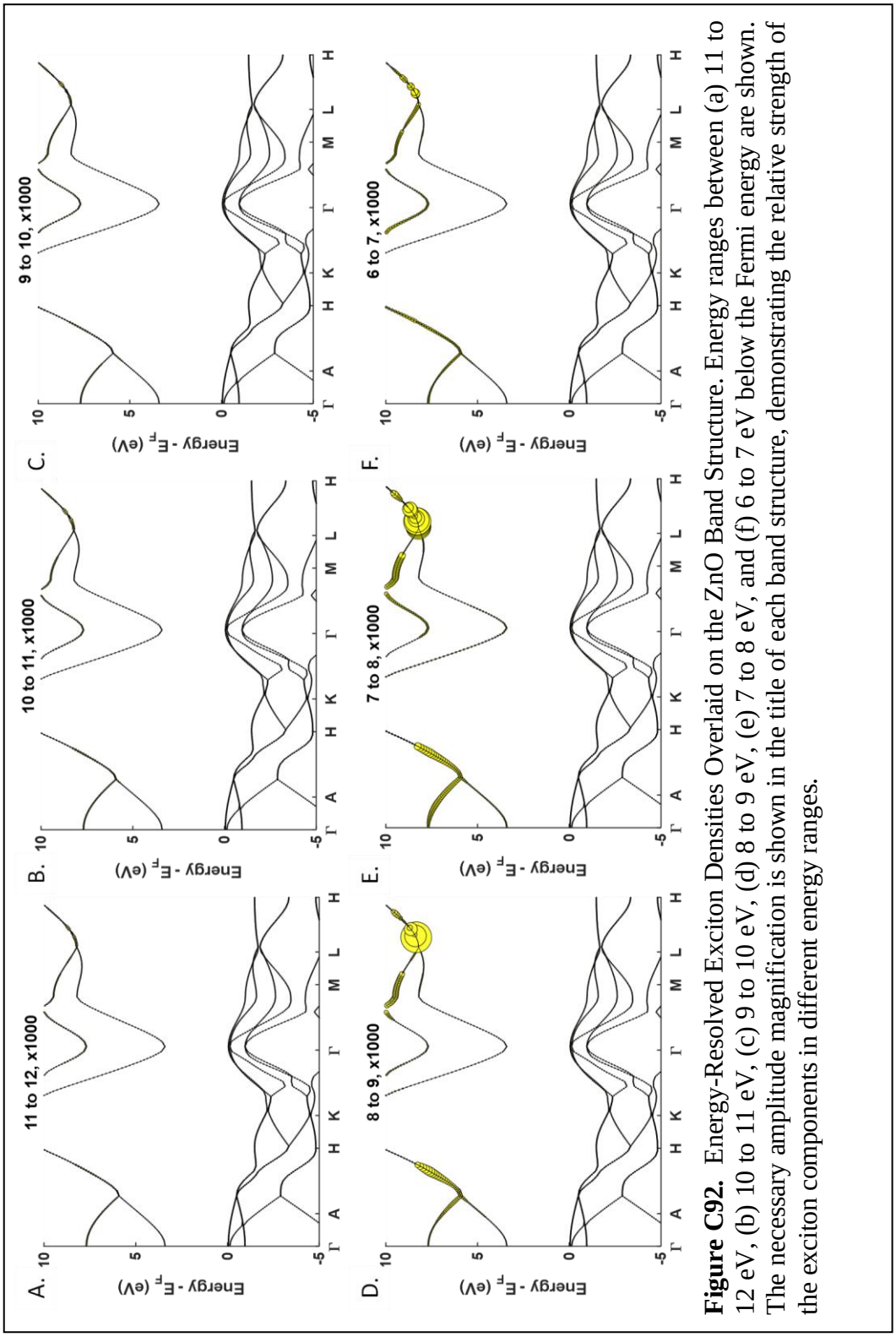

Figure C92. Energy-Resolved Exciton Densities Overlaid on the ZnO Band Structure. Energy ranges between (a) 11 to 12 eV, (b) 10 to 11 eV, (c) 9 to 10 eV, (d) 8 to 9 eV, (e) 7 to 8 eV, and (f) 6 to 7 eV below the Fermi energy are shown. The necessary amplitude magnification is shown in the title of each band structure, demonstrating the relative strength of the exciton components in different energy ranges.

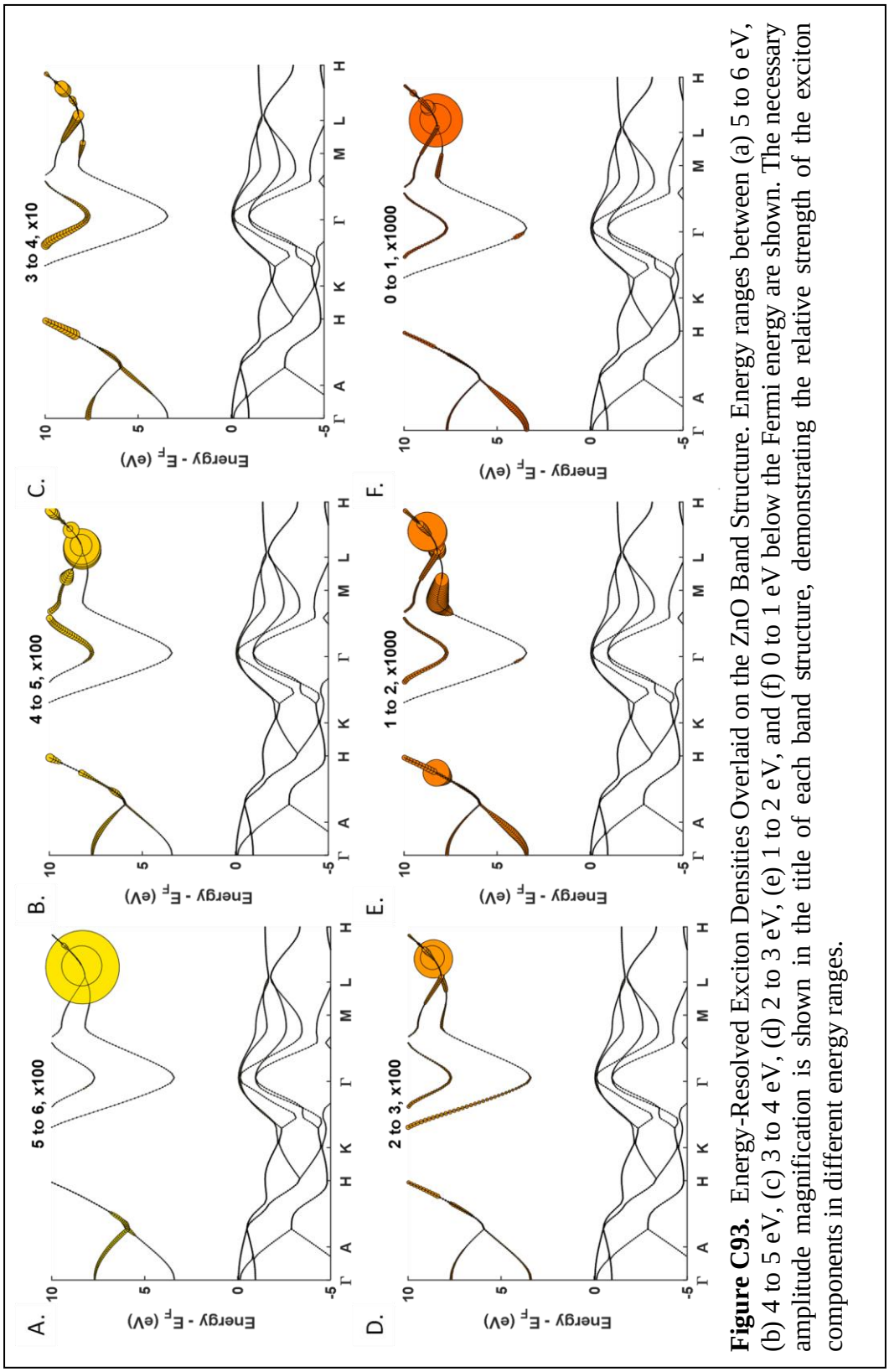

Figure C93. Energy-Resolved Exciton Densities Overlaid on the ZnO Band Structure. Energy ranges between (a) 5 to 6 eV, (b) 4 to 5 eV, (c) 3 to 4 eV, (d) 2 to 3 eV, (e) 1 to 2 eV, and (f) 0 to 1 eV below the Fermi energy are shown. The necessary amplitude magnification is shown in the title of each band structure, demonstrating the relative strength of the exciton components in different energy ranges.

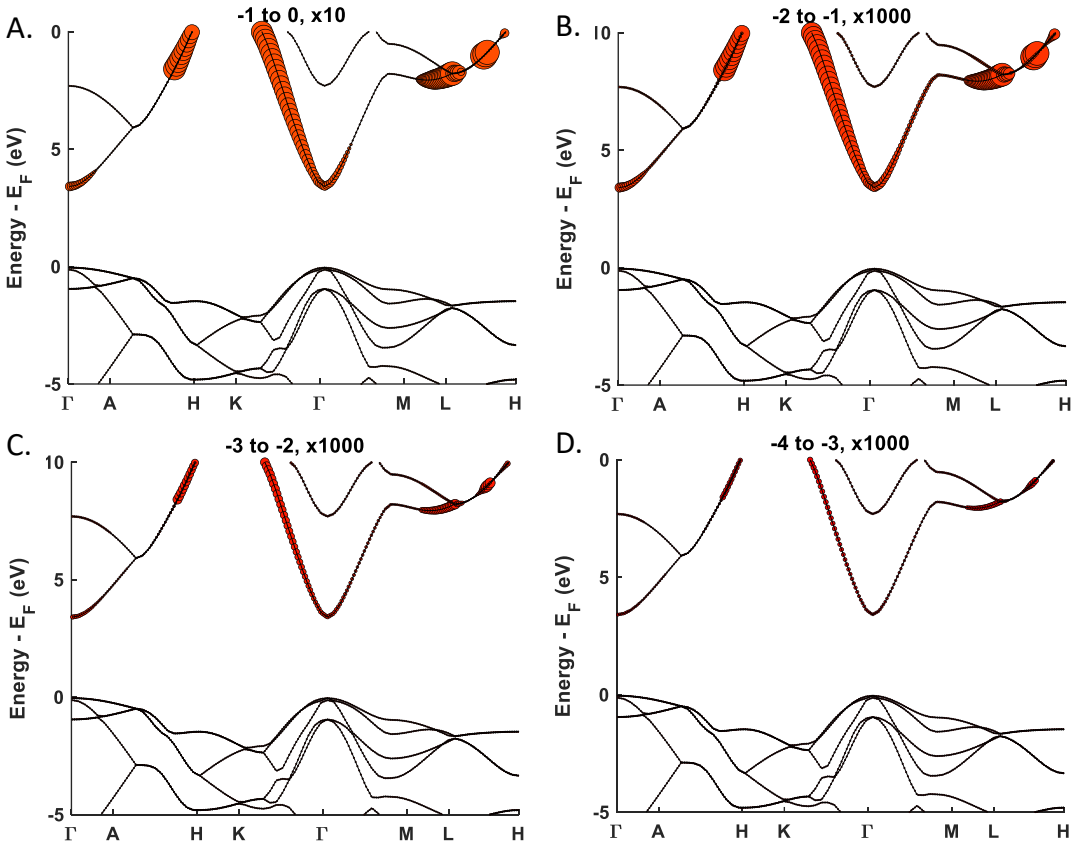

Figure C94. Energy-Resolved Exciton Densities Overlaid on the ZnO Band Structure. Energy ranges between (a) -1 to 0 eV, (b) -2 to -1 eV, (c) -3 to -2 eV, and (d) -3 to -4 eV below the Fermi energy are shown. The necessary amplitude magnification is shown in the title of each band structure, demonstrating the relative strength of the exciton components in different energy ranges.

c. Excited State Calculations

i. State filling band diagrams and Full Spectra

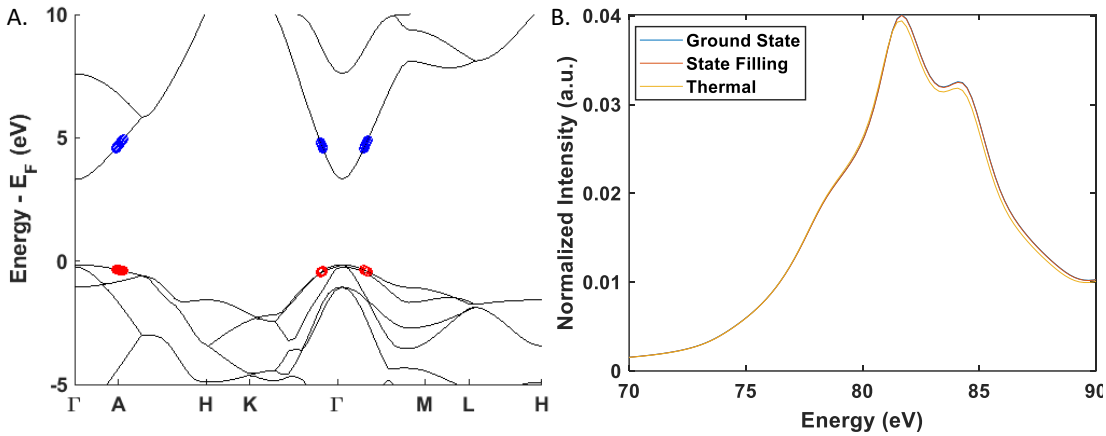

Figure C95. Excited State $M_{2,3}$ edge Absorption Spectrum. (a) State filling occupation used to model charge-transfer where the blue circles indicate electron occupation and red circles indicate holes overlaid on the band structure in black. (b) Broadened spectra for the ground state (blue), state filling (orange), and thermal expansion (yellow).

d. Hamiltonian Decompositions

i. Total Exciton Comparisons

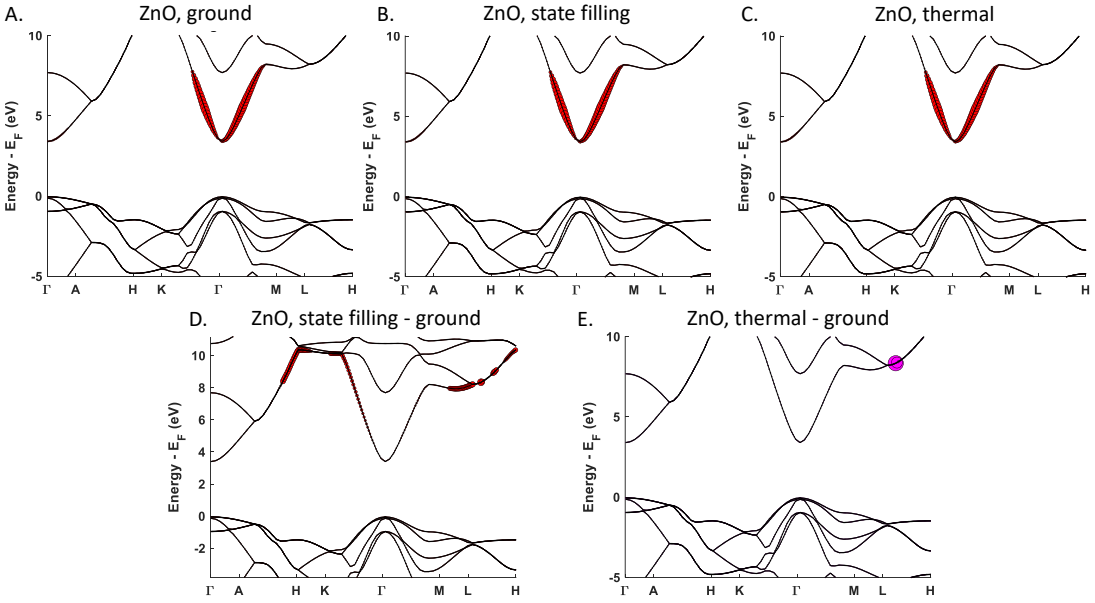

Figure C96. Total Core-Valence Exciton Densities. (a) Ground, (b) state filling, and (c) thermally expanded states' total core-valence exciton densities overlaid on the band structure of ZnO. Differentials for the (d) state filling, and (e) thermally expanded excited states.

ii. Hamiltonian Decomposition of Exciton Components for ground, state filling, and thermally expanded models.

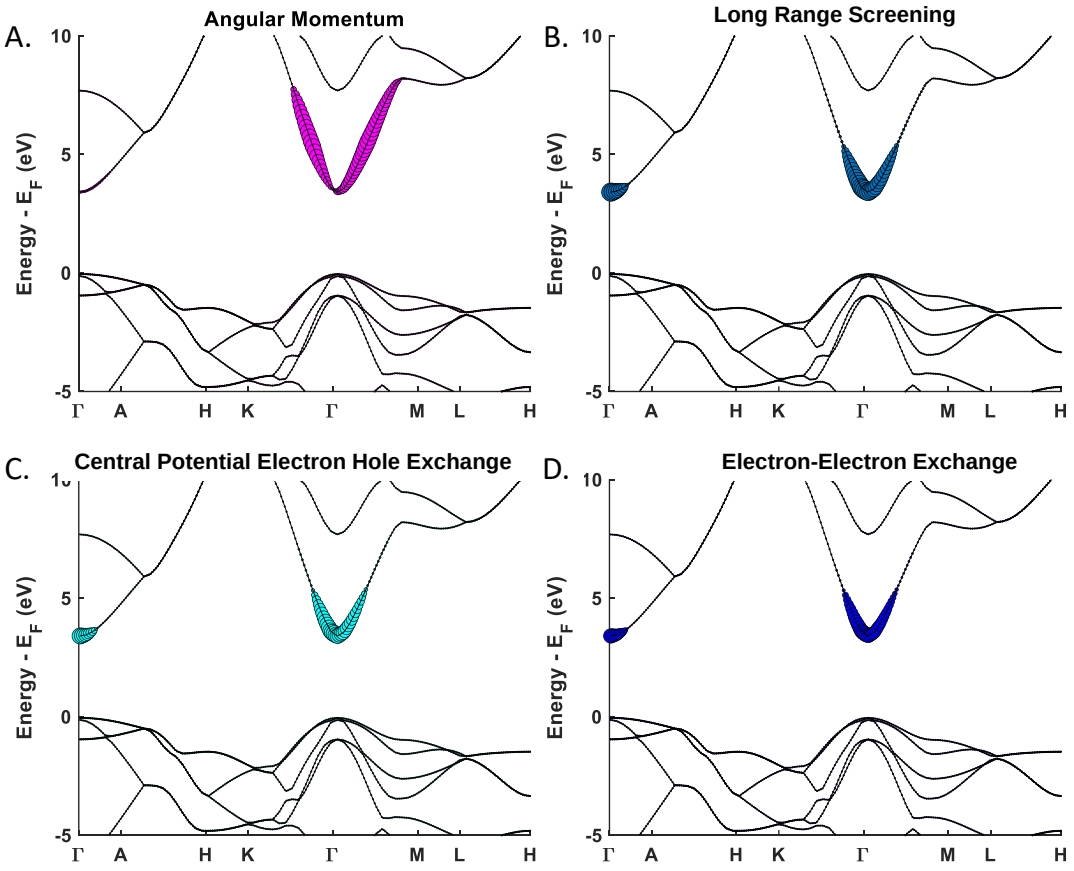

Figure C97. XUV transition Hamiltonian Decomposition of Core-Valence Exciton for the Ground State of ZnO. The (a) angular momentum, (b) core-hole screening, (c) electron-hole exchange, and (d) electron-electron exchange core-valence exciton densities are calculated and normalized to determine the relative contribution of each of these processes to the overall XUV exciton and thus absorption spectrum.

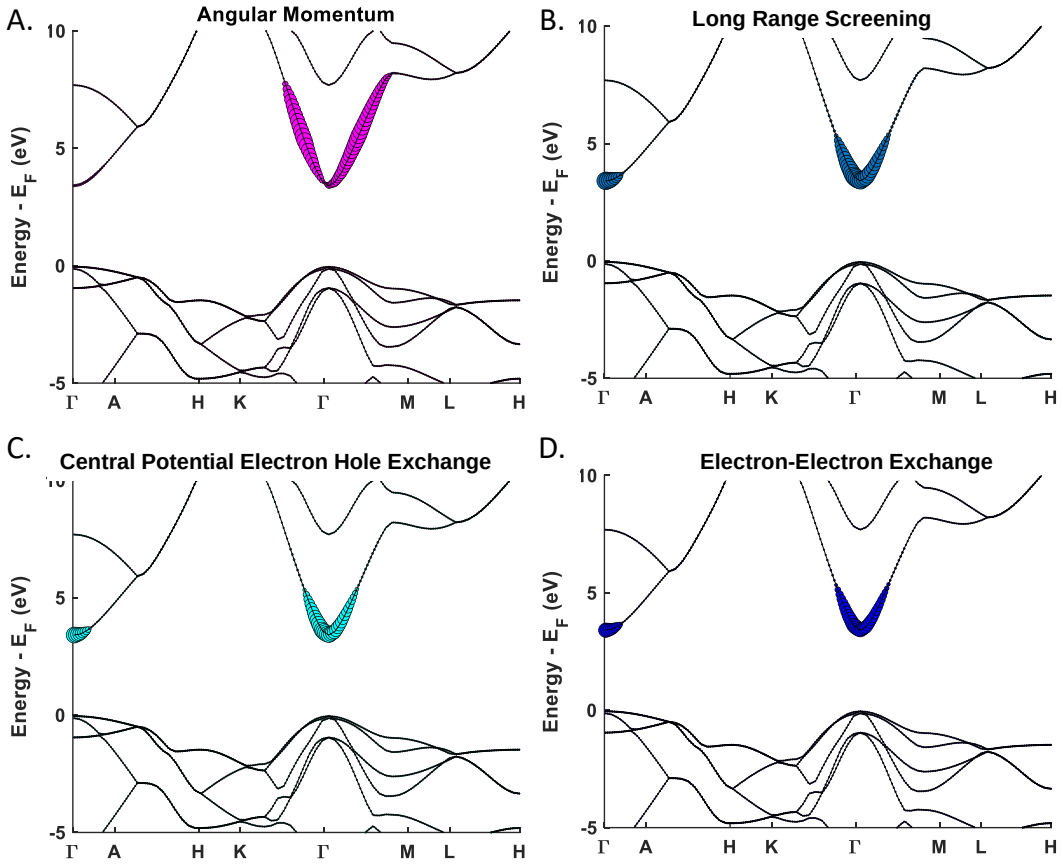

Figure C98. XUV transition Hamiltonian Decomposition of Core-Valence Exciton for the State Filling State of ZnO. The (a) angular momentum, (b) core-hole screening, (c) electron-hole exchange, and (d) electron-electron exchange core-valence exciton densities are calculated and normalized to determine the relative contribution of each of these processes to the overall XUV exciton and thus absorption spectrum.

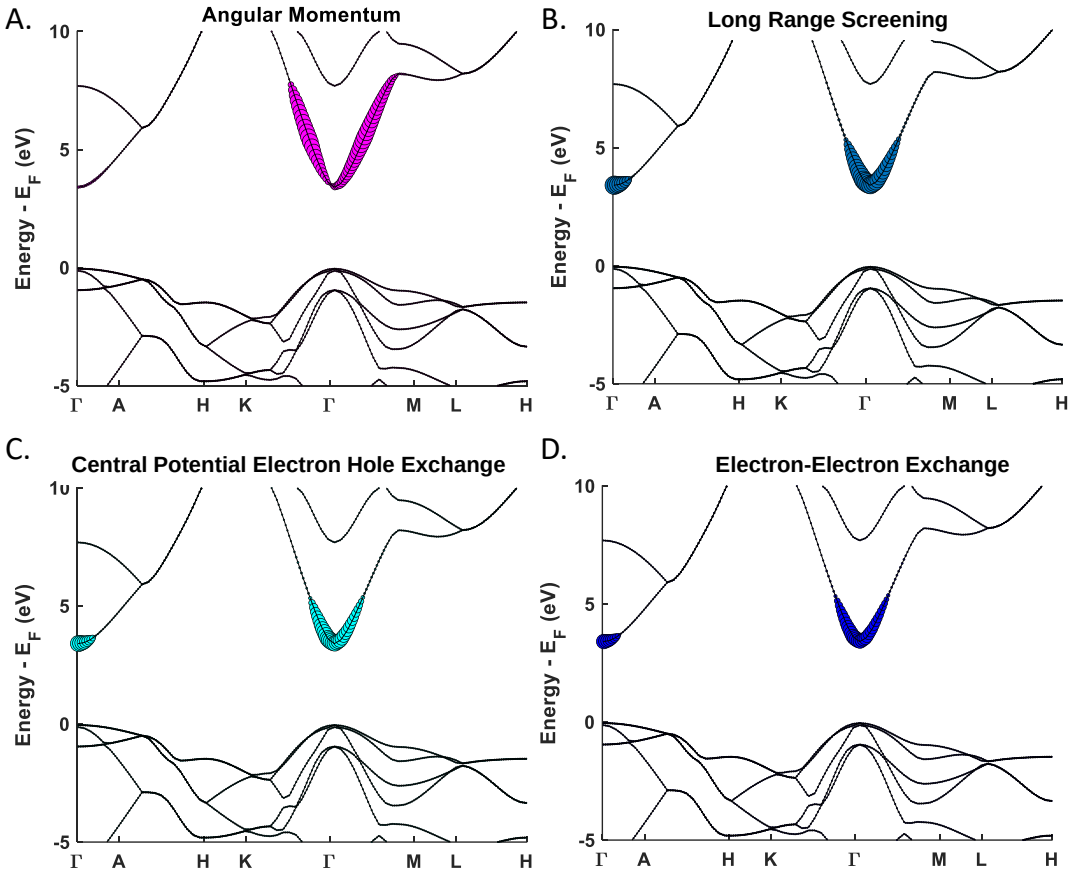

Figure C99. XUV transition Hamiltonian Decomposition of Core-Valence Exciton for the Thermally Expanded State of ZnO. The (a) angular momentum, (b) core-hole screening, (c) electron-hole exchange, and (d) electron-electron exchange core-valence exciton densities are calculated and normalized to determine the relative contribution of each of these processes to the overall XUV exciton and thus absorption spectrum.

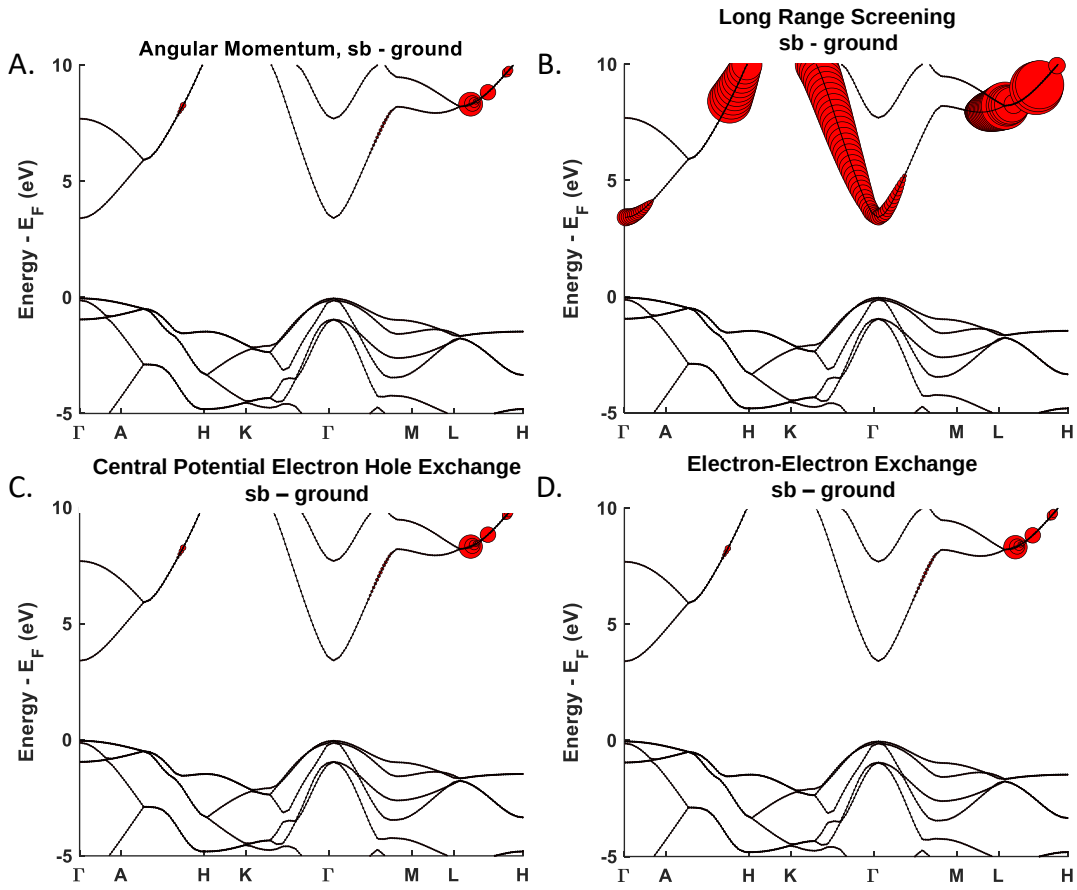

Figure C100. Differential XUV transition Hamiltonian Decomposition of Core-Valence Exciton for the State-Filling Excited State of ZnO. The magnitude of the state-filling minus the ground state components for the (a) angular momentum, (b) core-hole screening, (c) electron-hole exchange, and (d) electron-electron exchange core-valence exciton densities are calculated and normalized to determine the relative contribution of each of these processes to excited state effects.

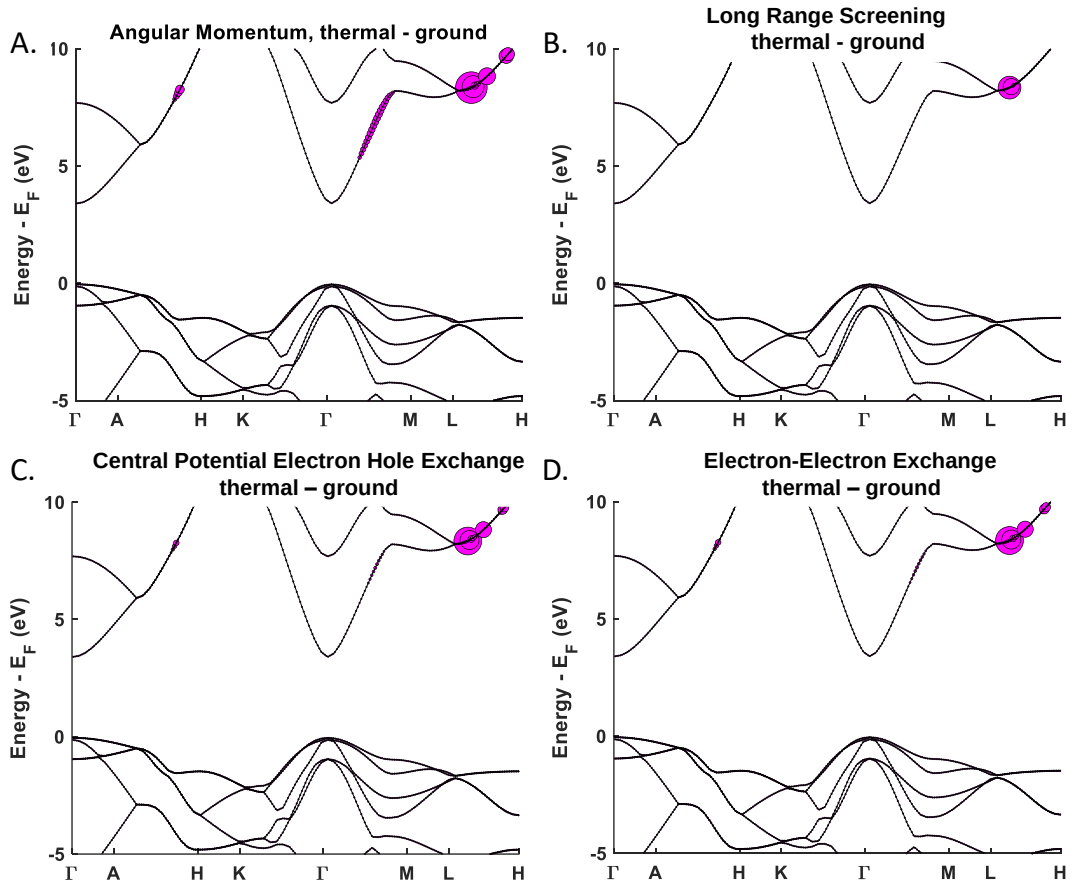

Figure C101. Differential XUV transition Hamiltonian Decomposition of Core-Valence Exciton for the Thermally Expanded Excited State of ZnO. The magnitude of the state-filling minus the ground state components for the (a) angular momentum, (b) core-hole screening, (c) electron-hole exchange, and (d) electron-electron exchange core-valence exciton densities are calculated and normalized to determine the relative contribution of each of these processes to excited state effects.

C10. Comparisons 3

a. Thermal Expansion Calculations

Table 3. Percent Thermal Expansion for the Transition Metal Oxides, 300 K to 650 K

	TiO_2	Cr_2O_3	MnO_2	Fe_2O_3	Co_3O_4	NiO	CuO	ZnO
% Expansion	1	0.6	0.3	0.8	0.3	1.2	0.4	0.7

b. Physical Properties for Hamiltonian Contribution Explanations

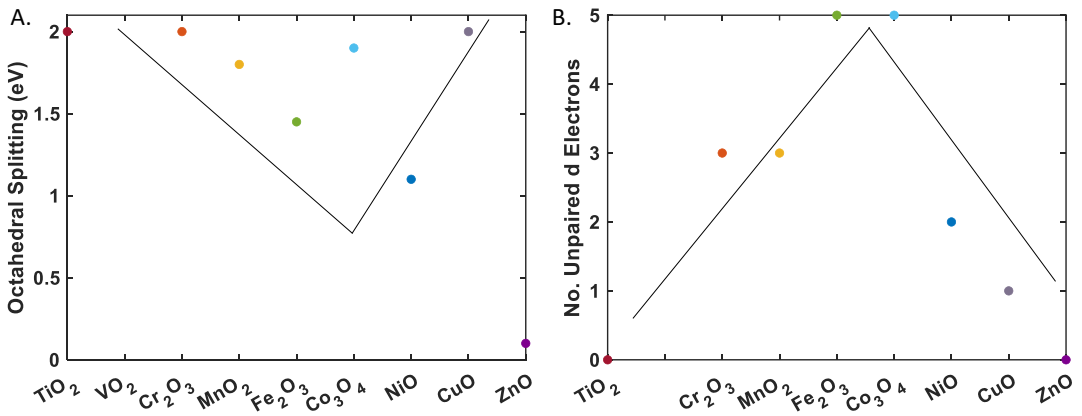

Figure C102. Material Property Trends. (a) Octahedral field splitting values for each of the transition metal oxides investigated. (b) Number of unpaired electrons for each of the transient metal oxides. Black lines are guides for the eye to indicate the trends in these material properties across the periodic table.

APPENDIX D: SUPPLEMENTARY INFORMATION FOR VALIDATION OF THE COGEF METHOD AS A PREDICTIVE TOOL FOR POLYMER MECHANOCHEMISTRY

I. General Methods

CoGEF calculations were performed using Spartan ′18 Parallel Suite according to previously reported methods.[1] Chemical structures were composed in ChemDraw, saved as .mol files, and then imported into Spartan. Structures were truncated to include tethers that accurately reflect the structure of the molecules used in the experimental studies. Ground state energies were calculated using DFT at the B3LYP/6-31G* level of theory in vacuum, unless specified otherwise. For the three mechanophores in the heterolytic category, CoGEF calculations were also performed using a polarizable continuum model (dielectric constant of 37) to simulate a polar solvent. Starting from the equilibrium geometry of the unconstrained molecule (relative energy = 0 kJ/mol), the distance between the terminal anchor atoms of the truncated structure was increased in increments of 0.05 Å and the energy was minimized at each step. This operation was carried out automatically using the Energy Profile calculation in Spartan. Calculations were run until a chemical transformation was predicted to occur, as evidenced by the rupture and reorganization of one or more covalent bonds. In some cases, an initial equilibrium conformer calculation was performed using Molecular Mechanics (MMFF) before performing the steps outlined above. The maximum number of geometry optimization cycles was increased beyond the default value using the GEOMETRYCYCLE option to ensure convergence at each step in the CoGEF profile.

Determination of F_{max}. The maximum force predicted for each mechanochemical transformation was calculated from the slope between contiguous points in the energy–displacement curve. In most cases, F_{max} coincides with the displacement immediately prior to a discontinuity in the relative energy profile. The value of F_{max} is thus calculated from the slope between the two data points preceding the abrupt attenuation in energy. More rarely, a continuous change in energy is observed that approaches an apparent plateau value at long displacements. In these cases, F_{max} occurs at the inflection point in the CoGEF curve. The value of the slope is divided by the Avogadro constant and adjusted to provide force in units of nJ/m (nN).

---

(1) (a) Beyer, M. K. The Mechanical Strength of a Covalent Bond Calculated by Density Functional Theory. *J. Chem. Phys.* **2000**, *112*, 7307–7312. (b) Kryger, M. J.; Munaretto, A. M.; Moore, J. S. Structure-Mechanochemical Activity Relationships for Cyclobutane Mechanophores. *J. Am. Chem. Soc.* **2011**, *133*, 18992–18998.

(2) Robb, M. J.; Kim, T. A.; Halmes, A. J.; White, S. R.; Sottos, N. R.; Moore, J. S. Regioisomer-Specific Mechanochromism of Naphthopyran in Polymeric Materials. *J. Am. Chem. Soc.* **2016**, *138*, 12328–12331.

Determination of E_{max}. The maximum energy relative to the energy of the unconstrained molecule at equilibrium is reported as E_{max}. The value of E_{max} is determined from the CoGEF curve at the displacement corresponding to F_{max}. Typically, this means that E_{max} represents the highest relative energy on the CoGEF curve; however, for instances in which the CoGEF profile exhibits a sigmoidal shape and/or a discontinuity is absent, E_{max} corresponds to the relative energy at the inflection point.

Determination of Force–Bond Angle. Force–bond angles were calculated according to the previously described method using structural models from CoGEF calculations at the displacement corresponding to F_{max}.[2] The external force vector was approximated using the coordinates of the two terminal atoms that define the distance constraint in the CoGEF calculation.

II. Supplementary Figures

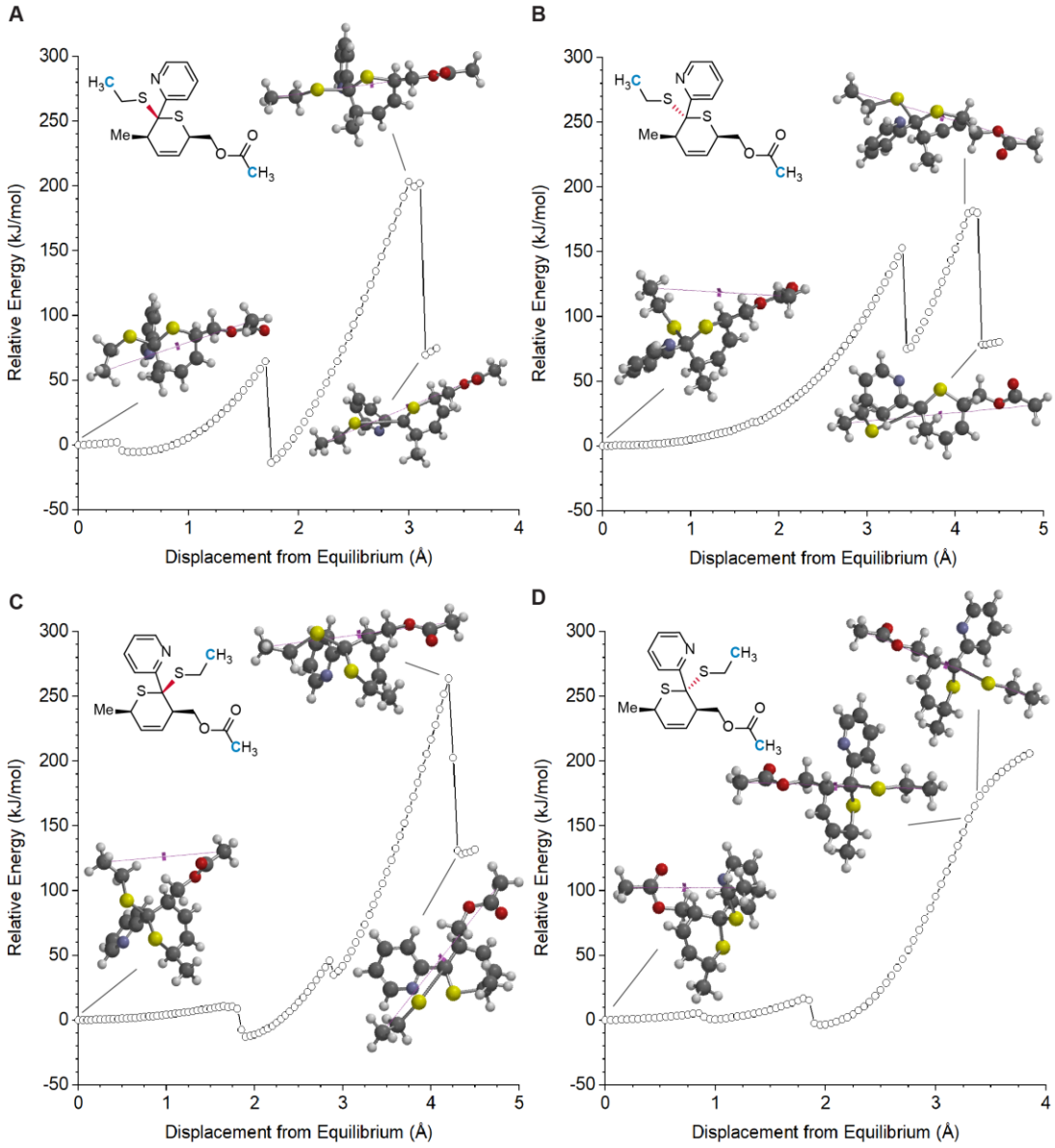

Figure D1. CoGEF results for four possible isomers of a hetero-Diels–Alder adduct corresponding to the reactive subunits of reported mechanophore **36**. All isomers are predicted to undergo C–S bond scission rather than the formal retro-[4+2] cycloaddition reaction.

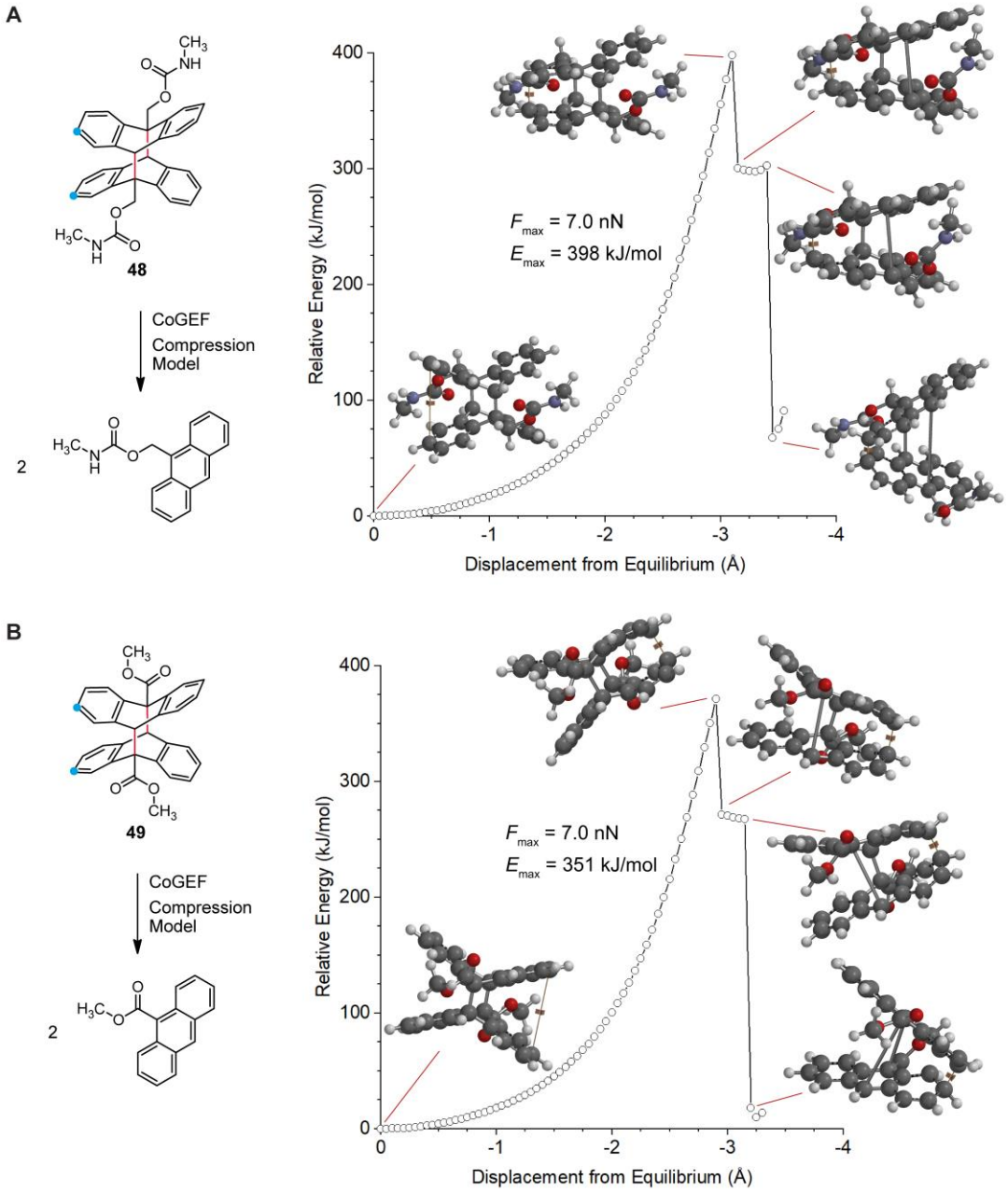

Figure D2. CoGEF calculations performed in an alternative compression mode for head-to-tail anthracene dimer mechanophores (A) **48** and (B) **49**. The distance between carbon atoms labeled with a blue dot was decreased incrementally starting from the force-free equilibrium geometry. At each step, the geometry was optimized at the B3LYP/6-31G* level of DFT. Both molecules are predicted to undergo a formal retro-[4+4] cycloaddition reaction upon simulated compression. The transformation proceeds through an apparent stepwise pathway suggesting an intermediate with diradicaloid character.

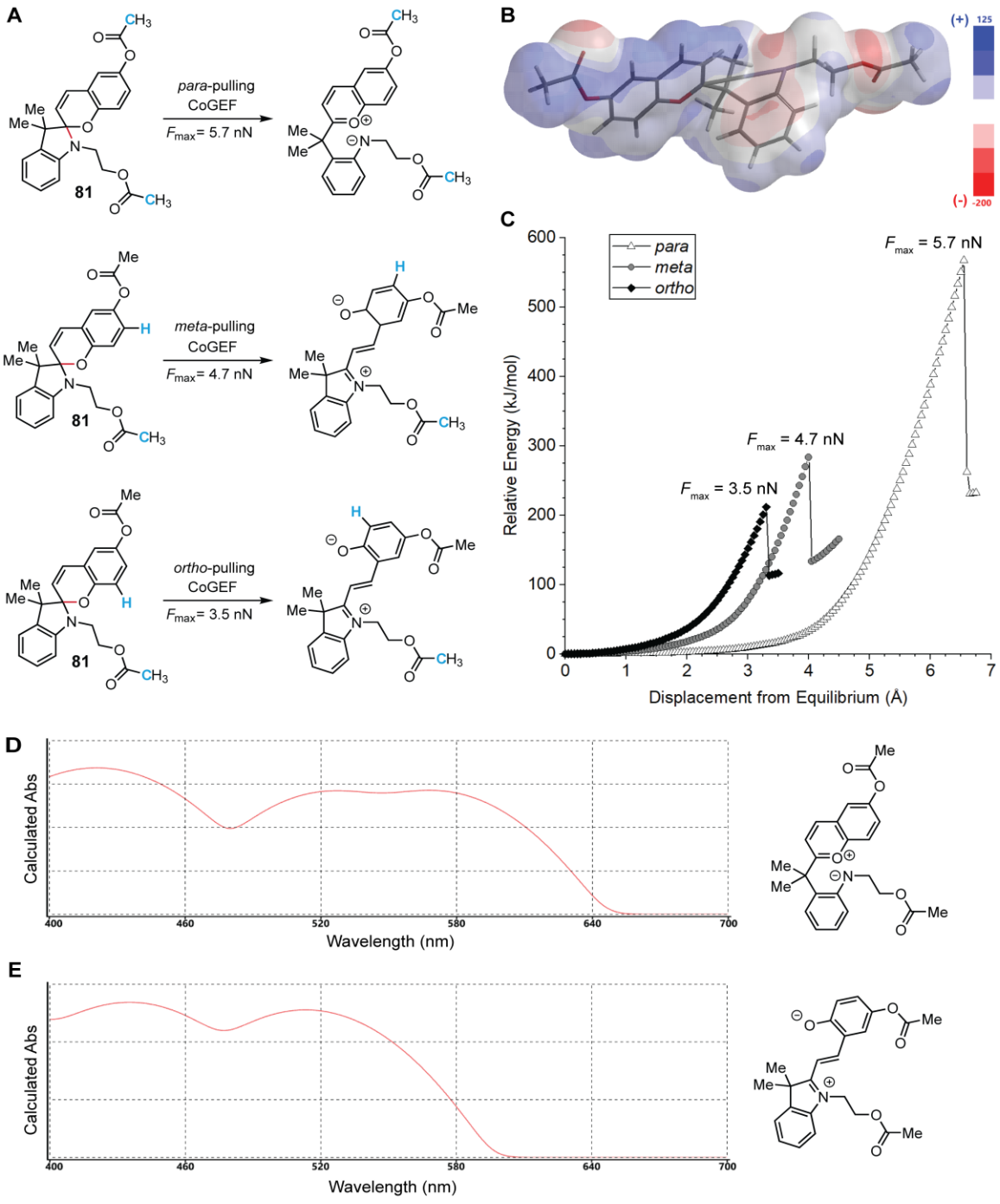

Figure D3. Investigation of regiochemical effects on the predicted mechanochemical reactivity of spiropyran **81**. (A) Changing the pulling position results in the anticipated scission of the C–O pyran bond leading to formation of the merocyanine. (B) Electrostatic potential map of the product predicted by CoGEF (*para*-pulling) indicating heterolytic fragmentation of the C–N bond. (C) CoGEF profiles associated with the schemes in panel A. (D, E) Visible absorption spectra calculated at the B3LYP/6-31G* level of TD-DFT for the product resulting from C–N bond scission, and the expected merocyanine species.

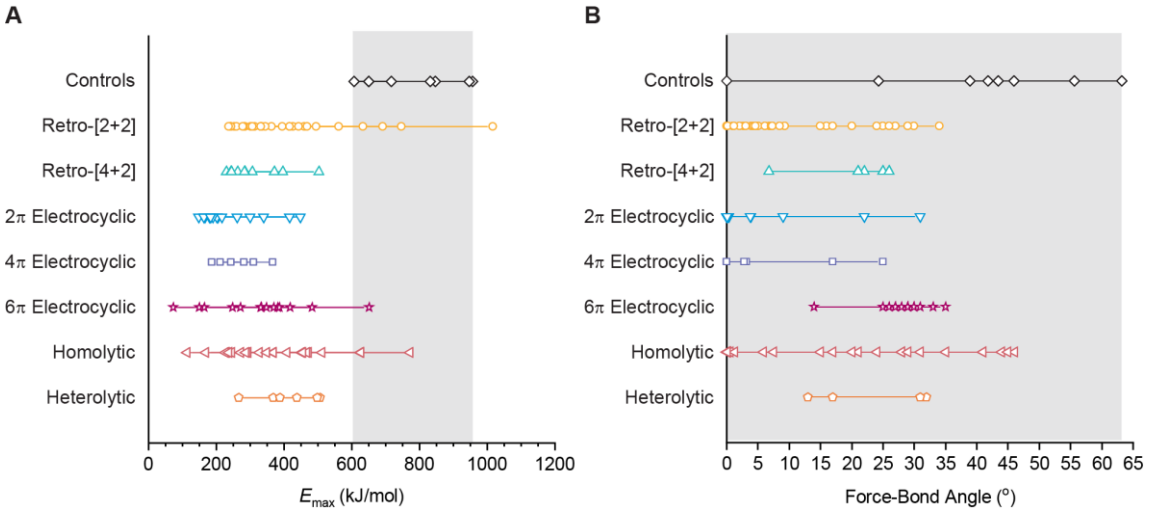

Figure D4. Summary of (A) E_{max} values and (B) force–bond angles determined using the CoGEF method for each mechanochemical reaction class. The CoGEF results for control structures are universally indistinguishable from the mechanophores when alternative quantitative metrics E_{max} and force–bond angle are compared, indicating that these metrics are poor predictors of mechanochemical activity. Data from calculations that are inconsistent with reported experimentally determined reactivity are excluded.

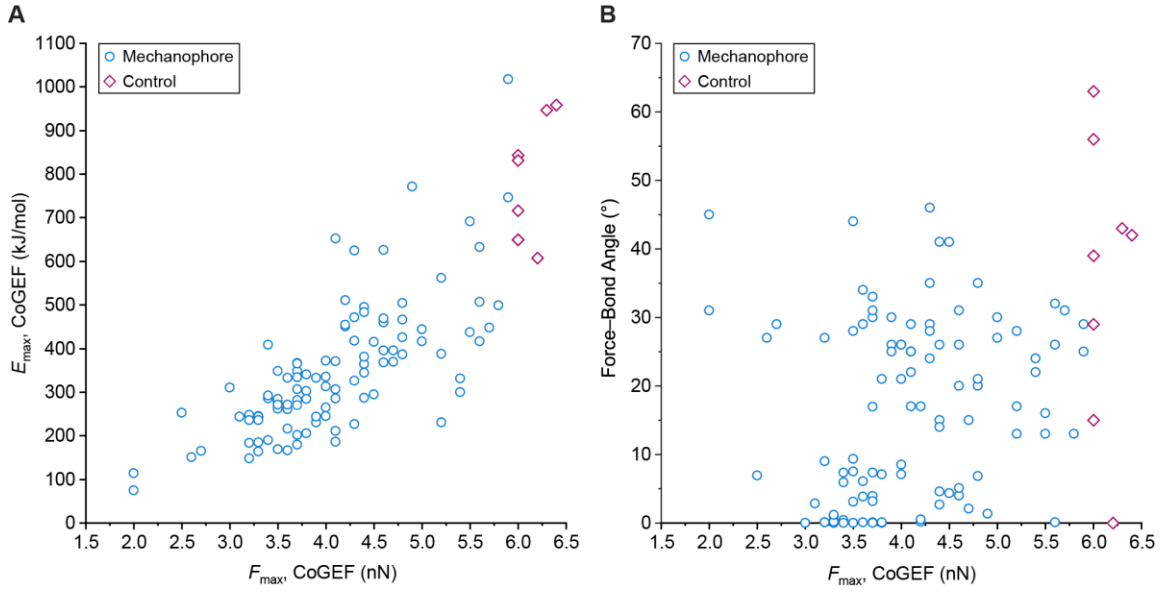

Figure D5. Relationship between calculated values of (A) E_{max} and (B) force–bond angle with the calculated values of F_{max} determined with the CoGEF method at the B3LYP/6-31G* level of density functional theory. There is a positive correlation between values of E_{max} and F_{max}, while there is no apparent correlation between force–bond angle and values of F_{max}.

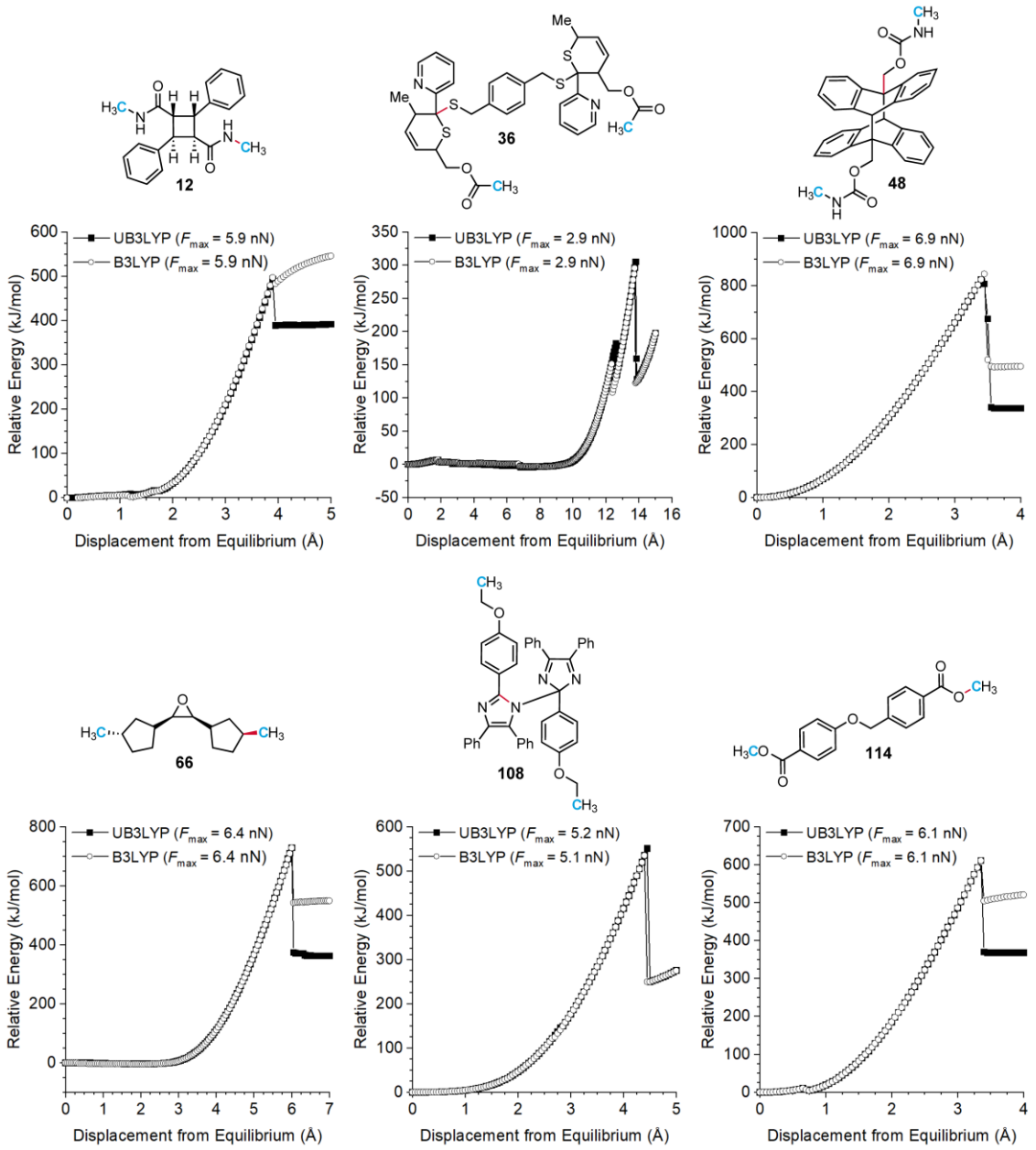

Figure D6. CoGEF calculations performed using unrestricted DFT (UB3LYP/6-31G*) on representative mechanophores for which CoGEF calculations at the B3LYP/6-31G* level of DFT predict reactions that are inconsistent with the reported experimental behavior. Use of the UB3LYP functional has minimal influence on the results of the CoGEF simulations. The same chemical transformations are predicted in each case.

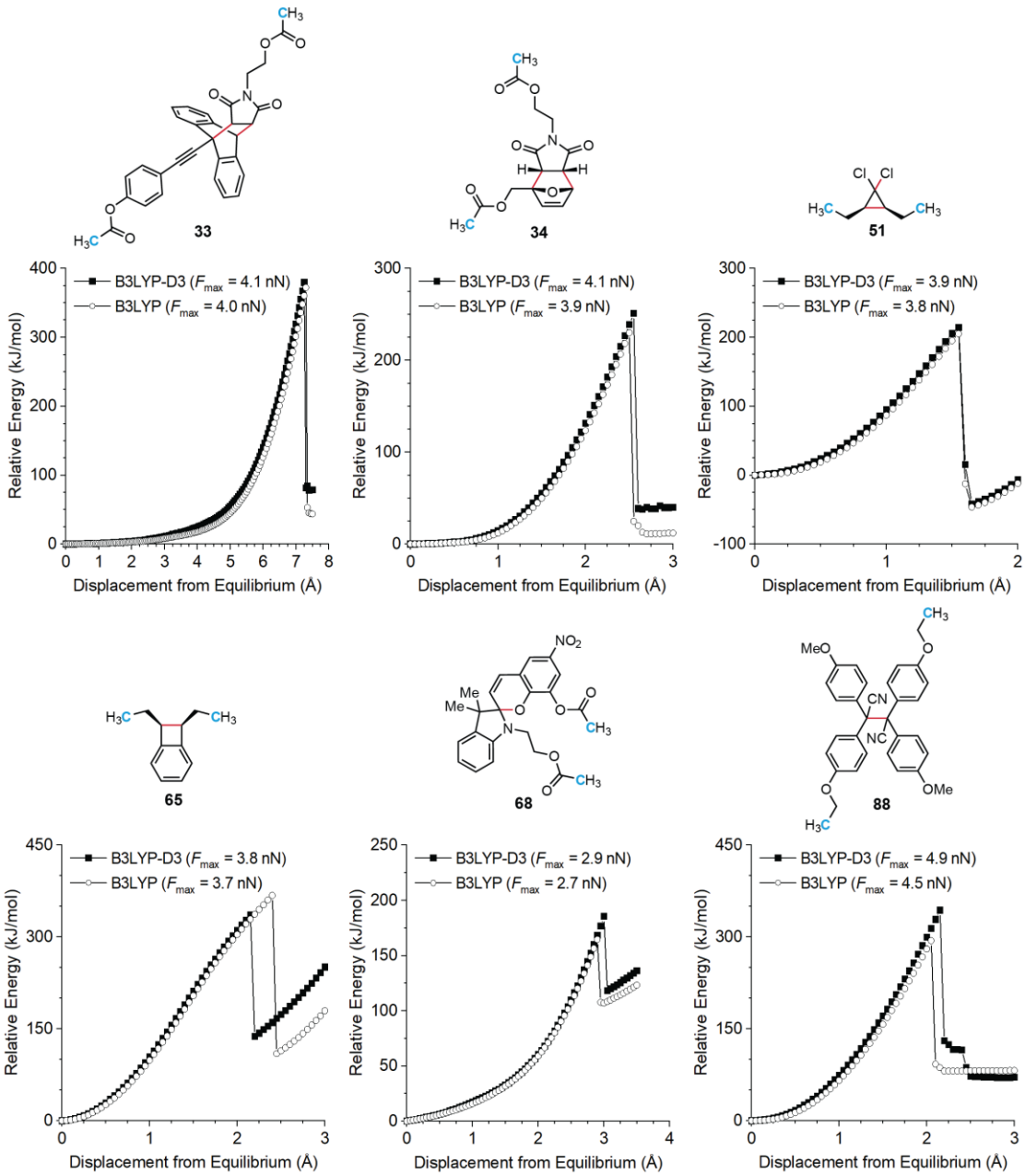

Figure D7. Comparison of CoGEF calculations performed on representative mechanophores at the B3LYP/6-31G* level of DFT and using a dispersion-corrected functional (B3LYP-D3/6-31G*). Use of the dispersion-corrected B3LYP-D3 functional has minimal influence on the results of the CoGEF simulations. The same chemical transformations are predicted in each case.

III. Summaries of Individual CoGEF Calculations

A summary of the results of each individual CoGEF calculation are presented on the pages below. All calculations were performed using DFT at the B3LYP/6-31G* level of theory in vacuum, unless specified otherwise. A reaction scheme depicts the structure of the truncated molecule and the product(s) predicted from the CoGEF calculation. The atoms colored blue indicate the anchor positions (i.e., pulling points) for defining the distance constraint and the bonds that are predicted to cleave are colored red. Representative images of computed structures at critical points in the CoGEF profile are included that depict the force-free equilibrium geometry as well as the structure(s) immediately before and after bond cleavage events. The length of the distance constraint is included below each computed structure and the corresponding positions on the CoGEF curve are denoted. Electrostatic potential maps are included for the products predicted by CoGEF calculations in the heterolytic category. The calculated values of F_{max}, E_{max}, and force–bond angle are tabulated for each calculation. Note that the former bonds persist as artifacts in Spartan after a reaction is predicted to occur. For references to the primary literature describing the experimental reactivity of each compound, refer to the tables in the main text.

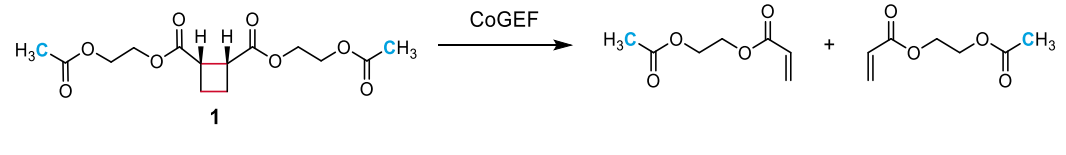

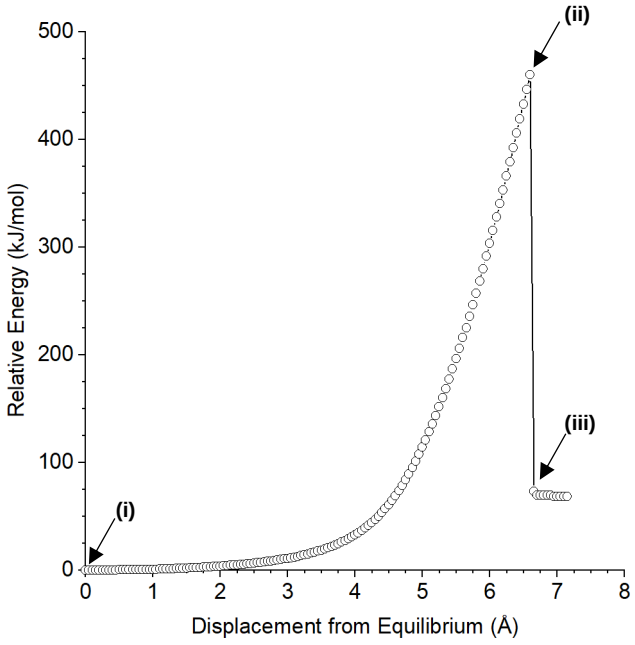

(i) Equilibrium Geometry

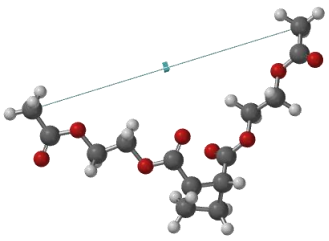

13.344 Å

(ii) Immediately Prior to Bond Cleavage

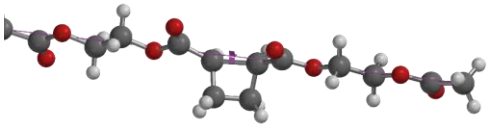

20.294 Å

(iii) Immediately After Bond Cleavage

20.344 Å

Summary of CoGEF Results	
F_{max}	4.6 nN
E_{max}	460 kJ/mol
Force-Bond Angle	4°

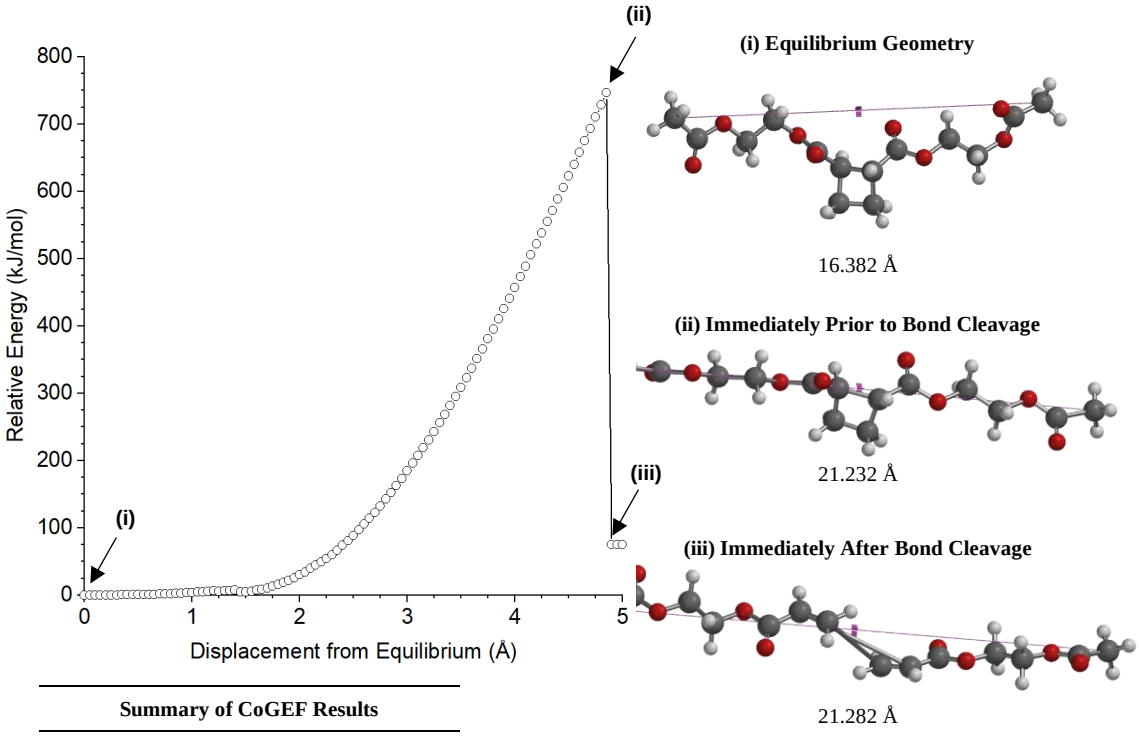

Summary of CoGEF Results	
F_{max}	5.9 nN
E_{max}	746 kJ/mol
Force-Bond Angle	25°

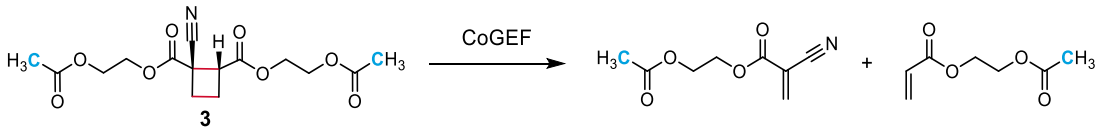

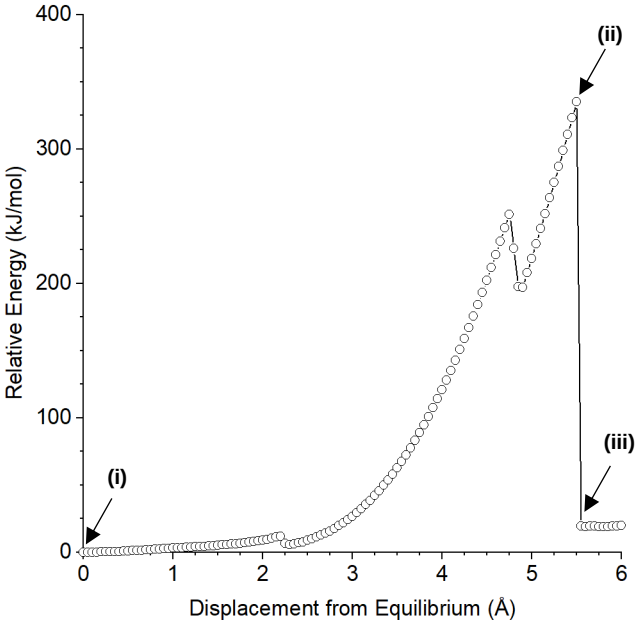

(i) Equilibrium Geometry

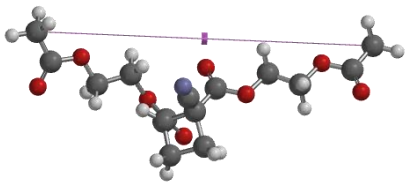

14.479 Å

(ii) Immediately Prior to Bond Cleavage

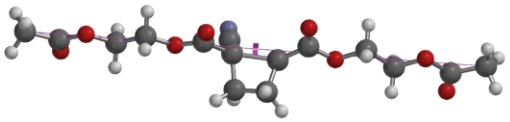

19.979 Å

(iii) Immediately After Bond Cleavage

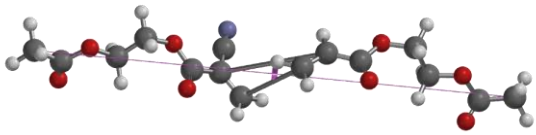

20.029 Å

Summary of CoGEF Results	
F_{max}	4.0 nN
E_{max}	335 kJ/mol
Force-Bond Angle	7.1°

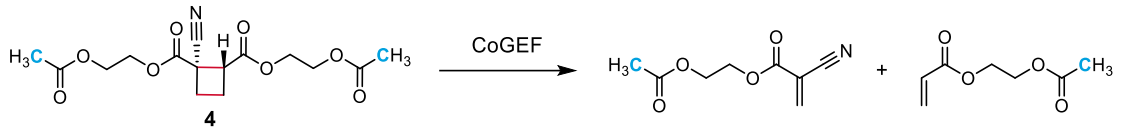

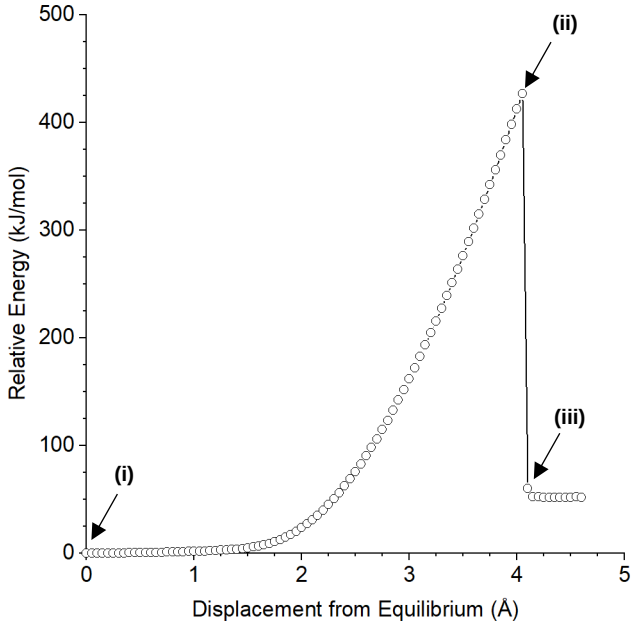

Summary of CoGEF Results

F_{max}	4.8 nN
E_{max}	426 kJ/mol
Force-Bond Angle	20°

(i) Equilibrium Geometry

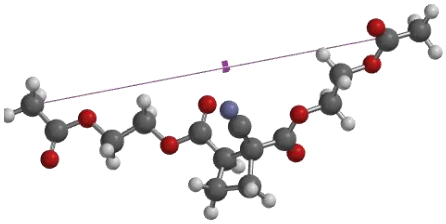

16.271 Å

(ii) Immediately Prior to Bond Cleavage

20.321 Å

(iii) Immediately After Bond Cleavage

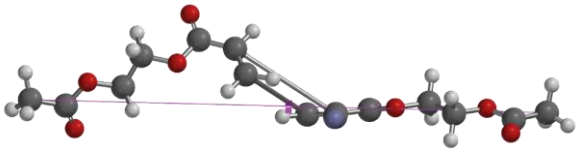

20.371 Å

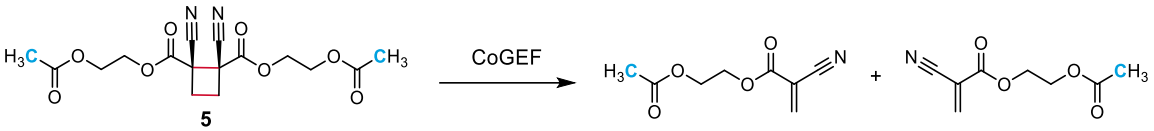

5

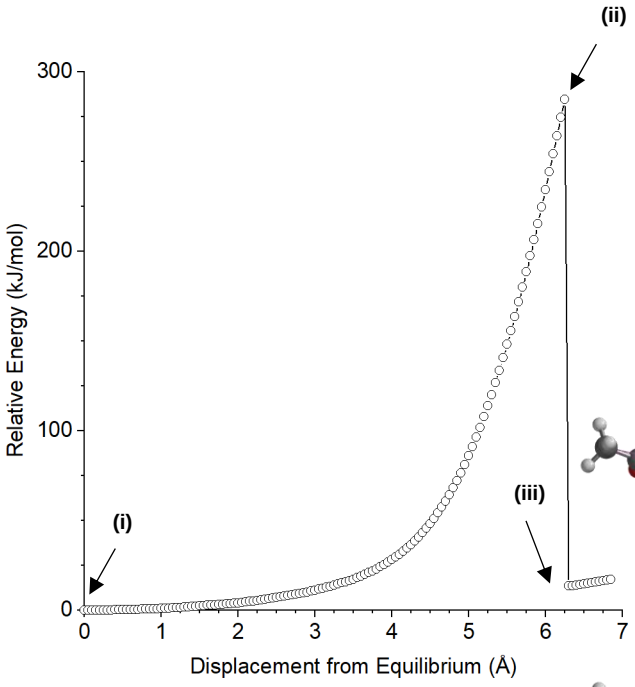

(i) Equilibrium Geometry

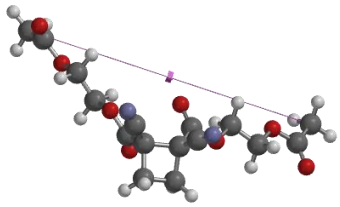

13.303 Å

(ii) Immediately Prior to Bond Cleavage

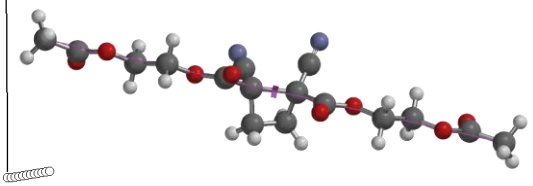

19.553 Å

(iii) Immediately After Bond Cleavage

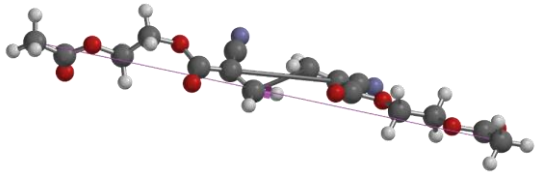

19.603 Å

Summary of CoGEF Results	
F_{max}	3.4 nN
E_{max}	285 kJ/mol
Force-Bond angle	7.3°

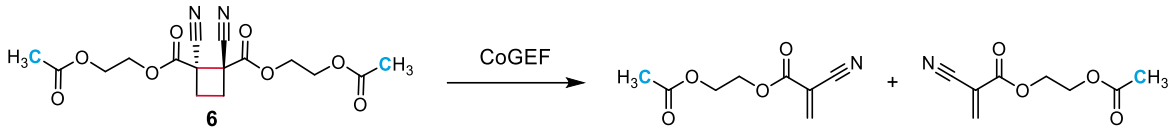

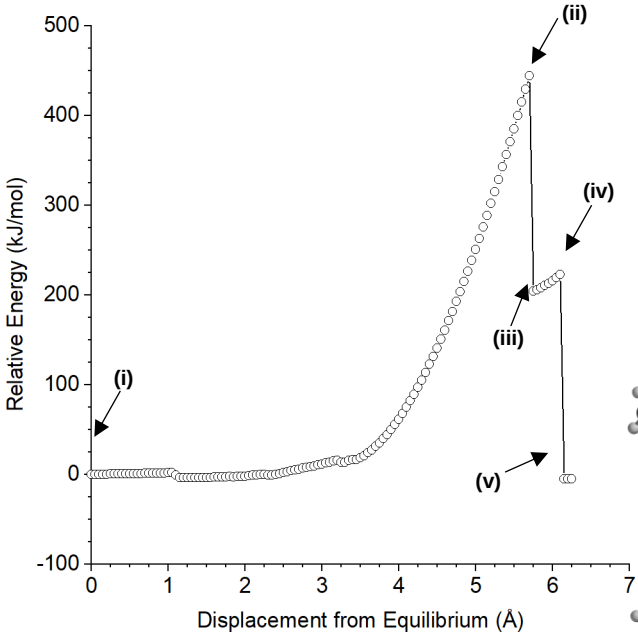

(i) Equilibrium Geometry

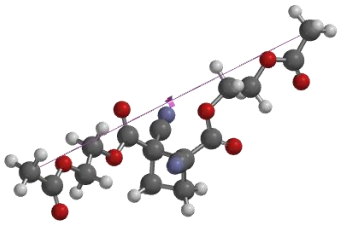

14.667 Å

(ii) Immediately Prior to First Bond Cleavage

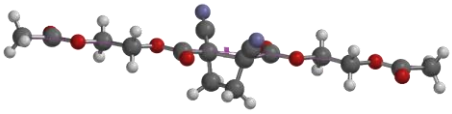

20.417 Å

(iii) Immediately After First Bond Cleavage

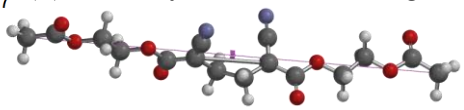

20.467 Å

(iv) Immediately Prior to Second Bond Cleavage

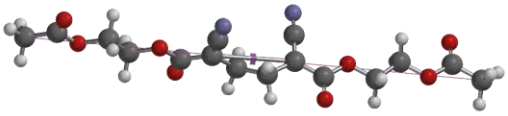

20.817

(iv) Immediately After Second Bond Cleavage

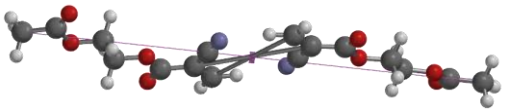

20.867 Å

Summary of CoGEF Results	
F_{max}	5.0 nN
E_{max}	444 kJ/mol
Force-Bond Angle	27°

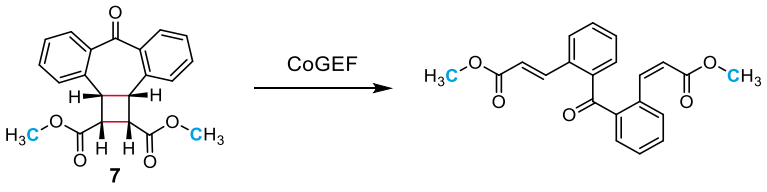

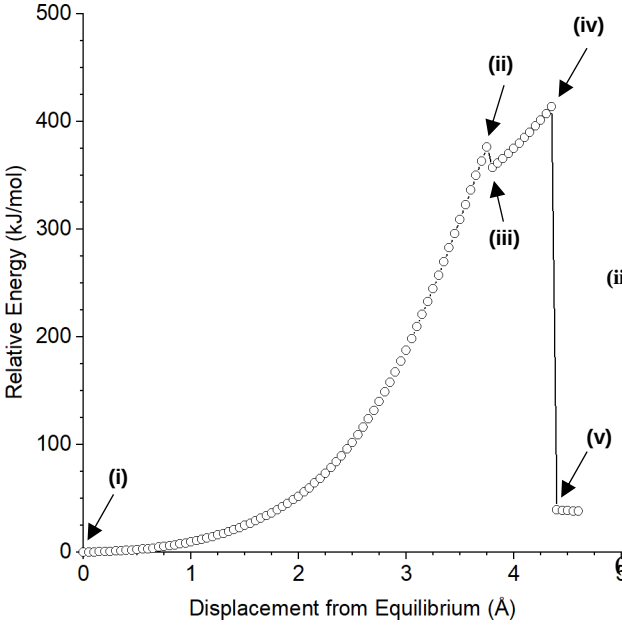

Summary of CoGEF Results	
F_{max}	4.5 nN
E_{max}	413 kJ/mol
Force-Bond Angle	4.3°

(i) Equilibrium Geometry

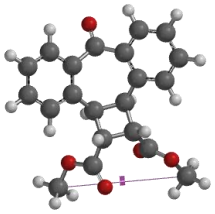

6.295 Å

(ii) Immediately Prior to First Bond Cleavage

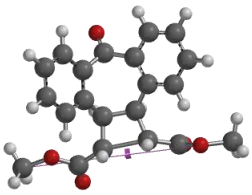

10.045 Å

(iii) Immediately After First Bond Cleavage

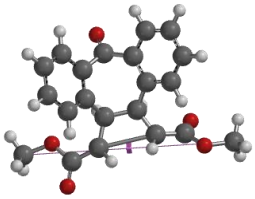

10.095 Å

(iv) Immediately Before Second Bond Cleavage

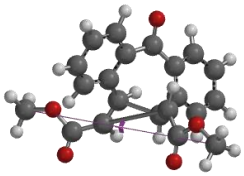

10.645 Å

(v) Immediately After Second Bond Cleavage

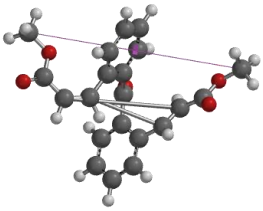

10.695 Å

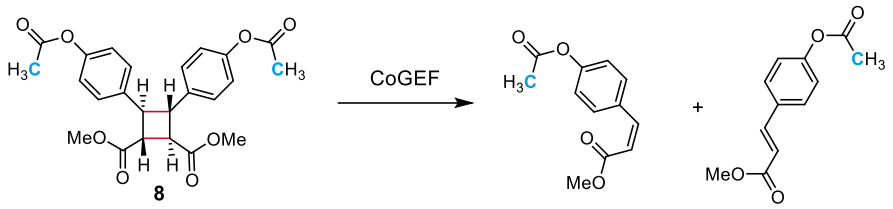

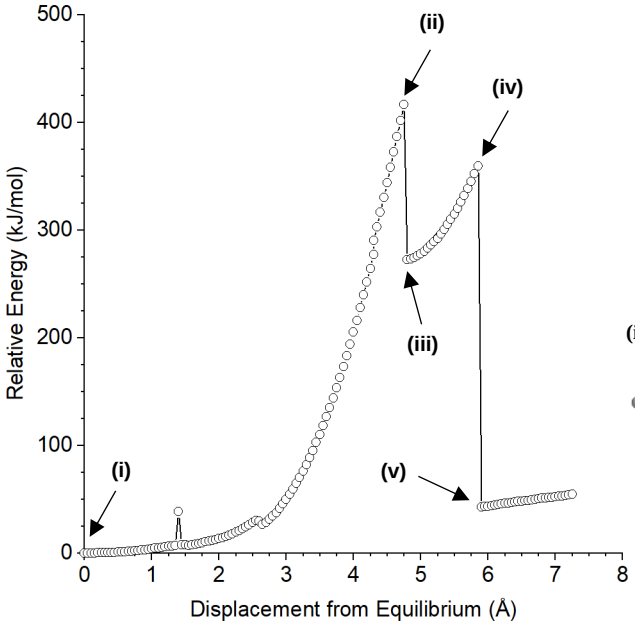

Summary of CoGEF Results	
F_{max}	5.0 nN
E_{max}	417 kJ/mol
Force-Bond Angle	30°

(i) Equilibrium Geometry

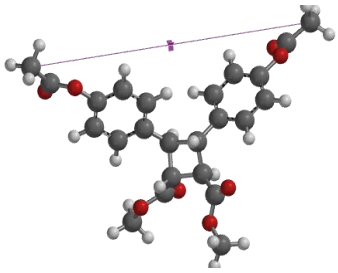

14.256 Å

(ii) Immediately Prior to First Bond Cleavage

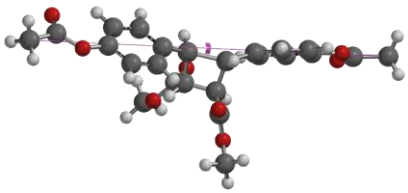

19.006 Å

(iii) Immediately After First Bond Cleavage

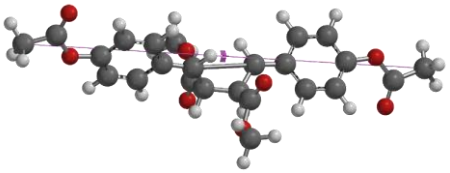

19.056 Å

(iv) Immediately Prior to Second Bond Cleavage

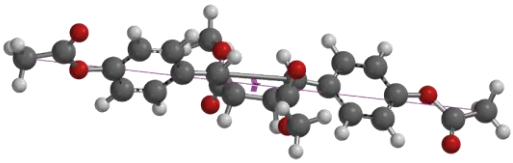

20.106

(v) Immediately After Second Bond Cleavage

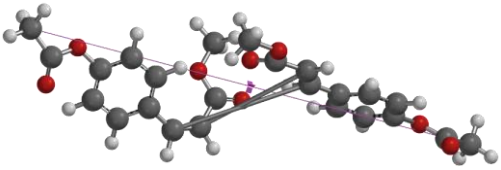

20.156 Å

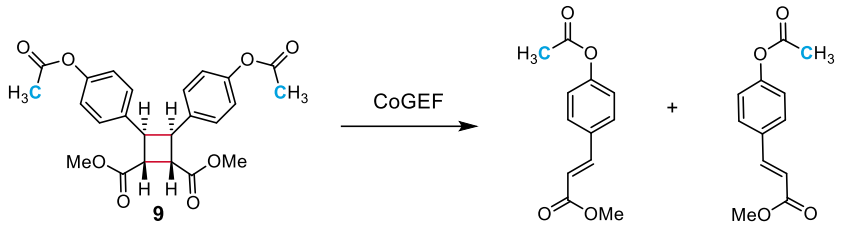

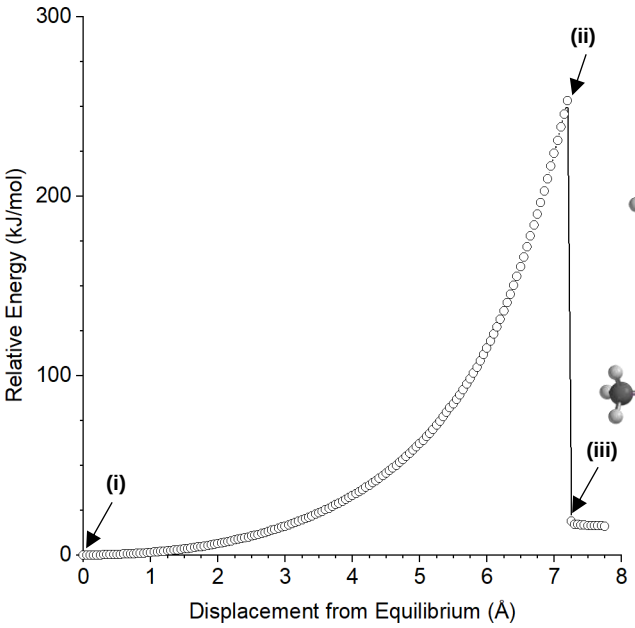

(i) Equilibrium Geometry

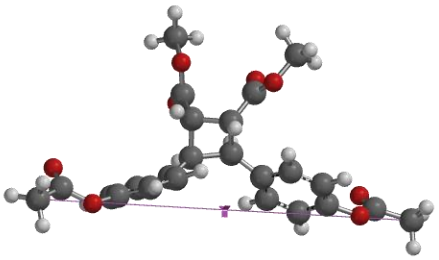

10.962 Å

(ii) Immediately Prior to First Bond Cleavage

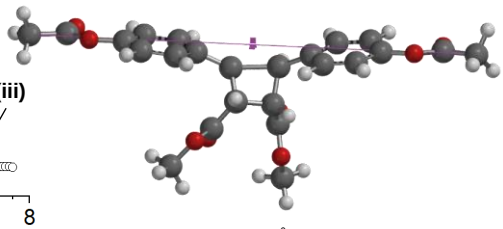

18.162 Å

(iii) Immediately After First Bond Cleavage

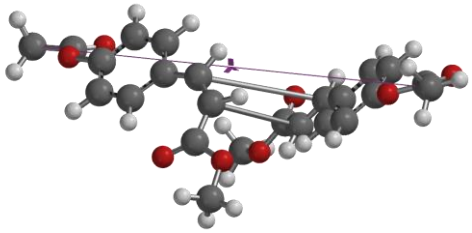

18.212 Å

Summary of CoGEF Results	
F_{max}	2.5 nN
E_{max}	253 kJ/mol
Force-Bond Angle	6.9°

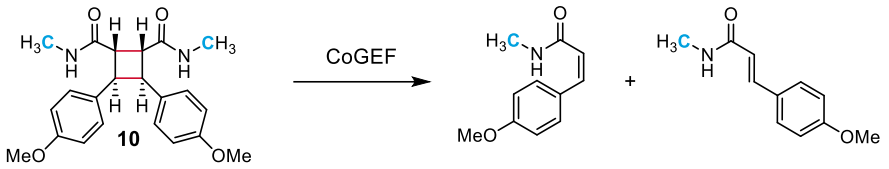

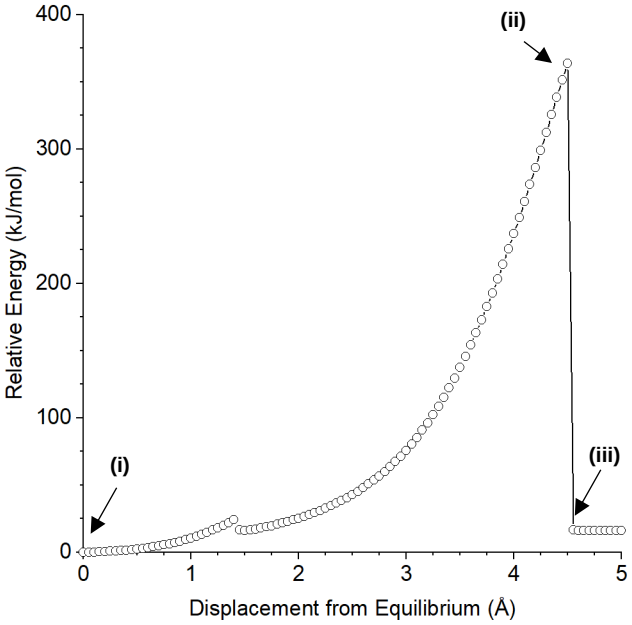

Summary of CoGEF Results	
F_{max}	4.4 nN
E_{max}	364 kJ/mol
Force-Bond Angle	2.7°

(i) Equilibrium Geometry

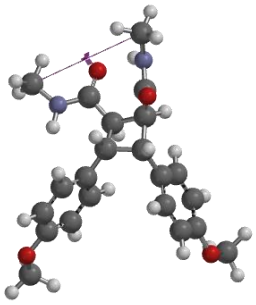

5.759 Å

(ii) Immediately Prior to First Bond Cleavage

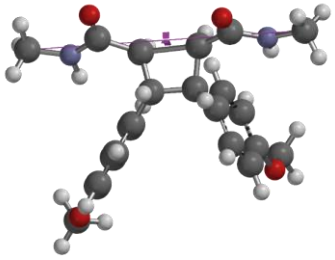

10.259 Å

(iii) Immediately After First Bond Cleavage

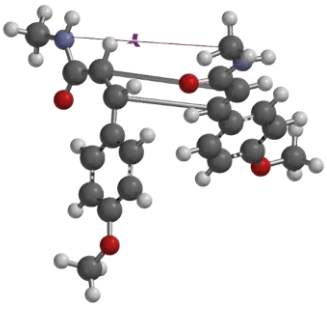

10.309 Å

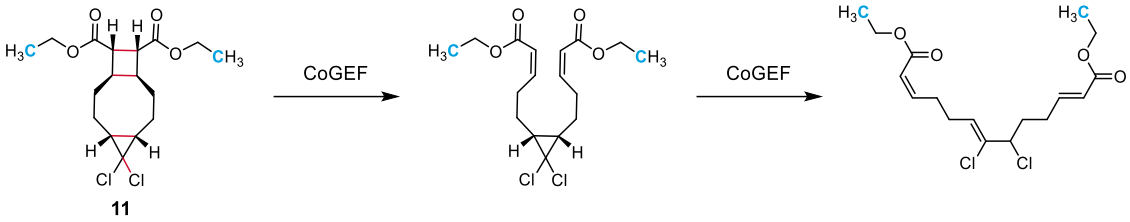

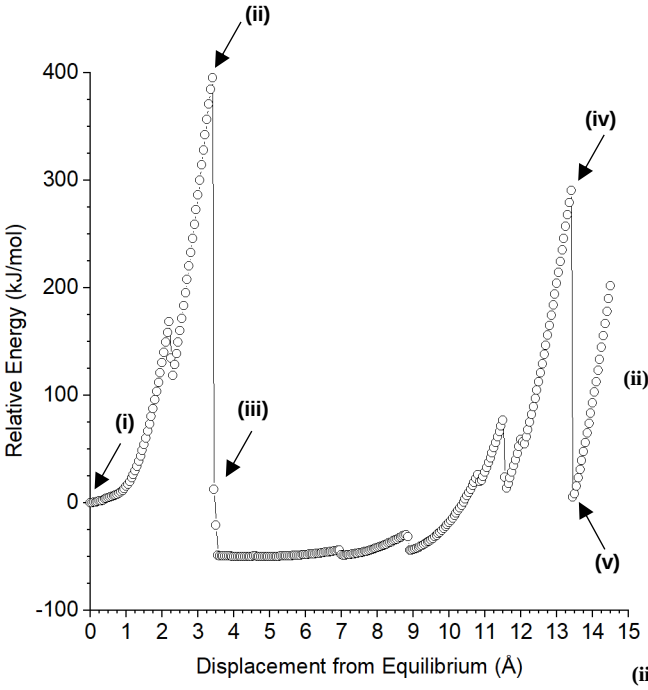

(i) Equilibrium Geometry

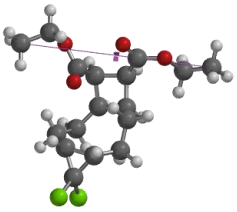

9.485 Å

(ii) Immediately Prior to First Bond Cleavage

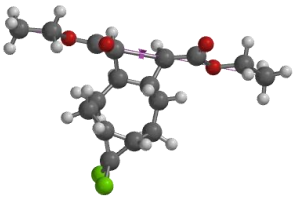

12.885 Å

(iii) Immediately After First Bond Cleavage

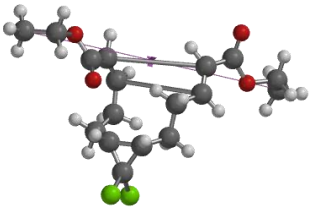

12.935 Å

(iv) Immediately Before Second Bond Cleavage

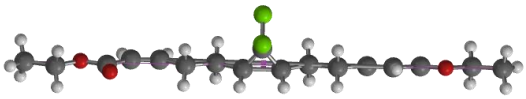

22.885 Å

(v) Immediately After Second Bond Cleavage

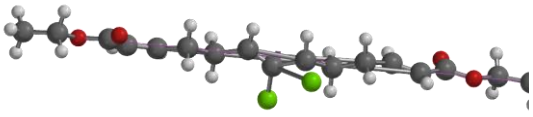

22.935 Å

Summary of CoGEF Results		
	cyclobutane	***g*DCC**
F_{max}	4.7 nN	3.8 nN
E_{max}	395 kJ/mol	291 kJ/mol
Force-Bond Angle	2.1°	0.4°

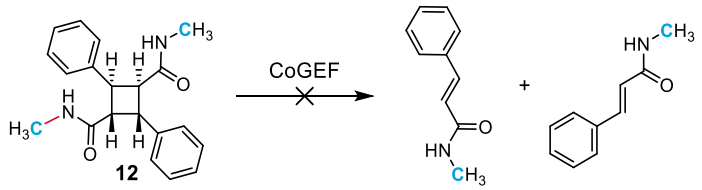

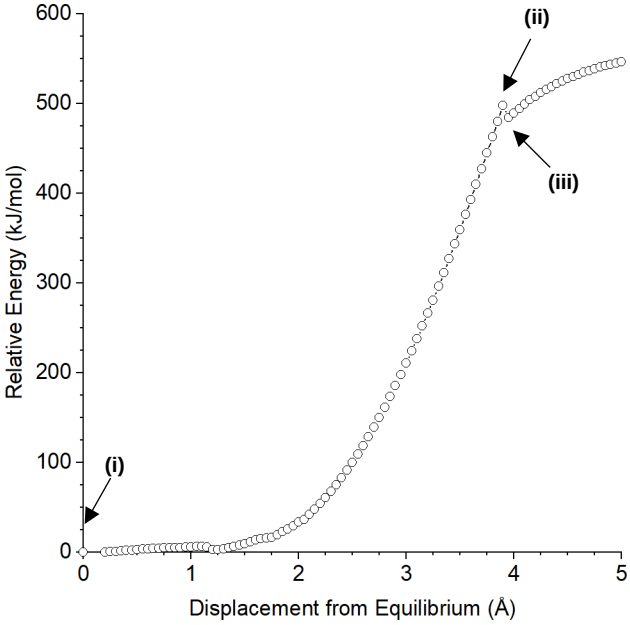

(i) Equilibrium Geometry

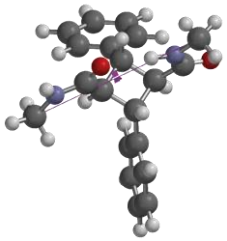

7.497 Å

(ii) Immediately Prior to Bond Cleavage

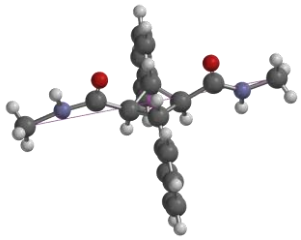

11.397 Å

(iii) Immediately After Bond Cleavage

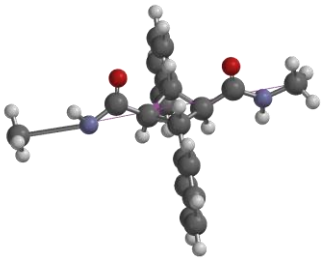

11.5447 Å

Summary of CoGEF Results	
F_{max}	5.9 nN
E_{max}	498 kJ/mol
Force-Bond Angle	44°

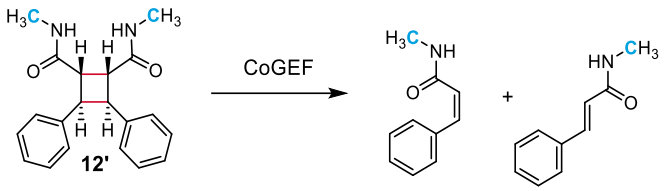

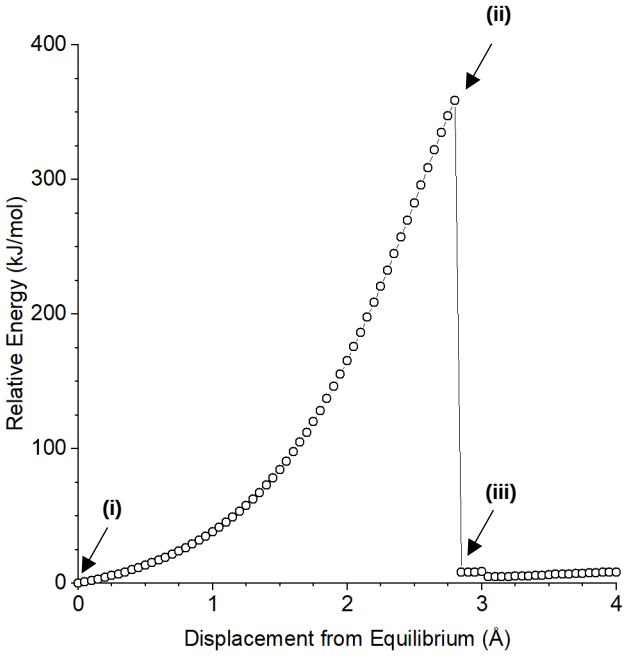

(i) Equilibrium Geometry

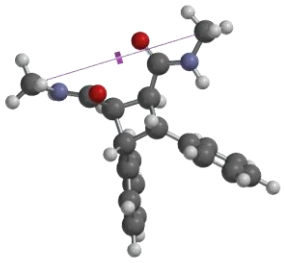

7.519 Å

(ii) Immediately Prior to Bond Cleavage

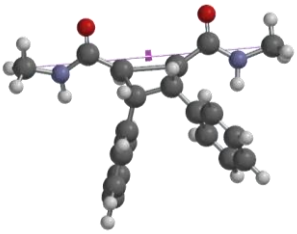

10.319 Å

(iii) Immediately After Bond Cleavage

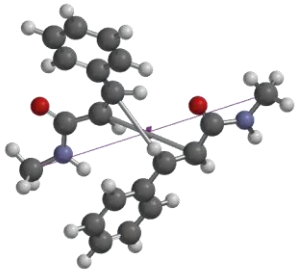

10.369 Å

Summary of CoGEF Results	
F_{max}	4.4 nN
E_{max}	359 kJ/mol
Force-Bond Angle	2.2°

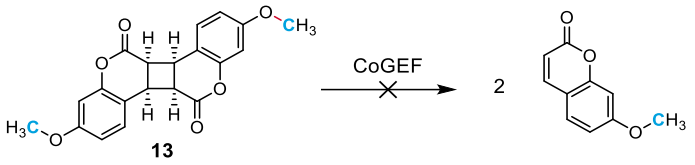

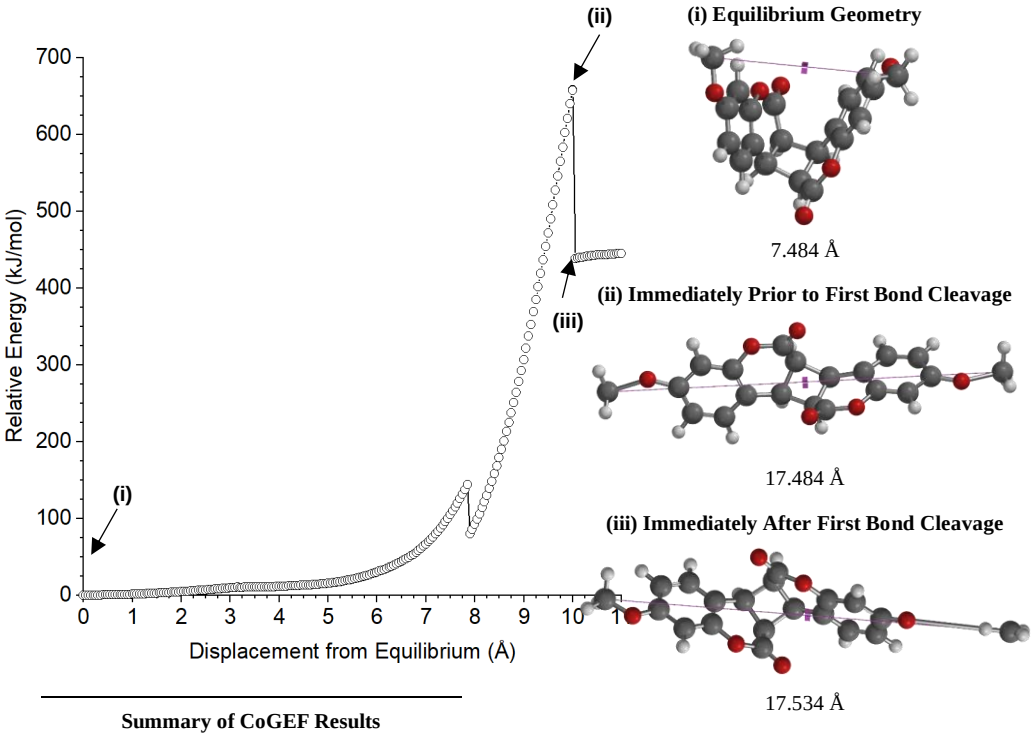

Summary of CoGEF Results	
F_{max}	6.3 nN
E_{max}	658 kJ/mol
Force-Bond Angle	28°

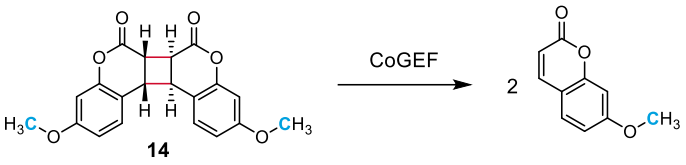

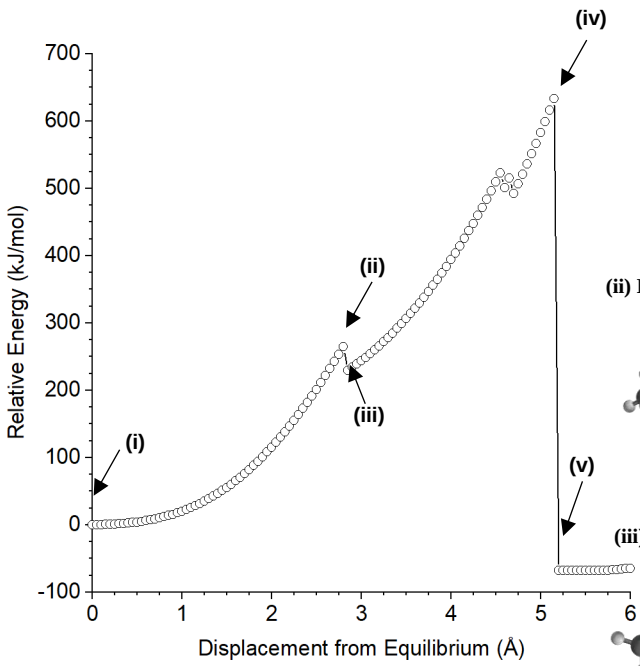

Summary of CoGEF Results	
F_{max}	5.6 nN
E_{max}	633 kJ/mol
Force-Bond Angle	26°

(i) Equilibrium Geometry

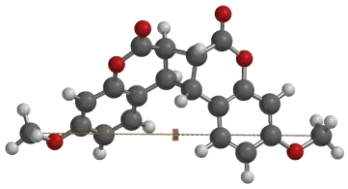

13.066 Å

(ii) Immediately Prior to First Bond Cleavage

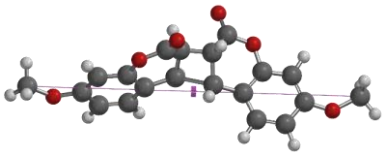

15.866 Å

(iii) Immediately After First Bond Cleavage

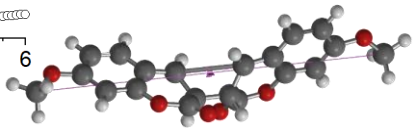

15.916 Å

(iv) Immediately Before Second Bond Cleavage

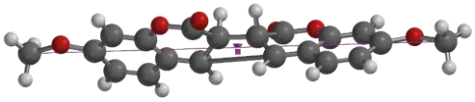

18.216 Å

(v) Immediately After Second Bond Cleavage

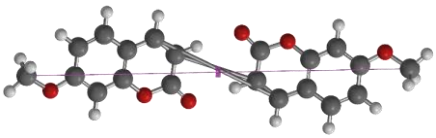

18.266 Å

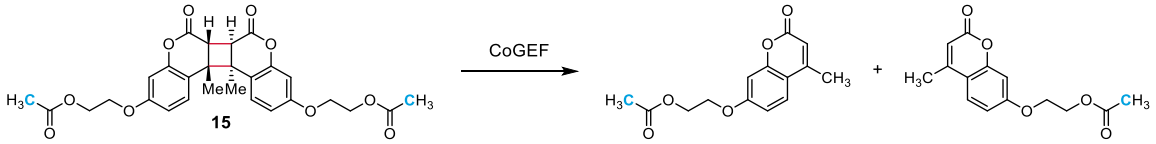

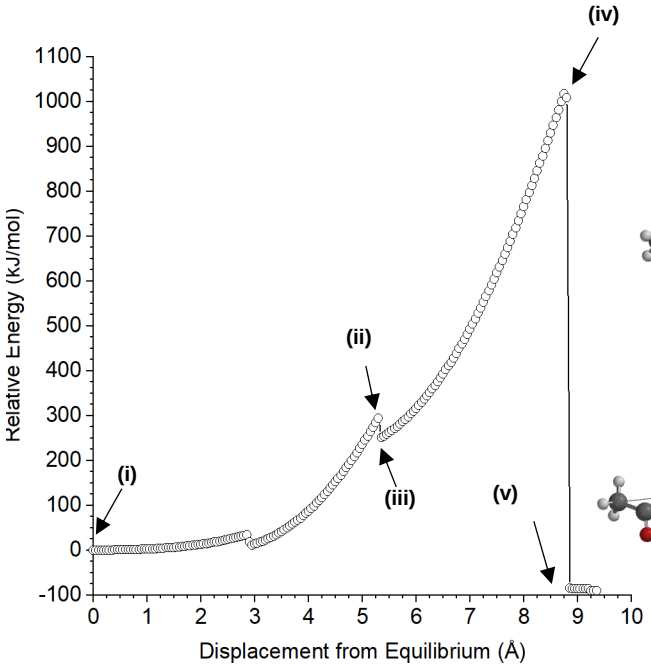

(i) Equilibrium Geometry

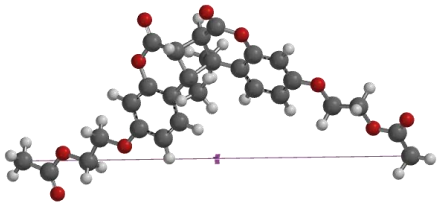

20.607 Å

(ii) Immediately Prior to First Bond Cleavage

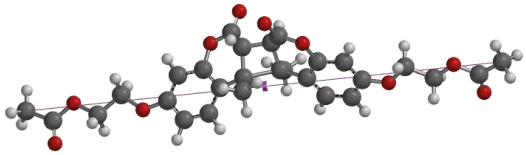

25.907 Å

(iii) Immediately After First Bond Cleavage

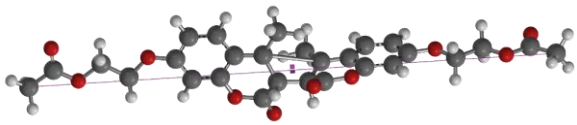

25.957 Å

(iv) Immediately Before Second Bond Cleavage

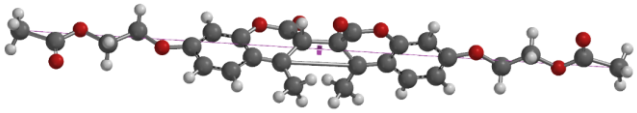

29.407 Å

(v) Immediately After Second Bond Cleavage

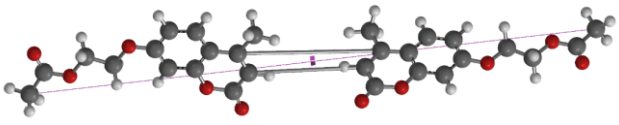

29.457 Å

Summary of CoGEF Results	
F_{max}	5.9 nN
E_{max}	1017 kJ/mol
Force-Bond Angle	29°

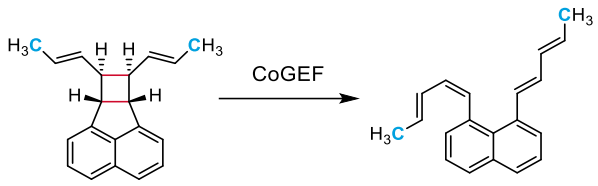

16

(i) Equilibrium Geometry

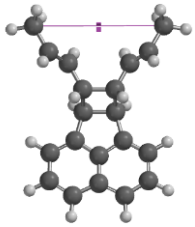

6.366 Å

(ii) Immediately Prior to First Bond Cleavage

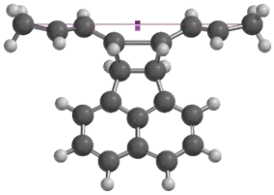

10.066 Å

(iii) Immediately After First Bond Cleavage

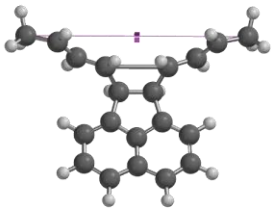

10.116 Å

(v) Immediately Prior to Second Bond Cleavage

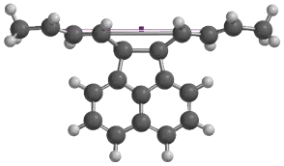

12.216 Å

(vi) Immediately After Second Bond Cleavage

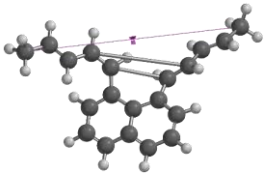

12.266 Å

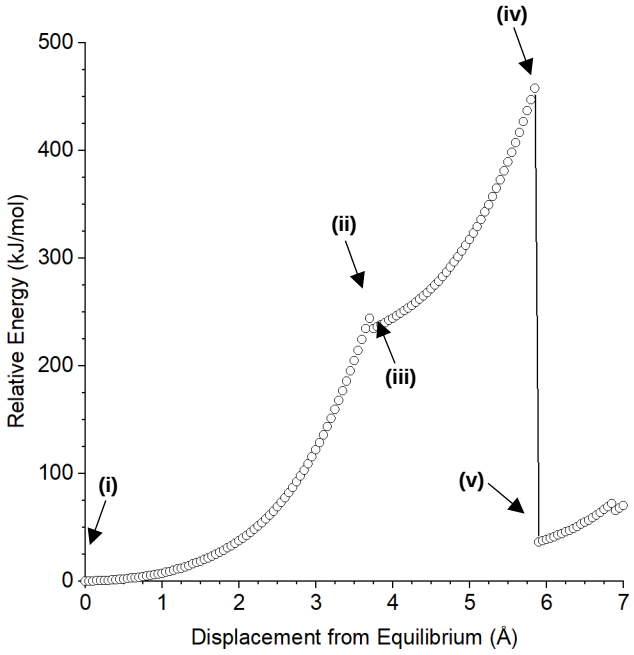

Summary of CoGEF Results	
F_{max}	3.3 nN
E_{max}	244 kJ/mol
Force-Bond Angle	0.0°

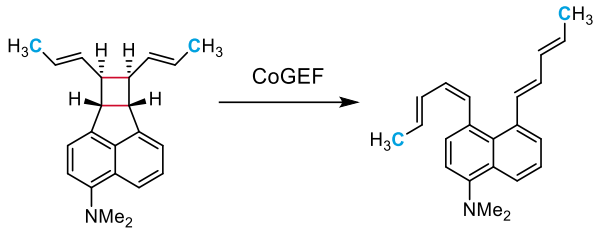

17

(i) Equilibrium Geometry

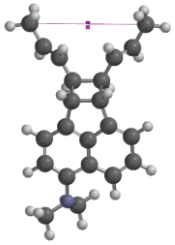

6.351 Å

(ii) Immediately Prior to First Bond Cleavage

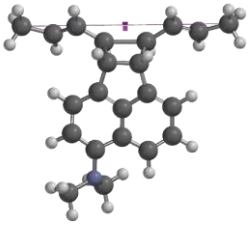

10.051 Å

(iii) Immediately After First Bond Cleavage

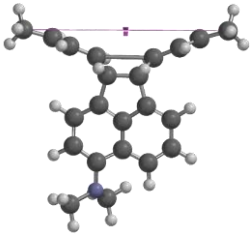

10.101 Å

(v) Immediately Prior to Second Bond Cleavage

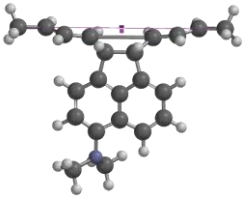

11.351 Å

(vi) Immediately After Second Bond Cleavage

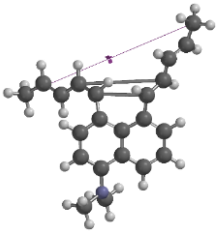

11.401 Å

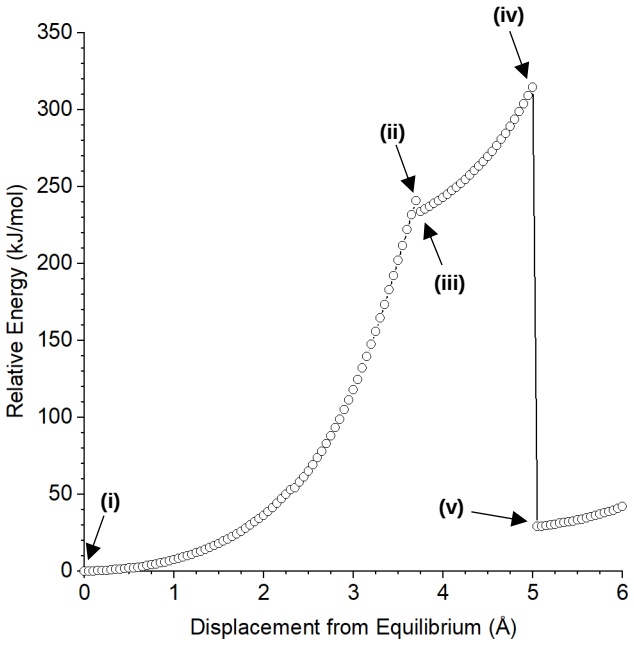

Summary of CoGEF Results	
F_{max}	3.3 nN
E_{max}	241 kJ/mol
Force-Bond Angle	1.0°

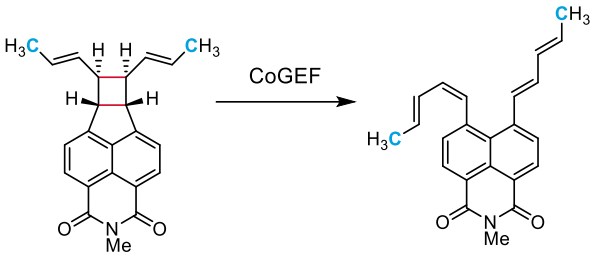

18

(i) Equilibrium Geometry

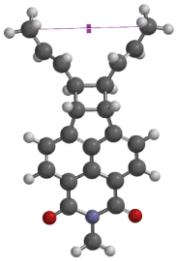

6.319 Å

(ii) Immediately Prior to First Bond Cleavage

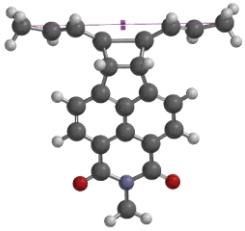

10.069 Å

(iii) Immediately After First Bond Cleavage

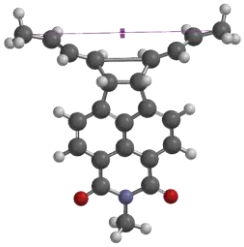

10.119 Å

(v) Immediately Prior to Second Bond Cleavage

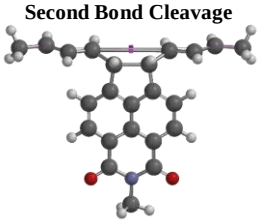

12.569 Å

(vi) Immediately After Second Bond Cleavage

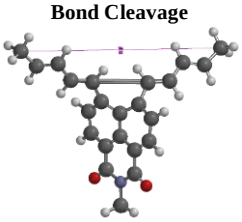

12.619 Å

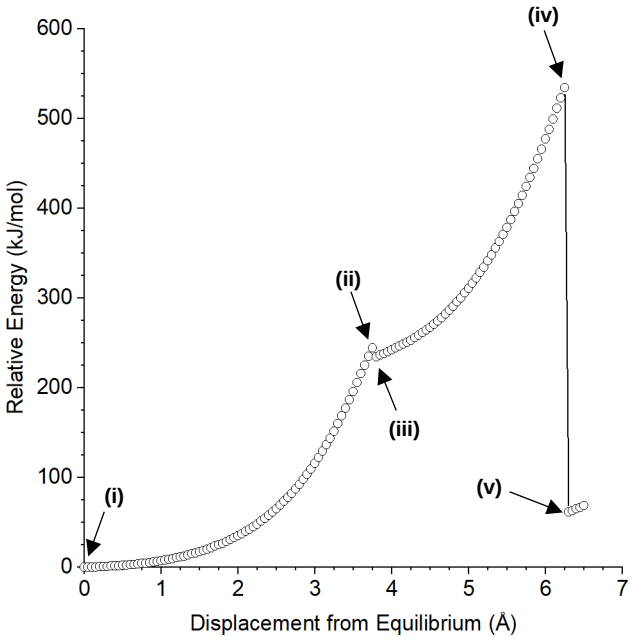

Summary of CoGEF Results	
F_{max}	3.3 nN
E_{max}	244 kJ/mol
Force-Bond Angle	0.2°

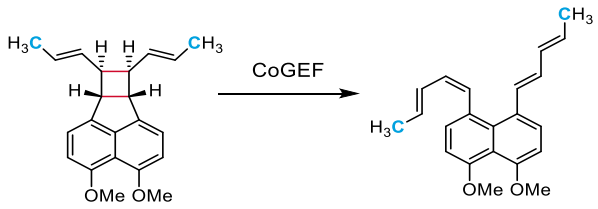

19

(i) Equilibrium Geometry

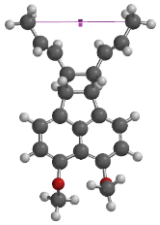

6.325 Å

(ii) Immediately Prior to First Bond Cleavage

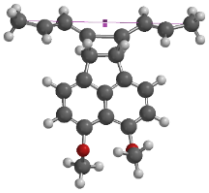

10.025 Å

(iii) Immediately After First Bond Cleavage

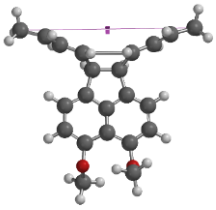

10.075 Å

(v) Immediately Prior to Second Bond Cleavage

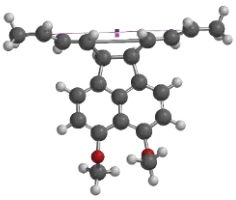

11.325 Å

(vi) Immediately After Second Bond Cleavage

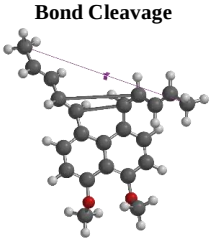

11.375 Å

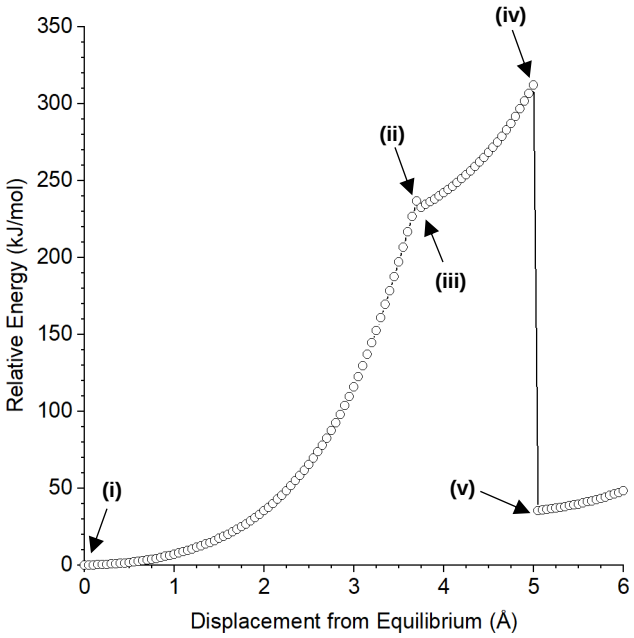

Summary of CoGEF Results	
F_{max}	3.3 nN
E_{max}	236 kJ/mol
Force-Bond Angle	1.2°

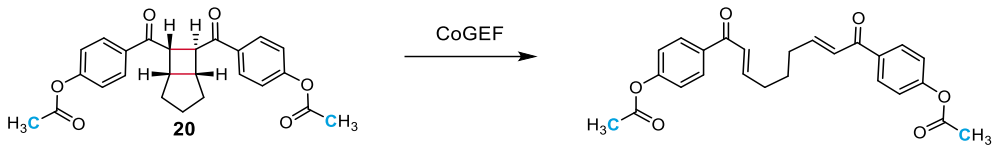

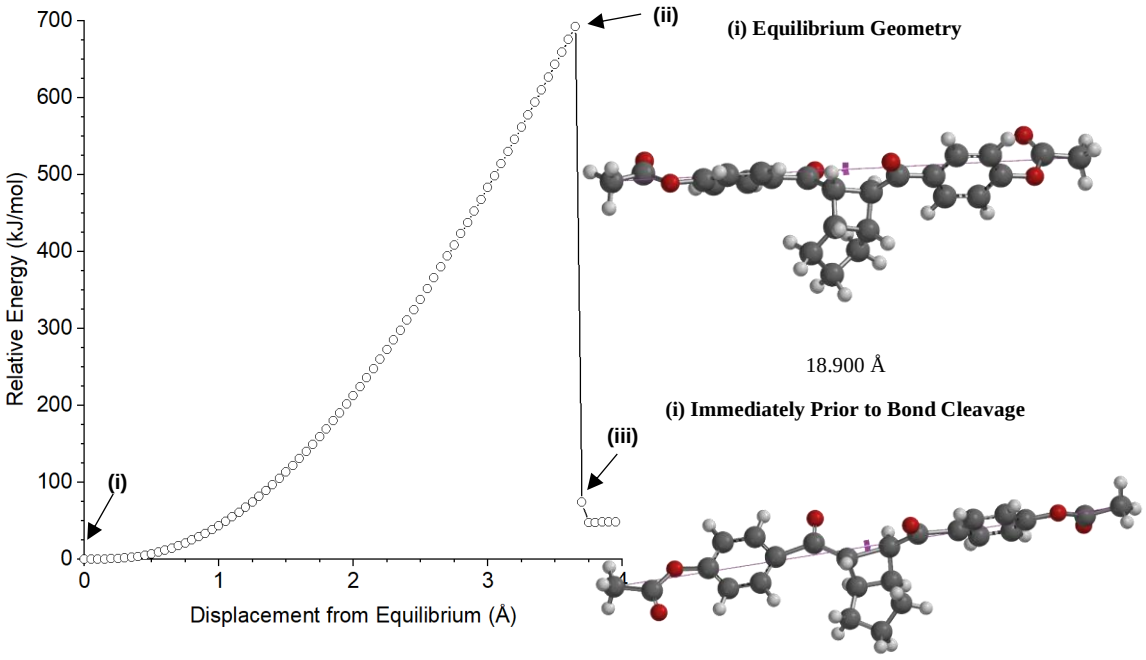

Summary of CoGEF Results	
F_{max}	5.5 nN
E_{max}	692 kJ/mol
Force-Bond Angle	16°

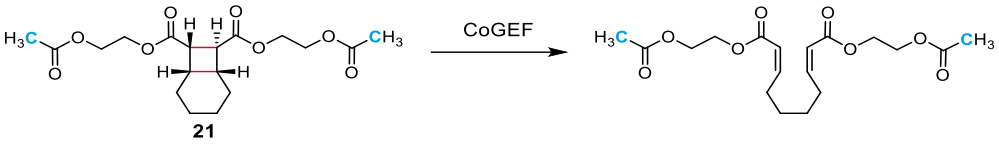

21

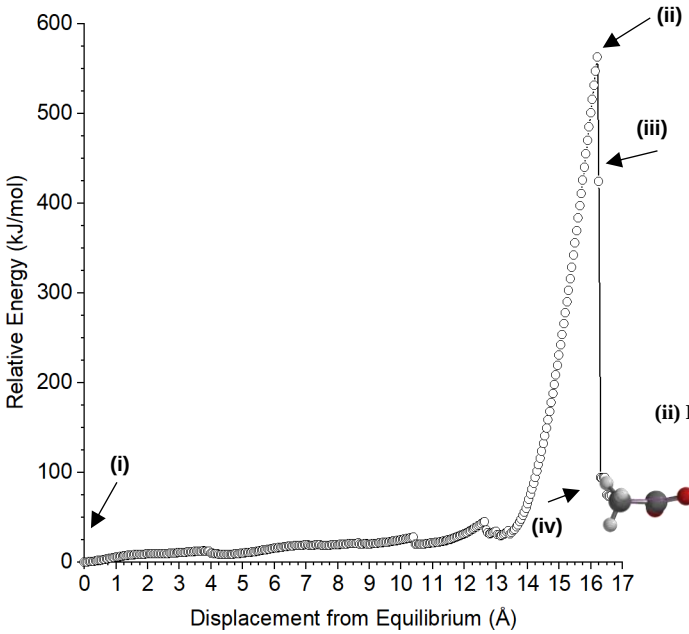

(i) Equilibrium Geometry

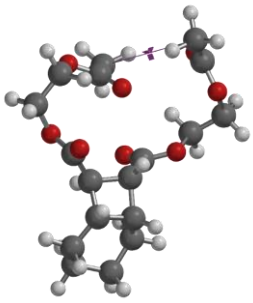

4.462 Å

(ii) Immediately Prior to First Bond Cleavage

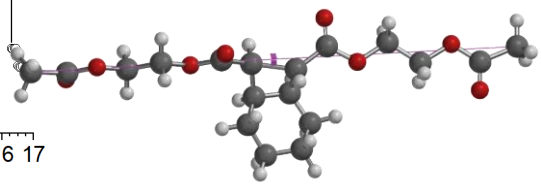

20.662 Å

(iii) Immediately After First Bond Cleavage

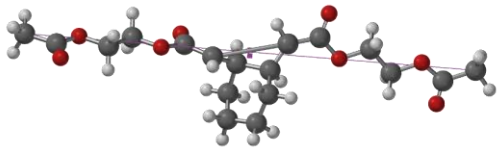

20.712 Å

(iv) Immediately After Second Bond Cleavage

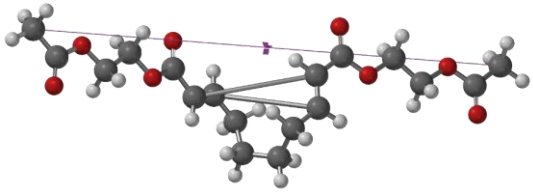

20.762 Å

Summary of CoGEF Results	
F_{max}	5.2 nN
E_{max}	562 kJ/mol
Force-Bond Angle	17°

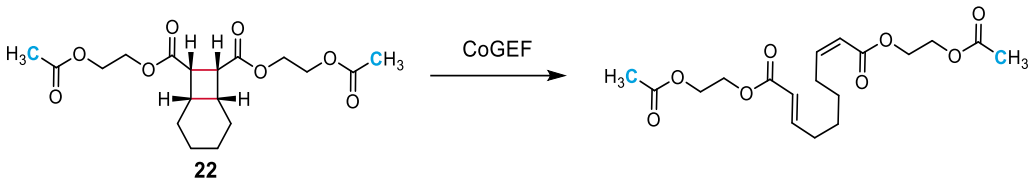

22

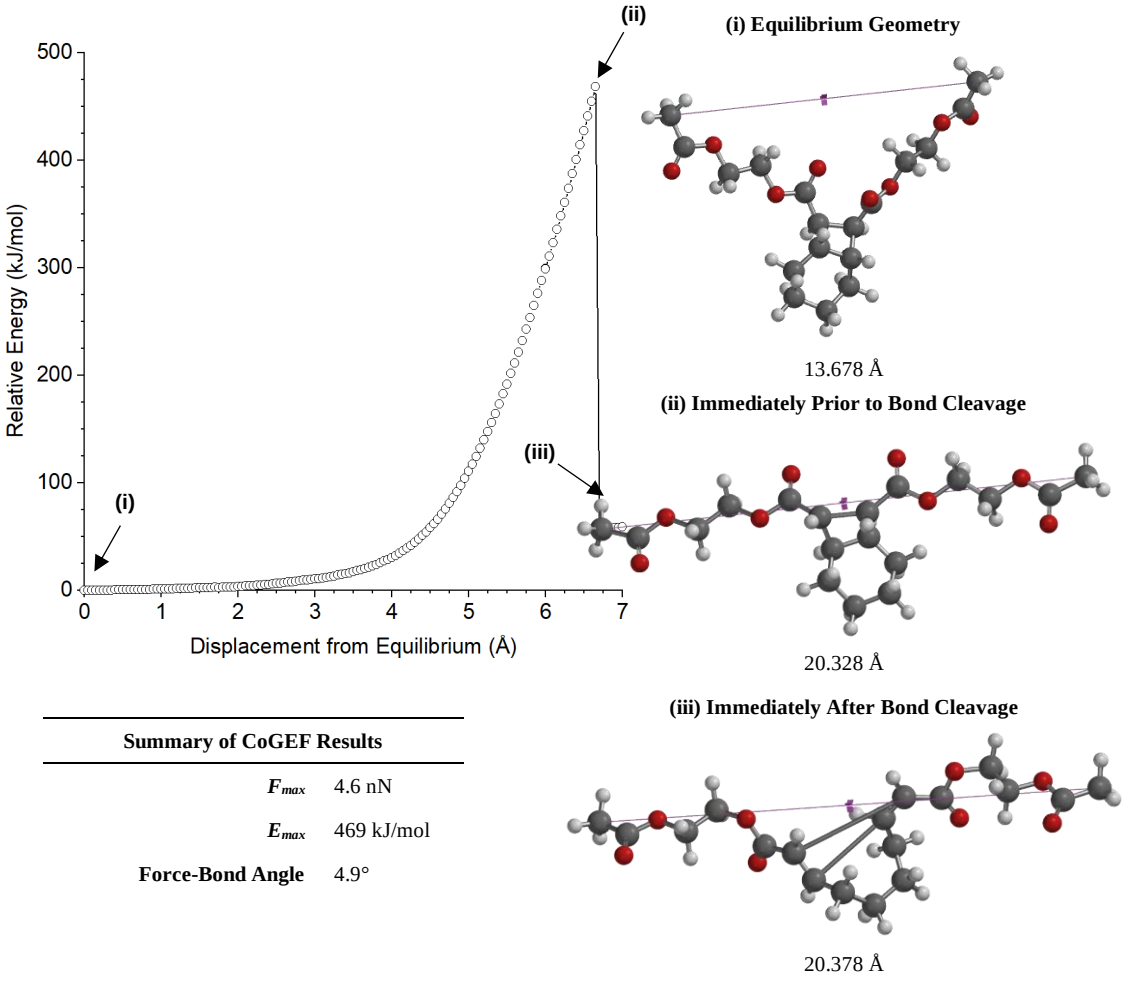

(i) Equilibrium Geometry

13.678 Å

(ii) Immediately Prior to Bond Cleavage

20.328 Å

(iii) Immediately After Bond Cleavage

20.378 Å

Summary of CoGEF Results	
F_{max}	4.6 nN
E_{max}	469 kJ/mol
Force-Bond Angle	4.9°

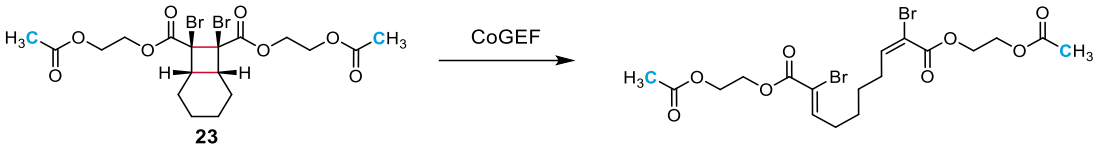

23

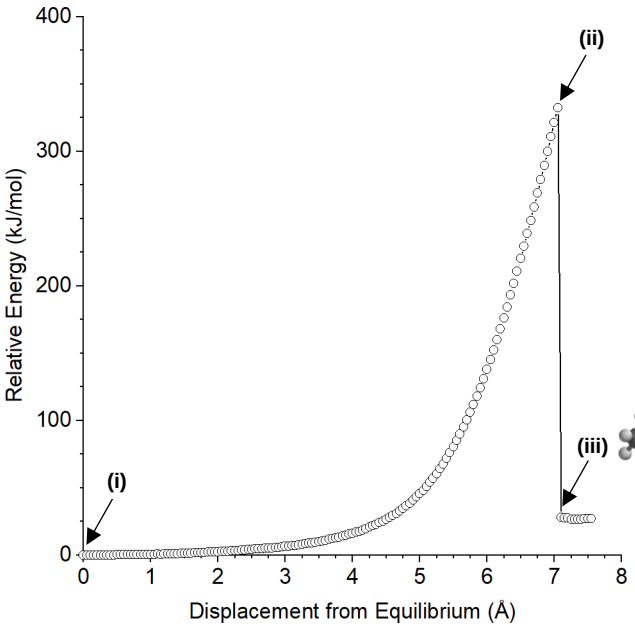

(i) Equilibrium Geometry

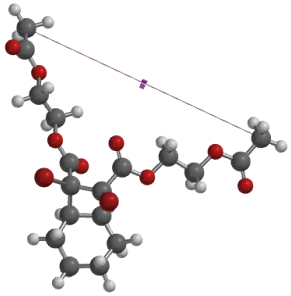

12.604 Å

(ii) Immediately Prior to First Bond Cleavage

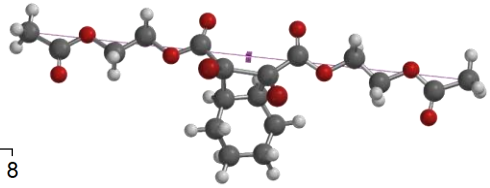

19.654 Å

(iii) Immediately After First Bond Cleavage

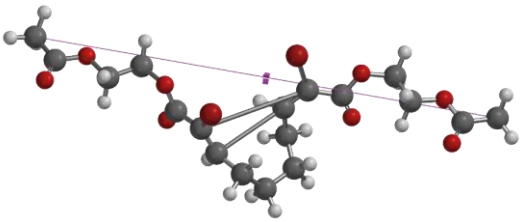

19.704 Å

Summary of CoGEF Results	
F_{max}	3.6 nN
E_{max}	332 kJ/mol
Force-Bond Angle	6.2°

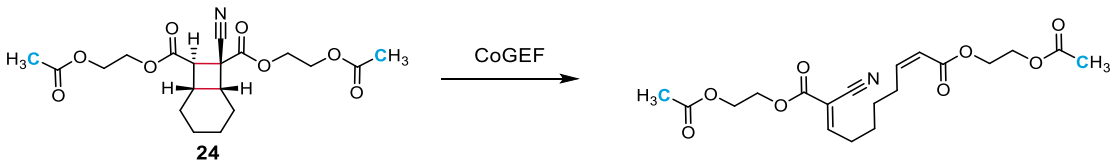

24

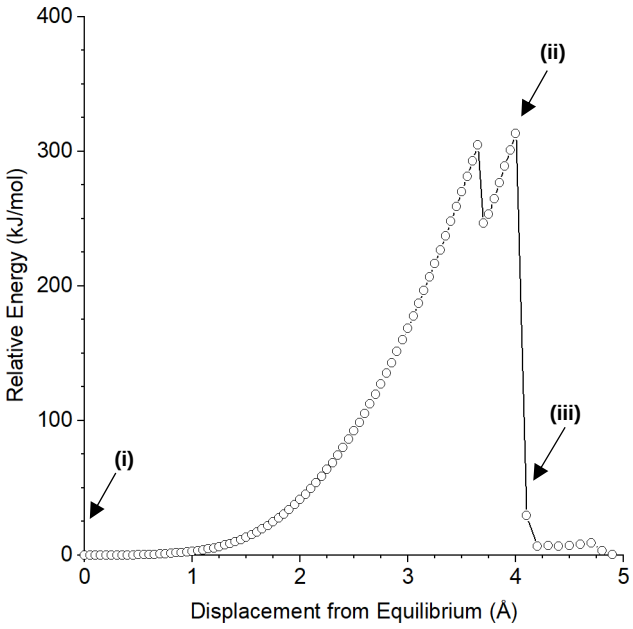

(i) Equilibrium Geometry

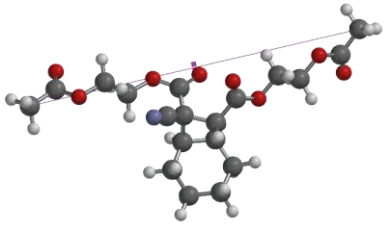

15.909 Å

(ii) Immediately Prior to Bond Cleavage

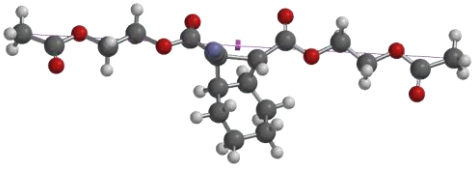

19.909 Å

(iii) Immediately After Bond Cleavage

20.009 Å

Summary of CoGEF Results	
F_{max}	4.0 nN
E_{max}	313 kJ/mol
Force-Bond Angle	8.5°

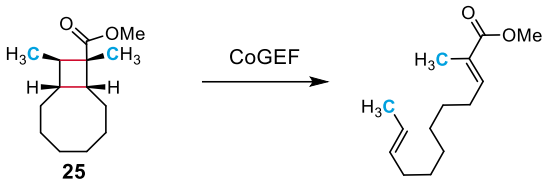

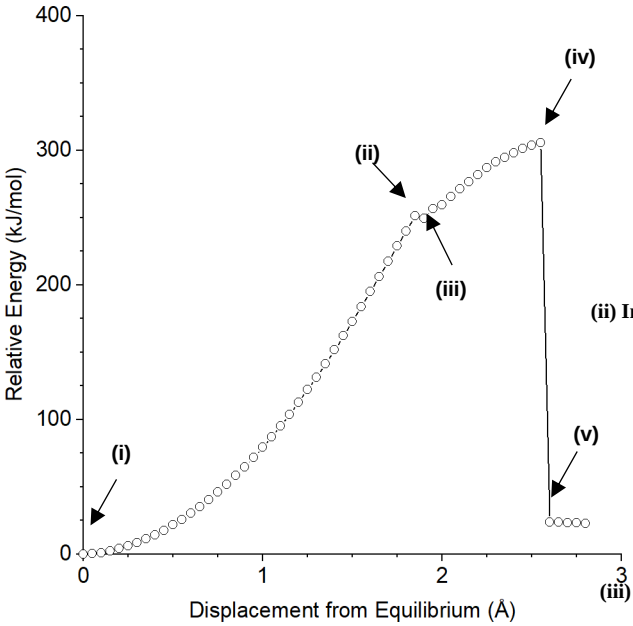

Summary of CoGEF Results	
F_{max}	3.8 nN
E_{max}	302 kJ/mol
Force-Bond Angle	7.1°

(i) Equilibrium Geometry

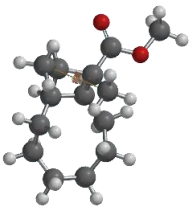

3.052 Å

(ii) Immediately Prior to First Bond Cleavage

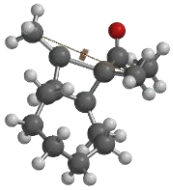

4.902 Å

(iii) Immediately After First Bond Cleavage

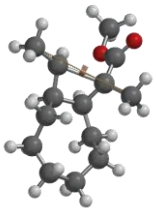

4.952 Å

(iv) Immediately Prior to Second Bond Cleavage

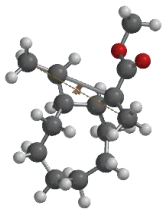

5.552 Å

(v) Immediately After Second Bond Cleavage

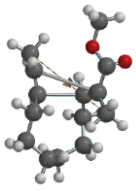

5.602 Å

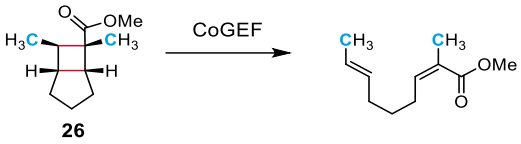

26

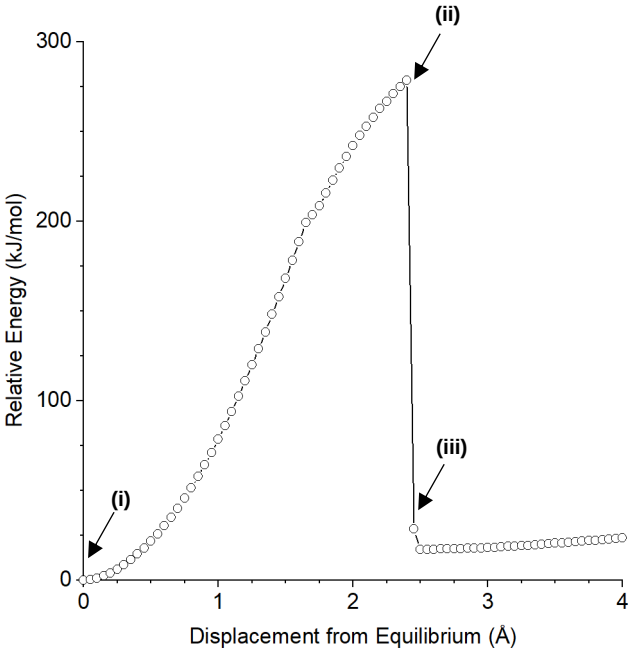

Summary of CoGEF Results	
F_{max}	3.5 nN
E_{max}	278 kJ/mol
Force-Bond Angle	3.1°

(i) Equilibrium Geometry

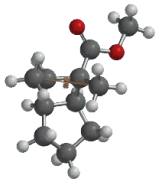

3.057 Å

(ii) Immediately Prior to Bond Cleavage

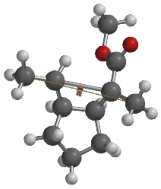

5.457 Å

(iii) Immediately After Bond Cleavage

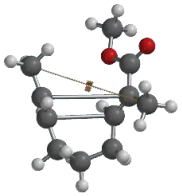

5.507 Å

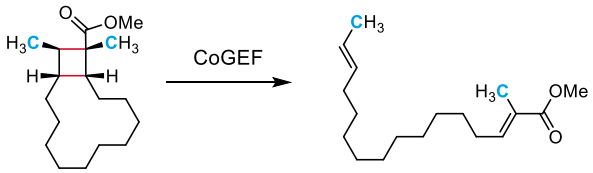

27

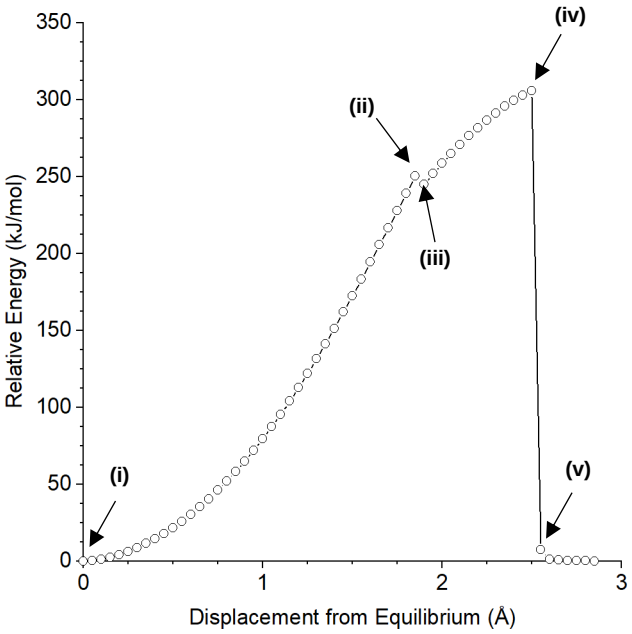

Summary of CoGEF Results	
F_{max}	3.7 nN
E_{max}	306 kJ/mol
Force-Bond Angle	7.3°

(i) Equilibrium Geometry

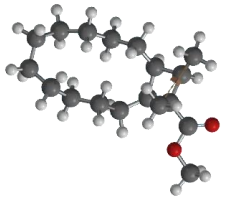

3.051 Å

(ii) Immediately Prior to First Bond Cleavage

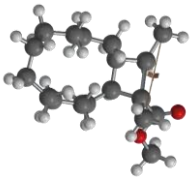

4.901 Å

(iii) Immediately After First Bond Cleavage

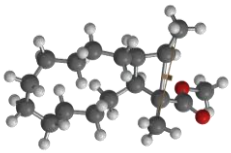

4.951 Å

(iv) Immediately Prior to Second Bond Cleavage

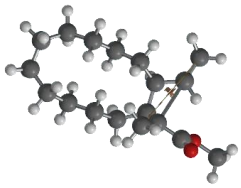

5.551 Å

(v) Immediately After Second Bond Cleavage

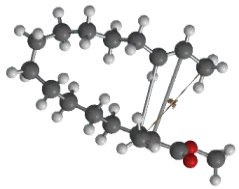

5.601 Å

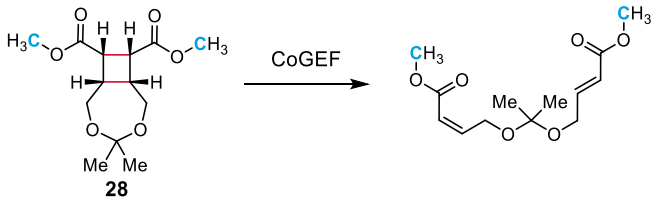

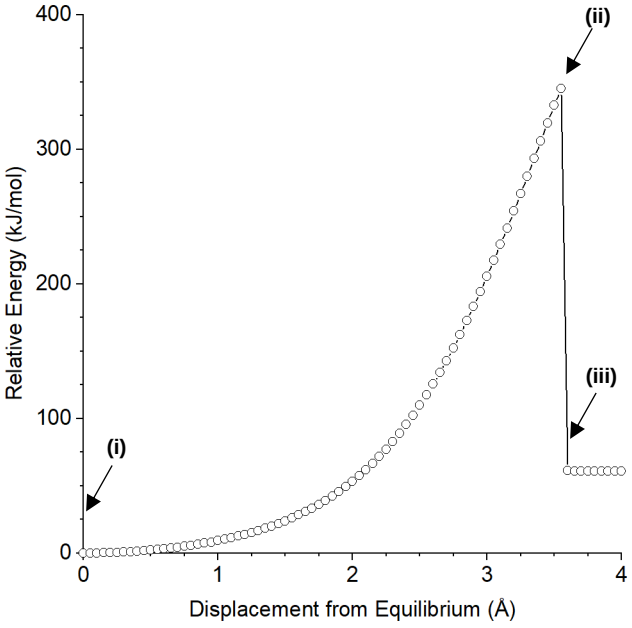

Summary of CoGEF Results

F_{max}	4.4 nN
E_{max}	345 kJ/mol
Force-Bond Angle	4.6 °

(i) Equilibrium Geometry

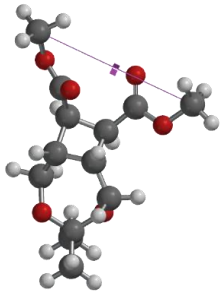

6.476 Å

(ii) Immediately Prior to Bond Cleavage

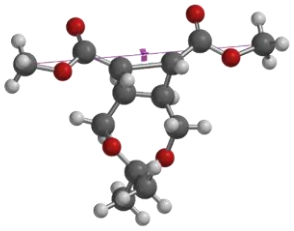

10.026 Å

(iii) Immediately After Bond Cleavage

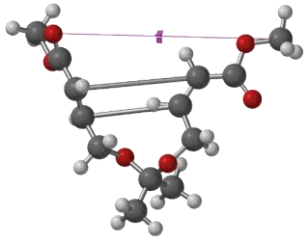

10.076 Å

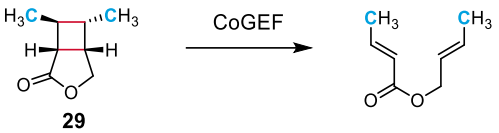

29

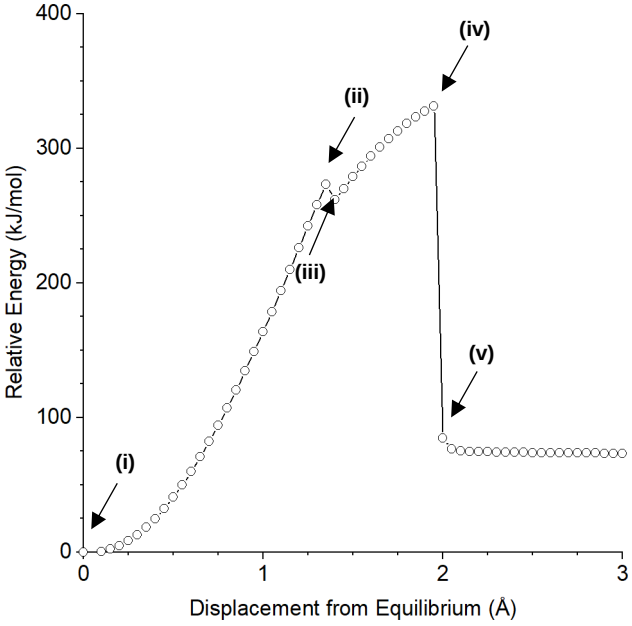

Summary of CoGEF Results	
F_{max}	5.4 nN
E_{max}	331 kJ/mol
Force-Bond Angle	24°

(i) Equilibrium Geometry

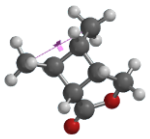

3.769 Å

(ii) Immediately Prior to First Bond Cleavage

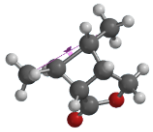

5.119 Å

(iii) Immediately After First Bond Cleavage

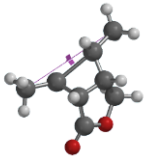

5.169 Å

(iv) Immediately Prior to Second Bond Cleavage

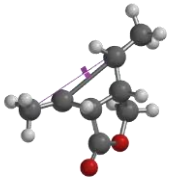

5.719 Å

(v) Immediately After Second Bond Cleavage

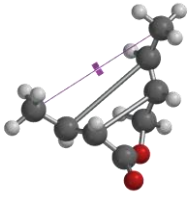

5.769 Å

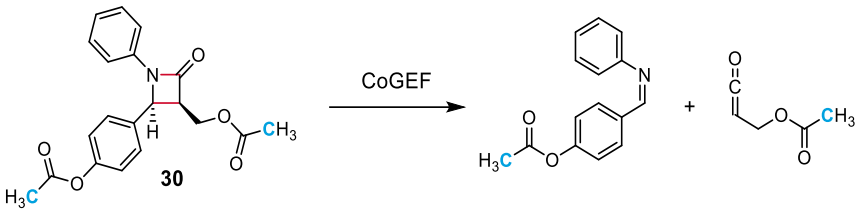

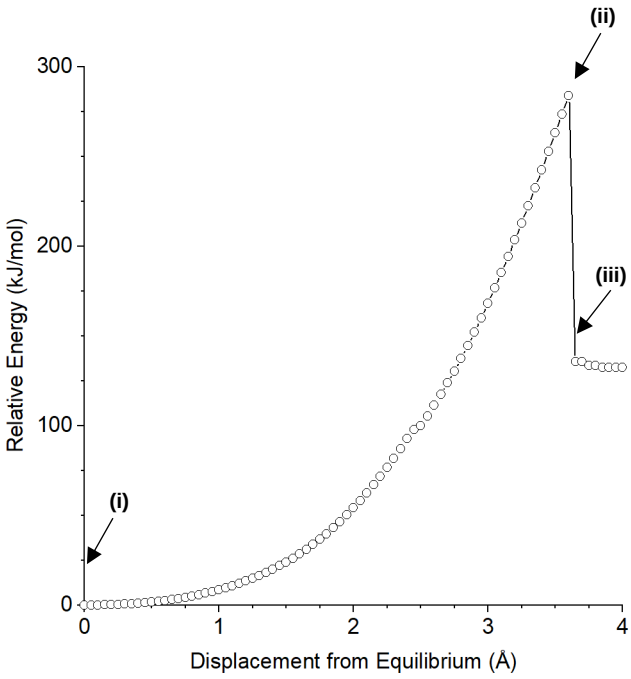

(i) Equilibrium Geometry

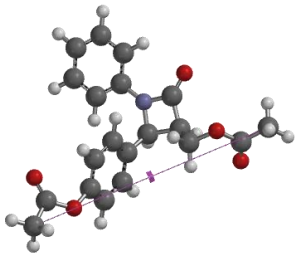

11.759 Å

(ii) Immediately Prior to Bond Cleavage

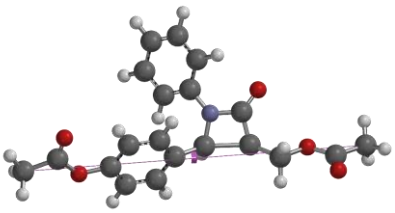

15.359 Å

(iii) Immediately After Bond Cleavage

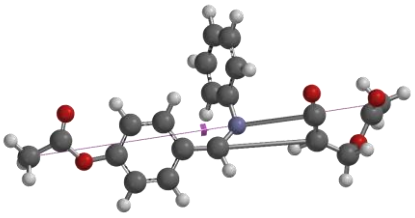

15.409 Å

Summary of CoGEF Results	
F_{max}	3.5 nN
E_{max}	284 kJ/mol
Force-Bond Angle	9.3°

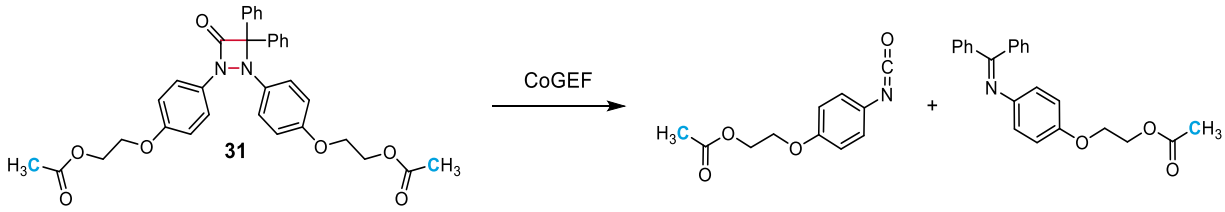

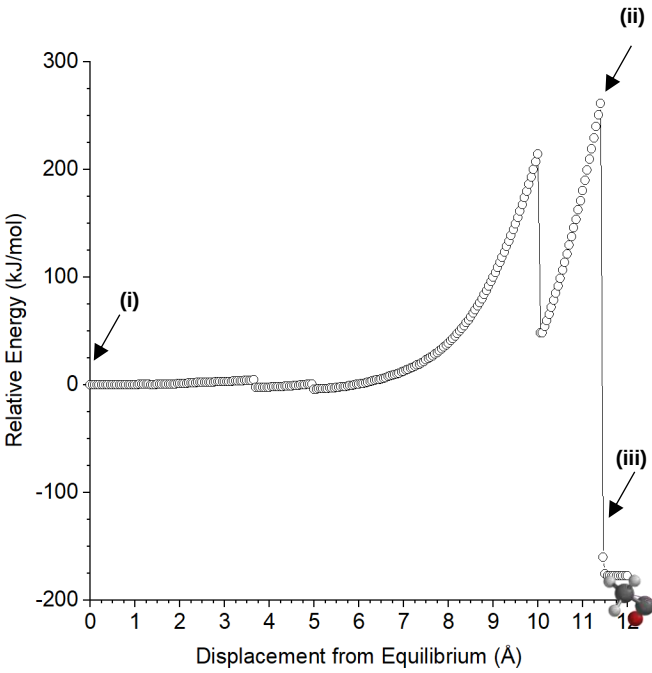

Summary of CoGEF Results

F_{max}	3.6 nN
E_{max}	260 kJ/mol
Force-Bond Angle	34°

(i) Equilibrium Geometry

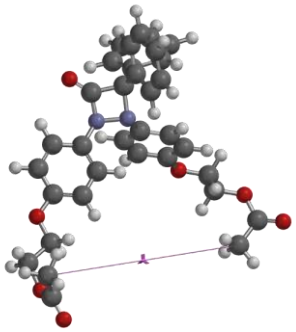

14.018 Å

(ii) Immediately Prior to Bond Cleavage

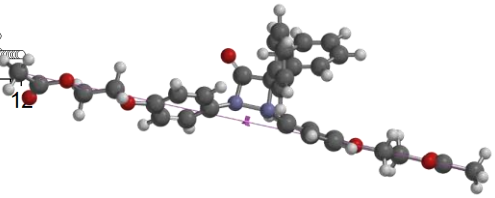

25.418 Å

(iii) Immediately After Bond Cleavage

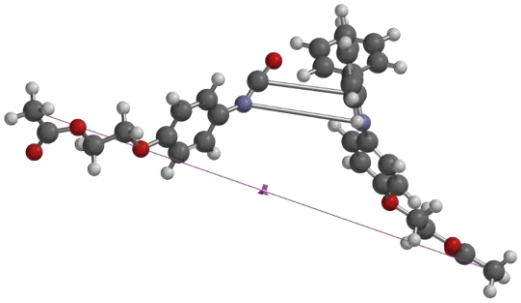

25.468 Å

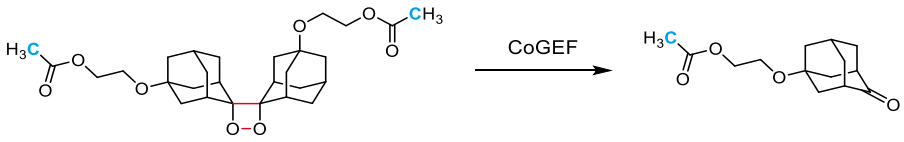

32

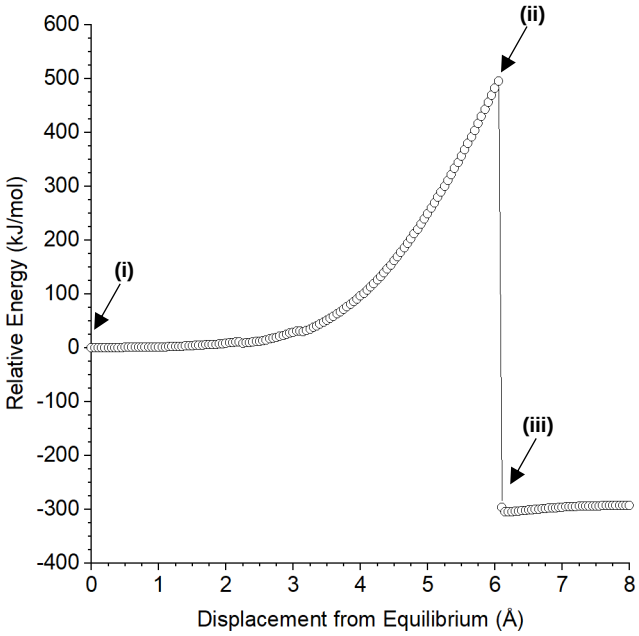

Summary of CoGEF Results	
F_{max}	4.4 nN
E_{max}	495 kJ/mol
Force-Bond Angle	15°

(i) Equilibrium Geometry

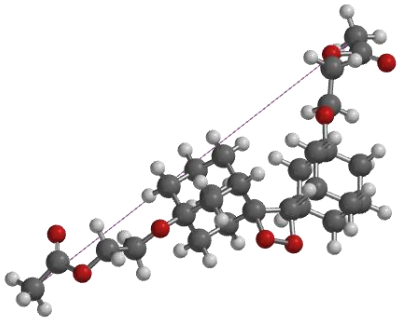

18.153 Å

(ii) Immediately Prior to Bond Cleavage

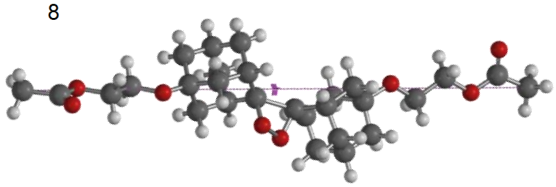

24.203 Å

(iii) Immediately After Bond Cleavage

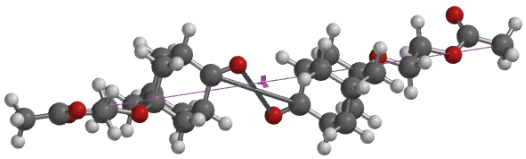

24.253 Å

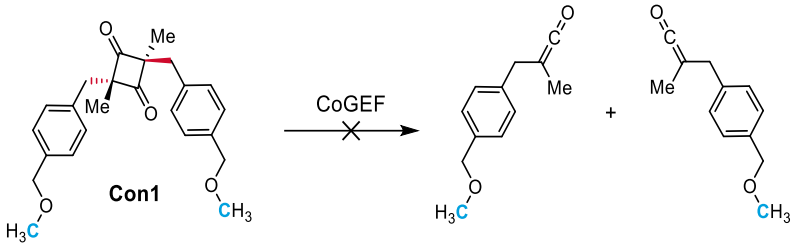

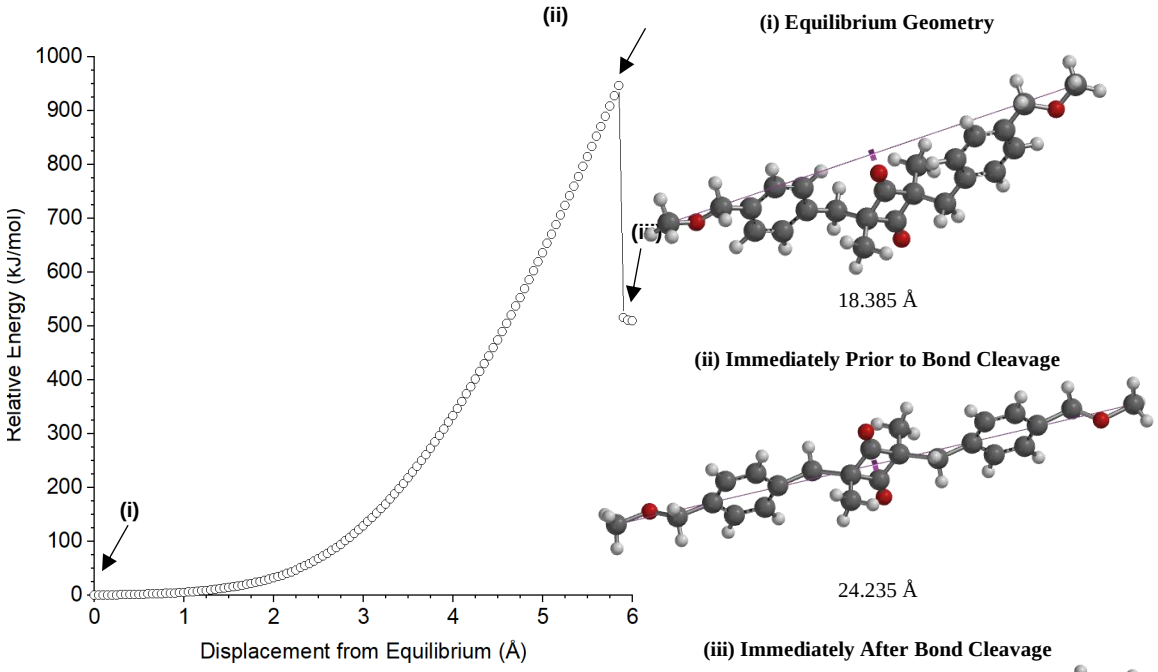

Summary of CoGEF Results	
F_{max}	6.3 nN
E_{max}	947 kJ/mol
Force-Bond Angle	43°

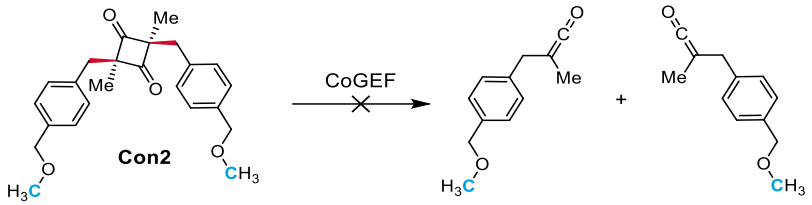

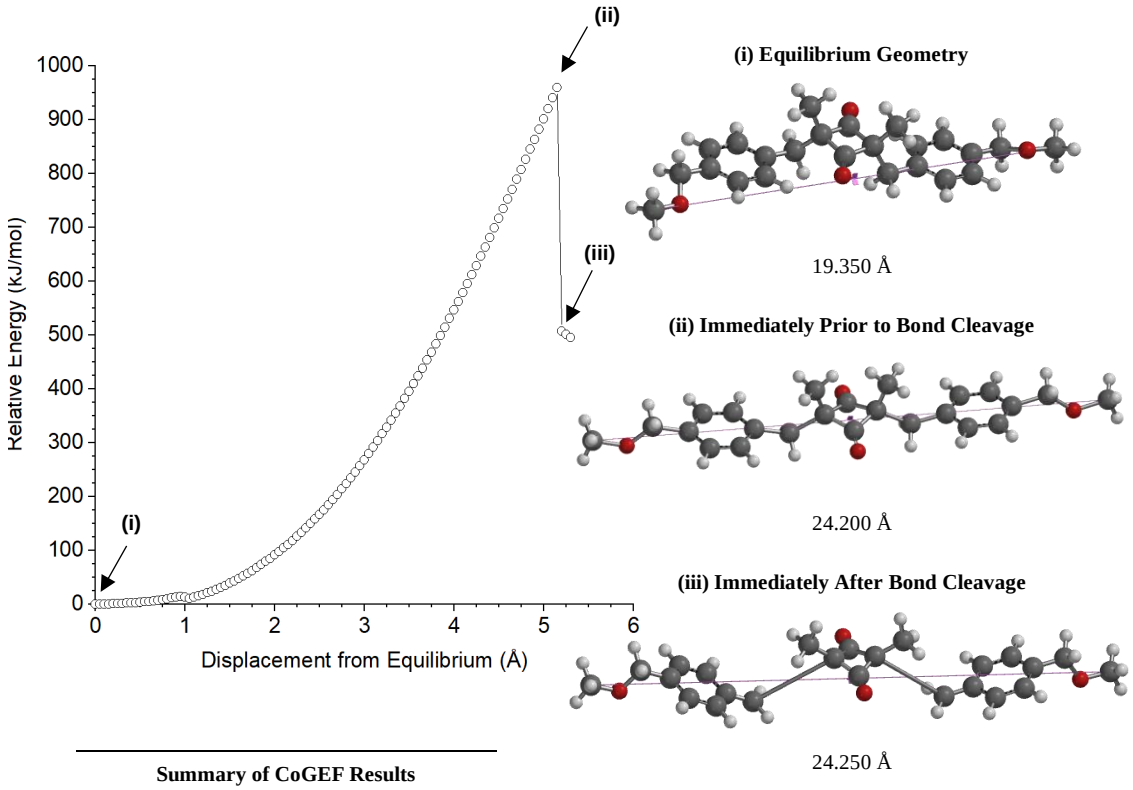

Summary of CoGEF Results	
F_{max}	6.4 nN
E_{max}	959 kJ/mol
Force-Bond Angle	42°

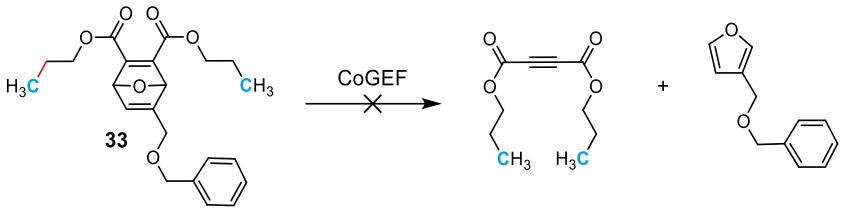

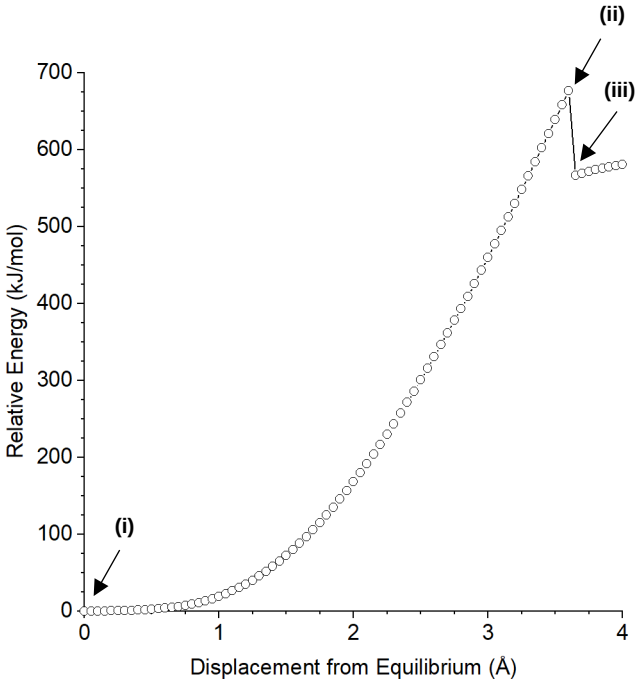

(i) Equilibrium Geometry

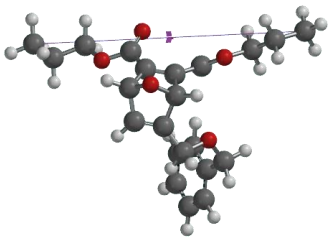

12.509 Å

(ii) Immediately Prior to Bond Cleavage

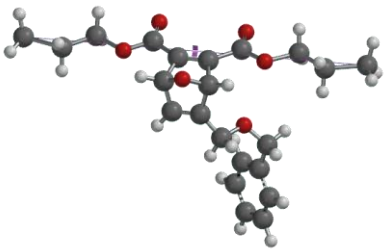

16.109 Å

(iii) Immediately After Bond Cleavage

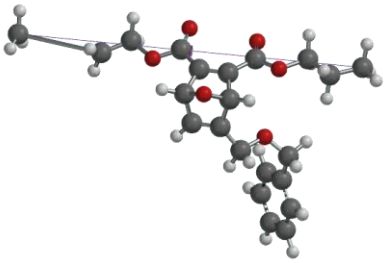

16.159 Å

Summary of CoGEF Results	
F_{max}	6.2 nN
E_{max}	676 kJ/mol
Force-Bond Angle	78°

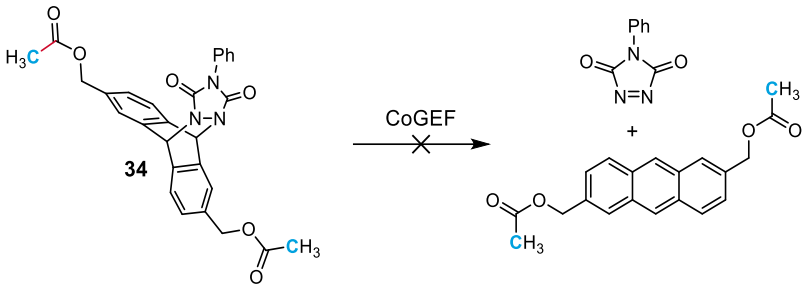

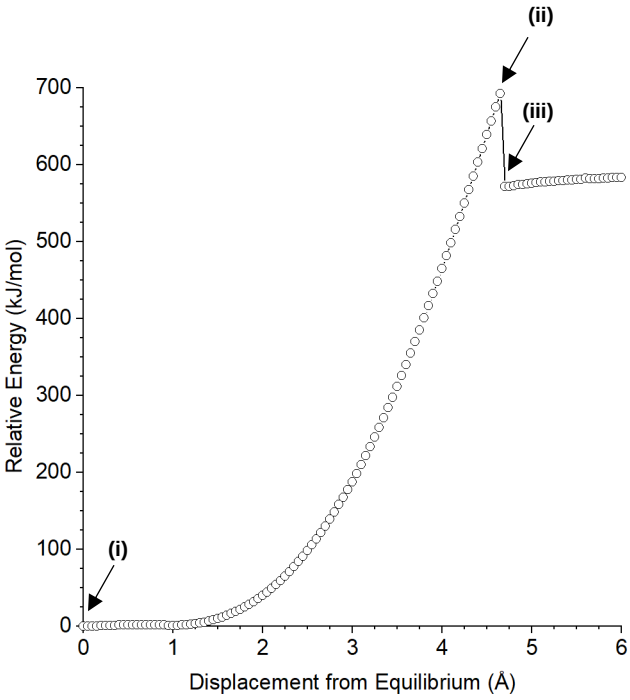

(i) Equilibrium Geometry

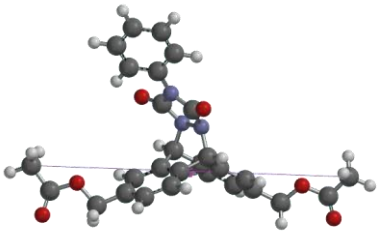

15.358 Å

(ii) Immediately Prior to Bond Cleavage

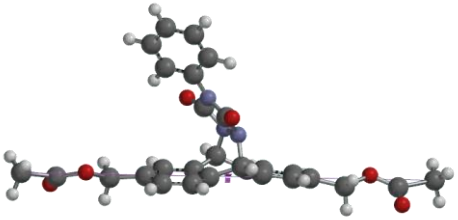

20.008 Å

(iii) Immediately After Bond Cleavage

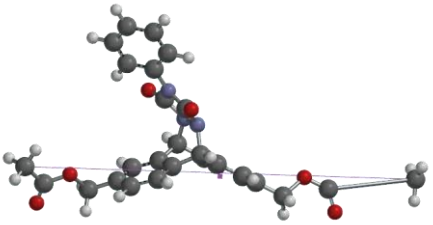

20.058 Å

Summary of CoGEF Results	
F_{max}	6.0 nN
E_{max}	693 kJ/mol
Force-Bond Angle	85°

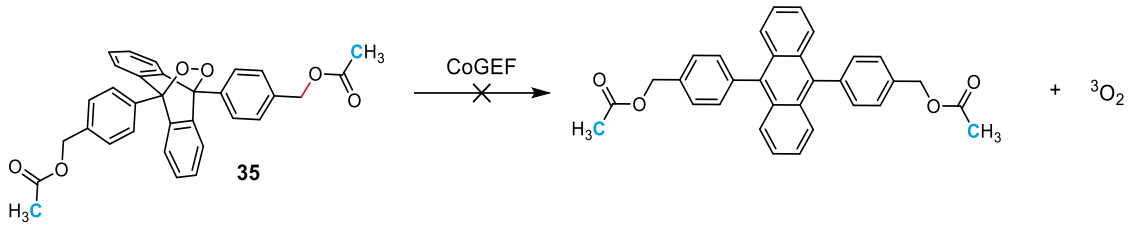

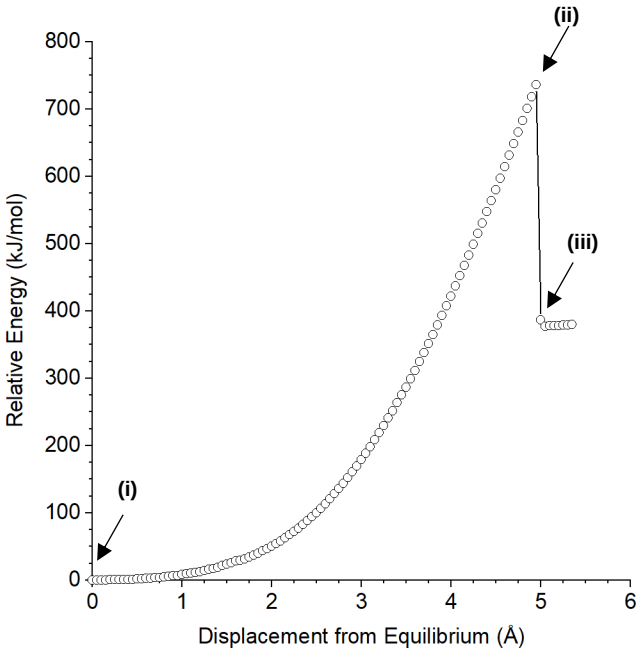

Summary of CoGEF Results	
F_{max}	5.8 nN
E_{max}	736 kJ/mol
Force-Bond Angle	66°

(i) Equilibrium Geometry

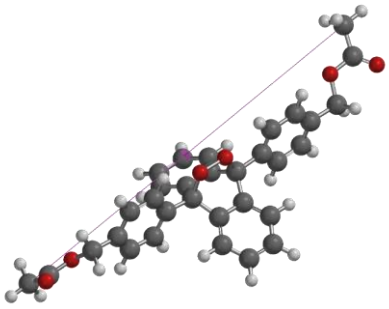

19.243 Å

(ii) Immediately Prior to Bond Cleavage

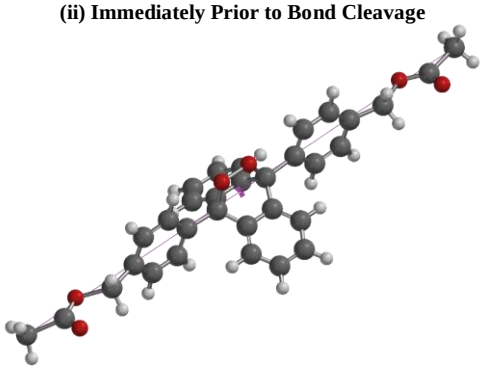

24.193 Å

(iii) Immediately After Bond Cleavage

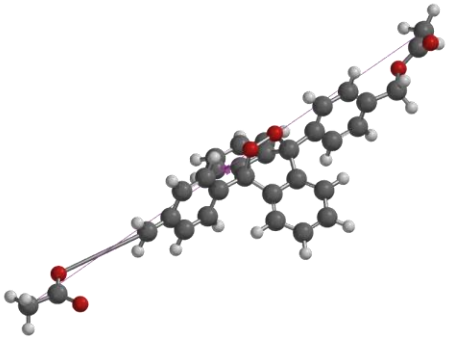

24.243 Å

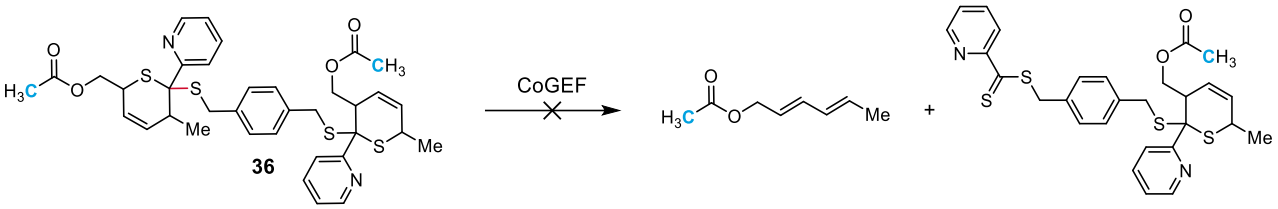

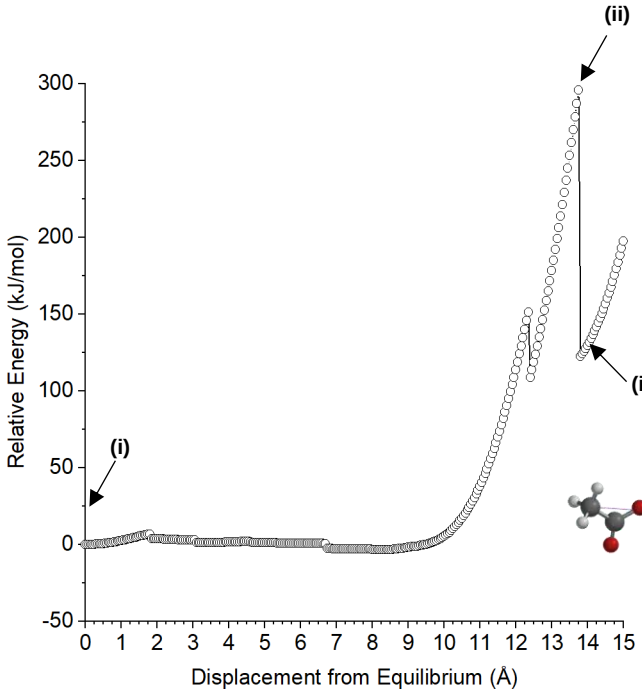

(i) Equilibrium Geometry

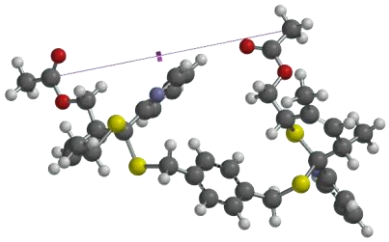

13.209 Å

(ii) Immediately Prior to Bond Cleavage

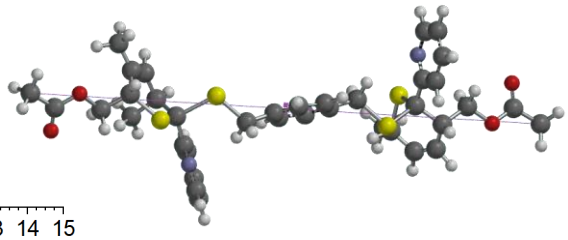

26.959 Å

(iii) Immediately After Bond Cleavage

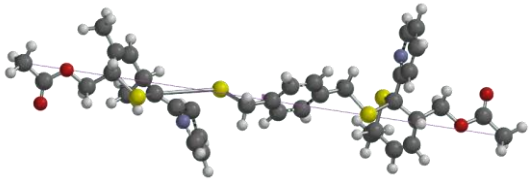

27.009 Å

Summary of CoGEF Results	
F_{max}	2.9 nN
E_{max}	295 kJ/mol
Force-Bond Angle	32°

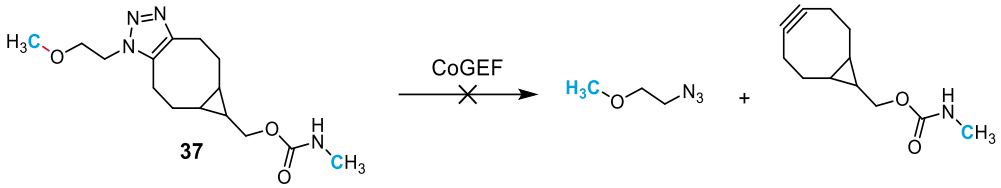

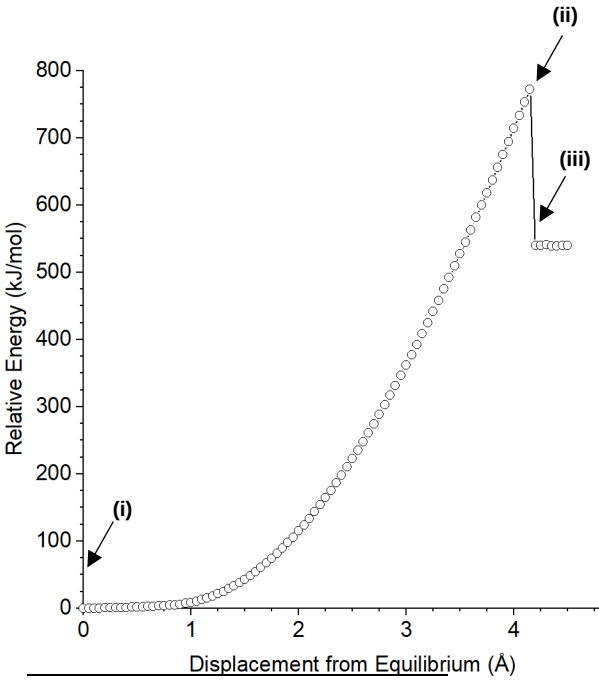

(i) Equilibrium Geometry

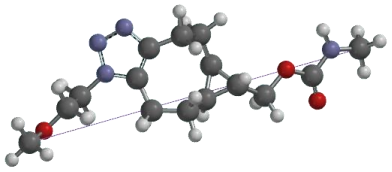

15.627 Å

(ii) Immediately Prior to Bond Cleavage

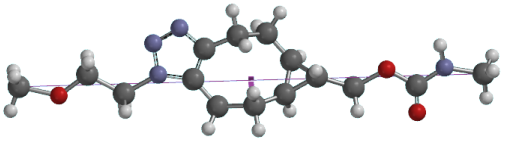

19.777 Å

(iii) Immediately After Bond Cleavage

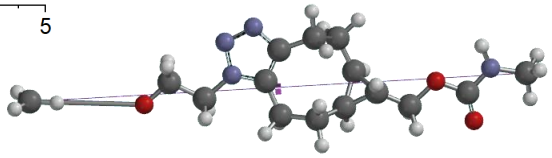

19.827 Å

Summary of CoGEF Results

F_{max}	6.5 nN
E_{max}	772 kJ/mol
Force/Bond angle	8.9°

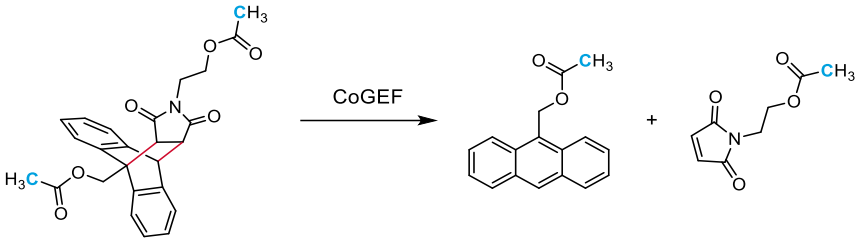

38

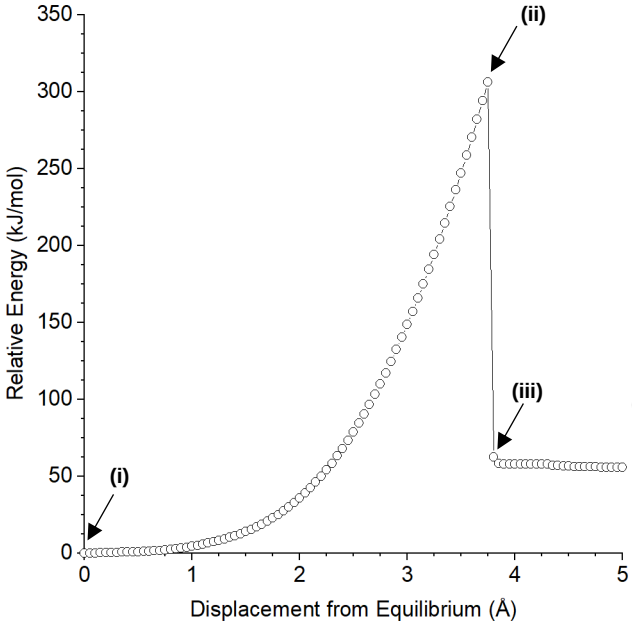

Summary of CoGEF Results	
F_{max}	4.1 nN
E_{max}	306 kJ/mol
Force/Bond angle	25°

(i) Equilibrium Geometry

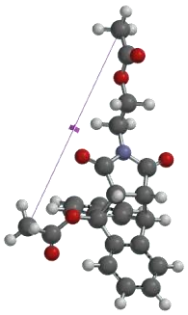

10.918 Å

(ii) Immediately Prior to Bond Cleavage

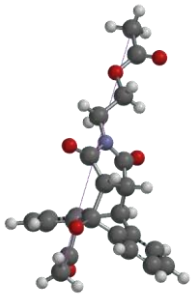

14.668Å

(iii) Immediately After Bond Cleavage

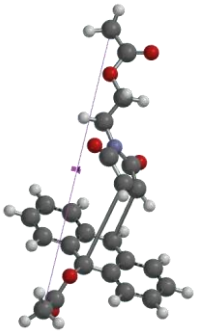

14.718 Å

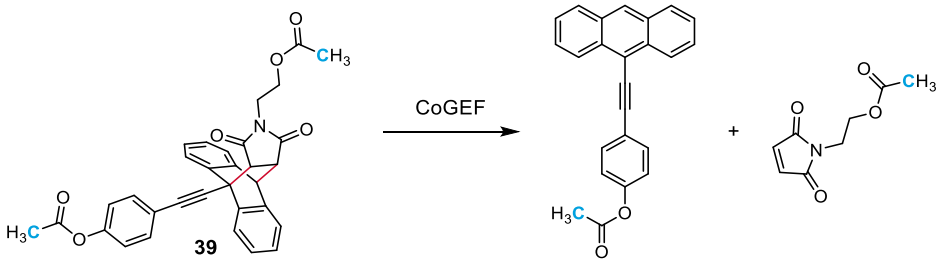

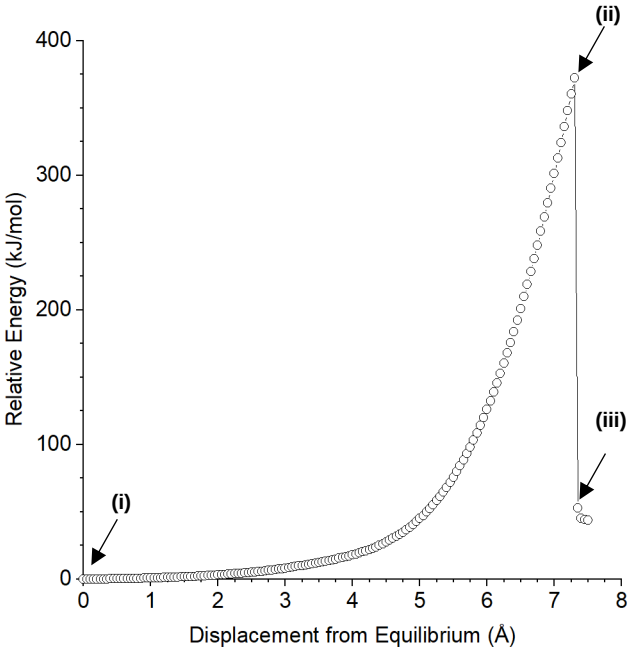

Summary of CoGEF Results	
F_{max}	4.0 nN
E_{max}	372 kJ/mol
Force-Bond Angle	26°

(i) Equilibrium Geometry

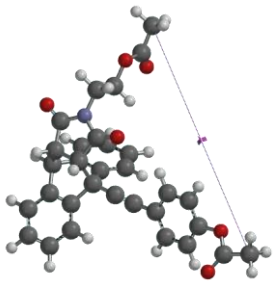

14.542 Å

(ii) Immediately Prior to Bond Cleavage

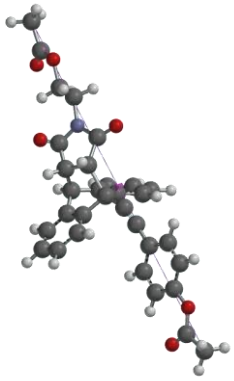

21.842 Å

(iii) Immediately After Bond Cleavage

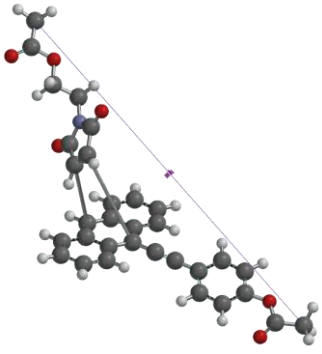

21.892 Å

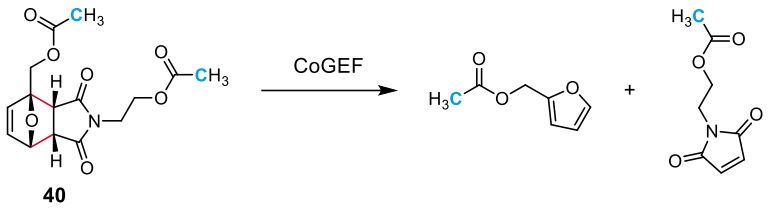

40

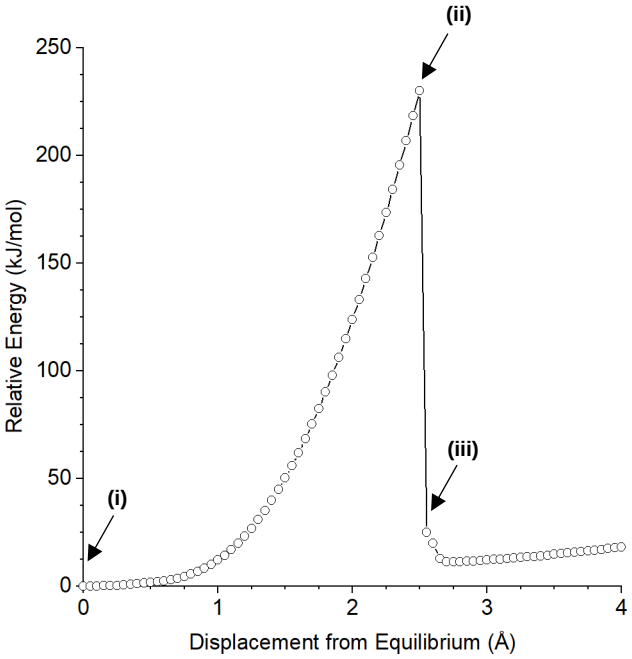

Summary of CoGEF Results	
F_{max}	3.9 nN
E_{max}	230 kJ/mol
Force-Bond Angle	26°

(i) Equilibrium Geometry

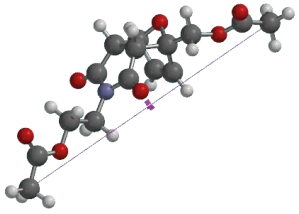

13.422 Å

(ii) Immediately Prior to Bond Cleavage

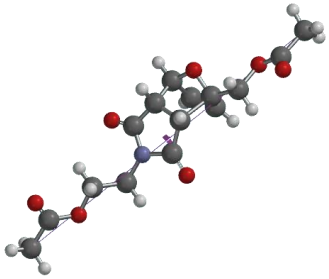

15.922 Å

(iii) Immediately After Bond Cleavage

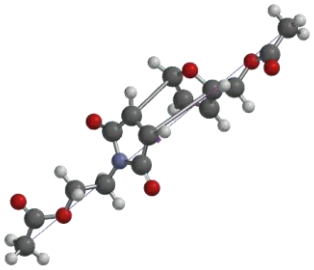

15.972 Å

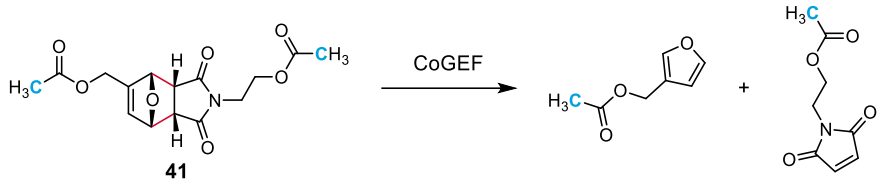

41

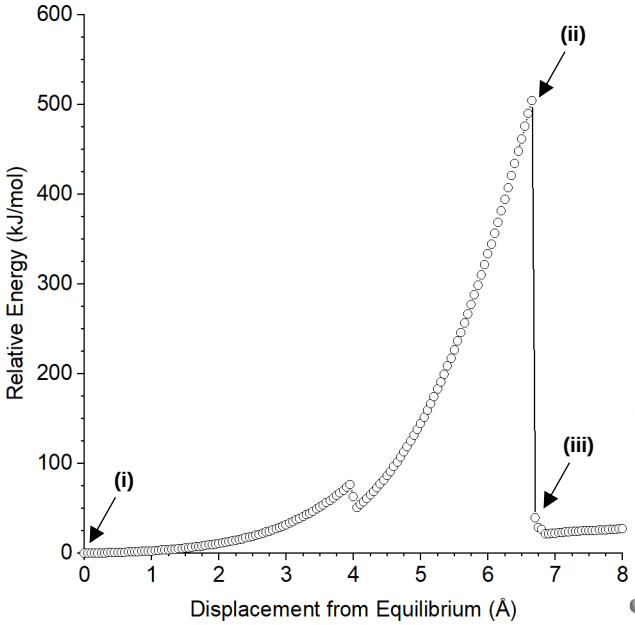

(i) Equilibrium Geometry

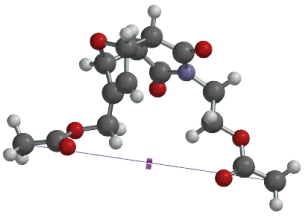

10.731 Å

(ii) Immediately Prior to Bond Cleavage

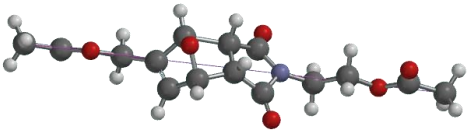

17.381 Å

(iii) Immediately After Bond Cleavage

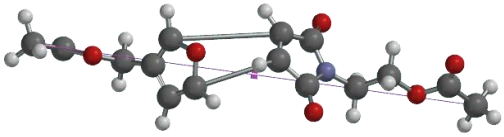

17.431 Å

Summary of CoGEF Results	
F_{max}	4.8 nN
E_{max}	504 kJ/mol
Force-Bond Angle	6.8°

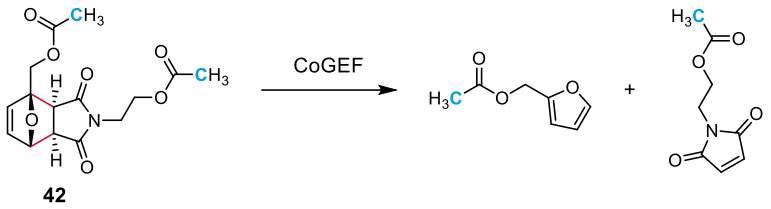

42

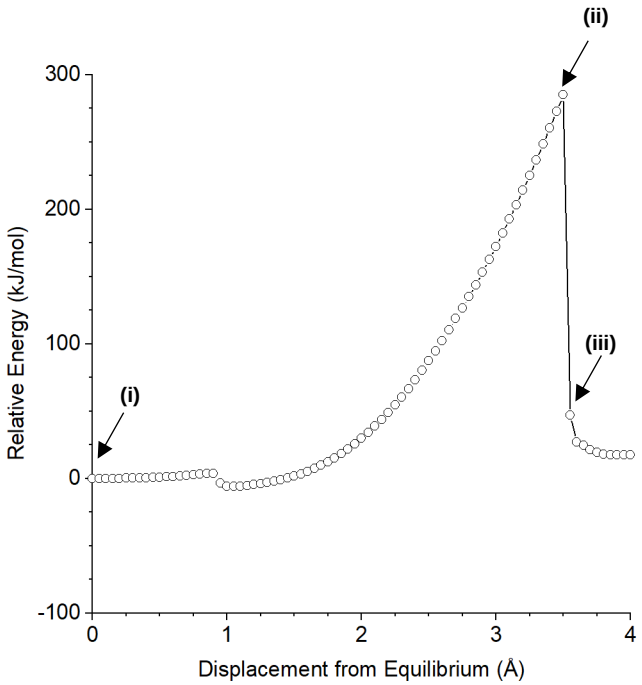

(i) Equilibrium Geometry

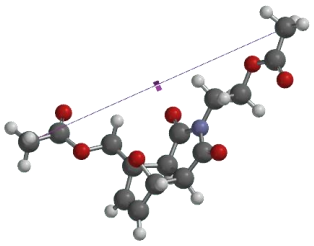

12.433 Å

(ii) Immediately Prior to Bond Cleavage

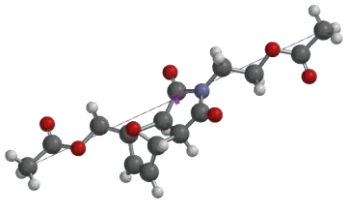

15.933Å

(iii) Immediately After Bond Cleavage

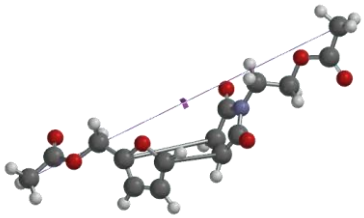

15.983 Å

Summary of CoGEF Results	
F_{max}	4.1 nN
E_{max}	285 kJ/mol
Force-Bond Angle	22°

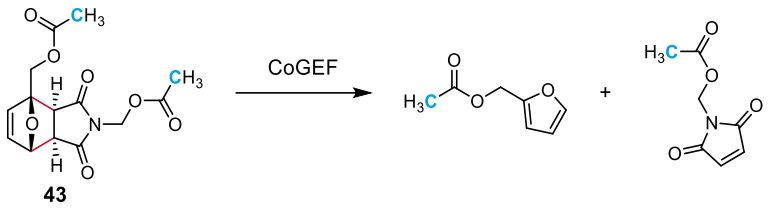

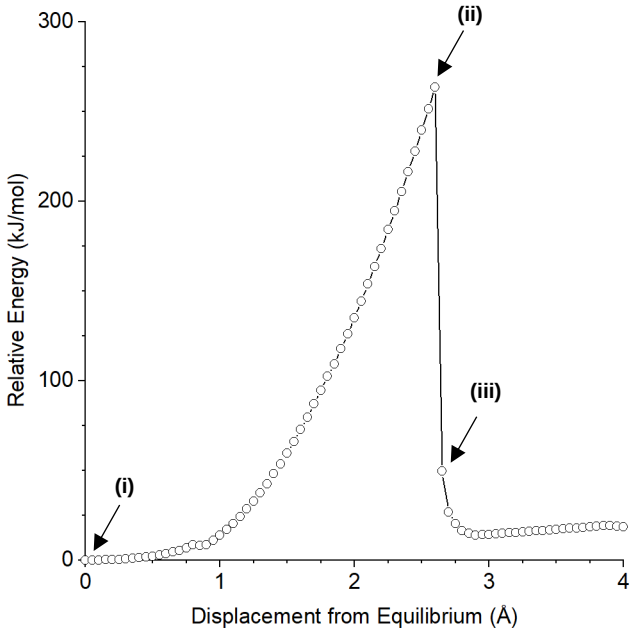

(i) Equilibrium Geometry

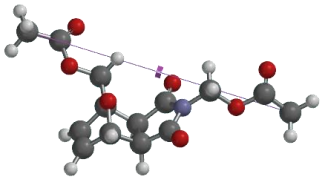

11.874 Å

(ii) Immediately Prior to Bond Cleavage

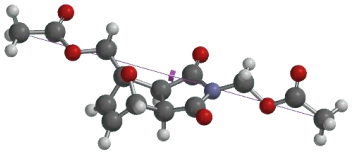

14.474 Å

(iii) Immediately After Bond Cleavage

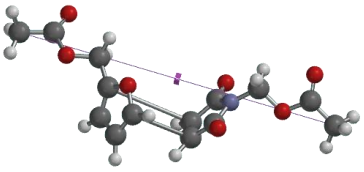

14.524 Å

Summary of CoGEF Results	
F_{max}	4.0 nN
E_{max}	264 kJ/mol
Force-Bond Angle	21°

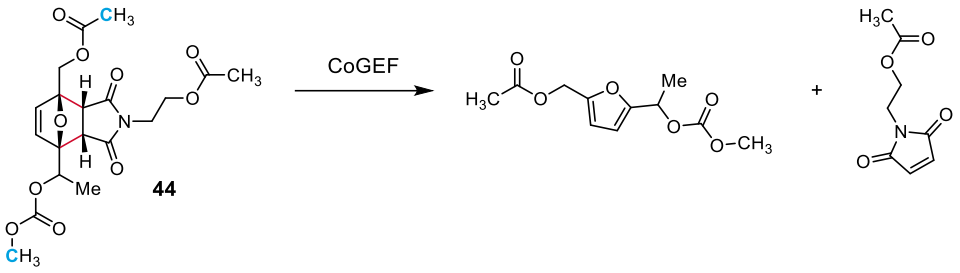

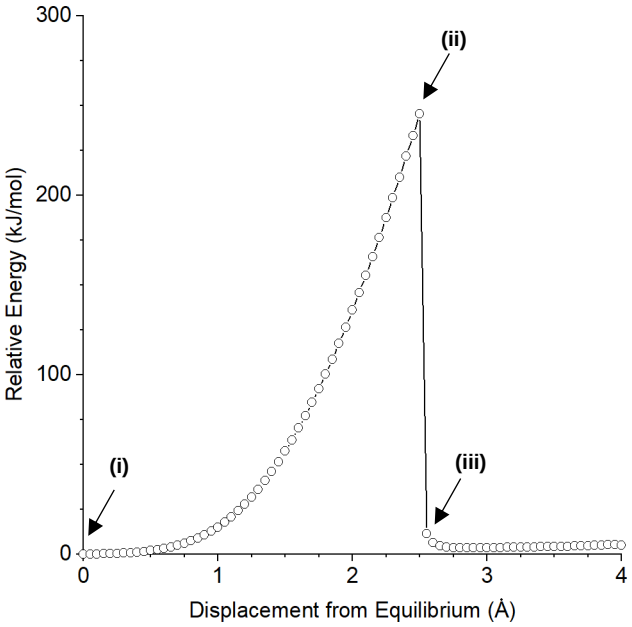

Summary of CoGEF Results	
F_{max}	4.0 nN
E_{max}	245 kJ/mol
Force-Bond Angle	26°

(i) Equilibrium Geometry

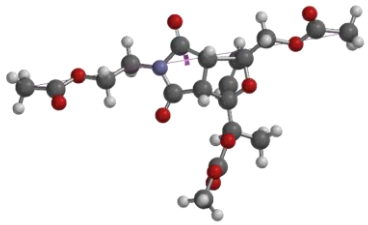

13.491 Å

(ii) Immediately Prior to Bond Cleavage

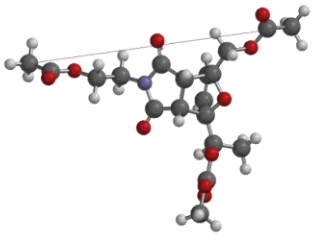

15.991 Å

(iii) Immediately After Bond Cleavage

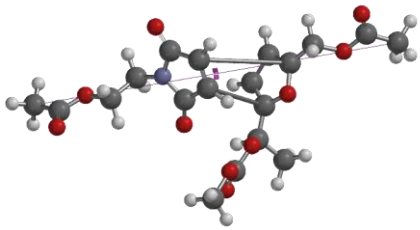

16.041 Å

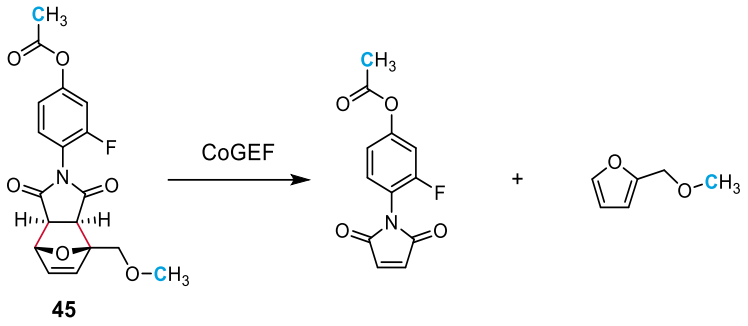

45

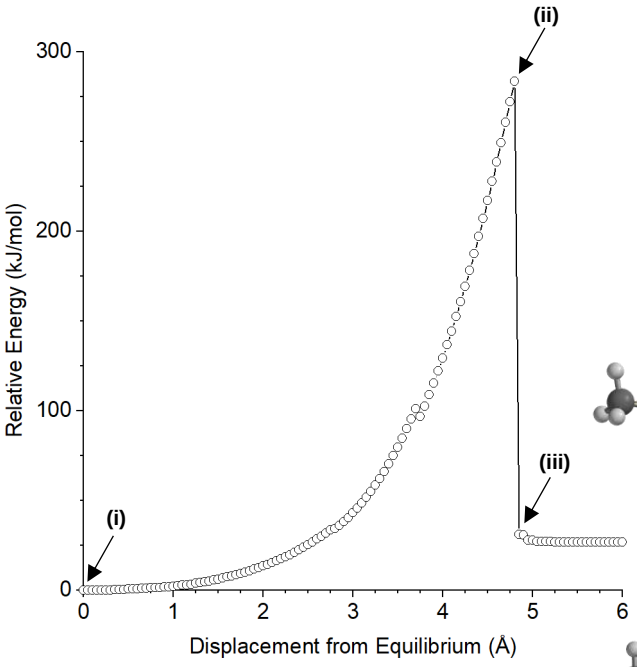

(i) Equilibrium Geometry

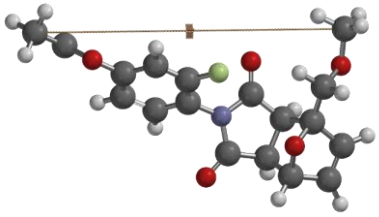

11.583 Å

(ii) Immediately Prior to Bond Cleavage

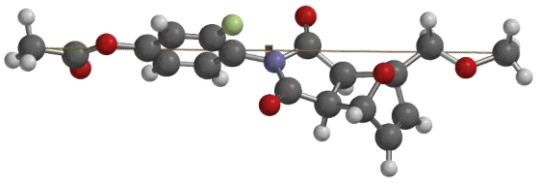

16.383 Å

(iii) Immediately After Bond Cleavage

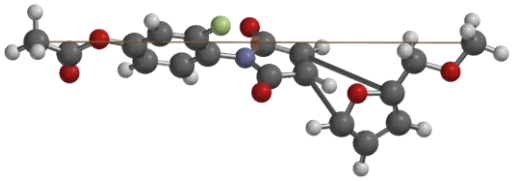

16.433 Å

Summary of CoGEF Results	
F_{max}	3.8 nN
E_{max}	284 kJ/mol
Force-Bond Angle	21°

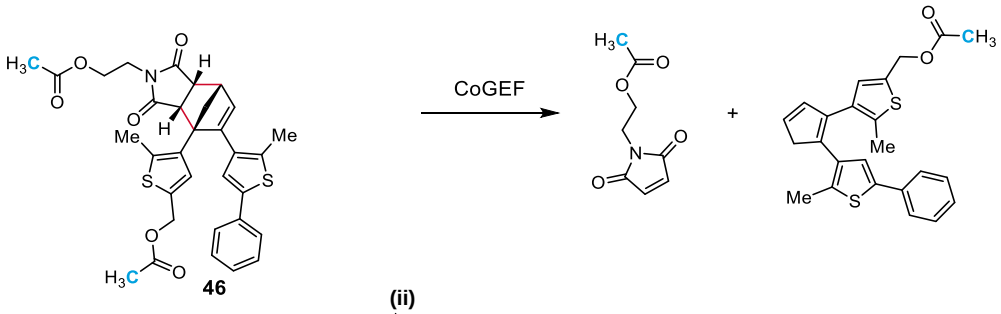

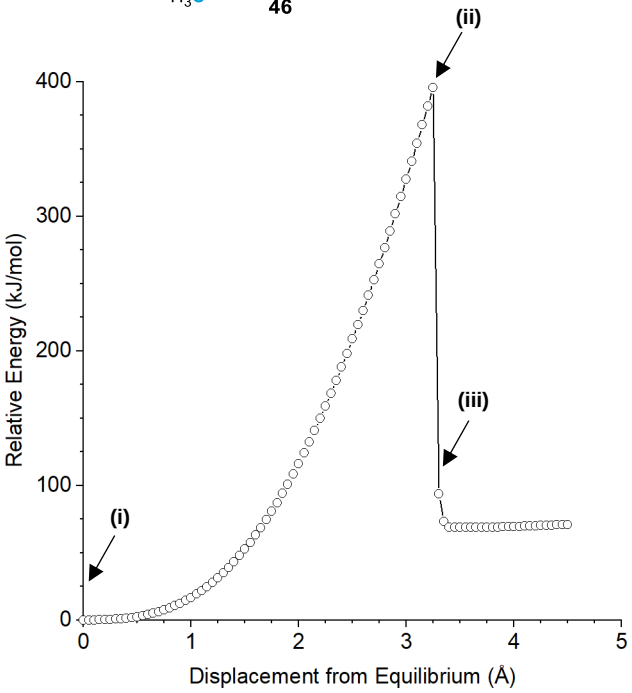

Summary of CoGEF Results	
F_{max}	4.6 nN
E_{max}	396 kJ/mol
Force-Bond Angle	26°

(i) Equilibrium Geometry

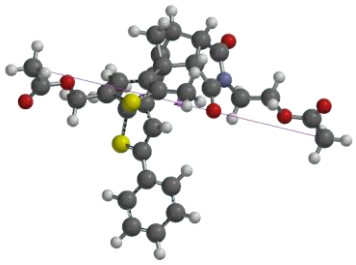

17.075 Å

(ii) Immediately Prior to Bond Cleavage

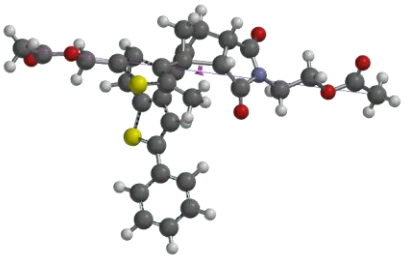

20.325 Å

(iii) Immediately After Bond Cleavage

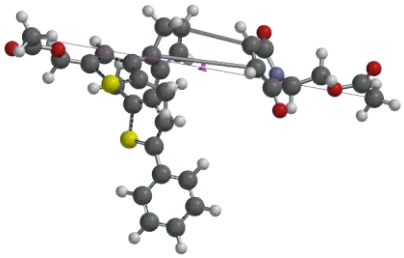

20.375 Å

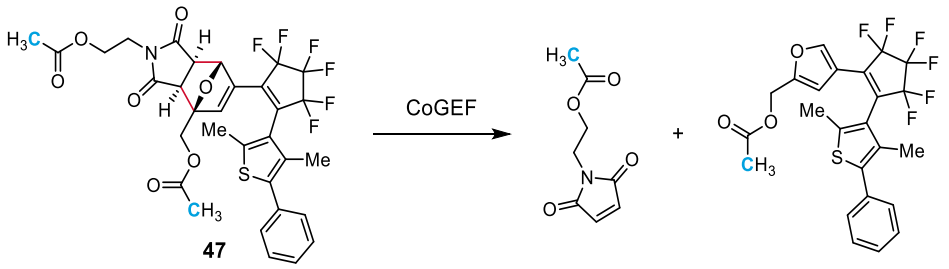

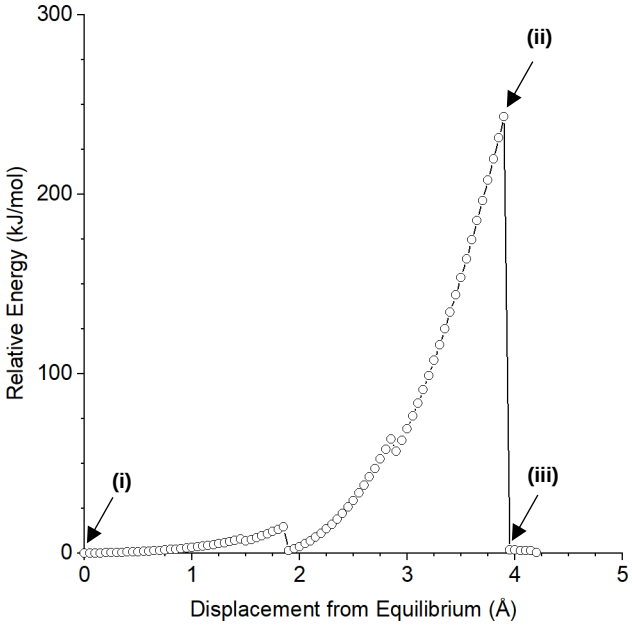

Summary of CoGEF Results	
F_{max}	3.9 nN
E_{max}	243 kJ/mol
Force-Bond Angle	25°

(i) Equilibrium Geometry

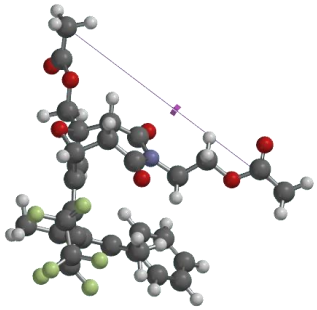

12.087 Å

(ii) Immediately Prior to Bond Cleavage

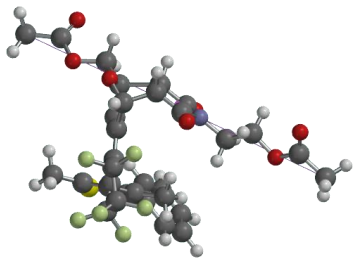

15.987 Å

(iii) Immediately After Bond Cleavage

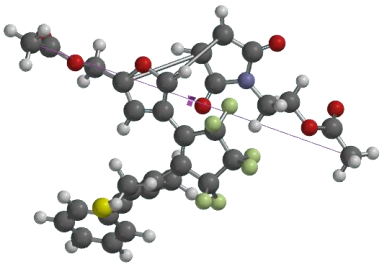

16.037 Å

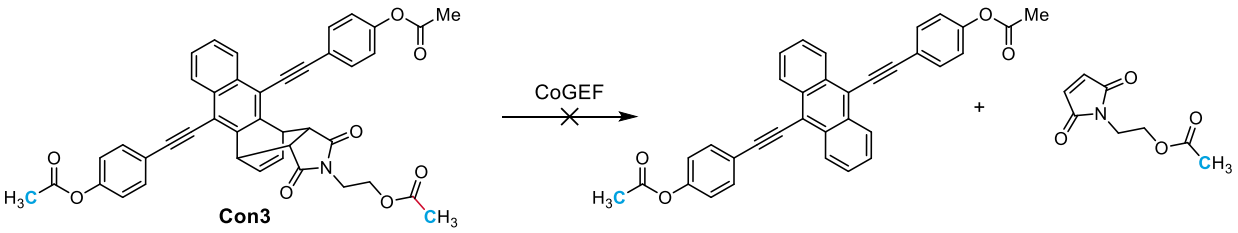

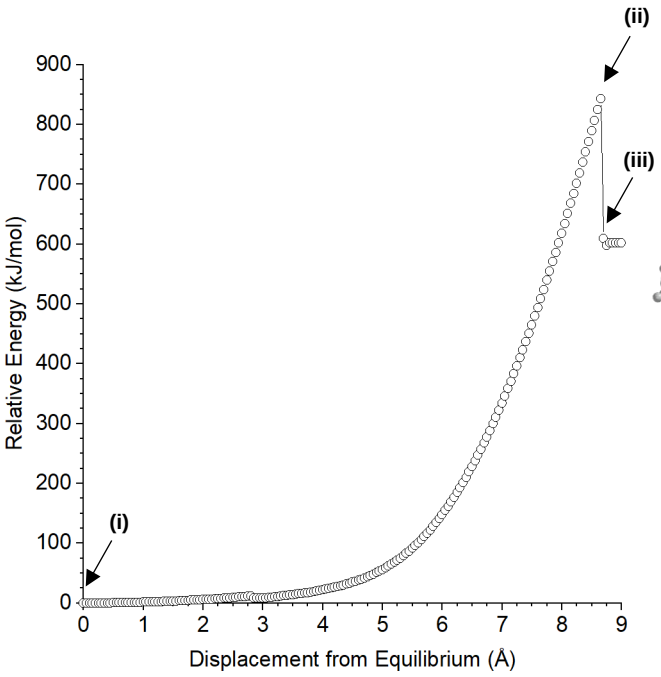

Summary of CoGEF Results	
F_{max}	6.0 nN
E_{max}	843 kJ/mol
Force-Bond Angle	29°

(i) Equilibrium Geometry

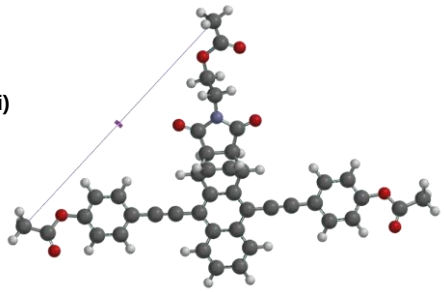

16.84 Å

(ii) Immediately Prior to Bond Cleavage

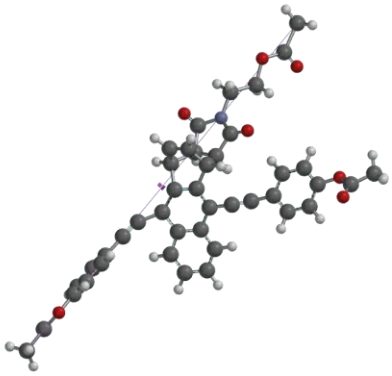

25.49 Å

(iii) Immediately After Bond Cleavage

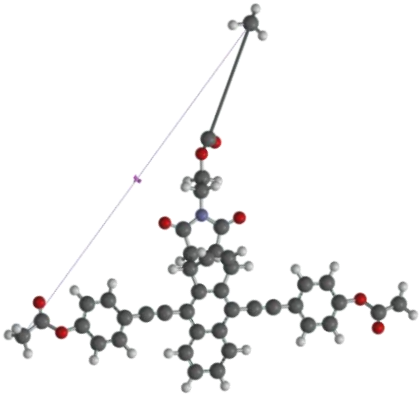

25.54 Å

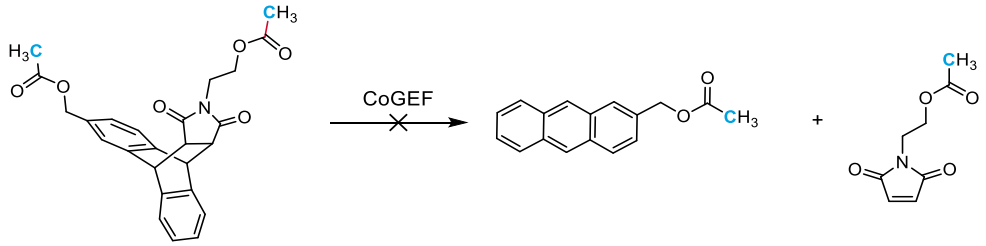

Con4

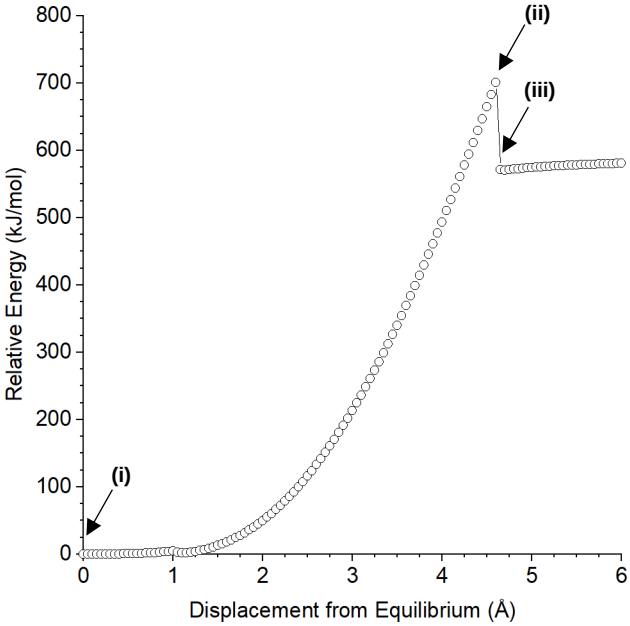

Summary of CoGEF Results	
F_{max}	6.0 nN
E_{max}	832 kJ/mol
Force-Bond Angle	15°

(i) Equilibrium Geometry

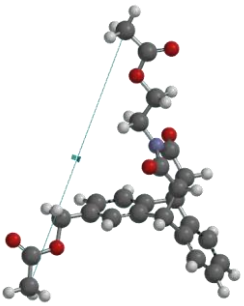

16.321 Å

(ii) Immediately Prior to Bond Cleavage

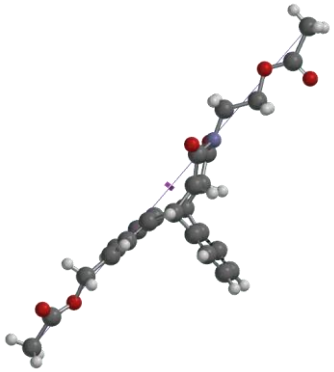

20.821 Å

(iii) Immediately After Bond Cleavage

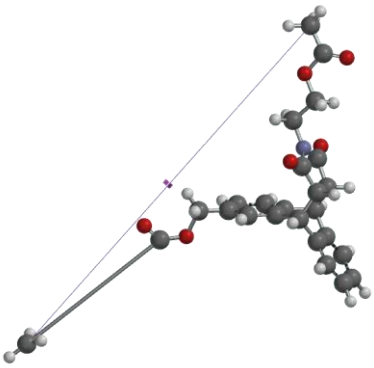

20.871 Å

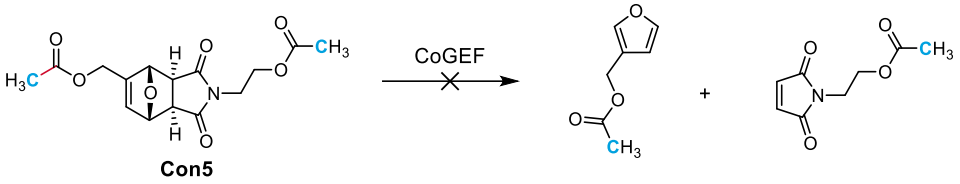

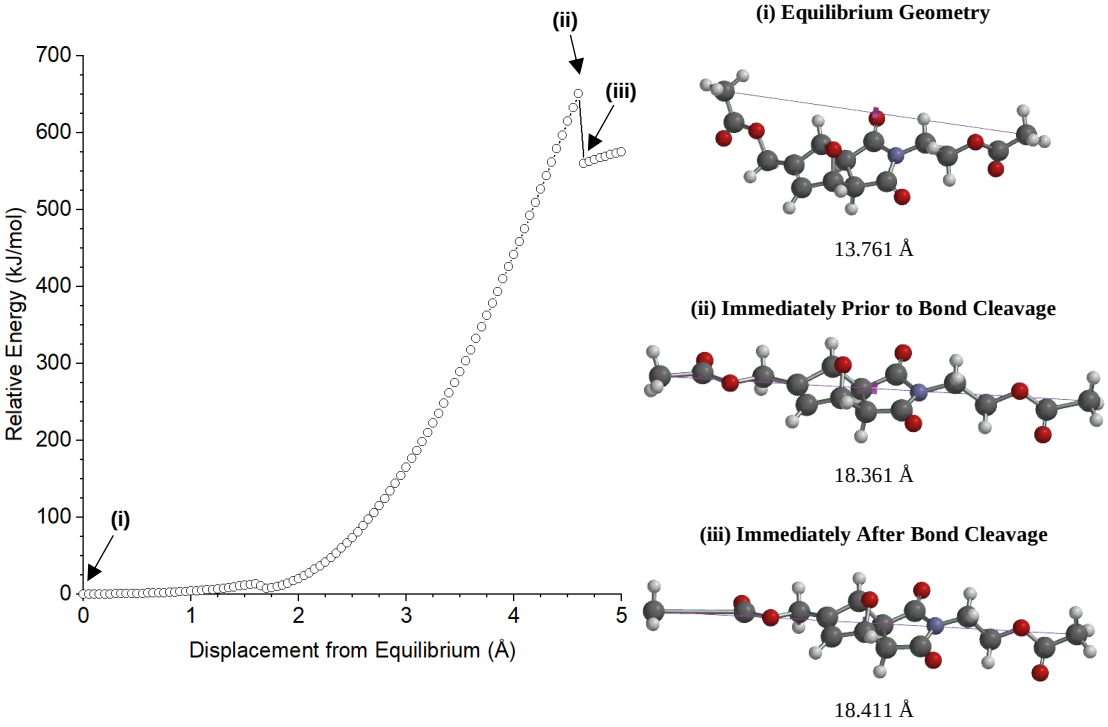

Summary of CoGEF Results	
F_{max}	6.0 nN
E_{max}	650 kJ/mol
Force-Bond Angle	39°

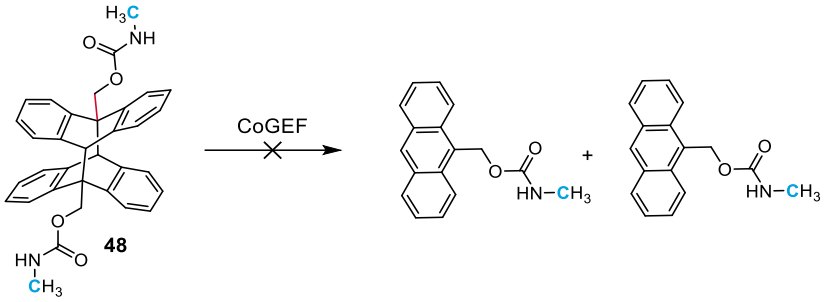

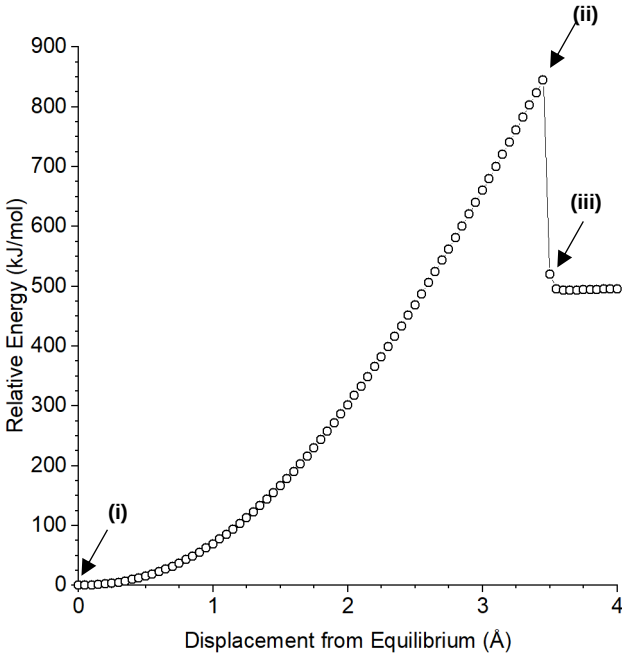

Summary of CoGEF Results	
F_{max}	6.9 nN
E_{max}	844 kJ/mol
Force-Bond Angle	53°

(i) Equilibrium Geometry

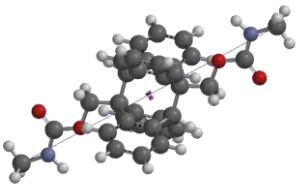

15.288 Å

(ii) Immediately Prior to Bond Cleavage

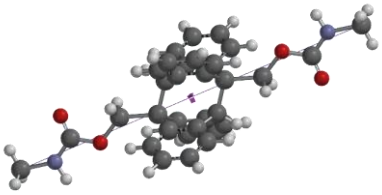

18.738 Å

(iii) Immediately After Bond Cleavage

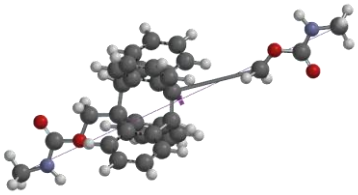

18.788 Å

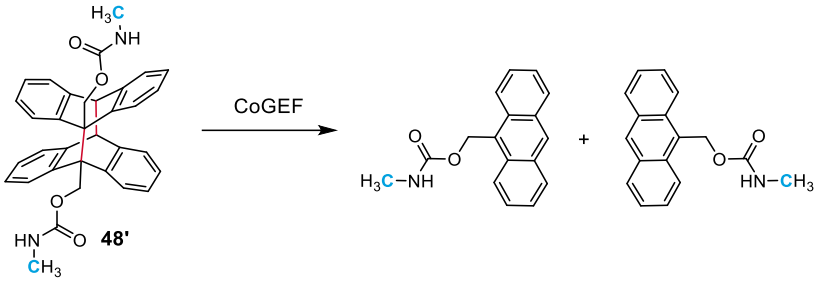

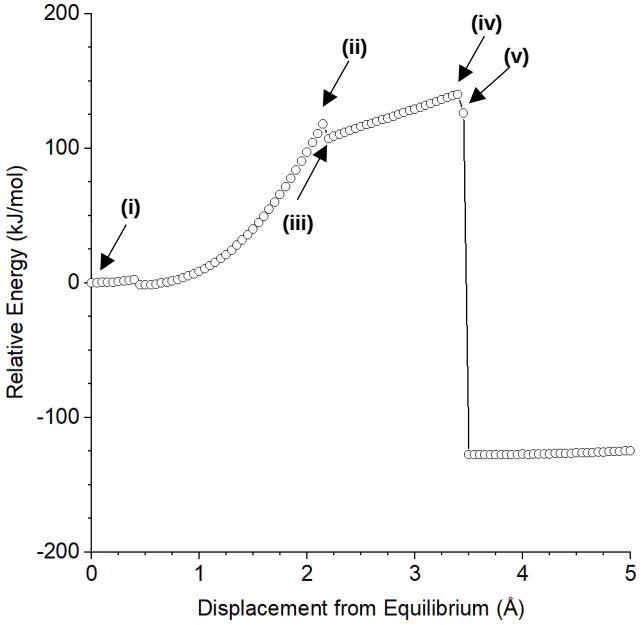

Summary of CoGEF Results	
F_{max}	2.3 nN
E_{max}	140 kJ/mol
Force-Bond Angle	5.7°

(i) Equilibrium Geometry

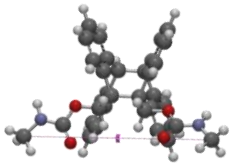

11.492 Å

(ii) Immediately Prior to First Bond Cleavage

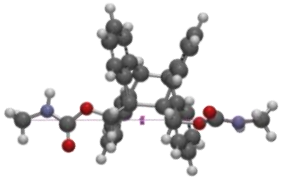

13.642 Å

(iii) Immediately After First Bond Cleavage

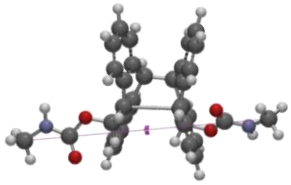

13.692 Å

(iv) Immediately Prior to Second Bond Cleavage

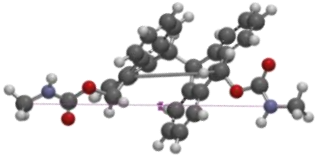

14.892 Å

(v) Immediately After Second Bond Cleavage

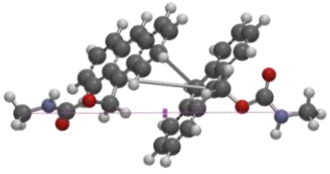

14.942 Å

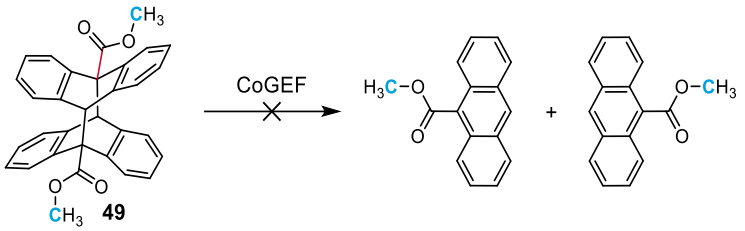

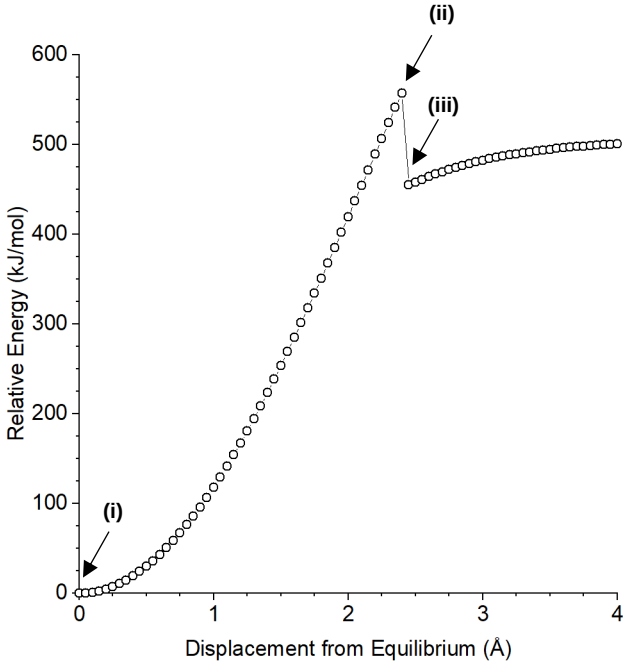

Summary of CoGEF Results	
F_{max}	5.8 nN
E_{max}	557 kJ/mol
Force-Bond Angle	57.8°

(i) Equilibrium Geometry

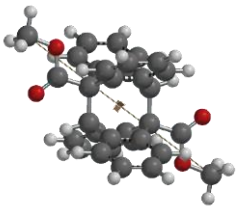

10.728 Å

(ii) Immediately Prior to Bond Cleavage

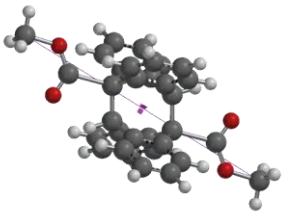

13.128 Å

(iii) Immediately After Bond Cleavage

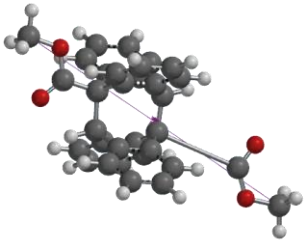

13.178 Å

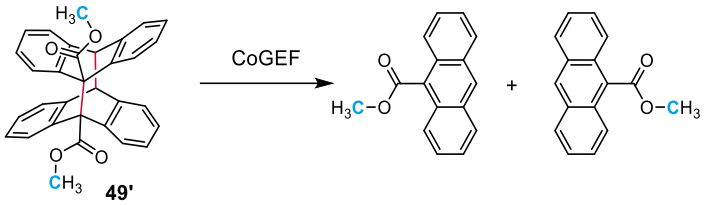

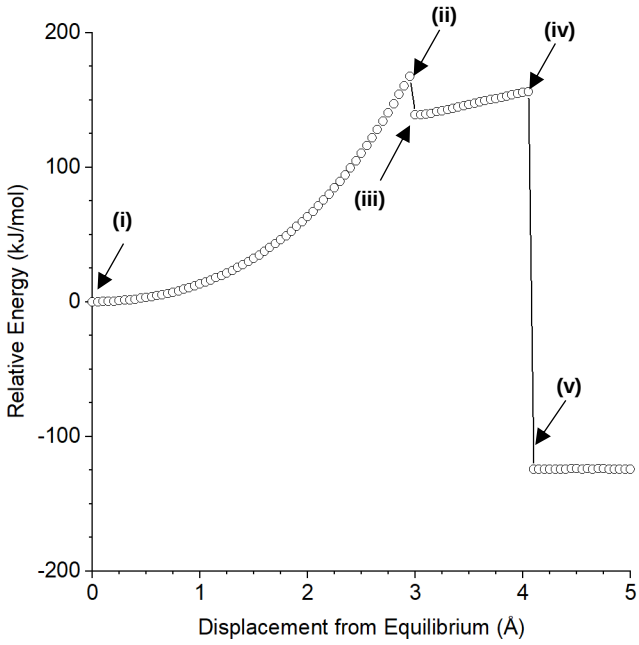

Summary of CoGEF Results	
F_{max}	2.2 nN
E_{max}	167 kJ/mol
Force-Bond Angle	0.5°

(i) Equilibrium Geometry

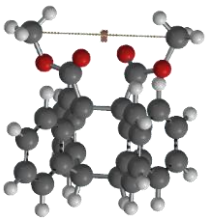

6.033 Å

(ii) Immediately Prior to First Bond Cleavage

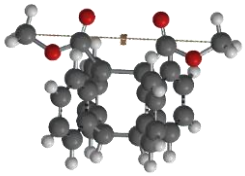

8.983 Å

(iii) Immediately After First Bond Cleavage

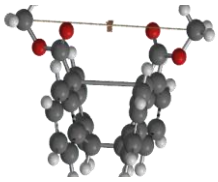

9.033 Å

(iv) Immediately Prior to Second Bond Cleavage

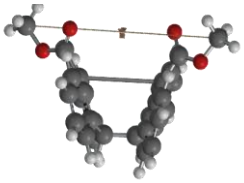

10.083 Å

(v) Immediately After Second Bond Cleavage

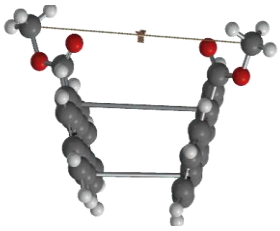

10.133 Å

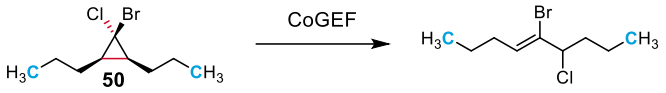

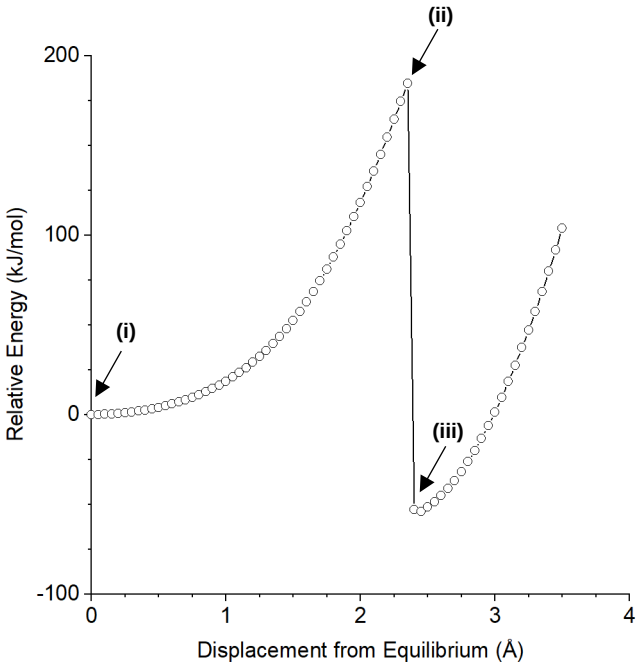

(i) Equilibrium Geometry

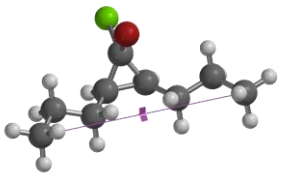

7.809 Å

(ii) Immediately Prior to Bond Cleavage

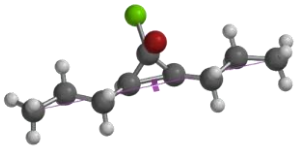

10.359 Å

(iii) Immediately After Bond Cleavage

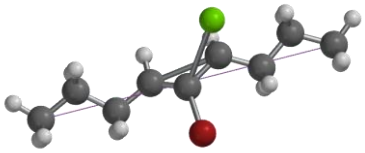

10.359 Å

Summary of CoGEF Results	
F_{max}	3.6 nN
E_{max}	216 kJ/mol
Force-Bond Angle	0.1°

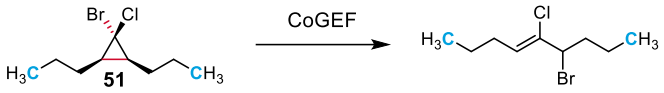

(i) Equilibrium Geometry

(ii)

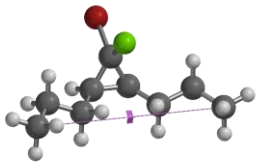

7.824 Å

(ii) Immediately Prior to Bond Cleavage

(i)

(iii)

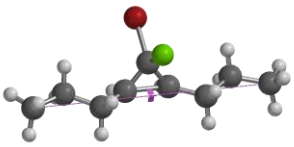

10.174 Å

(iii) Immediately After Bond Cleavage

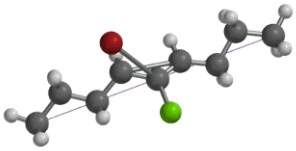

10.224 Å

Summary of CoGEF Results	
F_{max}	3.3 nN
E_{max}	184 kJ/mol
Force-Bond Angle	0.1°

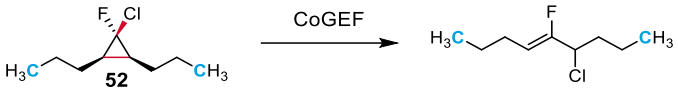

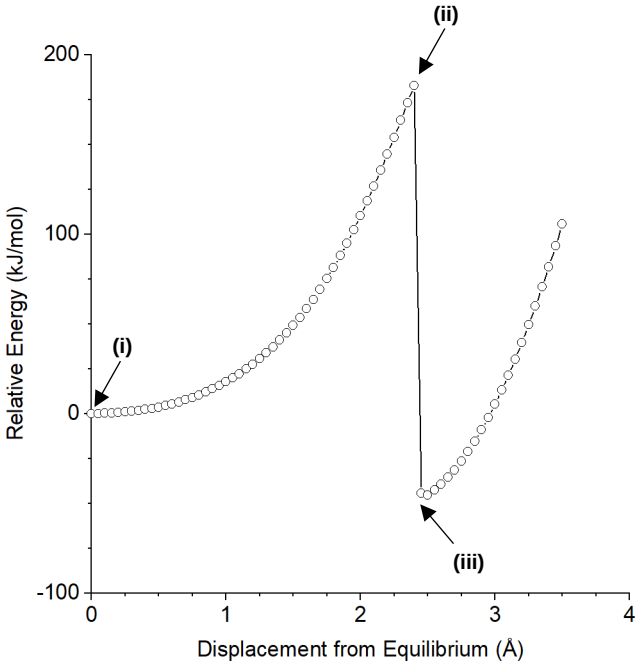

(i) Equilibrium Geometry

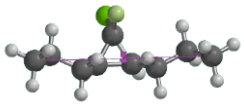

7.776 Å

(ii) Immediately Prior to Bond Cleavage

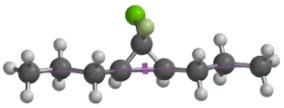

10.176 Å

(iii) Immediately After Bond Cleavage

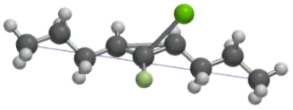

10.226 Å

Summary of CoGEF Results	
F_{max}	3.5 nN
E_{max}	262 kJ/mol
Force-Bond Angle	0.0°

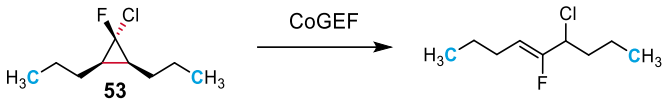

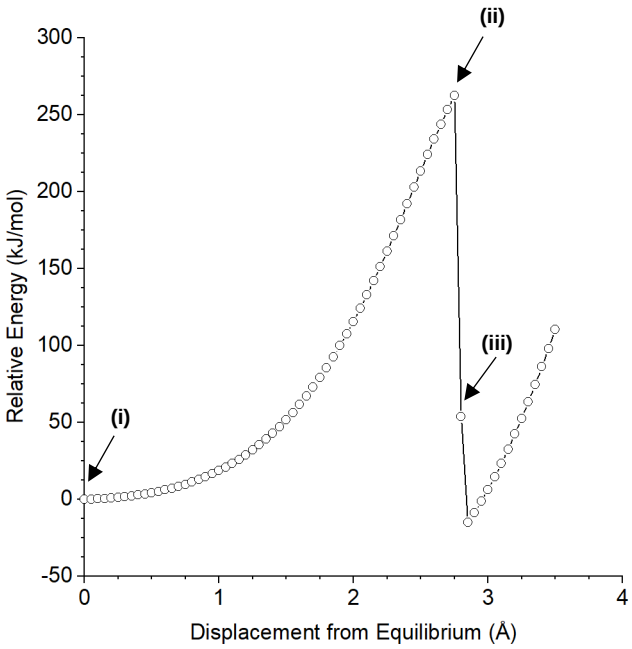

(i) Equilibrium Geometry

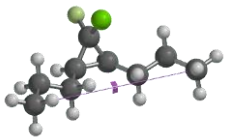

7.816Å

(ii) Immediately Prior to Bond Cleavage

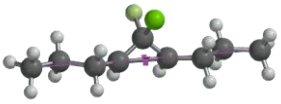

10.566 Å

(iii) Immediately After Bond Cleavage

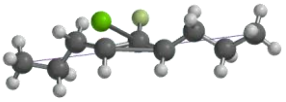

10.616Å

Summary of CoGEF Results	
F_{max}	3.2 nN
E_{max}	183 kJ/mol
Force-Bond Angle	0.1°

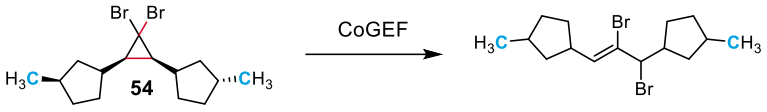

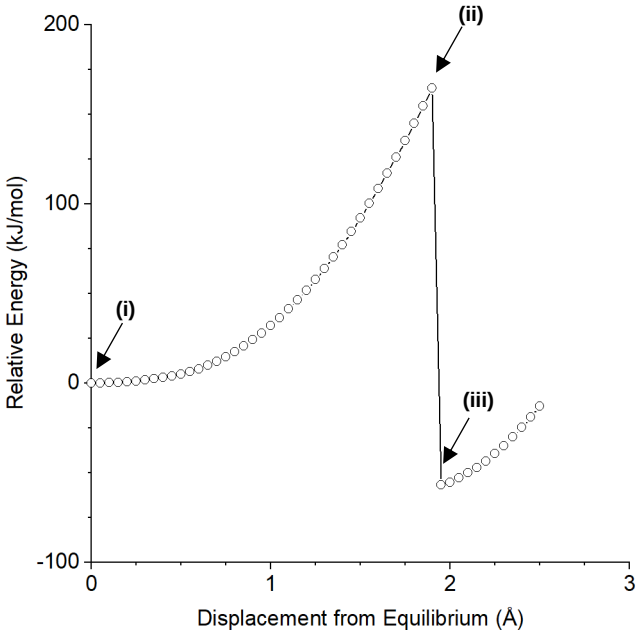

Summary of CoGEF Results

F_{max}	3.3 nN
E_{max}	164 kJ/mol
Force-Bond Angle	0.3°

(i) Equilibrium Geometry

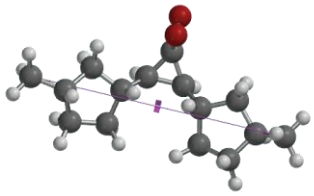

10.675 Å

(ii) Immediately Prior to Bond Cleavage

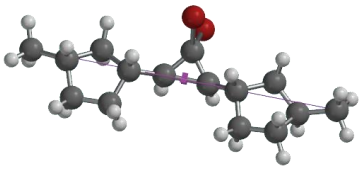

12.575 Å

(iii) Immediately After Bond Cleavage

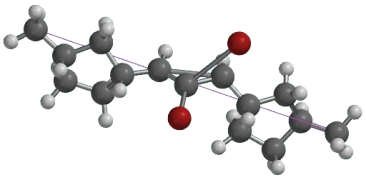

12.625 Å

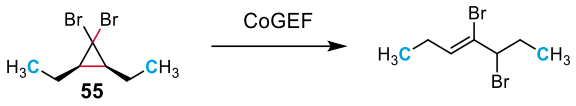

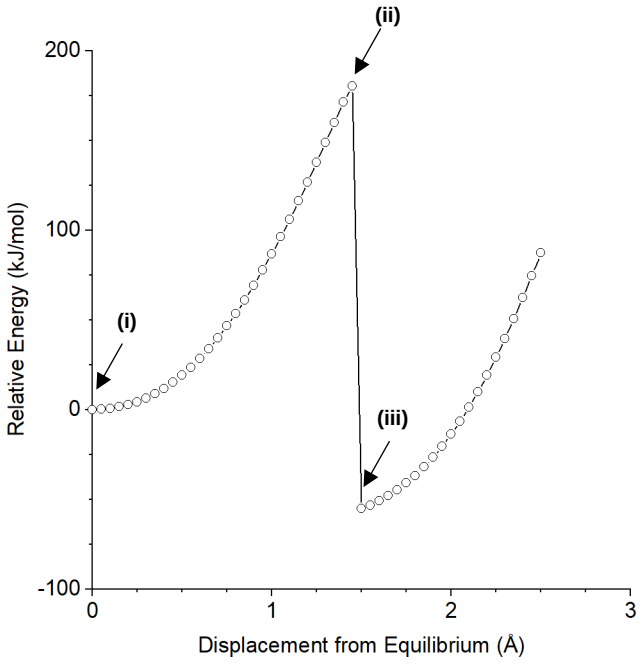

(i) Equilibrium Geometry

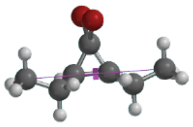

6.081 Å

(ii) Immediately Prior to Bond Cleavage

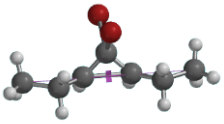

7.531 Å

(iii) Immediately After Bond Cleavage

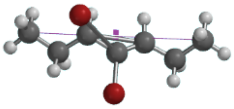

7.581 Å

Summary of CoGEF Results	
F_{max}	3.7 nN
E_{max}	180 kJ/mol
Force-Bond Angle	0.1°

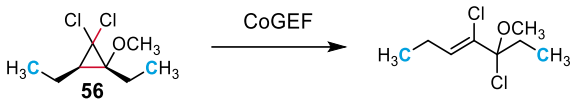

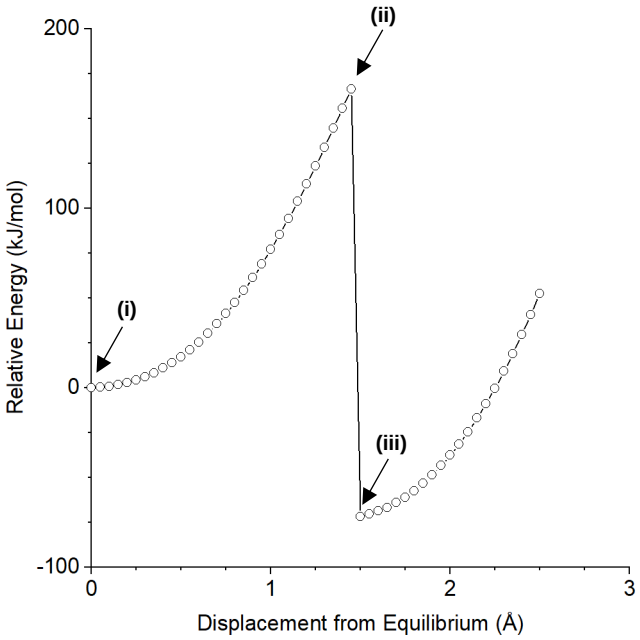

(i) Equilibrium Geometry

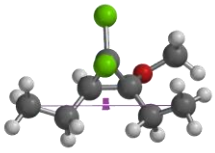

5.971 Å

(ii) Immediately Prior to Bond Cleavage

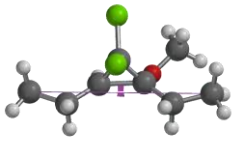

7.421 Å

(iii) Immediately After Bond Cleavage

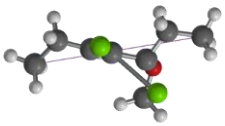

7.471 Å

Summary of CoGEF Results	
F_{max}	3.6 nN
E_{max}	166 kJ/mol
Force-Bond Angle	3.8°

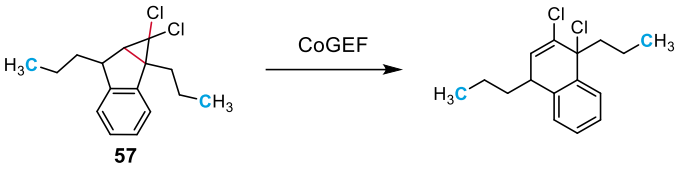

57

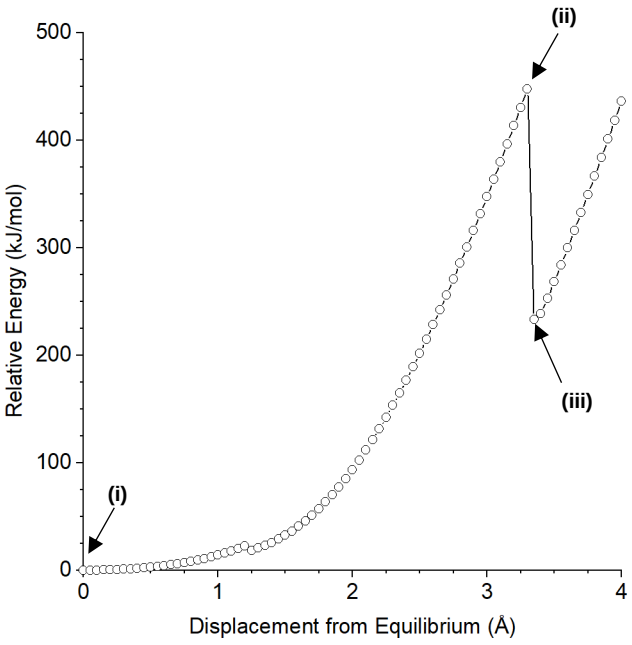

(i) Equilibrium Geometry

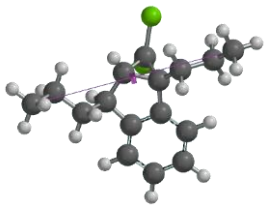

8.972 Å

(ii) Immediately Prior to Bond Cleavage

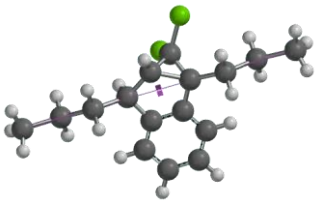

12.272 Å

(iii) Immediately After Bond Cleavage

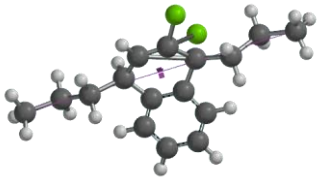

12.322 Å

Summary of CoGEF Results	
F_{max}	5.7 nN
E_{max}	448 kJ/mol
Force-Bond Angle	31°

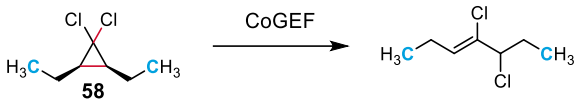

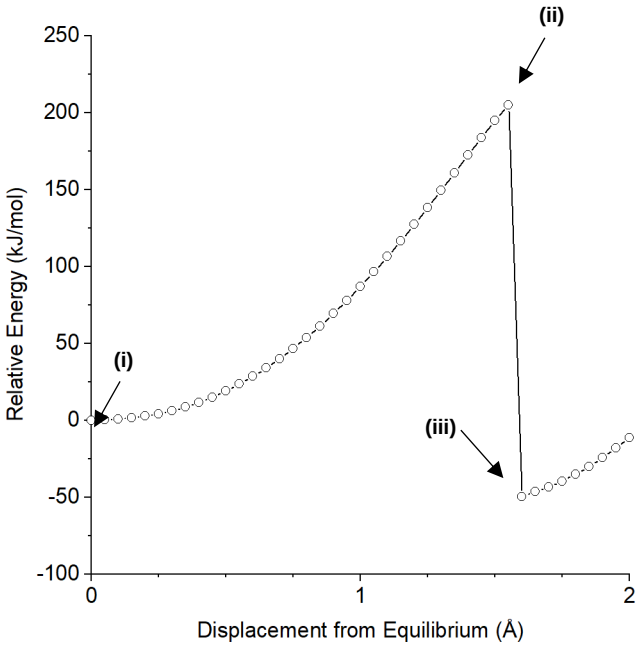

(i) Equilibrium Geometry

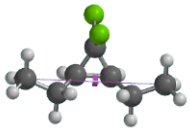

6.079 Å

(ii) Immediately Prior to Bond Cleavage

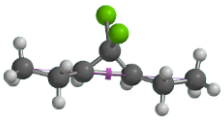

7.629 Å

(iii) Immediately After Bond Cleavage

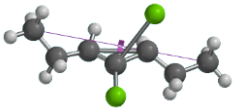

7.679 Å

Summary of CoGEF Results	
F_{max}	3.8 nN
E_{max}	205 kJ/mol
Force-Bond Angle	0.0°

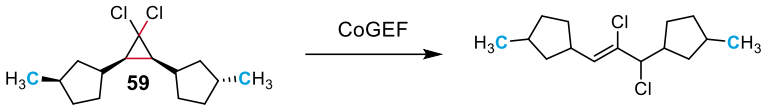

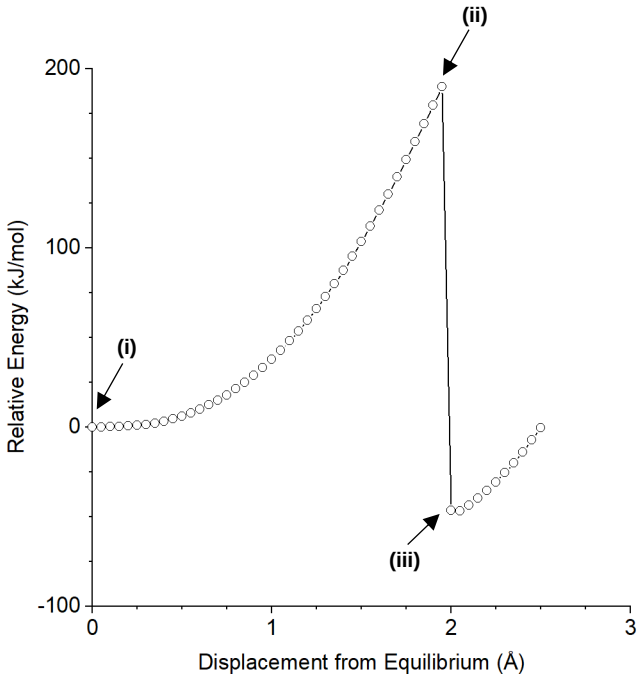

(i) Equilibrium Geometry

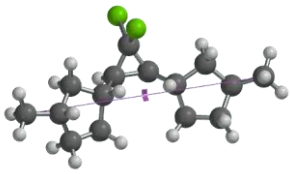

10.746 Å

(ii) Immediately Prior to Bond Cleavage

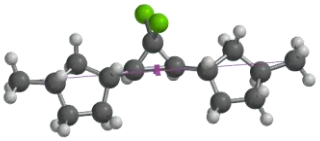

12.696 Å

(iii) Immediately After Bond Cleavage

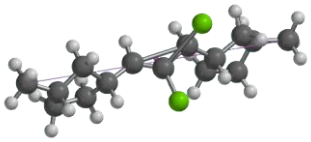

12.746 Å

Summary of CoGEF Results	
F_{max}	3.4 nN
E_{max}	190 kJ/mol
Force-Bond Angle	0.4°

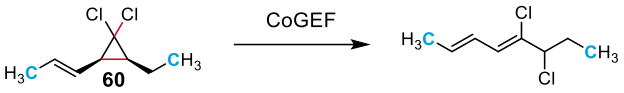

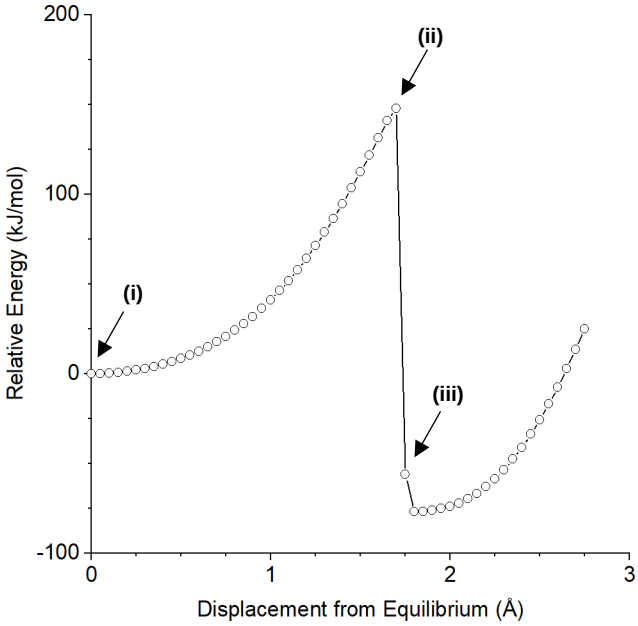

(i) Equilibrium Geometry

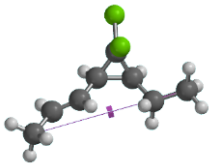

6.904 Å

(ii) Immediately Prior to Bond Cleavage

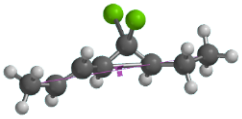

8.604 Å

(iii) Immediately After Bond Cleavage

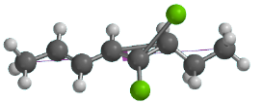

8.654 Å

Summary of CoGEF Results	
F_{max}	3.2 nN
E_{max}	148 kJ/mol
Force-Bond Angle	9.0°

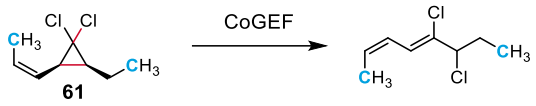

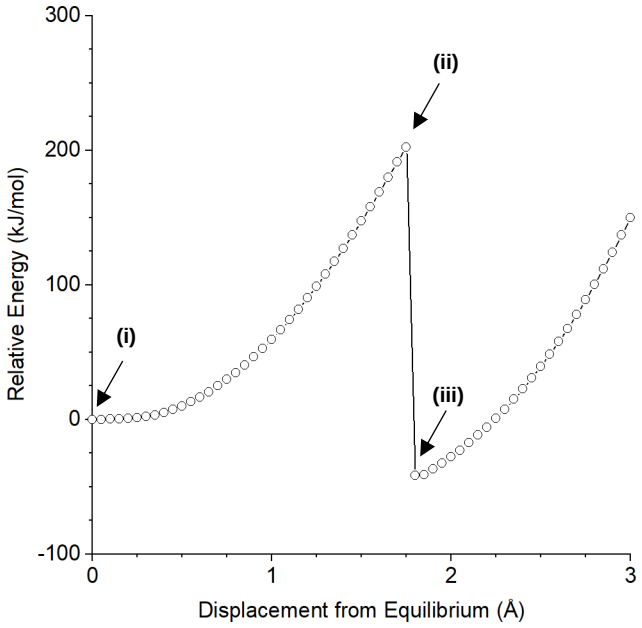

(i) Equilibrium Geometry

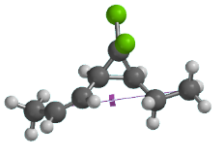

6.787 Å

(ii) Immediately Prior to Bond Cleavage

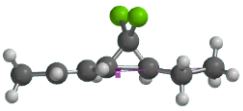

8.537 Å

(iii) Immediately After Bond Cleavage

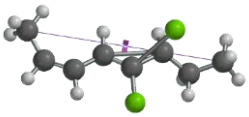

8.587 Å

Summary of CoGEF Results	
F_{max}	3.7 nN
E_{max}	202 kJ/mol
Force-Bond Angle	3.9°

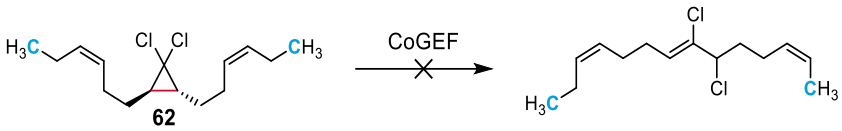

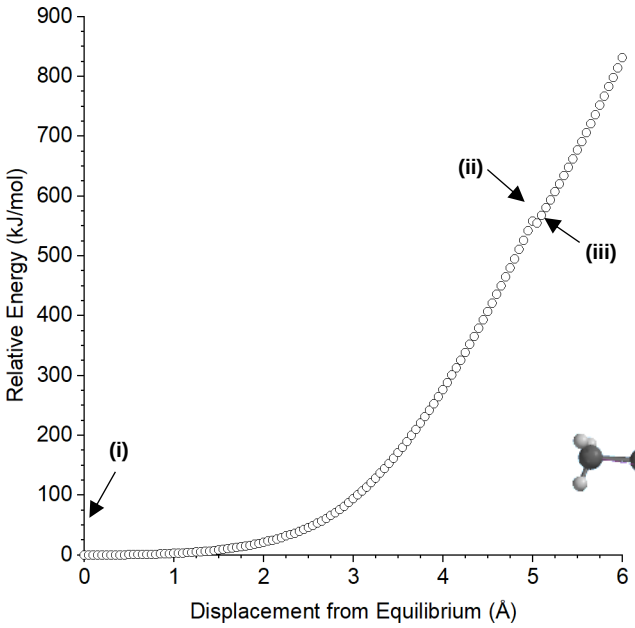

(i) Equilibrium Geometry

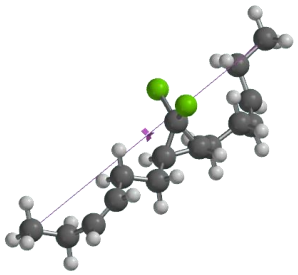

13.974 Å

(ii) Immediately Prior to Bond Cleavage

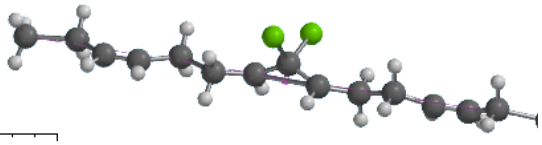

21.174 Å

(iii) Immediately After Bond Cleavage

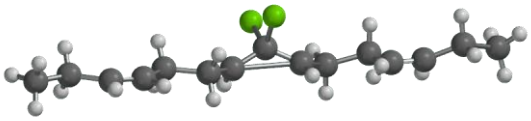

21.224 Å

Summary of CoGEF Results	
F_{max}	5.2 nN
E_{max}	557 kJ/mol
Force-Bond Angle	20°

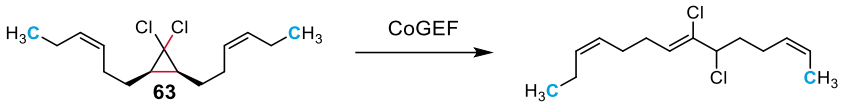

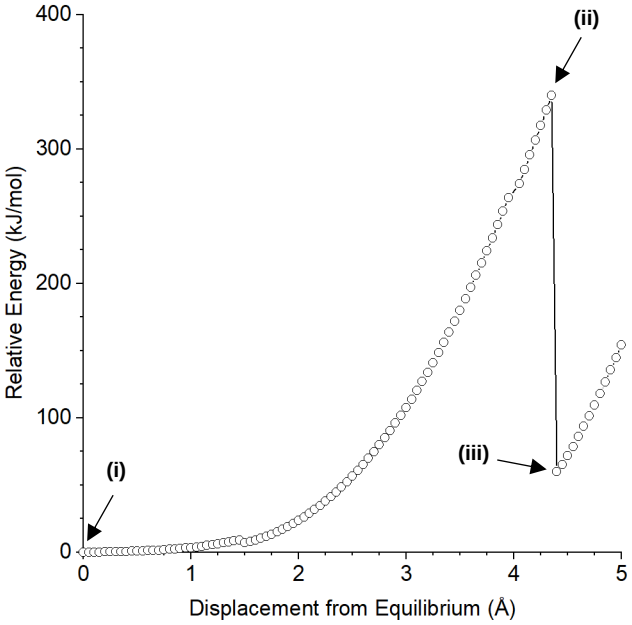

(i) Equilibrium Geometry

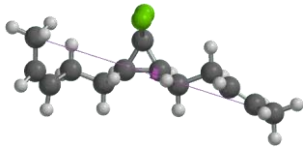

11.037 Å

(i) Immediately Prior to Bond Cleavage

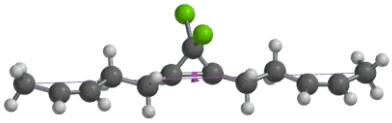

15.337 Å

(ii) Immediately After Bond Cleavage

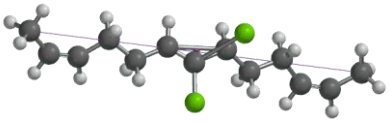

15.387 Å

Summary of CoGEF Results	
F_{max}	3.8 nN
E_{max}	340 kJ/mol
Force/Bond angle	0.1°

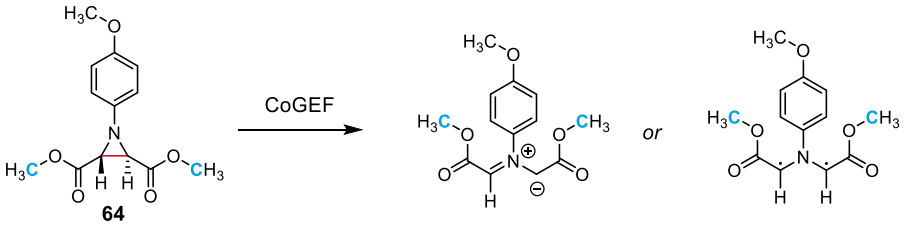

64

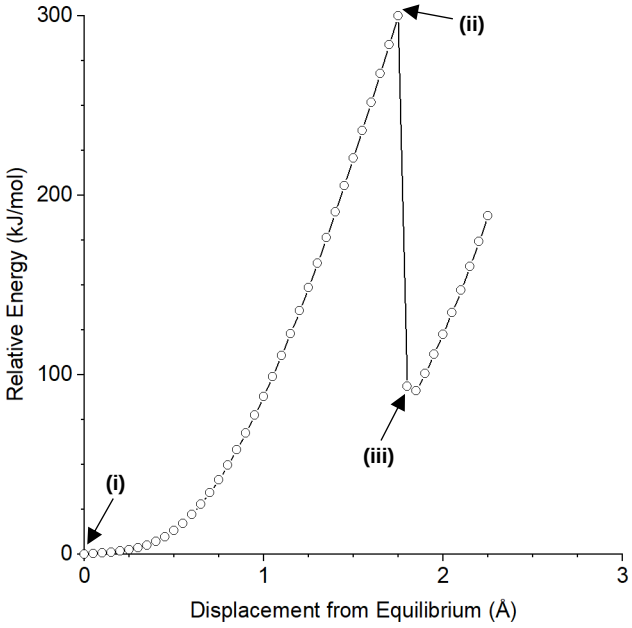

(i) Equilibrium Geometry

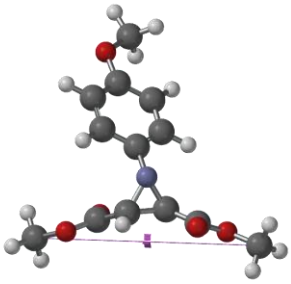

8.232 Å

(ii) Immediately Prior to Bond Cleavage

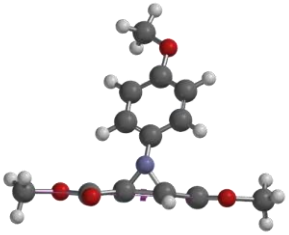

9.982 Å

(iii) Immediately After Bond Cleavage

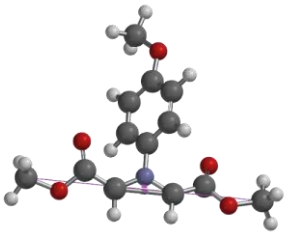

10.032 Å

Summary of CoGEF Results	
F_{max}	5.4 nN
E_{max}	300 kJ/mol
Force-Bond Angle	22°

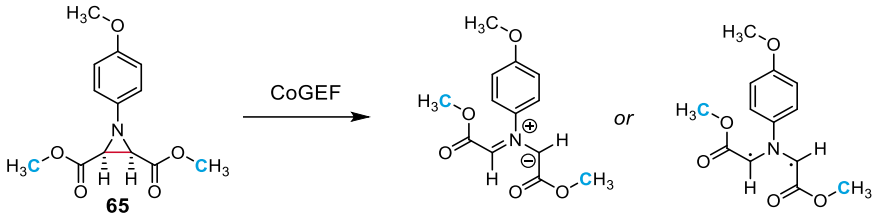

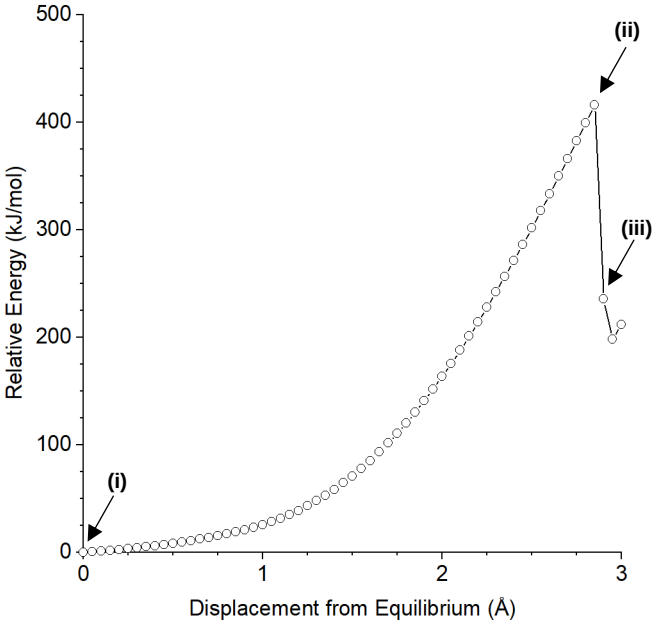

Summary of CoGEF Results	
F_{max}	5.6 nN
E_{max}	416 kJ/mol
Force-Bond Angle	0.1°

(i) Equilibrium Geometry

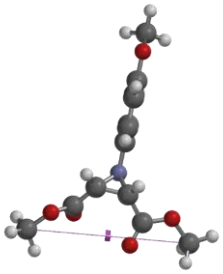

7.37 Å

(ii) Immediately Prior to Bond Cleavage

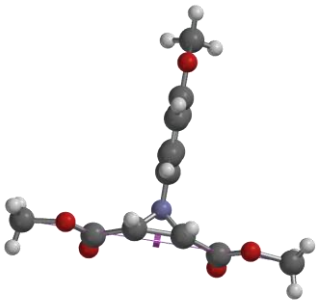

10.22 Å

(iii) Immediately After Bond Cleavage

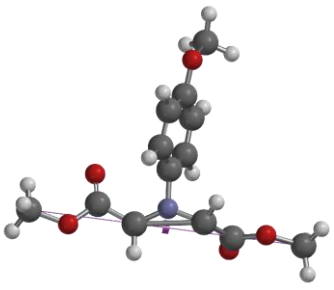

10.27 Å

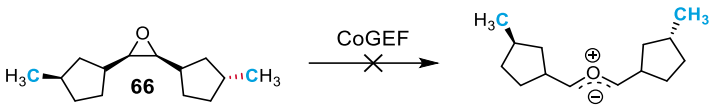

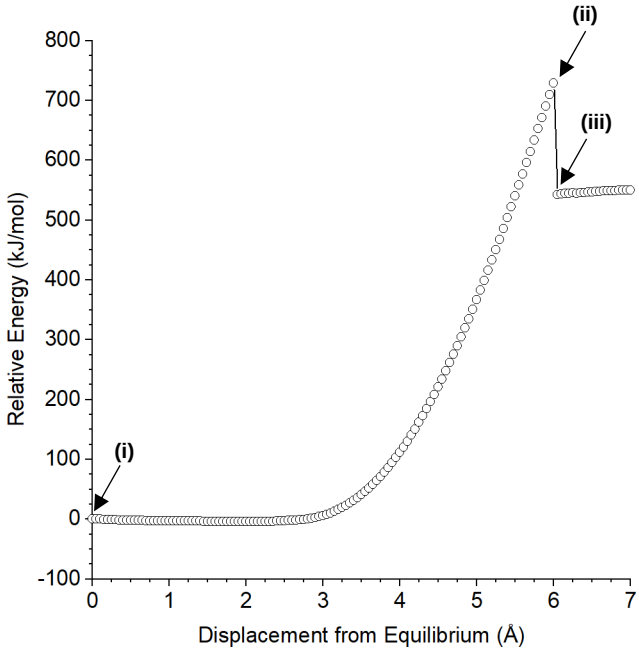

(i) Equilibrium Geometry

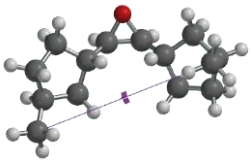

8.113 Å

(ii) Immediately Prior to Bond Cleavage

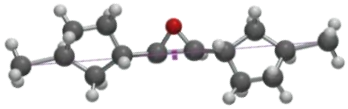

14.113 Å

(iii) Immediately After Bond Cleavage

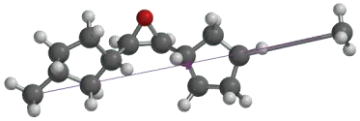

14.163 Å

Summary of CoGEF Results	
F_{max}	6.4 nN
E_{max}	729 kJ/mol
Force-Bond Angle	0.8°

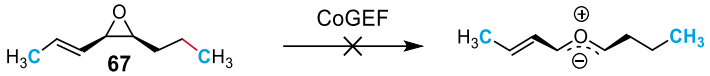

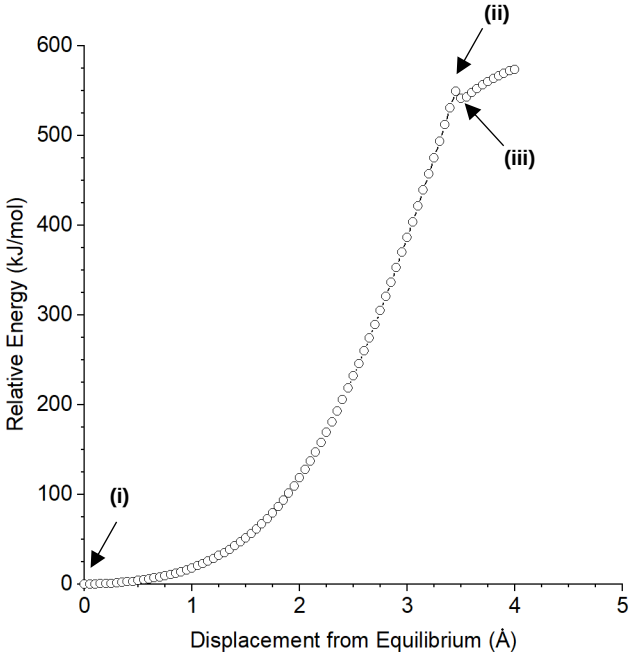

(i) Equilibrium Geometry

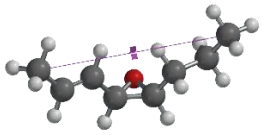

7.555 Å

(ii) Immediately Prior to Bond Cleavage

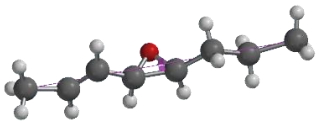

11.005 Å

(iii) Immediately After Bond Cleavage

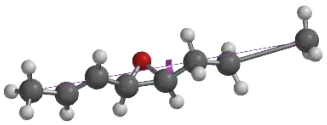

11.055 Å

Summary of CoGEF Results	
F_{max}	6.2 nN
E_{max}	549 kJ/mol
Force-Bond Angle	1.5°

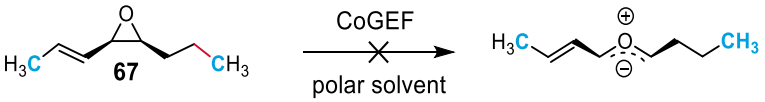

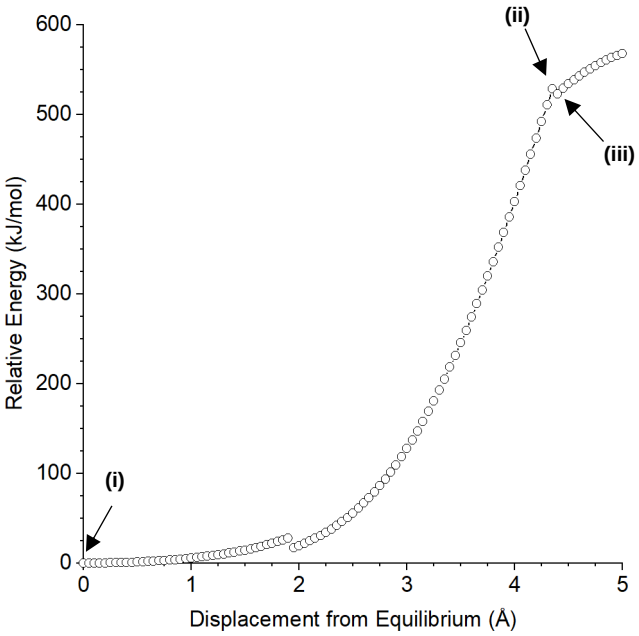

(i) Equilibrium Geometry

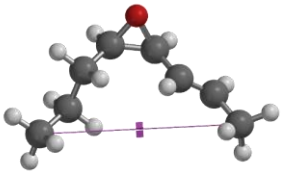

6.606 Å

(ii) Immediately Prior to Bond Cleavage

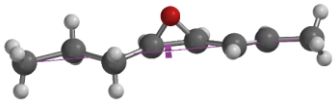

10.956 Å

(iii) Immediately After Bond Cleavage

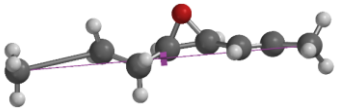

11.006 Å

Summary of CoGEF Results	
F_{max}	6.1 nN
E_{max}	529 kJ/mol
Force-Bond Angle	1.6°

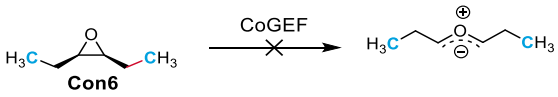

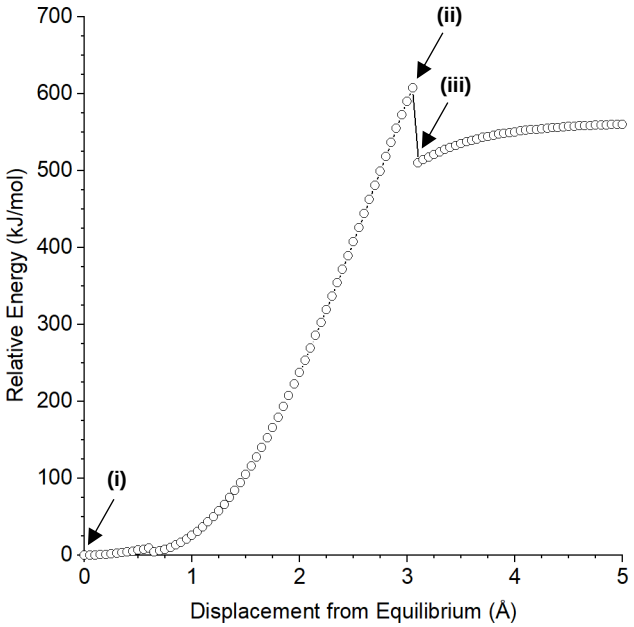

(i) Equilibrium Geometry

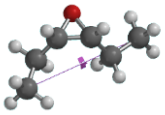

5.523 Å

(ii) Immediately Prior to Bond Cleavage

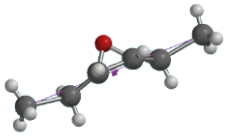

8.573 Å

(iii) Immediately After Bond Cleavage

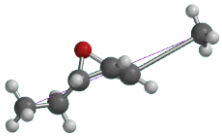

8.623 Å

Summary of CoGEF Results	
F_{max}	6.2 nN
E_{max}	607 kJ/mol
Force-Bond Angle	0.0°

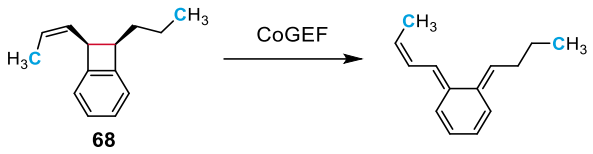

68

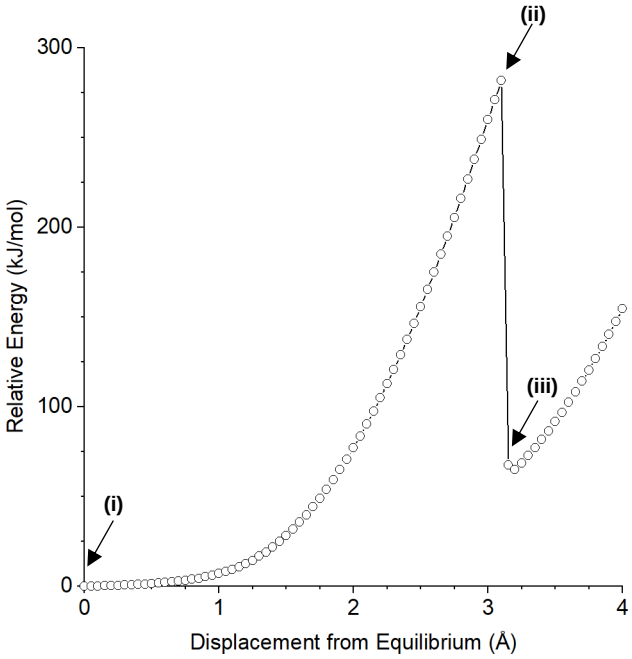

(i) Equilibrium Geometry

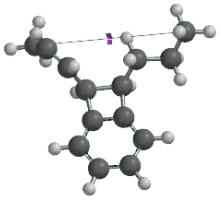

7.067 Å

(ii) Immediately Prior to Bond Cleavage

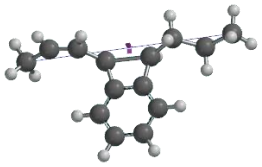

10.167 Å

(iii) Immediately After Bond Cleavage

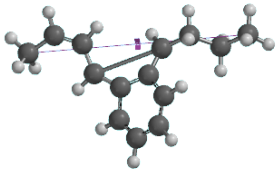

10.217 Å

Summary of CoGEF Results	
F_{max}	3.7 nN
E_{max}	282 kJ/mol
Force/Bond angle	3.2°

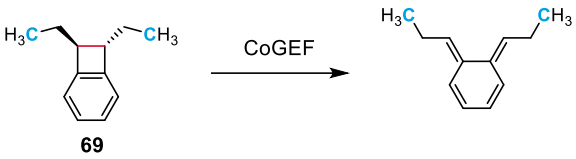

69

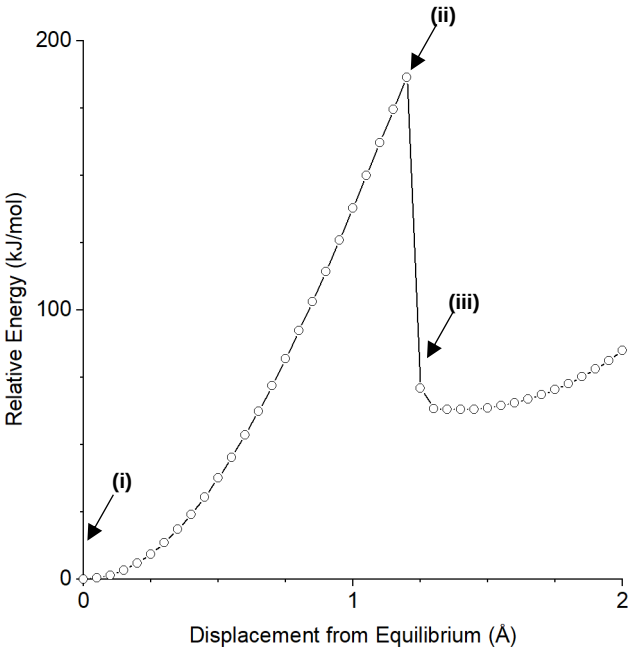

(i) Equilibrium Geometry

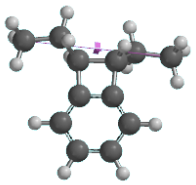

6.463 Å

(ii) Immediately Prior to Bond Cleavage

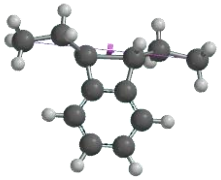

7.663 Å

(iii) Immediately After Bond Cleavage

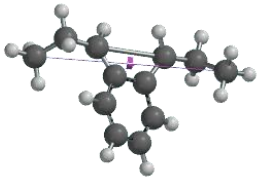

7.713 Å

Summary of CoGEF Results	
F_{max}	4.1 nN
E_{max}	186 kJ/mol
Force/Bond angle	17°

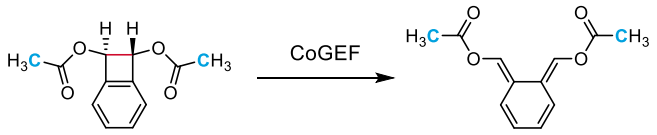

70

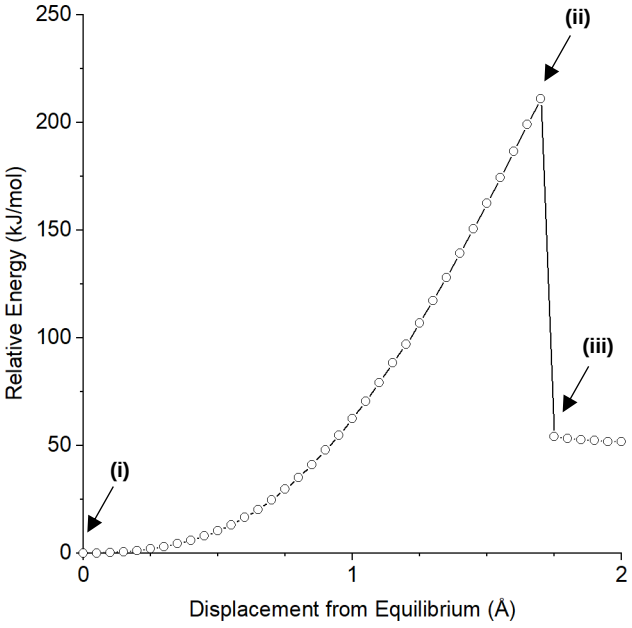

(i) Equilibrium Geometry

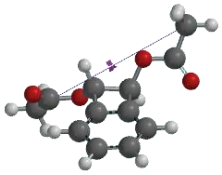

7.936 Å

(ii) Immediately Prior to Bond Cleavage

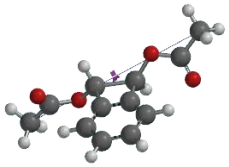

9.636 Å

(iii) Immediately After Bond Cleavage

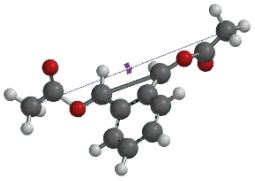

9.686 Å

Summary of CoGEF Results	
F_{max}	4.1 nN
E_{max}	211 kJ/mol
Force-Bond Angle	25°

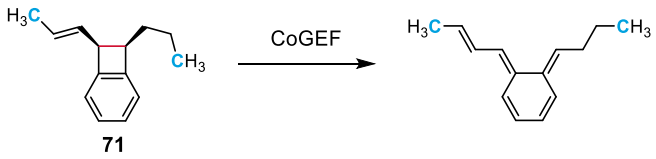

71

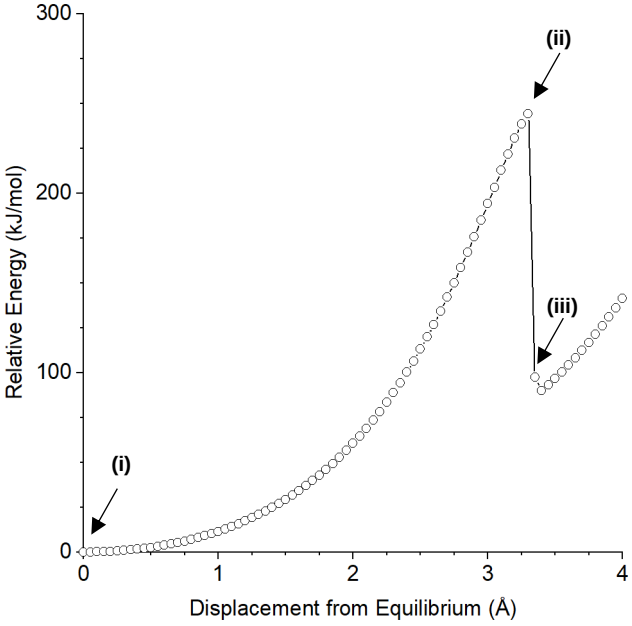

(i) Equilibrium Geometry

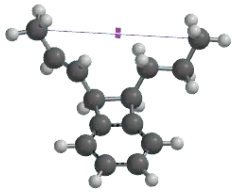

7.011 Å

(ii) Immediately Prior to Bond Cleavage

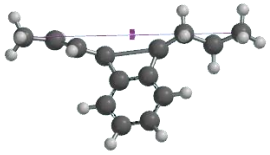

10.161 Å

(iii) Immediately After Bond Cleavage

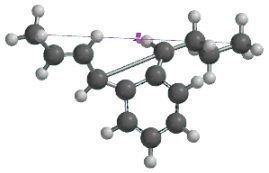

10.211 Å

Summary of CoGEF Results	
F_{max}	3.1 nN
E_{max}	244 kJ/mol
Force-Bond Angle	2.8°

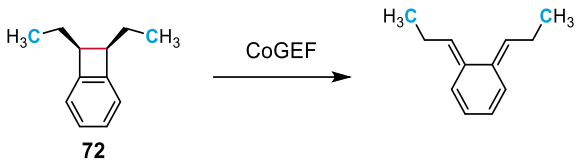

72

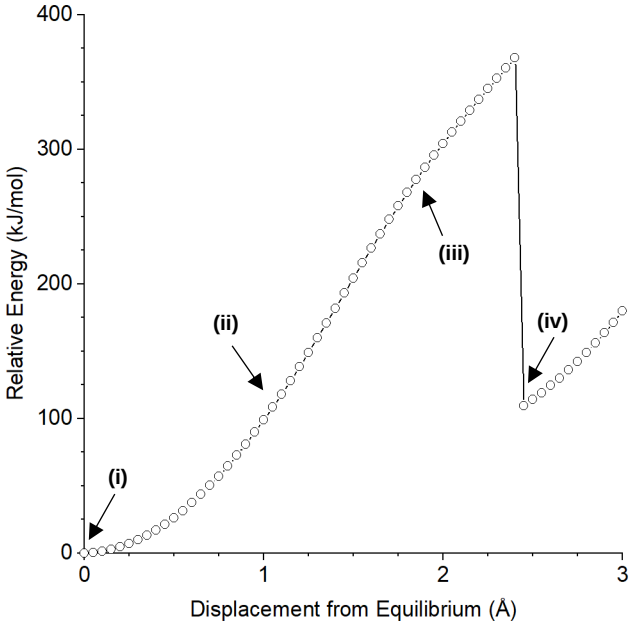

Summary of CoGEF Results	
F_{max}	3.7 nN
E_{max}	367 kJ/mol
Force/Bond angle	0.0°

(i) Equilibrium Geometry

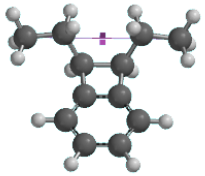

6.123 Å

(ii) Prior to Bond Cleavage

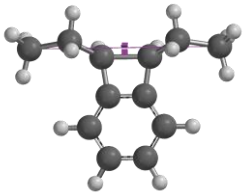

7.273 Å

(iii) After Bond Cleavage

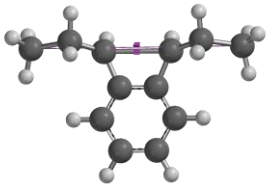

8.123

(iv) After Formation of Double Bonds

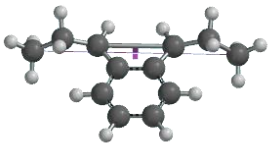

8.573 Å

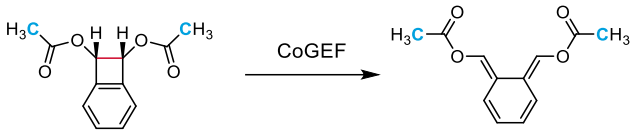

73

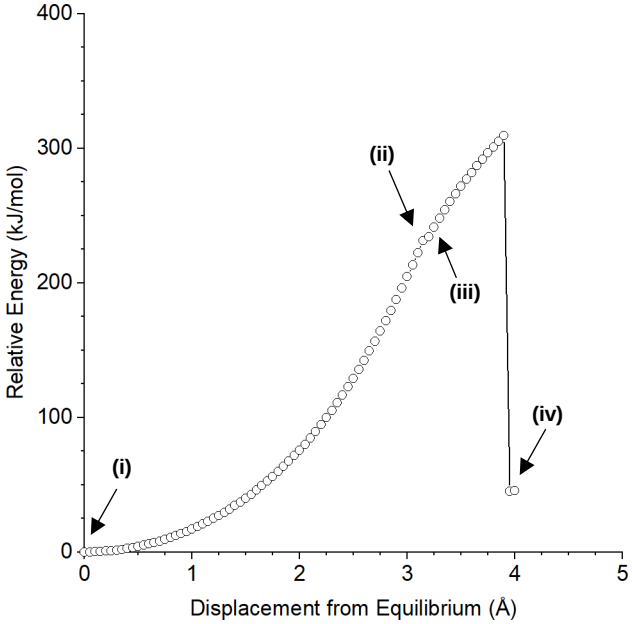

Summary of CoGEF Results	
F_{max}	3.0 nN
E_{max}	310 kJ/mol
Force-Bond Angle	0.0°

(i) Equilibrium Geometry

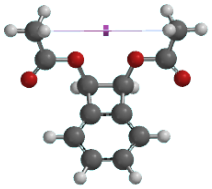

6.275 Å

(ii) Immediately Prior to Bond Cleavage

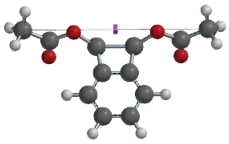

9.425 Å

(iii) Immediately After Bond Cleavage

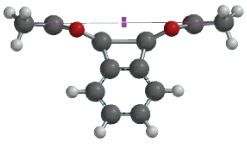

9.475 Å

(iv) After Formation of Double Bonds

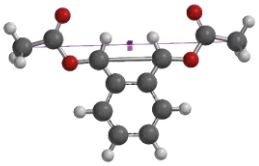

10.225 Å

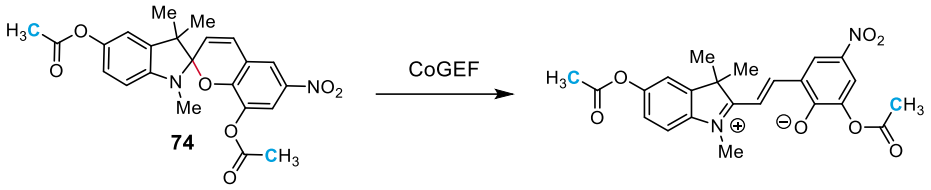

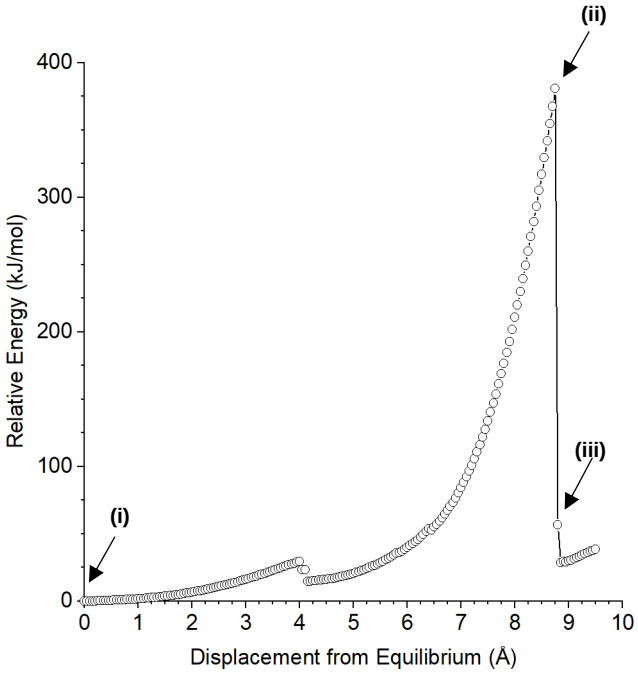

(i) Equilibrium Geometry

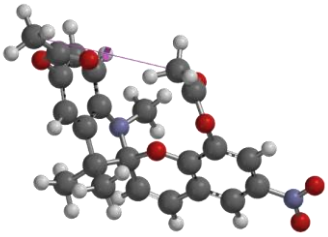

6.048 Å

(ii) Immediately Prior to Bond Cleavage

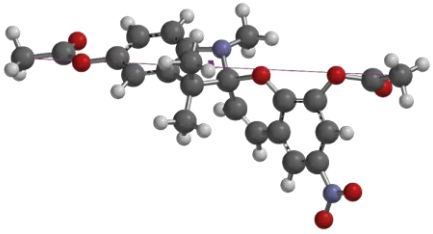

16.648 Å

(iii) Immediately After Bond Cleavage

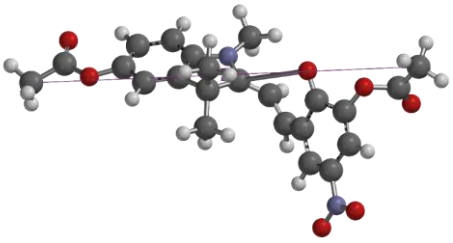

16.698 Å

Summary of CoGEF Results	
F_{max}	4.4 nN
E_{max}	381 kJ/mol
Force-Bond Angle	14°

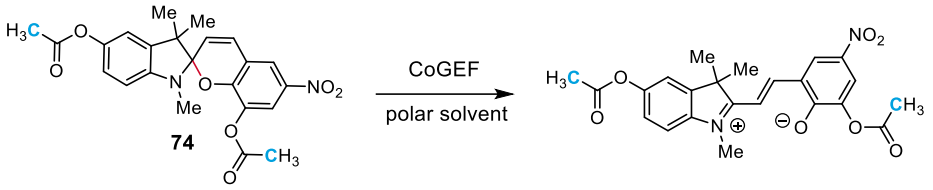

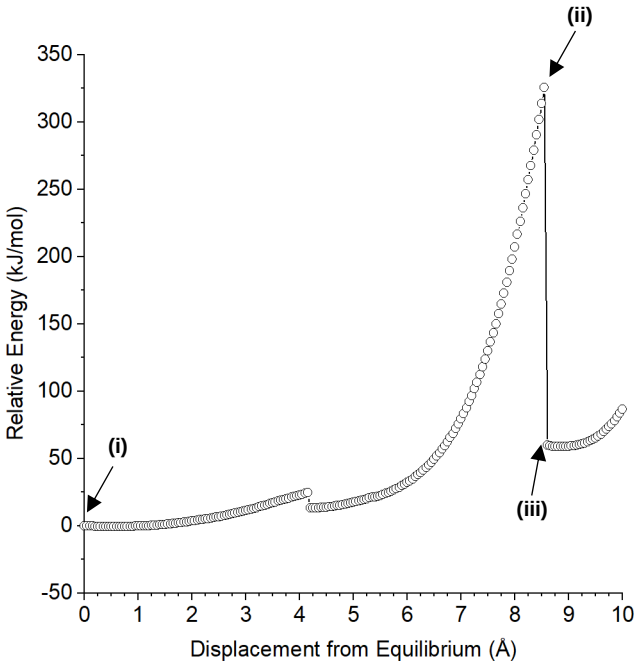

(i) Equilibrium Geometry

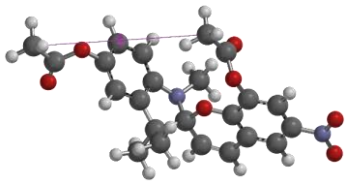

7.920 Å

(ii) Immediately Prior to Bond Cleavage

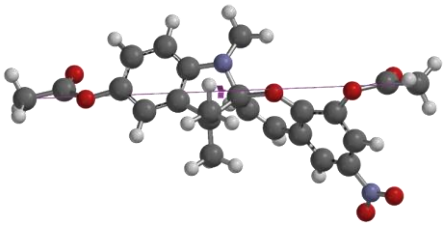

16.470 Å

(iii) Immediately After Bond Cleavage

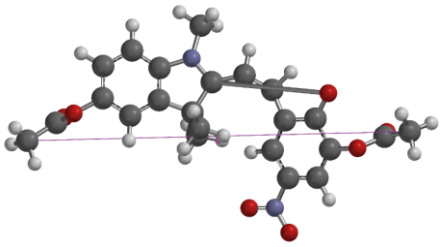

16.520 Å

Summary of CoGEF Results	
F_{max}	4.0 nN
E_{max}	325 kJ/mol
Force-Bond Angle	14°

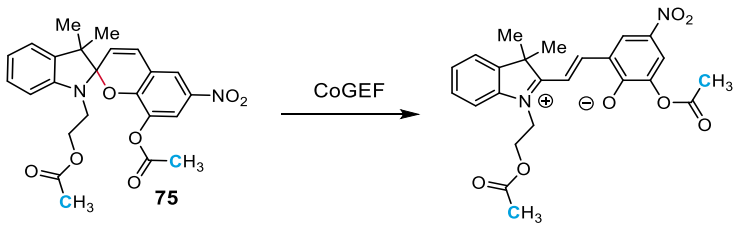

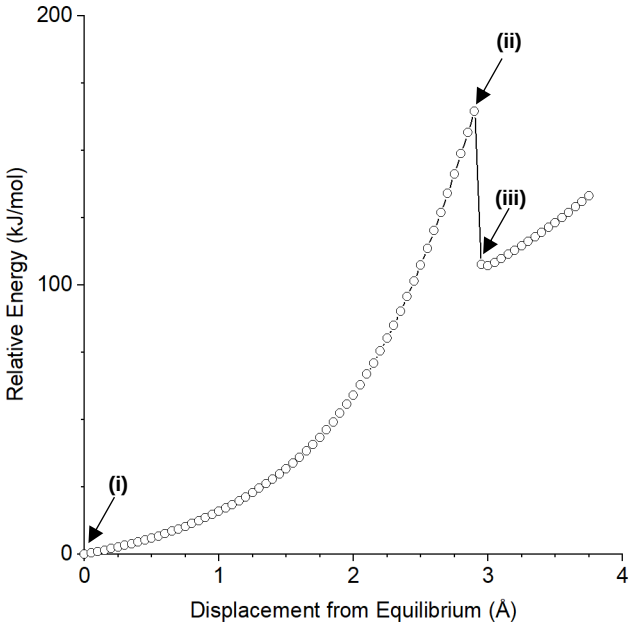

(i) Equilibrium Geometry

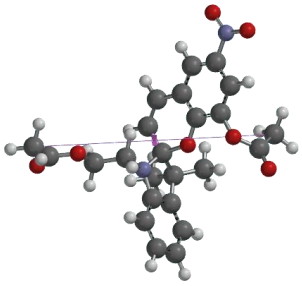

11.600 Å

(ii) Immediately Prior to Bond Cleavage

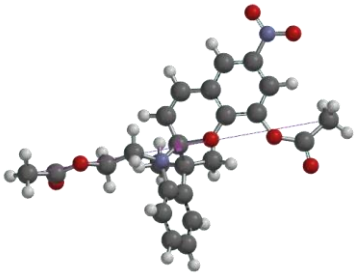

14.500 Å

(iii) Immediately After Bond Cleavage

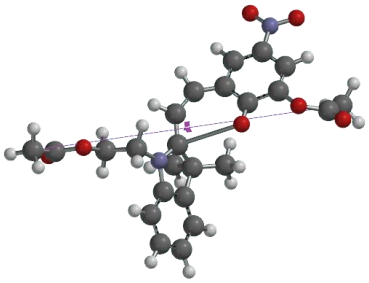

14.550 Å

Summary of CoGEF Results	
F_{max}	2.7 nN
E_{max}	165 kJ/mol
Force-Bond Angle	29°

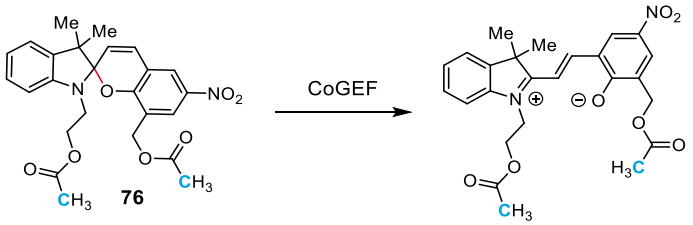

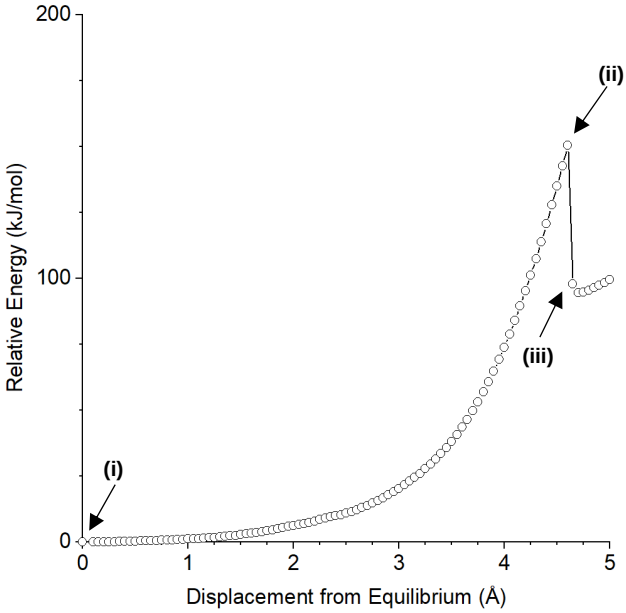

Summary of CoGEF Results	
F_{max}	2.6 nN
E_{max}	150 kJ/mol
Force-Bond Angle	27°

(i) Equilibrium Geometry

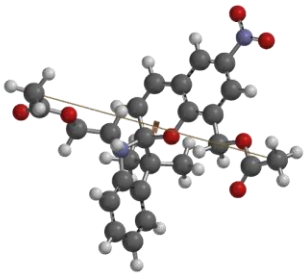

11.322 Å

(ii) Immediately Prior to Bond Cleavage

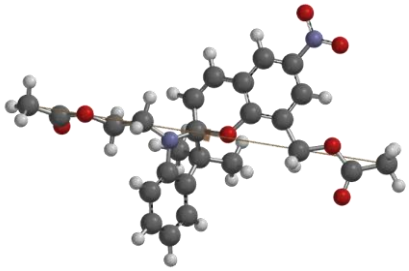

15.922 Å

(iii) Immediately After Bond Cleavage

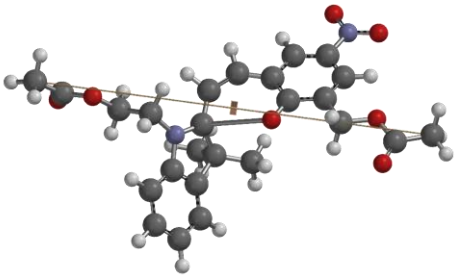

15.972 Å

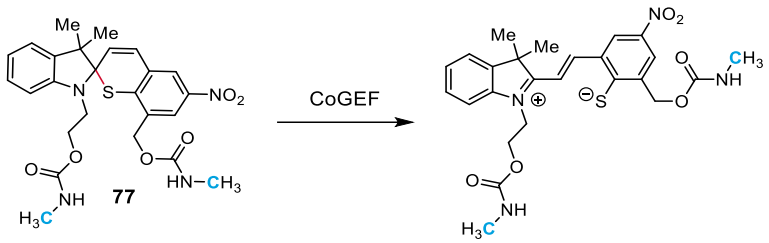

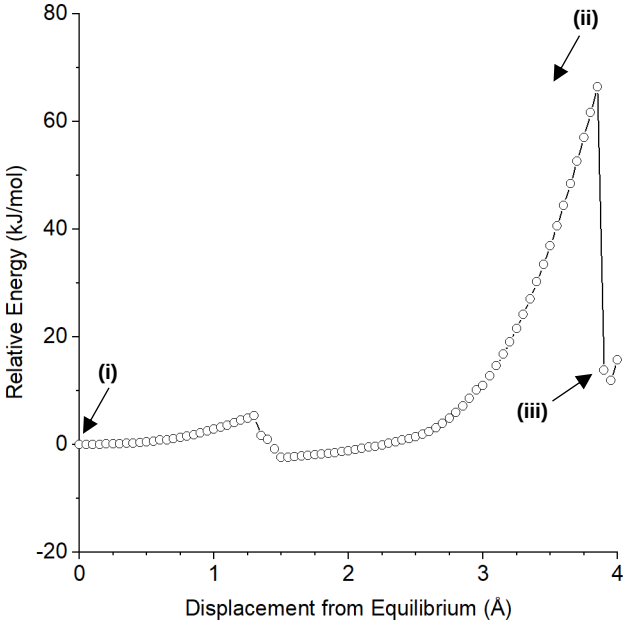

Summary of CoGEF Results	
F_{max}	2.0 nN
E_{max}	74 kJ/mol
Force-Bond Angle	31°

(i) Equilibrium Geometry

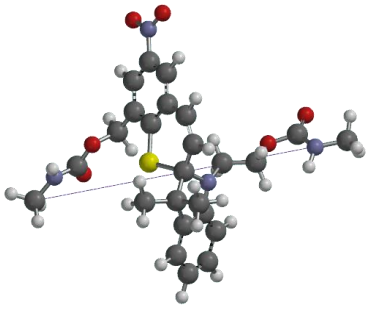

14.303 Å

(ii) Immediately Prior to Bond Cleavage

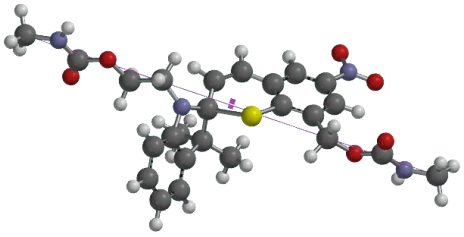

18.803 Å

(iii) Immediately After Bond Cleavage

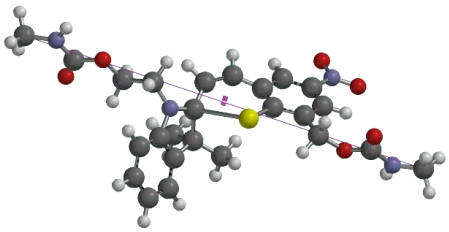

18.853 Å

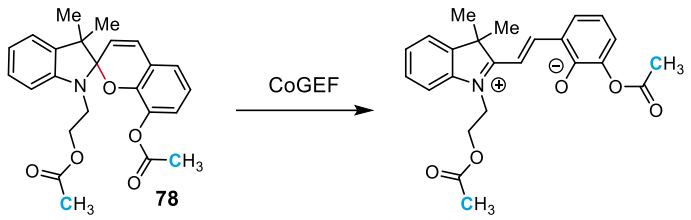

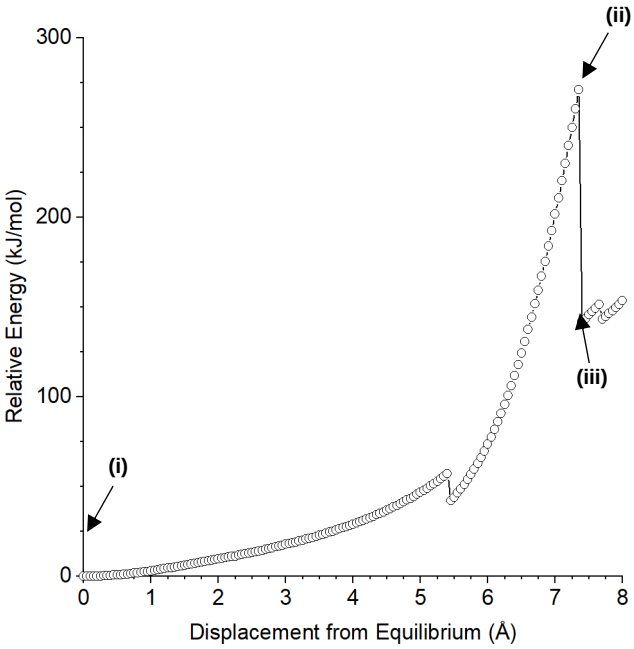

(i) Equilibrium Geometry

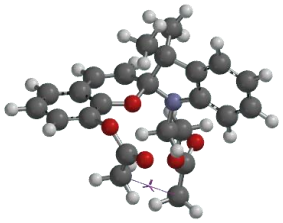

7.625 Å

(ii) Immediately Prior to Bond Cleavage

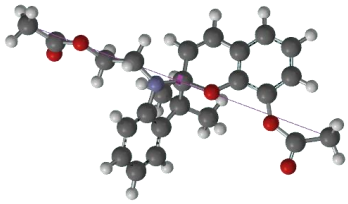

14.975 Å

(iii) Immediately After Bond Cleavage

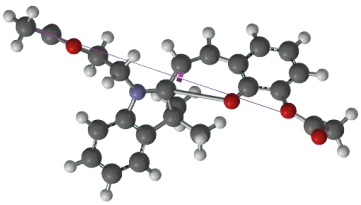

15.025 Å

Summary of CoGEF Results	
F_{max}	3.5 nN
E_{max}	271 kJ/mol
Force-Bond Angle	28°

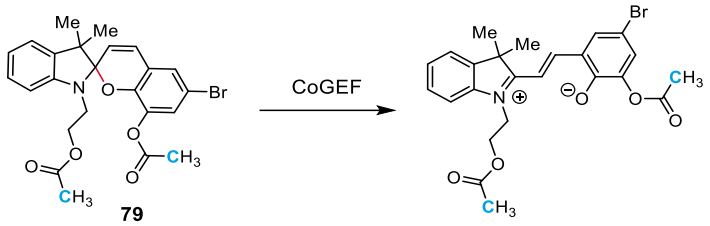

79

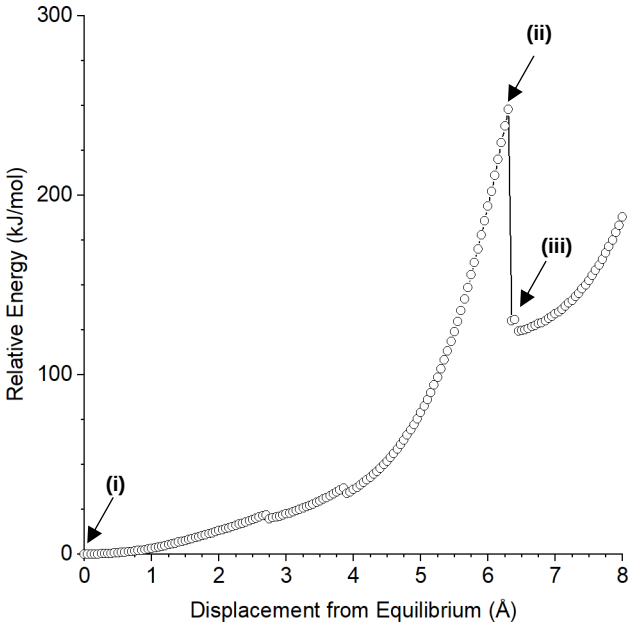

(i) Equilibrium Geometry

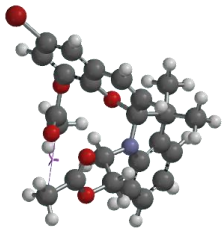

8.544 Å

(ii) Immediately Prior to Bond Cleavage

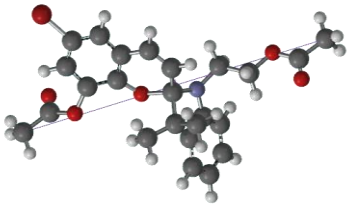

14.844 Å

(iii) Immediately After Bond Cleavage

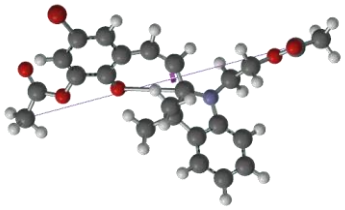

14.894 Å

Summary of CoGEF Results	
F_{max}	3.2 nN
E_{max}	248 kJ/mol
Force-Bond Angle	27°

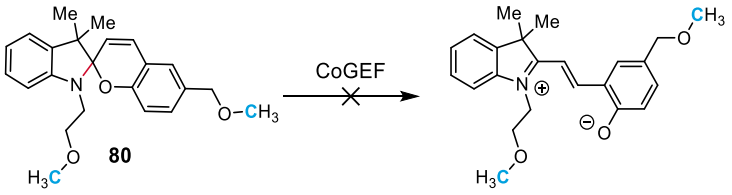

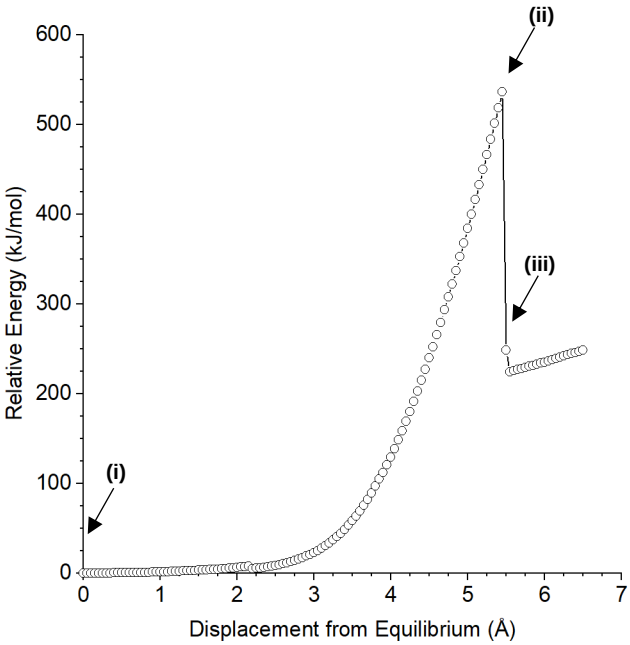

Summary of CoGEF Results	
F_{max}	5.9 nN
E_{max}	536 kJ/mol
Force-Bond Angle	47°

(i) Equilibrium Geometry

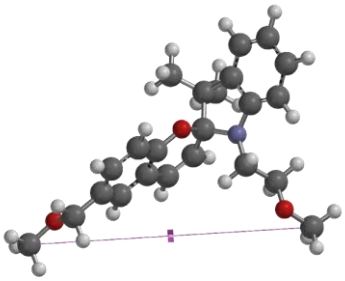

11.447 Å

(ii) Immediately Prior to Bond Cleavage

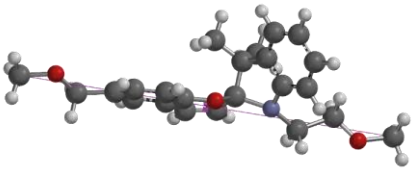

16.897 Å

(iii) Immediately After Bond Cleavage

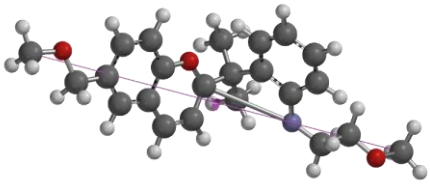

16.947 Å

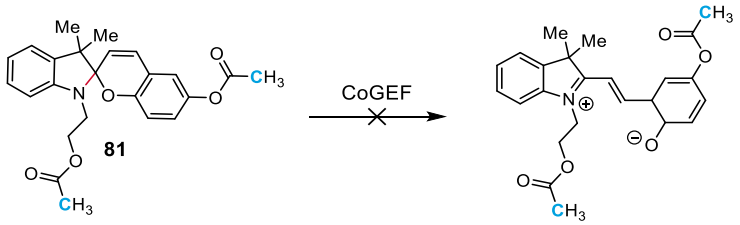

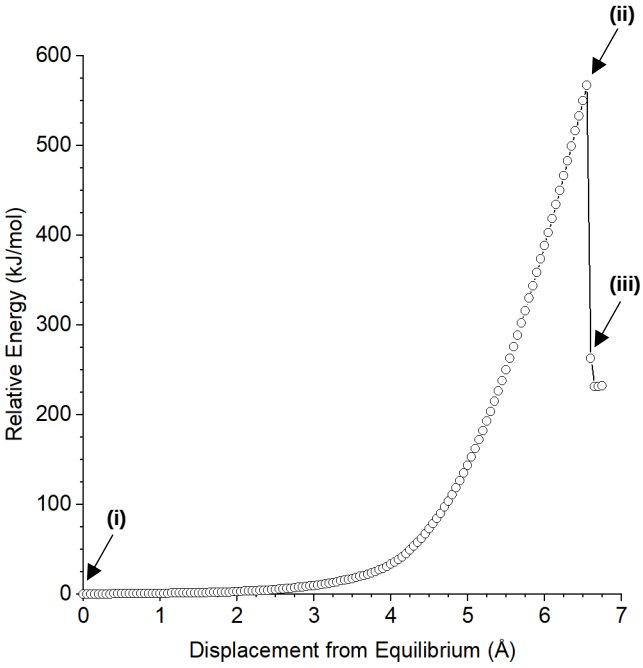

(i) Equilibrium Geometry

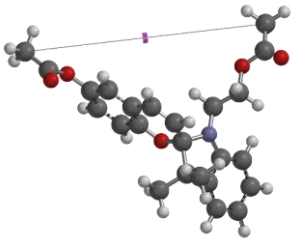

11.638 Å

(ii) Immediately Prior to Bond Cleavage

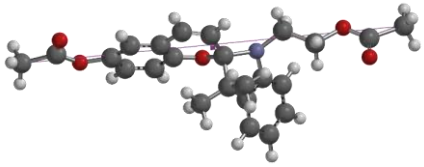

18.188 Å

(iii) Immediately After Bond Cleavage

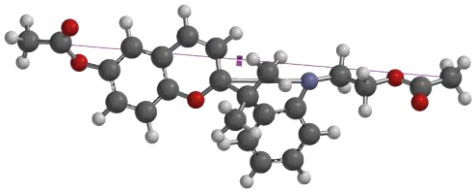

18.238 Å

Summary of CoGEF Results	
F_{max}	5.7 nN
E_{max}	567 kJ/mol
Force-Bond Angle	49°

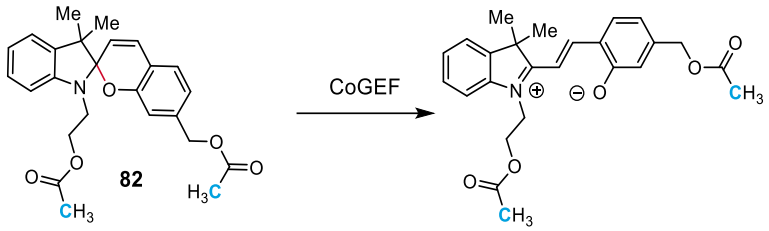

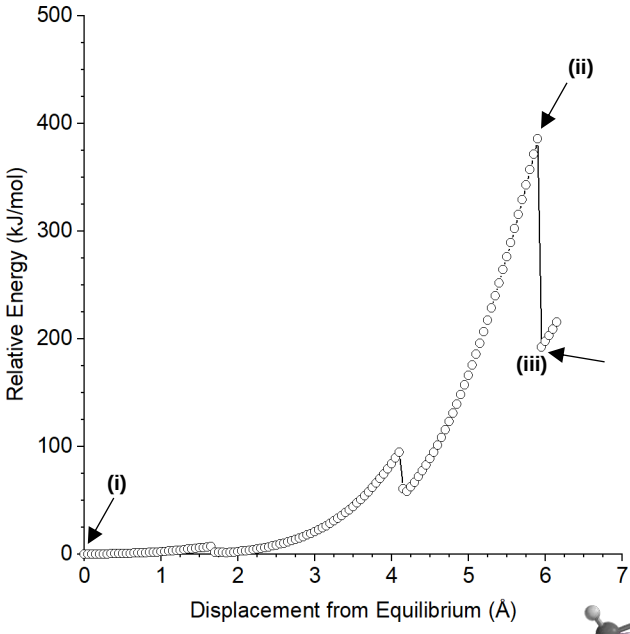

(i) Equilibrium Geometry

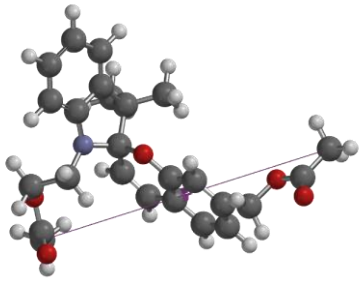

12.787 Å

(ii) Immediately Prior to Bond Cleavage

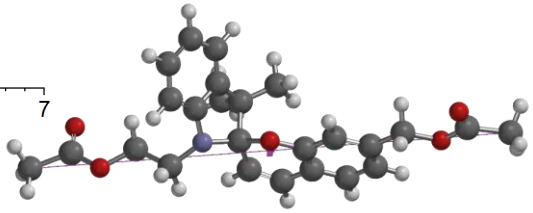

18.687 Å

(iii) Immediately After Bond Cleavage

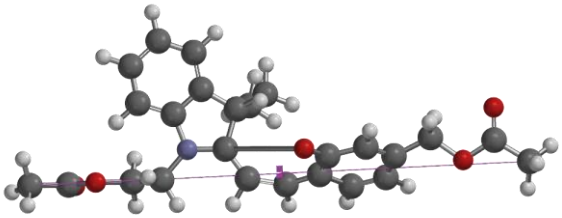

18.737 Å

Summary of CoGEF Results	
F_{max}	4.8 nN
E_{max}	386 kJ/mol
Force-Bond Angle	35°

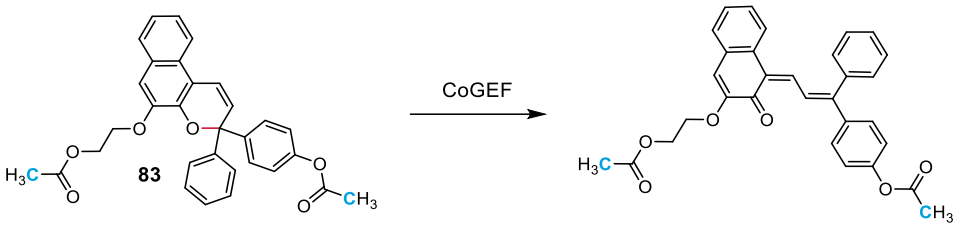

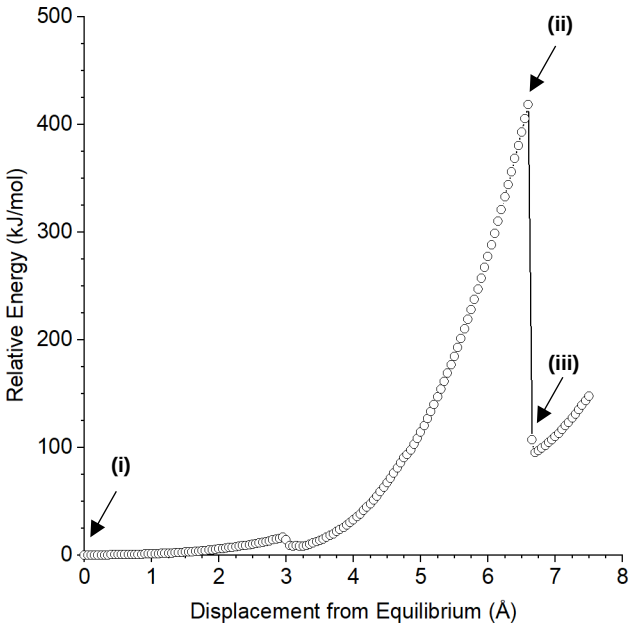

(i) Equilibrium Geometry

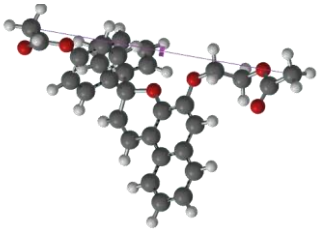

13.325 Å

(ii) Immediately Prior to Bond Cleavage

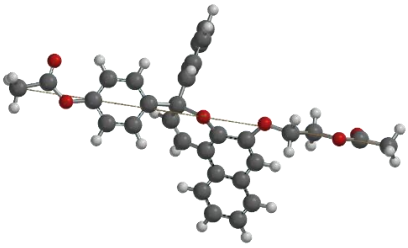

19.925 Å

(iii) Immediately After Bond Cleavage

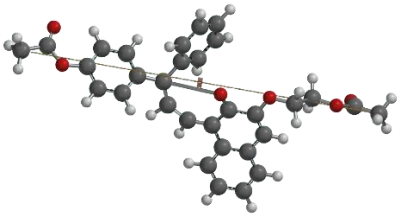

19.975 Å

Summary of CoGEF Results	
F_{max}	4.3 nN
E_{max}	418 kJ/mol
Force-Bond Angle	29°

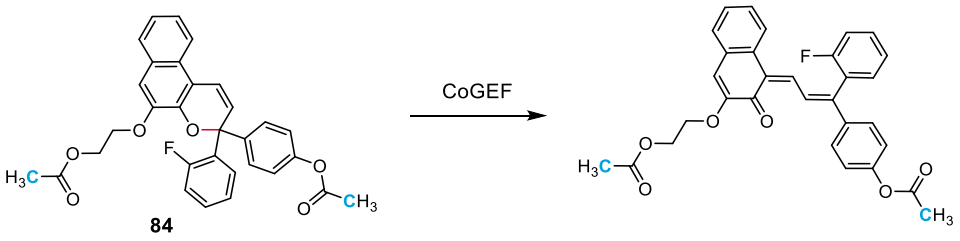

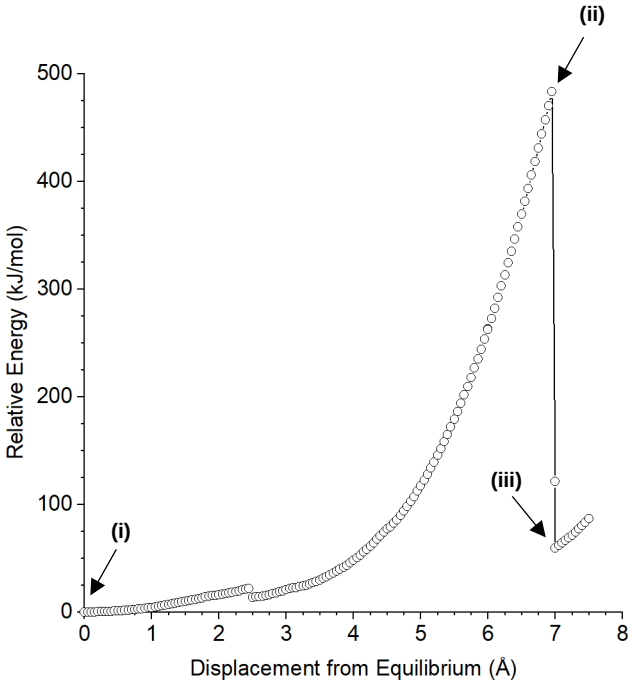

(i) Equilibrium Geometry

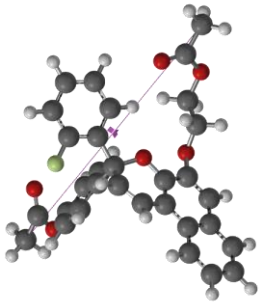

13.160 Å

(ii) Immediately Prior to Bond Cleavage

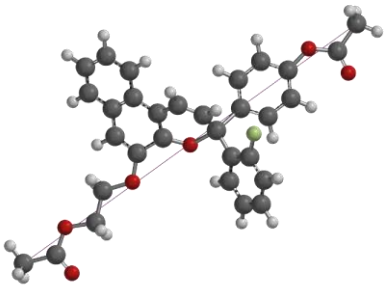

20.110 Å

(iii) Immediately After Bond Cleavage

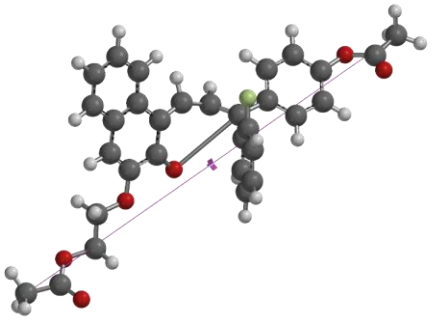

20.160 Å

Summary of CoGEF Results	
F_{max}	4.4 nN
E_{max}	483 kJ/mol
Force-Bond Angle	26°

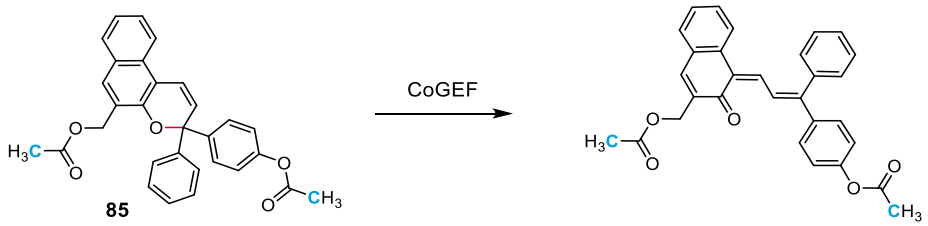

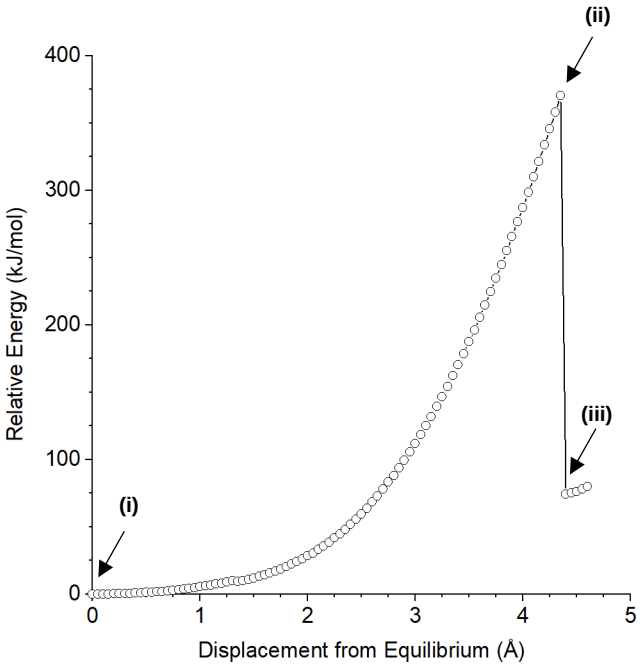

Summary of CoGEF Results	
F_{max}	4.1 nN
E_{max}	370 kJ/mol
Force-Bond Angle	29°

(i) Equilibrium Geometry

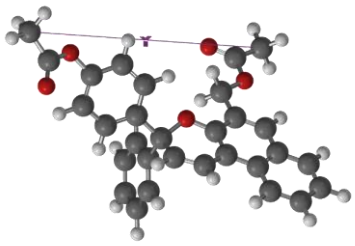

13.153 Å

(ii) Immediately Prior to Bond Cleavage

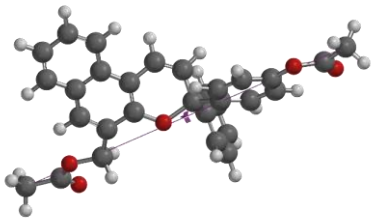

17.503 Å

(iii) Immediately After Bond Cleavage

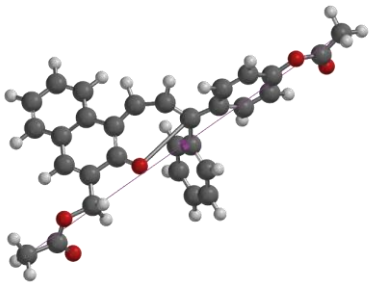

17.553 Å

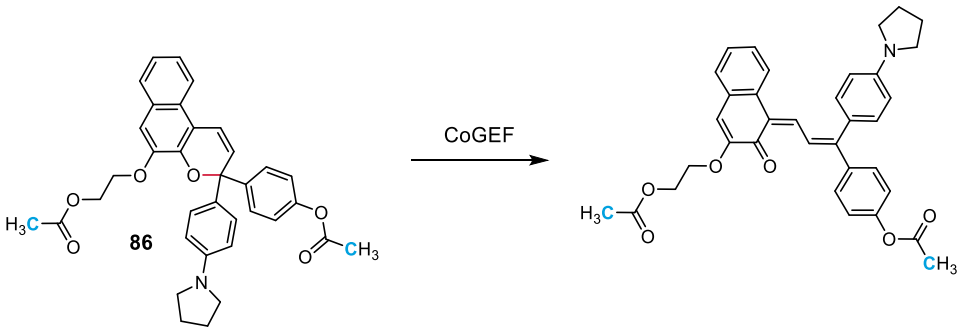

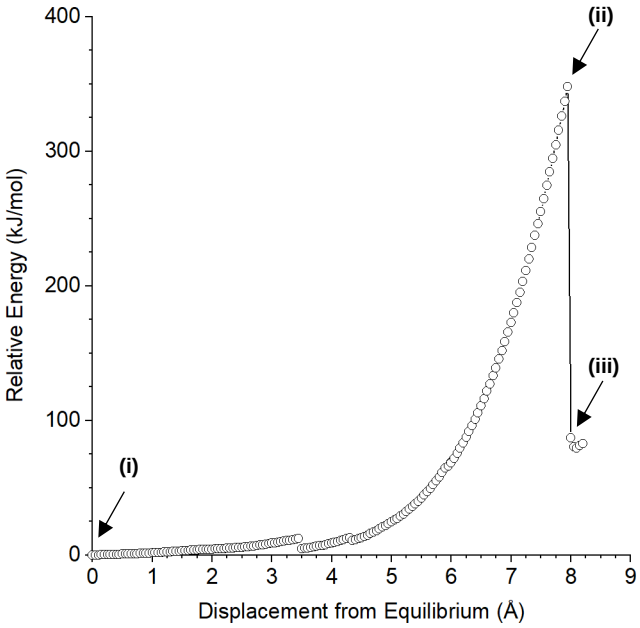

Summary of CoGEF Results	
F_{max}	3.7 nN
E_{max}	348 kJ/mol
Force-Bond Angle	30°

(i) Equilibrium Geometry

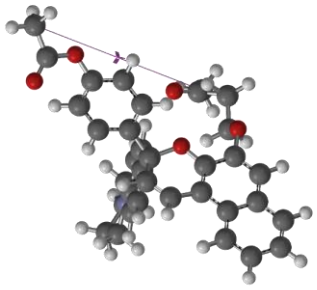

11.651 Å

(ii) Immediately Prior to Bond Cleavage

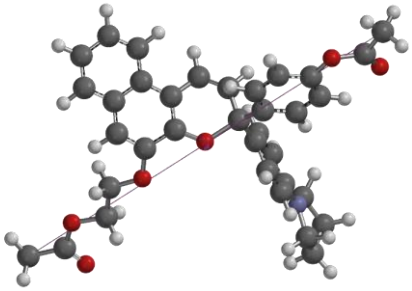

19.601 Å

(iii) Immediately After Bond Cleavage

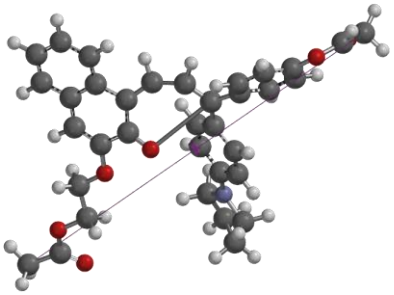

19.651 Å

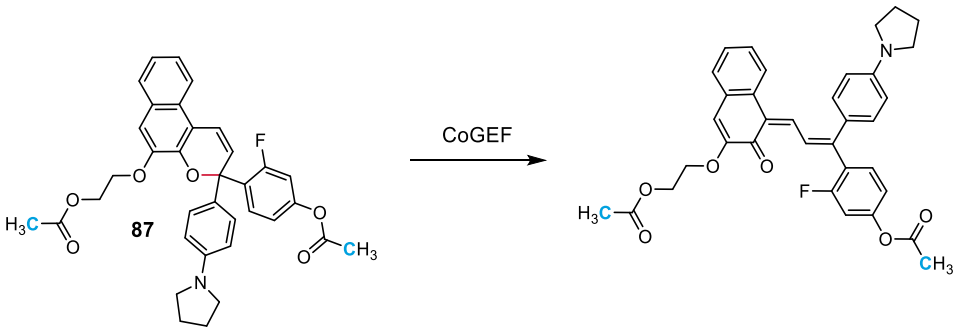

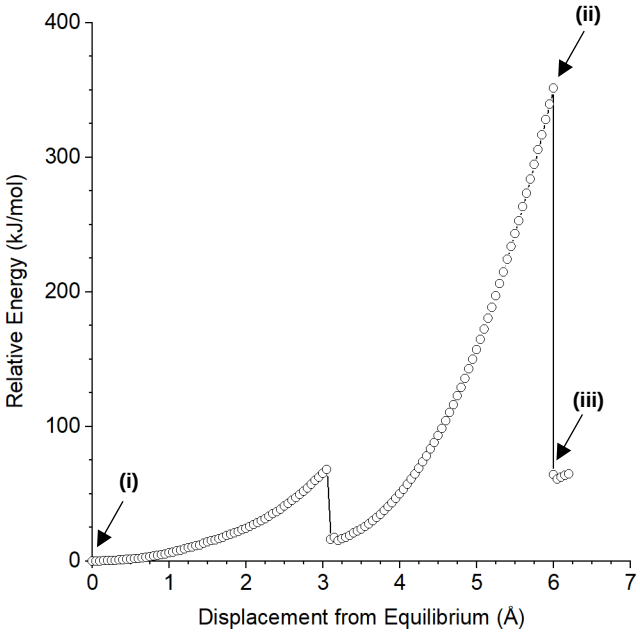

Summary of CoGEF Results	
F_{max}	3.7 nN
E_{max}	334 kJ/mol
Force-Bond Angle	33°

(i) Equilibrium Geometry

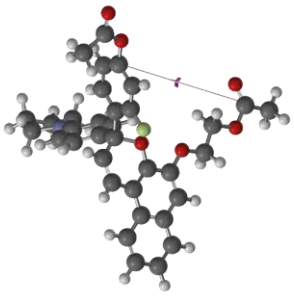

11.190 Å

(ii) Immediately Prior to Bond Cleavage

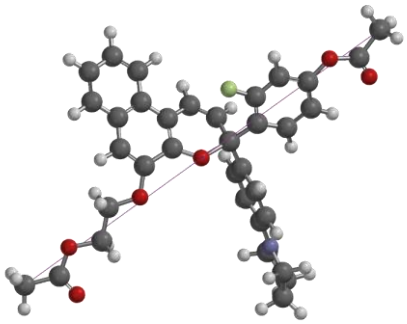

19.590 Å

(iii) Immediately After Bond Cleavage

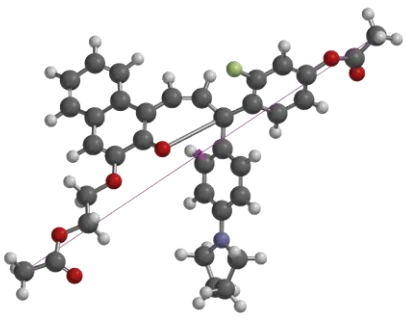

19.640 Å

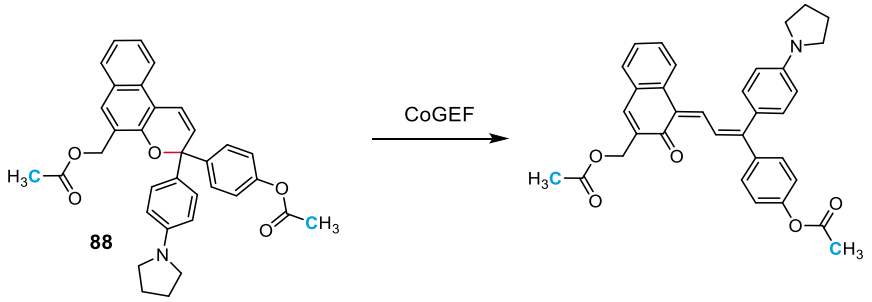

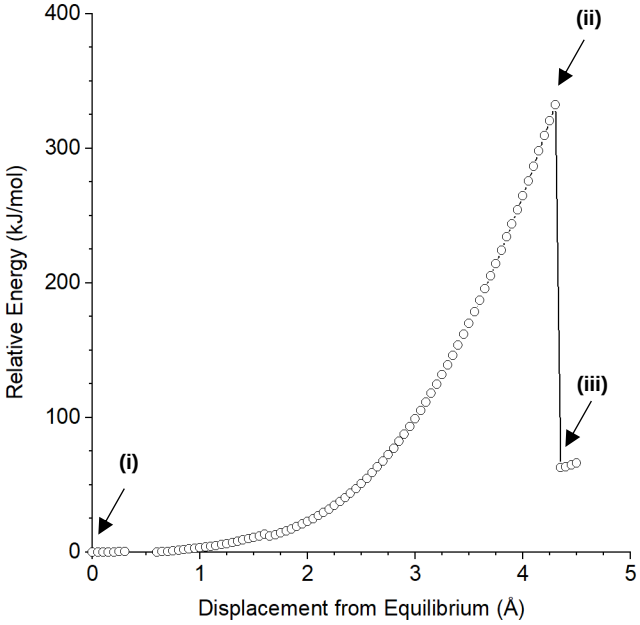

Summary of CoGEF Results	
F_{max}	3.9 nN
E_{max}	332 kJ/mol
Force-Bond Angle	30°

(i) Equilibrium Geometry

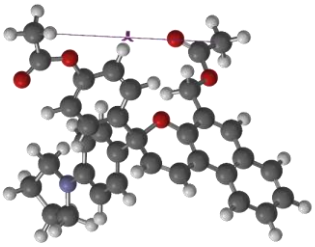

13.054 Å

(ii) Immediately Prior to Bond Cleavage

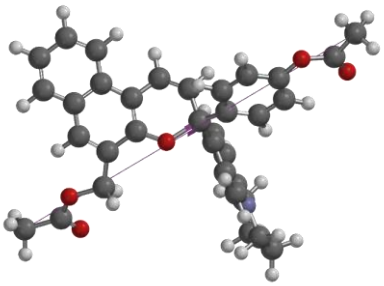

17.354 Å

(iii) Immediately After Bond Cleavage

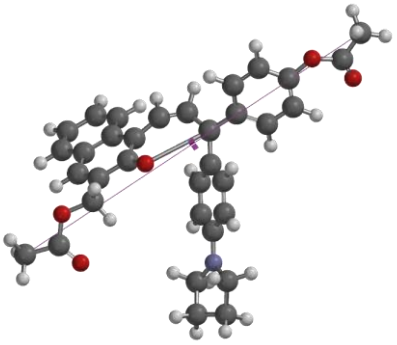

17.404 Å

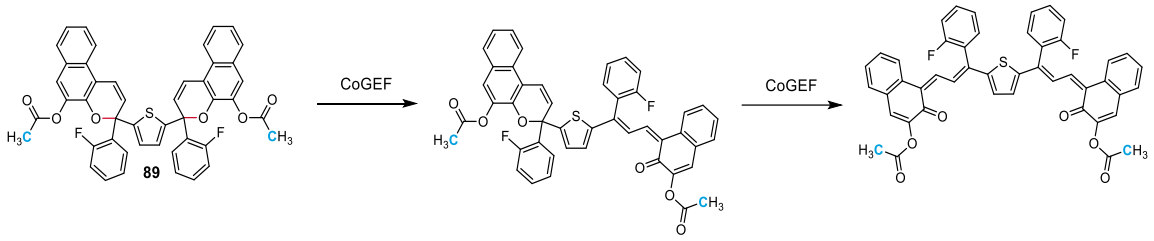

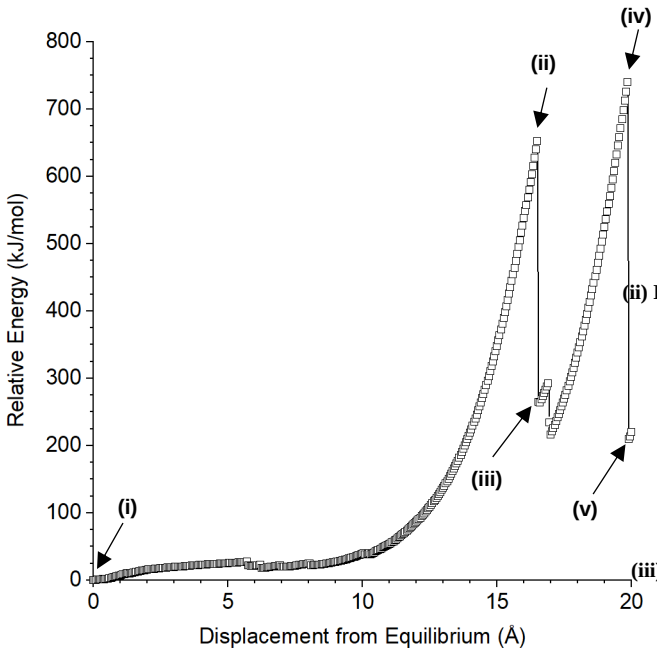

(i) Equilibrium Geometry

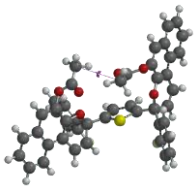

4.159 Å

(ii) Immediately Prior to First Bond Cleavage

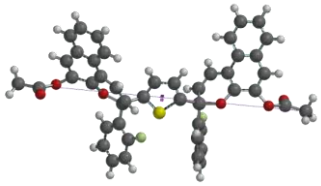

20.659 Å

(iii) Immediately After Bond First Cleavage

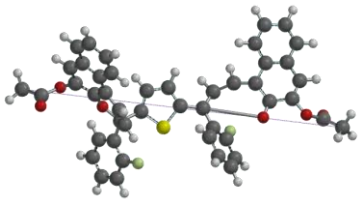

20.709 Å

(iv) Immediately Prior to Second Bond Cleavage

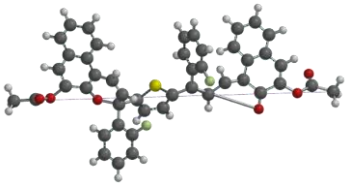

24.009 Å

(v) Immediately After Bond Second Cleavage

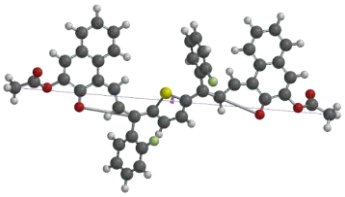

24.059 Å

Summary of CoGEF Results (S,S)	
F_{max}	4.1 nN (first) 4.6 nN (second)
E_{max}	652 kJ/mol (first) 740 kJ/mol (second)
Force-Bond Angle	25° (first), 27° (second)

The results presented here correspond to the (S,S)-isomer of compound **82**. The CoGEF results for the (R,S)-isomer are similar:

Summary of CoGEF Results (R,S)	
F_{max}	4.1 nN (first) 4.5 nN (second)
E_{max}	644 kJ/mol (first) 727 kJ/mol (second)
Force-Bond Angle	24° (first), 26° (second)

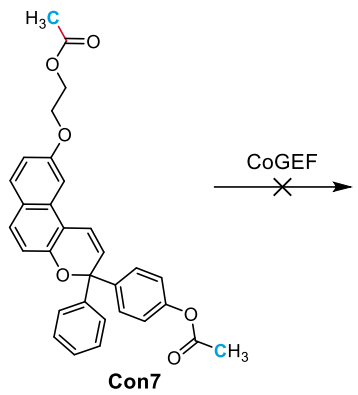

Con7

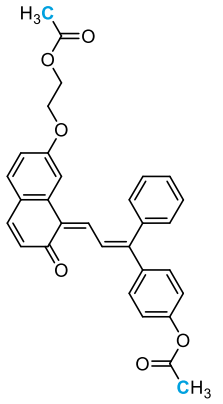

(i) Equilibrium Geometry

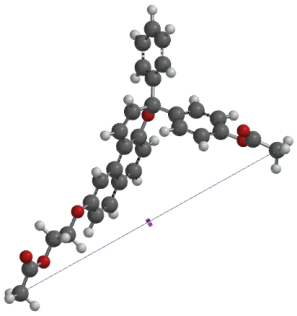

16.735 Å

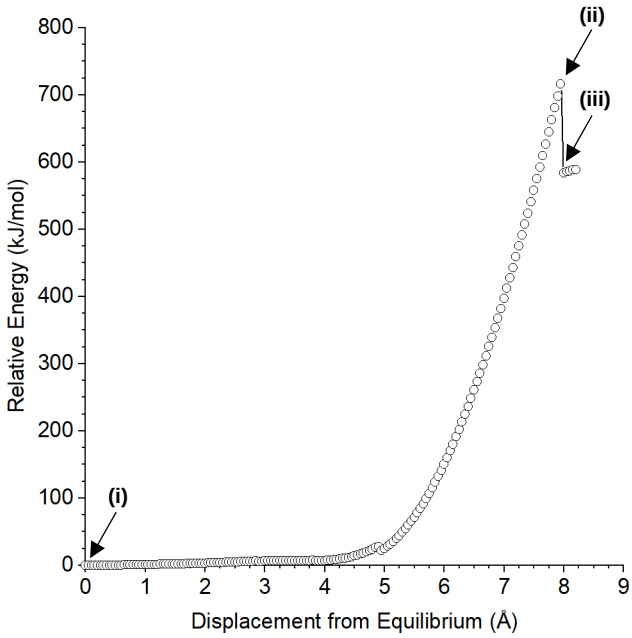

(ii) Immediately Prior to Bond Cleavage

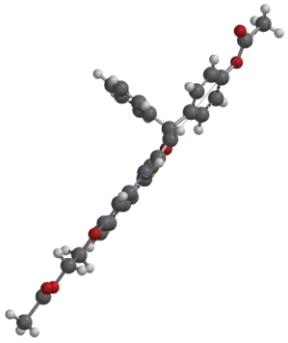

24.685 Å

(iii) Immediately After Bond Cleavage

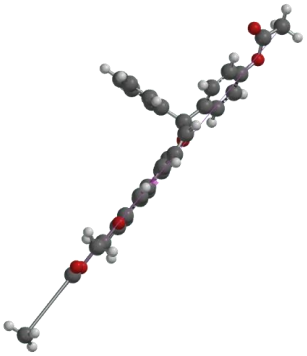

24.735 Å

Summary of CoGEF Results	
F_{max}	6.0 nN
E_{max}	716 kJ/mol
Force-Bond Angle	63°

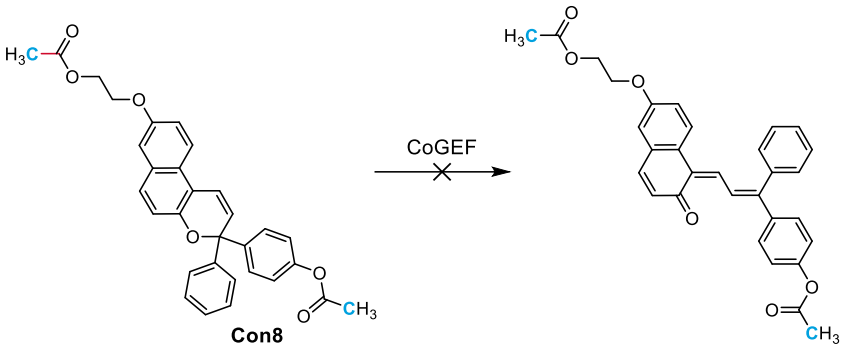

(i) Equilibrium Geometry

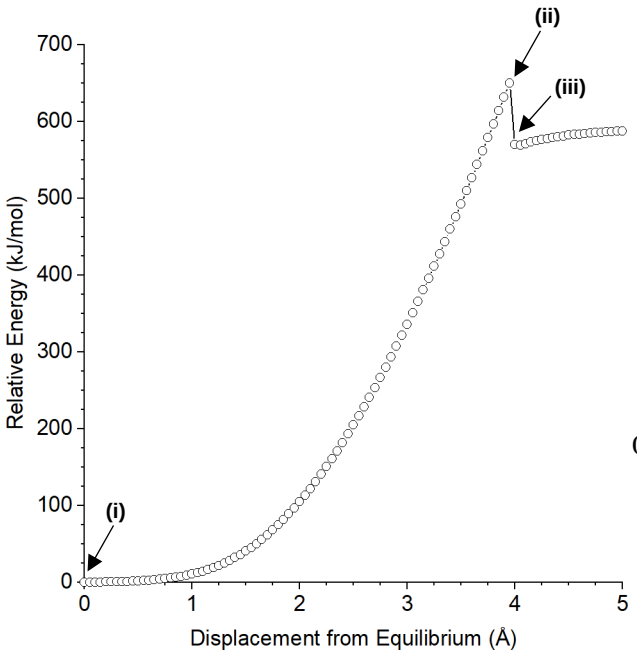

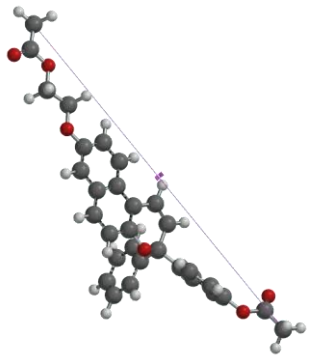

21.141 Å

(ii) Immediately Prior to Bond Cleavage

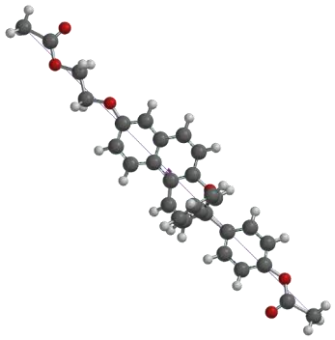

25.091 Å

(iii) Immediately After Bond Cleavage

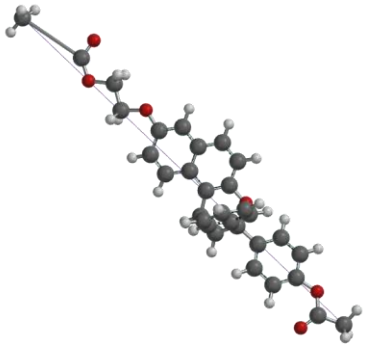

25.141 Å

Summary of CoGEF Results	
F_{max}	6.0 nN
E_{max}	650 kJ/mol
Force-Bond Angle	56°

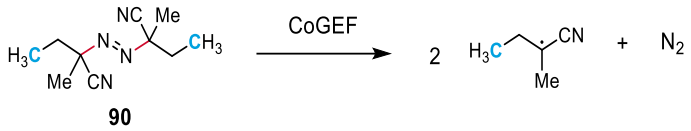

90

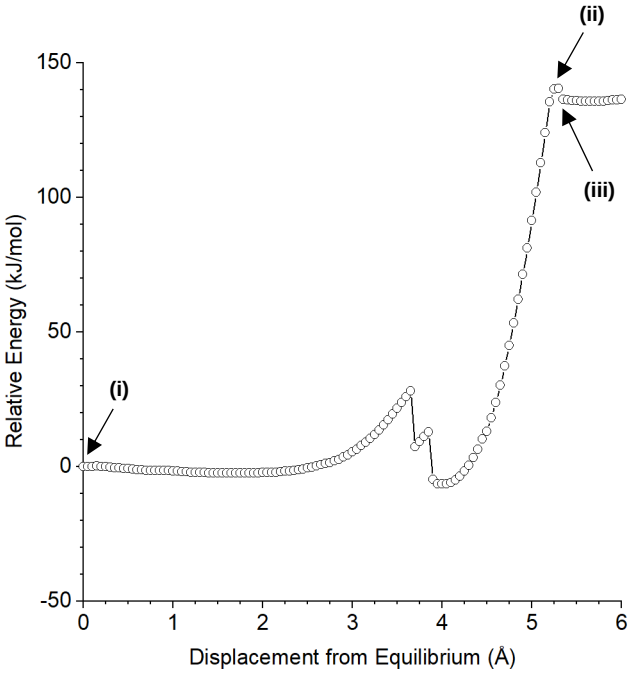

(i) Equilibrium Geometry

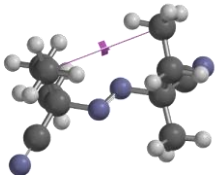

4.452 Å

(ii) Immediately Prior to Bond Cleavage

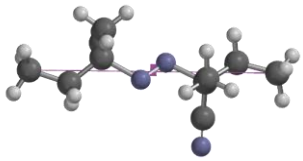

9.652 Å

(iii) Immediately After Bond Cleavage

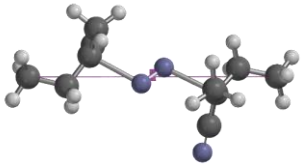

9.702 Å

Summary of CoGEF Results	
F_{max}	3.7 nN
E_{max}	140 kJ/mol
Force-Bond Angle	29°

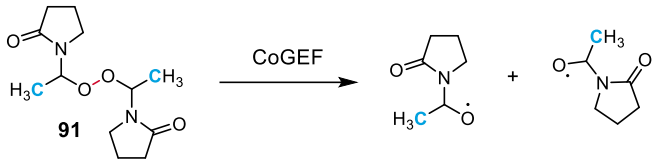

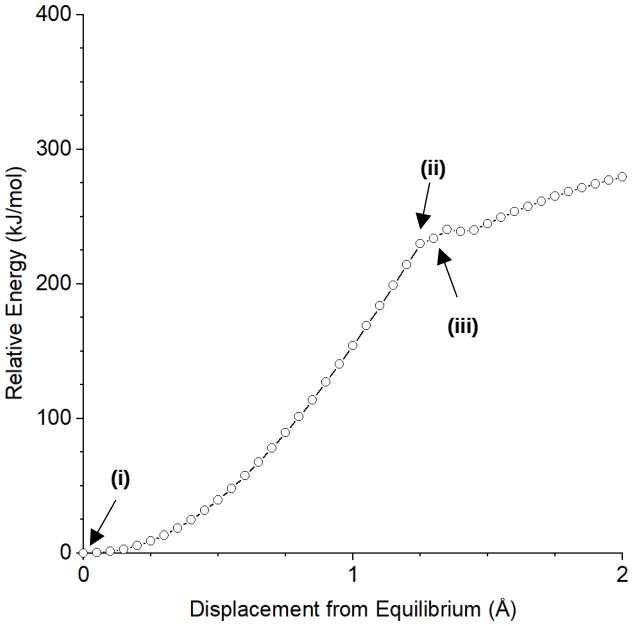

Summary of CoGEF Results	
F_{max}	5.2 nN
E_{max}	230 kJ/mol
Force-Bond Angle	28°

(i) Equilibrium Geometry

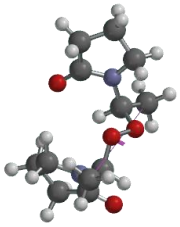

5.818 Å

(ii) Immediately Prior to Bond Cleavage

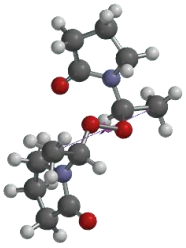

7.068 Å

(iii) Immediately After Bond Cleavage

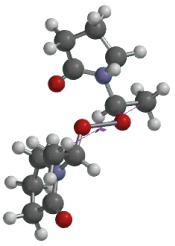

7.118 Å

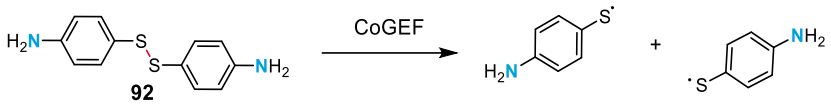

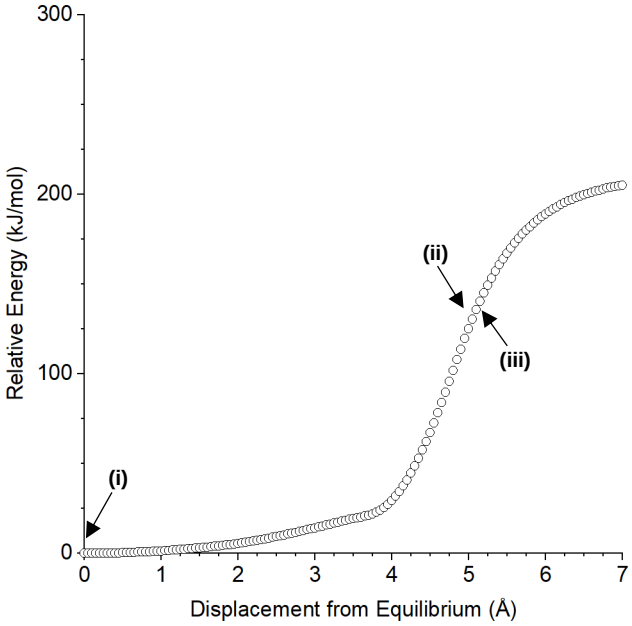

(i) Equilibrium Geometry

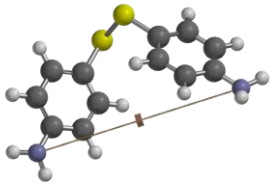

9.023 Å

(ii) Immediately Prior to Bond Cleavage

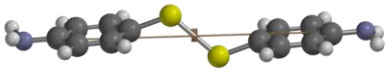

13.923 Å

(iii) Immediately After Bond Cleavage

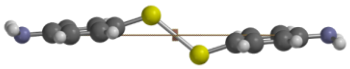

13.973 Å

Summary of CoGEF Results	
F_{max}	2.0 nN
E_{max}	114 kJ/mol
Force-Bond Angle	45°

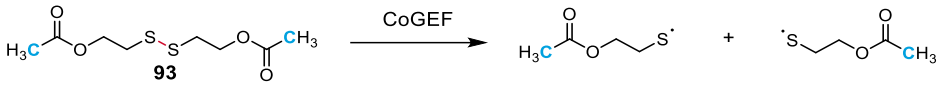

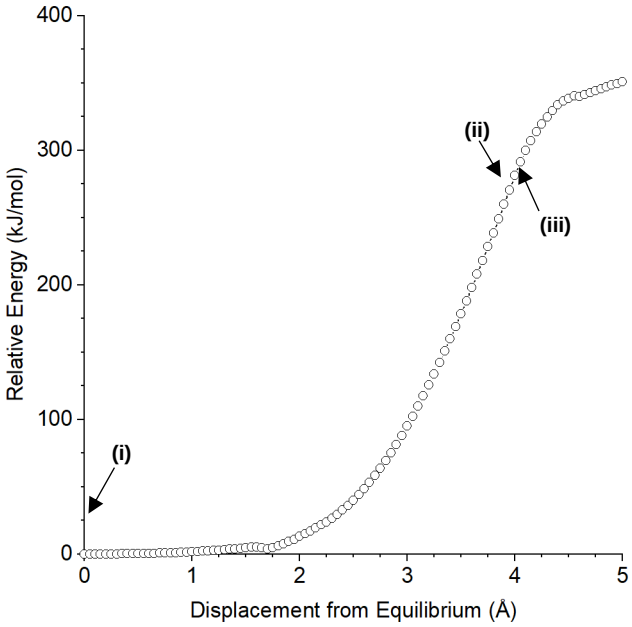

(i) Equilibrium Geometry

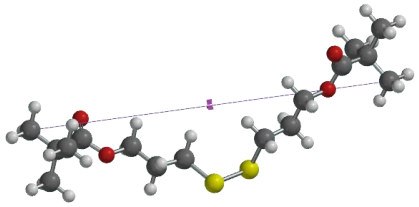

11.920 Å

(ii) Immediately Prior to Bond Cleavage

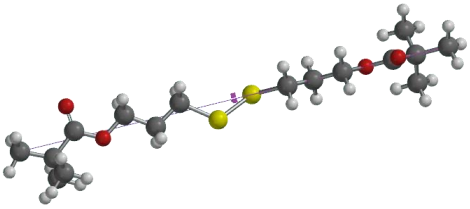

15.920 Å

(iii) Immediately After Bond Cleavage

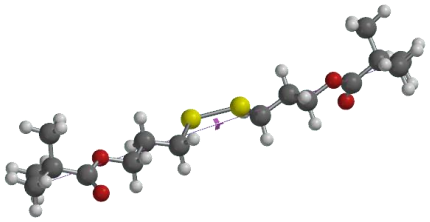

15.970 Å

Summary of CoGEF Results	
F_{max}	3.6 nN
E_{max}	271 kJ/mol
Force-Bond Angle	29°

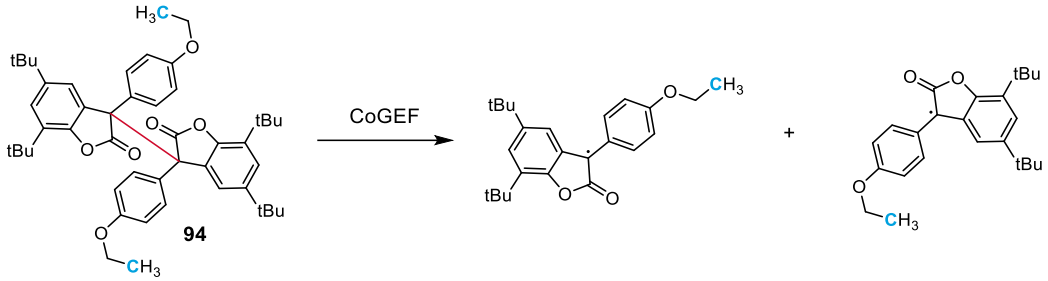

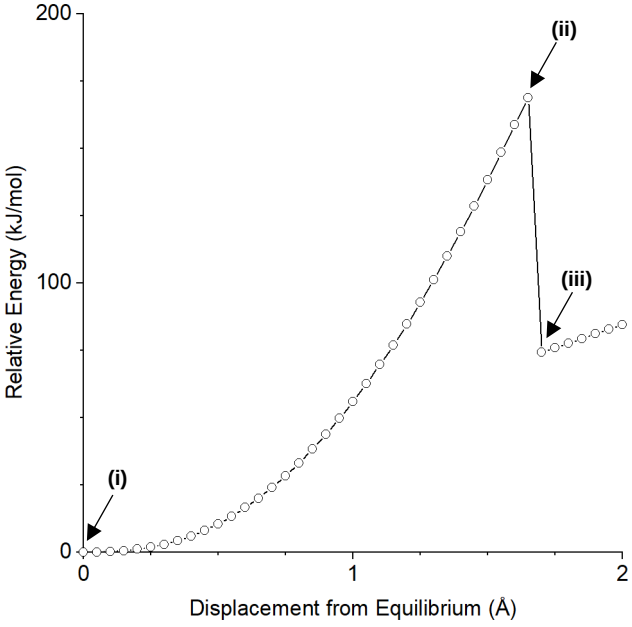

Summary of CoGEF Results	
F_{max}	3.5 nN
E_{max}	169 kJ/mol
Force-Bond Angle	44°

(i) Equilibrium Geometry

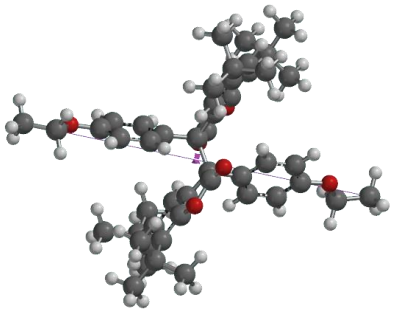

16.559 Å

(ii) Immediately Prior to Bond Cleavage

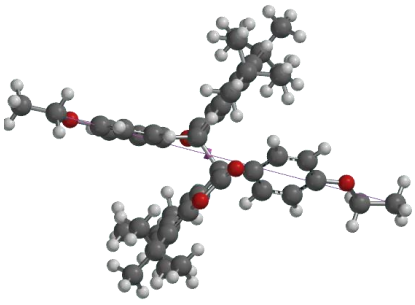

18.209 Å

(iii) Immediately After Bond Cleavage

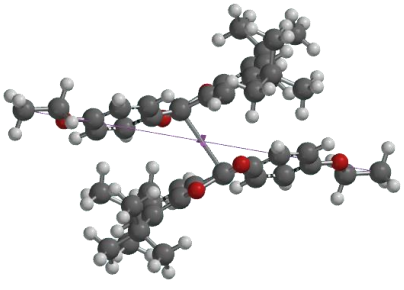

18.259 Å

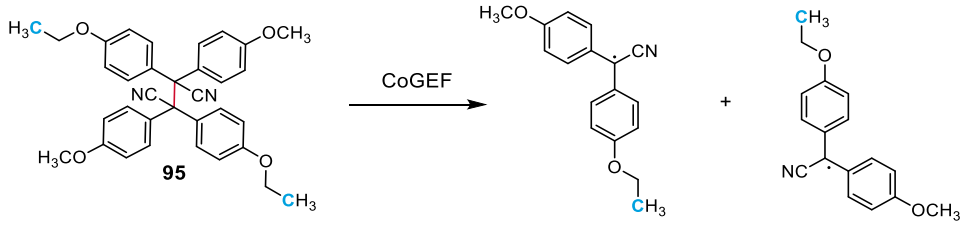

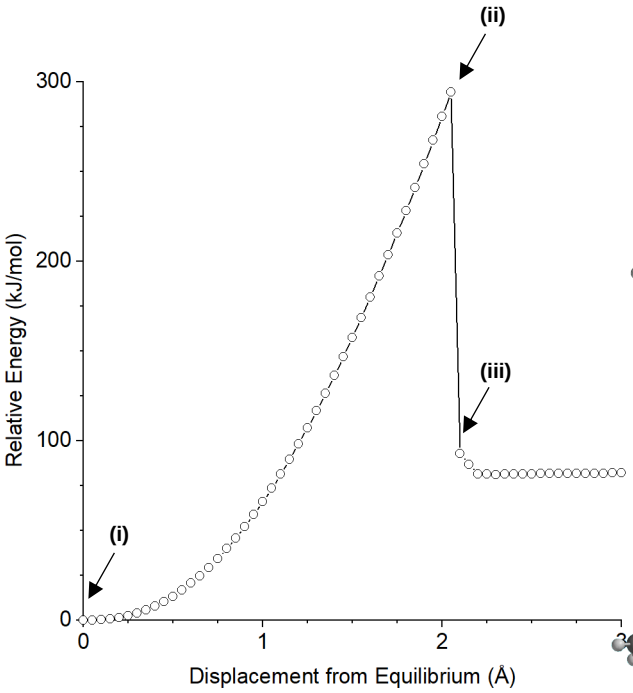

(i) Equilibrium Geometry

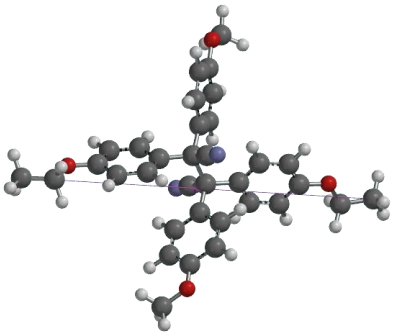

16.700 Å

(ii) Immediately Prior to Bond Cleavage

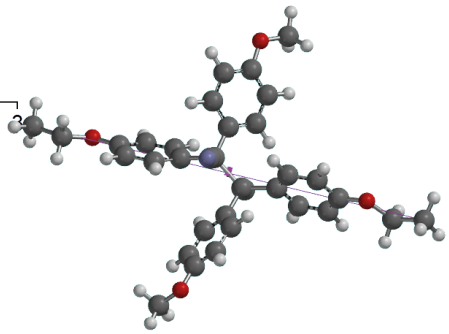

18.750 Å

(iii) Immediately After Bond Cleavage

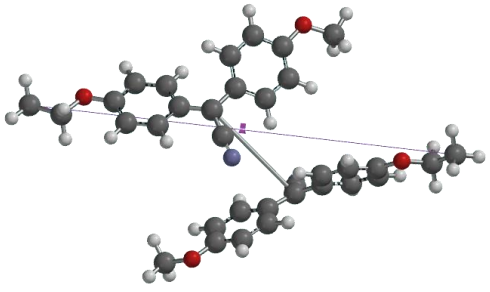

18.800Å

Summary of CoGEF Results	
F_{max}	4.5 nN
E_{max}	294 kJ/mol
Force-Bond Angle	41°

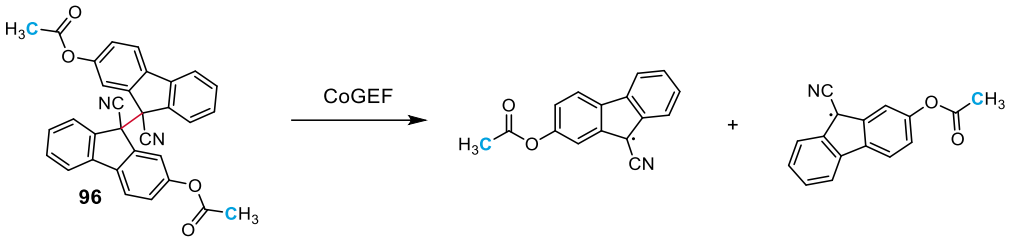

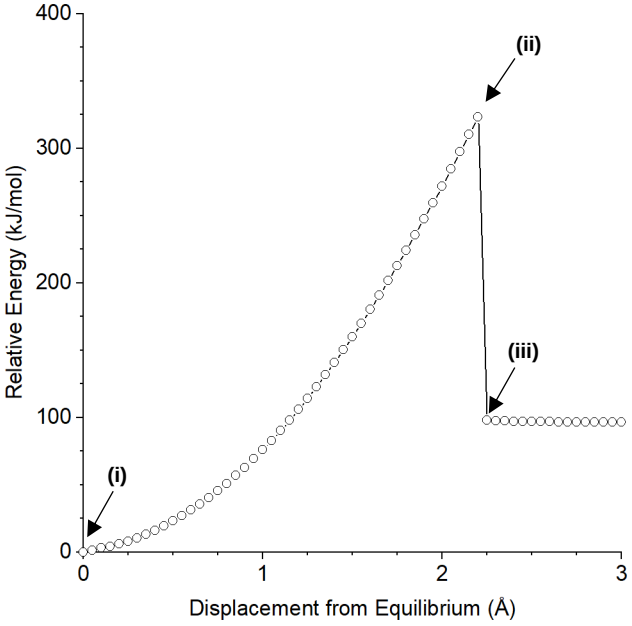

(i) Equilibrium Geometry

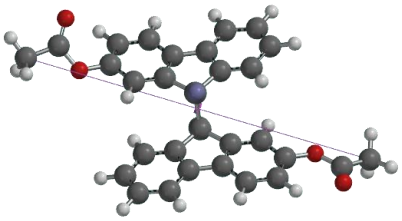

15.307 Å

(ii) Immediately Prior to Bond Cleavage

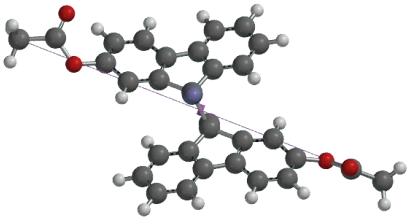

17.507 Å

(iii) Immediately After Bond Cleavage

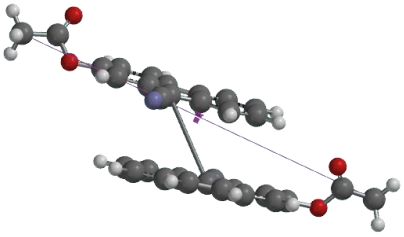

17.557 Å

Summary of CoGEF Results	
F_{max}	4.3 nN
E_{max}	326 kJ/mol
Force-Bond Angle	46°

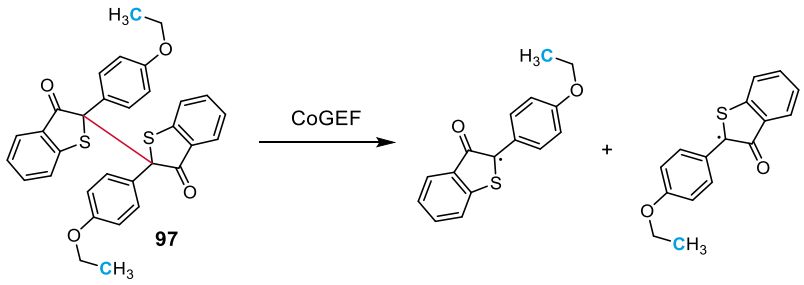

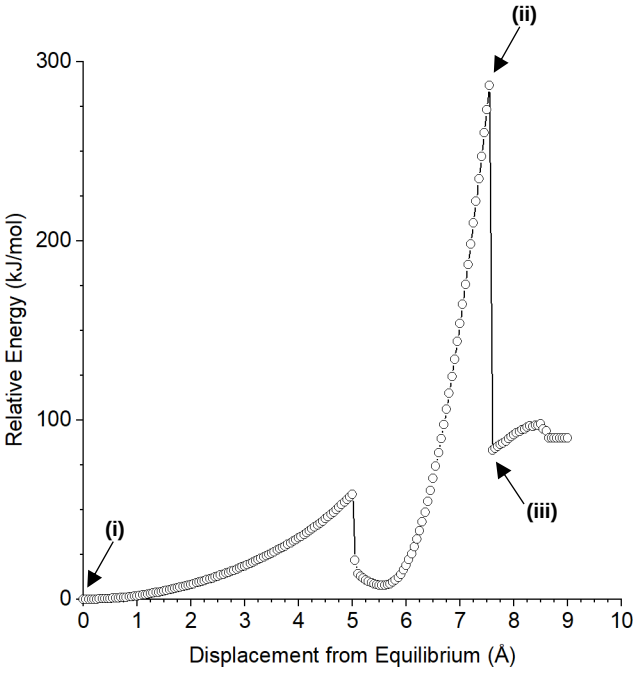

(i) Equilibrium Geometry

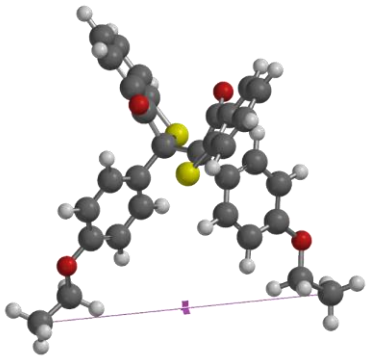

11.109 Å

(ii) Immediately Prior to Bond Cleavage

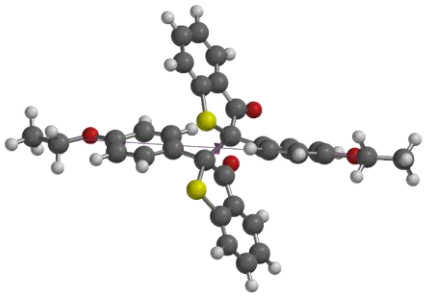

18.659 Å

(iii) Immediately After Bond Cleavage

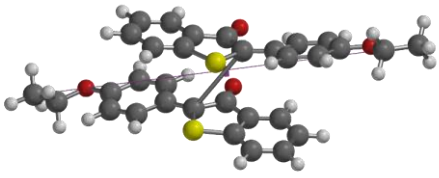

18.709 Å

Summary of CoGEF Results	
F_{max}	4.4 nN
E_{max}	287 kJ/mol
Force-Bond Angle	41°

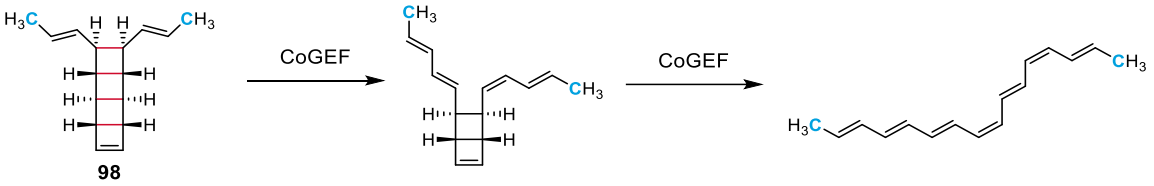

(i) Equilibrium Geometry

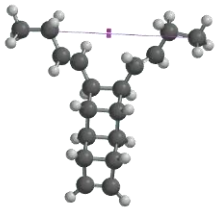

6.269 Å

(ii) Immediately Prior to First Bond Cleavage

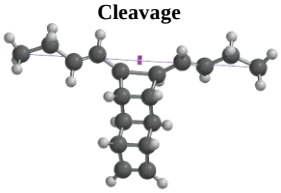

10.019 Å

(iii) Immediately After First Bond Cleavage

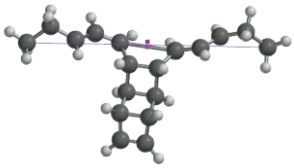

10.069 Å

(iv) Immediately Prior to Second Bond Cleavage

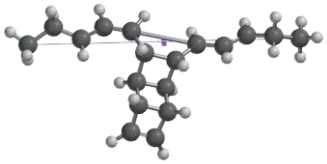

10.169 Å

(v) Immediately After Second Bond Cleavage

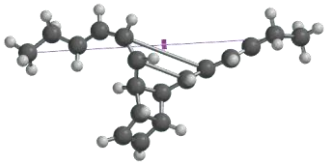

10.219 Å

(vi) Immediately Prior to Third Bond Cleavage

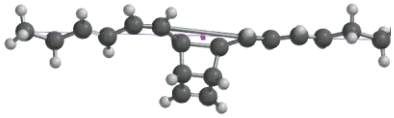

15.219 Å

(vii) Immediately After Third Bond Cleavage

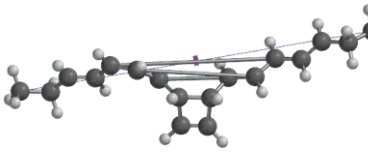

15.269 Å

(viii) Immediately After Fourth Bond Cleavage

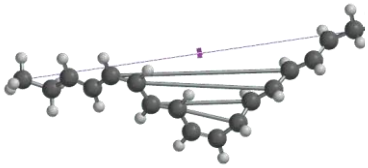

15.319 Å

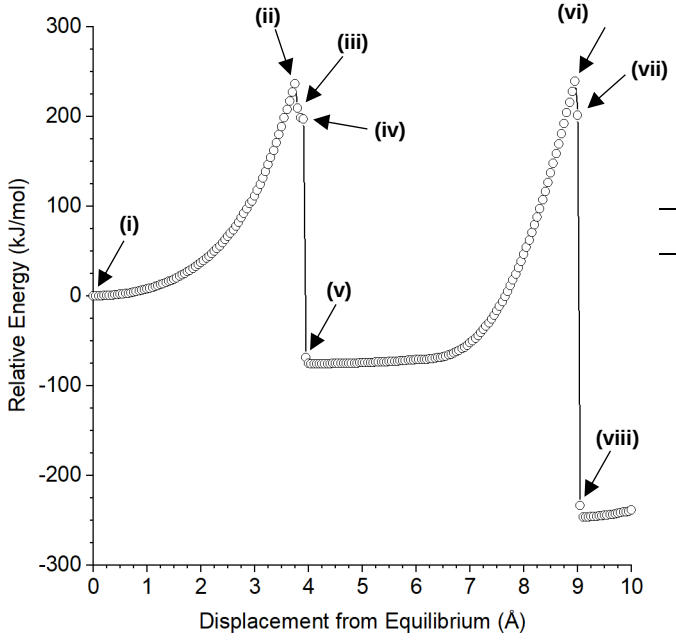

Summary of CoGEF Results	
F_{max}	3.2 nN (first) 3.9 nN (second)
E_{max}	236 kJ/mol (first) 239 kJ/mol (second)
Force-Bond Angle	0.1° (first), 4.4° (second)

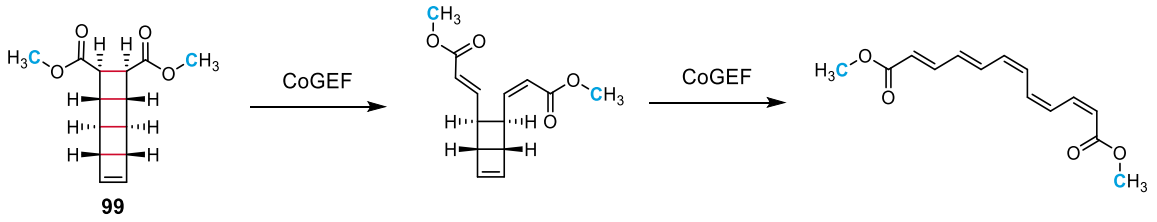

99

(i) Equilibrium Geometry

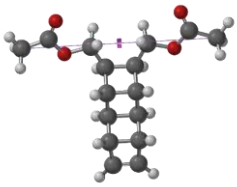

10.304 Å

(ii) Immediately Prior to First Bond Cleavage

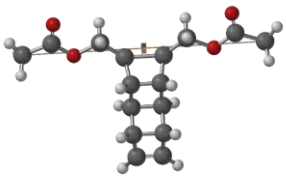

12.554 Å

(iii) Immediately After First Bond Cleavage

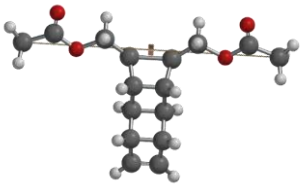

12.604 Å

(iv) Immediately Prior to Second Bond Cleavage

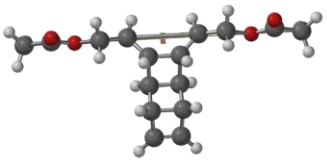

13.754 Å

(v) Immediately After Second Bond Cleavage

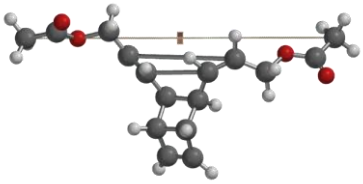

13.804 Å

(vi) Immediately Prior to Third Bond Cleavage

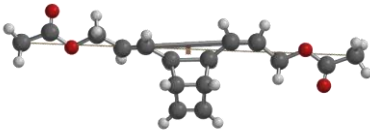

17.554 Å

(vii) Immediately After Third Bond Cleavage

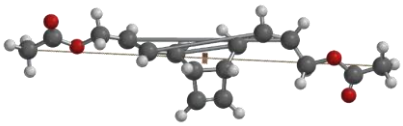

17.604 Å

(viii) Immediately After Fourth Bond Cleavage

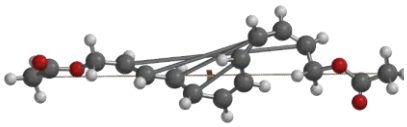

17.654 Å

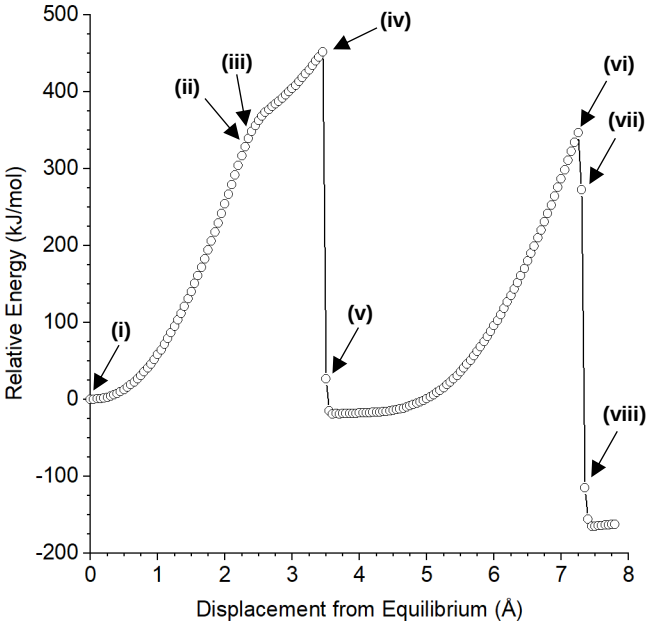

Summary of CoGEF Results	
F_{max}	4.2 nN 4.0 nN
E_{max}	451 kJ/mol 346 kJ/mol
Force-Bond Angle	0.2° (first) 3.4° (second)

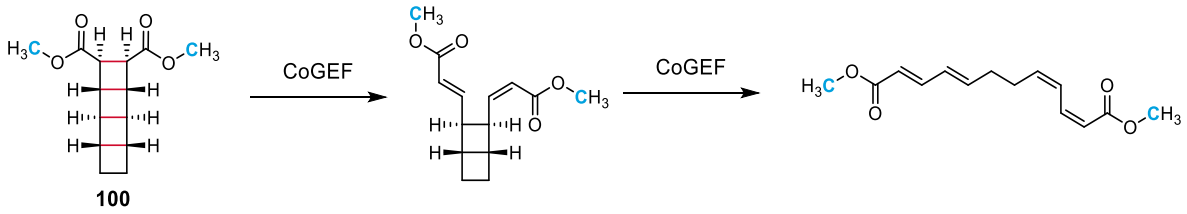

100

(i) Equilibrium Geometry

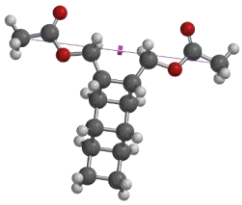

10.308 Å

(ii) Immediately Prior to First Bond Cleavage

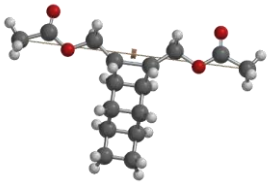

12.458 Å

(iii) Immediately After First Bond Cleavage

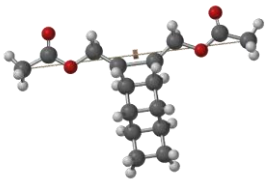

12.508 Å

(iv) Immediately Prior to Second Bond Cleavage

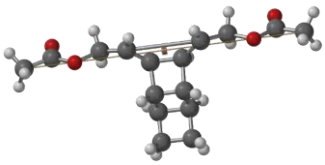

14.208 Å

(v) Immediately After Second Bond Cleavage

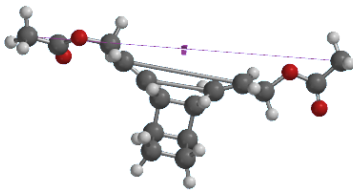

14.258 Å

(vi) Immediately Prior to Third Bond Cleavage

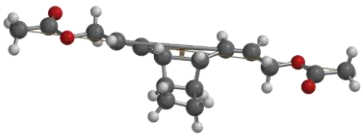

17.508 Å

(vii) Immediately After Third Bond Cleavage

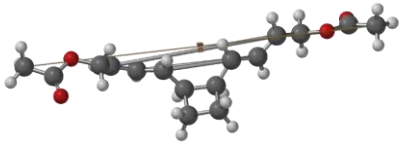

17.558 Å

(viii) Immediately After Fourth Bond Cleavage

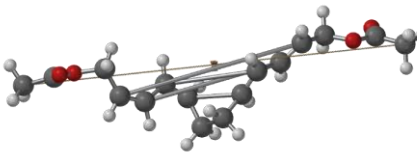

17.708 Å

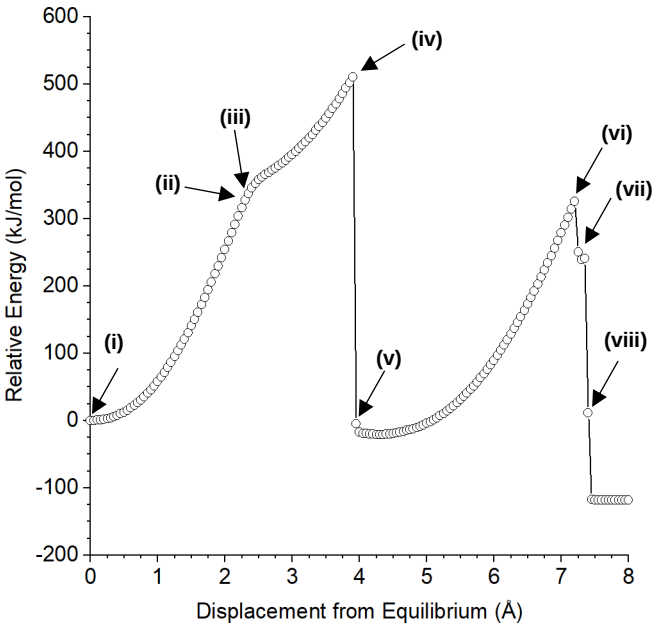

Summary of CoGEF Results	
F_{max}	4.2 nN (first) 3.9 nN (second)
E_{max}	511 kJ/mol (first) 326 kJ/mol (second)
Force-Bond Angle	0.5° (first) 4.0° (second)

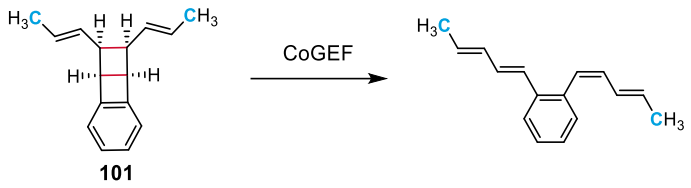

101

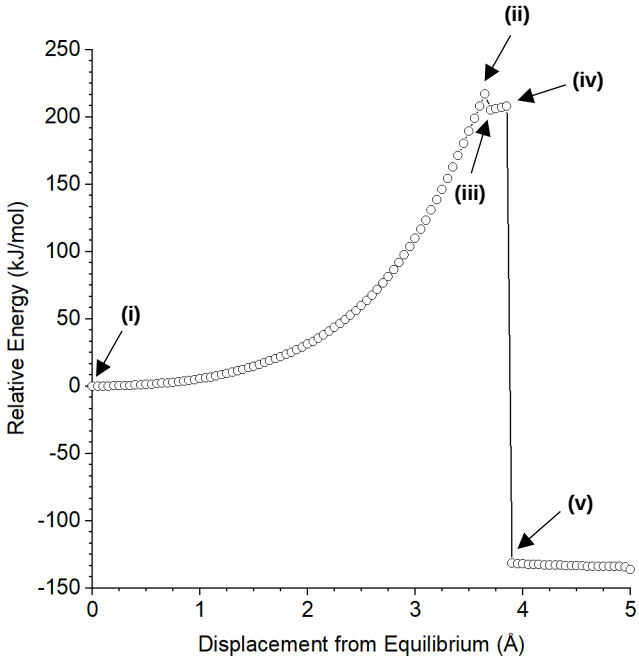

Summary of CoGEF Results	
F_{max}	3.1 nN
E_{max}	207 kJ/mol
Force-Bond Angle	0.1°

(i) Equilibrium Geometry

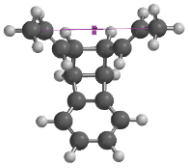

6.368 Å

) Immediately Prior to First Bond Cleavage

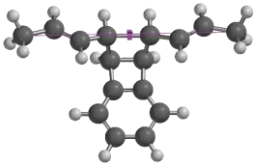

10.018 Å

ii) Immediately After First Bond Cleavage

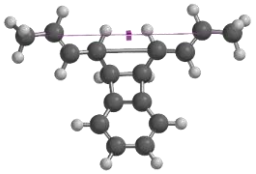

10.068 Å

(iv) Immediately Prior to Second Bond Cleavage

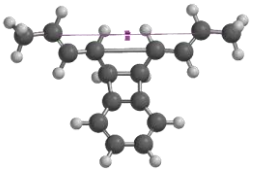

10.218 Å

(v) Immediately After Second Bond Cleavage

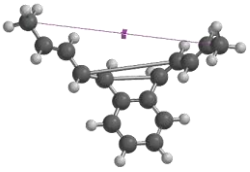

10.268 Å

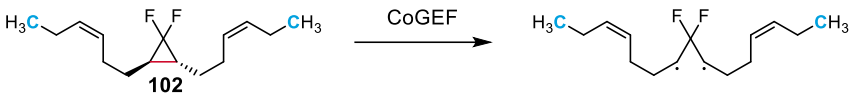

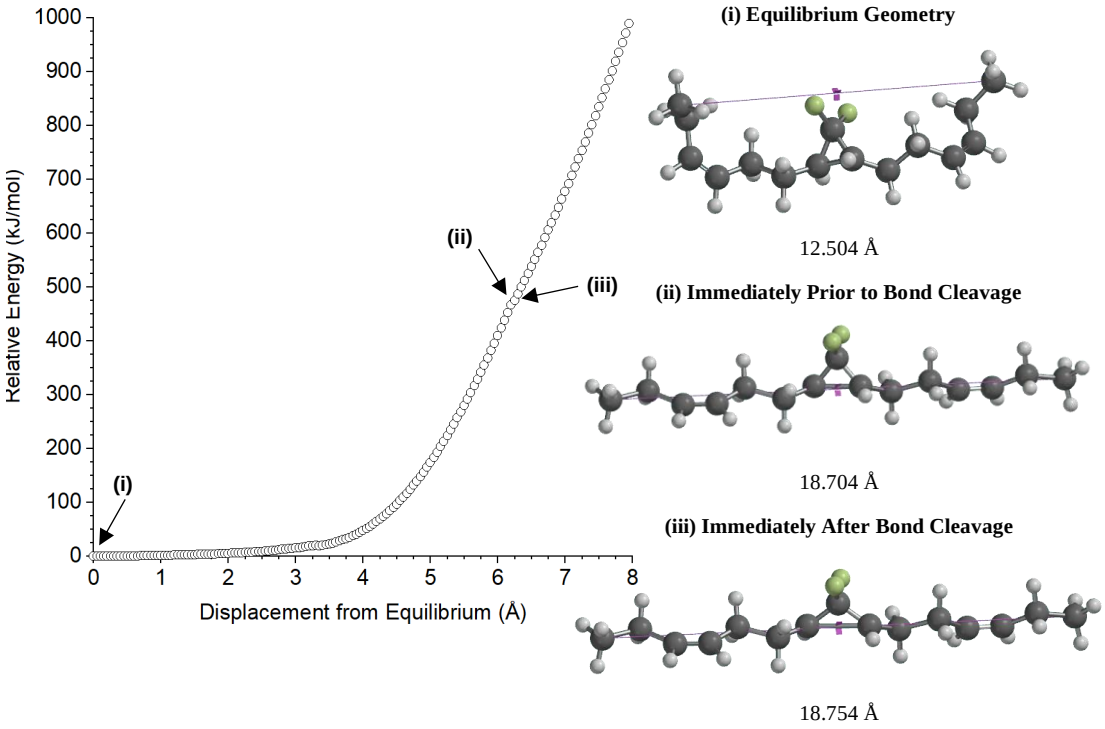

Summary of CoGEF Results	
F_{max}	4.8 nN
E_{max}	466 kJ/mol
Force-Bond Angle	21°

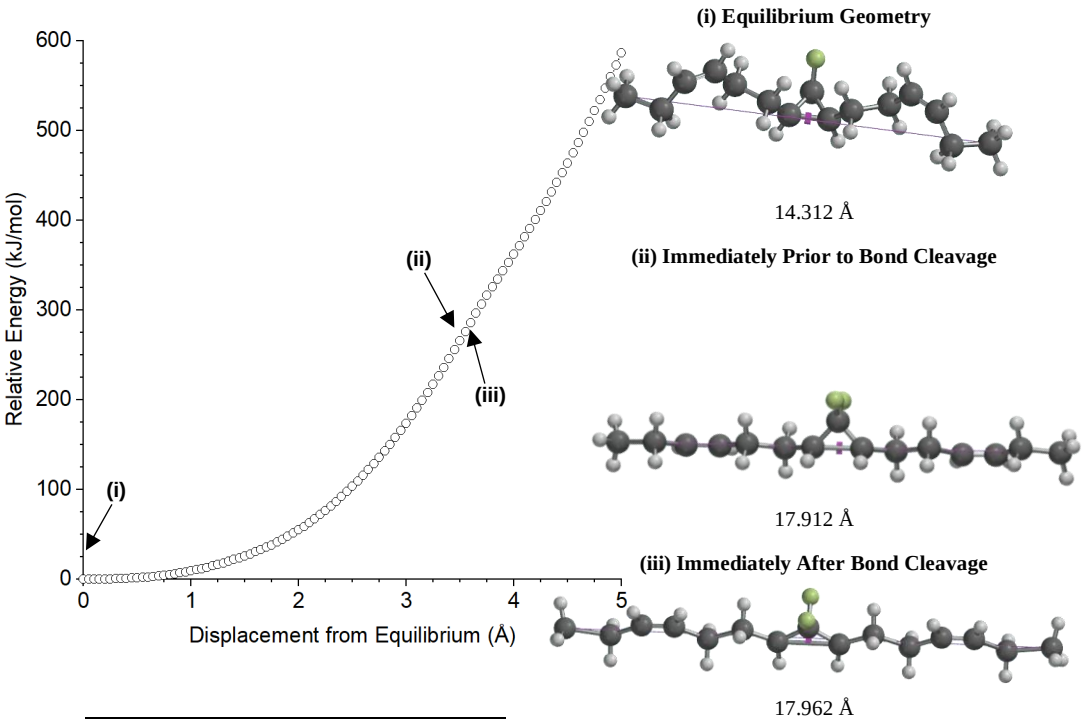

Summary of CoGEF Results	
F_{max}	3.4 nN
E_{max}	292 kJ/mol
Force-Bond Angle	0.0°

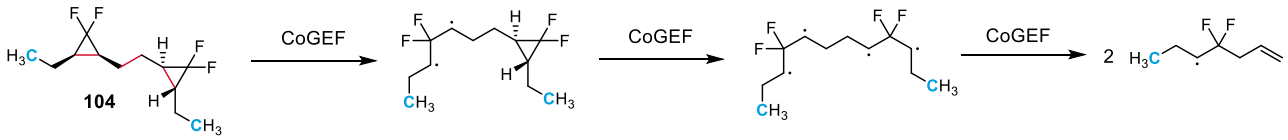

(i) Equilibrium Geometry

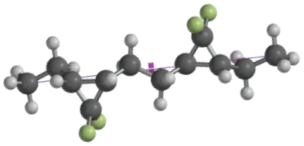

10.904 Å

(ii) Immediately Prior to First Bond Cleavage

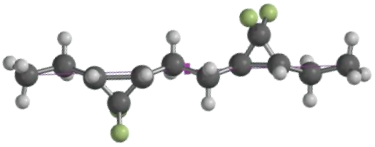

13.104 Å

(iii) Immediately After First Bond Cleavage

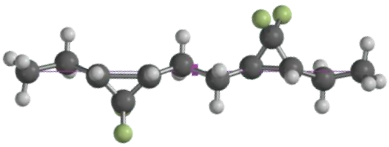

13.154 Å

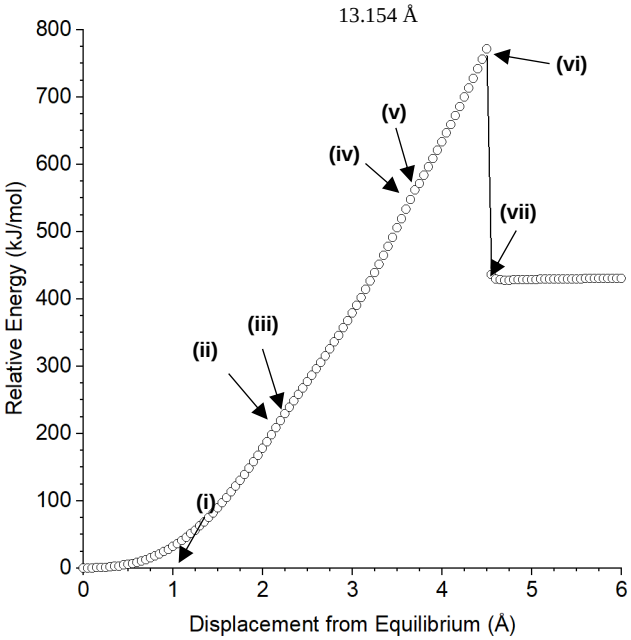

(iv) Immediately Prior to Second Bond Cleavage

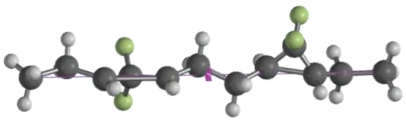

14.604 Å

(v) Immediately After Second Bond Cleavage

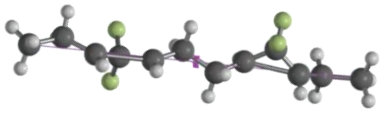

14.654 Å

(vi) Immediately Prior to Disproportionation

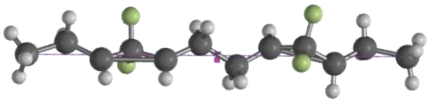

15.404 Å

(vii) Immediately After Disproportionation

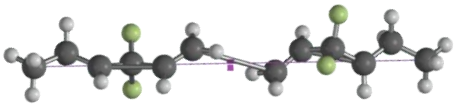

15.454 Å

Summary of CoGEF Results	
F_{max}	4.9 nN
E_{max}	771 kJ/mol
Force-Bond Angle	1.3°

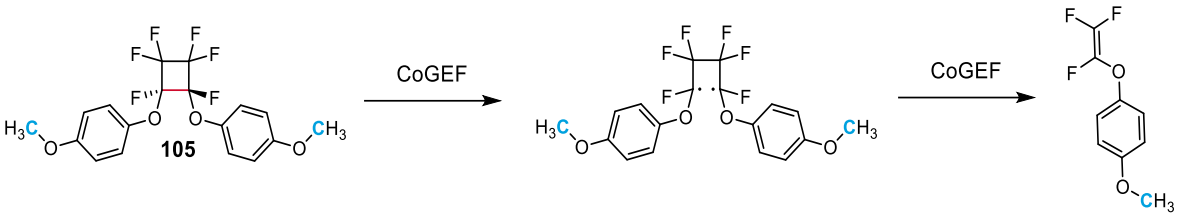

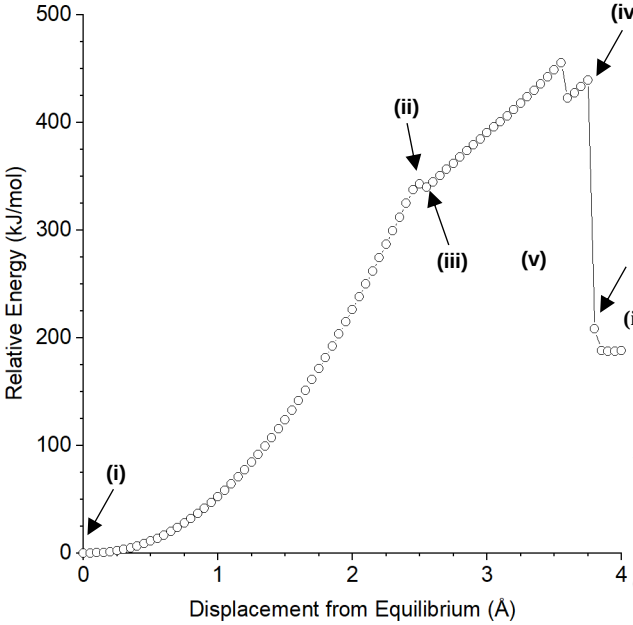

(i) Equilibrium Geometry

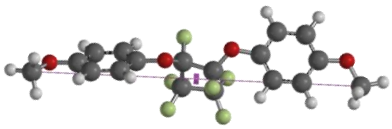

15.764 Å

(ii) Immediately Prior to First Bond Cleavage

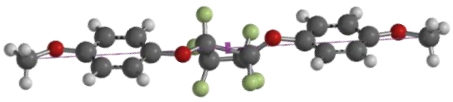

18.214 Å

(iii) Immediately After First Bond Cleavage

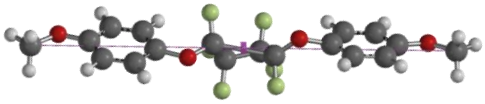

18.264 Å

(iv) Immediately Before Second Bond Cleavage

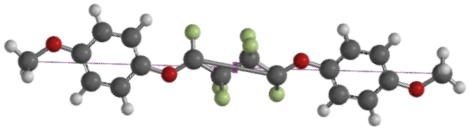

19.514 Å

(v) Immediately After Second Bond Cleavage

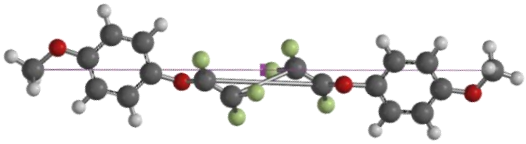

19.562 Å

Summary of CoGEF Results	
F_{max}	4.2 nN
E_{max}	455 kJ/mol
Force-Bond Angle	17°

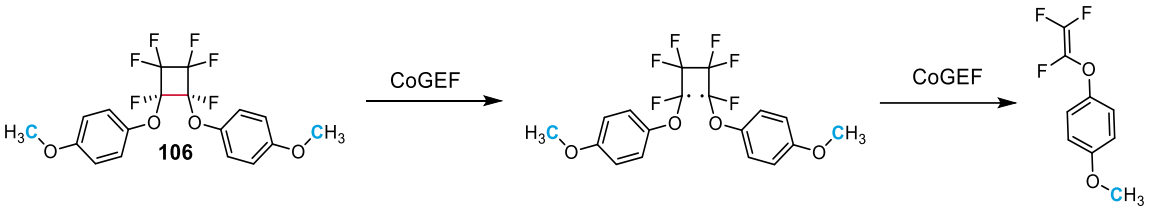

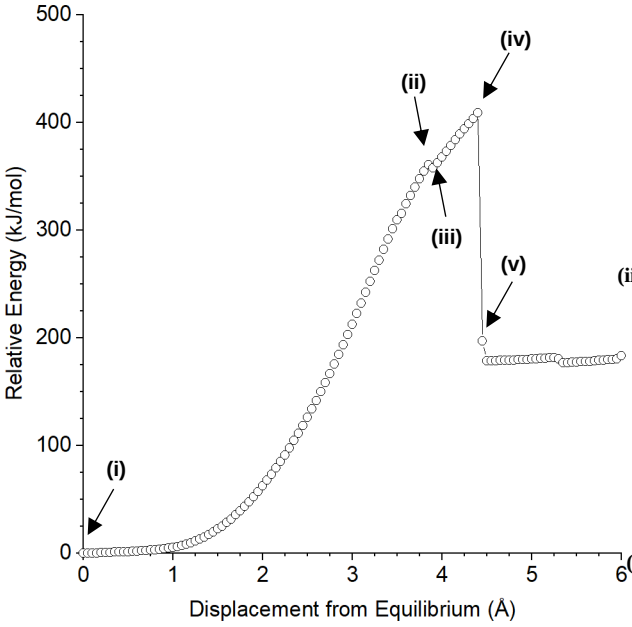

Summary of CoGEF Results	
F_{max}	3.4 nN
E_{max}	409 kJ/mol
Force-Bond Angle	5.9°

(i) Equilibrium Geometry

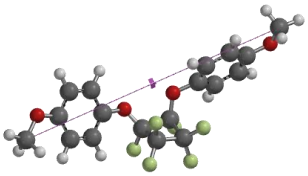

14.522 Å

(ii) Immediately Prior to First Bond Cleavage

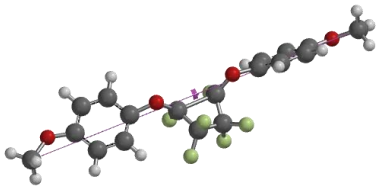

17.772 Å

(iii) Immediately After First Bond Cleavage

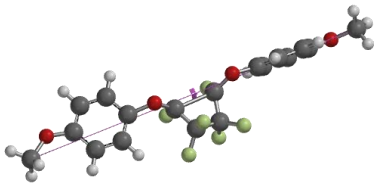

17.822 Å

(iv) Immediately Before Second Bond Cleavage

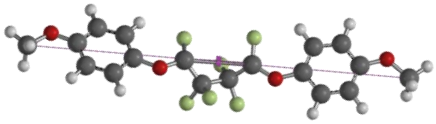

18.922 Å

(v) Immediately After Second Bond Cleavage

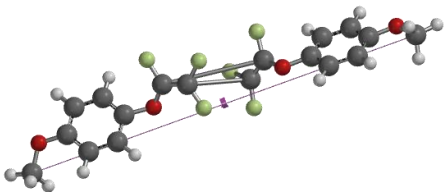

18.972 Å

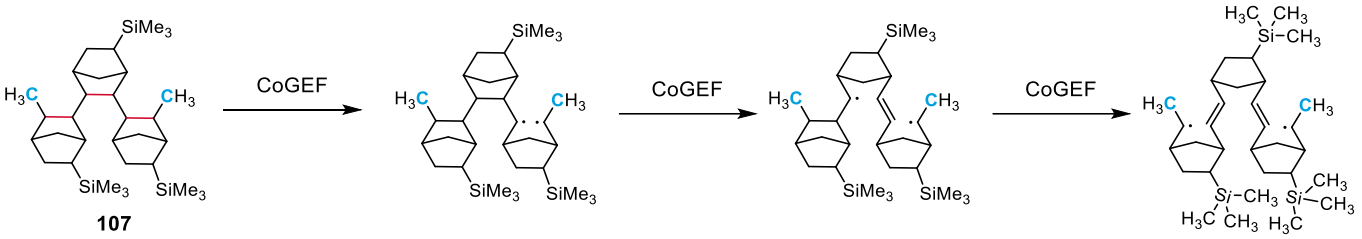

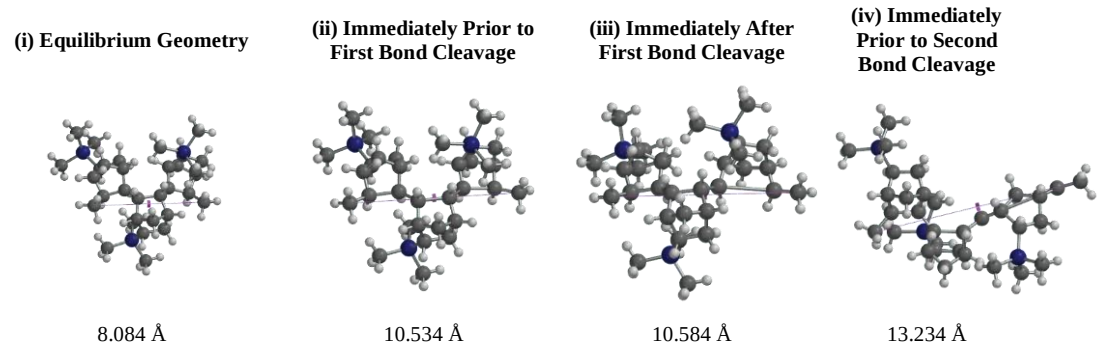

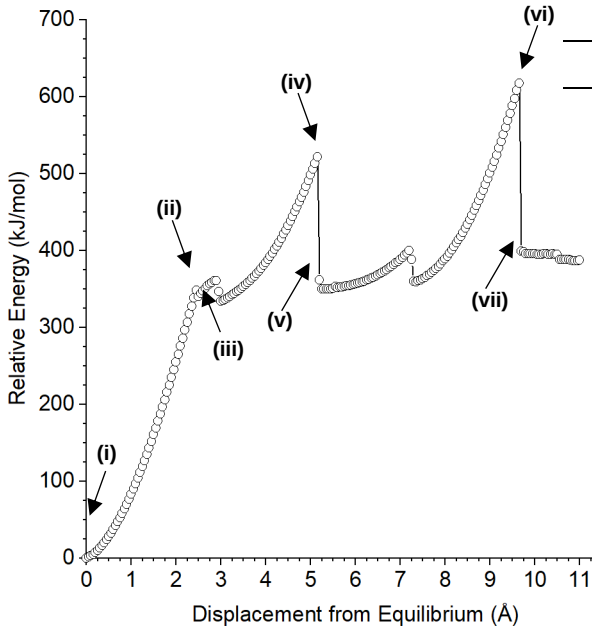

Summary of CoGEF Results

F_{max}	3.5 nN (first) 2.6 nN (second) 3.5 nN (third)
E_{max}	348 kJ/mol (first) 521 kJ/mol (second) 617 kJ/mol (third)
Force-Bond Angle	7.5° (first) 16° (second) 7.0° (third)

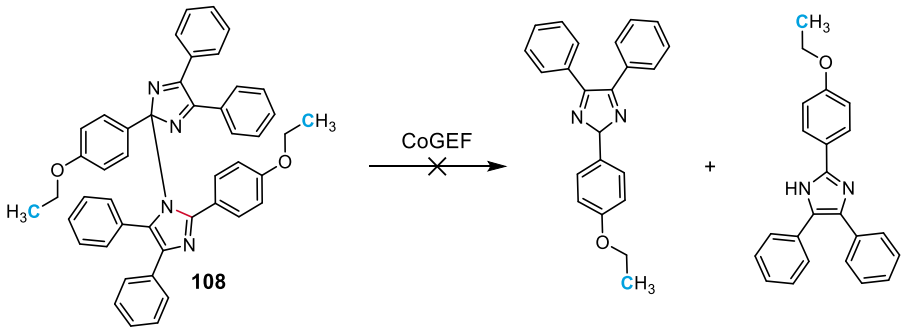

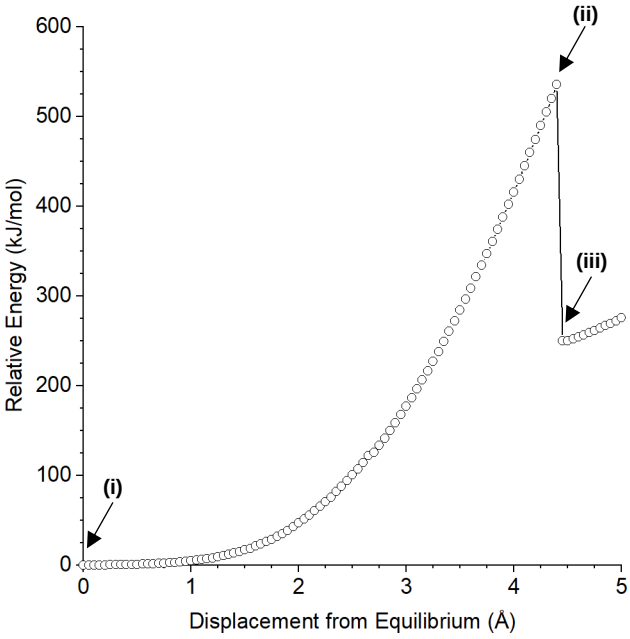

Summary of CoGEF Results	
F_{max}	5.1 nN
E_{max}	536 kJ/mol
Force-Bond Angle	43°

(i) Equilibrium Geometry

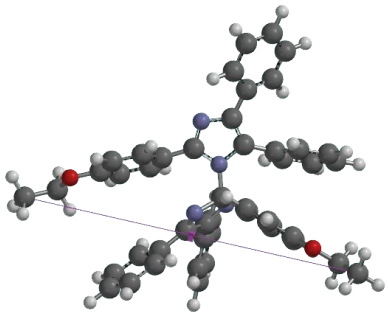

15.861 Å

(ii) Immediately Prior to Bond Cleavage

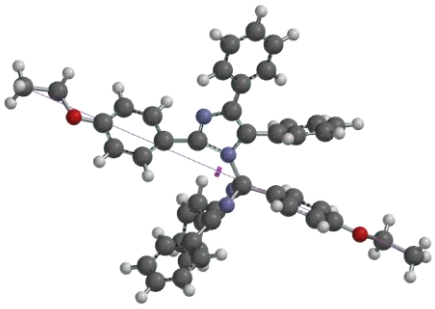

20.261 Å

(iii) Immediately After Bond Cleavage

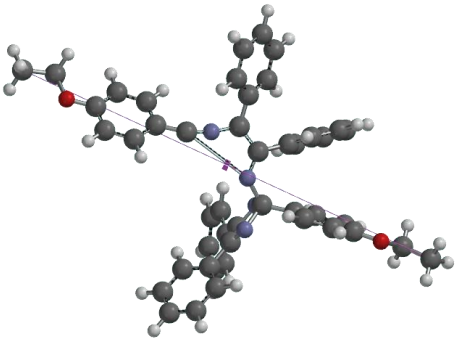

20.311 Å

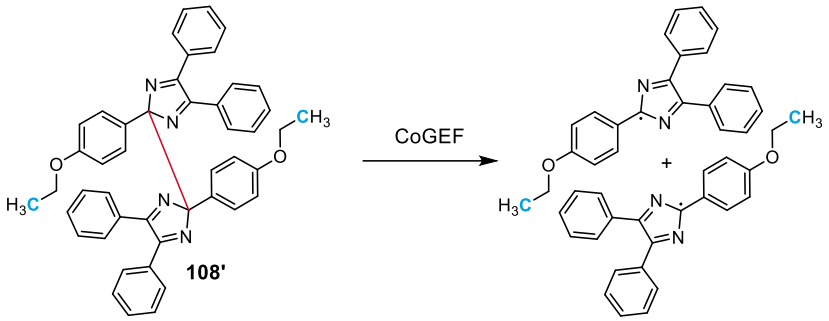

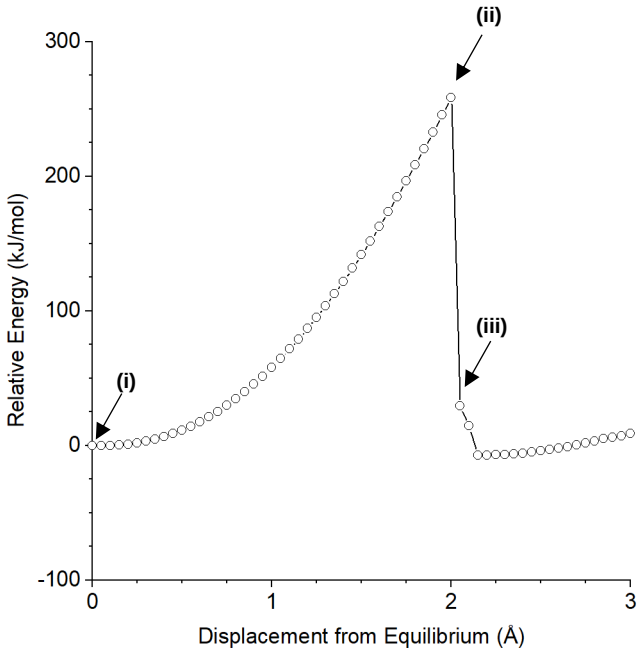

Summary of CoGEF Results	
F_{max}	4.3 nN
E_{max}	258 kJ/mol
Force-Bond Angle	40°

(i) Equilibrium Geometry

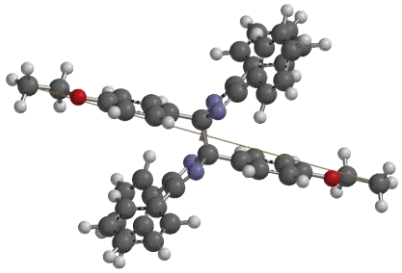

16.537 Å

(ii) Immediately Prior to Bond Cleavage

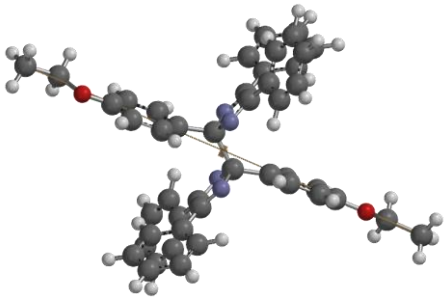

18.537 Å

(iii) Immediately After Bond Cleavage

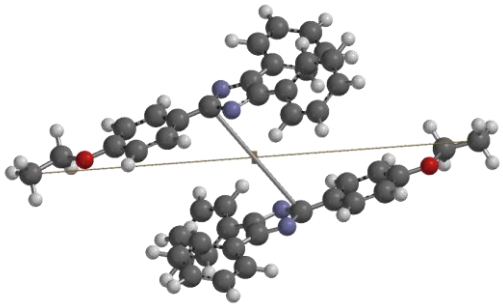

18.587 Å

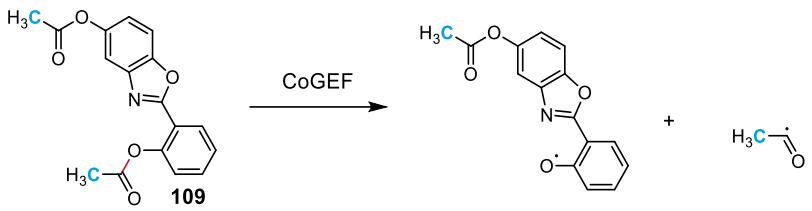

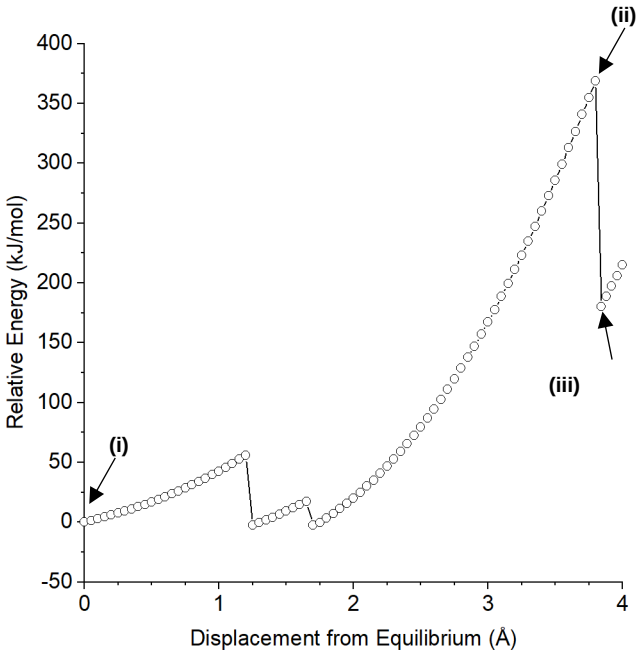

(i) Equilibrium Geometry

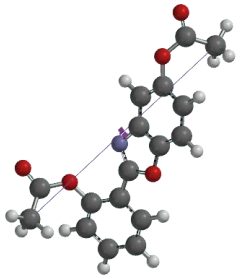

11.66 Å

(ii) Immediately Prior to Bond Cleavage

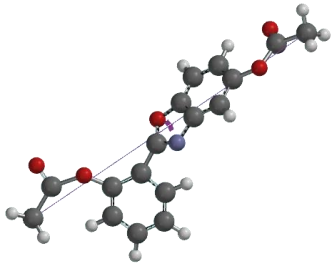

15.41 Å

(iii) Immediately After Bond Cleavage

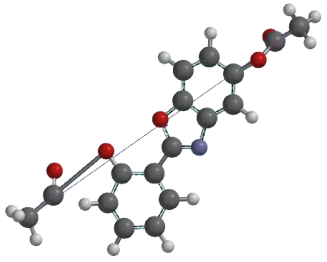

15.46 Å

Summary of CoGEF Results	
F_{max}	4.7 nN
E_{max}	369 kJ/mol
Force-Bond Angle	15°

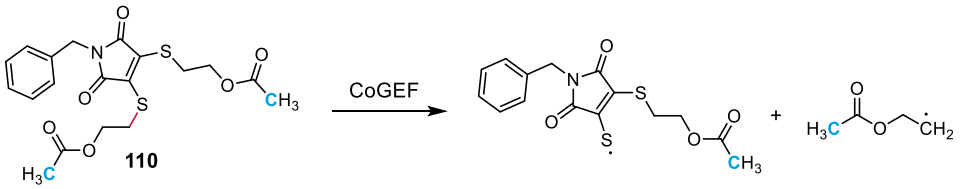

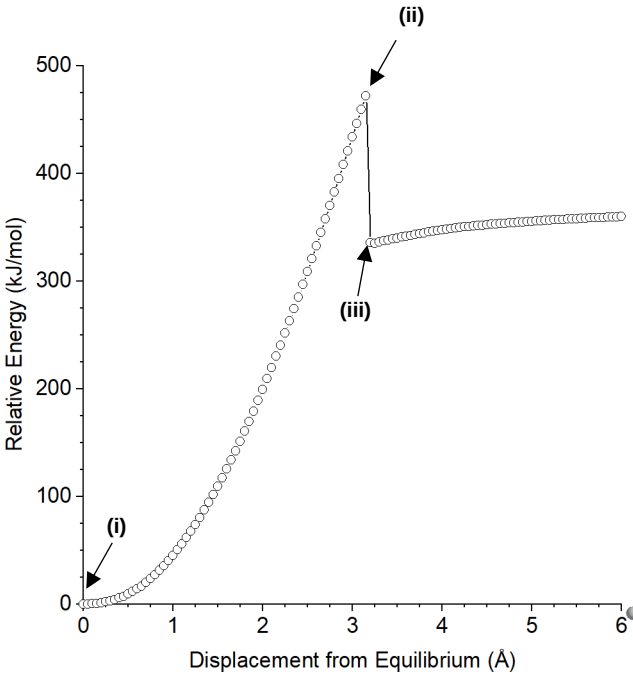

(i) Equilibrium Geometry

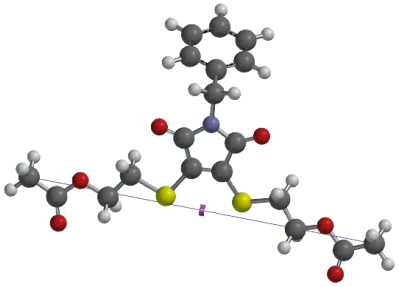

15.926 Å

(ii) Immediately Prior to Bond Cleavage

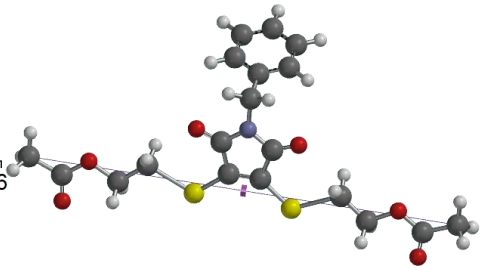

19.076 Å

(iii) Immediately After Bond Cleavage

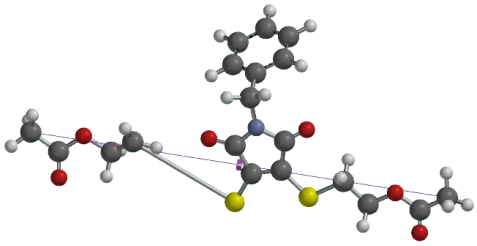

19.126 Å

Summary of CoGEF Results	
F_{max}	4.3 nN
E_{max}	472 kJ/mol
Force-Bond Angle	24°

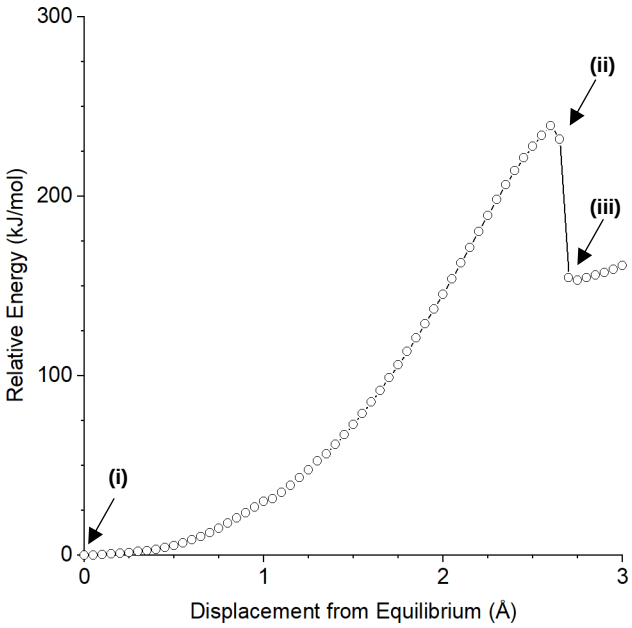

(i) Equilibrium Geometry

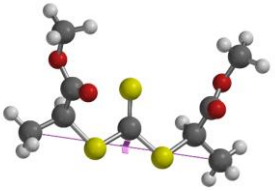

8.199 Å

(ii) Immediately Prior to Bond Cleavage

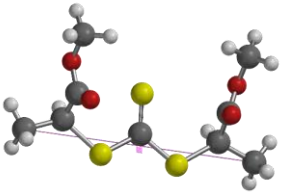

9.699 Å

(iii) Immediately After Bond Cleavage

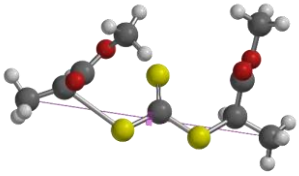

9.749 Å

Summary of CoGEF Results	
F_{max}	4.3 nN
E_{max}	227 kJ/mol
Force-Bond Angle	35°

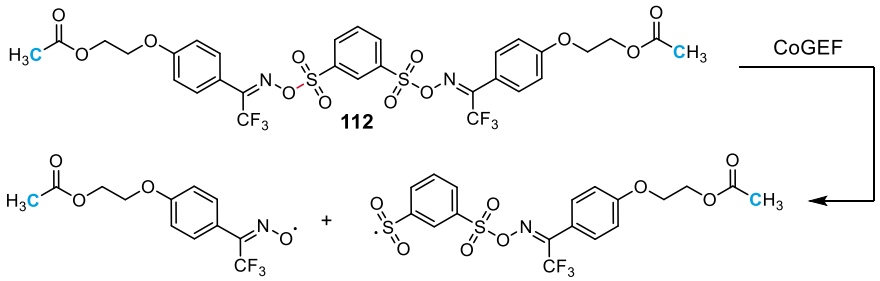

(i) Equilibrium Geometry

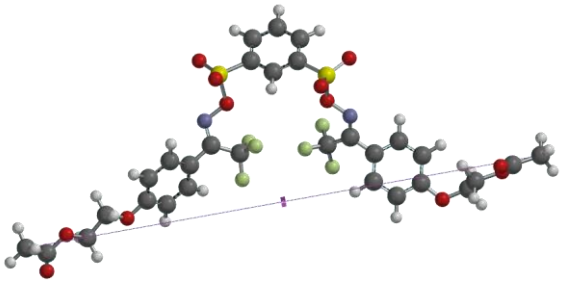

26.482 Å

(ii) Immediately Prior to Bond Cleavage

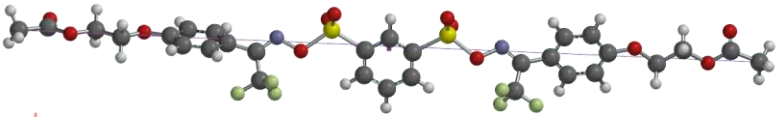

38.432 Å

(iii) Immediately After Bond Cleavage

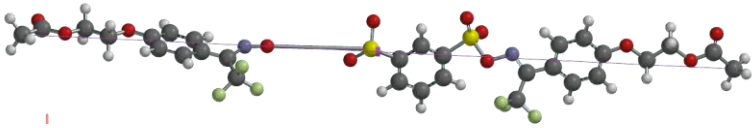

38.482 Å

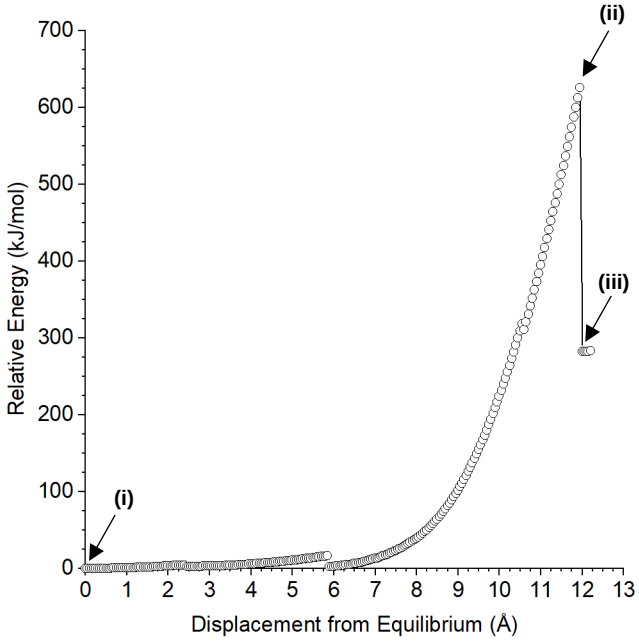

Summary of CoGEF Results	
F_{max}	4.3 nN
E_{max}	625 kJ/mol
Force-Bond Angle	28°

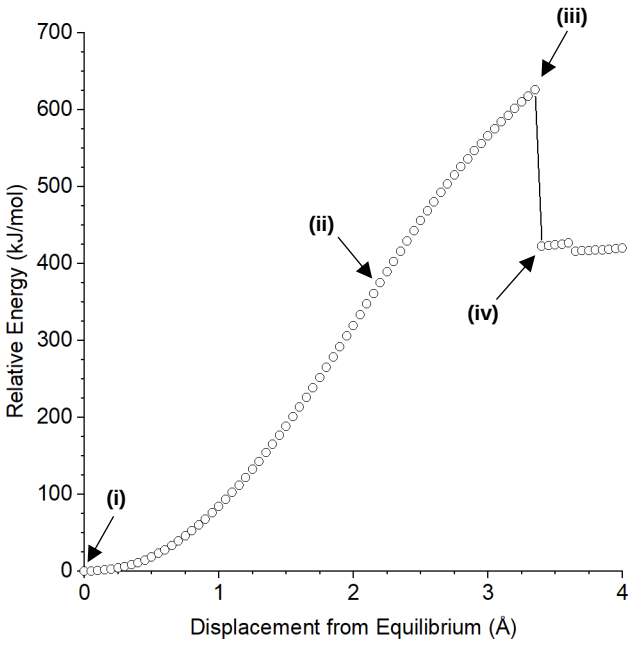

(i) Equilibrium Geometry

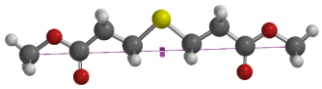

12.527 Å

(ii) At F_{max}

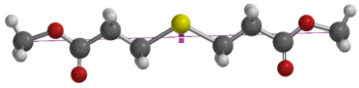

14.677 Å

(iii) Immediately Prior to Bond Cleavage

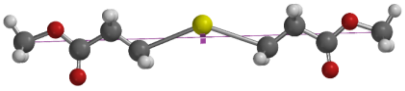

15.877 Å

(iv) Immediately After Bond Cleavage

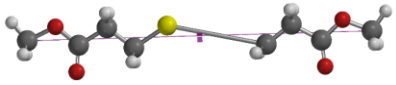

15.927 Å

Summary of CoGEF Results	
F_{max}	4.6 nN
E_{max}	626 kJ/mol
Force-Bond Angle	20°

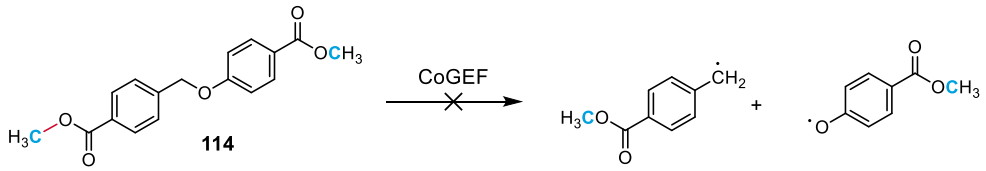

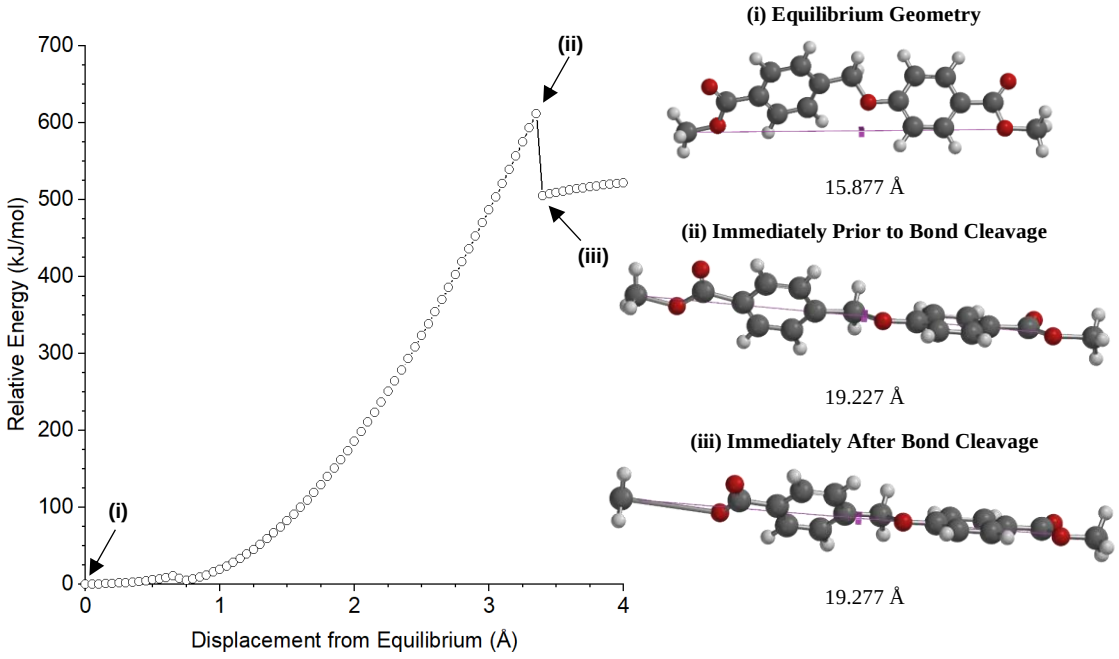

Summary of CoGEF Results	
F_{max}	6.1 nN
E_{max}	611 kJ/mol
Force-Bond Angle	37°

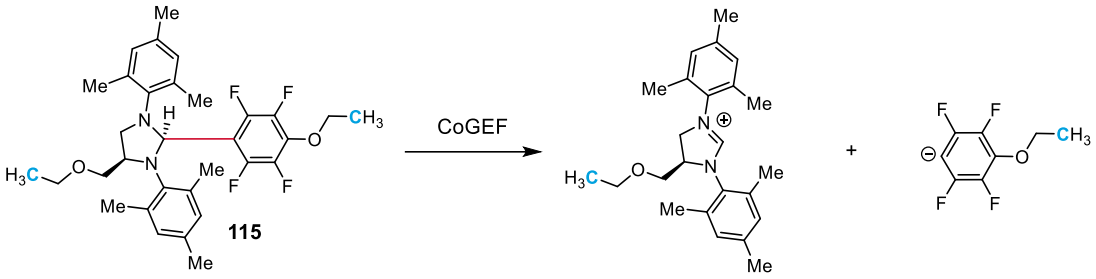

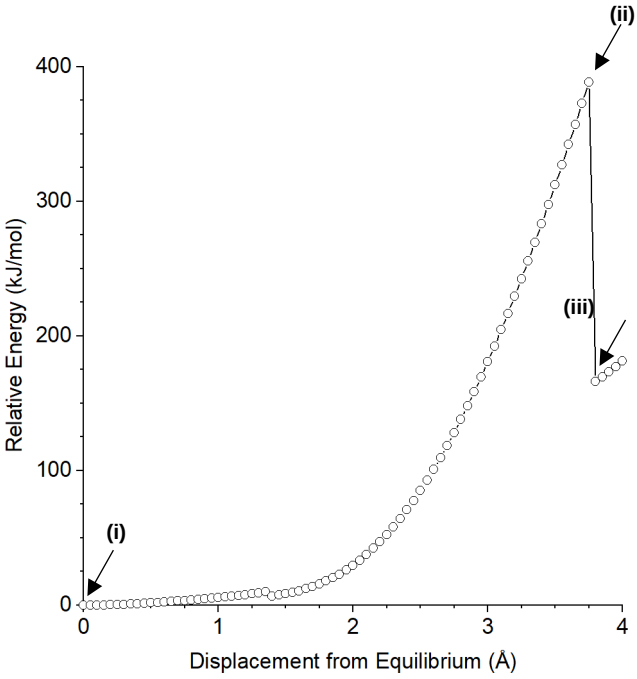

(i) Equilibrium Geometry

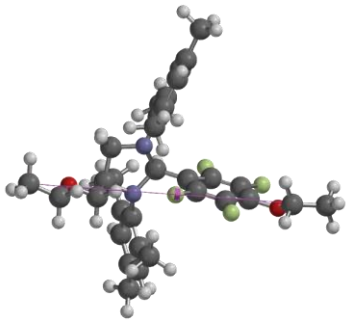

13.275 Å

(ii) Immediately Prior to Bond Cleavage

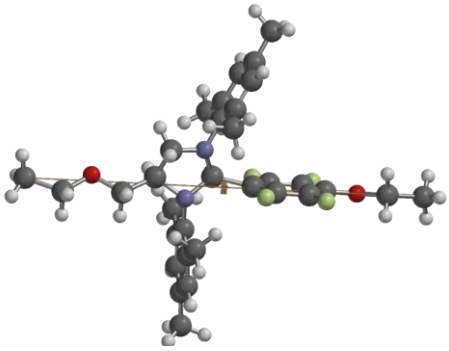

17.025 Å

Summary of CoGEF Results	
F_{max}	5.2 nN
E_{max}	388 kJ/mol
Force-Bond Angle	13°

(iii) Immediately After Bond Cleavage

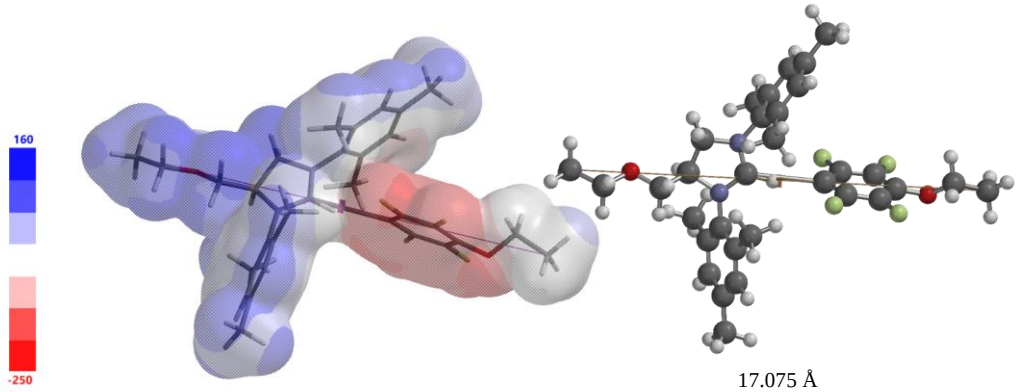

17.075 Å

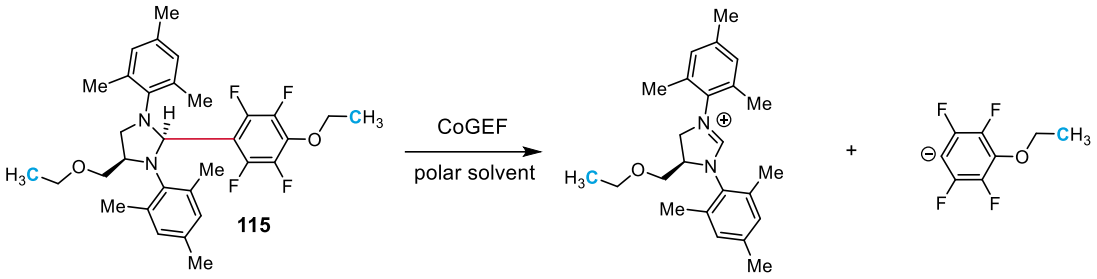

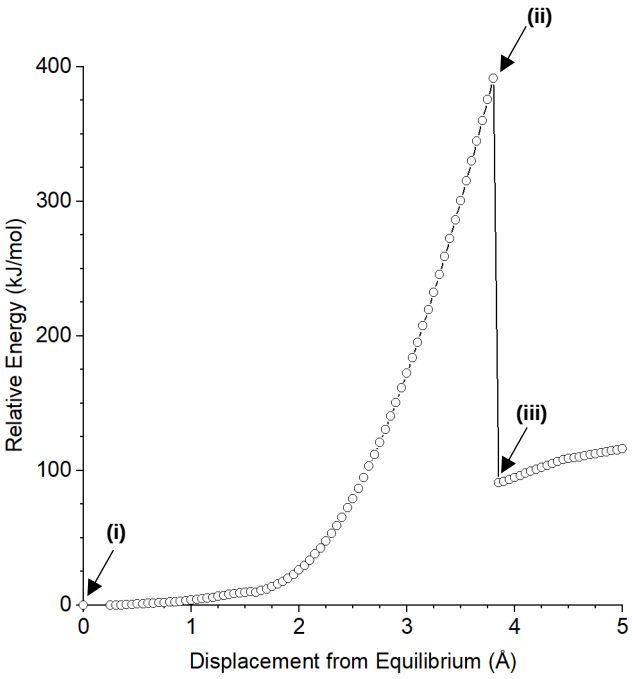

(i) Equilibrium Geometry

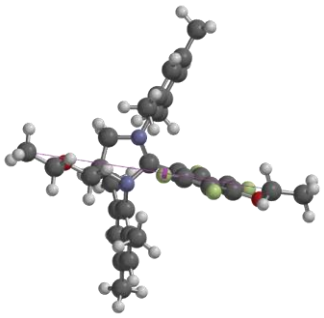

13.275 Å

(ii) Immediately Prior to Bond Cleavage

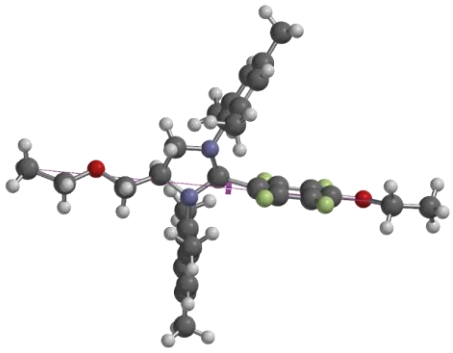

17.075 Å

(iii) Immediately After Bond Cleavage

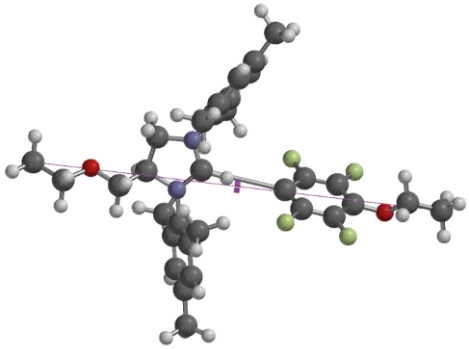

17.125 Å

Summary of CoGEF Results	
F_{max}	5.2 nN
E_{max}	391 kJ/mol
Force-Bond Angle	13°

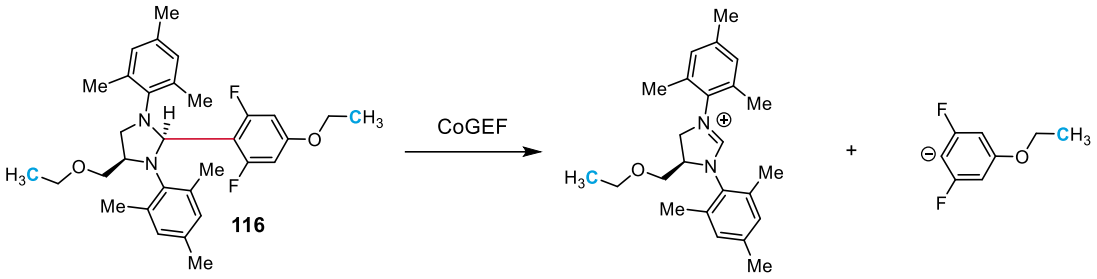

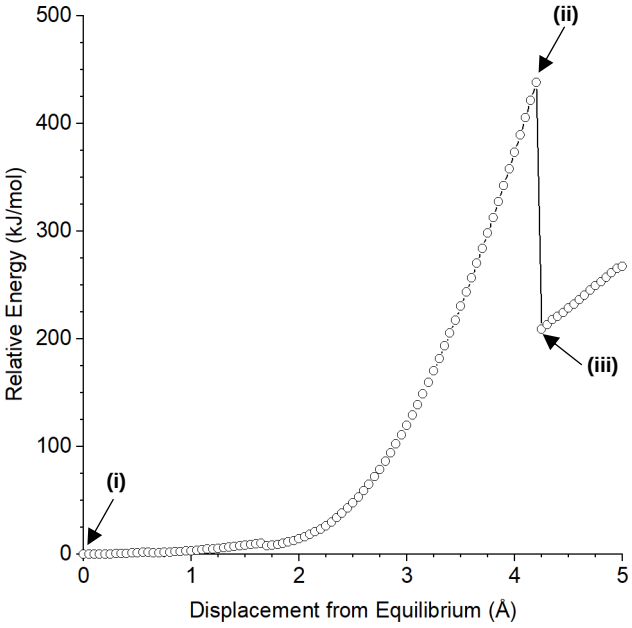

(i) Equilibrium Geometry

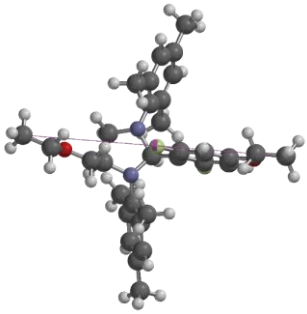

12.940 Å

(ii) Immediately Prior to Bond Cleavage

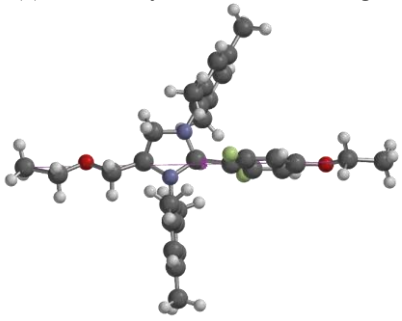

17.140 Å

Summary of CoGEF Results	
F_{max}	5.5 nN
E_{max}	438 kJ/mol
Force-Bond Angle	13°

(iii) Immediately After Bond Cleavage

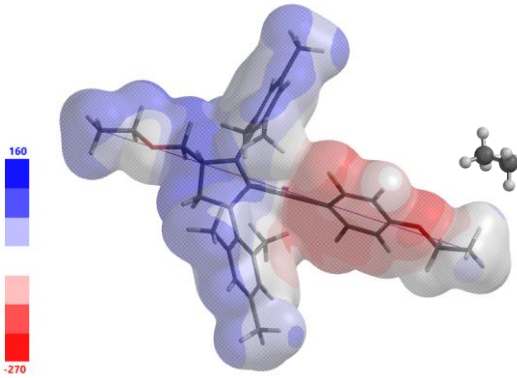

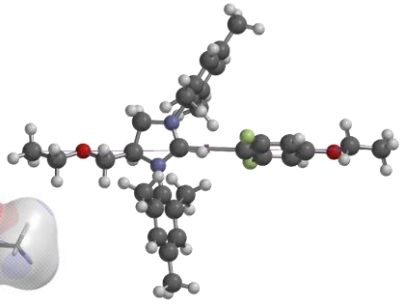

17.190 Å

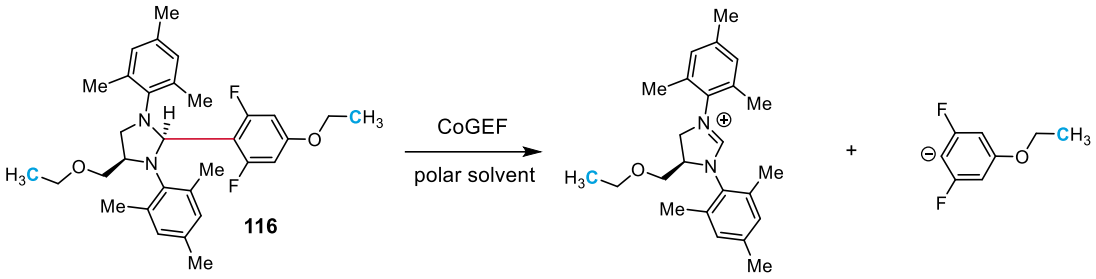

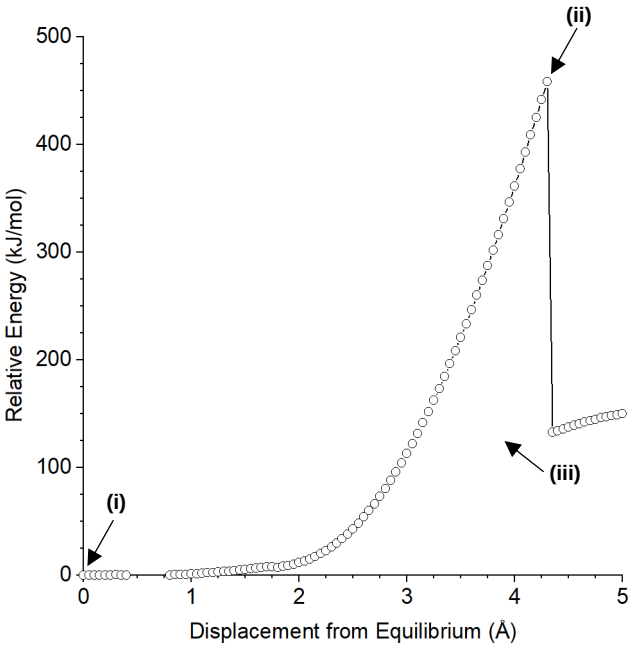

(i) Equilibrium Geometry

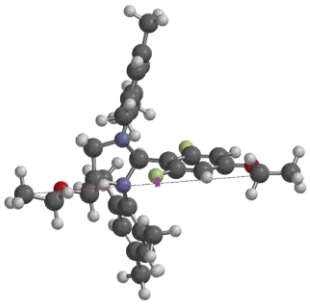

12.940 Å

(ii) Immediately Prior to Bond Cleavage

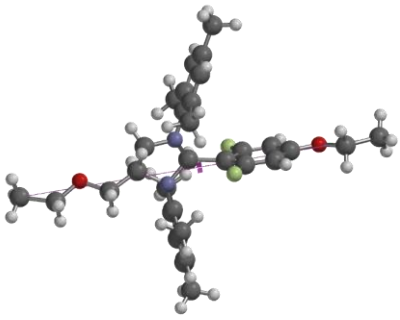

17.240 Å

(iii) Immediately After Bond Cleavage

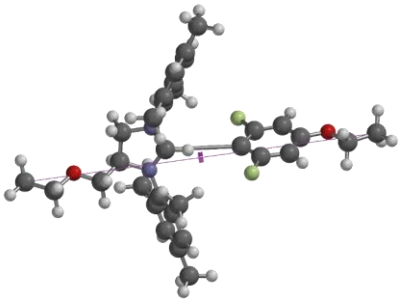

17.290 Å

Summary of CoGEF Results	
F_{max}	5.5 nN
E_{max}	458 kJ/mol
Force-Bond Angle	12°

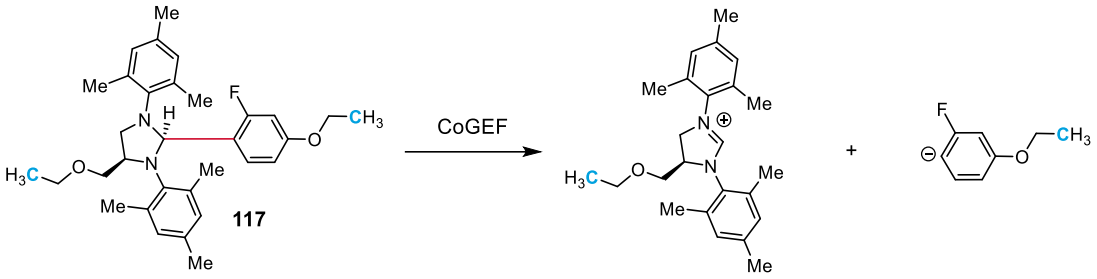

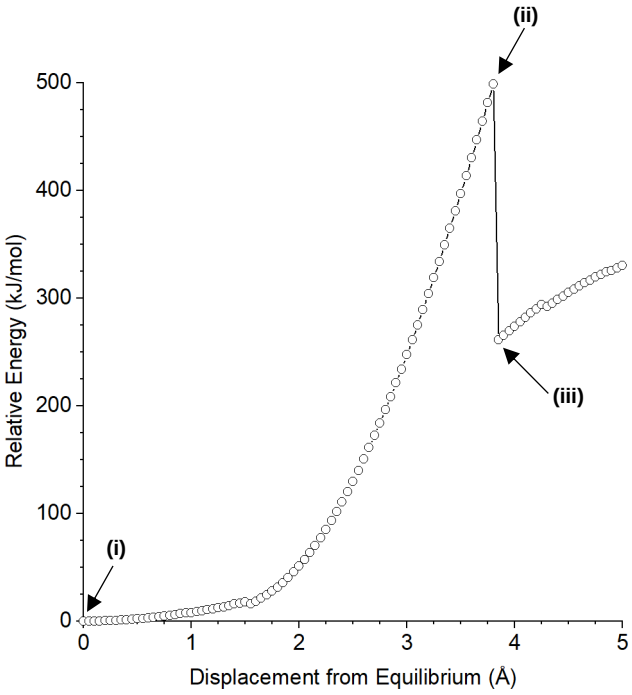

Summary of CoGEF Results	
F_{max}	5.8 nN
E_{max}	499 kJ/mol
Force-Bond Angle	14°

(i) Equilibrium Geometry

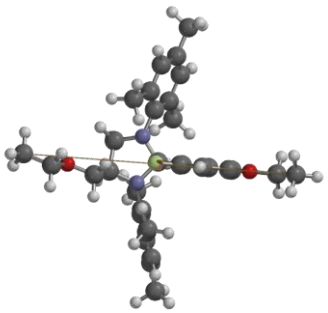

13.522 Å

(ii) Immediately Prior to Bond Cleavage

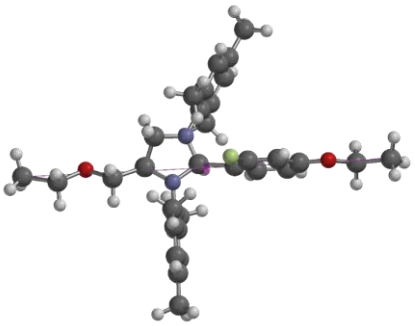

17.322 Å

(iii) Immediately After Bond Cleavage

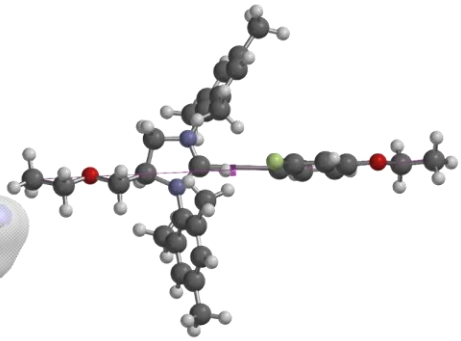

17.372 Å

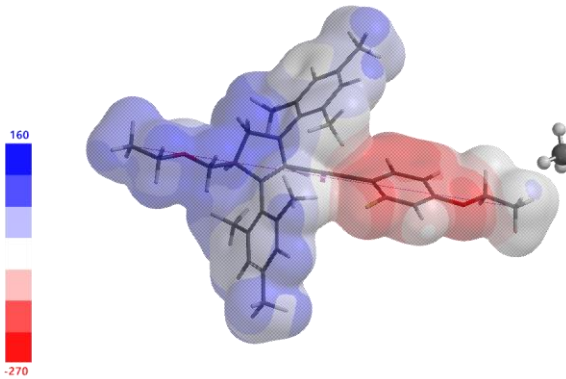

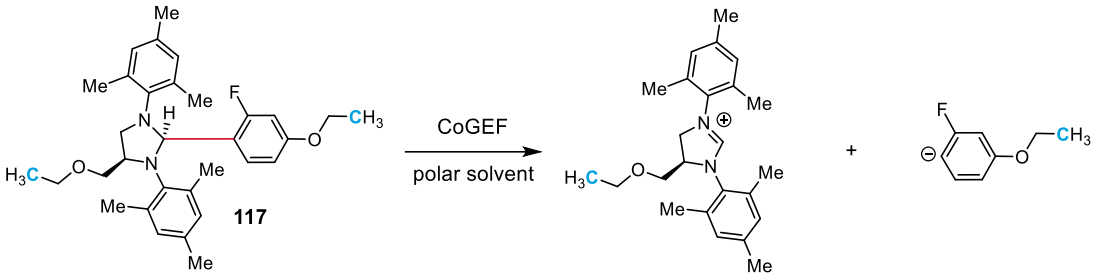

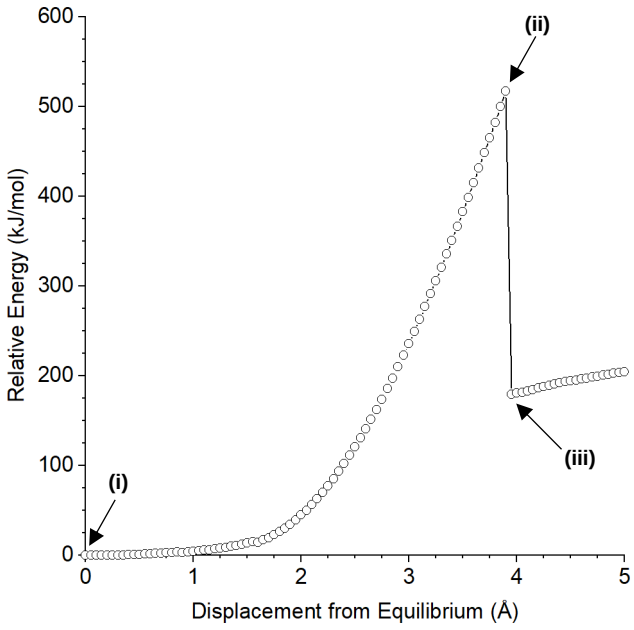

Summary of CoGEF Results	
F_{max}	5.8 nN
E_{max}	517 kJ/mol
Force-Bond Angle	14°

(i) Equilibrium Geometry

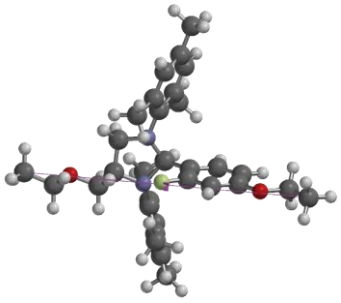

13.522 Å

(ii) Immediately Prior to Bond Cleavage

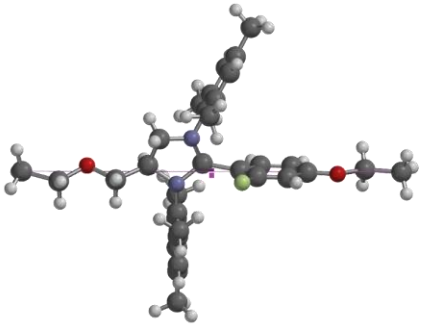

17.422 Å

(iii) Immediately After Bond Cleavage

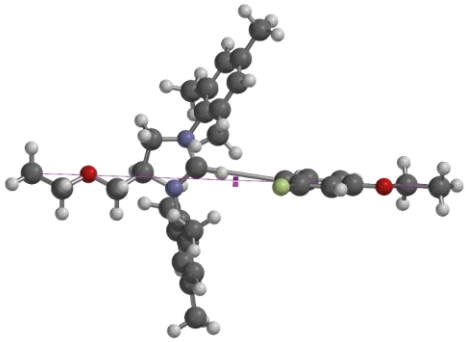

17.472 Å

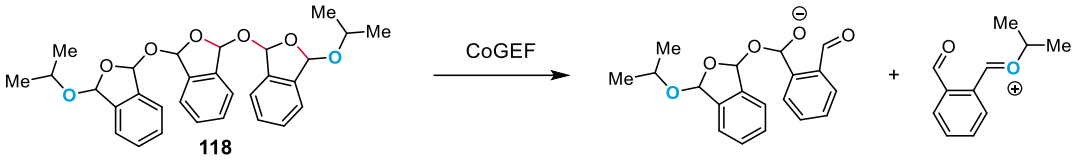

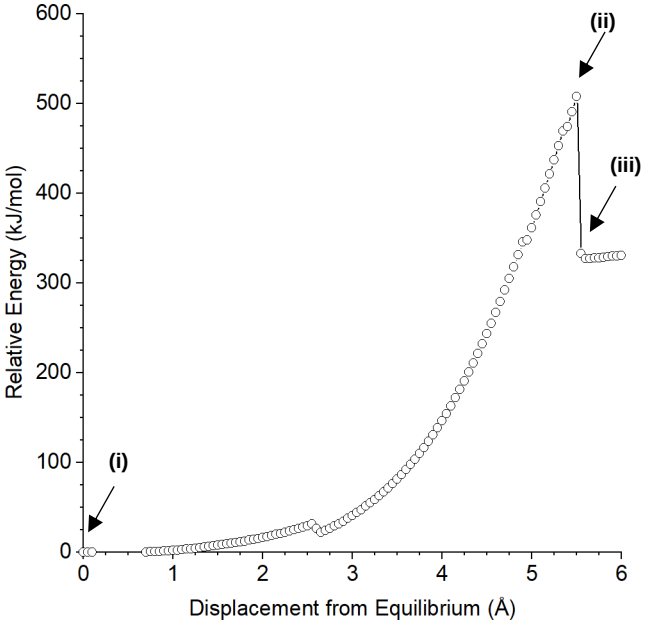

(i) Equilibrium Geometry

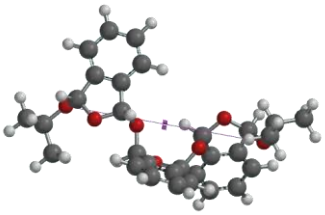

10.099 Å

(ii) Immediately Prior to Bond Cleavage

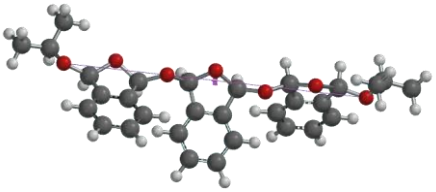

15.599 Å

(iii) Immediately After Bond Cleavage

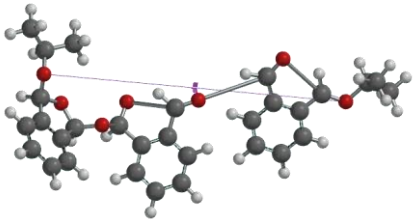

15.649 Å

Summary of CoGEF Results	
F_{max}	5.6 nN
E_{max}	507 kJ/mol
Force-Bond Angle	32°

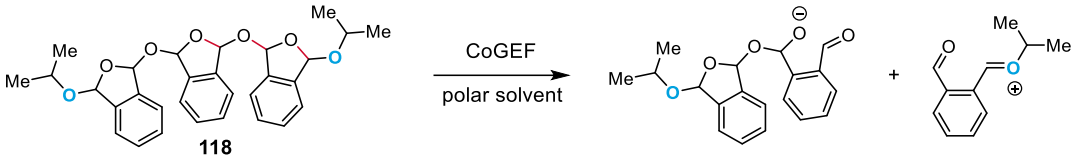

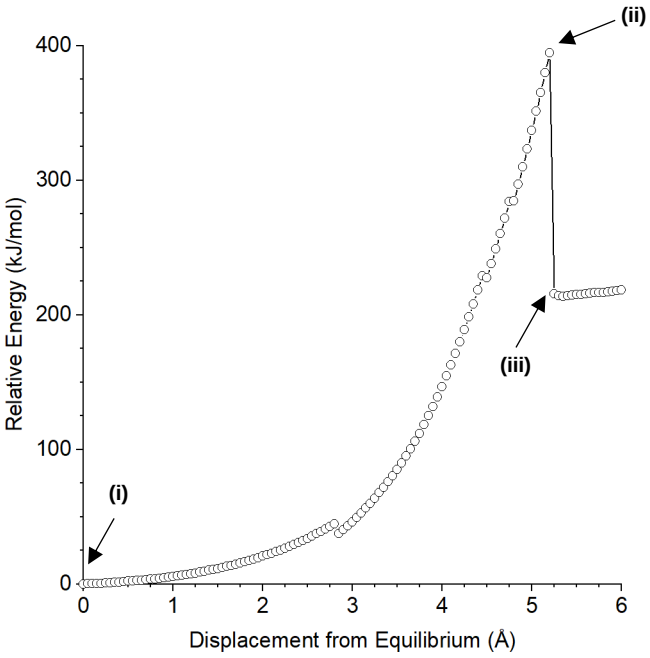

(i) Equilibrium Geometry

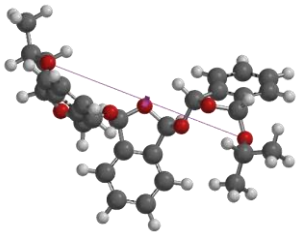

10.099 Å

(ii) Immediately Prior to Bond Cleavage

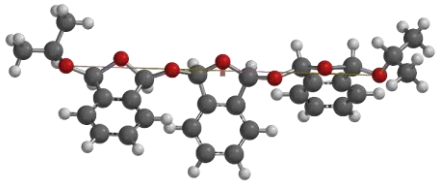

15.299 Å

(iii) Immediately After Bond Cleavage

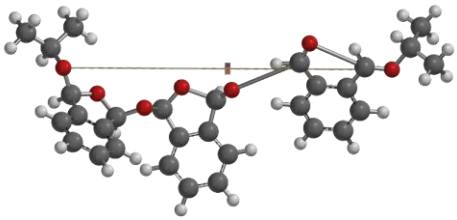

15.349 Å

Summary of CoGEF Results	
F_{max}	4.9 nN
E_{max}	395 kJ/mol
Force-Bond Angle	33°

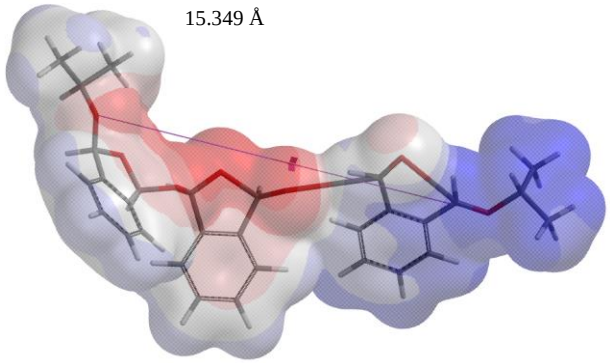

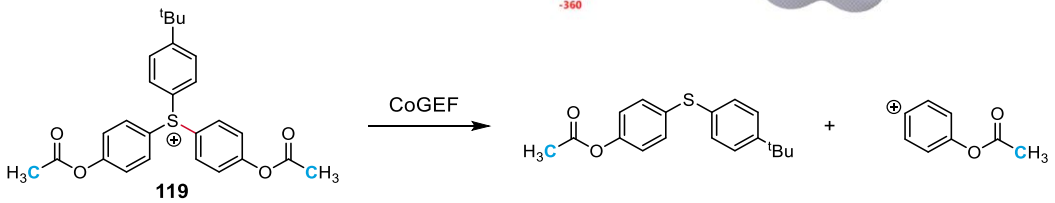

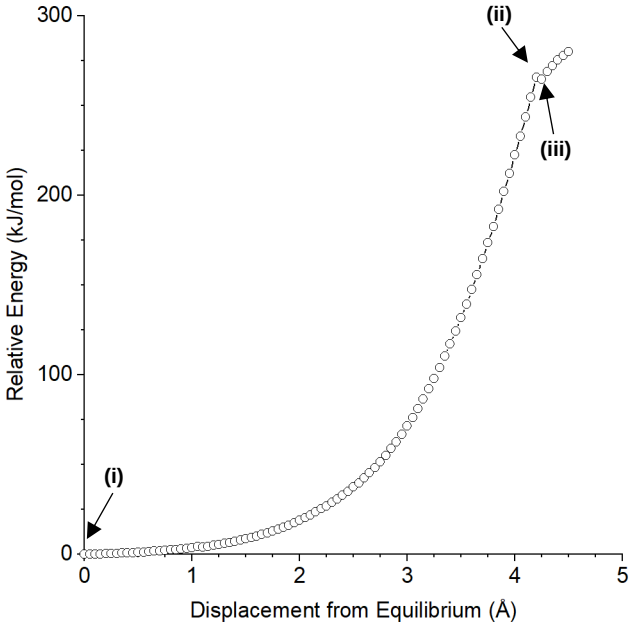

(i) Equilibrium Geometry

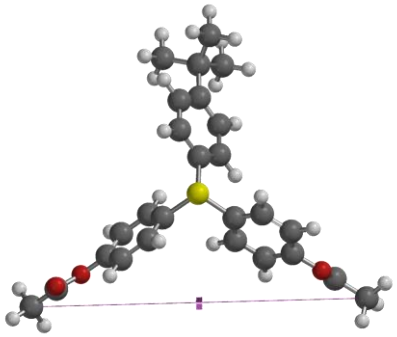

13.405 Å

(ii) Immediately Prior to Bond Cleavage

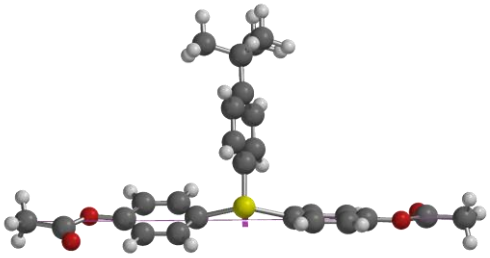

17.605 Å

(iii) Immediately After Bond Cleavage

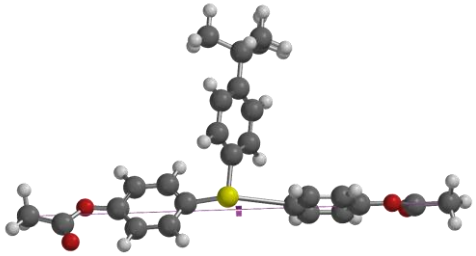

17.655 Å

Summary of CoGEF Results	
F_{max}	3.7 nN
E_{max}	266 kJ/mol
Force-Bond Angle	17°

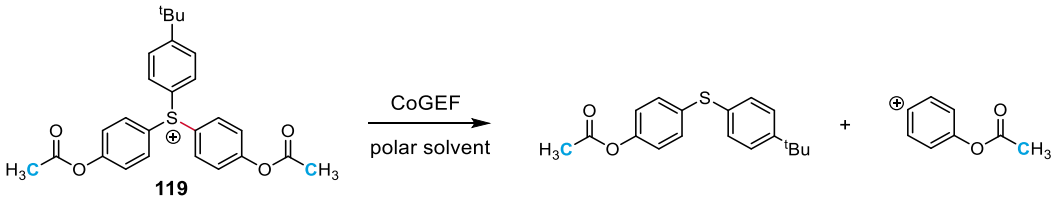

(ii) **(i) Equilibrium Geometry**

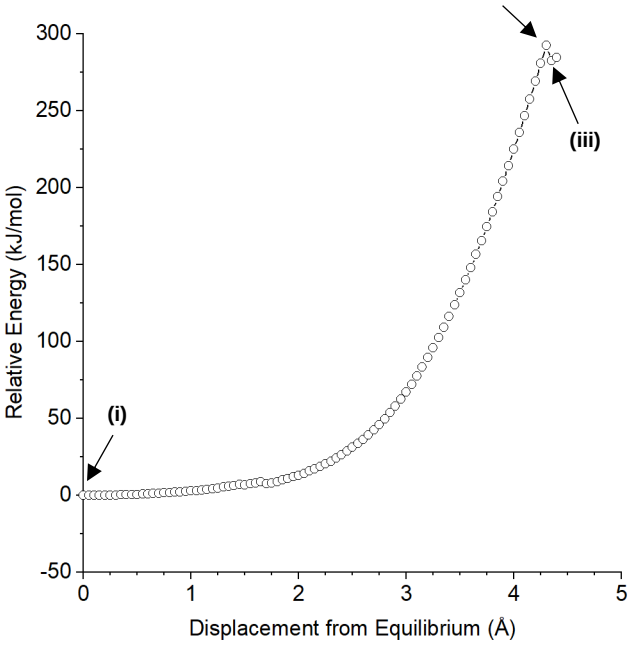

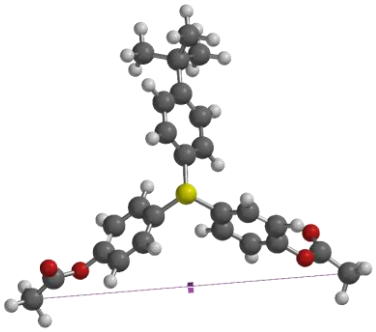

13.405 Å

(ii) Immediately Prior to Bond Cleavage

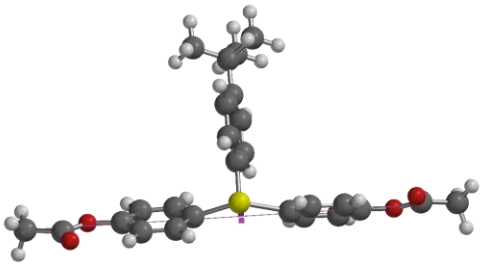

17.705 Å

(iii) Immediately After Bond Cleavage

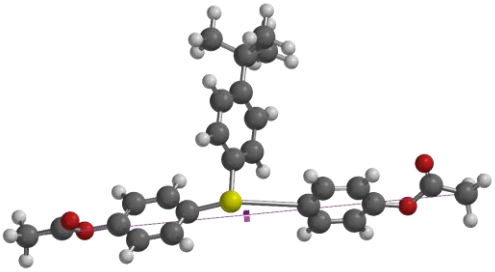

17.755 Å

Summary of CoGEF Results	
F_{max}	3.9 nN
E_{max}	292 kJ/mol
Force-Bond Angle	18°

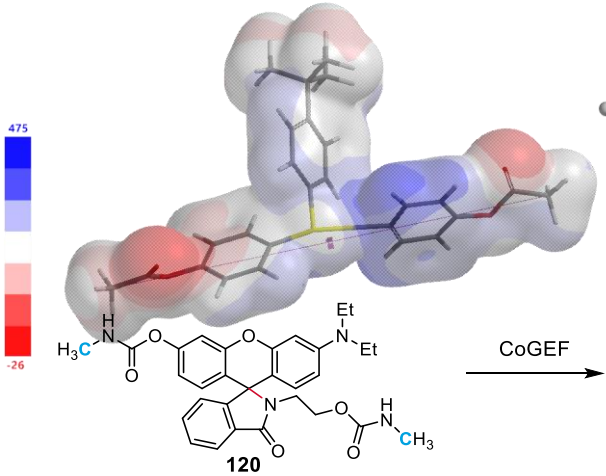

CoGEF

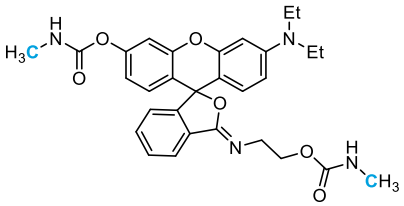

(ii) **(i) Equilibrium Geometry**

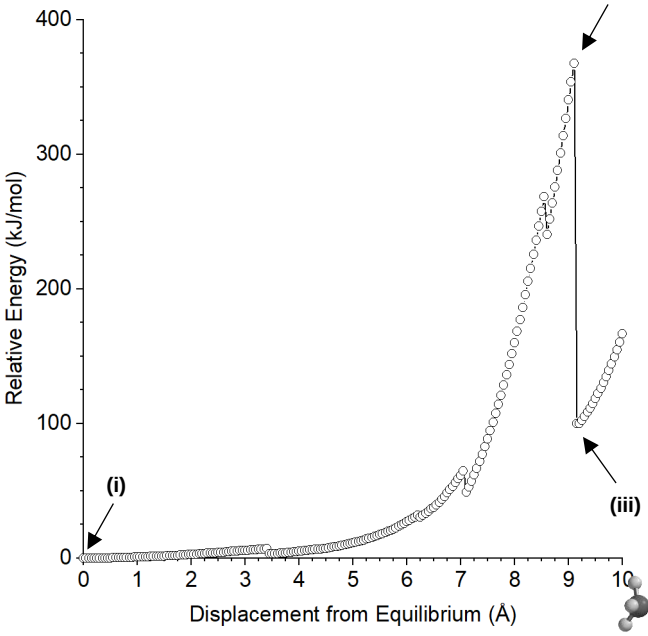

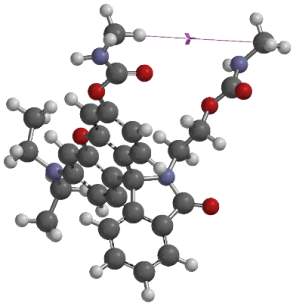

9.989 Å

(ii) Immediately Prior to Bond Cleavage

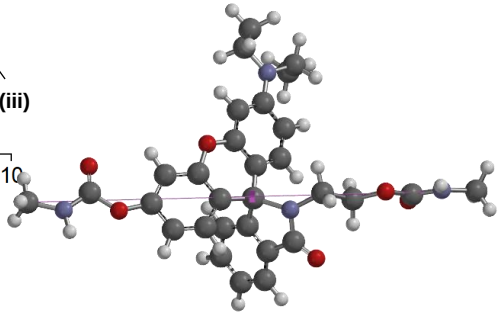

19.089 Å

Summary of CoGEF Results	
F_{max}	4.6 nN
E_{max}	368 kJ/mol
Force-Bond Angle	32°

(iii) Immediately After Bond Cleavage

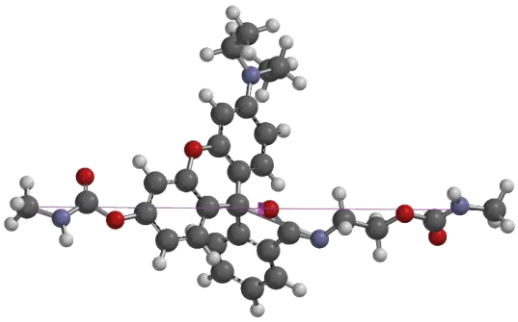

19.139 Å

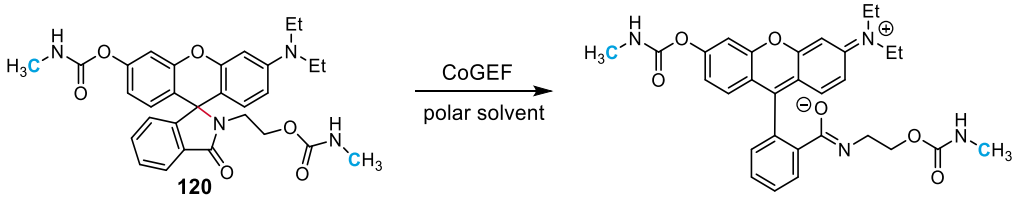

120

(ii)

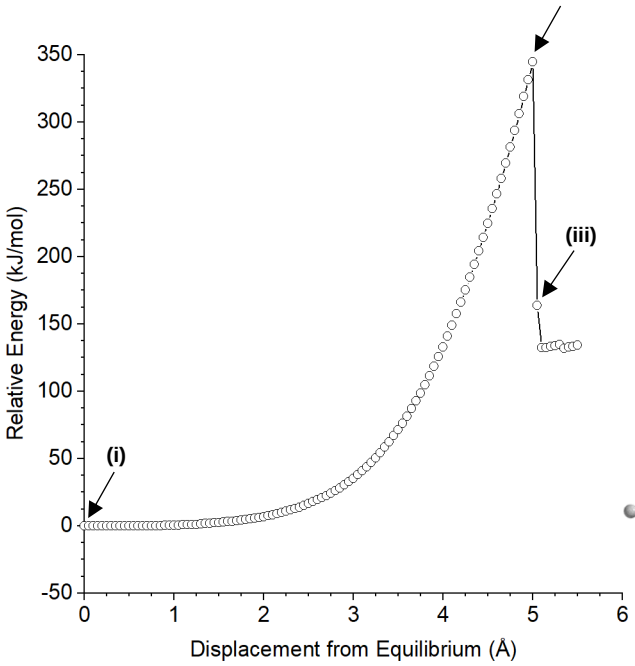

(i) Equilibrium Geometry

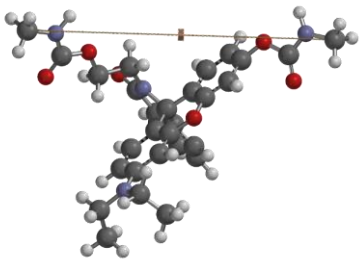

14.019 Å

(ii) Immediately Prior to Bond Cleavage

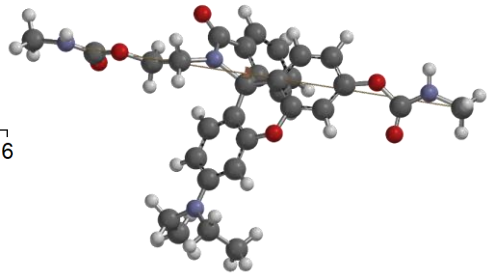

19.019 Å

Summary of CoGEF Results	
F_{max}	4.3 nN
E_{max}	345 kJ/mol
Force-Bond Angle	32°

(iii) Immediately After Bond Cleavage

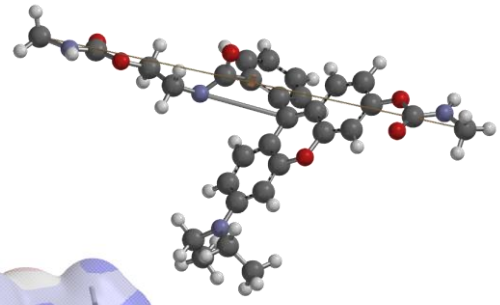

19.069 Å